An interdisciplinary approach to understanding the TTP pathway

by

Victoria Veronika Rink

A thesis submitted to the University of Birmingham for the degree of

DOCTOR OF PHILOSOPHY

School of Mathematics, College of Engineering and Physical Sciences
Institute of Inflammation and Ageing, College of Medical and Dental Sciences
The University of Birmingham
August 2024

UNIVERSITY OF
BIRMINGHAM

University of Birmingham Research Archive

e-theses repository

This unpublished thesis/dissertation is copyright of the author and/or third parties. The intellectual property rights of the author or third parties in respect of this work are as defined by The Copyright Designs and Patents Act 1988 or as modified by any successor legislation.

Any use made of information contained in this thesis/dissertation must be in accordance with that legislation and must be properly acknowledged. Further distribution or reproduction in any format is prohibited without the permission of the copyright holder.

Abstract

Dysregulated expression of inflammatory mediators as a product of complex immune and non-immune cell interactions is a hallmark of chronic inflammatory diseases. Understanding and identifying drivers of dysregulated gene expression in the context of the inflammatory response enables researchers to understand pathogenic mechanisms better and to develop novel therapies. Much of this work previously focused on epigenetic and transcriptional regulators. However, changes in the transcriptome are not solely caused by changes in transcription. Post-transcriptional regulation of the stability and translation initiation of pro-inflammatory and immuno-modulatory mRNAs is a critical factor in determining their expression. The stability of mRNAs is controlled primarily by a set of RNA-binding proteins that recognise cis-regulatory elements in the 3' untranslated regions. A prominent member of these proteins, TTP, vividly demonstrated, in several animal models, its role in the production of inflammatory mediators. TTP acts downstream of the p38 MAPK pathway as a regulatory switch between the on- and off-phase of the inflammatory response. Its regulation, however, is highly complex, and the dynamic interplay between the components involved is not yet fully understood.

This thesis aims to improve understanding of the dynamic regulation of the p38 MAPK-TTP signalling axis through mathematical modelling. A model based on ordinary differential equations and mass action kinetics was developed, describing TTP regulation by integrating the known properties of the components and interactions involved. To explore different properties of the model, two previously described p38 MAPK pathway models were adapted for integration with the newly built TTP model.

One of the resulting p38 MAPK-TTP models focuses on describing the pathway dynamics quantitatively, using data from bone marrow-derived macrophages and the murine macrophage

cell line RAW274.7. The calibrated model was then challenged by computationally simulating pathway mutants and comparing the results with data obtained from such mutant mice. The results underscore the need for further refinements and extensions to our model. They specifically highlighted the importance of considering the role of TTP in inhibiting mRNA translation, which is often overlooked compared to its mRNA degrading properties. The results further emphasised that the phosphatase DUSP1, while important, is insufficient to describe p38 MAPK regulation within our model accurately. Additionally, the results of inhibitor experiments underscore the need for caution in interpreting previous results and designing future experiments regarding the TTP phosphatase PP2A, as it affects TTP regulation on multiple levels.

The second model qualitatively explores potential oscillatory p38 MAPK activation patterns and their impact on TTP. A set of genetic engineering tools was developed for application in live-cell microscopy to investigate the dynamics of TTP activation experimentally. Captured live-cell microscopy data suggested that the stress induced by the imaging conditions affects TTP subcellular localisation. Consequently, the microscopy conditions need to be optimised before going forward. A fixed microscopy time-course experiment utilising activated cells expressing distinct TTP mutants, which resulted in different TTP activity, showed no differences in subcellular localisation over time in contrast to the literature, which suggests localisation to P-bodies or the nucleus.

With this interdisciplinary work, we have designed mathematical and experimental toolkits to improve our knowledge of the p38 MAPK-TTP signalling axis, which is relevant to various inflammatory diseases.

‘‘*Her kind plays many roles in the body, from nursery school teachers to professional killers. Therefore, she bears many faces and personalities depending on which role she is playing. By default, Macrophage is a humble, easy-going cell manifesting as a mother figure who speaks in a polite manner. However, she can brutally kill intruders without showing empathy or mercy.*’’

Cells at work - Wiki

Acknowledgements

I want to use this opportunity to express gratitude to the people who made it possible for me to write this thesis.

My supervisors, Sara Jabbari and Andy Clark deserve a big thank you for their scientific guidance. A big shout to Sara here, who was also a significant mental and emotional supporter, who helped me more or less unscathed through the more challenging patches of this PhD and for being THE perfect supervisor imaginable. Also, a big thank you to Andy for being a great mentor and role model scientist who inspires with his integrity, dedication, and passion for science. John O'Neil supported me day-to-day in the laboratory. He helped me out practically when the amount of mice legs seemed overwhelming and even performed some essential work on ELISAs after I left the laboratory for writing. Also, a big Thank you to Laura Bravo, who initiated the project. Sally Clayton and Kalbinder Daley took over a big chunk of the organizational work, which keeps the laboratory running. They thus helped me a lot in my day-to-day struggles. Thanks to all of you for being amazing!

The Clark Group, especially Chloe and Oliwia, made coming into the laboratory a daily delight. Thank you for your laughter, silly stories, and companionship.

Next, I would like to emphasise the role of Marco, my husband. You helped me every step of the way. You helped me design my experiments, discuss my data and solve problems. Your support gave me the confidence and energy to overcome each obstacle and grow as a scientist. You put so much time and work into the proof-reading of this thesis while also staying on top of your work that you almost forgot to care for yourself. Your heart's blood is on every page of this thesis, and I couldn't have done it without you. Growing with you through this time was the best decision I ever made.

A big thank you to my (extended) family, my Mum Luitgard (I love you), Volker, Amanda and Heribert for always supporting me!

Another big thank you to the MIDAS Orga Team and all my MIDAS student colleagues. I am grateful for my time in Birmingham with you.

I was further supported by many people from the RRG and outside. To avoid missing someone here, I will not name them. Instead, I hope they know who they are and that I am grateful and sad to leave them behind in Birmingham.

I am very grateful to the Wellcome Trust, who kindly funded this endeavour (Grant - reference: 220107/Z/20/Z).

Table of Contents

Abstract ..... **I**
Acknowledgements ..... **IV**
Table of Contents ..... **I**
List of Figures ..... **XII**
List of Tables ..... **XVII**
List of Abbreviations ..... **XX**
Chapter One **1**
1 General Introduction **2**
1.1 Overview 2
1.2 Inflammation 3
1.2.1 The acute inflammatory response 3
1.2.2 Macrophages in inflammation 7
1.2.2.1 Macrophage development 8
1.2.2.2 Macrophage activation and polarisation 9
1.2.2.3 Macrophage function in inflammatory environments 12
1.2.3 Inflammatory diseases – pathogenesis and treatment 13
1.3 p38 MAPK - an inflammatory signalling pathway 17
1.3.1 p38 MAPK activation 17
1.3.2 The p38 MAPK family 20
1.3.3 Downstream substrates of p38 MAPK 20
1.3.4 Regulation of p38 MAPK pathway signalling 23
1.3.4.1 Protein interactions 24
1.3.4.2 p38 MAPK phosphatases 25
1.3.5 p38 MAPK as a treatment target in disease 29
1.4 TTP 31
1.4.1 TTP function 31
1.4.1.1 Target mRNA binding 32
1.4.1.2 TTP-target degradation 34
1.4.2 TTP regulation 38
1.4.2.1 Transcriptional TTP regulation 38
1.4.2.2 Post-transcriptional TTP regulation 39
1.4.2.3 Post-translational TTP regulation 39
1.5 Mathematical modelling of signalling pathways during inflammation 46
1.5.1 The modelling process in systems biology 46
1.5.1.1 Goal setting and initial exploration 47
1.5.1.2 Model selection 48

1.5.1.3 Model design 50
1.5.1.4 Model validation and application 55
1.5.2 Optimal model identification approach by Balsa-Canto 57
1.5.3 Examples of biological systems models in inflammation 60
1.5.3.1 p38 MAPK pathway models 60
1.5.3.2 TTP models 67
1.6 Project overview and aims 68
Chapter Two 72
2 Materials and Methods 73
2.1 Cell isolation and maintenance 73
2.1.1 Murine BMDMs 73
2.1.1.1 Animal husbandry 73
2.1.1.2 Deriving BMDMs 73
2.1.1.3 BMDM seeding 74
2.1.2 Cell lines 75
2.1.2.1 Preparation of frozen cell lines for long-term storage 75
2.1.2.2 Reconstitution of cells from frozen stocks 76
2.1.2.3 Maintenance of cell lines 76
2.1.2.4 Seeding of RAW264.7 cells 77
2.2 Cloning 78
2.2.1 Plasmid and Oligo Tables 78
2.2.2 Construct generation 81
2.2.2.1 PCR for insert preparation and site-directed deletion or mutagenesis 82
2.2.2.2 Agarose gel electrophoresis 83
2.2.2.3 Purification from PCR reactions 84
2.2.2.4 Restriction digests 84
2.2.2.5 Dephosphorylation of linearised plasmid 85
2.2.2.6 Phosphorylation of PCR amplified inserts 85
2.2.2.7 Ligation reaction 86
2.2.2.8 Gibson assembly reactions 87
2.2.2.9 Site-directed mutagenesis 88
2.2.3 Plasmid preparation 88
2.2.3.1 Transformation in *E. coli* 88
2.2.3.2 Plasmids mini preparations 89
2.2.3.3 Plasmid Mira-preparations 90
2.2.3.4 Glycerol stocks 91
2.2.4 Introduction of constructs into cells 91
2.2.4.1 Transfection of standard plasmids into HEK293T cells and HeLa cells 91
2.2.4.2 Transfection of lentiviral plasmids into HEK293T cells 92
2.2.4.3 Harvesting and concentration of lentiviral particles 93
2.2.4.4 Measurement of viral yield 94

2.2.4.5 Transduction and establishment of stable overexpressing cell lines 94
2.3 Time-course Microscopy Reporter cells 96
2.3.1 Sample Preparation 96
2.3.1.1 Seeding 96
2.3.1.2 Stimulation 96
2.3.1.3 Fixation 97
2.3.1.4 Staining 97
2.3.2 Image acquisition 97
2.3.3 Image analysis 98
2.4 Time-course experiments with inflammatory stimuli and inhibitors 99
2.4.1 Assessment of RNA expression 99
2.4.1.1 RNA extraction 99
2.4.1.2 cDNA synthesis 100
2.4.1.3 Standard curve 100
2.4.1.4 Absolute qPCR reactions 101
2.4.2 Assessment of protein expression via Western Blot 103
2.4.2.1 Protein isolation 103
2.4.2.2 Protein measurement 103
2.4.2.3 Standard curve 104
2.4.2.4 SDS-PAGE using Stain-Free™ protein gels 104
2.4.2.5 SDS page using PhosTag gels 105
2.4.2.6 Western blot transfer and Stain-Free imaging 105
2.4.2.7 Membrane staining and development 106
2.4.2.8 Densitometry and total quantification 107
2.4.3 Assessment of protein expression by ELISA 107
2.5 Mathematical Modelling toolboxes 109
2.5.1 Structural identifiability analysis 109
2.5.2 Global parameter ranking 109
2.5.3 Parameter estimation 111
Chapter Three 113
3 Mathematical modelling of the p38 MAPK-TTP signalling axis during inflammatory responses in macrophage populations 114
3.1 Introduction 114
3.2 Model formulation 116
3.2.1 Scope of the model 116
3.2.2 Selection of the model structure 117
3.2.3 Model design 119
3.2.3.1 TTP core model 119
3.2.3.2 Kulawik p38 MAPK model 126
3.2.3.3 Kulawik p38 MAPK-TTP model 132

3.2.4 Analysis of model structure 140
3.2.4.1 Structural identifiability analysis of the p38 MAPK-TTP model 141
3.2.4.2 Parameter ranking of the p38 MAPK-TTP model 144
3.3 Experimental design 148
3.3.1 Model organisms 148
3.3.2 Model inputs 149
3.3.3 Measurement of model components 149
3.4 Parameter estimation of the Kulawik p38 MAPK-TTP model in BMDMs 152
3.4.1 BMDMs total quantification data 152
3.4.2 BMDM parameter estimation 157
3.4.2.1 One-step model parameter estimation 159
3.4.2.2 Two-step model parameter estimation 163
3.4.3 Model validation BMDMs 172
3.4.3.1 Comparison of WT and *Dusp1*$^{-/-}$ mutant BMDMs 172
3.4.3.2 Comparison of WT and *Zfp36*$^{aa/aa}$ mutant BMDMs 181
3.4.3.3 BMDM inhibitor experiments 187
3.5 Parameter estimation RAW264.7 cells 191
3.5.1 Comparison of BMDMs and the RAW264.7 cell line 191
3.5.1.1 p38 MAPK 192
3.5.1.2 DUSP1 193
3.5.1.3 Unphosphorylated TTP 193
3.5.1.4 Phosphorylated TTP 194
3.5.1.5 *Tnf* mRNA 195
3.5.2 Parameter estimation RAW264.7 cells 197
3.5.3 Model comparison of RAW264.7 and BMDM simulations 201
3.6 Discussion 203
3.6.1 Experimental Design 203
3.6.2 BMDM data and parameter estimation 206
3.6.3 BMDM model validation through pathway disruptions 212
3.6.4 Comparison of WT BMDMs and RAW264.7 cells 218
3.7 Chapter summary 221
Chapter Four 224
4 Mathematical Modelling of the p38 MAPK-TTP signalling axis in individual cells 225
4.1 Introduction 225
4.2 Model formulation 227
4.2.1 Definition of the model scope 227
4.2.2 Presentation of the Tomida p38 MAPK model 228
4.2.3 Design of the Tomida p38 MAPK-TTP model 235
4.2.4 Comparison of the Tomida and Kulawik p38 MAPK-TTP models 243

4.3 Establishing microscopy reporter cell lines 247
4.3.1 Experimental design of cloning 247
4.3.2 Establishing TTP mutant reporter cell lines 249
4.3.3 Establishment of KTR and TTP-colocalisation reporters 255
4.4 Microscopy setup and time-course experiments 257
4.4.1 Experimental design live-cell microscopy 257
4.4.2 Microscopy experiments of fixed HeLa-TTP reporters 262
4.4.2.1 Microscopy of HeLa-TTP reporter cells co-expressing DCP1a 263
4.4.2.2 Microscopy of HeLa-TTP reporter cells co-expressing MK2 266
4.5 Discussion 269
4.5.1 Tomida p38 MAPK-TTP model 269
4.5.2 Microscopy 270
4.5.2.1 Live-cell microscopy 270
4.5.2.2 DCP1a fixed cell experiment 272
4.5.2.3 MK2 fixed cell experiment 273
4.5.2.4 Automated image analysis 274
4.6 Chapter summary 277
Chapter Five 279
5 Conclusion 280
Chapter Six 284
6 References 285
Chapter Seven I
7 APPENDIX II
7.1 MATLAB scripts II
7.2 Preliminary experiments of Chapter 3 XV
7.2.1 Dose-response curve of Calyculin A XV
7.2.2 Standard curve total protein XVI
7.2.3 Standard curve phosphorylated protein XX
7.2.4 Standard curve qPCR XXIII
7.3 Individual experiments of Chapter 3 XXIV
7.3.1 WT BMDMs XXIV
7.3.1.1 Experiment 1 XXIV
7.3.1.2 Experiment 2 XXXIII
7.3.1.3 Experiment 3 XXXVII
7.3.2 *Dusp1*$^{-/-}$ BMDMs XL
7.3.2.1 Experiment 1 XL
7.3.2.2 Experiment 2 XLIV
7.3.2.3 Experiment 3 XLVIII
7.3.3 *Zfp36*$^{aa/aa}$ BMDMs LII

7.3.3.1 Experiment 1 LII
7.3.3.2 Experiment 2 LVI
7.3.3.3 Experiment 3 LIX
7.3.4 RAW264.7 cells LXIII
7.3.4.1 Experiment 1 LXIII
7.3.4.2 Experiment 2 LXVII
7.3.4.3 Experiment 3 LXXI
7.4 Adaption of the Kulawik p38 MAPK-TTP model LXXV
7.5 Parameter estimation results LXXXI
7.5.1 Example images parameter estimation LXXXI
7.5.2 p38 MAPK parameter estimation without DUSP1 data LXXXI
7.6 Cloning Results – Agarose Gels LXXXVI
7.7 Full plasmid sequences and plasmid maps XCI
7.8 Microscopy XCI
7.9 Image analysis XCII

List of Figures

Figure 1.1 Schematic overview of the inflammatory response upon injury. 6
Figure 1.2 Schematic overview of the polarisation states of activated macrophages. 11
Figure 1.3 Overview p38 MAPK activation by TLR4 and IL-1β. 19
Figure 1.4 Overview of inflammation-related p38 MAPK substrates. 23
Figure 1.5 Schematic overview of the phosphatase-mediated p38 MAPK pathway regulation. 28
Figure 1.6 Schematic overview of TTP-mediated mRNA degradation. 37
Figure 1.7 Schematic overview of TTP regulation. 44
Figure 1.8 Model diagram of the exemplary phosphorylation chain. 51
Figure 1.9 Overview of the iterative model building process. 59
Figure 1.10 Mathematical model of p38 MAPK activation with oscillatory dynamics by Tomida et al. 61
Figure 1.11 Mathematical model of LPS-dependent p38 MAPK-pathway activation by Hendriks et al. 65
Figure 1.12 Mathematical model of IL-1β-dependent p38 MAPK/MK2 activation by Kulawik et al. 66
Figure 3.1 Model diagram of the core TTP pathway. 120
Figure 3.2 Computational simulation of the core TTP model. 125
Figure 3.3 Computational simulation of target mRNA expression in TTP KO phenotype versus WT using the TTP core model. 126
Figure 3.4 Model diagram of the Kulawik p38 MAPK model. 128
Figure 3.5 Computational simulation Kulawik p38 MAPK model. 132
Figure 3.6 Model diagram of the Kulawik p38 MAPK-TTP pathway. 134
Figure 3.7 Computational simulation of the Kulawik p38 MAPK-TTP model. 140
Figure 3.8 Comparison TTP-target mRNA expression before and after nominal parameter adaption of the Kulawik p38 MAPK-TTP model. 140
Figure 3.9 Screenshot of the GenSSI results recommending changes to model structure. 143
Figure 3.10 Order 1 identifiability tableau of the Kulawik p38 MAPK-TTP model. 144
Figure 3.11 Relative and global parameter ranking of the Kulawik p38 MAPK-TTP model. 146
Figure 3.12 Schematic overview of the 19 sampling times of 8 h time-course experiment including 30 min pretreatment with inhibitors. 151
Figure 3.13 Measuring p38 MAPK-TTP pathway components by total quantification of Western blot and qPCR data obtained from BMDMs treated with LPS over an 8 h time-course. 156

Figure 3.14 Overview of BMDM p38 MAPK-TTP time-course experiment for visualisation of pathway dynamics. 156

Figure 3.15 Model diagram of the updated Kulawik p38 MAPK-TTP pathway model. 158

Figure 3.16 Computational simulation of the Kulawik p38 MAPK-TTP model using an exemplary estimated parameter set for LPS-treated BMDMs where all parameters were estimated simultaneously. 162

Figure 3.17 Computational simulation of the upstream p38 MAPK section of the Kulawik p38 MAPK-TTP model using an estimated parameter set with the best relative global MABS score for LPS-treated BMDMs. 167

Figure 3.18 Computational simulation of the downstream TTP section of the Kulawik p38 MAPK-TTP model using an estimated parameter set with the best MABS score for LPS-treated BMDMs. 169

Figure 3.19 Relative MABS of residuals of the BMDM parameter estimation. 170

Figure 3.20 Computational simulation of the downstream TTP section of the Kulawik p38 MAPK-TTP model with switched TTP degradation rates. 171

Figure 3.21 Measuring p38 MAPK-TTP pathway components by total quantification of Western blot and qPCR data obtained from *Dusp1*$^{-/-}$ and WT BMDMs treated with LPS over an 8 h time-course. 177

Figure 3.22 Computational simulation of LPS-treated WT and *Dusp1*$^{-/-}$ BMDMs using the calibrated Kulawik p38 MAPK-TTP model. 181

Figure 3.23 Measuring p38 MAPK-TTP pathway components by total quantification of Western blot and qPCR data obtained from *Zfp36*$^{aa/aa}$ and WT BMDMs treated with LPS over an 8 h time-course. 185

Figure 3.24 Computational simulation of LPS-treated WT and *Zfp36*$^{aa/aa}$ BMDMs using the calibrated Kulawik p38 MAPK-TTP model. 187

Figure 3.25 Measuring p38 MAPK-TTP pathway components by total quantification of Western blot and qPCR data obtained from WT BMDMs with or without Calyculin A stimulated with LPS over an 8 h time-course. 190

Figure 3.26 Measuring p38 MAPK-TTP pathway components by total quantification of Western blot and qPCR data obtained from RAW264.7 cells and WT BMDMs treated with LPS over an 8 h time-course. 197

Figure 3.27 Relative MABS of the RAW264.7 parameter estimation. 199

Figure 3.28 Computational simulation of the calibrated Kulawik p38 MAPK-TTP model for LPS-treated RAW264.7 cells. 200

Figure 3.29 Computational simulation of LPS-treated WT RAW264.7 cells and BMDMs using the calibrated Kulawik p38 MAPK-TTP model. 202

Figure 3.30 Comparison *Tnf* mRNA expression normalised to peak p38 MAPK phosphorylation between *Zfp36*$^{aa/aa}$ and WT BMDMs. 217

Figure 3.31 Comparison of secreted TNF-α protein expression between *Zfp36*$^{aa/aa}$ and WT BMDMs using ELISA. 217

Figure 4.1 Model diagram of the Tomida p38 MAPK model. 229
Figure 4.2 Computational single-cell simulation of the Tomida p38 MAPK model. 233
Figure 4.3 Computational multicellular simulation of the Tomida p38 MAPK model. 234
Figure 4.4 Model diagram of the Tomida p38 MAPK-TTP pathway. 236
Figure 4.5 Computational single-cell simulation of the Tomida p38 MAPK-TTP model. 241
Figure 4.6 Computational multicellular simulation of the Tomida p38 MAPK-TTP model. 243
Figure 4.7 Computational simulation of LPS-treated WT BMDMs using the nominal Tomida and calibrated Kulawik p38 MAPK-TTP model. 246
Figure 4.8 Cloning scheme of the TTP mutant reporter constructs for live-cell microscopy. 250
Figure 4.9 DNA gel electrophoresis verifying the correct PCR amplifications of the hTTP insert and the pmRuby2_mNeonGreen backbone for Gibson assembly. 251
Figure 4.10 Control DNA gel electrophoresis verifying the correct PCR amplifications for SDMs of hTTP at position Ser-80. 252
Figure 4.11 Control DNA gel electrophoresis verifying the correct PCR amplifications of the mNeonGreen_hTTP_WT insert and RE digest of the pLentiX_TetOne_Puro backbone for blunt-end ligation. 254
Figure 4.12 Example diagnostic RE digests of the newly generated construct pLentiX_TetOne_mNG_hTTP_WT to identify bacterial colonies with the correct insert orientation following blunt-end cloning. 255
Figure 4.13 Cloning scheme of the DCP1a (P-body) Colocalisation and MK2 KTR reporter constructs for live-cell microscopy. 256
Figure 4.14 Time-course of Doxycycline treated TetOne_hTTP_WT HeLa cells. 258
Figure 4.15 Time-lapse analysis of TetOne_mNG_hTTP_WT HeLa cells stimulated with IL-1β. 261
Figure 4.16 Representative images of fixed TetOne_mNG_hTTP_WT/AA/EE HeLa cells co-expressing mR2_DCP1a. 263
Figure 4.17 Time-course experiment of fixed TetOne_mNG_hTTP_WT/AA/EE HeLa cells co-expressing mR2_DCP1a treated with 30 ng/mL IL-1β. 266
Figure 4.18 Time-course experiment of fixed TetOne_mNG_hTTP_WT HeLa cells co-expressing mR2_MK2 treated with 30 ng/mL IL-1β. 268
Figure 7.1 Dose-response curve of the PP2A inhibitor Calyculin A in RAW264.7 cells. XVI
Figure 7.2 Preliminary experiment for identification of the TTP standard curve for total quantification. XVIII
Figure 7.3 Preliminary experiment for identification of the DUSP1 standard curve for total quantification. XIX
Figure 7.4 Measurement of the percentage of phosphorylated p38 MAPK in the active recombinant protein of p38 MAPK using PhosTag gel Western Blotting. XXI
Figure 7.5 Preliminary experiment for identification of the p38 MAPK standard curve for total quantification. XXII

Figure 7.6 Control DNA gel electrophoresis verifying correct linearisation of the TNF plasmid following AgeI RE digest. XXIII

Figure 7.7 WT BMDM Experiment 1: Total quantification Western blot data of BMDMs treated with LPS over an 8 h time-course measuring p38 MAPK-TTP pathway components. XXX

Figure 7.8 BMDM WT Experiment 1: Standard curves and total quantification of Western blot and qPCR data obtained from BMDMs treated with LPS over an 8 h time-course measuring p38 MAPK-TTP pathway components. XXXII

Figure 7.9 WT BMDM Experiment 2: Total quantification Western blot data of BMDMs treated with LPS over an 8 h time-course measuring p38 MAPK-TTP pathway components... XXXIII

Figure 7.10 WT BMDM Experiment 2: Standard curves and total quantification of Western blot and qPCR data obtained from BMDMs treated with LPS over an 8 h time-course measuring p38 MAPK-TTP pathway components. XXXVI

Figure 7.11 WT BMDM Experiment 3: Total quantification Western blot data of BMDMs treated with LPS over an 8 h time-course measuring p38 MAPK-TTP pathway components. XXXVII

Figure 7.12 WT BMDM Experiment 3: Standard curves and total quantification of Western blot and qPCR data obtained from BMDMs treated with LPS over an 8 h time-course measuring p38 MAPK-TTP pathway components. XXXVIII

Figure 7.13 *Dusp1*$^{-/-}$ BMDM Experiment 1: Representative total quantification Western blot data of *Dusp1*$^{-/-}$ BMDMs treated with LPS over an 8 h time-course measuring p38 MAPK-TTP pathway components. XL

Figure 7.14 *Dusp1*$^{-/-}$ BMDM Experiment 1: Total quantification of Western blot and qPCR data obtained from *Dusp1*$^{-/-}$ BMDMs treated with LPS over an 8 h time-course measuring p38 MAPK-TTP pathway components. XLII

Figure 7.15 *Dusp1*$^{-/-}$ BMDM Experiment 2: Total quantification Western blot data of *Dusp1*$^{-/-}$ BMDMs treated with LPS over an 8 h time-course measuring p38 MAPK-TTP pathway components. XLV

Figure 7.16 *Dusp1*$^{-/-}$ BMDM Experiment 2: Standard curves and total quantification of Western blot and qPCR data obtained from *Dusp1*$^{-/-}$ BMDMs treated with LPS over an 8 h time-course measuring p38 MAPK-TTP pathway components..... XLVI

Figure 7.17 *Dusp1*$^{-/-}$ BMDM Experiment 3: Total quantification Western blot data of *Dusp1*$^{-/-}$ BMDMs treated with LPS over an 8 h time-course measuring p38 MAPK-TTP pathway components. XLIX

Figure 7.18 *Dusp1*$^{-/-}$ BMDM Experiment 3: Standard curves and total quantification of Western blot and qPCR data obtained from *Dusp1*$^{-/-}$ BMDMs treated with LPS over an 8 h time-course measuring p38 MAPK-TTP pathway components..... L

Figure 7.19 *Zfp36*$^{aa/aa}$ BMDM Experiment 1: Representative total quantification Western blot data of *Zfp36*$^{aa/aa}$ BMDMs treated with LPS over an 8 h time-course measuring p38 MAPK-TTP pathway components. LIII

Figure 7.20 *Zfp36*$^{aa/aa}$ BMDM Experiment 1: Standard curves and total quantification of Western blot and qPCR data obtained from *Zfp36*$^{aa/aa}$ BMDMs treated with LPS over an 8 h time-course measuring p38 MAPK-TTP pathway components. LV

Figure 7.21 *Zfp36*$^{aa/aa}$ BMDM Experiment 2: total quantification Western blot data of *Zfp36*$^{aa/aa}$ BMDMs treated with LPS over an 8 h time-course measuring p38 MAPK-TTP pathway components. LVI

Figure 7.22 *Zfp36*$^{aa/aa}$ BMDM Experiment 2: Standard curves and total quantification of Western blot and qPCR data obtained from *Zfp36*$^{aa/aa}$ BMDMs treated with LPS over an 8 h time-course measuring p38 MAPK-TTP pathway components. LVII

Figure 7.23 *Zfp36*$^{aa/aa}$ BMDM Experiment 3: Total quantification Western blot data of *Zfp36*$^{aa/aa}$ BMDMs treated with LPS over an 8 h time-course measuring p38 MAPK-TTP pathway components. LX

Figure 7.24 *Zfp36*$^{aa/aa}$ BMDM Experiment 3: Standard curves and total quantification of Western blot and qPCR data obtained from *Zfp36*$^{aa/aa}$ BMDMs treated with LPS over an 8 h time-course measuring p38 MAPK-TTP pathway components. LXII

Figure 7.25 RAW264.7 Experiment 1: Total quantification Western blot data of RAW264.7 cells treated with LPS over an 8 h time-course measuring p38 MAPK-TTP pathway components. LXIII

Figure 7.26 RAW264.7 Experiment 1: Standard curves and total quantification of Western blot and qPCR data obtained from RAW264.7 cells treated with LPS over an 8 h time-course measuring p38 MAPK-TTP pathway components. LXVI

Figure 7.27 RAW264.7 Experiment 2: Total quantification Western blot data of RAW264.7 cells treated with LPS over an 8 h time-course measuring p38 MAPK-TTP pathway components. LXVII

Figure 7.28 RAW264.7 Experiment 2: Standard curves and total quantification of Western blot and qPCR data obtained from RAW264.7 cells treated with LPS over an 8 h time-course measuring p38 MAPK-TTP pathway components. LXX

Figure 7.29 RAW264.7 Experiment 3: Total quantification Western blot data of RAW264.7 cells treated with LPS over an 8 h time-course measuring p38 MAPK-TTP pathway components. LXXI

Figure 7.30 RAW264.7 Experiment 3: Standard curves and total quantification of Western blot and qPCR data obtained from RAW264.7 cells treated with LPS over an 8 h time-course measuring p38 MAPK-TTP pathway components. LXXIV

Figure 7.31 Computational simulation of the Kulawik p38 MAPK-TTP model comparing two sets of nominal parameters. LXXIX

Figure 7.32 Example image of parameter estimation output with a realistic error profile of the p38 MAPK pathway. LXXXI

Figure 7.33 Computational simulation of the upstream p38 MAPK section of the Kulawik p38 MAPK-TTP model using an estimated parameter set with the best MABS score for LPS-treated BMDMs with DUSP1 data excluded from the parameter estimation process. LXXXIII

Figure 7.34 Computational simulation of the of the downstream TTP section of the Kulawik p38 MAPK-TTP model using an estimated parameter set with the best MABS score for LPS-treated BMDMs with DUSP1 data excluded from the parameter estimation process. .. LXXXV

Figure 7.35 Control DNA gel electrophoresis verifying the correct RE digest of pLentiX_TetOne_Puro and PCR amplifications of the inserts mNeonGreen_hTTP_AA and mNeonGreen_hTTP_EE. LXXXVI

Figure 7.36 Diagnostic RE digests of the newly generated constructs pLentiTetOne_mNG_hTTP_AA/EE to identify bacterial colonies with the correct insert orientation following blunt-end cloning. LXXXVIII

Figure 7.37 Control DNA gel electrophoresis verifying the correct PCR amplification of the BB pmNeonGreen-mRuby2-FRET-10 and the inserts 14-3-3, DCP1a, GRBP1, and MK2 for Gibson assembly. LXXXVIII

Figure 7.38 Diagnostic RE digests of the newly generated construct pWPI_mRuby2_DCP1a/MK2 to identify bacterial colonies with the correct insert orientation following blunt-end cloning. LXXXIX

Figure 7.39 Control DNA gel electrophoresis verifying the correct RE digest of pWPI-IRES-Bla-Ak and PCR amplifications of the inserts R2_DCP1a, R2_G3BP1, R2_14-3-3b, and R2_MK2 for blunt end ligation. XC

Figure 7.40 Example for p38 MAPK activation by 30 ng/mL IL-1β. XCI

List of Tables

Table 2.1 Cell lines, their origins and culture media 75

Table 2.2 Plasmids 78

Table 2.3 Oligos 79

Table 2.4 Components PCR 82

Table 2.5 Cycling Conditions 83

Table 2.6 Components restriction digest 85

Table 2.7 Components of T4 PNK reaction 86

Table 2.8 Components of T4 DNA Ligase reaction 87

Table 2.9 Components of HiFi DNA Assembly reaction 87

Table 2.10 Components of Site-Directed Mutagenesis reaction 88

Table 2.11 Components of transfection solution 92

Table 2.12 Components of transfection solution Lenti-vector 93

Table 2.13 Composition of a cDNA reverse transcription reaction 100

Table 2.14 Overview qPCR standard curve 102

Table 2.15 Components of an RT qPCR reaction 102

Table 2.16 Cycle conditions of an RT qPCR reaction 102

Table 2.17 Recombinant protein for Western blot standard curve 104

Table 2.18 Western Blotting Antibodies 106
Table 3.1 Dependent variables of the core TTP pathway. 121
Table 3.2 Independent variables of the core TTP pathway. 121
Table 3.3 Overview of interactions of the core TTP pathway. 122
Table 3.4 Overview of parameters of the core TTP pathway model 122
Table 3.5 Overview of variables of Kulawik p38 MAPK pathway model 129
Table 3.6 Interactions and processes described by Kulawik p38 MAPK pathway model 129
Table 3.7 Overview of parameters of the Kulawik p38 MAPK pathway model 130
Table 3.8 Overview of variables of Kulawik p38 MAPK-TTP pathway model 135
Table 3.9 Interactions and processes described by Kulawik p38 MAPK-TTP pathway model 135
Table 3.10 Overview of parameters of the Kulawik p38 MAPK-TTP pathway model 136
Table 3.11 Ranked importance factors calculated from global parametric sensitivity analysis 147
Table 3.12 Parameter set for the example one-step Kulawik p38 MAPK-TTP model parameter estimation 160
Table 3.13 Parameter set of parameter estimation with best relative global MABS for the Kulawik p38 MAPK module 165
Table 3.14 Global relative MABS ranking of p38 MAPK parameter estimation runs 166
Table 3.15 Parameter set of parameter estimation for the Kulawik p38 MAPK-TTP model with fixed p38 MAPK parameters. 168
Table 3.16 Parameter set of parameter estimation for the RAW264.7 cell Kulawik p38 MAPK-TTP model. 198
Table 4.1 Variables of the Tomida p38 MAPK model. 230
Table 4.2 Interactions of the Tomida p38 MAPK model. 230
Table 4.3 Parameters of the Tomida p38 MAPK model. 231
Table 4.4 Variables of the Tomida p38 MAPK-TTP model. 237
Table 4.5 Interactions of the Tomida p38 MAPK-TTP model. 237
Table 4.6 Parameters of the Tomida p38 MAPK-TTP model. 238
Table 7.1 Variables and initial conditions of the Kulawik p38 MAPK-TTP model adapted to LPS-stimulated BMDMs LXXVII
Table 7.2 Nominal parameter values of the Kulawik p38 MAPK-TTP model adapted to LPS-stimulated BMDMs LXXVIII
Table 7.3 Parameter set of parameter estimation with best relative global MABS for the Kulawik p38 MAPK module with DUSP1 data excluded LXXXII
Table 7.4 Global relative MABS ranking of p38 MAPK parameter estimation runs without DUSP1 data LXXXII

Table 7.5 Parameter set of parameter estimation for the Kulawik p38 MAPK-TTP model with fixed p38 MAPK parameters and DUSP1 data excluded.....LXXXIV

List of Abbreviations

a.u.	Arbitrary unit
AA	Alanine-Alanine, instead of Serine-Serine
ACPA	anticitrullinated protein antibodies
AmpR	Ampicillin resistance
ANOVA	Analysis of variance
AP-1	Activator protein 1
ARE	AU-rich element
ASK	Apoptosis signal-regulating kinase
ATF	Activating transcription factor
ATP	Adenosine triphosphate
AUF-1	AU-rich binding factor-1
BB	Backbone
BCA	Bicinchoninic acid
BMDM	Bone marrow-derived macrophage
BSA	Bovine serum albumin
C/N-ratio	Cytoplasm to nucleus ratio
C/P-ratio	Cytoplasm to P-body ratio
CAF1	Ccr4 associated factor 1
CCCH	Cysteine-cysteine-cysteine-histidine
CCR4	carbon catabolite repression 4
CMV	Cytomegalovirus
CREB	cAMP response element binding protein
CXCL	C-X-C motif chemokine ligand
DAMP	Damage associated molecular pattern
DAPI	4′,6-diamidino-2-phenylindole
DCP1	Decapping protein 1
ddH2O	Double-distilled water
DMEM	Dulbecco's modified eagle medium
DMSO	Dimethyl sulfoxide
DNA	Desoxyribonucleic acid
Dox	Doxycycline
DUSP	Dual-specific phosphatase
EDTA	Ethylenediaminetetraacetic acid
EE	Glutamate-Glutamate, instead of Serine-Serine
EGFP	Enhanced green fluorescent protein
ELISA	Enzyme-linked immunosorbent assay
ELK-1	ETS Transcription Factor 1
EMP	Erythro-myeloid progenitor
ERK	Extracellular signal-regulated kinases
FCS	Fetal calf serum
FRET	Foerster resonance energy transfer
GMO	Genetically modified organism
HIV	Human immunodeficiency virus
HRP	Horse radish peroxidase
HSP	Heat shock protein
HuR	Human antigen R

iCLIP	Individual nucleotide resolution crosslinking and immunoprecipitation
IFN	Interferon
Ig	Immunoglobulin
IL-X	Interleukin-X
IRAK	IL-1 receptor associated kinase
IRES	Internal ribosome entry site
JAK	Janus kinase
JNK	Jun-amino-terminal kinases
KanR	Kanamycin resistance
KSRP	KH splicing regulatory protein
KLD	Kinase-Ligase-DpnI
KTR	Kinase translocation reporter
LB	Lysogeny broth
LLM	Large language model
LPS	Lipopolysaccharide
LV	Lentivirus
MABS	Mean of the absolute
MAP2K	MAPK kinase
MAP3K	MAPK kinase kinase
MAPK	Mitogen associated protein kinase
M-CSF	Macrophage
MEKK	MAPK/ERK kinases
MEM	Modified eagle medium
miRNA	Micro RNA
MK2/3	MAPK activated protein kinase 2/3
MKK	MAPK kinase
MKP	MAPK phosphatase
MNK1/2	MAPK-interacting kinase 1/2
MoM	Monocyte-derived macrophage
mRNA	Messenger RNA
MSK1/2	Mitogen and stress activated protein kinase 1/2
MSQR	Mean square root
NeoR	Neomycin resistance
NES	Nuclear export signal
NF-κB	Nuclear factor kappa-light-chain-enhancer of activated B cells
NLS	Nuclear localisation signal
NOT	Negative on TATA-less
ODE	Ordinary differential equation
PAMP	Pathogen associated molecular pattern
PAR-iCLIP	Photoactivatable ribonucleoside-enhanced individual nucleotide resolution crosslinking and immunoprecipitation
P-body	Processing body
PBS	Phosphate-buffered saline
PCR	Polymerase chain reaction
PEG	Polyethylene glycol
PNK	Polynucleotide kinase
PP2A/C	Protein phosphatase 2 A/C
PRR	Pattern recognition receptor

PTR	Post-transcriptional regulation
PVDF	Polyvinylidene difluoride
RA	Rheumatoid Arthritis
RANK	receptor activator of nuclear factor κ B
RBP	RNA binding protein
RE	Restriction enzyme
RIPA	Radio-immunoprecipitation assay
RM	Repeated measure
RNA	Ribonucleic acid
RPMI	Rosswell park memorial institute
RRE	Rev response element
RT	Room temperature
SAP-1	SRF accessory protein 1
SDM	Site-directed mutagenesis
SDS	Sodium dodecyl sulfate
SG	Stress granule
STAT	Signal transducer and activator of transcription
SV-40	Simian Virus 40
TAB	TAK1 binding protein
TAK	TGF-β activated kinase
TBST	Tris-buffered saline with Tween
TF	Transcription factor
TGF	Tumour growth factor
Th cell	T-helper cell
TIR	Toll-IL-1R
TLR	Toll-like receptor
TNF	Tumour necrosis factor
TRAF	TNF receptor associated factor
TRM	Tissue-resident macrophage
TTP	Tristetraprolin
TZF	Tandem zinc finger
UTR	Untranslated region
VSV	Vesicular stomatitis virus
WB	Western Blotting
WPRE	Woodchuck hepatitis virus posttranscriptional regulatory element
WT	Wild type
ZFP36	Zinc finger protein 36

CHAPTER ONE

General Introduction

1 General Introduction

1.1 Overview

Inflammation is a protective response of the body following a sterile or infectious injury with the goal of removing the triggering stimulus and restoring the body's preinjury state. In case of infection, it initiates the development of immune memory. However, in chronic inflammatory disease, inflammation and the associated immune responses are not resolved, and the initial protective mechanism becomes distorted and damages tissues, potentially incapacitating organ functions. For example, in the case of Rheumatoid arthritis (RA), chronic inflammation in the joints leads to tissue degradation and debilitating pain. A central aspect contributing to the pathogenesis and progression of such a chronic inflammatory disease is the dysregulated expression of inflammatory mediators, with macrophages being one of their major producers. Inhibition of the pro-inflammatory cytokine tumour necrosis factor α (TNFα), for example, has become a cornerstone of RA treatment.

Consequently, improving the understanding of the regulation of inflammatory gene expression enables researchers to comprehend pathogenic mechanisms better and discover novel therapies. One important post-transcriptional regulatory mechanism often overlooked is messenger ribonucleic acid (mRNA) degradation. This process is primarily regulated through RNA-binding proteins (RBP) that recognise cis-regulatory elements in the 3'untranslated regions (UTR) of many inflammatory and immunoregulatory mRNAs. One of the best-studied RBPs is Tristetraprolin (TTP), which induces its target-mRNA degradation through recruitment of the cytoplasmic mRNA degradation machinery and has demonstrated its essential role in regulating of inflammatory mediators, including TNFα. TTP expression and activity are heavily regulated on multiple levels by the prominent p38 mitogen-associated protein kinase (MAPK) signalling

pathway. Even before its role in the phosphorylation of TTP was established, the p38 MAPK pathway had been recognised as an important regulator of pro-inflammatory gene expression.

The complex regulation of TTP by p38 MAPK represents a challenge when trying to dissect its activity state and impact on target mRNA stability throughout the inflammatory response. This thesis intends to leverage an interdisciplinary approach combining mathematical modelling, from the field of applied mathematics, with molecular biology wet-lab experiments, from the field of immunology, to study the dynamics of the p38 MAPK-TTP signalling axis during the inflammatory response.

1.2 Inflammation

The acute inflammatory response is an intricate and highly synchronised series of cellular and humoral tissue responses, usually occurring within the first few hours upon sterile and infectious injury (1,2). Tissue-resident and blood-born innate immune cells, especially macrophages, are essential for regulating the onset and resolution of the inflammatory response (3). However, while inflammation is integral to combat pathogens and initiate tissue repair, its dysregulation can lead to excessive tissue damage, chronic disease, autoimmune disorders and even cancer (4). It is essential to understand the complex regulatory mechanisms involved in the inflammatory response to combat this dysregulation and develop therapeutics that resolve inflammation-mediated pathologies while conserving or promoting the tissue repair functions of the system.

1.2.1 The acute inflammatory response

The inflammatory response is initiated by local tissue-resident cells sensing damage or pathogen-associated molecular patterns (DAMPs, PAMPs) at the site of injury and infection. In response to these stimuli, tissue-resident cells produce molecular immune mediators such as

cytokines. Respective responsive tissue-resident cells include fibroblasts, macrophages, and mast cells. The released inflammatory mediators cause changes to adjacent blood vessels, increasing their diameter and vascular permeability, blood flow and accumulating fluid and plasma proteins such as fibrinogen and complement factors from the circulation. These changes result in the four main macroscopic observable characteristics of inflammation: pain, redness, heat and swelling (4,5).

Produced chemokines, a subgroup of cytokines capable of regulating leukocyte migration, generate a gradient within the tissue and the blood circulation system, thereby attracting immune cells from the circulation. Other released cytokines activate the endothelial lining of the blood vessels to upregulate cell-adhesion molecules, which interact with immune cells allowing them to attach, and enter the tissue via cellular extravasation. The local immune mediator cocktail also allows for the polarisation and activation of the recruited immune cells, enabling them to perform the specific functions required. The first cells to be recruited in large numbers are typically neutrophils. Their primary function is phagocytosis and the elimination of infectious agents. Neutrophils are later followed by monocytes, which differentiate into monocyte-derived macrophages (MoM) and obtain a pro-inflammatory phenotype. Besides phagocytosis, macrophages exert important signalling functions by presenting antigens and producing cytokines (3–5).

When the inflammation-triggering agent has been removed, the resolution of the inflammatory response initiates, during which the tissue is cleared of cellular debris, immune mediators, and pro-inflammatory immune cells. Anti-inflammatory immune cells and anti-inflammatory signalling molecules that promote wound healing and tissue restoration are the prime actors and factors during this phase (2). Here, macrophages switch their phenotype from a pro-inflammatory state to an anti-inflammatory one and contribute to the clearance of cellular

debris. They also secrete anti-inflammatory mediators and tissue regeneration-promoting molecules before they mature into tissue-resident macrophages (TRM) or undergo apoptosis (3,6). Consequently, among immune cells involved in the inflammatory response, macrophages are particular as they are present and essential in all stages of the inflammatory response, from recognition of damage or pathogens, activation of the endothelial lining, pathogen clearance, recruitment of other innate immune cells, initiation of the adaptive immune response, and finally restoration of tissue homeostasis. We will describe these cells in more detail, as they are the primary model organism of this work, and our endevour of understanding signalling pathways is pursued in the context of macrophage function and dysregulation. Figure 1.1 summarises the inflammatory response from onset to resolution, focusing on macrophages.

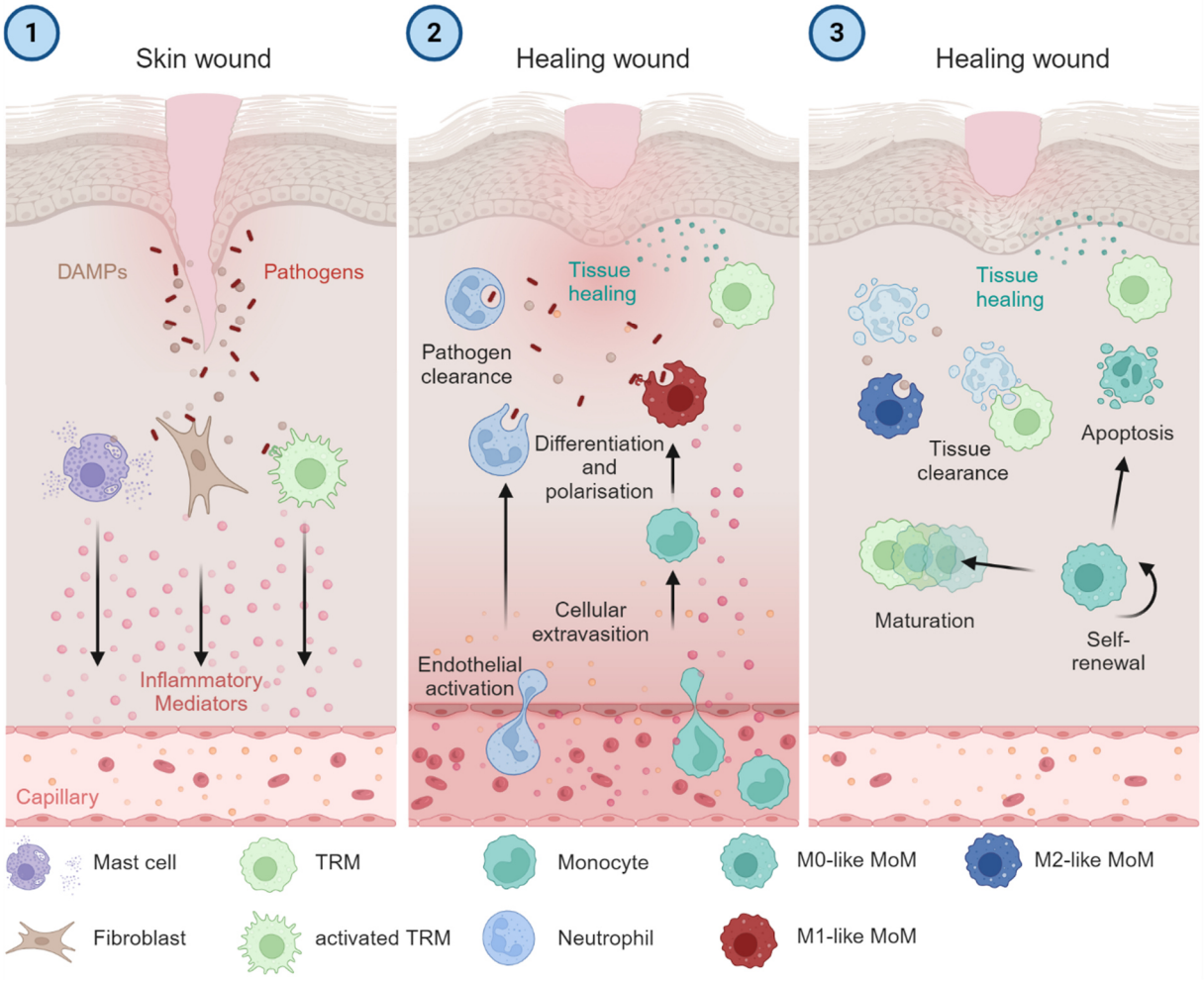


Figure 1.1 Schematic overview of the inflammatory response upon injury.

The inflammatory response is depicted in three steps: 1) During an infectious injury, molecular mediators (DAMPs and PAMPs) are recognised by tissue-resident cells (e.g. TRM, mast cells, fibroblasts). These cells initiate the inflammatory response by producing and secreting inflammatory mediators. 2) The secreted inflammatory mediators activate endothelial cells, which upregulate adhesion molecules and promote attachment and extravasation of immune cells, first neutrophils, then monocytes. Monocytes, upon arrival, differentiate into MoM and obtain a pro-inflammatory M1-like phenotype. Neutrophils and M1-like MoMs then clear the tissue from pathogens while producing more pro-inflammatory mediators. Endothelial activation further leads to an increase in diameter and vascular permeability, which leads to increased blood flow and accumulation of plasma proteins and fluid in the adjacent tissue. TRMs contribute to wound healing by secreting tissue-regenerating molecules. 3) Once the inflammatory stimuli are removed, neutrophils undergo apoptosis, and MoMs obtain a pro-resolution phenotype and, together with TRM, clear the tissue from any remaining cellular debris and immune-regulatory mediators. MoMs then either undergo apoptosis themselves or proliferate and mature into TRMs. This image was created using Biorender, adapting the template “The inflammatory response” from Louis Ngai (7).

1.2.2 Macrophages in inflammation

Over 100 years ago, Elie Metchnikoff first described a population of large mononuclear phagocytic cells and named them ‘macrophages’, which in Greek means ‘big eaters’. As the name suggests, one of the main functions of macrophages is engulfing invading microbes, apoptotic cells, and cellular debris. This function alone would make macrophages an essential part of the innate immune system. They also function as sentinels for pathogens and other injuries, are one of the major producers of pro- and anti-inflammatory mediators, and coordinate acquired immunity through communication with the adaptive immune system. They also exert important functions outside of inflammation, such as regulating haematopoiesis in the bone marrow. As varying as their functions are, they are heterogenous in their properties and localisation throughout the body. Nearly every tissue maintains its own specialised subset of TRMs, in addition to blood-derived monocytes that differentiate into macrophages upon entering tissues, where they polarise and change their properties depending on the signals present in the local environment. In their function as phagocytes and major cytokine producers, they express pattern recognition receptors (PRR). When activated by DAMPS and PAMPS, PRRs induce intricate signalling cascades that regulate function and production of inflammatory mediators. Due to their importance for the immune system, macrophages are consequently at the centre stage of many pathologies with detrimental effects caused by the dysregulation of their functions. Hence, they are a popular target for therapeutics, managing said diseases (4,8–10). In this chapter, we have a closer look at how macrophages develop, how they polarise and activate, how they function with a focus on cytokine production, and their role in pathogenesis, specifically in RA.

1.2.2.1 Macrophage development

Macrophages can arise from hematopoietic stem cells in the bone marrow during myelopoiesis. The stem cells undergo multiple differentiation steps that give rise to the common myeloid progenitors, granulocyte and macrophage progenitors, macrophage/dendritic cell progenitors, and finally, the circulating precursors, monocytes, which then can differentiate into macrophages upon entering peripheral tissues (11). In vitro, this process can be mimicked by cultivating cells from the bone marrow in the presence of macrophage colony-stimulating factor (M-CSF), which we use in our experiments for our bone marrow-derived macrophages (BMDMs) (12). *In vivo* this factor is expressed in specific microenvironments of the bone marrow and in local tissues during the inflammatory response, driving macrophage lineage commitment, and proliferation (13).

While circulating monocytes can contribute to maintaining and replenishing the long-lived, highly specialised TRMs, most originated differently, from three embryonic waves of haematopoiesis. During the first two waves, macrophages originate in the yolk sac from erythro-myeloid progenitors (EMP). The first wave occurs in the yolk sack and gives rise to yolk sack macrophages, also called primitive macrophages, which seed every tissue and give rise to microglia in the brain. The second wave occurs once EMPs seed the fetal liver and result in fetal monocytes, which, upon seeding into tissues, gradually dilute down the primitive macrophages, giving rise to the majority of adult TRMs. The third embryonic wave is mediated by hematopoietic stem cell-derived monocytes in the fetal liver at birth. In most tissues, the embryonic-derived macrophages seem to maintain themselves through their longevity and limited self-renewal. Only tissues with high cellular turnover, such as the heart, skin and gut, likely rely primarily on macrophage replenishment from BMDMs (11).

TRMs acquire additional features and tissue-specific functions in their organ-specific microenvironment and contribute to local tissue homeostasis (14). Examples of specialised TRMs include, among others, microglia in the brain and spinal cord, epidermal Langerhans cells, intestinal macrophages, Kupfer cells in the liver, red and white pulp macrophages of the spleen, alveolar macrophages, peritoneal macrophages, as well as osteoclasts and synovial macrophages in joints. All of them exhibit important tissue-dependent homeostatic roles. Microglia, for example, prune synapses, red pulp macrophages scavenge senescent erythrocytes and recycle heme, peritoneal macrophages regulate gut IgA production, osteoclasts reabsorb bone matrix, and synovial macrophages form protective immunological barriers between synovial connective tissue and the joint cavity, which contains potentially harmful proinflammatory mediators such as bone particles (14–17).

However, Macrophage heterogeneity does not stop at this level. An additional layer can be found in differentiated activated macrophages. Dependent on microenvironmental signals, macrophages can polarised towards inflammatory and anti-inflammatory phenotypes, which will be covered in more detail in the next chapter on macrophage activation.

1.2.2.2 Macrophage activation and polarisation

Differentiated macrophages can display differing activation states depending on the microenvironmental signals to which they are exposed. These states were first discovered in 1970 when interferon (IFN)γ produced by T helper cells (Th)1, was shown to change the phenotype of resting macrophages, increasing their capability to present antigens, produce pro-inflammatory mediators, and phagocytose pathogens (18). This process became known as the classical macrophage activation, and the macrophages were named M1 macrophages based on their connection to the Th1 response, which involves the cytokines TNFα, interleukin (IL)-1β, and IL-6, in addition to IFNγ. Later, an alternative activation pathway of macrophages was

observed, induced by the Th2 cell-associated cytokines IL-10, IL-4, IL-13, and tumour growth factor (TGF)-β, which resulted in an overall anti-inflammatory phenotype. Those cells were consequently named M2 macrophages (19). However, this historically strict classification into M1 and M2 subtypes is an oversimplification of reality. The subtypes are better-considered extremes of opposing polarisation states within a fluid spectrum (20,21).

Nevertheless, these classifications are valuable as they allow for a simplified view and easier description of the observed immunological responses and integration into a nomenclature system. Therefore, we will address the different activation states as M1-like and M2-like. Because we are primarily interested in macrophages during the inflammatory response, we always refer to an activated M1-like form if no information about the subtype is given. Figure 1.2 shows a schematic overview of macrophage polarisation, including activation triggers and secreted proteins.

M1-like polarisation and subsequent functional activation of macrophages are regulated by various surface receptors, including cytokine receptors and PRRs (22). In recent years, more and more innate immune receptors have been identified, which allow for the recognition of a broad spectrum of molecules and surprising flexibility and specificity in the immune response. An important group of PRRs are the toll-like receptors (TLR), transmembrane receptors that can detect extracellular and intracellular PAMPS. To date, more than 13 different TLRs have been identified in Mammalia. Each recognises different ligands, including viral and bacterial DNA and RNA, gram-negative and positive bacterial and fungal surface molecules, and parasites. Besides PRRs, cytokine receptors such as IFNγ- and TNF-receptors contribute to macrophage polarisation and activation. TLRs and cytokine receptors induce a vast range of signalling pathways, such as the nuclear factor kappa-light-chain-enhancer of activated B cells (NF-κB) and MAPK pathways. These signalling pathways then activate different transcription

factors, such as NF-κB and activator protein 1 (AP-1), which lead to the production of inflammatory cytokines, chemokines, and anti-microbial molecules (22). As the MAPK signalling cascades are the main interest of our modelling endeavour, we will describe them in more detail in Chapter 1.3.

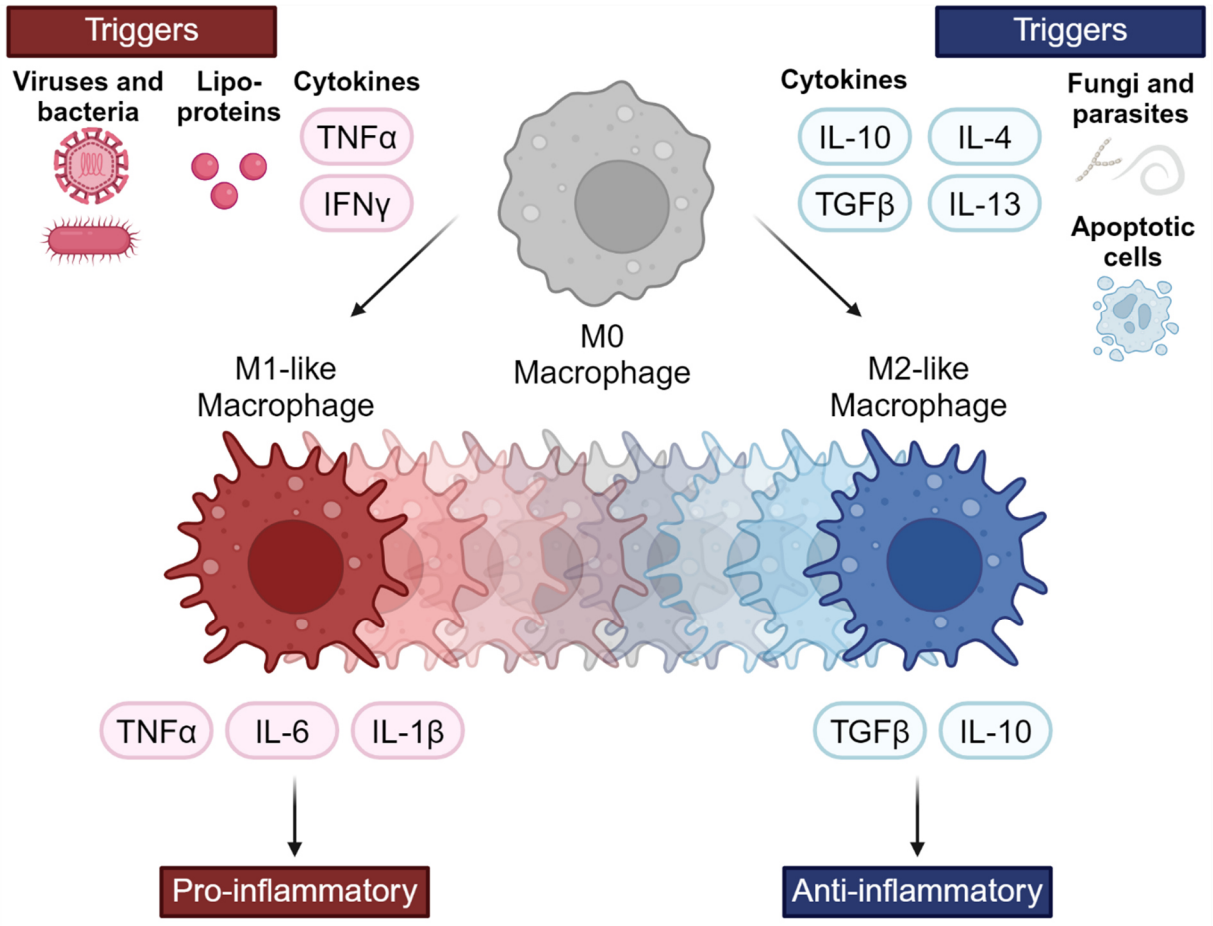


Figure 1.2 Schematic overview of the polarisation states of activated macrophages.

The M1-like polarisation state is induced by various PAMPs, especially from viruses and bacteria, but also lipoproteins and cytokines such as TNFα and IFNγ. The M2-like polarisation state is triggered in response to PAMPs from fungi and parasites, apoptotic cells and various cytokines, including IL-10, IL-4 and IL-13. These polarisation states represent the extremes of a spectrum of macrophage phenotypes. M-1-like macrophages produce pro-inflammatory mediators such as TNF-α, IL-6, and IL-1β, while M2-like macrophages produce anti-inflammatory cytokines, including TGF-β and IL-10. A steady-state macrophage can also be called an M0 macrophage. This image was adapted from Atri et al. and was created using Biorender (7,19).

1.2.2.3 Macrophage function in inflammatory environments

During the inflammatory response, TRMs produce cytokines and chemokines at the site of insult that activate the vascular endothelial cells and recruit other immune cells, among others, circulating monocytes. Adhesion molecules, expressed by activated endothelial cells of the vascular lining, promote adherence of the monocytes, and chemokines induce migration into the surrounding tissue, where they differentiate into MoMs and further migrate to the site of infection or damage. There, upon activation, they perform their primary anti-microbial functions. These include phagocytosis, antigen uptake, antigen presentation, and production of inflammatory mediators (4,8). Macrophages secrete many immune regulatory and effector molecules, including enzymes, complement components, coagulation factors, reactive oxygen species, arachidonic acid intermediates, and cytokines. These molecules can contribute directly to microbial killing, affect the type and strength of immune reactions, and enable tissue repair (4,8). We will focus here exclusively on the latter due to their relevance to our mathematical model.

The classical cytokines produced by M1-like macrophages include, among others, IL-1β, IL-6, IFNβ, and TNF-α. Cytokines are small proteins that can act in an autocrine, paracrine, and/or endocrine manner, thus affecting the local tissue environment as well as distant cells through the circulation. Based on their structure, they can be grouped into families. Of those, the IL-1 and TNF families are relevant to this thesis. The most prominent member of the IL-1 family is IL-1β; we use it in this project as a pro-inflammatory stimulus resulting in IL-1 receptor (IL-1R) signalling through NF-κB and MAPK pathways. IL-1β activates the vascular endothelium and immune cells. This activation contributes to local tissue destruction and increases the extravasation of effector cells.

The members of the TNF family, of which TNF-α is the most prominent one and used as an inflammatory readout in this project, are all critical regulators of the immune response. Both the NF-κB and MAPK pathways promote TNF-α expression. TNF-α activates the vascular endothelium and increases vascular permeability locally. Additionally, it acts systemically, contributing to fever, mobilisation of metabolites, and shock (4,8).

A subgroup of cytokines exhibits specific chemoattractant properties. These were consequently termed chemokines. They are important for recruiting effector immune cells from circulation, including neutrophils and monocytes. Chemokines enable adherence to and exit through the blood vessel wall and direct migration along a gradient towards the side of injury or infection. Macrophages produce a large variety of chemokines, including, among others, C-X-C motif chemokine ligand (CXCL) 1, CXCL2, and CXCL8 (4,8).

In summary, cytokines and chemokines mediate the recruitment and activation of immune cells during the inflammatory response and are thus essential for resolving the triggering infection or injury. However, dysregulation of these inflammatory mediators can have devastating consequences, which we will address in the next chapter about inflammatory diseases.

1.2.3 Inflammatory diseases – pathogenesis and treatment

When dysregulated, inflammation can lead to destructive and pathological consequences. Disruption of the well-orchestrated balance between pro-inflammatory and anti-inflammatory processes can cause insufficient or excessive immune responses. Insufficient inflammatory responses are characterised by repeated infections and impairments in wound healing. In contrast, excessive inflammation typically includes exaggerated activation and disrupted resolution of the inflammatory response. Over time, this contributes to tissue damage and impairment of organ function. The result of ongoing, non-resolving immune responses are

chronic inflammatory diseases, which often either have their origin in autoimmunity or allergy, as it is the case for RA or asthma, respectively (4,23).

RA is a chronic inflammatory autoimmune disease primarily that affects the synovium and can result in irreversible joint destruction and considerable disability affecting 0.5% to 1% of adults worldwide (24,25). RA development is thought to be primarily initiated and driven by autoimmune antibodies, including rheumatoid factor anti-IgG antibodies and anticitrullinated protein antibodies (ACPA) (26–28). Production of autoimmune antibodies is considered one possible way of how tolerance mechanisms of the adaptive immune system can break down and cause autoimmune disease. These autoantibodies react with surface proteins within the synovial tissue and induce an inflammatory response. Consequently, local macrophage-like and fibroblast-like synoviocytes are activated, which induces the production of inflammatory mediators and activation of the endothelium promoting the recruitment and infiltration of further immune cells into the joint. Macrophages, as a major source of inflammatory cytokines and chemokines, are regarded as central to RA pathogenesis. In RA synovium, the macrophage population is heterogeneous in origin and function (29). The three main subsets comprise TRM-like synoviocytes, osteoclasts and MoMs. The pro-inflammatory RA synovial tissue environment leads to the polarisation of MoMs towards an M1-like phenotype (30,31). M1-like macrophages produce inflammatory mediators, likely through TLR-activation, in response to various DAMPs in the RA synovium. ACPAs can also activate macrophages through simultaneous Fc-receptor engagement and TLR4 binding (32,33). Pro-inflammatory macrophages further contribute to RA pathogenesis by the production of matrix-degrading enzymes, expression of receptor activator of nuclear factor κ B (RANK), antigen presentation as well as stimulation of neovascularisation (34). Bone erosion in RA is mainly caused by increased formation and activation of bone-resorbing osteoclasts, a type of TRM, induced by

RANK ligand (RANKL), produced by T cells, and TNF, IL-6 and IL-1 produced by macrophages (35).

The substantial implications of dysregulated gene expression in the pathogenesis of RA and other chronic inflammatory diseases prompted researchers to try identifying the drivers of this dysregulation. This promised a better understanding of the underlying pathogenic mechanism and a potential discovery of novel therapies.

A result of this endeavour is the use of corticosteroids. These are a group of synthetic small-molecule drugs with powerful anti-inflammatory properties with the ability to downregulate the expression of a variety of cytokines, including TNF-α, in monocytes and macrophages. Corticosteroids are broadly used to treat various inflammatory diseases, including asthma, allergies, RA, inflammatory bowel disease, and multiple sclerosis. However, severe side effects can arise when used in high doses or over long periods, thus limiting their usability (36).

During the last 15 years, a new class of treatments has been established based on biological compounds allowing more targeted treatments. In RA, monoclonal antibodies against TNF-α, IL-6R, and IL-1β have been approved. Especially anti-TNF-α antibodies were highly effective and are now considered integral to RA management. However, anti-TNF antibodies also come with their own set of side effects (37).

Targeting cytokines by targeting signalling pathways involved in their production is also possible. One pathway that is already used for the treatment of inflammatory disease is the Janus kinase (JAK) signal transducer and activator of transcription (STAT) pathway. The pathway is involved in receptor signalling of various cytokines, including IL-2, IL-4, and IL-6. However, in 2023, the FDA issued a black box warning due to severe side effects, highlighting the need to develop new anti-inflammatory drugs (38,39).

Another well-researched pathway in RA, which was once considered one of the most promising therapeutic targets, is the p38 MAPK pathway. However, so far, the therapeutic potential has not been harvested (39). A better understanding of the pathway might open avenues for therapeutic exploitation. Therefore, we will present the p38 MAPK pathway in more detail in the next chapter.

1.3 p38 MAPK - an inflammatory signalling pathway

p38 MAPK is a prominent member of the MAPK family, considered an essential regulator of the inflammatory response. MAPK signalling pathways are present in all eukaryotes and are characterised by a three-tiered kinase cascade. This kinase cascade comprises a MAPK kinase kinase (MAP3K), which phosphorylates a MAPK kinase (MAP2K), which again phosphorylates a MAPK by dual phosphorylation of the highly conserved Thr-X-Tyr (X = any amino acid) activation motif, which all MAPK family members share. The identity of the amino acid X is a defining characteristic of each MAPK subfamily. These sequential phosphorylation events allow the amplification and spread of the initial signal within the cell. At the end of this chain, the MAPK phosphorylates its substrates, such as transcription factors, histones and RNA-binding proteins or another layer of downstream kinases, ultimately changing the expression profiles of the cell (40). MAPKs can be subdivided into three main groups based on their sequence homology: extracellular signal-regulated kinases (ERK), Jun-amino-terminal kinases (JNK) and p38 MAPKs (41). ERK1/2 signalling is typically triggered by mitogens and is well established as a cell-cycle regulator (42). JNK has been primarily associated with the M1-like phenotype polarisation of macrophages, while the p38 MAPK pathway is considered a major regulator of pro-inflammatory gene expression (40).

1.3.1 p38 MAPK activation

The p38 MAPK pathway can be activated by various stress-associated stimuli, including hypoxia, oxidative stress, UV irradiation, and osmotic shock (43) but also by inflammatory cytokines such as IL-1β and TNF-α, as well as PAMPs and DAMPs that activate TLRs (40,44,45).

Of those TLRs, TLR4 is of particular interest to us, as its main activator, lipopolysaccharide (LPS), a component of the cell wall of Gram-negative bacteria, is used as one of the primary inflammatory stimuli throughout this thesis. Upon binding of LPS, TLR4 forms a homodimer to activate signalling through its intracellular Toll-IL-1R (TIR) domain (4,46–48). As the name suggests, IL-1β receptors contain the same evolutionarily conserved domain, which, in this case, would be activated through IL-1β binding. For both receptors, TIR initiates downstream signalling pathways by recruiting the adaptor protein MyD88 (49). MyD88, in turn, recruits IL-1 receptor associated kinase (IRAK) 1 and IRAK4 together with the ubiquitin E3 ligase TNF receptor-associated factor 6 (TRAF6), the E2 ligase ubiquitin conjugating enzyme 13 (UBC13) and the cofactor Uve1A. Phosphorylation of TRAF6 by autoactivated IRAK leads then to the generation of a polyubiquitin scaffold, which allows for the recruitment of TAK1 binding protein 1 (TAB1) and TAB2, as well as the MAP3K TGF-β activated kinase (TAK) 1. TAK1 phosphorylation by IRAK constitutes the first step of the p38 MAPK signalling pathway. As a side note, TAK1 also activates the NF-κB signalling pathway (50), and there also exists a MyD88-independent signalling pathway for TLR4, which, however, does not activate the p38 MAPK pathway (4,10,48).

Apart from TAK1, p38 MAPK signalling can be regulated by 8 more MAP3Ks including the mixed lineage kinases (MLKs) dual leucine zipper-bearing kinase (DLK), zipper-sterile-alpha motif kinase (ZAK), thousand and one amino acid 1/2 (TAO1/2), tumour-progression locus 2 (TPL2), the MAPK/ERK kinases 3/4 (MEKK3/4), and apoptosis signal-regulating kinase 1 (ASK1). These MAP3Ks also activate other MAPK signalling pathways, primarily JNK (51). This shows how intertwined and connected the MAPK signalling pathways are. Apart from TAK1, MEKK3 and ASK1 have been reported to be activated by IL-1R and TLR4 activation (52,53). All MAP3Ks mentioned above phosphorylate the MAP2Ks MKK3 and MKK6, which

selectively recognise p38 MAPK. MKK4 has also been described to phosphorylate p38 MAPK under certain circumstances, however, it primarily phosphorylates JNK (54). Two T-cell-specific p38 MAPK activation pathways have been described that involve its autophosphorylation (55,56). On a side note, ERK1/2 are also activated in the context of LPS stimulation (57), which highlights that all of the three main MAPK family members play a role during the inflammatory response. Figure 1.3 shows an overview of the TLR4 and IL-1R-mediated MAPK activation, focusing on p38 MAPK.

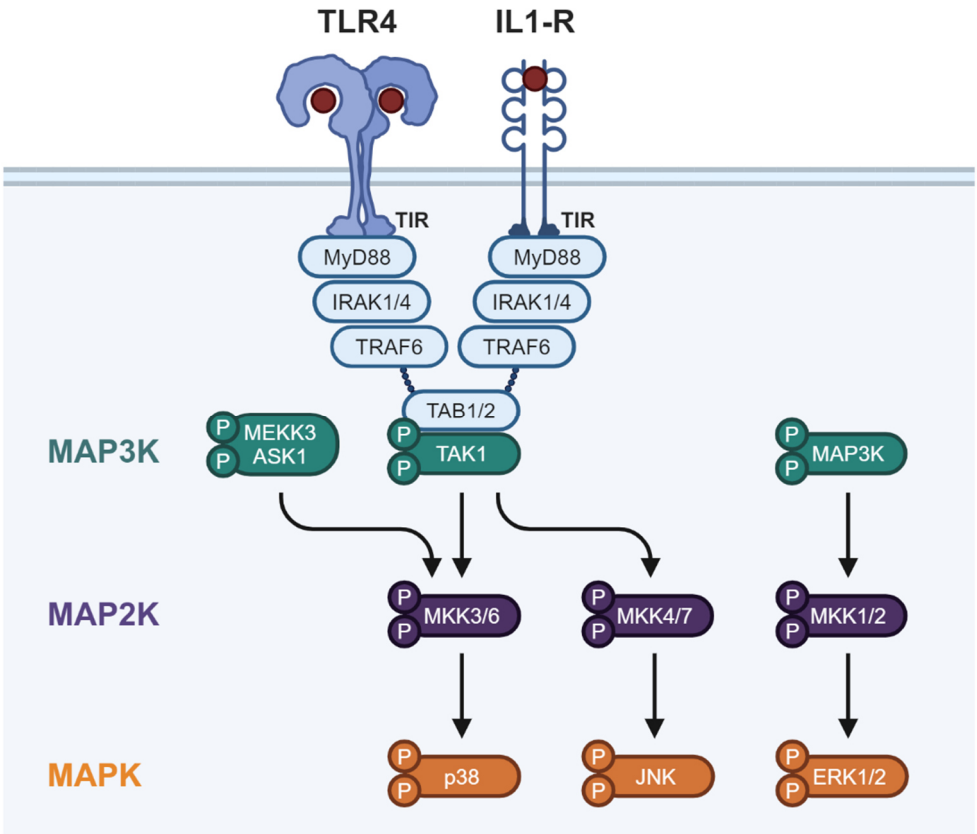


Figure 1.3 Overview p38 MAPK activation by TLR4 and IL-1β.

Upon binding of LPS to TLR4 or IL-1β to IL-1R, the TIR domain activates, allowing recruitment and activation of IRAK1/4 and TRAF6. IRAK1/4 and TRAF activation leads to a ubiquitin scaffold forming, which recruits TAB1/2 and TAK1. Phosphorylation of TAK1 is the first step of the p38 MAPK cascade. TLR4 and IL-1β also activate the p38 MAPK-specific MAP3Ks MEKK3 and ASK1. The MAP3Ks then phosphorylate the MAP2Ks MKK3 and MKK6, which phosphorylate p38 MAPK. TAK1 also activates the JNK cascade through MKK4/7.

TLR4 and IL-1R signalling also activate the ERK1/2 signalling pathway through MKK1/2. The image was created using Biorender, based on the MAPK template by Mina Nashed (7).

1.3.2 The p38 MAPK family

The p38 MAPK family is defined by a Gly in the Thr-X-Tyr MAPK phosphorylation motif and comprises four members which differ in their expression, substrate specificity, and sensitivity to inhibitors: p38α, which is encoded by the *MAPK14* gene, p38β encoded by *MAPK11*, p38γ encoded by *MAPK12*, and p38δ encoded by *MAPK13* (40). Of the four family members, p38α is the best studied and is almost ubiquitously expressed by all cell types. It was identified as the first family member in 1994 and found to be a 38 kDa protein phosphorylated in response to LPS treatment (58). The other three isoforms of the p38 MAPK family, which share around 60% sequence homology with p38α, were identified a few years later (59–62). The importance of p38α, within its family, was highlighted by the mouse p38α knockout mutant, which is embryonically lethal in mice, compared to the remaining isoforms, where knockout mice do not exhibit an apparent phenotype (63–66). In this thesis, we will primarily focus on p38α, and to some degree p38β, because the other two family members are not involved in TTP phosphorylation, which is the central pathway for our mathematical model. Also, these two can be considered mostly redundant in the context of the inflammatory response (67).

1.3.3 Downstream substrates of p38 MAPK

p38 MAPK can recognise more than 100 protein substrates through its common docking domain, which specifically binds to the docking domain or other docking motifs of their substrates (68,69). Those p38 MAPK target proteins include transcription factors, chromatin remodelling agents, structural proteins, DNA/RNA binding proteins, regulatory proteins, and other protein kinases, which again have a multitude of substrates. Downstream kinases of p38 include the MAPK-activated protein kinase 2/3 (MK2/3), mitogen and stress-activated protein

kinase 1/2 (MSK1/2) and MAPK-interacting kinase 1/2 (MNK1/2) (67,70–73). The focus is usually on MK2 and MK3, though, which are considered the most important ones due to their high specificity as a substrate for p38 MAPK and their significance in post-transcriptional gene regulation (71).

Due to the large number of substrates, it is unsurprising that the p38 MAPK pathway plays a crucial role in regulating a broad spectrum of cellular processes. This includes cell survival in response to stress, where p38 MAPK regulates DNA repair through autophagy, cell cycle arrest, and apoptosis (67,74–77). Additionally, mild stress responses, like cell differentiation that require a lot of morphological changes, involve p38 MAPK pathway activation, often initiated by cytokines. Tissues in which p38 MAPK has been shown to exert differentiation control include the bones, adipose tissue, and muscle (67,78–80). The function we are primarily interested in, though, is p38 MAPKs role in inflammation.

As mentioned above, p38 MAPK can directly phosphorylate and activate several transcription factors. Some of these, such as activating transcription factor 2 (ATF2), early growth response protein 1 (EGR-1), STAT1, as well as the members of the ternary complex factor family ETS Transcription Factor 1 (ELK-1) and SRF accessory protein 1 (SAP-1), are major regulators of pro-inflammatory gene expression (81–84). Through ATF2, which forms heterodimers with AP-1 family members, and the ternary complex family, which controls the expression of AP-1 family members, p38 MAPK contributes to the regulation of AP-1, which is, next to NF-κB, the most prominent pro-inflammatory transcription factor (85–87).

The p38 MAPK pathway might also affect the NF-κB pathway through MSK1/2-dependent phosphorylation of histone H3, which modifies chromatin structure and promotes the recruitment of NF-κB to pro-inflammatory promotors (88). Through MSK1/2 but also MK2,

p38 MAPK also activates other transcription factors, such as members of the ATF/cAMP response element binding protein (CREB) family, including CREB itself, which is involved in the transcriptional regulation of cytokine expression, including TNF-α (89–92).

MK2, and to some extent MK3, control pro-inflammatory gene expression primarily on the post-transcriptional level through phosphorylation of RNA-binding proteins, including TTP, which is an important regulator of mRNA stability (93–96). MK3 has a comparable relationship with MK2, as does p38β to p38α. They are closely related and seem to have similar substrate specificity, subcellular localisation, and activity patterns. However, MK3 is expressed at low levels and consequently displays a much lower kinase activity in general (97). Historically, post-transcriptional regulation has often been overlooked in favour of transcriptional regulation. However, RNA stability has been shown to be essential for the expression dynamics of many pro-inflammatory genes and, critically, the resolution of inflammation in later phases of the inflammatory response (98–100). In the following chapters about the RNA-binding protein TTP, we will also closely look at posttranscriptional regulation (PTR) and its role in the inflammatory response.

Apart from its well-documented pro-inflammatory functions, p38 MAPK signalling also regulates feedback mechanisms and, with that, anti-inflammatory gene expression. p38 MAPK has been described to limit TLR signalling and its own activation by phosphorylating TAB1 and/or TAB3, which prevent TAK1 phosphorylation and, subsequently, NF-κB and MAPK signalling (101). Via MSK1/2-mediated phosphorylation of CREB and histone H3, p38 MAPK also regulates the expression of the well-known anti-inflammatory cytokines IL-10, as well as the mRNA destabilizing protein TTP, and the MAPK phosphatase dual-specificity protein phosphatase 1 (DUSP1) (91,102). Specifically, DUSP1 is an important negative regulator of p38 MAPK and JNK activation.

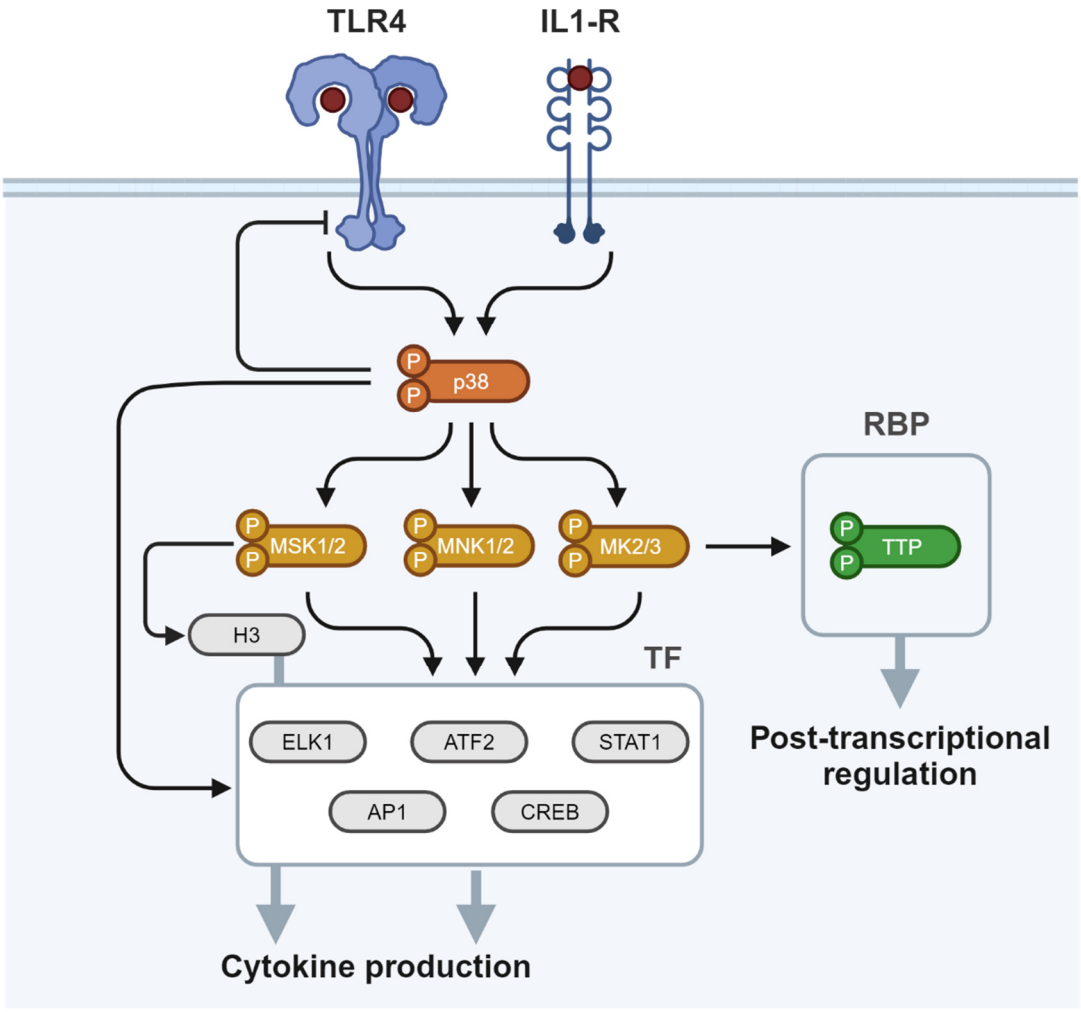


Figure 1.4 Overview of inflammation-related p38 MAPK substrates.

TLR4 and IL-1β activation leads to p38 MAPK phosphorylation through the p38 MAPK kinase cascade. Phosphorylated p38 MAPK has a plethora of substrates, including the kinases MSK1/2, MNK1/2, and MK2/3. These kinases, and in some instances p38 MAPK itself, then phosphorylate transcription factors (TF) and the histone H3, which induces cytokine production. P38 MAPK inhibits its own phosphorylation through phosphorylation of TAB1. Through MK2/3 p38, MAPK also regulates cytokine expression on the post-transcriptional level by phosphorylating RNA-binding proteins (RBPs), including TTP. The image was created using Biorender, based on the MAPK template by Mina Nashed (7).

1.3.4 Regulation of p38 MAPK pathway signalling

The magnitude, duration, and spatial distribution of p38 MAPK activity are tightly regulated to prevent excessive inflammatory responses. This fine-tuning is achieved by various mechanisms, including posttranslational modifications, where many possible modifications can

be introduced, protein interactions, control of subcellular localisation and stability, and deactivation by phosphatases. Some of these mechanisms will be discussed in detail next.

1.3.4.1 Protein interactions

Unphosphorylated p38 MAPK was reported to form a complex with its downstream kinases MK2 (71,103). This complex formation stabilises both proteins and increases pathway specificity by preventing MK2 activation by other non-specific MAPKs (71,104–107). Indeed, some p38 MAPK substrates, such as CREB, are also phosphorylated by MK2, which suggests that the p38 MAPK/MK2 complex might cooperatively phosphorylate at least some substrates (107,108). Consequently, subcellular localised stoichiometry between p38 MAPK, MK2, and other substrates, as well as activators, is likely an important factor determining p38 MAPK activity, specificity, and function (71). MK2, containing a nuclear localisation signal (NLS), is primarily located in the nucleus in resting cells, however, many of its targets are found in the cytoplasm. Consequently, MK2 has been shown to be exported from the nucleus upon phosphorylation by p38 MAPK (109,110). Because of this relationship, MK2-reporter constructs have been used as kinase-translocation reporter (KTR) to measure p38 MAPK activity in live-cell microscopy (111,112). There also have been reports that p38 MAPK might be co-exported with MK2 from the nucleus upon phosphorylation (113), or alternatively, the complex separates before the export of MK2 to the cytoplasm. In this context, p38 MAPK/MK2 complex formation, of course, would require localisation of unphosphorylated p38 MAPK and its phosphorylation in the nucleus. However, the subcellular localisation of the p38 MAPK pathway is not yet properly defined, and there have been contradicting reports for p38 MAPK subcellular localisation (114). For example, Wood et al. and Brand et al. presented evidence of p38 MAPK being in both the cytoplasm and the nucleus in resting cells. Upon phosphorylation at the outer membrane, however, it would translocate to the nucleus (115,116). In contrast, other

publications report that p38 MAPK is primarily located in the nucleus in resting cells and exported upon phosphorylation (113). As different cell types and stimuli were used in these reported experiments, the observed discrepancies might hint at cell type- and stimulus-specific regulation of the subcellular localisation (117).

1.3.4.2 p38 MAPK phosphatases

Tight regulation of the magnitude and duration of p38 MAPK activation is primarily achieved through its dephosphorylation by phosphatases. Depending on their specificity, these phosphatases can be separated into three groups: Tyrosine phosphatases, serine/threonine phosphatases, and DUSPs (67). At least 13 DUSP family members, known in mammalian cells, exhibit substrate specificity for MAPKs (118). Because of this, the terms DUSP and MAPK phosphatase (MKP) are sometimes used interchangeably, although they are not precisely equivalent. *In vitro*, most DUSPs can dephosphorylate multiple MAPK family members, and each MAPK can be dephosphorylated by multiple DUSPs, which indicates some level of functional redundancy (119). Selectivity is likely achieved through expression kinetics and sub-cellular compartmentalization (118,119). *DUSP1*, for example, is characterised as an immediate early gene, which is defined by a rapid and transient increase in expression upon stimulation and has been reported to be primarily localised to the nucleus (120–122), while DUSP6 accumulates slowly over time after stimulation and is localised to the cytoplasm (119,123). An alternative mode of action has been proposed that involves MKPs competing with upstream kinases and downstream substrates about the shared binding site on MAPKs (68,124). Of the DUSP family, specifically DUSP1, DUSP2, DUSP8, DUSP10, and DUSP16 showed preferential binding to p38 MAPK in *in vitro* overexpression studies (125–129). Of these, DUSP1, DUSP2, and DUSP10 have been associated with regulating the innate immune response and inflammation, based on the phenotypes of their knockout mutants (130–132).

Upon LPS treatment, *Dusp2*$^{-/-}$ mouse macrophages showed decreased inflammatory gene expression combined with some reduced p38 MAPK activity and *Dusp10*$^{-/-}$ mice macrophages exhibited increased inflammatory gene expression but no increase in p38 MAPK activity (130,132). In contrast, the function of DUSP1 has been primarily associated with p38 MAPK signalling. DUSP1 knockout (*Dusp1*$^{-/-}$) mice are viable and healthy under sterile conditions (133). However, if challenged with LPS, *Dusp1*$^{-/-}$ mice show significantly increased p38 MAPK activation and serum cytokines levels, including IL-1β and TNF-α, as well as other inflammatory mediators compared to wild-type mice. Consequently, macrophages isolated from *Dusp1*$^{-/-}$ mice likewise exhibited prolonged and exaggerated p38 MAPK activation combined with the overexpression of pro-inflammatory cytokines (118,131,134,135). This lack of negative regulation of the p38 MAPK signalling pathway makes the mice susceptible to sepsis, LPS-induced bone loss, cardiac dysfunction, and lethal endotoxemia (136–139). It further worsens several chronic inflammatory conditions, including experimental colitis, anaphylaxis, and experimental models of RA (140–142). All these observations highlight the importance of DUSP1 regulating p38 MAPK during the inflammatory response. DUSP1 is additionally of particular interest, as p38 MAPK itself, through MSK1/2-mediated phosphorylation of CREB/ATF transcription factors, induces DUSP1 expression (83,102,143,144). Furthermore, p38 MAPK has been shown to regulate *DUSP1* mRNA stability likely through the RNA binding protein TTP (145,146), as well as DUSP1 protein stability and catalytic activity on the post-translational level (124,147). By inducing the expression of its own negative regulator, p38 MAPK initiates a feedback loop that can lead to oscillations in p38 MAPK activity (148).

Apart from p38 MAPK-mediated post-translational modifications, DUSP1 is also regulated by its TLR-dependent acetylation, which promotes DUSP-p38 MAPK interaction and subsequent

inactivation of p38 MAPK. Furthermore, DUSP1 stability is regulated by ERK1/2 and IRAK-M-mediated phosphorylation, which both increase DUSP1 stability by reducing its ubiquitin-dependent degradation, as well as by phosphorylation, through JNK, which reportedly decreases its stability (149–153).

Interestingly, DUSP1 expression has been reported to be upregulated by glucocorticoids, suggesting that at least part of the anti-inflammatory properties of this class of drugs may be mediated through p38 MAPK inhibition (154–156). DUSP1 does not only regulate p38 MAPK but also JNK and, under some circumstances, ERK1/2 activity, which might explain the detrimental effects of long-term p38 MAPK inhibition in clinical trials. When p38 MAPK is continuously inhibited, this effectively removes the important anti-inflammatory regulator DUSP-1 from the feedback loop as well, potentially resulting in JNK and ERK1/2 overactivity. The following section will deliver a closer look at the limitations of p38 MAPK inhibitors in clinical settings. To conclude, outside of the DUSP family, also the Ser/Thr phosphatase protein phosphatase A (PP2A) and several protein tyrosine phosphatases (PTP) have been reported to dephosphorylate p38 MAPK (157–162), with p38 MAPK having again been reported to regulate PP2A expression/activity (163–166). The p38 MAPK regulation presented in this chapter is visualised in Figure 1.5.

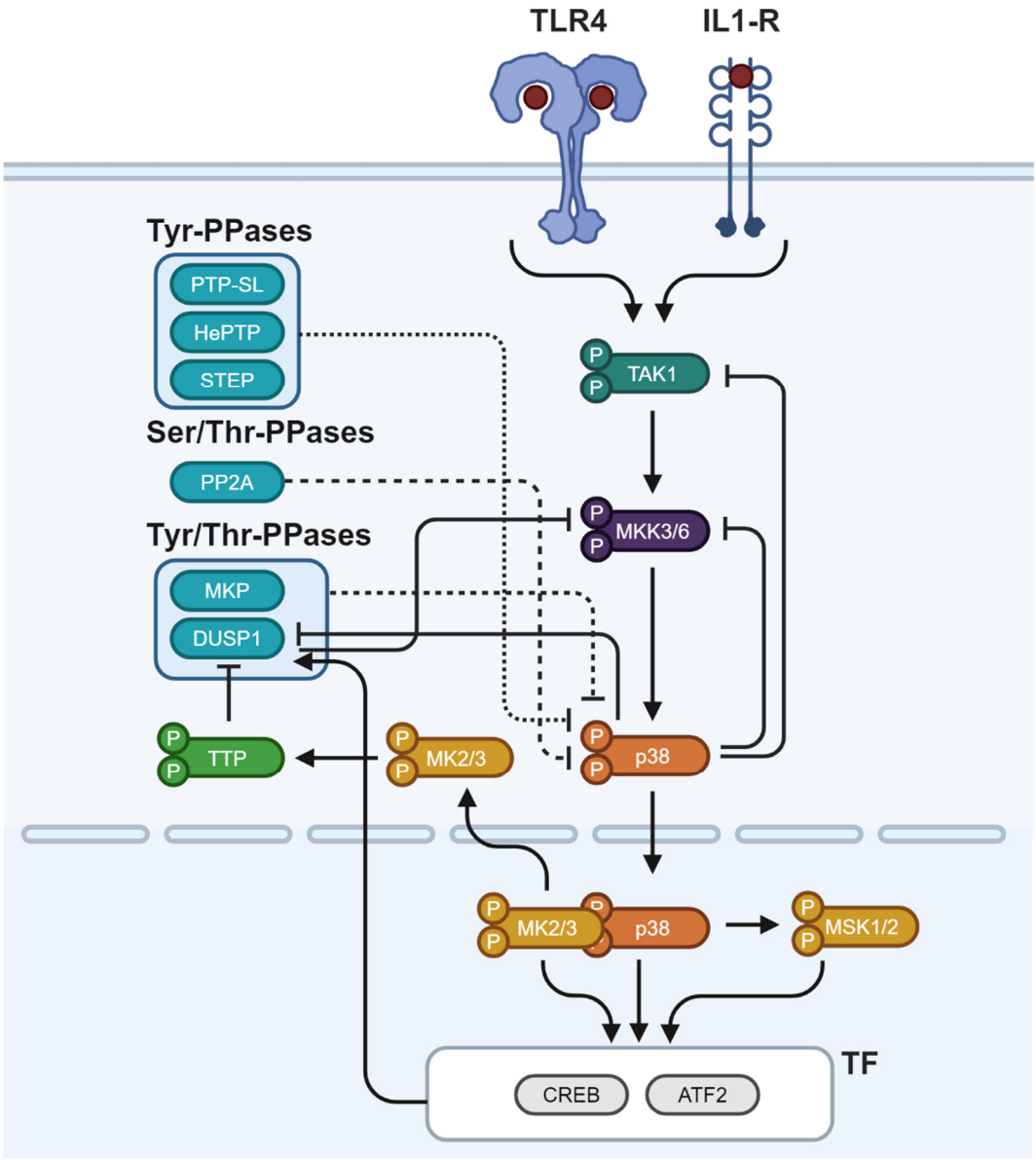


Figure 1.5 Schematic overview of the phosphatase-mediated p38 MAPK pathway regulation.

The Tyr-protein phosphatases (PPases) PTP-SL, HePTP, and striatal enriched phosphatase (STEP), the Ser/Thr-PPase PP2A, and the Tyr/Thr-PPases, which we summarise here as MKP, have been implicated in p38 MAPK regulation through dephosphorylation. Of the Tyr/Thr-PPases, DUSP1 is specifically interesting due to its multi-level interconnectedness with the p38 MAPK pathway. p38 MAPK directly and mediated through MSK1/2 and MK2/3 activates the transcription factors CREB and ATF, which regulate DUSP1 transcription. DUSP1 then dephosphorylates p38 MAPK and, at the same time, limits MAP2K binding. p38 MAPK further regulates DUSP1 expression on the post-transcriptional level via the mRNA-destabilizing protein TTP. p38 MAPK has also been reported to regulate PP2A activity/expression. Translocation of the nucleus leads to interaction with MK2, which phosphorylates TTP upon translocation to the cytoplasm. Additionally, autoregulatory negative feedback loops involving limiting TAK1 activity and MKK6 expression are presented. To reduce complexity, we omitted the

interconnection with the ERK, JNK, and NF-κB pathway and all p38 MAPK-regulatory elements that have not been associated with the inflammatory response in macrophages. The image was adapted from Canovas et al. and generated in Biorender (7,67).

1.3.5 p38 MAPK as a treatment target in disease

Dysregulation of p38 MAPK activity is associated with various inflammatory diseases, including cardiac diseases, cancer, pulmonary disease, neurodegenerative disease, and RA (85,167–169). In RA, strongly activated p38 MAPK has been observed in endothelial cells, fibroblasts, osteoclasts, and macrophages within the synovial tissues (84,170). p38 MAPK activation in RA contributes to cartilage and bone damage by promoting the synthesis of inflammatory cytokines, RANKL, and matrix metalloproteinases (171,172). It further contributes to the inflammatory phenotype by inducing the expression of cell adhesion molecules in endothelial cells (173,174). Consequently, developing p38 MAPK inhibitors was considered a promising anti-inflammatory therapy.

Although many p38 antagonists underwent clinical trials for RA and other inflammatory diseases, all of them failed in the clinics due to multiple challenges, including hepatoxicity and cardiotoxicity, but also lack of efficacy. In some cases, the inhibitor only led to short-term therapeutic success and lost its functionality later (175–178). Nevertheless, new inhibitors with lower off-target effects have been developed since then, and though none of them have been successful yet, phase I and II clinical trials have been ongoing for the last 25 years, expanding to disease areas outside of inflammation, including cancer, cardiovascular and neurodegenerative disease (67). Now, the p38 MAPK-MK2 signalling axis has emerged as a promising drug target, as MK2 has been associated with the regulation of mRNA stability of a plethora of pro-inflammatory mediators through the RNA binding protein TTP (179). Several MK2/MK3 inhibitors have been reported; of those, ATI-450 (also known as CDD-450), which

prevents p38 MAPK specific MK2 activation, showed promising results in phase I clinical trials (39,180–184). Overall, more tailored approaches, focusing on specific cell types or other members of the p38 MAPK signalling pathway, could make it possible to harvest its unused potential for the treatment of inflammatory diseases. To better understand the potential of intervening in the MK2 signalling axis, we will present more information on TTP and its function in the PTR of inflammatory mediators.

1.4 TTP

The RNA-binding protein TTP, encoded by the *zinc finger protein 36* (*ZFP36*) gene, is the best-studied member of the ZFP36 family, which also include ZFP36L1 and ZFP36L2 in most mammals (185). Of the three family members, TTP was described first in 1989 by Varnum et al. under the name TPA-induced sequence 11 (TIS11) as a gene expressed in response to tetradecanoyl phorbol acetate (TPA) (186). They all share a highly conserved tandem cysteine-cysteine-cysteine-histidine (CCCH) zinc finger domain, which binds the cofactor Zn^{2+} and is considered a canonical RNA-binding domain (187,188). Apart from the tandem CCCH domain, as its name suggests, TTP also contains three proline-rich motifs, each consisting of four consecutive prolines (189). It also exhibits conserved N-terminal and C-terminal domains that both have been identified as mRNA decay activation domains (190) as well as an NLS and nuclear export signal (NES) (191). Apart from this, TTP is considered highly unstructured, which has consequences for its stability, as we will explore in the upcoming chapter about post-translational TTP regulation. TTP's importance for regulating the inflammatory response is powerfully demonstrated by the severe pro-inflammatory phenotype of *Zfp36*$^{-/-}$ mice. These mice develop a complex syndrome of arthritis, cachexia, and autoimmunity, which bear resemblance to human disease pathogenesis such as RA and systemic lupus erythematosus. Especially striking was the discovery that treatment of *Zfp36*$^{-/-}$ mice with TNF-α antibodies prevented the development of most symptoms, which established *Tnf* mRNA as one of the primary targets of TTP early on (192). In the following sub-chapters, we will expand our TTP knowledge by exploring its function and regulation.

1.4.1 TTP function

TTP was first considered a potential transcription factor due to its sequence similarity to known transcription factors and its initial description as a nuclear protein in murine fibroblasts (193–

195). However, Experiments performed by Blackshear et al. suggested that TTP is not involved in TNF-α transcriptional regulation (196). The actual function of TTP was revealed by Carballo et al. in 1998, using cells isolated from *Zfp36*$^{-/-}$ mice (196). This publication showed that the *Tnf* mRNA half-life was doubled in LPS-stimulated macrophages isolated from TTP-deficient mice. They subsequently demonstrated that TTP regulates *Tnf* mRNA stability by binding the RNA directly at AU-rich elements (ARE), which are established mediators of RNA instability, within the 3'prime UTR of its target mRNAs (197,198).

1.4.1.1 Target mRNA binding

TTP's mode of action starts by recognizing and binding RNA-specific cis-regulatory elements, the AREs. AREs are nucleotide sequences, typically 50 to 150 nucleotides long, that usually contain multiple, potentially overlapping AUUUA pentamers located in an AU-rich region within the 3'UTR of mRNAs (198). The conservation of AREs was first described in *TNF* mRNA in 1986, together with the observation that AREs are particularly enriched in mRNAs encoding inflammatory mediators (199). In the same year, AREs were established as potent and selective mediators of mRNA degradation (200). Over the years, additional roles of AREs in RNA stabilization, and general RNA processing, transport, and translation were identified (201). Bioinformatics studies provided the estimate that AREs are present in around 7% of human protein-coding genes (202,203). Furthermore, the importance of AREs in immune regulation is demonstrated by the severe chronic inflammatory arthritis and Crohn's-like inflammatory bowel disease developed by mice lacking AREs in the 3' UTR of *Tnf* mRNA (204). TTP and its family members are not the only RBPs recognising AREs and regulating mRNA stability. Other well-established RBPs include AU-rich binding factor-1 (AUF1) and KH splicing regulatory protein (KSRP), which primarily promotes RNA degradation, as well as Human antigen R (HuR), which is mainly associated with RNA stabilization (205–207).

TTP has a high affinity for the minimal ARE nonamer "UUAUUUAUU", but it may also bind to a shortened "UAUUUAU" motif (208,209). The binding is mediated through TTP's tandem zinc finger (TZF) domain, demonstrated by Carballo et al. through mutating the TZF domain and the observation that mutation of the residues within the domain completely abrogated RNA binding (188). A recent paper by Lai et al. showed that mutating the TZF domain *in vivo* led to a phenotype closely resembling that of *Zfp36*$^{-/-}$ mice (210). Hudson et al. published the NMR structure of the RNA-TZF domain interaction of the TTP family member ZFP36L2 (211), describing on the structural level how both ZFP36L2 TZF domains are necessary for high-affinity binding. Although the presence of the TTP target sequence in the 3'UTR of an mRNA is a good first hint, it is not sufficient to identify a physiological TTP target.

A high standard for identifying an actual physiological TTP target was demonstrated for *Tnf* mRNA. Not only did the *Zfp36*$^{-/-}$ model exhibit excessive TNF-α protein levels as one of its major hallmarks, but treatment with anti-TNF-α antibodies suppressed the development of the inflammatory phenotype of this mouse model (192). The causative role of TNF-α was further confirmed by crossing *Zfp36*$^{-/-}$ mice with mice lacking TNF-α receptors, which led to the same outcome as observed for anti-TNF-α antibody treatment (212). These observations were followed by confirmation of TNF-α overproduction in macrophages in *Zfp36*$^{-/-}$ mice, which were associated with increased *Tnf* mRNA levels and mRNA stability (196). *Tnf* mRNA has also been shown to contain the ideal TTP binding motif, and the direct binding of TTP to *Tnf* mRNA has been confirmed by various *in vitro* studies (196).

Another similarly well-established target of TTP is the myeloid cell growth factor *Gm-csf* mRNA (208,213). Apart from these, many new TTP targets have been proposed, with varying levels of data backing them up. An especially useful online tool is the TTP atlas provided by the May Perutz Labs, which contains photoactivatable ribonucleoside-enhanced individual

nucleotide resolution crosslinking and immunoprecipitation (PAR-iCLIP) profiles of TTP wild-type (WT), *Zfp36*$^{-/-}$, and *Zfp36*$^{aa/aa}$ murine BMDMs stimulated with LPS, as well as genome-wide mRNA expression profiles and RNA stability analyses from TTP WT and TTP$^{-/-}$ datasets under the same conditions (214,215). *Zfp36*$^{aa/aa}$ mice will be introduced in detail in the following chapter about post-translational TTP regulation. Among these proposed TTP-target mRNAs, several are relevant for the inflammatory response: *CXL1*, *CXCL2*, *IL-1b*, *IL-2*, *IL-6*, *IL-10*, *IL-12*, *IL-17*, *ZFP36*, *TLR4*, *DUSP1*, *DUSP6* (208,215).

1.4.1.2 TTP-target degradation

Following mRNA binding, TTP promotes the degradation of the bound mRNAs mainly through the recruitment of members of the cytoplasmic mRNA degradation machinery. This way of regulating mRNA stability allows for rapid adaption of the mRNA pool to environmental stimuli, ultimately altering the protein pool and as such the cellular functions.

The cytoplasmic exonucleolytic mRNA decay machinery exerts five types of ribonucleolytic activities, namely deadenylation, decapping, endonucleolytic decay, and 5'-3' as well as 3'-5' exonucleolytic decay. The order and combination of these activities vary depending on the mRNA substrate and cellular environment. The exonuclease-mediated mRNA decay pathway starts with deadenylation, the progressive shortening of the poly(A) tail, which in eukaryotes is primarily mediated by the multiprotein complexes carbon catabolite repression 4/ Ccr4 associated factor 1/negative on TATA-less (CCR4/CAF1/NOT) and poly(A)-nuclease 2 (PAN2)/PAN3 (216,217). Subsequently, the decapping complex is recruited, comprising the decapping protein 1 (DCP1) and DCP2 (218). After hydrolysis of the 5' m7G cap structure, degradation is carried out from the 5' end by the 5'-3' exonuclease 1 (XRN1) and/or from the 3'end by the exosome pathway (219,220).

TTP exhibits a conserved N-terminal and C-terminal domain that both have been identified as mRNA decay activation domains (190). Both domains are required for the recruitment of the deadenylase CAF1 of the CCR4-NOT deadenylation complex through direct binding of the CCR4-NOT transcription complex subunit 1 (CNOT1) and CNOT9 (221–223). TTP has further been reported to recruit the decapping enzymes DCP1/2, the exonuclease XRN1, and exosome-related proteins (190,224,225). To summarise, Figure 1.6 provides a schematic overview of TTP-mediated mRNA degradation.

Another mechanism through which TTP might regulate RNA stability is by promoting processing body (P-body) formation and the recruitment of mRNAs to those structures. P-bodies are well-established, non-membranous cytosolic aggregates of mRNAs and proteins related to mRNA decay and translational repression (226). Enriched proteins include, among others, major enzymes of the 5'-3' decay pathway, such as XRN1, DCP1/2, and CCR4 (219,227,228). Although these proteins are not exclusively located into P-bodies, and the formation of macroscopically observable P-bodies is not required for general RNA decay to occur (229), P-bodies might accelerate mRNA decay by bringing the RNA decay machinery and mRNAs in close proximity to each other. Studies, like one by Chan et al. in 2018, support the idea that active decay might occur within P-bodies, although probably in an RNA-specific manner (230–232). Wang et al. reported that only subsets of mRNAs within P-bodies are destined for degradation, while others even seem to be protected (233). This would also explain somewhat contradicting reports that P-body-associated mRNAs are translationally repressed instead of degraded (232,234). A more integrating model of P-body function by Frank et al. suggests that they form when the decay machinery is working over capacity. According to this model, if high levels of mRNAs are destined for mRNA decay, they are recruited to P-bodies

to allow efficient degradation, and at the same time, to functionally silence them prior to degradation by sequestration of RNAs from polysomes (229).

Independent of the question of whether P-bodies are actual hubs for transcript-dependent RNA degradation or rather translational repression, or both, TTP, as well as other RBPs that regulate RNA stability, co-localise with these RNP granules or even actively contribute to their nucleation (229,235). Additionally, TTP has been shown to localise to P-bodies in its active unphosphorylated form. One mechanism by which it might contribute to their formation was suggested to be by delivering ARE-mRNAs (229,235,236).

Over the years, several roles outside of mRNA degradation have been proposed for TTP, including direct miRNA-mediated mRNA degradation, pre-mRNA splicing, NF-κB inhibition, and inhibition of mRNA translation (208,237–239). However, apart from the latter one, none of them have gathered a substantial body of evidence to be considered validated TTP functions at this point.

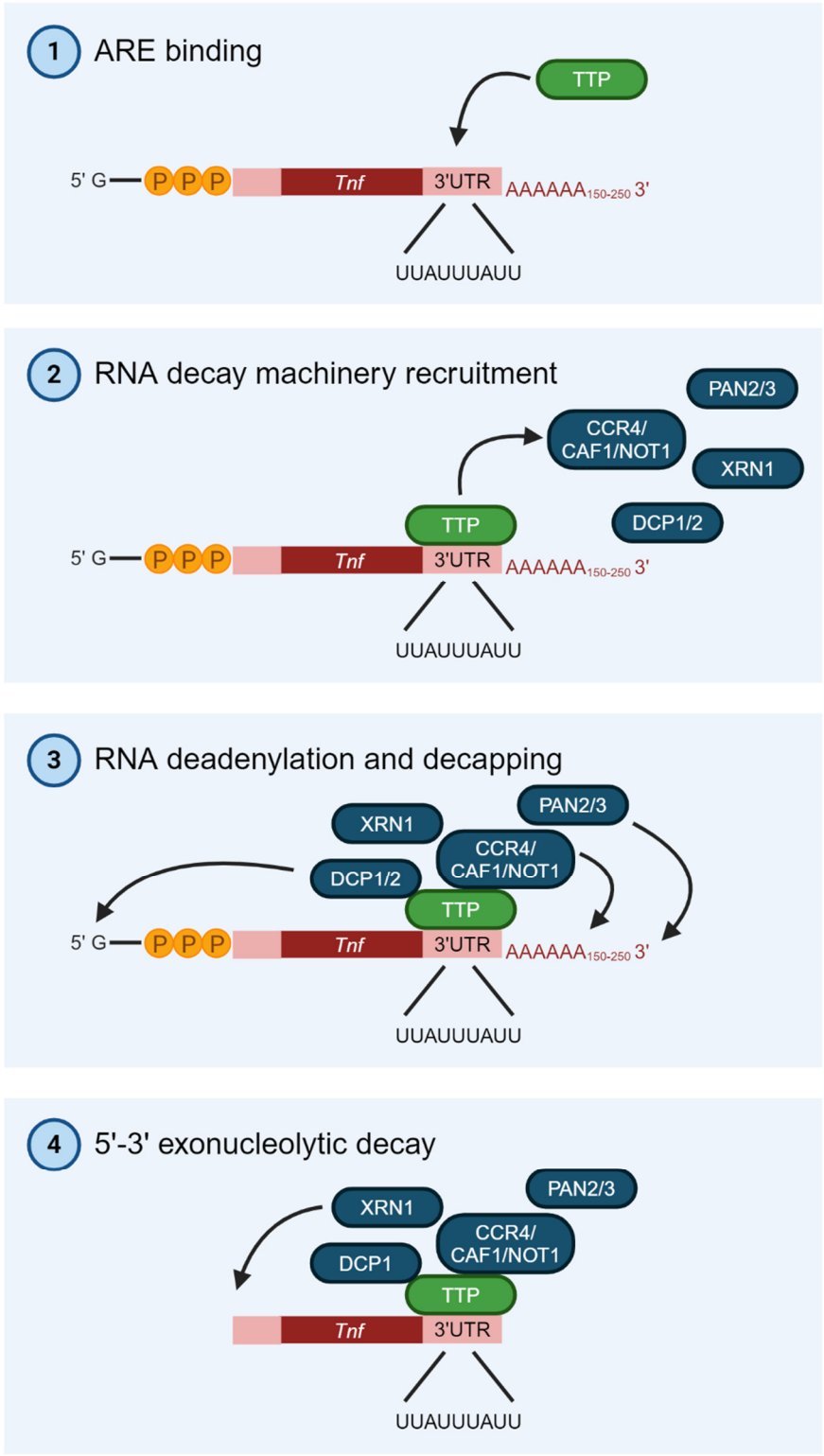


Figure 1.6 Schematic overview of TTP-mediated mRNA degradation.

1) Unphosphorylated TTP recognises, and binds ARE in the 3'UTR of its target mRNAs. 2) Upon binding TTP, members of the RNA decay machinery are recruited by interacting with the CCR4/CAF1/NOT1 complex. 3)

Deadenylation of the RNA through the PAN2/3 deadenylation complex and CCR4/CAF1 deadenylases is followed by decapping through DCP1/2. 4) XRN1 degrades the nucleotides of the remaining mRNA. The image was created in Biorender (7).

1.4.2 TTP regulation

As TTP is crucial for controlling the expression of many pro-inflammatory and immune-regulatory mRNAs, it is no surprise that its own expression and function are highly regulated on multiple levels. One of the major pathways involved is the p38 MAPK-MK2 signalling axis. TTP expression levels can be dynamically regulated not only on the transcriptional level but also on the post-transcriptional level by RBPs and micro RNAs as well as by post-translational modification affecting protein stability, RNA-binding affinity, protein-protein interactions, and subcellular localisation. In addition, it is important to remember that TTP usually does not exist as the sole regulatory factor of its target mRNAs. Multiple RBPs might compete for the same binding sites and directly interact with each other or change the RNA secondary structure and, as such, ARE-binding.

1.4.2.1 Transcriptional TTP regulation

The *ZFP36* gene is 2.5 kB long, including the 5' and 3' UTR, and consists of two exons and one intron. The gene locus occupies around 12 kB on human chromosome 19q13.1. In mice, *Zfp36* is located on chromosome 7 within a linkage group at its proximal end (240,241). TTP falls into the group of immediate early genes, and its mRNA transcription is rapidly and transiently induced by various mitogenic and inflammatory stimuli. The inducibility of TTP is dependent on several promoter elements within its 5' proximal region and transcriptional regulatory elements within its intron. The promoter elements contain binding motifs for transcription factors such as NF-κB, CREB, small worm phenotype and mothers against decapentaplegic homolog 3/4 (SMAD3/4), ELK-1, specificity protein 1 (SP1), EGR-1, and AP2

(242,243). p38 MAPK is involved in transcriptional regulation of TTP via ELK-1, EGR-1, and CREB phosphorylation (89,90,244). The processed mRNA of the *ZFP36* gene is around 1.7 kB in length and is subject to post-transcriptional control mechanisms.

1.4.2.2 Post-transcriptional TTP regulation

The TTP mRNA contains an AU-rich region that controls the rapid turnover of its mRNA. The biological importance of its post-transcriptional control has been demonstrated through a mouse model with deleted AREs in the 3'UTR of TTP, which resulted in the protection of these mice from induction of several inflammatory disease models in mice (245). Furthermore, several miRNAs have been reported to control TTP mRNA stability (246–249). On top of that, TTP performs an autoregulatory feedback loop by binding its own AREs and promoting mRNA degradation (250,251).

1.4.2.3 Post-translational TTP regulation

Post-translational modifications not only allow dynamic regulation of TTP expression by affecting its stability but also its RNA-binding affinity, its ability to recruit the mRNA decay machinery, and its subcellular localisation, thus, its overall activity and function. Phosphorylation is by far the best-studied modification of TTP. Especially kinase cascades such as the p38 MAPK pathway allow rapid signal amplification and attachment of di-anionic phosphates to TTP, which can again be rapidly removed by respective phosphatases.

TTP is extensively phosphorylated *in vivo* and *in vitro* cell models, with at least 14 phosphorylation sites confirmed in mice with corresponding sites in human TTP (93,252). A complete list can be viewed on the PhosphoSitePlus website (253). This circumstance is readily detectable in Western Blotting (WB), resulting in multiple bands of TTP upon treatment of cells with inflammatory stimuli. The function of most of these phosphorylations is still unknown.

The two best-studied phosphorylation sites are Ser-52 and Ser-178 in mice and Ser-60 and Ser-186 in humans. Both are targets of MK2 and have been shown to affect various aspects of TTP function. MK2-mediated phosphorylation increases TTP protein levels by stabilizing the protein and preventing its proteasomal degradation through the default unstructured protein degradation pathway (93). This stabilization is impressively demonstrated in *Mk2/3*$^{-/-}$ mice, where TTP levels are strongly reduced, but the remaining TTP is highly functionally active. This leads us to the next function of MK2 phosphorylation, namely the inactivation of TTP. MK2-mediated TTP phosphorylation reduces its binding affinity to ARE-mRNAs and impedes Ccr4/Caf1/Not complex recruitment. The data are, however, somewhat contradictory regarding the reduction of binding affinity to AREs. While some groups observed TTP binding effects (212,254,255), others specifically reported no phosphorylation-dependent effect on ARE binding and the presence of TTP in polysomes (93,256–258). Though the exact mechanism is not clearly determined, it is undisputed that MK2-phosphorylation inhibits TTP activity and stabilises the protein. These processes seem to be at least partially mediated by the 14-3-3 adaptor protein that has been shown to bind TTP upon phosphorylation (93,208,256,259). Recently, a transgenic mouse strain has been developed, in which Ser-52 and Ser-178 of the endogenous TTP gene were substituted with alanine, rendering these positions non-phosphorylatable by MK2. Consequently, TTP is unstable and inducible only in low levels but highly active. Overall, these mice exhibit no apparent phenotype and are fertile. Intriguingly, these mice display a strongly attenuated response against LPS and are protected from inflammatory disorders such as endotoxemia and experimental RA, highlighting the physiological relevance of the p38 MAPK-mediated regulation of TTP (260). Macrophages isolated from *Zfp36*$^{aa/aa}$ mice exhibit reduced secretion of TNF-α. However, double KOs of MK2/MK3 combined with *Zfp36*$^{aa/aa}$ secrete even lower levels of TNF-α, hinting towards

additional mechanisms apart from Ser-52 and Ser-178 phosphorylation. One potential mechanism could be the third TTP residue that has been identified to be phosphorylated by MK2: Ser-316 in mice. This phosphorylation site lies within the conserved C-terminal RNA decay activation domain of TTP and has been shown to contribute to the recruitment of the CCR4-NOT deadenylase complex together with Ser-52 and Ser-178 (93,261). Of course, MK2's potential role in TTP CREB-mediated transcription might also be involved. Finally, the serine-threonine phosphatase PP2A has been identified to target TTP and to act as an antagonist to the p38 MAPK pathway by activating and destabilizing TTP. PP2A has been reported to compete with 14-3-3 for TTP binding, which protects it from dephosphorylation by PP2A. PP2A comprises a core heterodimer of the catalytic subunit PP2A-C and the regulatory subunit PP2A-A as well as an interchangeable third subunit PP2A-B. PP2A-B has several isoforms that compete for binding of the heterodimer and allow for substrate specificity. This is important to us, as our group are currently working on identifying the PP2A-B isoform responsible for TTP recognition. This would allow us to understand the dephosphorylation dynamics of TTP better, as expression of the isoforms varies throughout the inflammatory response. Furthermore, regulation of PP2A expression and activity has been associated with p38 MAPK activity (163,164,166,262).

Another important feature of TTP regulation is its localisation. p38 MAPK pathway activity regulates the shuttling of TTP between the nucleus and the cytoplasm as well as localisation to P-bodies and stress granules (SG). TTP levels have originally been described in fibroblasts to be low in unstimulated cells and primarily localised to the nucleus (194). At the same time, cellular stimulation with mitogens leads to its rapid CRM1-dependent translocation from the nucleus to the cytoplasm (187,263), which is mediated by its N-terminal NES sequence (191). Translocation of TTP to the cytoplasm has also been associated with its phosphorylation and

14-3-3 binding (193,264). Due to its NLS and NES, TTP is thought to undergo constant nucleocytoplasmic shuttling (191). However, in macrophage cell lines and primary mouse macrophages, TTP has been shown to be primarily cytosolic (196,263,265). Brook et al. later showed nuclear localisation of TTP in macrophages upon treatment with protease inhibitors and where *Zfp36*$^{aa/aa}$ overexpressor mutants were utilised (266). However, a colleague recently tried to reproduce these results in a less artificial environment without overexpression of TTP and was unable to detect TTP in the nuclear fraction of LPS-treated macrophage cell lines and primary cells using WB (personal communication, unpublished). Regardless, the functional relevance of nuclear localisation still needs to be clarified. It potentially could serve as a protective function, as pro-longed TTP activity has been shown to promote apoptosis, or a not yet identified nuclear functions in transcription, alternative splicing of pre-mRNA splicing, or premature RNA degradation (238,267).

TTP has also been reported to locate into P-bodies and SGs in a phosphorylation-dependent manner (229,268–270). However, there are reports that TTP might localise to P-bodies independent of its phosphorylation status (268). MK2 phosphorylation-dependent 14-3-3 binding has been shown to prevent TTP association with SGs (259). TTP has also been shown to promote the transfer of ARE-containing mRNA into P-bodies and the communication between these and SGs. The theory is that unphosphorylated TTP selects translationally stalled RNAs from SGs and promotes their degradation in P-bodies.

Although p38 MAPK is necessary, it is insufficient for the complete inhibition of TTP function, which is not surprising considering the large number of reported TTP phosphorylation sites. In *ZFP36*$^{aa/aa}$ mice, the affinity for deadenylases in the presence of okadaic acid, a PP2A inhibitor, is reduced, hinting towards additional phosphorylation sites affecting TTP stability. An additional kinase, ERK, has previously been indicated in regulating TTP stability and

localisation (266), with Ser-220 (murine) being proposed as a potential phosphorylation site of ERK2 (193). In fact, combined ERK and p38 MAPK activity has been demonstrated to be sufficient for completely inhibiting TTP-mediated TNF-α mRNA decay. Apart from phosphorylations, two ubiquitinations and one methylation site have also been reported in TTP. However, no functional contribution of these modifications has yet been elucidated.

Another means of regulating the activity of an RBP, such as TTP, is by directly changing the availability of cis-regulatory elements. This includes mechanisms that change the length of 3'UTR, as it is the case for TTP-mediated NLRP3 regulation, or secondary mRNA structures (271–275). Additionally, RBPs can competitively bind the same motif, where the best-documented example is the competition between TTP, KSRP, and the RNA-stabilizing protein HuR (276).

The pathway complexity renders it challenging to maintain a coherent picture estimating the effects of the p38 MAPK pathway on the dynamic regulation of TTP and its target mRNAs. Figure 1.7 attempts to create an overview of most TTP regulatory elements described in this chapter. One approach which either allows exploration of the full complexity of the pathways involved or their step-by-step dissection and reduction to the most crucial elements and these elements' individual contributions to the pathway is the mathematical modelling of biological systems. In the next chapter, we will explore the fundamentals of mathematical modelling in the context of biological systems and present how other researchers used it to understand the inflammatory response better.

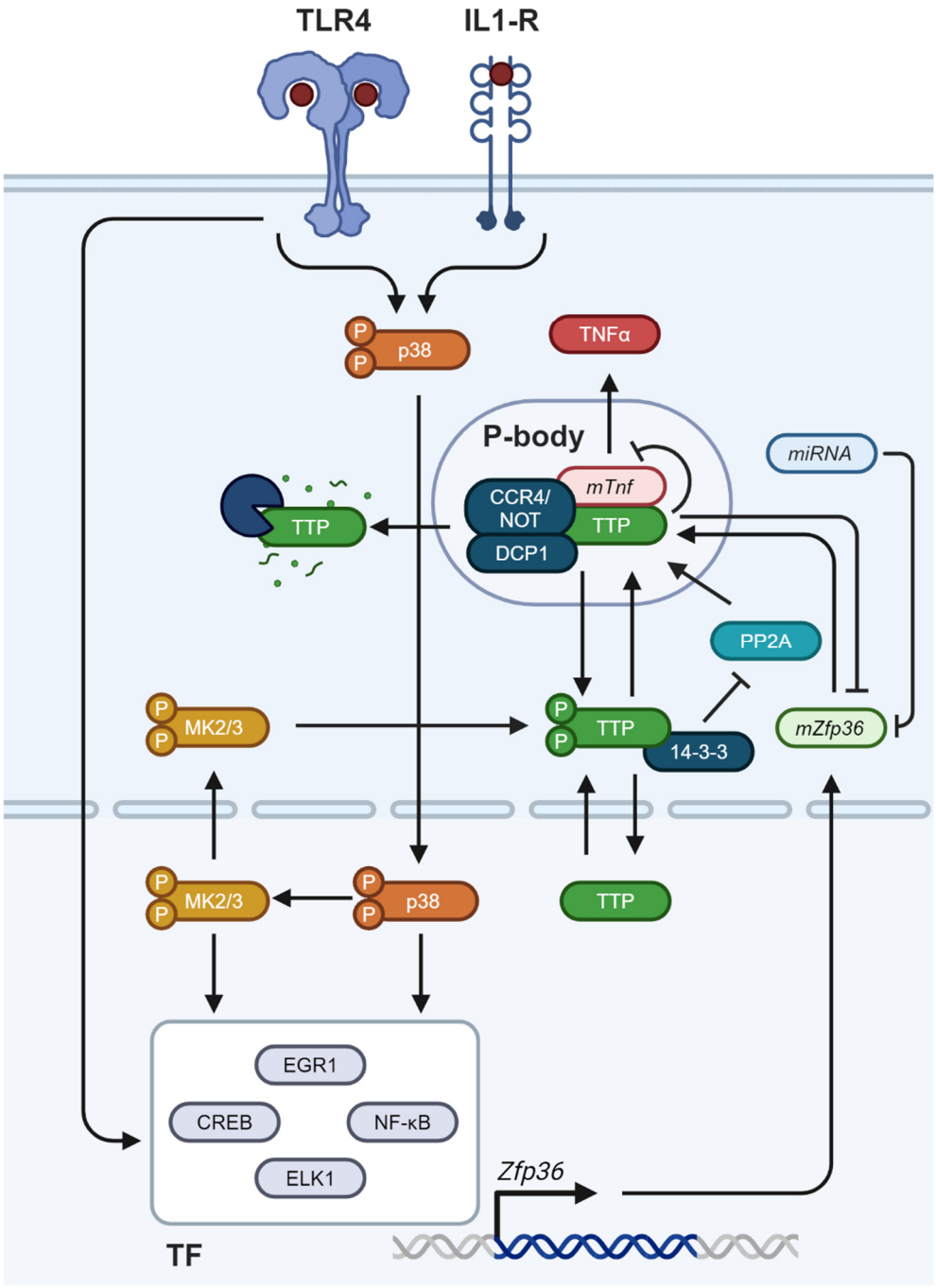


Figure 1.7 Schematic overview of TTP regulation.

TTP transcription is regulated by various TFs, including NF-κB, EGR1, CREB, and ELK1. Inflammatory cytokines and PAMPs activate PRRs, such as TLR4, and/or cytokine receptors, such as IL-1R, which activate NF-κB and p38 MAPK signalling pathways. Phosphorylated p38 MAPK translocates into the nucleus, where it phosphorylates its downstream kinase MK2, and together, they phosphorylate the TFs EGR1, CREB, and ELK1. On the post-transcriptional level, Zfp36 mRNA is regulated through miRNAs and RBPs, which includes TTP itself. Unphosphorylated TTP protein locates to P-bodies and mediates mRNA degradation through interaction with the cytoplasmic RNA degradation machinery, specifically the CCR4 NOT deadenylase complex and the

decapping protein DCP1. Unbound, unphosphorylated TTP shuttles between the nucleus and the cytoplasm, is highly unstable, and becomes rapidly degraded via the default unstructured protein degradation pathway. Phosphorylation of TTP by MK-2, which translocates to the cytoplasm upon phosphorylation to p38 MAPK, and binding of 14-3-3, protects TTP from degradation and limits its dephosphorylation through PP2A. However, phosphorylation of TTP also renders it inactive by preventing its interaction with the mRNA decay machinery and potentially binding to its target mRNAs. The image was created in Biorender (7).

1.5 Mathematical modelling of signalling pathways during inflammation

Mathematical models could be described as a simplified representation of reality expressed in mathematical language. Combining the abstract model with empirical experiments and integrating data allows for real-world applications and prediction of system behaviour. In the scientific process, comparing experimental data with model simulations, in case of discrepancies, can reveal missing components, lead to the rejection of a hypothesis, and direct future experimental designs. Once a model is established, perturbations, such as drug simulations, genetic mutations, or disease states, can be quickly introduced and analysed, allowing for testing new hypotheses. Furthermore, computer simulations of the model permit the exploration of purely theoretical or elaborate and costly experimental designs. Finally, mathematical models can be used to better understand complex pathways by highlighting interactions that might be otherwise overlooked due to their complex nature (277). Despite all these potential benefits of mathematical modelling, some biologists may be hesitant to apply this valuable tool. Breaking down the modelling process and understanding the individual components of utilised equations can improve accessibility. Therefore, this chapter will focus on exploring the main principles of building a mathematical model and some previously published models describing the p38 MAPK-TTP signalling axis.

1.5.1 The modelling process in systems biology

Numerous approaches and methods are used in the modelling process, and the resulting models can take many forms, depending on the biological system they describe. They can range from describing a specific biological observation with only a few simple mathematical equations to large, complex networks of hundreds of equations. Algorithmic improvements, together with the increase in computing power in recent years, allowed for the widespread application of mathematical modelling approaches. The description of increasingly complex phenomena, to

the point that whole-cell models seem to be more now a question of time and effort than feasibility (278). However, complexity brings along its own set of challenges. Often, it is favourable to focus on identifying the simplest possible depiction of the biological process, which still reveals all features to answer a specific set of questions. Consequently, how a model is constructed relies primarily on the goals and purposes of the model. A great introduction to this topic is provided in the book "A First Course in Systems Biology" by Prof. Eberhard O. Voit, which's structure is used for the explanations here. Independently of the specific biological question, according to Voit, the modelling process can be roughly divided into five phases (279, p. 22): The goal setting and exploration phase, 2) the model selection phase, where the model type is determined, 3) the model design phase, comprising the definition of model components and interactions, design of the equations and estimation of rate constants within the model, followed by 4) the model analysis and diagnosis phase and finally 5) the model application phase.

1.5.1.1 Goal setting and initial exploration

The first step of the modelling process is to set the goals and purpose for the model and answer questions regarding the preferred degree of complexity, available contextual information, data needs, and availability. Once the goals are clear, one important question is which scale for the model is most appropriate. The scale can range from individual chemical interactions of small molecules, individual cells, and human organs to whole ecosystems. Additionally, a relevant time scale for the model needs to be defined. Biochemical system models can span several organizational scales, such as genes, proteins, and cell-to-cell interactions. However, adding too many organizational scales early in the modelling process can increase the number of unknown parameters significantly leading to models, which less accurately depict the biological system at hand, potentially limiting their predictive capabilities.

One of the main determinants of the appropriate model scale is data availability. If data is scarce compared to the complexity of the model, over-fitting of the data can occur, which means that the model may be great at simulating the original data set used to calibrate the model. However, it becomes unreliable if the scenario is altered slightly. A similar problem arises if the available data has a high experimental noise level. The "gold standard" for mathematical modelling is numerical data from total quantification experiments. This data type allows comparability between experiments across time and even between research groups. It is quite an exciting thought that research data generated worldwide could be combined directly into mathematical models if this standard were implemented. Nevertheless, prevalent qualitative and semi-quantitative data can provide valuable input about the overall behaviour of model components and potential restraints (279). For this project, we had the opportunity to design our experiments to fit our mathematical model and vice versa and develop the model and the experimental plan alongside each other.

1.5.1.2 Model selection

In the model selection phase, the appropriate type of model and its overall structure are determined based on the previously determined goals and data availability. A commonly used array of decisions can help define what kind of model works best.

The first decision to make is whether a mechanistic (also called explanatory model) or a black box model is preferable. These two extremes represent how detailed the model needs to be to fit the predefined goals. A black box model simply connects one observation with another without addressing the why of the relationship. An explanatory model, on the other hand, connects an observation directly to its biological processes. While explanatory models provide more insight, they are typically more complex than black box models and require more input.

The next decision must be made between using a static versus a dynamic model. The underlying question is whether the biological process of interest changes over time or not. In static models, one explores only the dependencies of the model components, which can be very useful in large network models. In a dynamic model, one explores how these components change over time. For dynamic models, another decision needs to be made regarding whether one is interested in continuous or discrete time scales. This decision is essential, as it determines the type of equation used, again determining the type of mathematical analysis available later. Typically, differential equations are applied for continuous models, while discrete models usually require iterative recursive maps.

The next consideration includes the question of whether the model should assume that the model components are spatially distributed or rather homogeneous. A typical example of heterogeneous distribution of model components is protein distribution between several subcellular compartments, such as the nucleus and cytoplasm. Most model components have some type of spatial distribution; however, if this property is not essential to the outcome of the model, it is often easier to omit this fact. Including some form of approximation like this into a model is essential as, although depicting the whole reality is desirable, it is principally not achievable.

Following the decision about spatial distribution, one chooses between open and closed system models. Open models have some external input from or release output into the environment, while closed models have neither of these characteristics.

Finally, one needs to consider if a deterministic or stochastic model is more appropriate. Deterministic models assume that all information is completely known, and consequently, once all numerical settings are defined, all future outcomes are defined. This model type ignores

random features such as biological fluctuations and experimental noise. Experimental noise can be visualised, though, by including confidence intervals in the computational simulations of a deterministic model. Stochastic, also called probabilistic models, add randomization features to the model structure. This model type is more accurate than the deterministic models because biological data always contains variability and uncertainties. However, adding those probabilistic or random aspects into the equations can complicate downstream applications like parameter estimation, as established computational toolboxes might not allow for this type of equation (279).

1.5.1.3 Model design

Once the type of model is decided on, the model design process starts, which includes the definition of the main model components, its equations as well as the parameter estimation.

System Components

Model components classically include dependent and independent variables, processes and interactions, signals and process modulations, and parameters. Variables in this context represent biological entities of interest, which can be single entities, like individual cells, but also a pool of entities, such as a concentration of proteins. A variable is considered dependent when it changes its value depending on an external input or another variable. On the other hand, one speaks of an independent variable if this is not the case. Processes and interactions typically either involve a variable or connect the variables within the system. An example would be the degradation of a protein pool or protein phosphorylation. Parameters comprise numerical characteristics of the model, such as kinetic rate constants, e.g., protein degradation rates. Parameters stay constant during a specific computational simulation and are highly specific to the observed biological system and environment.

The formulation of a model typically starts with drawing a model diagram and establishing lists of all the model components. This allows us to bring the information into an assessable structure, facilitating the later writing of the model equations. In these model diagrams, variables are drawn as nodes, which are connected through edges, depicted by an arrow, representing the flow of material. The material flow typically happens at a specific rate, which represents the parameter of this process. Additionally, models might contain a flow of information, which does not affect variables directly but rather the processes they undergo, for example by increasing or decreasing the rate of protein degradation. For this, a different type of arrow is used that connects a sender variable with the edge, connecting two variables, or more specifically, their process parameters. Figure 1.8 shows a simple phosphorylation chain induced by an external signal to exemplify these features. It consists of the dependent variables P_1 and P_2, with P_1 being the unphosphorylated and P_2 being the phosphorylated protein species, the external stimulus and independent variable S, and the phosphorylation rate φ_{P1} and the dephosphorylation rate ρ_{P2}. Usually, but not shown for this example, four lists are created alongside the model diagram including dependent variables, independent variables, interactions, and parameters.

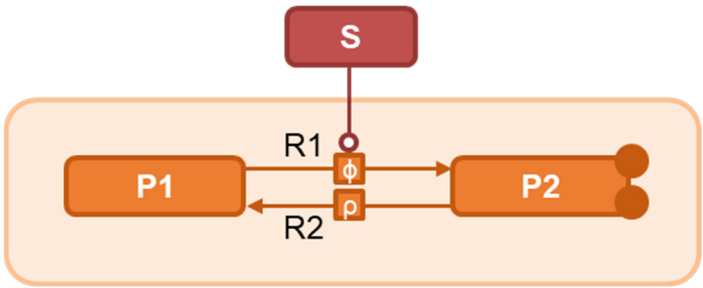


Figure 1.8 Model diagram of the exemplary phosphorylation chain.

The graphic summarises the model components included in the exemplary phosphorylation chain, how they relate to each other, and the main reactions involved. This overview was then used to formulate the model equations 1.1 to 1.2. The key dependent variables P_1 and P_2, and the independent variable S are represented as nodes. Coloured

circles on the nodes mark phosphorylated protein species. Arrows, also called edges in this context, indicate the flow of material between variables and represent the main reactions within the model numbered R1 to R2. The parameters are represented as small squares on the reaction arrows labelled with the Greek letters φ or ρ referring to the specific type of reaction, namely the rate of phosphorylation and dephosphorylation, respectively.

Model equations

Once the model diagram and the component lists are established, the information needs to be translated into equations according to the previously chosen model structure. We will use the example from the previous chapter and the model structure we will use throughout this thesis to exemplify this process here. As a model structure, we chose an ordinary differential equation (ODE) model, which is mechanistic, dynamic, continuous, spatially homogenous, open, and deterministic. The reason why we chose this model structure will be laid out in Chapter 3.2.2. In an ODE model, each dependent variable is described by its own differential equation, describing its change over time. We also base the description of the model processes on the principles of general mass action kinetics. The use of this principle in modelling nonlinear dynamic biological systems models originates from biochemical systems theory, a well-established modelling framework originally designed to estimate enzyme interactions accurately without limiting mathematical analysis. In practice, the principle of mass action kinetics entails that the terms in each equation comprise a product of the parameters and all dependent and independent variables involved in the specific process. By summing up all individual reactions that affect a specific variable, we receive a representation of how this variable changes over time. In our example, we have two processes: the phosphorylation of P_1 at the rate φ_{P1} in response to stimuli S and the constant dephosphorylation of P_2 at the rate ρ_{P2}. The concentration of P_1 decreases if it is phosphorylated and increases when P_2 is dephosphorylated and vice versa. Translated into equations, this results in the following equations:

$$\frac{dP_1}{dt} = -\varphi_{P1}{}^{*}S^{*}P_1 + \rho_{P2}{}^{*}P_2, \quad (1.1)$$

$$\frac{dP_2}{dt} = +\varphi_{P1}{}^{*}S^{*}P_1 - \rho_{P2}{}^{*}P_2, \quad (1.2)$$

with the initial conditions $P_1(0)=P_10$ and $P_2(0)=P_20$. Here '*' represents a multiplication sign, which is introduced for improved readability of the equations.

Two main approaches are used to solve ODEs: analytical and computational. Analytical methods involve solving the ODEs in terms of the symbolic parameters (and therefore, progress can be made without needing their specific values), but this quickly becomes impossible for ODEs that accurately capture complex biological behaviours. Computational simulations require numerical values for the parameters, and the ensuing simulations allow visual (as well as numerical) evaluation of the model behaviour, which makes models more easily accessible to a broad audience. For qualitative analysis, a nominal parameter set and initial conditions can be chosen through trial and error to match our expectations or mimic available semi-quantitative or qualitative data. These numerical values can then be used to simulate the data using computational tools like MATLAB. Using qualitative model simulations allows for various possibilities to explore the model structure, how it behaves in different environments, and if the model can simulate the system as expected. This process can help identify if model structure changes need to be made early on. However, to get a model with reasonable real-world predictive capabilities, the initial concentrations and parameters must either be measured directly or, if this is not feasible, estimated from other datasets (279).

Parameter estimations

Parameter values can be obtained in many ways. The parameter estimation process is rarely straightforward and often comprises the bottleneck in mathematical modelling. One can discriminate between two main approaches: bottom-up and top-down. These constitute two

extremes of the parameter estimation process, but most approaches lie in between. In a bottom-up estimation, parameter values are measured individually for each system component and process. An example would be measuring the maximum phosphorylation rate φ_{P1}, the dephosphorylation rate ρ_{P2}, and initial concentrations of the non-phosphorylatable protein P_1 and the phosphorylated protein P_2 directly. The bottom-up approach has traditionally been used in biological system models and has previously dominated the field. However, it often fails for various reasons that are not entirely understood. For example, data obtained *in vitro* in artificial environments, such as extracellular measurement of kinase activities, is often so artificial that they cannot be directly transferred into cellular systems or whole organisms. Additionally, due to their large number, identifying each parameter individually is a work-intensive, costly, and slow procedure (279).

Consequently, the computation-heavy top-down approach is on the rise. For this approach, the dependent variables of the model are measured under different conditions or time points. In our previous example, this would be the concentration of the total protein (P_1+P_2) and phosphorylated protein P_2 over a relevant time span, potentially with different stimuli profiles and concentrations or with inhibitors present. In the top-down estimation of nonlinear models, the data, together with the symbolic equations, are then entered into an optimisation algorithm, which uses a search algorithm iteratively to determine a parameter set that minimises the difference between the model and the experimental data (279). This process is computation-heavy compared to the bottom-up approach but allows for the measurement of the readout of the variables from within its biological system. Also, the data obtained in this process contains information about connections within the system that are not deducible when individual measurements are performed in the bottom-up approach.

While tidy formulae exist for estimating parameters for linear systems (e.g. via the least squares method), no such formulae exist for nonlinear systems such as those used in this thesis. Furthermore, the model may be non-identifiable, i.e. it is possible that two different sets of parameters give identical simulations and residual error, and they might not even be the best possible fit to describe the data, as often multiple non-optimal solutions exist (279 p.142). Balsa-Canto et al. established a MATLAB toolbox named AMIGO2 and an iterative model identification process that aims to help with the problems of top-down parameter estimation of nonlinear models that will be described in more detail in Chapter 1.5.2 (280,281).

1.5.1.4 Model validation and application

After a parameter set has been estimated, and as such, the model calibrated, one can analyse the quality of the estimation by quantifying the model's goodness of fit to the experimental data or visually comparing model dynamics.

To test if the now calibrated model can describe the biological system at hand, one can test how well the model simulation can describe new data sets. Here, experimental data generated using, for example, inhibitors or mutant mouse models introduces perturbations into the system and allows one to explore if the underlying model assumptions are correct in varying circumstances. If this is not the case, re-evaluation of the assumptions and refinement and extension of the model structure becomes necessary. This process is important and valuable as it allows one to find knowledge gaps or fallacies in one's understanding of the biological system, which can inform future experiments. If the model structure is altered, one can compare the new and old models quantitatively with each other using mathematical post-analysis tools as they are, for example, implemented in the AMIGO2 toolbox (280,282).

After some extensions and refinements, and once the quality of the parameter estimation is sufficient so that the model can simulate different model perturbations reliably, we can finally apply the model for its intended use. One common academic use of modelling is exploring the design and operating principles of the biological system. Asking questions like, "Why has the biological system evolved in this way and not differently?" allows for exploring different biological design elements and why one is better suited than the other (279). For example, one could ask what the benefits of three-tiered kinase cascades are, a principle widespread in mammalian cells, compared to single-level, two-level, or higher-level kinase cascades. Another often-used application explores how to reach an optimal state or avoid undesired states, for example, in the context of disease treatment and development or optimisation of biotechnological processes. For these purposes, single- and multi-objective dynamic optimisation approaches can be employed to identify the optimal combination of changes required to reach one or multiple predefined goals (283). Computational optimal experimental design procedures are another means of applying mathematical models, especially in the day-to-day life of a lab-based biologist. This process can also be part of the iterative parameter estimation process, as it allows for the determination of experimental design that generates high-precision, information-dense data while minimising the complexity and cost of the experiments. Once the model is validated, the expected outcomes of experiments can also be explored *in silico* through simulations.

The last two applications in optimal control and optimal experimental design are also implemented into the AMIGO2 toolbox, which will be described in the next chapter. Of course, the modelling process does not end here. Together with our understanding of biological systems, the mathematical model continues to grow and change, aiding us in the process by compiling our knowledge in an easily accessible, surveyable, and adaptable way.

1.5.2 Optimal model identification approach by Balsa-Canto

Balsa-Canto and Banga published an iterative model identification procedure for nonlinear biological models, with parameter estimation at its centre (281). For their process of model identification, they assume that during the modelling process, instead of one single model, many competing model variations exist or come into existence over time, which vary in some detail of how the biological system is mathematically represented. The goal of the model identification process is, therefore, not only to estimate a parameter set which best fits the data but also to identify which model variation is the best to do so. Although we will not use all these aspects within this thesis and instead focus primarily on their approach regarding parameter estimation, the overall process provides valuable insights into the complete modelling process, analysis methods, and application of biological system models. Their model identification process aims to allow parameter estimation with the maximum accuracy while providing solutions for the most common issues with nonlinear parameter estimation. This process is necessary due to the previously described challenges of nonlinear model parameter estimation, including problems with non-identifiability, overfitting, and local non-optimal solutions.

The optimal model identification approach involves the following steps: 1) Structural identifiability analysis. This step evaluates if the model structure enables us to identify a unique value for each parameter, assuming ideal experimental conditions. Combined with the global ranking of the model parameters according to parametric sensitivities, this allows for the refinement of the model structure while obtaining important information for parameter estimation. These two analysis methods will be described in more detail in Chapter 3.2.4. 2) *A-priori* practical identifiability: This step allows us to examine if unique parameter values can be identified given a specific experimental design. (necessary since it is rare in practice to be

able to generate all the data one needs) 3) Optimal experimental design: We have mentioned this principle briefly as a potential future model application in the previous chapter. It is implemented to obtain information-dense datasets for parameter estimation while limiting experimental costs. 4) Parameter estimation using local and global optimisation algorithms. 5) *A-posteriori* practical identifiability: This step allows for the quantification of the quality of the parameter estimates while comparing multiple models.

Figure 1.9 gives an overview highlighting the connection of each of the steps. It depicts the iterative nature of mathematical modelling, introduced by refinements and extensions of the model over time.

To us, the most valuable property of this publication by Balsa-Canto et al. is that they combined all these steps and more into a free MATLAB toolbox named Advanced Model Identification using Global Optimisation (AMIGO), enabling any researcher with access to MATLAB to use the approach for their projects (280). The applications used within this thesis are described in detail within their respective Material and Method chapters.

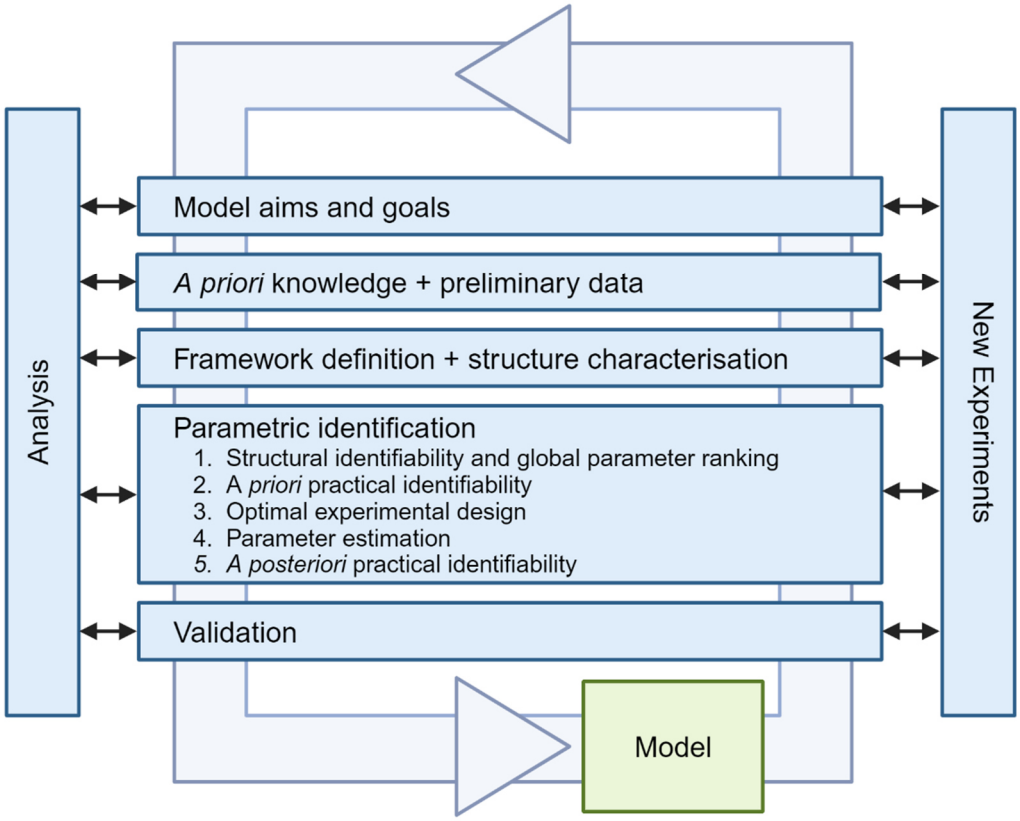


Figure 1.9 Overview of the iterative model building process.

Model building starts with the definition of the aims and goals of the model. The model structure is then established based on a priori knowledge and preliminary data. Next, the parameters may be estimated by fitting the model to experimental data. For this purpose, structural and practical identifiability a priori, as well as parametric sensitivities, can be determined to guide this process. With the help of optimal experimental design, one can decide on an experimental plan to obtain data for the parameter estimation process. Once the data has been obtained, parameter estimation can be performed. This leads to a first working model that needs to be validated with a new set of experiments. In most cases the validation step reveals deficiencies in the model structure. If this is the case, a new model structure and experimental design need to be planned and executed. This process is then repeated until the validation phase is satisfactory and the model goals are achieved. This image was adapted from Banga et al. using Biorender (7,284).

1.5.3 Examples of biological systems models in inflammation

In this chapter, a selection of previously published models describing the p38 MAPK signalling pathway and TTP regulation will be presented. Examining existing models can help identify whether the planned model is relevant and extends existing knowledge. For our p38 MAPK-TTP model, two p38 MAPK models, one published by Tomida et al. and one by Kulawik et al., were especially influential and inspired our model design upstream of TTP, as well as our experimental design, and the overall aims of this thesis.

1.5.3.1 p38 MAPK pathway models

Considering the role of the p38 MAPK pathway in developing inflammatory diseases, it is unsurprising that a whole battery of models exists describing various aspects of this pathway.

Tomida et al. published a p38 MAPK ODE model based on live-cell microscopy data of IL-1β stimulated HeLa cells expressing a p38 MAPK KTR. The model describes an oscillatory activation pattern of p38 MAPK with cell-to-cell heterogeneity, introduced through the DUSP1 inhibitory feedback loop (148). Zhang et al. later examined the effect of time delays in this model by introducing delay differential equations and analysed the oscillatory properties in more detail (285). Oscillations are a common pattern in the modelling of biological systems, often introduced through delayed inhibitory feedback loops, and have been described for various inflammatory signalling pathways including ERK1/2 and NF-κB (286–288). Figure 1.10 displays the core data that forms the basis of the model of Tomida et al., as well as their published model diagram and an example for their simulations. We were intrigued by the model and the potential effects these oscillatory patterns might have on TTP expression, activity, and function. Consequently, we decided to explore potential TTP oscillatory activation patterns as a goal of this thesis.

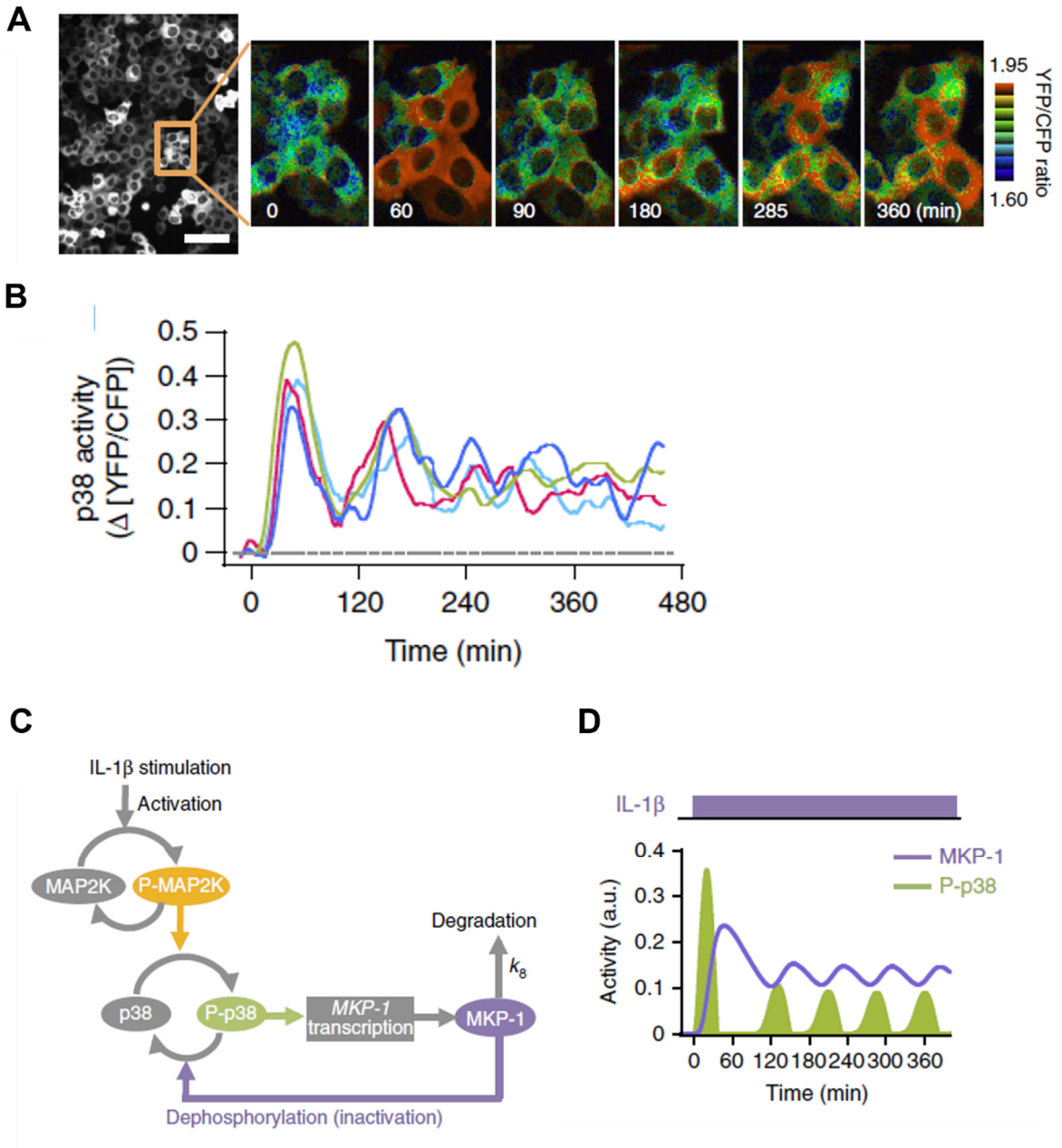


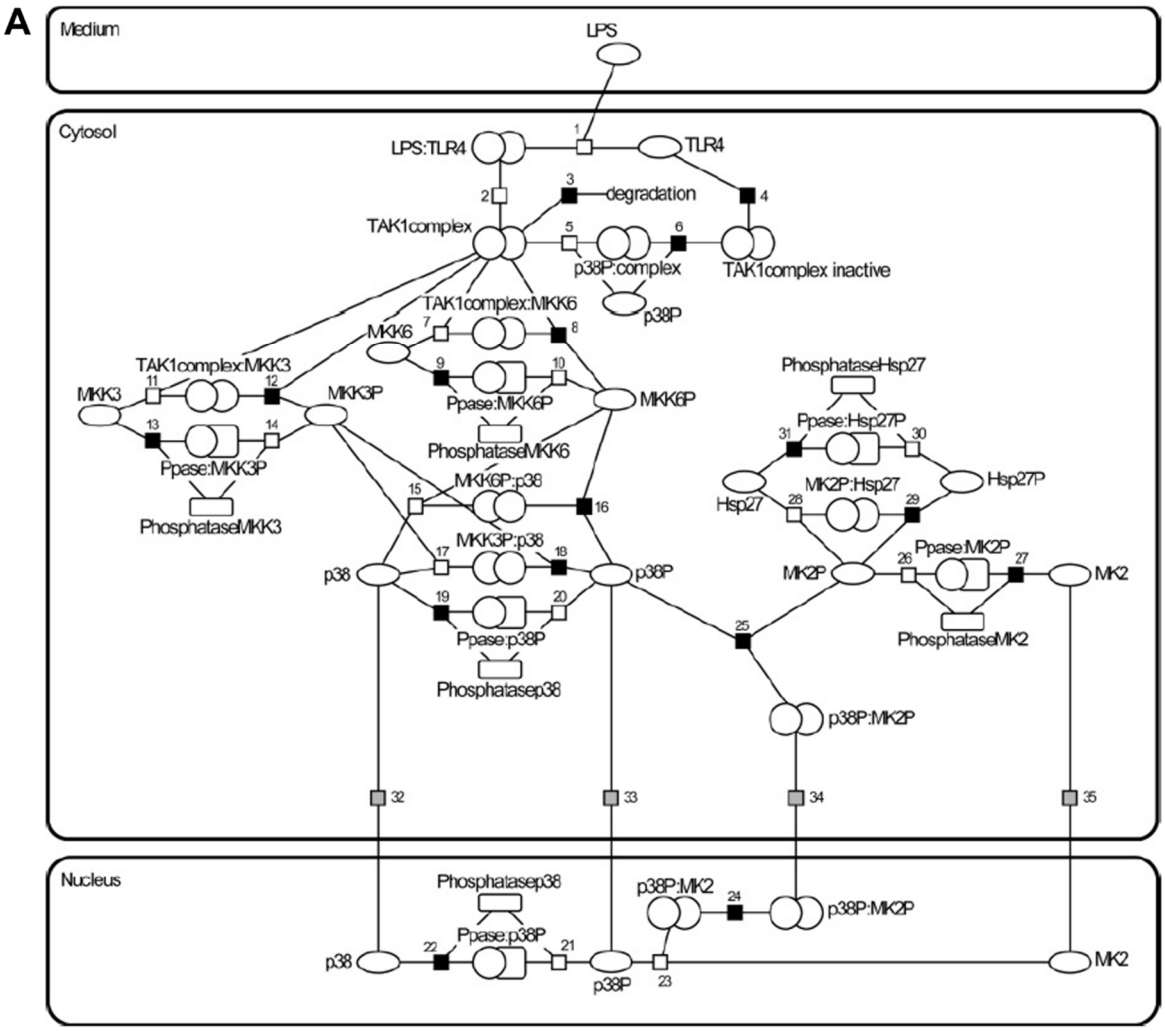
Figure 1.10 Mathematical model of p38 MAPK activation with oscillatory dynamics by Tomida et al.

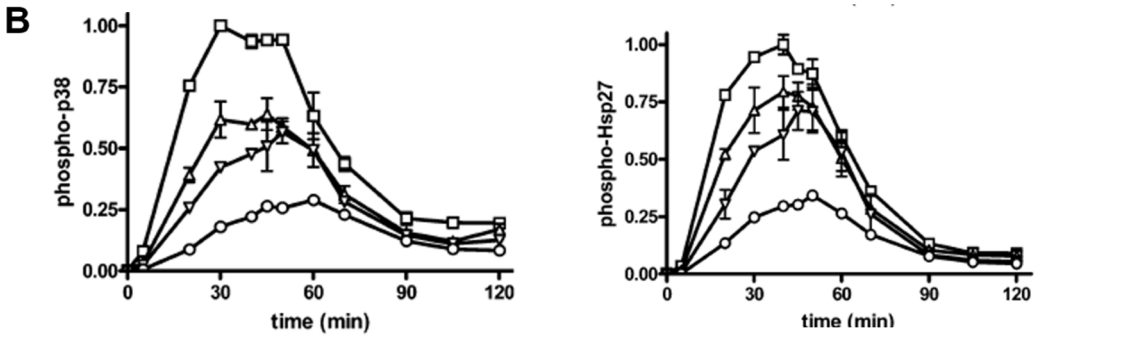
A) Microscopy images of HeLa cells expressing a p38 MAPK activity reporter stimulated with IL-1β. B) Measured p38 MAPK activity in individual cells. C) Model diagram of the p38 MAPK model published by Tomida et al. D) Model simulation of p38 MAPK and MKP-1 activity. The images were obtained from the original publication (148).

The main limitation of the p38 MAPK model by Tomida et al. lies in its purely qualitative nature, as only nominal parameters were implemented, which limits its predictive capabilities and applicability in future experimental design and hypothesis testing. Two models that overcome this limitation are published by Hendriks et al. and Kulawik et al., both describing validated p38 MAPK dynamic models, including parameter estimation using total quantification data (289,290). As mentioned, total quantification numerical data is considered the highest standard in mathematical modelling, making the data reusable and comparable between different experiments and experimental methods. The main limitation of the p38 MAPK model by Tomida et al. lies in its purely qualitative nature, as only nominal parameters were implemented, which limits its predictive capabilities and applicability in future experimental design and hypothesis testing. Two models that overcome this limitation are the ones published by Hendriks et al. and Kulawik et al., which both describe validated p38 MAPK dynamic models and include parameter estimation using total quantification data (148,289). As mentioned previously, total quantification numerical data is considered the highest standard in mathematical modelling, as it makes the data reusable and comparable between different experiments and experimental methods.

Hendriks et al. created their p38 MAPK model using data from differentiated U937 cells, a human monocyte cell line, stimulated with varying LPS concentration (289). They aimed to test whether the commonly used argument that improved knowledge of signalling dynamics using mathematical modelling delivers on the often-implied promise that this knowledge enables the design of more precise, efficacious, and safe medicines. They defined drug discovery-related questions such as: What are optimal drug targets and modes of inhibition, and are there opportunities for co-drugging? Their model contains the complete three-tiered kinase cascade of the p38 MAPK pathway, including TAK1, MKK3, and MKK6, p38, as well as MK2, with

heat shock protein 27 (Hsp27) phosphorylation as the readout for TNF-α expression. All the named components are included individually in their unphosphorylated and phosphorylated form and additionally as interaction-complexes. They also included different subcellular localisations, which required partial differential equations. Of all these components, the model considers their complex formation and dissociation rates, their activation and deactivation rates, and, if applicable, nuclear import and export rates, which results in over 50 parameters (Figure 1.11 A). The parameters of this highly complex model were estimated using the following data: The initial concentrations were measured using total quantification WB for all main components. Only the concentration of p38 and Hsp27 phosphorylation was measured throughout the inflammatory response in a semi-quantitative manner using ELISA (Figure 1.11 B). Consequently, most of their parameters are, as they themselves noted, only poorly estimated, which results in a so-called "sloppy" model (291). While the quality of the parameter estimation is a limiting factor, nevertheless, their inhibitor design and application of their model in drug discovery (Figure 1.11 C) were inspiring and influenced the long-term goals for the application of our model.


A
Medium
LPS
Cytosol
LPS:TLR4
TLR4
degradation
TAK1complex
p38P:complex
TAK1complex inactive
p38P
TAK1complex:MKK6
MKK6
Ppase:MKK6P
MKK6P
TAK1complex:MKK3
MKK3
MKK3P
Ppase:MKK3P
PhosphataseMKK3
PhosphataseMKK6
MKK6P:p38
MKK3P:p38
p38
p38P
Ppase:p38P
Phosphatasep38
PhosphataseHsp27
Ppase:Hsp27P
Hsp27P
Hsp27
MK2P:Hsp27
Ppase:MK2P
MK2P
MK2
PhosphataseMK2
p38P:MK2P
Nucleus
Phosphatasep38
p38P:MK2
Ppase:p38P
p38
p38P
MK2


B
phospho-p38
time (min)
phospho-Hsp27
time (min)

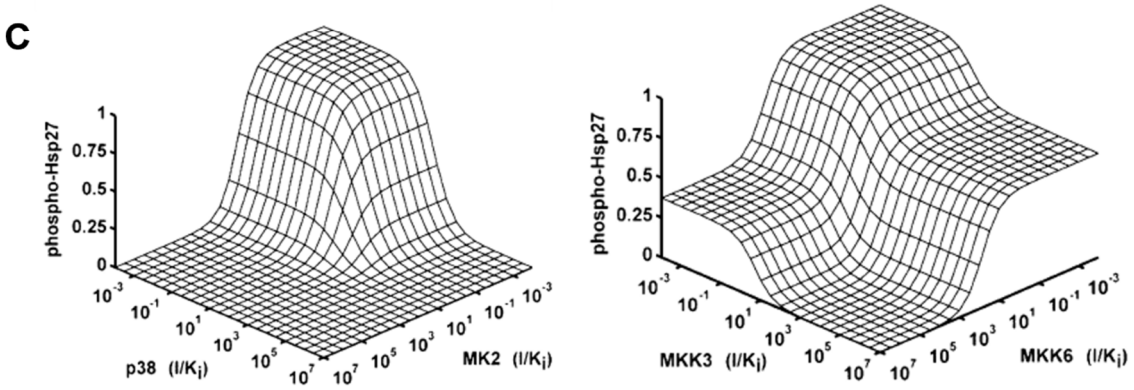

C
phospho-Hsp27
p38 (I/Ki)
MK2 (I/Ki)
phospho-Hsp27
MKK3 (I/Ki)
MKK6 (I/Ki)

Figure 1.11 Mathematical model of LPS-dependent p38 MAPK-pathway activation by Hendriks et al.

A) shows the model diagram of the LPS-induced p38 MAPK model published by Hendriks et al. B) shows PMA-differentiated U937 cells stimulated with varying concentrations of LPS for 120 min. Phospho-p38 (left) and phospho-Hsp27, as a placeholder for TNF-α (right), were measured. C) shows the simulation of co-drugging experiments of MK2 and p38 MAPK inhibitors (left) and MKK3 and MKK6 inhibitors (right). As readout, HSP27 expression levels were used. The images were obtained from their original publication (289).

Kulawik et al. developed a p38 MAPK model based on total quantification WB in BMDMs and hepatocytes in response to varying concentrations of IL-1β (290). Their model included p38 MAPK and MK2, both as unphosphorylated and phosphorylated species, and MKP as a placeholder for all p38 MAPK phosphatases (Figure 1.12 A). All upstream signalling is condensed in the stimulus-dependent phosphorylation rate of p38. For total quantification of total and phosphorylated p38 and MK2 (Figure 1.12 B and C), they used *in vitro* phosphorylated recombinant protein, purified from *E. coli,* and determined its phosphorylation percentage using mass-spectrometry. MKP concentrations were not measured. They estimated their parameters using large high-quality data sets and used p38 MAPK and MK2 inhibitor data to validate their model. This experimental design is of a very high standard for mathematical modelling and heavily inspired us to attempt a similar structure and approach for our p38 MAPK-TTP model.

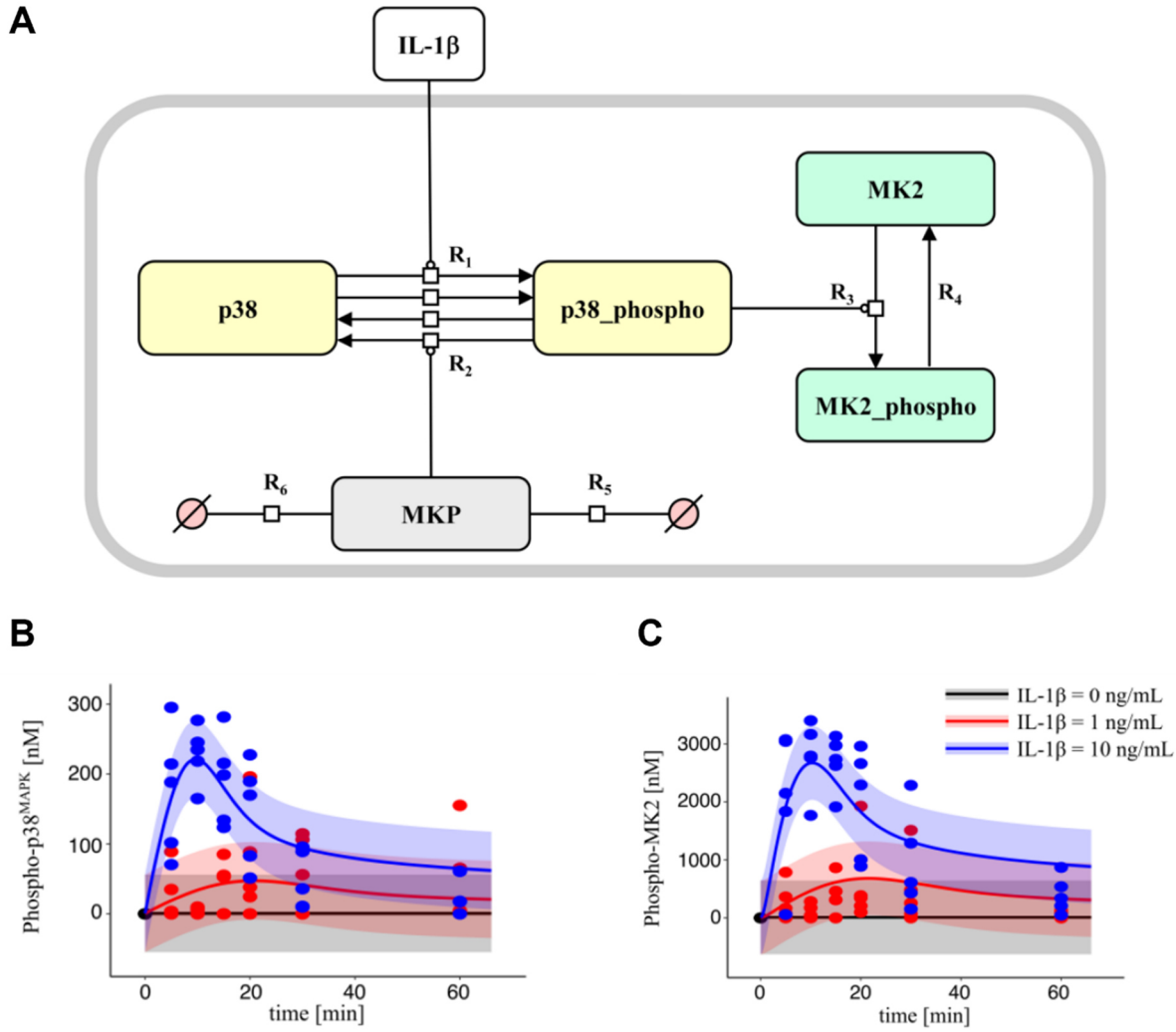


Figure 1.12 Mathematical model of IL-1β-dependent p38 MAPK/MK2 activation by Kulawik et al.

A) Model diagram of the p38 MAPK ODE model published by Kulawik et al. B) and C) show expression kinetics measurements of phosphorylated p38 MAPK and MK2 in BMDMs for different IL-1β concentrations (points) together with the simulation of the calibrated model (solid line). The images were obtained from their original publication (290).A) Model diagram of the p38 MAPK ODE model published by Kulawik et al. B) and C) show expression kinetics of phosphorylated p38 MAPK and MK2 in BMDM for different IL-1β concentrations (points) together with the simulation of the calibrated model (solid line). The images were obtained from their original publication (290).

1.5.3.2 TTP models

According to our knowledge, only a few mathematical models focus on TTP itself. By examining these existing TTP models we ensured that our planned model is novel and extends on existing knowledge.

We found one qualitative ODE model by Ronkina et al. exploring the effect of MK2-dependent *de novo* synthesis of TTP on system behaviour and resulting TNF-α levels (180). While this model perfectly fits the specific purpose, it does not quantitatively cover TTP dynamics.

Fähling et al. explored the regulation of hypoxia-inducible factor 1 (HIF-1) by TTP using three static models based on concepts of modular response analysis to find an explanation for the observation that *ZFP36* mRNA expression positively correlates with HIF-1 targets (292). Here, modular response analysis was used to evaluate the effects of perturbations on a network by looking at the effect of said perturbation on the regulatory strength between two adjacent nodes within the network (293,294).

Another qualitative dynamic model of TTP has been proposed by Aslam and Zaheer (295). This model contains *ZFP36* mRNA, degraded *ZFP36* mRNA, unphosphorylated TTP, and phosphorylated TTP, as well as *TNF* mRNA, degraded *TNF* mRNA, and TNF-α protein. They defined 14 equations describing biochemical reactions within this pathway and estimated nominal parameters through trial and error for computational simulations. They proposed a feedforward and a feedback loop for both TTP and TNF, which they explore in their publication.

1.6 Project overview and aims

A large body of literature has developed around TTP since its discovery, including its structure, expression patterns, and function. Its multi-level regulation by the p38 MAPK pathway is also well established. Although our current broad picture of TTP is, therefore, well developed, our understanding of the dynamic regulation of its activity within the inflammatory response is limited and mostly based on qualitative assumptions. The effects of the proposed oscillatory activity of p38 MAPK on TTP and the expression of its mRNA targets are especially difficult to grasp due to the complex regulatory mechanisms of the pathways involved. Consequently, we aim to develop two mathematical models of the p38 MAPK-TTP signalling axis to address these shortcomings.

Kulawik p38 MAPK-TTP model

The first one, inspired by the p38 MAPK model published by Kulawik et al., will focus on the detailed and quantitative depiction of p38 MAPK-TTP pathway dynamics and their effect on the PTR of pro-inflammatory cytokines in macrophages during the inflammatory response.

We found that previous data from our group and others analysing TTP's expression and target-mRNA degradation in macrophages was mostly focused on a limited number of time points, which makes it challenging to obtain a complete picture of its dynamics throughout the inflammatory response. In addition to the low temporal resolution, the data was semi-quantitative making it impossible to directly compare different experimental designs and extract sufficient numerical values for parameter estimation of our model. The lack of comparability between experiments was especially problematic for our modelling endeavour because the experimental designs only ever incorporated a limited number of p38 MAPK-TTP pathway components, never the complete picture. Consequently, we decided to create our own data set

for this model's parameter estimation, implementing total quantification WB and quantitative polymerase chain reaction (qPCR).

Possible applications of this model, after its completion, are to verify or challenge our hypotheses and pathway assumptions, optimise future experimental design, and simulate anti-inflammatory treatment strategies for drug target identification. The main research questions that we aim to address with this model can be summarised as follows:

i) What are the dynamic changes in relevant pathway components in murine macrophages during the inflammatory response?

ii) How does system perturbation affect key pathway components in murine macrophages, and is the model sufficient to predict these?

iii) Does the TTP pathway vary in the macrophage cell line RAW264.7 during inflammation, and how can we utilise our mathematical model to address this question?

iv) Can we use our mathematical model to inform the design of future experiments, with the goal of optimising data quality and minimising the experimental cost?

The quantitative data produced for model parameter estimation and validation will be used to address the following model assumptions about the p38 MAPK-TTP pathway:

Assumption 1: The reduced p38 MAPK pathway is sufficient to model TTP and target mRNA expression.

Assumption 2: Measuring DUSP1 expression is sufficient to model feedback inhibition of the p38 MAPK pathway.

Assumption 3: Measuring high and low phosphorylation species observed in WB is sufficient to model p38 MAPK-mediated TTP expression, phosphorylation, and activation.

Assumption 4: Measuring target mRNA expression is sufficient to discern TTP function for the mathematical model of the pathway.

Tomida p38 MAPK-TTP model

The aim of the Tomida p38 MAPK-TTP model is to capture the effects of oscillatory p38 MAPK activity on the TTP pathway and the subsequent expression of inflammatory mediators during the early inflammatory response.

Previous data from our group suggest, that TTP might change its subcellular localisation based on its activation status in an oscillatory manner. To measure p38 MAPK and TTP activity dynamically in individual cells, the method of choice was live-cell microscopy in combination with using fluorescent reporter proteins. The resulting data would be semi-quantitative in nature as it is impossible to measure the total amount of protein in this setting.

Long-term applications of the model would be primarily in testing inflammatory treatment strategies and testing of hypotheses regarding the oscillatory nature of the pathways involved. The main research questions that we hoped to address with this model can be summarised as follows:

i) How does the oscillatory activity of p38 MAPK affect TTP activity and expression of inflammatory mediators during the early inflammatory response?
ii) Can we measure TTP activity in individual cells using fluorescent reporters?
iii) What are the advantages of oscillatory regulation of TTP compared to a classic one, and what are the differences?

Additionally, the quantitative data produced for model parameter estimation of the Kulawik p38 MAPK-TTP model will be used to test if the following assumption is true:

Oscillatory activation of p38 MAPK is better suited to simulate the total quantification data on the cell population level.

CHAPTER TWO

Materials and Methods

2 Materials and Methods

2.1 Cell isolation and maintenance

2.1.1 Murine BMDMs

2.1.1.1 Animal husbandry

BMDMs used in the time-course experiments described below were derived from either C57/BL6J mice obtained from Jackson Laboratories, *Zfp36*$^{aa/aa}$ mice, or *Dusp1*$^{-/-}$ mice. The *Zfp36*$^{aa/aa}$ strain originated from the C57/BL6J background and was generated by knock-in incorporation of serine to alanine substitutions at codon Ser-52 and Ser-178 of the endogenous TTP protein, which renders the positions non-phosphorylatable, as described by Ross et al. 2015 (260). *Dusp1*$^{-/-}$ likewise originated from the C57/BL6J background and was derived as a knock-out strain, originally obtained from Bristol-Myers Squibb (133,142). Both mice strains exhibit no apparent phenotype if maintained under standard conditions. In the experiments described below, the C57/BL6J mice were used as WT reference for both modified strains.

Female and male mice aged between 10 and 14 weeks were used. The mouse cohorts were maintained on a 12-h light/12-h dark cycle at 25°C with ad libitum access to a standard chow diet and water at the Biomedical Service Unit of the University of Birmingham in accordance with Home Office guidelines.

2.1.1.2 Deriving BMDMs

Differentiated BMDMs were derived by humanely culling mice through cervical dislocation according to schedule 1. The hind legs were prepared and deboned using a scalpel to reveal the femur and tibia, which were cut at both ends to expose the bone marrow. The prepared bones were transferred into 500 µL microcentrifuge tubes, the bottoms of which were pierced using a

21-gauge needle. These tubes were placed in 1.5 mL collection tubes. The bone marrow was then flushed out by centrifugation at 1500 x g for 3 min at room temperature (RT) and re-suspended before being transferred into a falcon tube filled with 50 mL RPMI (Sigma-Aldrich) substituted with 10% heat-inactivated Fetal calf serum (FCS) (Sigma-Aldrich), 1% PenStrep (Sigma-Aldrich), 1% L-Glutamine (Sigma-Aldrich) and M-CSF (Sigma-Aldrich). 10 mL each of this cell suspension was seeded into plate dishes and incubated at 37°C and 5% CO_2 for seven days with medium exchange on day five.

2.1.1.3 BMDM seeding

On day 7, differentiated BMDMs were harvested and seeded for stimulation with 10 ng/mL LPS with and without 30 min pretreatment with 2.5 ng/mL of the PP2A inhibitor Calyculin A on the following day (The protocol continues in Chapter 2.4). For this purpose, the cells were washed with PBS and incubated for 20 min in 3 mL 5 mM sterile EDTA solution (Sigma-Aldrich) in PBS without calcium and magnesium (Thermo Fisher Scientific). EDTA and calcium and magnesium free PBS is used to prevent divalent cations from facilitating cell adhesion to a negatively charged surfaces such as protein-coated Falcon plastic ware (296). The now loosened cells were removed from the plate using a cell lifter and combined in 50 mL falcon tubes. The cell suspension was sedimented by centrifugation at 300 x g for 5 min at RT, the supernatant was discarded, and the cells were resuspended in 10 mL culture medium substituted with 10% heat-inactivated FCS. The cell number was determined using disposable counting slides (Immune System) and 1:1 Trypane blue solution (Sigma-Aldrich). 2 x 10^6 cells were seeded per well in 6-well plates and incubated overnight at 37°C and 5% CO_2.

2.1.2 Cell lines

Table 2.1 Cell lines, their origins and culture media

Cell line	Cell origin	Culture medium
HEK293T (297)	Human embryonic kidney cells stably expressing SV-40 T-antigen (kindly donated by Dr Chris Weston of the Centre of Liver and Gastrointestinal Research, University of Birmingham)	DMEM (Gibko) 10% FCS (Sigma Aldrich) 1% PenStrep (Sigma Aldrich) 1% L-Glutamine (Sigma Aldrich)
HeLa (298)	Human epithelial carcinoma cells (ATCC)	MEM (Gibco) 10% FCS 1% PenStrep
RAW269.72 (299)	Resemble murine adherent macrophages, originated from ascites of an Abelson murine leukaemia virus-induced tumour in BALB/c mice (ATCC)	DMEM 10% FCS (Sigma Aldrich) 1% PenStrep (XXX)

2.1.2.1 Preparation of frozen cell lines for long-term storage

Cell lines were frozen for long-term storage in FCS with 10% DMSO added. For this purpose, cells were grown to confluency in a T75 flask. After reaching confluency, RAW264.7 cells were detached from the flask bottom using a cell scraper, while HeLa and Hek293T cells were washed with PBS and detached by incubating with the supplier-recommended volume of TrypLE Express (Gibco) for 2 to 4 min. Next, the cell line-specific respective FCS-containing media was added and a third of the cell suspension sedimented by centrifugation at 300 x g for 5 min at RT. The resulting pellet was resuspended in 1 mL 10% DMSO in FCS and transferred into plastic cryovials, which were then placed in a Mr Frosty freezing container (Thermo Fisher

Scientific) filled with isopropanol (Merck), precooled to 4°C. The container was placed at -80°C overnight. The next day, the frozen vials were transferred to long-term vapor-phase liquid nitrogen storage.

2.1.2.2 Reconstitution of cells from frozen stocks

For reconstitution of frozen cells, the cells were rapidly thawed at 37°C, and the 1 mL suspension was diluted with 9 mL cell line-specific respective culture media. The cells were centrifuged at 300 x g for 10 min at RT, and the supernatant freezing media was removed. The resulting cell pellet was resuspended in the cell line-specific respective culture medium and transferred to culture flasks after viable-cell counting (cell culture flask size depending on cell number; T25 < $1x10^6$ < T75 < $5x10^6$ < T150). The cells were cultured at 37°C and 5% CO_2 overnight. The next day, the cells were microscopically controlled for cell attachment and non-attached and dead cells were removed by exchanging the culture medium.

2.1.2.3 Maintenance of cell lines

The cell lines were maintained in T-25, T-75, or T-150 flasks with 4, 12, or 24 mL, depending on flask size, of their respective culture medium at 37°C and 5% CO_2. Usually, twice a week, when the cells reached 90% confluency, the cells were subcultured. For this, cells were detached as described under 2.1.2.3. Following detachment, the cells were resuspended by pipetting, transferred into 15 mL falcon tubes, and sedimented by centrifugation at 300 x g for 5 min at RT. The supernatant was discarded, the cell pellet re-suspended in respective cell line-specific culture medium, and the desired amount of the cell suspension was transferred to a new medium containing culture flasks, keeping a subcultivation ratio of 1:3 to 1:10 depending on cell availability needs. Cells were used for experiments between passages 2 and 15.

2.1.2.4 Seeding of RAW264.7 cells

The day before the experiment, RAW264.7 cells were harvested and seeded for stimulation with 10 ng/mL LPS with and without 30 min pretreatment with 2.5 ng/mL of the PP2A inhibitor Calyculin A on the following day (The protocol continues in Chapter 2.4). For this purpose, the cells were detached, as described under 2.1.2.3. The cell suspension was sedimented by centrifugation at 300 x g for 5 min at RT, the supernatant discarded, and the cells resuspended in 1 mL culture medium substituted with 10% heat-inactivated FCS. The cell number was determined using disposable counting slides and 1:1 Trypane blue solution. 1.2 x 10^6 cells were seeded per well in 6-well plates and incubated overnight at 37°C and 5% CO_2.

2.2 Cloning

2.2.1 Plasmid and Oligo Tables

Table 2.2 Plasmids

Plasmid name	Purpose and properties
pGFP-TNFalpha	Addgene (#28089) qPCR standard *Tnf*
pMD2.G	Addgene (#12259) VSV-G envelope expressing plasmid
psPAX2	Addgene (#12260) 2nd generation lentiviral packaging plasmid
pLentiX_TetOne_Puro	Takara (#631849) Lentiviral vector for tetracycline-inducible expression of mammalian proteins
pWPI-IRES-Bla-Ak	Addgene (#154980) Lentiviral vector for expressing mammalian proteins
pmNeonGreen-mRuby2-FRET-10	Addgene (#58179), Fluorophores for reporter and FRET
pFRT-TODestFLAGHAhTTP	Addgene (#48738) Expresses hTTP
pT7-EGFP-C1-HsDCP1a	Addgene (#25030) Expresses DCP1a, P-body marker
pEGFP-C1-G3BP1-WT	Addgene (#135997) Expresses G3BP1, SG-marker
pcDNA3-HA-14-3-3b	Addgene (#13270) Expresses 14-3-3b, TTP interaction partner for FRET
pPBbsr-mKO-MK2	Addgene (#115492)

	p38 activity reporter mKO-MK2
pLentiCMV-Puro-DEST-p38KTRmCerulean3	Addgene (#59155) Lentiviral vector expressing p38 KTR
pLentiTetOne_mNG_hTTP_WT	Tetracycline-inducible lentiviral vector expressing mNeonGreen-tagged WT hTTP
pLentiTetOne_mNG_hTTP_AA	Tetracycline-inducible lentiviral vector expressing mNeonGreen-tagged AA hTTP (Ser to Ala substitution at Ser-60 and Ser-186)
pLentiTetOne_mNG_hTTP_EE	Tetracycline-inducible lentiviral vector expressing mNeonGreen-tagged EE hTTP (Ser to Glu substitution at Ser-60 and Ser-186)
pLentiTetOne_mNG	Tetracycline-inducible lentiviral vector expressing mNeonGreen
pWPI_mRuby2_DCP1a	Lentiviral vector expressing mRuby2-tagged DCP1a (P-body marker)
pWPI_mRuby2_14-3-3b	Lentiviral vector expressing mRuby2-tagged 14-3-3b (FRET partner TTP)
pWPI_mRuby2_G3BP1	Lentiviral vector expressing mRuby2-tagged G3BP1 (SG-marker)
pWPI_mRuby2_MK2	Lentiviral vector expressing mRuby2-tagged MK2 (KTR p38 MAPK)
pWPI_mRuby2	Lentiviral vector expressing mRuby2

Table 2.3 Oligos

Name	**Sequence 5' - 3'**	**Purpose**
1_BB_NG_fwd	TAAGCGGCCGCGAC TCTAG	PCR BB mNG Gibson assembly (forward)

1_BB_NG_rev	CTTGTACAGCTCGTCCATGC	PCR BB mNG Gibson assembly (reverse)
1_IN_mhTTP_rev	CTTGTACAGCTCGTCCATGC	PCR Insert hTTP (reverse)
1_IN_hTTP_fwd	gcatggacgagctgtacaagATGGATCTGACTGCCATC	PCR Insert hTTP (forward)
T1C4_hTTPA60_F	CCGCTCCACCGCACTAGTGGAGGGCCGC	AGC (Ser) to GCA (Ala) SDM position 60 (forward)
T1C4_hTTPA60_R	CCAGGCAGGCGGGAGGTG	AGC (Ser) to GCA (Ala) SDM position 60 (reverse)
T1C4_hTTPEA60_F	CCGCTCCACCGAGCTAGTGGAGGGCCG	Position 60 SDM AGC (Ser) to GAG (Glu) (forward)
T1C4_hTTPE60_R	CCAGGCAGGCGGGAGGTG	Position 60 SDM AGC (Ser) to GAG (Glu) (reverse)
T1C4_hTTPA186_F	CCAGAGCATCGCATTCTCCGGCCTGCC	AGC (Ser) to GCA (Ala) SDM position 186 (forward)
T1C4_hTTPA186_R	CGAAGCACAGGAGGGTGG	AGC (Ser) to GCA (Ala) SDM position 186 (reverse)
T1C4_hTTPE186_F	CCAGAGCATCGAGTTCTCCGGCCTGCC	Position 186 SDM AGC (Ser) to GAG (Glu) (forward)
T1C4_hTTPE186_R	CGAAGCACAGGAGGGTGG	Position 186 SDM AGC (Ser) to GAG (Glu) (reverse)
2_IN_NG_mhTTP_fwd	GCCACCATGGTGAGCAAG	PCR Insert (forward) mNG_hTTP WT/AA/EE mNG
2_IN_NG_mhTTP_rev	TTACTATCACTCAGAAACAGAGATGC	PCR Insert (reverse) mNG_hTTP_WT/AA/EE
2_IN_NG_rev	ttactatcaCTTGTACAGCTCGTCCATG	PCR Insert mNG (reverse)
3_BB_R2_woNG_fwd	TAAGCGGCCGCGACTCTAG	PCR BB R2 Gibson assembly (forward)

3_BB_R2_woNG_rev	CTTGTACAGCTCGTCCATCC	PCR BB R2 Gibson assembly (forward)
3_IN_DCP1a_fwd	TGTACAAGTCCGGACTCAGATCAATGGAGGCGCTGAGTC	PCR Insert DCP1a (forward)
3_IN_DCP1a_rev	TCTAGAGTCGCGGCCGCTTATCATAGGTTGTGGTTGTCTTTGTTC	PCR Insert DCP1a (reverse)
3_IN_C1_MK2_MCS_fwd	GGATGGACGAGCTGTACAAGCTCGAGATGCTGTCCAACTC	PCR Insert MK2 (forward)
3_IN_C1_MK2_MCS_rev	TCTAGAGTCGCGGCCGCTTAAATTGTTACCGCGGCCGC	PCR Insert MK2 (reverse)
T3C2_IN_mRuby2_fwd	GCCACCATGGTGTCTAAG	PCR Insert (forward) mR2_DCP1a/MK2 mR2
T3C2_IN_R2_C1_DCP1a_rev	TTATCATAGGTTGTGGTTGTC	PCR Insert (reverse) mR2_DCP1a
T3C2_IN_R2_C1_MK2_rev	TTATCAGTGGGCCAGAGC	PCR Insert (reverse) mR2_MK2

2.2.2 Construct generation

All overexpressing cell lines were generated using lentiviral transduction, as this allows the quick establishment of stable cell lines. The gene of interest inserts were produced using site-directed mutagenesis and Gibson assembly on non-lentiviral plasmids. Resulting arrays of protein of interest linked to their respective fluorescent markers were then amplified using polymerase chain reaction (PCR) and inserted into lentiviral vectors by blunt end ligation. We used one type of lentivirus system for constant overexpression, pWPI-IRES-Bla-Ak (Addgene)

(300), and a second one for Tet-driven induction of overexpression, Lenti-X™ Tet-One™ Inducible Expression System (Takara) (301). Lentivirus work was approved by the GMO committee of the University of Birmingham (approval Nr: MDS_2010).

2.2.2.1 PCR for insert preparation and site-directed deletion or mutagenesis

Using Q5 High-Fidelity 2X Master Mix (NEB) according to the manufacturer's instructions, PCR was employed to amplify inserts for blunt-end ligation and to amplify backbone and/or inserts for Gibson assembly and site-directed mutagenesis. The reaction mix was prepared as described in Table 2.4 in 25 µL reactions. Forward and reverse primers were mixed at a final concentration of 500 nM (desalted, Merck) with 1 ng of template plasmid. The PCRs were run for 30 cycles in a thermal cycler (T100, Biorad) according to conditions described in Table 2.5. We used the NEB Tm calculator tool (302) to identify the annealing temperature of the primer pairs while only considering the parts of the primers which directly bind to their respective template. The elongation time of the PCR reactions was set to 30 sec per kB amplified. All results of PCR reactions were assessed by Agarose gel electrophoresis as described in Chapter 2.2.2.2.

Table 2.4 Components PCR

Reagent	Amount/Volume
Q5 High-Fidelity 2x Master Mix	12.5 µL
10 µM forward primer stock	1.25 µL
10 µM reverse primer stock	1.25 µL
Template DNA	1 ng (plasmid)/100ng(gDNA) in 1 µL or 5 µL
Nuclease-free water	to 25 µL

Table 2.5 Cycling Conditions

Step	Temperature	Time
Initial denaturation	98°C	30 sec
30 cycles	98°C	10 sec
	Depending on primer pair	30 sec
	72°C	30 sec/kb
Final extension	72°C	2 min
Storage	4°C	∞

2.2.2.2 Agarose gel electrophoresis

Agarose gel electrophoresis was performed to analyse the outcome of restriction enzyme (RE) digests and PCR amplifications. For this purpose, 1% agarose gel was generated by mixing agarose powder (Sigma Aldrich) and 1x Bionic Buffer (Sigma Aldrich). The mixture was microwaved until the agarose completely dissolved and cooled to 50°C. SYBR Safe DNA gel stain (Thermo Fisher) was added 1:10,000 and mixed thoroughly to allow DNA visualisation. This mixture was poured into a running chamber and left to solidify for 30 min. The solidified gel was then placed into the electrophoresis unit (Biorad), filled with 1x Bionic buffer. To identify the size of the DNA constructs, 6 µL of 1 kB plus DNA ladder (NEB) was loaded onto the gel together with any DNA samples. Samples were mixed with 6x loading buffer (NEB) before being added to the gel wells. The agarose gel electrophoresis was then run at 180 V for 1.5h. The SYBR Safe signal was then visualised using a ChemiDoc MP imaging system (Biorad).

2.2.2.3 Purification from PCR reactions

DNA was purified for subsequent sensitive applications such as site-directed mutagenesis and Gibson assembly and for cloning applications where the used restriction enzymes were not heat-inactivatable. For this purpose, the Wizard SV gel and PCR clean-up system (Promega) was used according to the manufacturer's instructions.

The PCR product or RE digest was mixed with an equal amount of membrane binding solution and transferred onto a Minicolumn collection tube assembly. The setup was incubated for 1 min at RT to bind DNA to the column. After incubation, the column was centrifuged for 1 min at maximum speed, and the flow-through was discarded. The column was then washed twice, once with 700 µL and once with 500 µL membrane wash solution with added ethanol and centrifuged for 1 min and 5 min, respectively, at maximum speed. The flow-through was discarded after each washing step. The column assembly was centrifuged again for 1 min to allow evaporation of residual ethanol. The column was transferred from the collection tube to a 1.5 mL microcentrifuge tube, and 30 µL of nfH2O was added to the column, followed by an incubation of 5 min at RT. Finally, the column tube assembly was centrifuged for 1 min at full speed to elute DNA. The quality and amount of purified DNA were measured using a Nanodrop 2000 spectrophotometer (Thermo Scientific). The purified DNA was either directly used in follow-up applications or stored at -20°C.

2.2.2.4 Restriction digests

Restriction enzymes for vector linearisation, DpnI digest, and identification of correct insertion of insert after Gibson assembly and Blunt end ligation were purchased from NEB and used according to the manufacturer's instructions. 10 units of enzyme per µg of DNA was combined with DNA, Restriction buffer, and nuclease-free water according to Table 2.6. The mixture was

then incubated for 1 h at 37°C. When an RE digest preceded an application (e.g., ligation after DpnI digest and vector linearisation), REs were heat-inactivated if possible. To check if an RE digest was completed, agarose gel electrophoresis was performed as described above (Chapter 2.2.2.2). To verify the correctness of insertions, the bands produced by diagnostic RE digests were compared with virtual digests generated using the Benchling online tool (303).

Table 2.6 Components restriction digest

Reagent	Amount/Volume
Restriction enzyme (BstZ17I-HF, DpnI, NcoI, XhoI, BamHI, PmeI,	10 units per µg, usually 1 µL
DNA	Variable, usually 1 µg or less
10x restriction buffer	5 µl
Nuclease-free water	to 50 µl

2.2.2.5 Dephosphorylation of linearised plasmid

Following the linearisation of plasmid vectors, the DNA ends of the backbone were dephosphorylated to reduce the probability of plasmid relegation. For this purpose, Quick-CIP enzyme (NEB) was added to the restriction digest (Chapter 2.2.2.4) according to the manufacturer's instructions at a ratio of 1 to 5 to the total reaction volume. Following the restriction enzyme digest, the reaction was either heat-inactivated or immediately purified (see Chapter 2.2.2.3).

2.2.2.6 Phosphorylation of PCR amplified inserts

For both blunt-end and sticky-end ligation, inserts were phosphorylated to be ligated inserts into the vector. For this purpose, T4 polynucleotide Kinase (NEB) was used according to the manufacturer's instructions. Preceding this reaction, the insert was purified as described above

(Chapter 2.2.2.3). To calculate the required Moles of 5' ends for the reaction, the NEBiocalculator (304) mass to/from moles converter was used. The reaction mixture was set up as described in Table 2.7 and incubated for 30 min at 37°C, and afterwards heat inactivated at 65°C for 20 min.

Table 2.7 Components of T4 PNK reaction

Reagent	Amount/Volume
DNA	Up to 150 pmol
10x T4 PNK buffer	5 µl
10 mM ATP	5 µl
T4 PNK	1 µl
Nuclease-free water	To 50 µl

2.2.2.7 Ligation reaction

After backbone and insert preparation (this usually included phosphorylation of the insert, and linearisation, dephosphorylation, and purification of the vector), the vector and insert were ligated using T4 DNA Ligase (NEB) according to the manufacturer's instructions. To calculate pmol amounts of vector and insert, from DNA concentration and length, the NEBiocalculator (304) Mass to/from moles converter was used. The employed reaction mixture is summarised in Table 2.8. For sticky end cloning, the mixture was incubated for 10 min at RT, while for blunt end ligation, the reaction was either incubated for 2 h at RT or overnight at 16°C. Finally, the reaction was heat-inactivated at 65°C for 10 min and chilled on ice for direct use in transformations.

Table 2.8 Components of T4 DNA Ligase reaction

Reagent	Amount/Volume
10x T4 DNA Ligase Buffer	1 µl
Vector DNA	0.01 pmol
Insert DNA	0.03 pmol
Nuclease-free water	to 10 µl
T4 DNA Ligase	0.5 µl

2.2.2.8 Gibson assembly reactions

Gibson assembly was used as a cloning strategy in the process of construct generation whenever inserts needed to be transferred between non-lentiviral vectors. For this purpose, NEBuilder HiFi DNA Assembly Master Mix (NEB) was used according to the manufacturer's instructions. The reaction mix was set up as described in Table 2.9 in PCR reaction tubes and then incubated at 50°C for 15 min. Oligos used in Gibson assembly were designed using the web application NEBuilder (305). The amount of DNA used in these reactions was calculated using the NEBiocalculator (304) Mass to/from moles converter. Following incubation, samples were stored on ice for subsequent transformation or frozen at -20°C for long-term storage.

Table 2.9 Components of HiFi DNA Assembly reaction

Reagent	Amount/Volume
Vector DNA	0.03 pmol
Insert DNA	0.06 pmol
2x HiFi DNA Assembly Master Mix	10 µl
Nuclease-free water	to 20 µl

2.2.2.9 Site-directed mutagenesis

To substitute or introduce specific individual base pairs, Site-directed mutagenesis (SDM) was performed using the Q5 Hot Start High-Fidelity Master mix (NEB) and the Kinase, Ligase and DpnI (KLD)- enzyme mix (NEB) according to the manufacturer's instructions. First, a PCR was performed as described in Chapter 2.2.2.1 using primers designed using the web application NEBaseChanger (306). The PCR product was then treated with KLD-enzyme mix by setting up the reaction as described in Table 2.10 in a PCR reaction tube. The mixture was incubated for 5 min at RT, and the resulting constructs were directly used for transformation.

Table 2.10 Components of Site-Directed Mutagenesis reaction

Reagent	Amount/Volume
PCR product	1 µl
2x KLD reaction buffer	5 µl
10x KLD enzyme mix	1 µl
Nuclease-free water	3 µl

2.2.3 Plasmid preparation

After generating new constructs, plasmids were transformed into *E. coli*, to facilitate validation of the cloning outcome, subsequent propagation, and long-term storage in the form of isolated plasmid DNA as well as *E. coli* glycerol stocks. For validation, restriction enzyme digests and sequencing were used. All work with *E. coli* was covered under a GMO licence (MDS 20_10).

2.2.3.1 Transformation in *E. coli*

For transformation of newly assembled constructs or retransformation for propagation, either NEB 5-alpha (High efficiency) (NEB) (Genotype: fhuA2 Δ(argF-lacZ)U169 phoA glnV44 Φ80 Δ(lacZ)M15 gyrA96 recA1 relA1 endA1 thi-1 hsdR17) or NEB Stable Competent *E. coli* (High

Efficiency) (NEB) (Genotype: *F' proA+B+ lacIq Δ(lacZ)M15 zzf::Tn10 (TetR)/ Δ(ara-leu) 7697 araD139 fhuA ΔlacX74 galK16 galE15 e14- Φ80dlacZΔM15 recA1 relA1 endA1 nupG rpsL (StrR) rph spoT1 Δ(mrr-hsdRMS-mcrBC))* were used according to the manufacturer's instructions.

Competent cells were thawed on ice, and 1 ng of plasmid DNA (in a maximum of 1 µL) or the respective volume amount after cloning procedures (SDM 5 µL, Gibson Assembly 2 µL, Blunt end ligation 2 µL) was added to 50 µL of cells. The mixture was incubated on ice for 30 min, after which heat shock transformation was performed at 42°C for 30 sec. Cells were incubated on ice for 5 min before 950 µL of pre-warmed outgrowth medium was added (NEB 5-alpha: SOC, NEB stable: Stable outgrowth medium). The cells were placed in a shaking incubator at 30°C, 250 rpm, for 60 min. The E-coli were spread out on agar plates prepared from LB Agar (Sigma Aldrich) containing either 100 µg/mL Ampicillin (Sigma Aldrich) or 50 µg/mL Kanamycin (Sigma Aldrich) and incubated overnight at 37°C (NEB 5-alpha) or 30°C (NEB stable). All work with *E. coli* was done under sterile conditions.

2.2.3.2 Plasmids mini preparations

RE digests or Sanger sequencing was used to identify which colonies, grown on agar plates, contained the correct constructs. For both techniques, plasmid DNA was isolated from the bacteria colonies using the GeneJet Plasmid Miniprep Kit (Thermo Fisher) according to the manufacturer's instructions. 5 (where the upstream procedure was SDM, sticky end cloning or Gibson assembly) up to 20 (where the upstream procedure was blunt end cloning) 5.5 mL bacteria liquid cultures, containing either 100 µg/mL Ampicillin (Sigma Aldrich) or 50 µg/mL Kanamycin (Sigma Aldrich) were set up in 50 mL centrifuge tubes from colonies formed on agar plate in selective LB media (Merck). The lid on these tubes was loosely attached with tape for ventilation. The cultures were incubated for 15 h at 250 rpm and 37°C in a shaking

incubator. 5 mL of the bacteria culture was then centrifuged at 6800 x g for 2 min, and the remaining culture was stored in the fridge for upscaling after identification of the respective construct. The pelleted bacteria were resuspended in 250 µL resuspension buffer with 100 µg/mL RNase freshly added and transferred into a 1.5 mL microcentrifuge tube. 250 µL lysis buffer was added and incubated for 4 min at RT. The lysis was then stopped by adding 250 µL neutralisation buffer, and the mixture was centrifuged for 5 min to pellet cell debris and chromosomal DNA. After that step, the clear liquid was transferred onto a Gene Jet spin column and centrifuged for 1 min at 13,200 x g at RT. After discarding the flow-through, the column was washed twice using 500 µL Washing Solution for 30 sec at 13,200 x g at RT. The columns were then centrifuged another time for 1 min at 13,200 x g at RT. To elute the plasmid DNA from the column, 35 µL nfH20 was added to the column membrane and, after an incubation time of 2 min, centrifuged for 2 min at 13,200 x g at RT. DNA concentration and quality were measured using a Nanodrop 2000 spectrophotometer (Thermo Scientific). The plasmid DNA was stored at -20°C.

For blunt-end cloning, constructs were verified by RE digest. Sanger sequencing (Source Bioscience), using primers covering the area of interest from both the 5' and 3' direction to confirm sequence integrity, was carried out on all constructs used in subsequent experiments.

2.2.3.3 Plasmid Mira-preparations

For long-term stock preparation of plasmids, 50 mL Liquid culture was set up in selective LB media for 18 h at 37°C. To isolate the DNA, we adopted a protocol designed by Mira Pronobis et al. (307), named Mira-preparation. The GeneJet plasmid Miniprep kit (Thermo Fisher) was used as described above with the following modifications: 50 mL of the bacterial culture was centrifuged at 4000 x g for 10 min at 4°C. The pellet was then resuspended in 1.5 mL resuspension buffer, 1.5 mL lysis buffer, and 2 mL neutralisation buffer were used. The mixture

was then distributed into four 1.5 mL microcentrifuge tubes and centrifuged at 13,200 x g for 10 min at RT to sediment cell debris and chromosomal DNA. The clear supernatant was then collected using a 15 mL centrifuge tube and 1x volume of 96% molecular grade ethanol was added. The mixture was then loaded onto 5 Gene Jet Spin columns in sequential 700 µL aliquots. The remaining steps were the same for each column in both protocols. After elution, the plasmid DNA from the 5 columns was combined, yielding 175 µL of isolated plasmid in a concentration range of 500 to 2000 ng/µL.

2.2.3.4 Glycerol stocks

Apart from isolated plasmid DNA, constructs were also stored in the form of bacterial glycerol stocks for ease of use in the future. 5 mL liquid culture in selective LB medium, containing either 100 µg/mL Ampicillin or 50 µg/mL Kanamycin was set up and incubated for 18 h at 37°C under constant agitation. The cells were then pelleted by centrifugation for 5 min at 5000 x g, and the supernatant was discarded. The pellet was then resuspended in LB medium containing 20% glycerol and stored at -80°C. For recovery of bacteria, some of the frozen bacteria were scraped off with a pipette tip and streaked out on an LB agar plate containing selective antibiotics. After bacteria colonies were grown, an individual colony was used to set up an overnight liquid culture in a selective LB medium.

2.2.4 Introduction of constructs into cells

2.2.4.1 Transfection of standard plasmids into HEK293T cells and HeLa cells

Transfected Hek293T and HeLa cells were used during the validation phase of the cloning project. 5 µg of plasmid was transfected into cells seeded at 90% confluency in 6 well plates using Lipofectamine 3000 (Thermo Fisher) at the highest recommended concentration according to the manufacturer's instructions. Transfection solutions 1 and 2 were prepared as

described in Table 2.11, mixed well, combined, and then incubated for 15 min at RT for lipid-DNA complexation. Following incubation, the DNA-lipid complex was added to the cells. Two days post-transfection, the cells were checked for fluorescent protein expression or treated with media containing selective mammalian antibiotics for the resistance factor present on the plasmids.

Table 2.11 Components of transfection solution

Reagent	Amount/Volume	Transfection Solution 1/2
Opti-MEM	250 µl	Solution 1 and 2
Lipofectamine 3000	7.5 µl	Solution 1
P3000	10 µl	Solution 2
Plasmid	5 µg	Solution 2

2.2.4.2 Transfection of lentiviral plasmids into HEK293T cells

To generate lentiviral particles for cell transduction, a confluent T75 flask of Hek293T cells was transfected with a lentiviral system containing a lentiviral transfer plasmid, either based on pWPI-IRES-Bla-Ak (Addgene) or pLentiX_TetOne_Puro (Takara) encoding the gene of interest, a packaging plasmid psPAX2 (Addgene) and an envelope glycoprotein plasmid pMD2.G (Addgene). For transfection, Lipofectamine 3000 was used as described in Chapter 2.2.4.1, using the transfection mixture summarised in Table 2.12. The combined transfection solution was added to a T75 flask containing 6 mL Hek293T cell medium. The cells were then placed into a ventilated secondary container for lentivirus work and incubated at 37°C, 5% CO_2. After 6 h, the transfection media was discarded and replaced with 9 mL HEK293T cell medium.

Table 2.12 Components of transfection solution Lenti-vector

Reagent	Amount/Volume	Transfection Solution 1/2
Opti-MEM	1.5 mL	Solution 1/2
Lipofectamine 3000	41 µL	Solution 1
P3000	35 µL	Solution 2
Lenti-vector	14.4 µg	Solution 2
psPAX2	8.33 µg	Solution 2
pMD2.G	2.63 µg	Solution 2

2.2.4.3 Harvesting and concentration of lentiviral particles

Lentiviral particles were harvested and concentrated using two different methods. The first follows the protocol described by Jiang et al. (308), while the other utilises the PEG virus precipitation kit (Abcam) according to the manufacturer's instructions. The first method was used to purify particles for the generation of TTP expression reporter cells, while the other method was used for ease of use to produce the viral particles for expression of colocalisation partners, where the lower yield of the PEG precipitation was adequate for the intended purpose.

Protocol Jiang et al.

The first harvest of lentivirus-containing media was performed 24 h post-transfection. Here, the 9 mL media were replaced with 12 mL fresh HEK293T cell medium. The collected media was stored in a 50 mL tube within a secondary container at 4°C. The second harvest was performed 52 h post-transfection. The harvested media was combined and centrifuged at 3000 x g for 10 min to pellet any cell debris. Afterwards, the media was filtered from remaining impurities using a 0.45 µm pore filter (Millipore). The filtered media was then distributed and layered in 675 µL aliquots into conic 2 mL screw-top tubes filled with 450 µL of a sucrose cushion (10%

Sucrose, 50 mM Tris-HCl, 100 mM NaCl, 0.5 mM EDTA, pH=7.4) and centrifuged for 4 h at 10,000 x g. The pelleted virus was resuspended in 200 µL PBS and stored in 5 µL aliquots at -80°C.

Protocol PEG

For the PEG virus precipitation protocol, the virus-containing medium was harvested 3 days post-transfection and centrifuged for 15 min at 3200 x g and 4°C. The supernatant was transferred into a 50 mL centrifuge tube, and 1x PEG solution was added. The mixture was then refrigerated overnight. The following day, the mixture was centrifuged at 3200 x g for 40 min, the supernatant discarded, and the virus pellet resuspended with 100 µL virus resuspension solution. The concentrated viral particles were then aliquoted into 20 µL aliquots in PCR tubes and stored at -80°C.

2.2.4.4 Measurement of viral yield

We used the Lenti-X GoStix Plus quantitative lentiviral titre test (Takara) to measure the efficiency of virus production and concentration according to manufacturer's instructions. For this purpose, 20 µL of lentiviral supernatant or diluted concentrate was added to the sample well of the Lenti-X GoStix Plus cassette, followed by 80 µL of Chase Buffer. After 10 min of incubation at RT, the intensity of the band was measured using the GoStix Plus app (Takara). To compare virus yield, virus samples reaching > 90% transduction efficiency in HeLa cells were used.

2.2.4.5 Transduction and establishment of stable overexpressing cell lines

To transduce HeLa cells, 10 µL (Protocol Jiang et al.) or 20 µL (protocol PEG) of concentrated lentivirus were added to a 1 mL cell-specific culture medium. The medium was added to cells seeded at 50% confluency and incubated for 2 days in a secondary container at 37°C 5% CO_2.

Cells were then selected for construct expression by incubation with puromycin (Thermo Fisher) depending on the resistance gene present in the transduction cassette. Optimal concentrations of antibiotics that guaranteed killing cells not expressing selection factors within 2 days (2 µg/mL Puromycin for HeLa), were determined by previously performed dilution experiments. The resulting transduced cell populations were then expanded and frozen for long-term storage in liquid nitrogen (Chapter 2.1.2.1) or directly used in follow-up assays.

2.3 Time-course Microscopy Reporter cells

2.3.1 Sample Preparation

2.3.1.1 Seeding

For confocal microscopy, cells were seeded in specific 4 Well µ-Dish 35 mm (Ibidi) or µ-Slide 8 Well (bidi) imaging dishes. For this purpose, HeLa cells were detached according to their subculturing protocol, counted, and seeded at 25% confluency in HeLa culture medium in the recommended volume by the dish manufacturer. This allowed for Doxycycline stimulation, at 50% confluency, the next day. The cells were then incubated at 37°C, 5% CO_2, until Doxycycline induction and downstream imaging.

2.3.1.2 Stimulation

24 h before imaging, TetOne reporter TTP expression was induced by replacing the medium with 500-1000 ng/mL Doxycycline in HeLa cell medium. To minimise the environmental effects on live-cell microscopy, the cells were transported to the imaging facility incubator at this stage and incubated at 37°C and 5% CO2.

For stimulation of the inflammatory response in fixed-cell microscopy experiments, a master mix was prepared to contain 30 ng/mL IL-1β and 1000 ng/mL Doxycycline in HeLa culture medium, and the stimulus was administered by a medium exchange. After stimulation for a specified time, the cells were fixed for follow-up staining and microscopy analysis.

For live-cell microscopy, the cells were counter-stained for their nuclei, and their medium was exchanged for phenol red-free imaging medium containing 1000 ng/mL Doxycycline. After setting up the microscope and imaging the controls, the cells were stimulated on the microscope stand by IL-1β spike-in, leading to a final concentration of 30 ng/mL.

2.3.1.3 Fixation

Following stimulation, the cells were incubated for 20 min in fixation buffer (BioLegend) and washed thoroughly with PBS. Cells were stored in PBS, in the dark at 4°C, until counter-staining and microscopy.

2.3.1.4 Staining

Fixed cells were either incubated for 20 min with 1:1000 DRAQ5 (Thermo Scientific) or 5 min with 1:100 DAPI (Thermo Scientific). This was followed by thoroughly washing cells in PBS and storage of cells in PBS in the dark in the fridge until imaging.

For live-cell microscopy, staining was performed prior to stimulation. The nucleus was stained by incubating cells for 20 min in 1:1000 DRAQ5 in HeLa imaging medium containing 1000 ng/mL Doxycycline (Thermo Scientific) at 37°C. The solution was then aspirated, and cells were washed with PBS before replacing the Doxycycline incubation medium.

2.3.2 Image acquisition

Cells were imaged on a Zeiss LSM 780 running Zen Black software (Zeiss, Germany). As a control, parent cells not expressing a fluorescent marker, non-Doxycycline induced TTP cells, and mNeonGreen and mRuby overexpressors were imaged. When two reporters were supposed to be imaged simultaneously, one-reporter-only controls were utilised. Laser intensity and filter settings were set up so that no signal was detected in respective channels in control HeLa cells.

For microscopy, cells were located using the counter-stain marker where possible. All dishes were imaged at 650x magnification using an immersion oil with a refractory index of 1.33 (provided by the Institute of Biomedical Research (IBR), Birmingham).

2.3.3 Image analysis

The image analysis was performed using an automated workflow in Python, implementing Cellpose and ImageJ macros. The scripts can be found in Appendix 7.9.

First, the czi.files were converted to tiff using the Bio-Formats Plugin in ImageJ.

For P-body analysis, the channels were split. The P-body mask was generated through semi-automated thresholding in Image-J using the image of the split DCP1a channel. The cells were segmented using the Cellpose software. The resulting cell and P-body masks were then added and subtracted in ImageJ using Image Calculator to create a mask of TTP-positive cells without P-bodies and a mask with P-bodies per cell without the cytoplasm. Those masks were then used to measure intensity within each cell in ImageJ. ChatGPT 4.0 was used to write and troubleshoot the code. The resulting data was compiled from individual Excel files in Python, and the cytoplasm to P-body (C/P) ratio of the mean intensity of TTP expression was calculated.

For analysis of nuclear translocation, the Cellpose software was used to segment the cells and the nuclei of the cells. The cytoplasm mask was generated by creating an ROI from the nuclei mask and filling them in on top of the cell mask. Otherwise, the same image analysis process was used as for P-bodies. Instead of the C/P ratio, the cytoplasm to nucleus (C/N) ratio was calculated.

2.4 Time-course experiments with inflammatory stimuli and inhibitors

2.4.1 Assessment of RNA expression

2.4.1.1 RNA extraction

mRNA was isolated from RAW264.7 cells and BMDMs using a Monarch Total RNA Miniprep Kit (NEB) according to the manufacturer's instructions. First, cells seeded in 6-well plates (Chapter 2.1.1.32.1.2.4) were placed on ice. The medium was removed, and the cells were washed with cold 4°C PBS, after which 400 µL 1x DNA/RNA protection reagent was added per well. The plates were then wrapped in parafilm and frozen at -80°C for storage until the next steps of RNA isolation were performed. After removal from storage, plates were thawed at RT, 400 µL RNA lysis reagent was added per well, and the well content was mixed thoroughly. The resulting lysates were transferred into genomic DNA removal columns and centrifuged for 30 sec at 16,000 x g at RT. The flow-through was mixed with an equal amount of 95% molecular grade ethanol, transferred to an RNA Purification column, and centrifuged for 30 sec at 16,000 x g at RT. The resulting flow-through was discarded, and the columns were washed with 500 µL RNA Wash Buffer by centrifugation for 30 sec at 16,000 x g at RT. Columns were then incubated with 80 µL freshly prepared DNase I working solution for 15 min, followed by adding 500 µL RNA Priming buffer and centrifugation for 30 sec at 16,000 x g. Afterwards, each column was washed twice with 500 µL RNA Wash Buffer, the first with a 30 sec and the second with a 2 min centrifugation step at 16,000 x g at RT. The columns were finally dried by an additional 1 min 16,000 x g centrifugation stap at RT and transferred to RNase-free microcentrifuge tubes. RNA was finally eluted by adding 50 µL nuclease-free H_2O directly to the column and centrifugation for 30 sec at 16,000 x g at RT. RNA concentration

was determined using the Nanodrop 2000 spectrophotometer (Thermo Scientific). The isolated RNA was stored at -80°C.

2.4.1.2 cDNA synthesis

Complementary DNA (cDNA) was synthesised using the iScript cDNA Synthesis kit for RT-qPCR (Bio-Rad) according to the manufacturer's instructions. 500 ng of template RNA for BMDMs and 1000 ng for RAW264.7 cells was diluted in nuclease-free water to a total volume of 15 µL in PCR reaction tubes. The reagents were combined according to Table 2.13, added to the pre-diluted template RNA, mixed, and spun down briefly. The reaction tubes were then placed in a T100 Thermal Cycler (BioRad), and reverse transcription was performed by a 5 min incubation at 25°C, followed by incubation at 42°C for 30 min and heat inactivation of the reverse transcriptase at 85°C for 5 min. The cDNA was stored at -20°C. To determine possible contamination with genomic DNA of the samples and the master mix, minus-reverse transcriptase controls of template RNA and a non-template control were added per thermocycler run.

Table 2.13 Composition of a cDNA reverse transcription reaction

Component	Volume per reaction [µL]
5x iScript Advanced Reaction Mix	4
iScript Advanced Reverse Transcriptase	1
500/1000 ng RNA	15
Total volume	20

2.4.1.3 Standard curve

The qPCR standard curve for murine TNF-α was prepared using a plasmid containing the respective sequence, purchased from Addgene (#28089), and prepped as described in 2.2.3.3. Predicted complementary Taqman probe binding was verified before purchase using Benchling.

The presence of the entire sequence was confirmed using the Sanger sequencing service from SourceBioscience using the library primer EGFP_C_F. Subsequently, 5 µg of the pMurineTNF plasmid were digested with AgeI (NEB) according to the manufacturer's instructions and as described in chapter 2.2.2.4. The components were mixed and incubated at 37°C for 1 h, followed by a heat inactivation step at 65°C for 20 min. The quality of the linearisation process was verified using DNA gel electrophoresis as described in Chapter 2.2.2.2. The linearised plasmid at a concentration of 100 ng/µL (or 1.8 x 10^{10} molecules/µL, determined by NEBiocalculator (304)) was then aliquoted as a serial dilution (dilution factor from 100 to 1x10^{10}), and stored at -20°C.

2.4.1.4 Absolute qPCR reactions

Real-time quantitative (q)PCR of TNF mRNA was performed using FAM-TaqMan probes Mm00443258_m1 (Thermo Fisher Scientific) together with TaqMan Gene Expression Master Mix (Thermo Fisher Scientific) according to the manufacturer's instructions. The PCR reactions were set up in triplicates in 384-well plates by combining the reagents shown in Table 2.15 and run on a CFX384 Real-Time PCR detection system (Bio-Rad) with the cycle conditions listed in Table 2.16. The standard curve was run alongside samples for total quantification, starting at 3 molecules up to 1E+08 molecules in a well (Table 2.14). The quality of the standard curve was assessed by calculating the R^2 value of linear regression. No-template control, minus-reverse transcriptase control, and water samples were run on each plate to monitor contaminations and exclude false positive results.

Table 2.14 Overview qPCR standard curve

Standard No.	pDNA copy number	Standard No.	pDNA copy number
S1	1E+08	S10	3000
S2	30000000	S11	1000
S3	10000000	S12	300
S4	3000000	S13	100
S5	1000000	S14	30
S6	300000	S15	10
S7	100000	S16	3
S8	30000	S17	0
S9	10000		

Table 2.15 Components of an RT qPCR reaction

Component	Volume per reaction [µL]
TaqMan Gene Expression Master mix 2x	5
TaqMan Gene Expression Assay (20x)	0.5
cDNA template (10 ng/µL)	1.5
nfH2O	3
Total volume	10

Table 2.16 Cycle conditions of an RT qPCR reaction

Cycling step	Temperature [°C]	Time [min:sec]	# Cycles
UDG Incubation	50	2:00	1
AmpliTaq Gold, UP enzyme activation	95	10:00	1
Denaturation	95	0:15	40
Annealing and extension	60	1:00	
Optical read			

2.4.2 Assessment of protein expression via Western Blot

2.4.2.1 Protein isolation

To isolate protein, $2x10^6$ BMDMs, $1.2x10^6$ RAW264.7 cells, or $0.6x10^6$ HeLa cells per well were seeded and stimulated in 6-well plates, placed on ice, washed with ice-cold PBS, and incubated for 5 min in 100 µL lysis buffer per well. The lysis buffer was prepared from 10x RIPA buffer (Cell Signaling) with 1x cOmpleteULTRA protease inhibitor (Roche) and 1x PhosStop phosphatase inhibitor (Roche) in ddH_20. The now lysed cells were scraped off, transferred into QIAshredder columns, stacked into collection tubes (Qiagen) and centrifuged at maximum speed in a microcentrifuge for 2 min at 4°C. Then, the columns were discarded, and the collection tubes were centrifuged at 14.000 x g, 4°C, for 10 min. The resulting pellet was discarded while the supernatant was transferred into a pre-cooled microcentrifuge tube and stored at -20°C or -80°C for short- or long-term storage, respectively.

2.4.2.2 Protein measurement

Protein concentrations were measured using the Pierce BCA protein assay kit (Thermo Fisher Scientific) according to the manufacturer's instructions. Bovine serum albumin (BSA) standards were prepared by serial dilution of a 2000 µg/mL BSA stock in 1x RIPA buffer (BSA standard concentrations [µg/mL]: 0, 125, 250, 500, 750, 1000, 1500, 2000). Following this, the BCA working reagent was set up (50:1, BCA Reagent A:B), mixed well and stored in the dark before use. The frozen samples were thawed on ice, and the required volume was transferred into PCR tubes to prepare a dilution 1:4 in RIPA buffer. 10 µL of each standard and the prediluted sample were pipetted in triplicates into a clear polystyrene flat bottom 96-well plate. Then, 200 µL Working Reagent was added per well. The plate was mixed for 30 sec on a plate shaker and incubated for 30 min at 37°C. Afterwards, the absorbance at 563 nm was measured and analysed using the Synergy™ HT microplate reader.

2.4.2.3 Standard curve

A standard curve for p38 MAPK, TTP, and DUSP1 was generated using purchased recombinant protein (Table 2.17). The protein was aliquoted for single use and stored at -80°C in PCR tubes. For experiments, aliquots were thawed on ice, serially diluted in 1x RIPA, and otherwise treated the same way as samples described below under Chapter 2.4.2.4. Standard curve dilution concentrations used in experiments were determined by preliminary experiments.

Table 2.17 Recombinant protein for Western blot standard curve

Recombinant protein	Supplier	Stock concentration
Human p38 alpha/MAPK14 (Active)	Abcam	0.64 µg/µL
Human TTP	Abcam	0.09 µg/µL
Human MKP-1 (DUSP1)	Abcam	0.05 µg/µL

2.4.2.4 SDS-PAGE using Stain-Free™ protein gels

Protein samples were separated for WB via SDS PAGE using Criterion™ TGX Stain-Free™ Protein Gels (4–20%, 26 well, BioRad), a Criterion Gel Electrophoresis Cell (BioRad) and Running buffer (25 mM Tris, 190 mM glycine, 0.1%SDS, pH8.3) according to the manufacturer's instructions. Samples were diluted in 6x Laemmli SDS sample buffer with Mercaptoethanol (Thermo Fisher Scientific) and RIPA buffer to a concentration of 1.67 µg/µL, vortexed, quickly spun down, and boiled in a heating block for 5 min at 95°C. Afterwards, the samples were vortexed and spun down at maximum speed for 1 min in a microcentrifuge and stored on ice before being loaded onto the gels. For large-scale experiments, prepped samples were stored at -20°C for follow-up SDS page and WB. 20 µg of protein in 12 µL were loaded per well. 5 µL Pageruler Plus Prestained Protein Ladder (Thermo Fisher Scientific) was run alongside samples and loaded to the first and last lane. Electrophoresis was performed at 100

V until the dye constituting the visible running front had just left the gel (usually ~1.5 h). After protein separation, the gel was immediately removed from its gel cassette, and the Stain-Free signal for later normalisation was activated for 1 min using a ChemiDoc™ MP imaging system (BioRad). The image acquired during this activation was also used to evaluate the protein separation on the gel.

2.4.2.5 SDS page using PhosTag gels

To determine the percentage of phosphorylated p38 in the purchased active p38 recombinant protein, a sample of that protein was separated using SuperSep PhosTag gels (50 µmol/L, 100x100x6.6 mm, Wako) according to the manufacturer's instructions. Samples were treated as described in 2.4.2.4. The sample was run in conjunction with a PhosTag gel-specific protein ladder (Wako) and run for 1 h at 100 V in Running buffer (25 mM Tris, 190 mM glycine, 0.1%SDS, pH8.3). After the run, the gel was carefully removed from the cassette, placed into a dish containing Transfer buffer (25 mM Tris, 190 mM glycine, pH 8.3) with 10 mmol/L EDTA, and incubated for 20 min under gentle agitation. This was repeated 3 times with buffer exchange. Following this, the gel was soaked for another 10 min in transfer buffer without EDTA.

2.4.2.6 Western blot transfer and Stain-Free imaging

After pretreatment (Stain-Free activation or buffer soaking), the gels were directly transferred onto the preactivated PVDF membranes of Trans-Blot® Turbo™ transfer packs (BioRad), which were then assembled within the blotting chambers of the Trans-Blot® Turbo™ transfer system (BioRad) according to the manufacturer's instructions. Afterwards, blotting was performed for 7 min using the Turbo-settings. Stain-Free gel blots were incubated for 5 min in TBST (200 mM Tris base, 150 mM NaCl, 0.1% Tween 20), directly placed on the plate of the ChemiDoc™ MP imaging system and an image was acquired using the Stain-Free blot imaging

settings. The acquired picture, showing the total protein loaded on the gel, is later used to normalise the individual lanes.

2.4.2.7 Membrane staining and development

To hybridize with the primary antibody, blots were blocked for 5 min under gentle agitation in EveryBlot Blocking Buffer (BioRad) and incubated overnight on the plate shaker at 4°C with the respective primary antibody diluted in EveryBlot Blocking Buffer at the appropriate concentration (Table 2.18). On the next day, blots were washed 3 times for 5 min each in TBST and incubated for 1 h with Horseradish peroxidase (HRP)-conjugated secondary antibody in EveryBlot Blocking Buffer at the appropriate concentration (Table 2.18). Subsequently, the blots were washed 3 times for 5 min each in TBST again before chemiluminescence was measured using ECL™ Western Blotting Detection Reagents (Thermo Fisher Scientific) according to the manufacturer's instructions. The blots were incubated for 2 min at RT with 6 mL development solution (1:1 Detection Reagent 1 and 2) and directly imaged for chemiluminescence on the ChemiDoc™ MP imaging system. Blots were then washed and stored at -20°C or -80°C for short- or long-term storage. Where p38 was the imaging target, the blots were first imaged for Phospho-p38 and subsequently stripped for 40 min using 2x ReBlot Plus Mild Antibody Stripping solution (Merck) according to the manufacturer's instructions. After washing 5 times for 5 min in TBST, the stripping efficiency was checked by measuring chemiluminescence followed by a new hybridization as described in this protocol.

Table 2.18 Western Blotting Antibodies

Antibody	Supplier	Dilution
α-Phospho-p38 MAPK (Thr180/Tyr182) #9211	Cell Signaling	1:1000
α-p38 MAPK #9212	Cell Signaling	1:1000

α-DUSP1/MKP1 (E6T5S) #35217	Cell Signaling	1:1000
α-Tristetraprolin (D1I3T) #71632	Cell Signaling	1:1000
A-rabbit IgG, HRP-linked #7074	Cell Signaling	1:2000

2.4.2.8 Densitometry and total quantification

Signals were analysed and quantified using ImageLab (Bio-Rad). Lanes and bands were drawn to include the full Stain-Free signals and all bands visible. Signals were adjusted by background rolling circle subtraction using a disk size of 0.1 mm. Adjusted values were generated by normalising band values to the Stain-Free lane measurements. The analysis table was then exported to a Microsoft-Excel file. The standard curve was calculated using linear regression analysis. The quality of standard curves was assessed by calculating the R^2 value of the linear regression model, and the *FORECAST* function in Excel was used to perform total quantification. Values measured below the detection limit were excluded, indicated by a grey symbol in the individual WB analysis graphs (Appendix 7.3). To identify time-course values below the detection limit, images were obtained with longer exposure, leading to some values being oversaturated, especially in the standard curve. Oversaturated values and wonky lanes were excluded from the calculation of standard curve and time-course measurements. When less than three data points were left in the standard curve, time-course data points initially below the detection limit were calculated using interblot calibration (309).

2.4.3 Assessment of protein expression by ELISA

To measure the amount of TNFα protein secreted from WT BMDMs and mutant TTP expressing BMDMs, we used the Mouse TNF alpha Uncoated ELISA assay from Invitrogen.

For this, a 96-well ELISA plate (Corning) was coated with 100 µL/well of 1:250 diluted capture antibody in Coating Buffer overnight at 4°C, with the plate sealed. After the incubation, the wells were washed three times using 250 µL of Wash Buffer before they were blocked with 200 µL of 1x ELISA/ELISPOT Diluent for 1 h at RT. Afterwards, the wells were rinsed once using Wash Buffer before being used in the assay.

The standard for the ELISA was reconstituted immediately before a twofold series dilution in triplicates with ELISA/ELISPOT Diluent was performed (1000; 500; 250; 125; 62.5; 31.25; 15.625; 0 pg/mL). Each well finally contained 200 µL of the appropriately diluted volume of standard solution.

Samples comprising the cell supernatant collected during the BMDM LPS time-course experiments were diluted 1:4 in ELISA/ELISPOT Diluent before 200 µL in triplicates were added into wells. After adding standards and samples, the plate was sealed and incubated at RT for 2 h.

All wells were washed 3 times using 250 µL/well of Wash Buffer before 100 µL of 1:250 detection antibody in ELISA/ELISPOT Diluent was added to each well. The plate was again sealed and incubated for 1 h at RT before all wells were washed 3 times using 250 µL/well of Wash Buffer. 100 µL of 1:100 Streptavidin-HRP in ELISA/ELISPOT Diluent was added to each well, upon which the plate was again sealed and incubated at RT for 30 min. All wells were washed 5 times using 250 µL/well of Wash Buffer before 100 µL of 1x TMB solution was added to each well and incubated for 15 min. The reaction was stopped by adding 100 µL/well of stop solution. The plate was then read on a Synergy™ HT microplate reader at 450 nm.

2.5 Mathematical Modelling toolboxes

2.5.1 Structural identifiability analysis

The MATLAB toolbox GenSSI, published by Banga and Balsa-Canto (310), assesses global structural identifiability of linear and nonlinear dynamic models by using a generating series approach based on Lie derivates and creating a identifiability tableaus for visualisation purposes from the Jacobian of the series coefficients (311).

GenSSI uses, as format, an advanced multilanguage interface for CVODES and IDAS. To define the input for the toolbox, a problem file needs to be generated that contains the model function with all symbolic definitions. Here, the symbolic variables of dependent variables *x* and parameters *p* are created as well as their respective vector *model.sym.x* and *model.sym.p*. Then, the model equations are defined as column vectors under *model.sym.xdot*. The stimulus *g* called control in this toolbox is defined as *model.sym.g*. Observables *y* are defined as *model.sym.y* and initial conditions *x0* under *model.sym.x0*. In addition, a "run" script was defined. After running *genssiStartup.m*, the model can then be analysed using this runExample.file. Results are presented as text, identifying parameters as either globally, locally, or non-structurally identifiable, as well as identifiability tableaus. The complete code for GenSSI identifiability analysis of the Tomida and Kulawik TTP models can be found in Appendix 7.1.

2.5.2 Global parameter ranking

The AMIGO2 toolbox presented by Balsa-Canto et al. (280,282) includes a global sensitivity analysis of parameters and ranking based on the resulting importance factor. Global parametric sensitivity analysis is achieved by calculating the sensitivity of a large pool of parameter vectors created by Latin hypercube sampling.

Within the toolbox the importance factors are defined as follows:

$$\delta_{n_{lhs}n_d}^{msqr} = \frac{1}{n_{lhs}n_d}\sqrt{\sum_{mc=1}^{n_{lhs}}\sum_{d=1}^{n_d}([s_d]_{mc})^2} \tag{2.1}$$

$$\delta_{n_{lhs}n_d}^{mabs} = \frac{1}{n_{lhs}n_d}\sum_{mc=1}^{n_{lhs}}\sum_{d=1}^{n_d}|[s_d]_{mc}| \tag{2.2}$$

$$\delta_{n_{lhs}n_d}^{mean} = \frac{1}{n_{lhs}n_d}\sum_{mc=1}^{n_{lhs}}\sum_{d=1}^{n_d}[s_d]_{mc} \tag{2.3}$$

$$\delta_{n_{lhs}n_d}^{max} = \sum_{mc=1}^{n_{lhs}}[max_d\ s_d]_{mc} \tag{2.4}$$

$$\delta_{n_{lhs}n_d}^{min} = \sum_{mc=1}^{n_{lhs}}[min_d\ s_d]_{mc} \tag{2.5}$$

With $msqr$ standing for mean square root, n_d representing the total number of dependent variables, n_{lhs} the number of different values selected for each parameter using latin hypercube sampling, s_d the relative sensitivity of the dependent variable d, mc the index of the specific latin hypercube sampling parameter estimate. To perform global parameter ranking in AMIGO2, first a "run file" was created under the name "run_KulawikTTP_Grank", containing the name of the problem file, "Kulawik_TTP_Grank", as well as the command to call *AMIGO_Prep(inputs)* and *AMIGO_Grank(inputs)*. The problem file was set up containing information about the result folder (*inputs.pathd.results_folder*), model-related data (*inputs.model.i*) such as model type (*input_model_type*), file name to be run (*matlabmodel_file*) as well as a number of state variables (*n_st*), parameters (*n_par*), and stimuli (*n_stimulus*). Furthermore, their names are defined (*st/par/stimulus_names*), as well as model equations (*eqns*) and nominal parameter values (*par*).

This information was followed by experimental scheme-related data (*inputs.exps.i*), defining number of experiments (*n_exp*), initial conditions (*exp_y0{iexp}*) number of sampling times (*t_f{iexp}*), number of observables (*n_obs{iexp}*), their name for graphs (*obs_names{iexp}*)and their connection to variable name (*obs{iexp}*). Further, the type of stimulus (*u_interp{iexp}*), the duration of the experiment (*t_con{iexp}*), as well as value of stimulus (*u{1}*) are defined. In the next section, the data regarding unknown parameters (*inputs.PESol.i*) is given, defining which parameters are considered for analysis (*id_global_theta*), minimum and maximum value (*global_theta_min/max*) to be explored, as well as reference to nominal parameter values (*global_theta_guess*). For the simulation of the data, the initial value problem solver (*inputs.ivpsol.ivpsolver*) *ode15s* and the sensitivity solver (*senssolver*) "*sensma"t* were chosen. Rtol and Atol were set to *1.0D-7* (*rtol/atol*). The number of G-rank samples for global sensitivities (*inputs.rank.gr_samples*) was set to *10,000*. The full code for the global parameter ranking of the Tomida and Kulawik TTP models is found in Appendix 7.1.

2.5.3 Parameter estimation

Parameter estimation was performed using the MATLAB toolbox AMIGO2 published by Balsa-Canto et al. (280,282). Here, the parameter estimation problem is formulated as a nonlinear optimisation problem to minimise a given cost function, which again aims to minimise the distance between the model simulations and the experimental data. The toolbox allows the employment of various nonlinear problem solvers. In this thesis, we used the local solver nl2sol in combination with the hybrid solver eSS2 as well as the global solver SRES. The initial value problem solver can be chosen between *ode45*, *ode113*, *ode15s*, and CVODES.

To perform parameter estimation in AMIGO2, first a "run file" was created under the name "run_KulawikTTP_PE", containing the name of the problem file, "Kulawik_TTP_XXX_PE", as well as the command to call *AMIGO_Prep(inputs)* and *AMIGO_PE(inputs)*. The problem

file was set up to contain information about the result path, model definition, and experimental scheme. This is already described in detail in the previous Chapter 2.5.2. Specific for parameter estimation is the experimental data related information (*inputs.exps.data_i*). Here the data type, the experimental data as *ns(iexp) x n_obs(iexp)* matrix under *inputs.exps.exp_data{i}*, and the error data in the same format as the data are inserted. Furthermore, the unknowns related data needs to be chosen; this includes which parameters to include (*inputs.PEsol.id_global_theta*) as well as upper and lower boundaries for the estimation (*inputs.PEsol.global_theta _min/max*). Then, the cost function-related data (*inputs.PEsol.PEcost_type*) and (*inputs.nlpsol.nlpsover*) needs to be chosen. The full code for the parameter estimation of the Kulawik TTP model is found in Appendix 7.1. Data output comprises estimated parameters, simulation of parameters, various visualisation of residuals, and Crammer Rao correlation matrix.

CHAPTER THREE

Mathematical modelling of the p38 MAPK-TTP signalling axis during the inflammatory response in macrophage populations

3 Mathematical modelling of the p38 MAPK-TTP signalling axis during inflammatory responses in macrophage populations

3.1 Introduction

Macrophages, as a major source of inflammatory cytokines and chemokines, are central to developing chronic inflammatory diseases such as RA (32,312). In RA synovial tissue, the pro-inflammatory environment leads to the polarisation of monocyte-derived macrophages towards an "M1-like" phenotype (31,313), while DAMPs activate TLRs, thus stimulating the production of inflammatory mediators (33,314–317). A central pathway regulating TLR4-induced cytokine and chemokine expression in macrophages, is the p38 MAPK-TTP signalling axis (318,319). Here p38 MAPK promotes the expression of inflammatory mediators directly on the transcriptional level and indirectly by MK2-mediated phosphorylation and deactivation of TTP on the posttranscriptional level, which would otherwise work to downregulate the expression of these mediators (85,91,92,180). Because of this, p38 MAPK has been identified as a promising target for anti-inflammatory therapy (178). However, p38 MAPK inhibitors tested in clinical trials exhibited only transient anti-inflammatory activity and a broad range of adverse effects (67,175,178). The underlying reason for the limited effectivity is not entirely understood. Still, one potential drawback of continuous p38 MAPK inhibition could be that it prevents TTP expression in macrophages, abolishing TTP's mRNA destabilizing effects, paradoxically leading to an increase in the expression of pro-inflammatory mediators overall (85,320). Therefore, a better understanding of the p38 MAPK-TTP pathway structure and dynamics might allow to harvest the therapeutic potential concealed within this pathway.

In silico analysis of signalling pathways using mathematical modelling can help to obtain a comprehensive view by dissecting the importance and temporality of each pathway element to

identify and analyse targets for potential treatment strategies (289). ODE models are a well-established tool in pharmacological research and have been used extensively and successfully to simulate the kinetics of various signalling pathways, including the MAPK pathway (321).

This chapter describes the building, parameter estimation, and validation of a p38 MAPK-TTP ODE model calibrated on total quantification WB and qPCR data. Since the p38 MAPK pathway is a popular target for mathematical modelling, various models have already been published investigating different aspects of p38 MAPK biology (compare Chapter 1.5.3.1). One of these, published by Kulawik et al., inspired the experimental design for parameter estimation in this chapter, as well as the structure of the p38 MAPK section of the model (290). Parameter estimation and model analysis and validation were performed in accordance with a framework for ideal model identification described by Balsa-Canto et al. (compare Chapter 1.5.2) (281).

3.2 Model formulation

The modelling process can be broadly divided into five phases: Goal setting, model selection, model design, model analysis, and model application. In this sub-chapter we will tackle the first three for the Kulawik et al. inspired p38 MAPK-TTP model, up to the point where a defined model structure is established. To achieve that, symbolic equations, and nominal parameter values for the initial exploration of the model were based on already published data.

3.2.1 Scope of the model

Determining the scope of our model included defining its aim, identifying data availability and constraints, the temporal or spatial scope, potential application, and defining the main research questions to tackle with the help of this model.

The aim and the main questions to be addressed were already presented in Chapter 1.6. As a brief reminder, the aim of our Kulawik p38 MAPK-TTP model was to accurately capture the interactions and behaviours of the p38 MAPK-TTP signalling axis relevant to the posttranscriptional regulation of pro-inflammatory chemokines and cytokines in macrophages.

While a variety of publications already exist, presenting expression measurements of members of this pathway, we found the data insufficient to fully understand pathway dynamics and interactions in a quantitative, reproducible manner, especially because of the frequently low temporal resolution and the semi-quantitative nature of the data available. For this interdisciplinary project, we were able to tailor the experimental design to our mathematical model instead of, as is more common, making use of existing data. Consequently, the experimental design was defined as an important factor for this model (detailed in Chapter 3.3). The improvement of which will therefore also be part of the discussion.

Total quantification data can be considered the gold standard for mathematical modelling, as it enables data comparison and improves the reproducibility and predictive power of a model (279). As such, we decided to use total quantification methodology, in this case using standard-curve based total quantification WB and qPCR, to generate the data for the parameter estimation of the model.

The temporal scope was set to cover the first 8 h of the inflammatory response in as much detail as possible without compromising experimental practicality. During this timeframe, all major inflammatory response events we are interested in, such as the initial peak of p38 MAPK phosphorylation, the initial peak in DUSP1 expression, the initial peak in Tnf mRNA expression, and the main peak in TTP expression, should happen in BMDMs (148,210,290). Where results would suggest that later time points are needed, an experiment specifically looking at these could be designed, which is possible due to the use of total quantification data. We defined the spatial scope to cover protein and RNA pools within individual cells of macrophage populations, not discriminating between subcellular compartments. This decision is based on previous experiments performed by colleagues in our group and from the literature, which demonstrate that potential subcellular changes of TTP throughout the inflammatory response in BMDMs and RAW264.7 cells cannot be detected using multicellular quantitative approaches such as WBs (263,265,266). Based on this data, we decided that adding subcellular compartmentalization would not improve the explanatory power of the model.

3.2.2 Selection of the model structure

Based on the purpose we defined for our model and the planned data input, the structure of the model was decided from a pool of model characteristics, as laid out in Chapter 1.5.1.2. This decision was derived by asking several questions, such as whether we wanted an explanatory mechanistic or correlative black box model, whether the model should be static or dynamic,

continuous or discrete, deterministic or stochastic, spatially homogenous or heterogenous, open to environmental factors or closed, and whether any approximations are needed.

We aimed for a model with strong explanatory capacity, that can copy detailed biological processes. It needed to be dynamic, not static, to cover the temporal component of the inflammatory response as well as continuous and nonlinear because we are interested in detailed dynamic changes in a nonlinear system. First, we chose a deterministic model that clearly described the average biological processes. For this model, we further chose a homogenous spatial distribution for reasons discussed in the previous chapter (Chapter 3.2.1).

We further wanted an open model structure, allowing for environmental input in the form of inflammatory stimuli or inhibitors to disturb the system. In the context of required model approximations, as the whole plethora of signalling molecules involved in TLR4 signalling in macrophages is too complex to cover while meeting our aspired data quality requirements, we excluded all signalling components upstream of p38 as well as other pathways involved in TTP and TTP-target gene expression. With this simplification, we allowed ourselves to focus on the central pathway and keep the experimental design manageable.

A natural choice for a continuous model system is to represent it with differential equations. As we assumed spatial homogeneity, we will work with ordinary differential equations with a single independent variable, *t*. For the 'right-hand side' of the function of the central TTP model, we decided to go with the canonical generalised mass action system based on the modelling framework for biochemical systems theory (322). Using a canonical model design resulted in a homogenous structure, allowing easy analysis of the model, predictability, and compatibility with many already published models, including the p38 MAPK model presented by Kulawik et al. (290). The following section will use the now-defined model structure to

describe the design process of the actual mathematical model by defining its components and the underlying equations.

3.2.3 Model design

Designing a biological system model includes the definition of its components and resulting equations. Important classes of components in this context comprise variables, processes, and interactions, as well as parameters. In this section, an overview and reasoning for model components and equations will be given for the core TTP model, the implemented p38 MAPK model by Kulawik et al., as well as a combined Kulawik p38 MAPK-TTP model.

3.2.3.1 TTP core model

The idea for the model and its core structure was initiated by Dr Laura Bravo. To formulate the TTP pathway model we started with a model diagram (Figure 3.1) and a list of system components (Table 3.2, Table 3.3, Table 3.4, Table 3.5, Table 3.6) based on a scheme published by Clark and Dean (319). This scheme focuses primarily on the p38 MAPK- and PP2A-mediated posttranslational regulation of TTP and the difference in the degradation rate between unphosphorylated (unstable) and phosphorylated TTP (stable). First, we defined the dependent variables. For our model, we chose phosphorylated p38 MAPK protein, unphosphorylated and phosphorylated TTP protein, and the TTP-target mRNA (Table 3.1). For simplicity, we assume that p38 MAPK dephosphorylation increases linearly with time. To reflect this, we included the ODE time component ‘t’ into the equation (Table 3.2). We further defined independent variables that are not affected by the system and are usually constant within the model constraints. In our case, the independent variables comprise LPS as the inflammation-stimulating factor, time, and the protein phosphatase PP2A (Table 3.2). For our purposes, PP2A is assumed to be expressed constantly and not affected by LPS stimulation. The interactions and processes connecting the variables are summarised in Table 3.3.

Central here is the connection between unphosphorylated TTP and its phosphorylated state, where TTP becomes phosphorylated by the p38 MAPK signalling pathway (R1, in Figure 3.1; all other reactions within this chapter are connected to this figure as well) and dephosphorylated in a PP2A-dependent manner (R2). Other processes comprise the synthesis of unphosphorylated TTP induced by LPS (R3) and degradation of unphosphorylated (R4) as well as phosphorylated TTP (R5). Further reactions comprise LPS-induced target mRNA synthesis (R6) along with its unphosphorylated TTP-dependent (R7) and independent degradation (R8). The interactions and processes can be summarised as phosphorylation, dephosphorylation, synthesis, and degradation. Therefore, we structured the resulting parameters (Table 3.4) in the same categories: with γ_T and γ_{Rm} being the synthesis rates of TTP (T) and target mRNA (R_m), φ_T and φ_{Pp} being phosphorylation rates, with P_P standing for phosphorylated p38 MAPK, ρ_{Tp} and ρ_{Pp} being dephosphorylation rates, and δ_T, δ_{Tp}, δ_{Rm1}, and δ_{Rm2} being respective degradation rates.

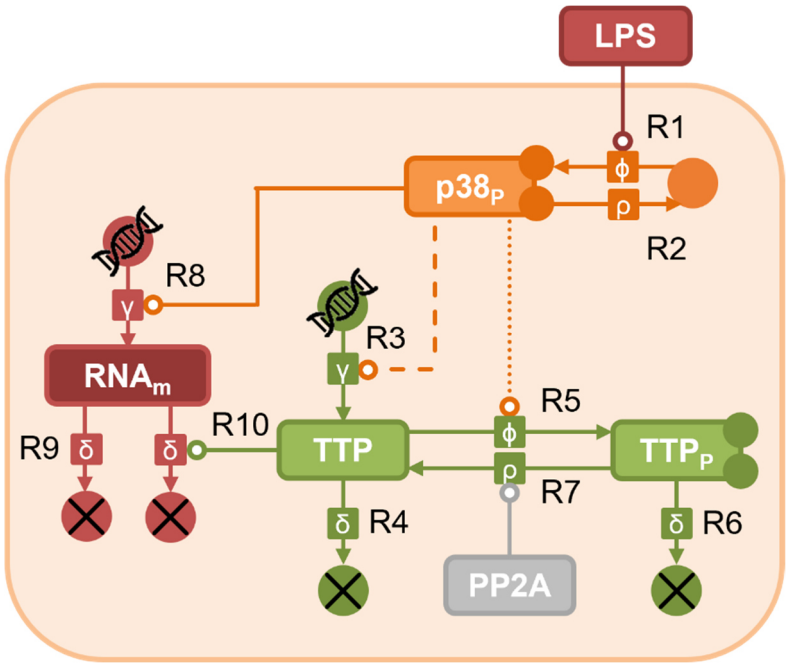


Figure 3.1 Model diagram of the core TTP pathway.

The graphic summarises the model components included in the TTP core model, how they relate to each other, and the main reactions involved. This overview was then used to formulate the model equations (3.1) to (3.4). The key dependent variables phosphorylated p38 MAPK ($p38_P$, orange), unphosphorylated TTP (green), phosphorylated TTP (TTP_P, green), and pro-inflammatory TTP-target mRNA (RNA_m, dark red), and the independent variables LPS (red) and PP2A (grey) are represented as nodes. Coloured circles on the nodes mark phosphorylated protein species. Arrows, also called edges in this context, indicate the flow of material between variables and represent the main reactions within the model numbered R1 to R9. Circles with a DNA helix indicate that new mRNA or, ultimately, protein is synthesised and enters the model. Circles with an X refer to the degradation of mRNA or protein, therefore material leaving the model system. The lines with circles at their ends represent a flow of information and connect a variable with the reactions they are affecting. The parameters are represented as small squares on the reaction arrows labelled with the Greek letters γ, δ, φ, or ρ, referring to the specific type of reaction, namely the rate of synthesis, degradation, phosphorylation, and dephosphorylation, respectively.

Table 3.1 Dependent variables of the core TTP pathway.

Dependent variables			
Symbol	**Description**	**Initial condition**	**Dimension**
P_P	Concentration of phosphorylated p38 MAPK	$P_P0 = 0$	$a.u.$
T	Concentration of unphosphorylated TTP	$T0 = 0$	$a.u.$
T_P	Concentration of phosphorylated TTP	$T_P0 = 0$	$a.u.$
R_m	Concentration of TTP-target mRNA	$R_m0 = 0$	$a.u.$

Table 3.2 Independent variables of the core TTP pathway.

Independent variables			
Symbol	**Description**	**Value**	**Dimension**
S	Concentration of stimulus LPS	1	$a.u.$
A	Concentration of PP2A	1	$a.u.$
t	Time component of the ODE	0-480	min

Table 3.3 Overview of interactions of the core TTP pathway

Interactions			
Reaction	**Description**	**No.**	**Ref.**
$\emptyset \xrightarrow{LPS} p38_P$	LPS-dependent production of phosphorylated p38 MAPK	R1	(319)
$\emptyset \leftarrow p38_P$	Dephosphorylation of p38 MAPK	R2	(319)
$\emptyset \xrightarrow{p38_P} TTP$	Phospho-p38-dependent TTP synthesis	R3	(319)
$\emptyset \leftarrow TTP$	Degradation of unphosphorylated TTP	R4	(319)
$TTP \xrightarrow{p38_P} TTP_P$	Phospho-p38-mediated TTP phosphorylation	R5	(319)
$\emptyset \leftarrow TTP_P$	Degradation of phosphorylated TTP	R6	(319)
$TTP \xleftarrow[PP2A]{} TTP_P$	PP2A-mediated TTP dephosphorylation	R7	(319)
$\emptyset \xrightarrow{p38_P} RNA_m$	p38 MAPK-dependent synthesis of target mRNA	R8	(319)
$\emptyset \leftarrow RNA_m$	TTP-independent degradation of target mRNA	R9	(319)
$\emptyset \xleftarrow[TTP]{} RNA_m$	TTP-dependent degradation of target mRNA	R10	(319)

Table 3.4 Overview of parameters of the core TTP pathway model

Parameters			
Symbol	**Description**	**Nominal value**	**Dimension**
φ_{Pp}	Synthesis rate of $p38_P$	$0.1*10^{-1}$	min^{-1}
ρ_{Pp}	Dephosphorylation rate of $p38_P$	$0.1*10^{-1}$	min^{-2}
γ_T	Synthesis rate of TTP	$1.0*10^{-1}$	min^{-1}
δ_T	Degradation rate of TTP	$0.2*10^{-1}$	min^{-1}
φ_T	Phosphorylation rate of TTP	$5.0*10^{+1}$	min^{-1}
δ_{Tp}	Degradation rate of phosphorylated TTP	$0.1*10^{-5}$	min^{-1}

ρ_{Tp}	Dephosphorylation rate of TTP	$0.5*10^{-1}$	min^{-1}
γ_{Rm}	Synthesis rate of target mRNA	$1.0*10^{-1}$	min^{-1}
δ_{Rm1}	Degradation rate 1 of target mRNA	$0.1*10^{-2}$	min^{-1}
δ_{Rm2}	Degradation rate 2 of target mRNA	$0.1*10^{-1}$	min^{-1}

The collected information was then translated into a set of ordinary differential equations, with each dependent variable being represented by its own equation:

$$\frac{dP_P}{dt} = +\varphi_{Pp}{}^{*}S - \rho_{Pp}{}^{*}t^{*}P_P, \quad (3.1)$$

$$\frac{dT}{dt} = +\gamma_T{}^{*}P_P + \rho_{Tp}{}^{*}A^{*}T_P - \delta_T{}^{*}T - \varphi_T{}^{*}P_P{}^{*}T, \quad (3.2)$$

$$\frac{dT_P}{dt} = +\varphi_T{}^{*}P_P{}^{*}T - \delta_{Tp}{}^{*}T_P - \rho_{Tp}{}^{*}A^{*}T_P, \quad (3.3)$$

$$\frac{dR_m}{dt} = +\gamma_{Rm}{}^{*}P_P - \delta_{Rm1}{}^{*}R_m - \delta_{Rm2}{}^{*}T^{*}R_m, \quad (3.4)$$

with the initial conditions $P_P(0) = P_P0$, $T(0) = T0$, $T_P(0) = T_P0$, and $R_m(0) = R_m0$. Here '*' represents a multiplication sign, which is introduced for improved readability of the equations.

Now that we have decided on the mathematical scaffold, we chose a set of nominal parameter values to visualise qualitative model properties. The first set of parameter values (Table 3.4) was designed without units and obtained by trial and error with the aim to fit our qualitative and quantitative assumptions of the involved processes. For example, unphosphorylated and phosphorylated TTP were assigned two distinct degradation rates, as their degradation rate disparity is thought to be one of the core regulatory modules of this pathway (319): unphosphorylated TTP is active and can degrade its target mRNA but is at the same time highly

unstable due to its lack of structure outside of its central zinc-finger domain and gets readily degraded by the proteasome via the default unstructured protein degradation pathway, while phosphorylated TTP is inactive but highly stabilised (323). We further chose a TTP synthesis rate that allows steady accumulation over the 8 h period in addition to high phosphorylation rates because this type of cellular process is commonly very fast (324), while PP2A is arbitrarily set to 1, as we assumed it to not change over time. These values resulted in simulations shown in Figure 3.2. For the simulation, the equations (3.1) to (3.4) were solved in MATLAB using the *ode23* function. The full MATLAB script for this can be found in Appendix 7.1. Phosphorylated p38 behaved in accordance with the literature (290) in this simulation, with a steep rise in concentration at the beginning of the inflammatory response, followed by a rapid decrease to a plateau level. Unphosphorylated TTP increased slowly over time, allowing for an initial peak in inflammatory TTP-target mRNA expression. Phosphorylated TTP quickly accumulated, reaching a peak, followed by a steady decrease over time, thus refreshing the pool of unphosphorylated TTP later in the inflammatory response. The initial model was also successful in describing the expression pattern of pro-inflammatory cytokines and chemokines, which many of which are considered immediate early genes (325), with a steep increase early in the inflammatory response induced by p38 phosphorylation followed by a decrease, primarily promoted by unphosphorylated TTP. A TTP-KO would consequently lead to a substantial dysregulation in the form of prolonged target mRNA expression (Figure 3.3).

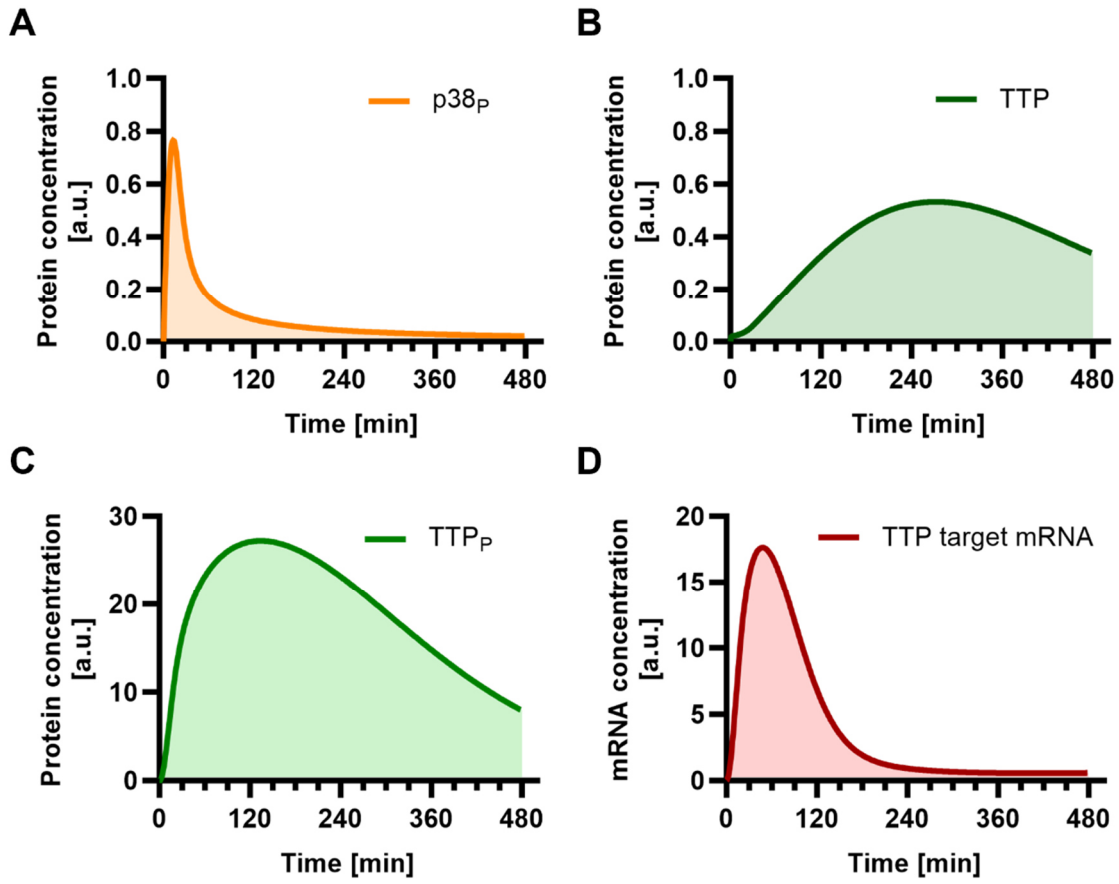


Figure 3.2 Computational simulation of the core TTP model.

The computational simulation of the TTP core model was generated in MATLAB using the *ode23* function to solve the ODE equations (3.1) to (3.4) as well as the nominal parameter values and initial conditions shown in Table 3.4, Table 3.1, and Table 3.2 for a time span of 480 min. The graphs show the expression change of A) phosphorylated p38, B) unphosphorylated TTP, C) phosphorylated TTP, and D) TTP-target mRNA following treatment with an inflammatory stimulus. The full MATLAB script for generating the graphs can be found in Appendix 7.1.

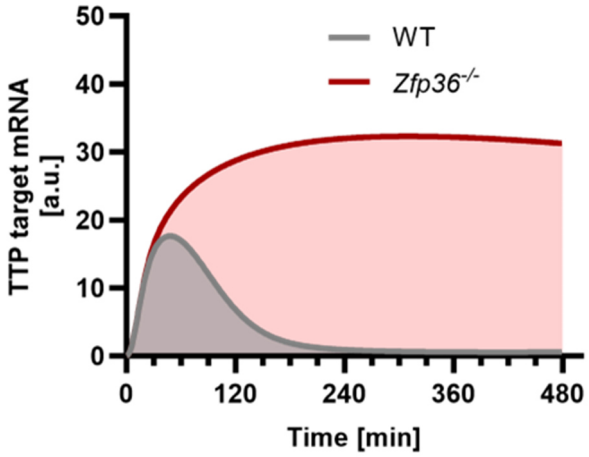


Figure 3.3 Computational simulation of target mRNA expression in TTP KO phenotype versus WT using the TTP core model.

The simulation shows target mRNA expression in the presence (TTP WT) and absence (TTP KO) of TTP. This was achieved by setting the TTP synthesis rate γ_T=0. The data for the simulation was created in MATLAB by solving equations (3.1) to (3.4) using the *ode23* function and the parameters from Table 3.4, Table 3.1, and Table 3.2 (except γ_T).

3.2.3.2 Kulawik p38 MAPK model

The p38 MAPK pathway, due to its importance in inflammation and cellular stress response in addition to its intricate dynamics, is a popular target for *in silico* analysis. Consequently, a whole battery of biological system models has already been described, capturing different aspects of the pathway (148,289,290). The advantages of exploring and implementing already validated elements of a model include achieving a better grasp of what is important for one's own model, inspiration for the experimental design and how to perform parameter estimation, and, when one is fortunate, even a validated set of parameters in a comparable biological system.

The reasons for choosing the Kulawik et al. model for upstream implementation were based on the similarity in model structure and their experimental design, which include high-quality data

using a total quantification approach in primary BMDMs. In addition, they included p38 MAPK phosphatases as dependent variables. The phosphatases are interesting to us because they comprise an important feedback loop within the pathway, and one of them, DUSP1, has been a research interest in the Clark research group for quite some time. DUSP1 further is an interesting target for anti-inflammatory therapy (326).

The Kulawik p38 MAPK model, represented by the model diagram in Figure 3.4, like our TTP core model, is based on mass action kinetics and consists of five nonlinear ODEs, with dependent variables being unphosphorylated and phosphorylated p38 MAPK (P, P_P), MKP (D) as a placeholder for all p38 MAPK specific phosphatases, unphosphorylated (K) and phosphorylated MK2 (K_P), and the inflammatory cytokine IL-1β (S) as an independent variable (290). Kulawik et al. further included saturating kinetics (Compare Equation 3.5), here with the saturation rate σ_S, for stimulus-dependent phosphorylation of p38 MAPK to simulate varying IL-1β concentrations (0 – 40 $mL^{-1}ng$) (290).

Instead of TLR4 activation, Kulawik et al. included IL-1R complex stimulation in their model. IL-1R-mediated p38 MAPK pathway activation is also present in macrophages and was chosen by the authors due to its role in hepatocyte biology (327). Like in our TTP core model, the signalling complex was summarised as stimulus-mediated p38 MAPK activation. They further assumed a basal activation of p38 MAPK, which they measured in their experiments. They combined contributing MAPK phosphatases (but not measuring them) with the argument that they lack specificity and to simplify the experimental design. A summary of all interactions and resulting parameters can be found in Table 3.6 and Table 3.7, respectively.

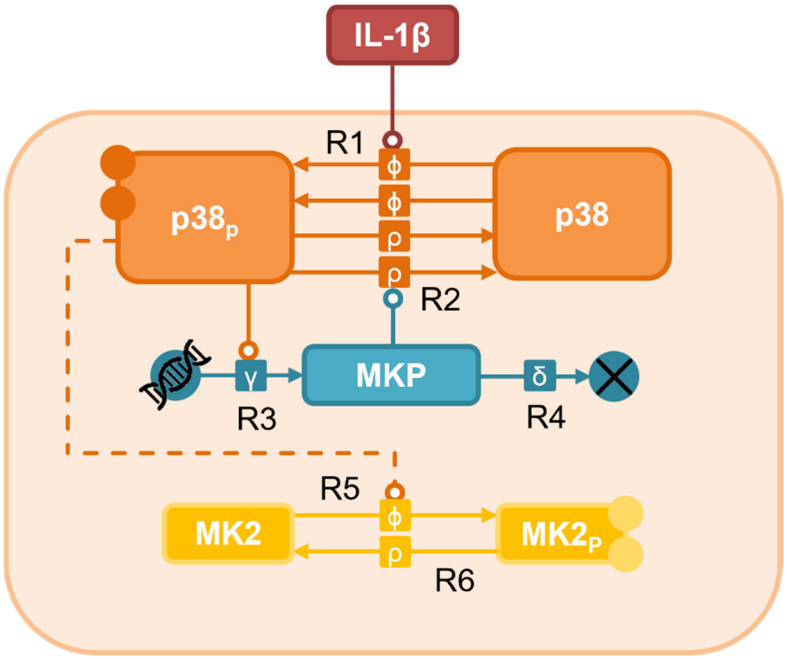


Figure 3.4 Model diagram of the Kulawik p38 MAPK model.

The graphic summarises the model components, reactions, and interactions included in the Kulawik p38 MAPK model. The dependent variables comprise unphosphorylated (p38, orange) and phosphorylated p38 ($p38_p$, orange), unphosphorylated (MK2, yellow) and phosphorylated MK2 ($MK2_p$, yellow), and the combined p38 MAPK phosphatases (MKP, blue). The sole independent variable is the stimulus IL-1β (red). Circles on the side of the variable mark phosphorylated protein species. Arrows indicate the flow of material between variables and represent the main reactions within the model numbered R1 to R6. Circles with a DNA helix indicate that new mRNA or, ultimately, protein is synthesised and enters the model. Circles with an X refer to the degradation of mRNA or protein, therefore material leaving the model system. The lines with circles at their ends represent a flow of information and connect a variable with the reactions they are affecting. The parameters are represented as small squares on the reaction arrows labelled with the Greek letters γ, δ, φ, or ρ, referring to the specific type of reaction, namely the rate of synthesis, degradation, phosphorylation, and dephosphorylation, respectively. Reactions 1 and 2 consist of two arrows each, representing the basal phosphorylation and degradation rates and the stimulus-dependent phosphorylation and dephosphorylation rates.

Table 3.5 Overview of variables of Kulawik p38 MAPK pathway model

Variables			
Symbol	**Description**	**Initial condition**	**Dimension**
S	Concentration of stimulus IL-1β	20	$mL^{-1}ng$
P	Concentration of unphosphorylated p38	$P0 = 40.3577$	μM
P_P	Concentration of phosphorylated p38	$P_P0 = 0.0013$	μM
D	Concentration of MKP	$D0 = 40$	μM
K	Concentration of unphosphorylated MK2	$K0 = 4.5514$	μM
K_P	Concentration of phosphorylated MK2	$K_P0 = 0.0856$	μM

Table 3.6 Interactions and processes described by Kulawik p38 MAPK pathway model

Interactions			
Reaction	**Description**	**No.**	**Ref.**
$p38 \xrightarrow{IL-1\beta} p38_P$	IL-1β-dependent phosphorylation of p38	R1a	(290)
$p38 \rightarrow p38_P$	Constant phosphorylation of p38	R1b	(290)
$p38 \xleftarrow[MKP]{} p38_P$	MKP-dependent dephosphorylation of $p38_P$	R2a	(290)
$p38 \leftarrow p38_P$	Constant dephosphorylation of $p38_P$	R2b	(290)
$\emptyset \xrightarrow{p38_P} MKP$	Phospho-p38-dependent MKP synthesis	R3	(290)
$\emptyset \leftarrow MKP$	Degradation of MKP	R4	(290)
$MK2 \xrightarrow{p38_P} MK2_P$	Phospho-p38-mediated MK2 phosphorylation	R5	(290)
$MK2 \leftarrow MK2_P$	MK2 dephosphorylation	R6	(290)

Table 3.7 Overview of parameters of the Kulawik p38 MAPK pathway model

Parameters			
Symbol	**Description**	**Nominal value**	**Dimension**
σ_S	Saturation rate of S	$0.52*10^{-1}$	$ng^{-1}mL$
φ_{P1}	Phosphorylation rate 1 of p38	$1.51*10^{-4}$	min^{-1}
φ_{P2}	Phosphorylation rate 2 of p38	$9.08*10^{-3}$	$min^{-1}ng^{-1}mL$
ρ_{Pp1}	Dephosphorylation rate 1 of $p38_P$	$1.00*10^{-5}$	min^{-1}
ρ_{Pp2}	Dephosphorylation rate 2 of $p38_P$	$3.10*10^{+1}$	$\mu M^{-1}\ min^{-1}$
γ_D	Synthesis rate of MKP	$8.41*10^{-3}$	$\mu M^{-1}\ min^{-1}$
δ_D	Degradation rate of MKP	$0.01*10^{+1}$	min^{-1}
φ_K	Phosphorylation rate of MK2	$1.02*10^{+1}$	$\mu M^{-1}\ min^{-1}$
ρ_{Kp}	Dephosphorylation rate of $MK2_P$	$7.14*10^{-1}$	min^{-1}

The mathematical equations presented by Kulawik et al. were adapted to fit our denotation conventions to simplify compatibility between models but were otherwise left unchanged. This results in the following set of ODEs:

$$\frac{dP}{dt} = -\varphi_{P1}{}^{*}P - \frac{\varphi_{P2}{}^{*}S^{*}P}{\sigma_S{}^{*}S + 1} + \rho_{Pp1}{}^{*}P_P + \rho_{Pp2}{}^{*}D^{*}P_P, \tag{3.5}$$

$$\frac{dP_P}{dt} = +\varphi_{P1}{}^{*}P + \frac{\varphi_{P2}{}^{*}S^{*}P}{\sigma_S{}^{*}S + 1} - \rho_{Pp1}{}^{*}P_P - \rho_{Pp2}{}^{*}D^{*}P_P, \tag{3.6}$$

$$\frac{dD}{dt} = +\gamma_D{}^{*}P_P{}^{*}D - \delta_D{}^{*}D, \tag{3.7}$$

$$\frac{dK}{dt} = -\varphi_K{}^{*}P_P{}^{*}K + \rho_{Kp}{}^{*}K_P, \tag{3.8}$$

$$\frac{dK_P}{dt} = +\varphi_K{}^{*}P_P{}^{*}K - \rho_{Kp}{}^{*}K_P, \tag{3.9}$$

with the initial conditions $P(0) = P0$, $P_P(0) = P_P0$, $D(0) = D0$, $K(0) = K0$, and $K_P(0) = K_P0$. Here '*' represents a multiplication sign, which is introduced for improved readability of the equations.

Parameter values of the p38 MAPK model were estimated by Kulawik et al. applying maximum likelihood estimation in a single multi-experiment fit using Data2Dynamics software (328). These values are summarised in Table 3.7. They also identified the cell volume of hepatocytes and BMDMs, allowing the presentation of data in the nano-molar dimensions. The model simulation in Figure 3.5 was created by implementing those parameters and the initial conditions, setting the IL-1β concentration to 20 ng/mL, and solving ODEs with the *ode23* solver in MATLAB (Appendix 7.1). While the experimental conditions are different, these provide a good starting point for the nominal values that we use to start our parameterisation process. Phosphorylated p38 MAPK, as in our core model, behaves as described by Kulawik et al. in this simulation, with a steep rise in concentration at the beginning of the inflammatory response, followed by a rapid decrease to a basal level (290). In the model, the observed initial increase was introduced through the stimulus-dependent phosphorylation of p38 MAPK, while its decrease is mediated by dephosphorylation of p38 MAPK through its MKPs. Because phosphorylated p38 MAPK stimulates expression of MKP, a negative feedback loop is formed by the two variables. The same is true for phosphorylated MK2, but with a less pronounced drop after the initial rise, whereas the concentration of combined MAPK phosphatases increases gradually over time. To leverage the work by Kulawik et al., the TPP core model and the Kulawik p38 MAPK pathway model will be combined in the next section.

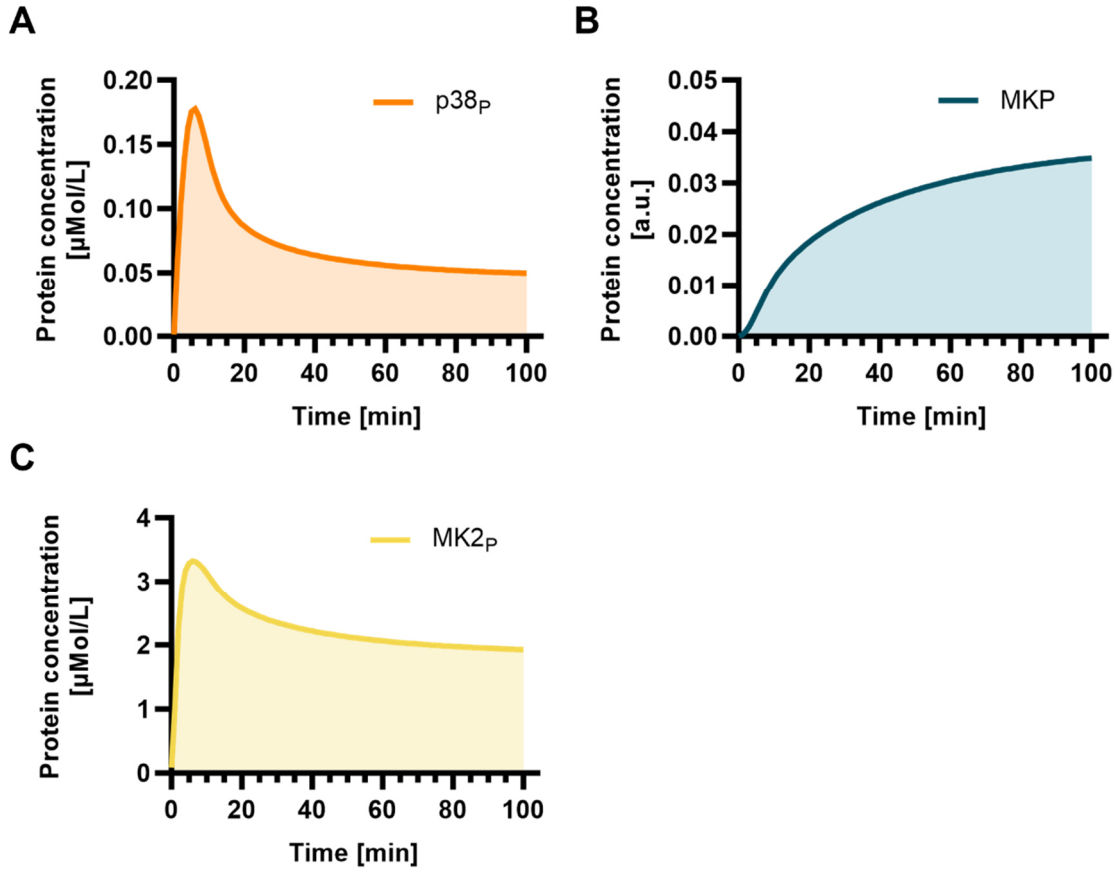


Figure 3.5 Computational simulation Kulawik p38 MAPK model.

The data for the simulation of the Kulawik p38 MAPK model was generated in MATLAB using the *ode23* function to solve the ODE equations (3.5) to (3.9) as well as the nominal parameter values and initial conditions shown in Table 3.7 and Table 3.5 for a time span of 100 min. The graphs show the expression change of A) phosphorylated p38, B) MKP, C) phosphorylated MK2 following treatment with 20 ng/mL IL-1β in hepatocytes. The full MATLAB script for generating the graphs can be found in Appendix 7.1.

3.2.3.3 Kulawik p38 MAPK-TTP model

We next combined the Kulawik p38 MAPK model and the TTP core model by replacing the ODE for phospho-p38 with the Kulawik model and by changing the phosphorylation of TTP from a p38-MAPK to an MK2-dependent mechanism (Figure 3.6). In this context, target mRNA and TTP synthesis are still dependent on p38 MAPK activity. This resulted in the following set of ODEs:

$$\frac{dP}{dt} = -\varphi_{P1}{}^{*}P - \frac{\varphi_{P2}{}^{*}S^{*}P}{\sigma_{S}{}^{*}S+1} + \rho_{Pp1}{}^{*}P_{P} + \rho_{Pp2}{}^{*}D^{*}P_{P}, \quad (3.5)$$

$$\frac{dP_{P}}{dt} = +\varphi_{P1}{}^{*}P + \frac{\varphi_{P2}{}^{*}S^{*}P}{\sigma_{S}{}^{*}S+1} - \rho_{Pp1}{}^{*}P_{P} - \rho_{Pp2}{}^{*}D^{*}P_{P}, \quad (3.6)$$

$$\frac{dD}{dt} = +\gamma_{D}{}^{*}P_{P}{}^{*}D - \delta_{D}{}^{*}D, \quad (3.7)$$

$$\frac{dK}{dt} = -\varphi_{K}{}^{*}P_{P}{}^{*}K + \rho_{Kp}{}^{*}K_{P}, \quad (3.8)$$

$$\frac{dK_{P}}{dt} = +\varphi_{K}{}^{*}P_{P}{}^{*}K - \rho_{Kp}{}^{*}K_{P}, \quad (3.9)$$

$$\frac{dT}{dt} = +\gamma_{T}{}^{*}P_{P} + \rho_{Tp}{}^{*}A^{*}T_{P} - \delta_{T}{}^{*}T - \varphi_{T}{}^{*}K_{P}{}^{*}T, \quad (3.10)$$

$$\frac{dT_{P}}{dt} = +\varphi_{T}{}^{*}K_{P}{}^{*}T - \delta_{Tp}{}^{*}T_{P} - \rho_{Tp}{}^{*}A^{*}T_{P}, \quad (3.11)$$

$$\frac{dR_{m}}{dt} = +\gamma_{Rm}{}^{*}P_{P} - \delta_{Rm1}{}^{*}R_{m} - \delta_{Rm2}{}^{*}R_{m}{}^{*}T, \quad (3.12)$$

With the initial conditions $P(0) = P0$, $P_P(0) = P_P0$, $D(0) = D0$, $K(0) = K0$, $K_P(0) = K_P0$, $T(0) = T0$, $T_P(0) = T_P0$, and $R_m(0) = R_m0$. Here '*' represents a multiplication sign, which is introduced for improved readability of the equations.

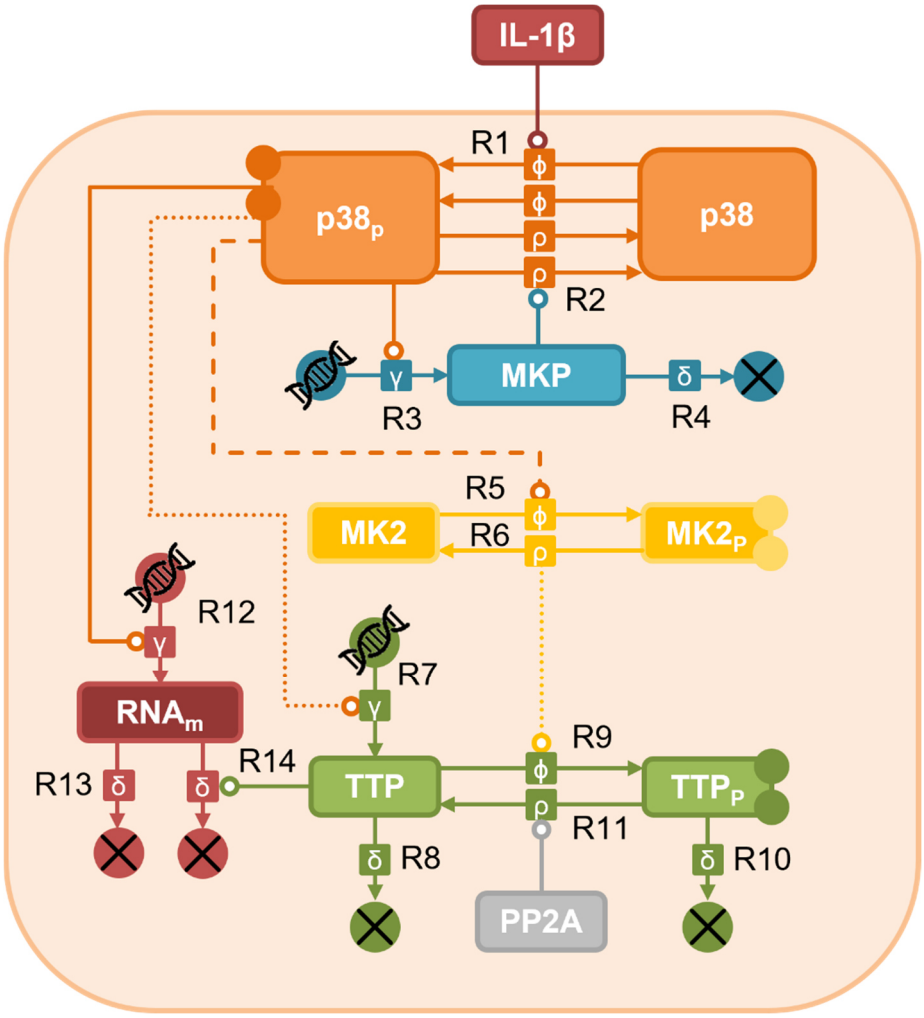


Figure 3.6 Model diagram of the Kulawik p38 MAPK-TTP pathway.

The graphic summarises the model components, reactions, and interactions included in the Kulawik p38 MAPK-TTP model. The dependent variables comprise unphosphorylated and phosphorylated p38 (orange), unphosphorylated and phosphorylated MK2 (yellow), the combined p38 MAPK phosphatases (blue), unphosphorylated and phosphorylated TTP (green), and TTP-target mRNA (red). The independent variables are the stimulus IL-1β and the TTP phosphatase PP2A. Circles on the side of the variable mark phosphorylated protein species. Arrows indicate the flow of material between variables and represent the main reactions within the model numbered R1 to R6. Circles with a DNA helix indicate that new mRNA or, ultimately, protein is synthesised and enters the model. Circles with an X refer to the degradation of mRNA or protein, therefore material leaving the model system. The lines with circles at their ends represent a flow of information and connect a variable with the reactions they are affecting. The parameters are represented as small squares on the reaction arrows labelled with the Greek letters γ, δ, φ, or ρ, referring to the specific type of reaction, namely the rate of synthesis, degradation, phosphorylation, and dephosphorylation, respectively. Reactions 1 and 2 consist of two arrows each, representing the basal phosphorylation and degradation rate as well as the stimulus-dependent phosphorylation and dephosphorylation rates.

Table 3.8 Overview of variables of Kulawik p38 MAPK-TTP pathway model

Variables			
Symbol	**Description**	**Initial condition**	**Dimension**
S	Concentration of stimulus IL-1β	20	$mL^{-1}ng$
P	Concentration of unphosphorylated p38	$P0 = 0.3577$	μM
P_P	Concentration of phosphorylated p38	$P_P0 = 0.0013$	μM
D	Concentration of MKP	$D0 = 0$	μM
K	Concentration of unphosphorylated MK2	$K0 = 4.5514$	μM
K_P	Concentration of phosphorylated MK2	$K_P0 = 0.0856$	μM
T	Concentration of unphosphorylated TTP	$T0 = 0$	$a.u.$
T_P	Concentration of unphosphorylated TTP	$T_P0 = 0$	$a.u.$
R_m	Concentration of TTP-target mRNA	$R_m0 = 0$	$a.u.$
A	Concentration of PP2A	1	$a.u.$

Table 3.9 Interactions and processes described by Kulawik p38 MAPK-TTP pathway model

Interactions			
Reaction	**Description**	**No.**	**Ref.**
$p38 \xrightarrow{IL-1\beta} p38_P$	IL-1β-dependent phosphorylation of p38	R1a	(290)
$p38 \rightarrow p38_P$	Constant phosphorylation of p38	R1b	(290)
$p38 \xleftarrow[MKP]{} p38_P$	MKP-dependent dephosphorylation of $p38_P$	R2a	(290)
$p38 \leftarrow p38_P$	Constant dephosphorylation of $p38_P$	R2b	(290)
$\emptyset \xrightarrow{p38_P} MKP$	Phospho-p38-dependent MKP synthesis	R3	(290)
$\emptyset \leftarrow MKP$	Degradation of MKP	R4	(290)
$MK2 \xrightarrow{p38_P} MK2_P$	Phospho-p38-mediated MK2 phosphorylation	R5	(290)

$MK2 \leftarrow MK2_P$	MK2 dephosphorylation	R6	(290)
$\emptyset \xrightarrow{p38_P} TTP$	Phospho-p38-dependent TTP synthesis	R7	(319)
$\emptyset \leftarrow TTP$	Degradation of unphosphorylated TTP	R8	(319)
$TTP \xrightarrow{MK2_P} TTP_P$	MK2-mediated TTP phosphorylation	R9	(319)
$\emptyset \leftarrow TTP_P$	Degradation of phosphorylated TTP	R10	(319)
$TTP \xleftarrow[PP2A]{} TTP_P$	PP2A-mediated TTP dephosphorylation	R11	(319)
$\emptyset \xrightarrow{p38_P} RNA_m$	p38 MAPK-dependent synthesis of target mRNA	R12	(319)
$\emptyset \leftarrow RNA_m$	TTP-independent degradation of target mRNA	R13	(319)
$\emptyset \xleftarrow[TTP]{} RNA_m$	TTP-dependent degradation of target mRNA	R14	(319)

Table 3.10 Overview of parameters of the Kulawik p38 MAPK-TTP pathway model

Parameters

Symbol	Description	Nominal value	Dimension
σ_S	Saturation rate of Stimulus	0.52*10^{-1}	$ng^{-1}mL$
φ_{P1}	Phosphorylation rate 1 of p38	1.51*10^{-4}	min^{-1}
φ_{P2}	Phosphorylation rate 2 of p38	9.08*10^{-3}	$min^{-1}ng^{-1}mL$
ρ_{Pp1}	Dephosphorylation rate 1 of p38P	1.00*10^{-5}	min^{-1}
ρ_{Pp2}	Dephosphorylation rate 2 of p38P	3.10*10^{+1}	$\mu M^{-1}\, min^{-1}$
γ_D	Synthesis rate of MKP	8.41*10^{-3}	$\mu M^{-1}\, min^{-1}$
δ_D	Degradation rate of MKP	0.01*10^{+1}	min^{-1}
φ_K	Phosphorylation rate of MK2	1.02*10^{+1}	$\mu M^{-1}\, min^{-1}$
ρ_{Kp}	Dephosphorylation rate of MK2P	7.14*10^{-1}	min^{-1}
γ_T	Synthesis rate of TTP	0.5*10^{-1}	$\mu M^{-1}\, min^{-1}$

δ_T	Degradation rate of TTP	$0.1*10^{-1}$	min^{-1}
φ_T	Phosphorylation rate of TTP	$0.1*10^{-1}$	$\mu M^{-1}\, min^{-1}$
δ_{Tp}	Degradation rate of TTP_P	$0.1*10^{-3}$	min^{-1}
ρ_{Tp}	Dephosphorylation rate of TTP_P	$0.2*10^{-1}$	min^{-1}
γ_{Rm}	Synthesis rate of RNA_m	$5.0*10^{-1}$	$\mu M^{-1}\, min^{-1}$
δ_{Rm1}	Degradation rate 1 RNA_m	$0.1*10^{-2}$	min^{-1}
δ_{Rm2}	Degradation rate 2 RNA_m	$2.0*10^{-1}$	min^{-1}

Simulation of the equations using the *ode23* solver in MATLAB is shown in Figure 3.7. Initial observations prompted us to update some nominal parameters of the TTP core model to maintain the correct qualitative behaviour of TTP pathway system components (Table 3.10) as described in Chapter 3.2.3.1. This includes, specifically, the TTP-target mRNA, which would have otherwise lost its distinctive expression pattern compared to the TTP core model (Figure 3.8). The main differences in model dynamics between the TTP core model and the combined Kulawik p38 MAPK-TTP model are the high plateau that phospho-p38 MAPK reaches after its initial peak, the strong signal amplification through MK2, and the change in TTP phosphorylation. Adaption of the parameters, following this combination of the two models, resulted in some interesting dynamics such as two peaks in TTP-target mRNA expression and an initial peak for unphosphorylated TTP. The initial increase in unphosphorylated TTP expression, observed in the model simulation, was mediated by phosphorylated p38 MAPK. The subsequent decrease in unphosphorylated TTP expression was caused by TTP phosphorylation mediated by phosphorylated MK2, which occured slightly delayed compared to the p38 MAPK mediated stimulation of TTP expression. This delay can be explained by the fact that MK2-phosphorylation itself is regulated by p38 MAPK. The later increase in

unphosphorylated TTP levels can be attributed to a reduction in MK2-mediated phosphorylation, which followed MK2's initial peak in activity.

Similarly, the dynamics of TTP-target mRNA expression were influenced by these processes. The the initial increase in TTP-target mRNA levels, as observed in the model simulation, was driven by phosphorylated p38 MAPK-mediated stimulation. The following rapid decrease in TTP-target mRNA corresponded to an increase in unphosphorylated TTP expression. The subsequent short increase in TTP-target mRNA was caused by a decrease in unphosphorylated TTP levels. The final decrease results from a combined effect of increased unphosphorylated TTP levels and reduced levels of phosphorylated p38 MAPK.

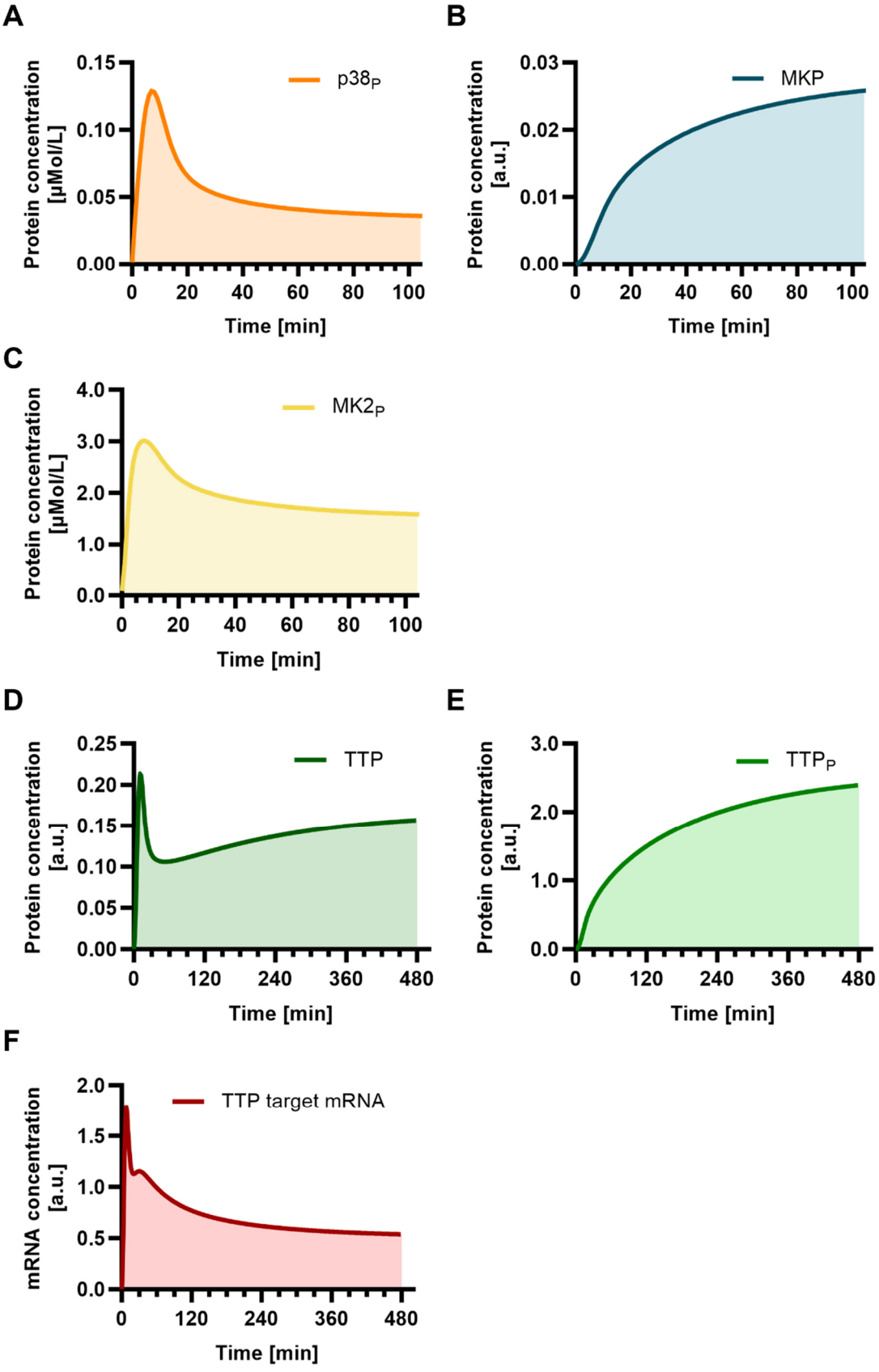

A
Protein concentration [µMol/L]
0.15
0.10
0.05
0.00
p38P
0
20
40
60
80
100
Time [min]
B
Protein concentration [a.u.]
0.03
0.02
0.01
0.00
MKP
0
20
40
60
80
100
Time [min]
C
Protein concentration [µMol/L]
4.0
3.0
2.0
1.0
0.0
MK2P
0
20
40
60
80
100
Time [min]
D
Protein concentration [a.u.]
0.25
0.20
0.15
0.10
0.05
0.00
TTP
0
120
240
360
480
Time [min]
E
Protein concentration [a.u.]
3.0
2.0
1.0
0.0
TTPP
0
120
240
360
480
Time [min]
F
mRNA concentration [a.u.]
2.0
1.5
1.0
0.5
0.0
TTP target mRNA
0
120
240
360
480
Time [min]

Figure 3.7 Computational simulation of the Kulawik p38 MAPK-TTP model.

The data for the simulation of the Kulawik p38 MAPK-TTP model was generated in MATLAB using the *ode23* function to solve the ODE equations (3.4) to (3.11) as well as the nominal parameter values and initial conditions shown in Table 3.10 and Table 3.8 for a time span of 480 min. The graphs show the expression change of A) phosphorylated p38, B) MKP, C) phosphorylated MK2, D) unphosphorylated TTP, E) phosphorylated TTP, and F) TTP-target mRNA, following treatment with 20 ng/mL IL-1β in hepatocytes. The full MATLAB script for the generating the graphs can be found in Appendix 7.1.

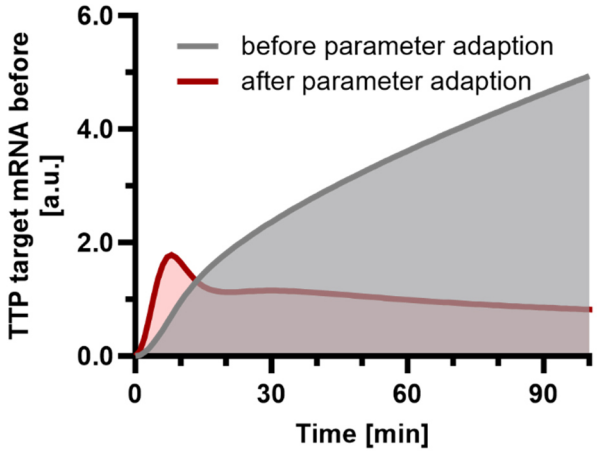


Figure 3.8 Comparison TTP-target mRNA expression before and after nominal parameter adaption of the Kulawik p38 MAPK-TTP model.

The data for the simulation of the TTP-target mRNA was generated in MATLAB using the *ode23* function to solve the ODE equations (3.4) to (3.11) as well as the nominal parameter values and initial conditions shown in Table 3.10, Table 3.1, Table 3.8, and Table 3.4 for a time span of 100 min. The graph shows the TTP-target mRNA expression before (grey) and after the update of the nominal parameters of the TTP model. The full MATLAB script for the generating the graphs can be found in Appendix 7.1.

3.2.4 Analysis of model structure

The simulation of mathematical equations and nominal parameter values in MATLAB presented in the last chapter gave us a first impression of qualitative model properties. Another, more quantifiable, way of gaining information about the quality of the model before having any contact with biological data is using the model analysis tools “structural identifiability” and “global parameter ranking”.

3.2.4.1 Structural identifiability analysis of the p38 MAPK-TTP model

Structural identifiability is a process of evaluating if, under ideal experimental conditions, such as measurement of all dependent variables with unlimited sampling times, unique values can be given to model parameters in the process of parameter estimation. A variety of ways have been described for testing structural identifiability, including approaches based on Taylor series (329), generating series based on Lie derivates (330), direct test (331), and profile likelihood (332). Here, we used the MATLAB toolbox GenSSI published by Banga and Balsa-Canto, which evaluates global and local structural identifiability of linear and nonlinear dynamic models by using a generating series approach based on Lie derivates and creating identifiability tableaus for visualisation purposes from the Jacobian of the series coefficients (333), as described in Chapter 2.5.1.

To analyse the structural identifiability of the Kulawik p38 MAPK-TTP model, we first had to change the term of the input variable S, which was nonlinear due to the saturating kinetics introduced by Kulawik et al. (290) (Compare Equation 3.5), as the GenSSI toolbox requires a linear input function for it to work. Therefore, we replaced here temporarily the saturating kinetics with a linear term, resulting in the following changes to the ODEs:

$$\frac{dP}{dt} = -\varphi_{P1}{}^{*}P - \boldsymbol{\varphi_{P2}}{}^{*}\boldsymbol{S}^{*}\boldsymbol{P} + \rho_{Pp1}{}^{*}P_P + \rho_{Pp2}{}^{*}D^{*}P_P, \qquad 3.13$$

$$\frac{dP_P}{dt} = +\varphi_{P1}{}^{*}P + \boldsymbol{\varphi_{P2}}{}^{*}\boldsymbol{S}^{*}\boldsymbol{P} - \rho_{Pp1}{}^{*}P_P - \rho_{Pp2}{}^{*}D^{*}P_P. \qquad 3.14$$

Kulawik et al. also identified the saturation rate as non-identifiable and fixed the value artificially for the parameter estimation. After removing the saturating kinetics, the GenSSI toolbox algorithm found most model parameters to be structurally globally identifiable. However, the toolbox excluded the degradation and dephosphorylation rate of phospho-TTP,

δ_{Tp} and ρ_{Tp}, as well as the independent variable PP2A (A) from the analysis process due to the number of parameters within this group exceeding the number of relations, meaning that it was not possible to perform structural identifiability analysis on these parameters. The software proposed changing PP2A from an independent variable to a dependent variable to solve this problem (Figure 3.9). Adding an additional ODE for PP2A is part of our long-term goals. However, at the time of writing, members of our group are still working on identifying the subunit of PP2A responsible for TTP dephosphorylation. This missing piece of information did not allow us to include the measurement of PP2A in our experimental design for the time being.

After removing the independent variable A from the equations, GenSSI found all model parameters globally structurally identifiable. This means the quality of the model structure should be sufficient to perform parameter estimation. The produced identifiability tableaus, which visualise the analysis process, are shown in Figure 3.10. In these tableaus, each column represents one parameter and each row the number of evaluated Lie derivates. When one of the Lie-Derivate runs is solved successfully for a parameter, the graph shows this run as a black value. Parameters with one or more non-zero ("black") runs per column are considered identifiable. For clarity, the reduced identifiability tableau of the 1st order is shown, which only depicts the evaluation for the number of derivates needed to achieve full structural identifiability, in this case, 16.

```
The remaining group of parameters, relations and the corresponding solutions:

--> Parameters:
deltaTp
  rhoTp
     PP

--> Relations:
(13*gammaT*((deltaT + (107*phiT)/1250)^2 - phiT*((295841*phiMK)/50000000 - (107*rhoMKp)/1250) + (107*PP

--> Symbolic solution(s) of the remaining parameters:
--> WARNING: The number of parameters is Larger than the number of relations!
             An explicit solution cannot be given for this subset of parameters.
             PLEASE CONSIDER AN EXTRA DERIVATIVE!
```

Figure 3.9 Screenshot of the GenSSI results recommending changes to model structure.

This screenshot shows the output of GenSSI regarding the Kulawik p38 MAPK-TTP model after removing the saturation kinetics for the stimulus. It highlighted the recommendation to add an additional dependent variable for PP2A (here PP).

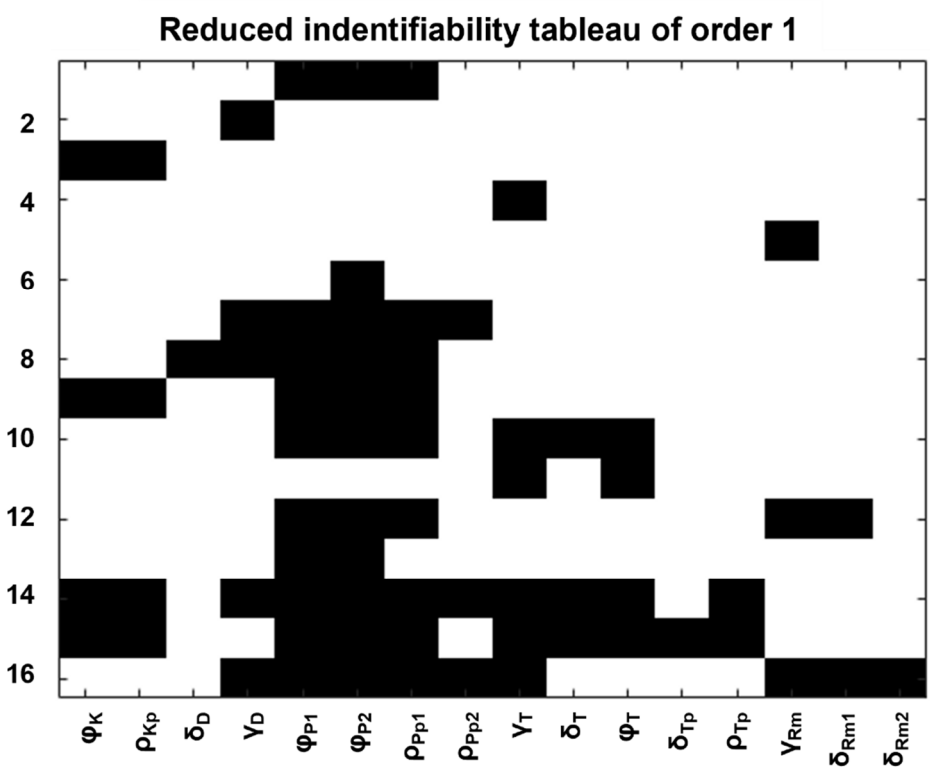


Figure 3.10 Order 1 identifiability tableau of the Kulawik p38 MAPK-TTP model.

Results of the GenSSI toolbox for the structural identifiability analysis of the Kulawik p38 MAPK-TTP model are shown as an identifiability tableau. The Y-axis shows the number of necessary Lie-Derivates until full identifiability was achieved, each row representing one derivate. Each column represents one parameter. The graph shows each Lie-Derivate that has been solved successfully for an individual parameter as a black value. Parameters with one or more non-zero ("black") runs per column are considered identifiable. After 16 derivates, all parameters were found to be structurally identifiable.

3.2.4.2 Parameter ranking of the p38 MAPK-TTP model

Global parameter ranking identifies the relative influence of individual parameters on the model output and ranks them accordingly. This can be done by calculating relative parametric sensitivities for a sufficiently large number of parameter vectors and by applying statistical methods to analyse the overall impact on the system (279). The method we use here was originally described by Brun and Reichert (334) and was implemented into the AMIGO2 toolbox (280). The toolbox uses Latin Hypercube sampling to create the pool of parameter vectors and ranks the parameters according to the calculated importance factor δ_{θ}^{msqr} (msqr/MSQR=mean square root), which is a direct measure of how sensitive the model or a specific variable is to a given parameter θ (For the detailed formula refer to Chapter 2.5.2) . Figure 3.11 A shows the relative sensitivity of dependent variables to changes in parameter values, whereas Figure 3.11 B depicts the ranking of parameters according to their impact on the overall model output. We defined parameters as highly important for the variable or the model that had a δ_{θ}^{msqr} larger than 0.08 (Figure 3.11 A) or 0.0125 (Figure 3.11 B), respectively. For an individual variable, usually, their respective synthesis rate was ranked as the most important, followed by the degradation rate. This is the case for D, T, T_P, and R_m. For T_P its phosphorylation rate is additionally highly important. For K and K_P the most important parameters are its phosphorylation and dephosphorylation rates. For P and P_P, φ_{P1} and ρ_{Pp1} had the highest impact of the parameters. Generally, for the whole model, the most important

($\delta_\theta^{msqr} > 0.013$) parameters comprise γ_T, δ_T, ρ_{Pp1}, whereas the least ($\delta_\theta^{msqr} < 0.0055$) important comprise φ_{P2}, ρ_{P2}, and δ_{Rm2}. Apart from δ_θ^{msqr}, the toolbox also produced the importance factors δ_θ^{mabs} (mabs/MABS=mean of the absolute), δ_P^{mean}, δ_P^{min}, and δ_P^{max} as outputs. Table 3.11 shows an overview of all importance factors. Here δ_P^{mabs}, like δ_θ^{msqr}, is a measure of model sensitivity with respect to a given parameter and comparing both can indicate outliers of the sensitivity analysis if they differ greatly from each other. Comparing δ_θ^{mabs} to δ_θ^{msqr} delivered some interesting differences: They differed in ρ_{Pp1} and φ_{P1}, which have the highest δ_P^{mabs} values. Comparing the overall trend between the two importance factors in Figure 3.11 B shows that δ_θ^{mabs} rates parameters stronger than δ_θ^{msqr} based on their position within the signalling pathway. Still, overall, they followed the same trend. The importance factor δ_θ^{mean} is useful to identify the algebraic sign of the mean effect changes. For us all degradation and dephosphorylation rates hold a negative sign while synthesis and phosphorylation rates have a positive sign. δ_θ^{min} and δ_θ^{max} give information on the range of the sensitivity analysis and can be of help to identify outliers, which we, however, did not observe. Understanding the importance of parameters on the model can help inform the experimental design and the parameter estimation, which will be covered in the next chapters.

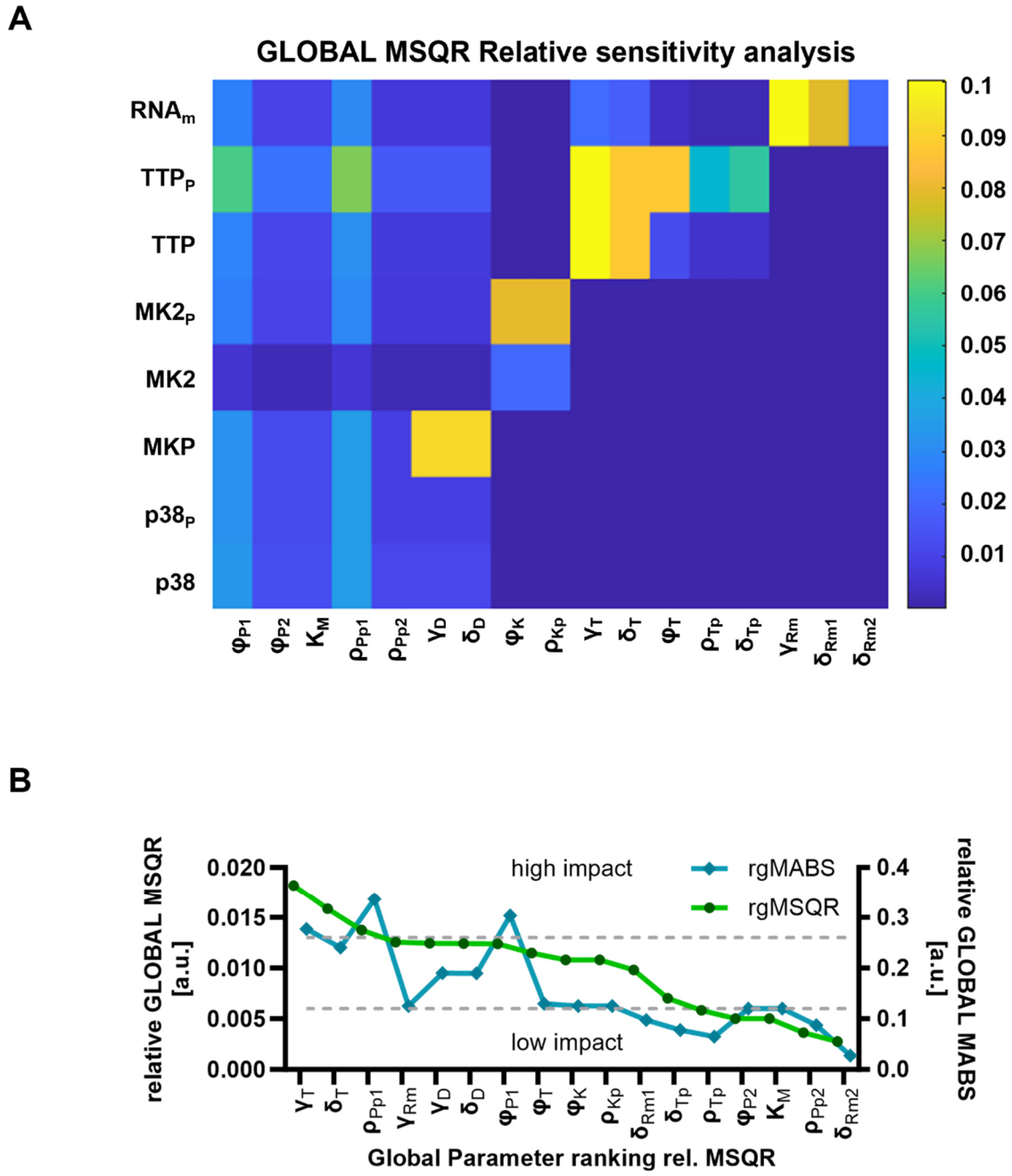


Figure 3.11 Relative and global parameter ranking of the Kulawik p38 MAPK-TTP model.

Calculation of parametric sensitivities of the Kulawik p38 MAPK-TTP model was performed using the AMIGO2 MATLAB toolbox. Shown are the relative parametric sensitivities of each model parameter with respect to the model variables (A) as well as the parameters ranked according to the importance factor δ_θ^{msqr}. The dotted lines show the categorization of the parameters into high and low impact. In addition to δ_θ^{msqr}, also δ_θ^{mabs} is shown under B), which enables quick comparison of where the ranking of the two differs.

Table 3.11 Ranked importance factors calculated from global parametric sensitivity analysis

Importance factors ranked according to δ_θ^{msqr}					
Parameter	δ_θ^{msqr}	δ_θ^{mabs}	δ_θ^{mean}	δ_θ^{max}	δ_θ^{min}
γ_T	1.82E-02	2.77E-01	2.23E-01	1.00E+00	-2.29E-01
δ_T	1.59E-02	2.41E-01	-1.96E-01	1.85E-01	-1.20E+00
ρ_{Pp1}	1.37E-02	3.36E-01	-2.32E-01	3.60E-01	-6.79E-01
γ_{Rm}	1.26E-02	1.25E-01	1.25E-01	1.00E+00	-1.33E-14
γ_D	1.24E-02	1.90E-01	7.10E-02	9.31E-01	-1.69E-01
δ_D	1.24E-02	1.90E-01	-7.12E-02	2.27E-01	-8.67E+00
φ_{P1}	1.24E-02	3.04E-01	2.05E-01	6.10E-01	-3.55E-01
φ_T	1.15E-02	1.30E-01	9.83E-02	8.83E-01	-3.55E-01
φ_K	1.08E-02	1.25E-01	7.35E-02	8.10E-01	-2.65E-01
ρ_{Kp}	1.08E-02	1.25E-01	-7.35E-02	4.49E-01	-1.04E+00
δ_{Rm1}	9.82E-03	9.77E-02	-9.77E-02	1.06E-14	-2.25E+00
δ_{Tp}	7.03E-03	7.78E-02	-7.34E-02	1.86E-02	-6.92E-01
ρ_{Tp}	5.83E-03	6.47E-02	-5.16E-02	5.82E-02	-4.60E-01
φ_{P2}	5.00E-03	1.20E-01	8.12E-02	2.40E-01	-1.38E-01
K_M	5.00E-03	1.20E-01	-8.12E-02	1.48E-01	-3.13E-01
ρ_{Pp2}	3.63E-03	8.72E-02	-5.39E-02	1.19E-01	-2.48E-01
δ_{Rm2}	2.74E-03	2.73E-02	-2.73E-02	2.45E-15	-1.00E+00

For the detailed formula of the importance factors refer to Chapter 2.5.2.

3.3 Experimental design

The experimental design process for the Kulawik p38 MAPK-TTP model aimed to identify the ideal set of experiments to perform parameter estimation while staying within the limits set by the availability of time, money, equipment, and expertise. In this chapter, we will describe the design and the given constraints. Various decisions were made, including which model organisms and cell types, which stimuli and inhibitors, and which methods were to be used. Additionally, we had to decide which dependent variables to measure directly and how to obtain total quantification data. In the decision-making process, we considered primarily the scope and goals we set for ourselves in Chapter 1.6, summarised as first creating a biological systems model capturing the first 8 h of inflammatory response in macrophages, followed by testing system perturbations and its comparison to the murine macrophage cell line RAW264.7.

3.3.1 Model organisms

We decided to use primary murine BMDMs and the murine macrophage cell line RAW264.7. Murine BMDMs have the advantage that well-established mutant mouse strains, *Dusp1*$^{-/-}$ and *Zfp36*$^{aa/aa}$, are available that are not only relevant to our pathway and allow measurements of model perturbations but are potentially crucial for model parameter estimation and understanding pathway dynamics. Historically, murine BMDMs were an important tool for our group to study p38 MAPK and TTP pathway dynamics; thus, having a validated model in murine BMDMs would be key to providing a viable tool for future experimental design. The RAW264.7 cell line was a starting point for experimental setup and a good way to reduce the number of mice needed for preliminary experiments. Furthermore, RAW264.7 cells have been essential tools in the past to identify mechanisms of TTP biology in our group as well as others (250,320,335,336), which was one of the reasons one of our goals was to use our model in understanding and defining the differences and limitations of this cell line.

3.3.2 Model inputs

In accordance with our goal to use the model for future experimental design, we chose LPS as the experimental inflammatory stimulus because it is the most used inflammatory agent in our laboratory and likely in many other laboratories as well. We decided to start experimenting with sustained administration of LPS, choosing the routinely used concentration of 10 ng/mL, which showed potent induction of the p38 MAPK pathway in the past. Choosing this concentration has the added benefit of making the model more applicable to our group's experimental design.

In addition to the inflammatory stimulus, we aimed to introduce a pathway disturbance using an inhibitor as a model input. In this case, the PP2A inhibitor, Calyculin A, at 2.5 nM. The experimental concentration for this inhibitor was determined through a dose-response curve experiment (Appendix 7.2.1 and supplementary Figure 7.1).

3.3.3 Measurement of model components

After defining the model inputs, we needed to decide on how to measure the dependent variables. WB is well established in our lab and the method of choice in the Kulawik et al. paper. Therefore, all the material, equipment, and validated antibodies for our targets were readily available. The main limitation of WB, in this instance, was the size of the gel, which determines the number of sampling times for our time-course. In our case that meant the use of 24-well gels, which were the version with the highest number of lanes, based on the available equipment. We decided to measure total and phosphorylated p38 MAPK, DUSP1, and TTP. DUSP1 expression measurements were included to assess whether they are sufficient to simulate p38 MAPK pathway dynamics. MK2 was omitted to reduce the size of the experiments as we were not sure we would have enough isolated protein to measure it. Unfortunately, no antibody for specifically phosphorylated TTP at positions Ser-52 and Ser-178 is available. For

now, we can circumvent this issue by measuring distinct bands of TTP on the Western blot individually, as when TTP is separated by SDS PAGE, it usually presents as at least two distinct bands. This is because TTP becomes hyperphosphorylated in the process of the inflammatory response, and the hyperphosphorylated TTP protein migrates slower on the gel due to the added charge and size, as shown by Cao et al. (337). It is important to note that, for most of the phospho-species the responsible kinase and the biological function have not yet been identified (267), and it is unclear whether their phosphorylation follows the same dynamics as the p38 MAPK pathway. In the absence of a better method, though, we can test if the measured dynamics are sufficient to explain TTP-target mRNA expression patterns. We decided to enable total quantification utilising commercially available recombinant human protein in the absence of available mouse protein. This is feasible because our antibodies were validated for both mice and humans. Initial standard curve concentrations were determined in preliminary Western blot experiments (supplementary Figure 7.5). For p38 MAPK, we also determined the percentage of phosphorylated protein species within the purchased active recombinant protein using PhosTag gel WB (46.6±0.23%, supplementary Figure 7.4).

To quantitatively measure TTP-target mRNA, our primary method of choice was RT qPCR, which is well-established in our laboratory. As the TTP-target mRNA, we decided to measure *Tnf,* which was chosen as it is sufficient to explain the development of the severe inflammatory syndrome in $TTP^{-/-}$ mouse strains and is one of the best studied and validated TTP-target mRNAs (192,338).

For our RT qPCR standard curve, we decided to use plasmid DNA to determine the exact copy number within a sample, which offers advantages compared to RNA in terms of stability, reproducibility, ease of generation, and validation. We obtained the *Tnf* plasmid from Addgene and confirmed the integrity of the *Tnf* primer binding site through Sanger sequencing. We then

linearised the plasmid using the restriction enzyme AgeI, the process of which was confirmed by DNA gel electrophoresis (supplementary Figure 7.6).

The number and distribution of measured time points define the temporal resolution of the data and determine which system behaviours can be observed and subsequently included in the model. Our choice to use 24-well Stain-Free gels for WB established the maximum number of sampling times due to gel capacity. In addition to the time-course samples, we allocated spaces for the standard curve, which required 5 lanes on the gel and one lane for the size marker. Therefore, we decided on the 19 sampling time points shown in Figure 3.12.

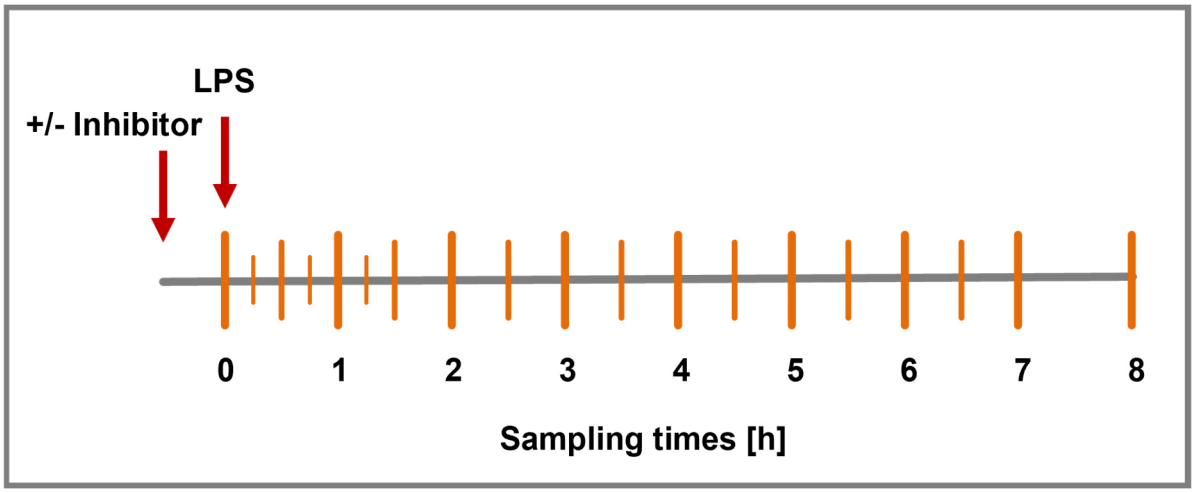


Figure 3.12 Schematic overview of the 19 sampling times of 8 h time-course experiment including 30 min pretreatment with inhibitors.

To determine the distribution of these sampling times within the 8 h time window of the experiment, we consulted scientific literature to understand the qualitative expression dynamics of our observables in RAW264.7 and BMDM cells. Regarding phosphorylated p38 MAPK, Kulawik et al. observed an initial peak between 0.25 h and 0.75 h after stimulation in BMDM, followed by a plateau phase. Hence, high resolution of the first hours of the inflammatory response is crucial to cover this dynamic. We set 15 min intervals as the minimum spacing between sampling times to facilitate successful protein and RNA isolation. During the plateau phase of p38 MAPK phosphorylation, we aimed for 30 min intervals to capture potential changes in phosphorylation levels. DUSP1 and *Tnf* mRNA expression were expected to peak within the first 1.5 h of the inflammatory response, with a slight time shift compared to p38 MAPK phosphorylation (148,339). We also expected the onset of TTP expression to be within the same time period (266). Therefore, we aimed to increase the high-resolution period to 1.5 h.

3.4 Parameter estimation of the Kulawik p38 MAPK-TTP model in BMDMs

Using the above-described conditions, we performed the total quantification of proteins and mRNA targets during the inflammatory response in BMDMs. Additionally, to obtain data for model validation, we treated the BMDMs with the PP2A inhibitor Calyculin A. The experiment was repeated 3 times. The same experiment, but without inhibitors, was also performed in *Dusp1*$^{-/-}$ and *Zfp36*$^{aa/aa}$ mice, with the goal of challenging our pathway assumptions for model validation.

3.4.1 BMDMs total quantification data

In this chapter we will describe the measured expression dynamics of our model pathway components. For each experiment, bone marrow was extracted from the hind legs of eight mice and cultivated in the presence of MCSF for 7 days to differentiate into BMDMs. These cells were counted and combined to ensure sufficient cell numbers for seeding. The cells were stimulated with 10 ng/mL LPS, followed by protein and RNA isolation at 19 distinct time points.

The Western Blots were quantified using the Image Lab software, the data normalised to total protein measured through the Stain-Free signal of the blots, and the total protein concentration was calculated using the standard curve as described in Chapter 2.4.2.8. The protein data is shown as pg per µg total protein, which for simplicity will be shortened to pg/µg in the following results description. The Western blots, their individual quantification, and the data handling are described in Appendix 7.3.1. Such evaluated and cleaned-up data of BMDM experiments is displayed in Figure 3.13. For clarity, each graph only depicts one target of

interest. Apart from the standard deviation, individual data points of the experimental replicates are shown in the background with a lighter symbol colour.

Phosphorylated p38 MAPK expression dynamics are presented in Figure 3.13 A. The average of the total p38 MAPK was used to determine the concentration of unphosphorylated p38 MAPK for later parameter estimation. Phosphorylated p38 MAPK already present in unstimulated cells at a concentration of 5 pg/µg. Following stimulation, the observed phosphorylation rapidly increased, reaching its maximum at 30 min with a concentration of 47 pg/µg. Afterwards, the concentration declined first more rapidly to around 23 pg/µg at 1.5 h and then more gradually over time, reaching 13 pg/µg after 8 h.

In Figure 3.13 B, the expression of DUSP1 is displayed. The first detectable value was measured after 45 min; the expression peaked after 1 h at 76 pg/µg and, afterwards, declined before bottoming out at around < 35 pg/µg. The plateau phase could only be captured in one of the 3 experiments, as for the others, the decrease after the peak led to values below the detection limit (compare Appendix 7.3.1).

Figure 3.13 C displays expression levels of unphosphorylated (TTP) and total TTP (TTP_T); however, the individual data points are shown only for unphosphorylated TTP, in addition to the average. For total TTP, Individual data points were omitted to improve clarity. Unphosphorylated TTP was not detectable in unstimulated cells and started to be within the detection range 0.5 h after stimulation. The unphosphorylated species then peaked at 1.25 h with an average of around 54 pg/µg. Following the peak, the signal decreased and commenced fluctuating around a lower level. Between 4 h and 5 h, a local maximum (34 pg/µg) in expression was observed.

Phosphorylated TTP, shown in Figure 3.13 D, was not detectable before stimulation but started to be observed around 0.25 h after stimulation, reaching a first local maximum at the 1 h time point around 30 pg/µg. After a brief slump, the concentration was observed to rise again to a peak at 4.5 h at around 80 pg/µg. Phosphorylated TTP then decreased at a close to constant rate, reaching a minimum after 7 h with expression levels around 37 pg/µg.

Tnf mRNA expression is displayed in Figure 3.13 E. Initially, without stimulation, the expression is low at 2 copy number (cn)/pg RNA. Expression, however, started to increase at 0.5 h and peaked after 1 h at 90 cn/pg. Afterwards, the expression decreased in stages, initially with a first substantial decrease between 1.5 h and 2 h, followed by a plateau-like phase until the 4 h time point, after which the concentration declined over the remaining time-course reaching 25 cn/pg at 8 h.

The combined overview picture in Figure 3.14 shows the varying dynamics within the p38 MAPK-TTP pathway during the inflammatory response. The first peak of phosphorylated p38 was followed by peaks of DUSP1, TTP and *Tnf* mRNA expression, with the peak of unphosphorylated TTP being slightly delayed compared to the *Tnf* peak.

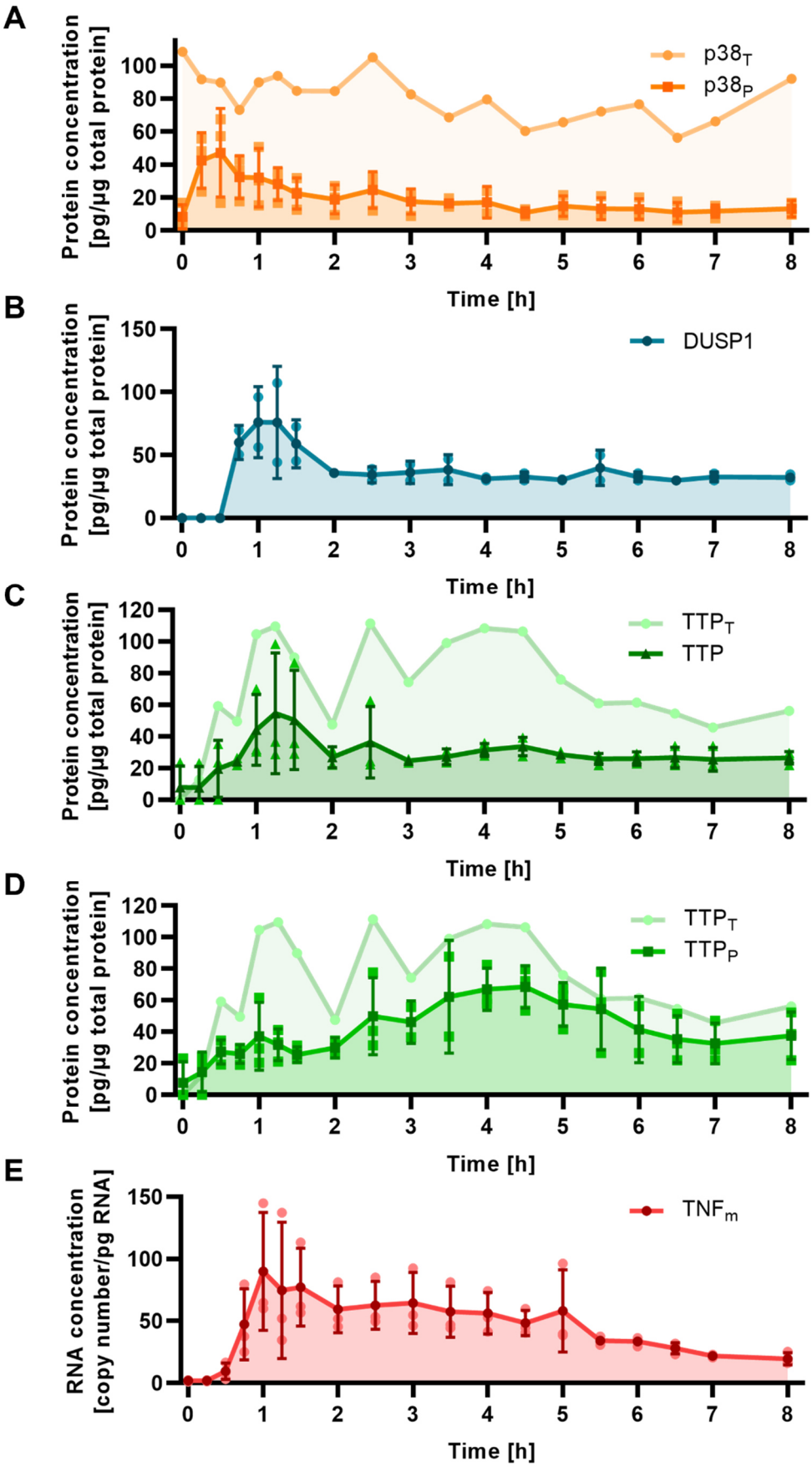

A
Protein concentration [pg/µg total protein]
p38T
p38P
Time [h]
B
Protein concentration [pg/µg total protein]
DUSP1
Time [h]
C
Protein concentration [pg/µg total protein]
TTPT
TTP
Time [h]
D
Protein concentration [pg/µg total protein]
TTPT
TTPP
Time [h]
E
RNA concentration [copy number/pg RNA]
TNFm
Time [h]

Figure 3.13 Measuring p38 MAPK-TTP pathway components by total quantification of Western blot and qPCR data obtained from BMDMs treated with LPS over an 8 h time-course.

BMDMs derived from the bone marrow of 8 mice were combined and treated with 10 ng/mL LPS for a period of 8 h. Protein concentrations of phospho-p38, total p38, DUSP1, phospho-TTP and TTP, as well as *Tnf* mRNA levels, were measured using WB and qPCR, respectively (n=3). The Western blot data of A) phospho-p38 ($p38_P$), B) DUSP1, C) total (TTP_T) and unphosphorylated TTP (TTP, lower band), and D) total and phosphorylated TTP (TTP_P, upper band) was quantified in Image Lab software, normalised to its Stain-Free signal, and the total protein concentrations were calculated using standard curves of recombinant protein. The total amount of E) *Tnf* mRNA was measured by running a standard curve consisting of known quantities of plasmid DNA alongside the samples for qPCR. Standard deviation is displayed as error bars, and the results of the individual experiments are included as lightly coloured symbols in the background to visualise variability.

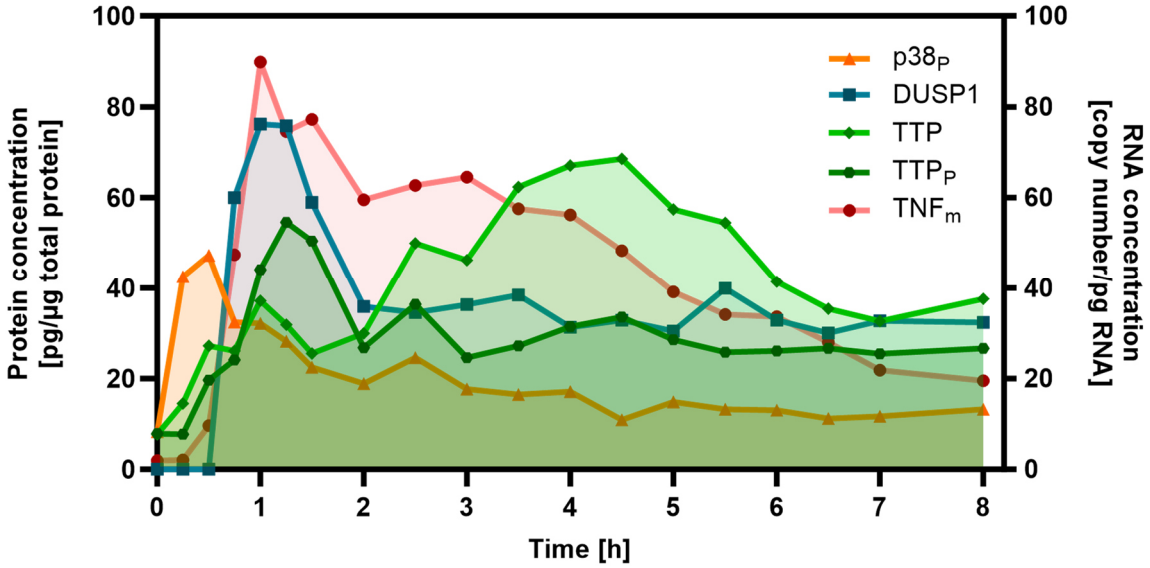


Figure 3.14 Overview of BMDM p38 MAPK-TTP time-course experiment for visualisation of pathway dynamics.

The data presented in Figure 3.13 is combined to highlight, how the different pathway components relate to each other throughout the inflammatory response. Protein concentration is indicated on the left y-axis, whereas the right y-axis depicts RNA concentration. All components are shown in their respective signature colours. For clarity, no standard deviation or individual data points are included.

3.4.2 BMDM parameter estimation

In this chapter, we will present the parameter estimation of the Kulawik p38 MAPK-TTP model with data obtained from BMDM experiments described in Chapter 3.4.1. We updated the model according to our experimental design by removing the saturation rate, and the variables MK2, $MK2_P$, and PP2A. The updated model and nominal parameters, together with the reasoning behind these changes, can be found in Appendix 7.4. Figure 3.15 shows the updated model diagram, and supplementary Table 7.1 and Table 7.2 summarise the model components. This resulted in the following set of ODEs:

$$\frac{dP}{dt} = -P^*\varphi_{P1} - S^*P^*\varphi_{P2} + {P_P}^*\rho_{Pp1} + D^*{P_P}^*\rho_{Pp2}, \quad 3.14$$

$$\frac{dP_P}{dt} = +P^*\varphi_{P1} + S^*P^*\varphi_{P2} - {P_P}^*\rho_{Pp1} - D^*{P_P}^*\rho_{Pp2}, \quad 3.15$$

$$\frac{dD}{dt} = +{\gamma_D}^*{P_P}^*D - {\delta_D}^*D, \quad 3.16$$

$$\frac{dT}{dt} = +{\gamma_T}^*P_P + {\rho_{Tp}}^*T_P - {\delta_T}^*T - {\varphi_T}^*T^*P_P, \quad 3.17$$

$$\frac{dT_P}{dt} = +{\varphi_T}^*T^*P_P - {\delta_{Tp}}^*T_P - {\rho_{Tp}}^*T_P, \quad 3.18$$

$$\frac{dR_m}{dt} = +{\gamma_{Rm}}^*P_P - {\delta_{Rm1}}^*R_m - {\delta_{Rm2}}^*{R_m}^*T, \quad 3.19$$

with the initial conditions $P(0) = P0$, $P_P(0) = P_P0$, $D(0) = D0$, $K(0) = K0$, $K_P(0) = K_P0$, $T(0) = T0$, $T_P(0) = T_P0$, and $R_m(0) = R_m0$. Here '*' represents a multiplication sign, which is introduced for improved readability of the equations.

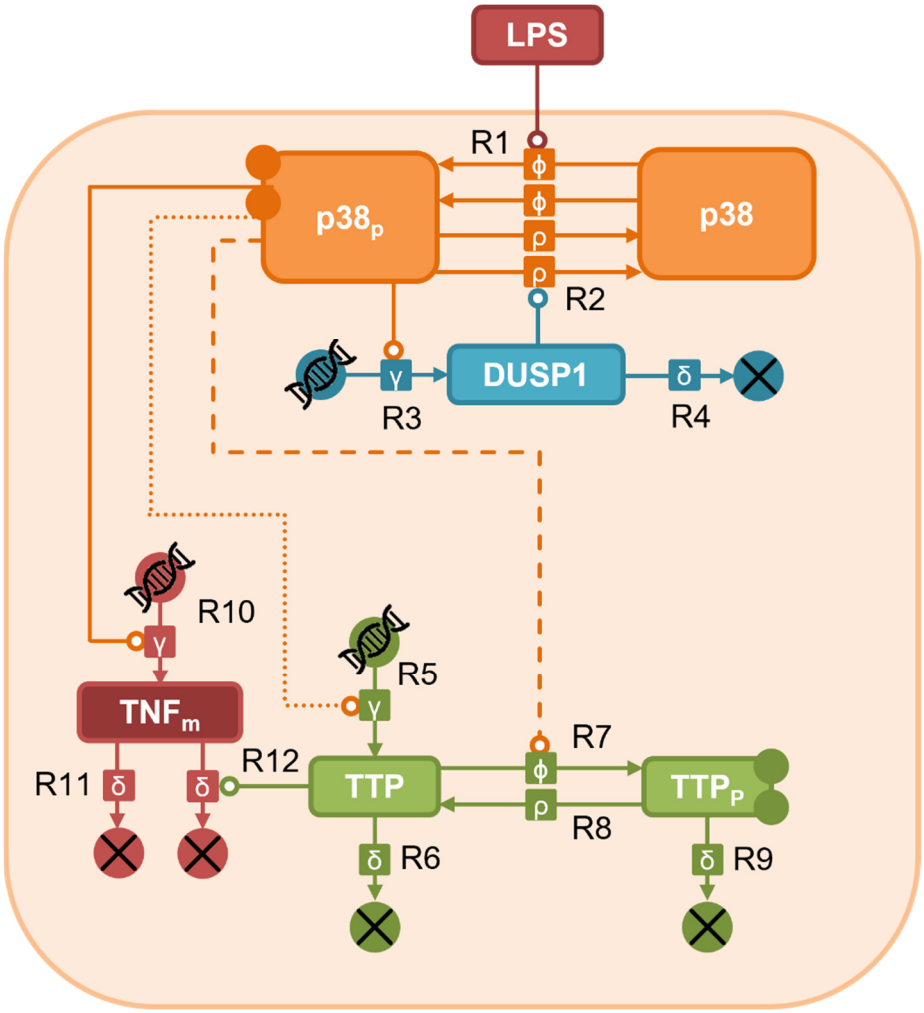


Figure 3.15 Model diagram of the updated Kulawik p38 MAPK-TTP pathway model.

The graphic summarises the model components, reactions, and interactions included in the updated Kulawik p38 MAPK-TTP model following experimental design. The dependent variables comprise unphosphorylated and phosphorylated p38 (orange), the p38 MAPK phosphatase DUSP1 (blue), unphosphorylated and phosphorylated TTP (green), and TTP-target mRNA (red). The sole independent variable is the stimulus LPS. Circles on the side of the variable mark phosphorylated protein species. Arrows indicate the flow of material between variables and represent the main reactions within the model numbered R1 to R12. Circles with a helix indicate that new mRNA or protein is synthesised and enters the model. Circles with a cross refer to the degradation of mRNA or protein, meaning material leaving the model. The lines with circles on the top represent the flow of information and connect variables with the reactions they are affecting. The parameters are represented as small squares on the reaction arrows labelled with the Greek letters γ, δ, φ, or ρ, referring to the specific type of reaction, namely for the rate of synthesis, degradation, phosphorylation, and dephosphorylation, respectively. Reactions 1 and 2 consist of two arrows each, representing the steady-state phosphorylation and degradation rates and the stimulus-dependent phosphorylation and dephosphorylation rates.

3.4.2.1 One-step model parameter estimation

We ran the AMIGO parameter estimation script (Appendix 7.1) with the combined nonlinear problem solvers (NLP) NLSQ2 and eSS2 for the calculation of the residuals (340,341). This combination of settings was recommended by Gabor et al. because they reduce the risk of overfitting to local solutions while staying computationally efficient (342). We also tested the global evolutionary-based NLP solver SRES published by Runarsson et al. (343). However, the parameter estimates did not vary in quality from those obtained from the NLSQ2/eSS2 NLP.

First, we tested how the algorithm can handle the parameter estimation of all parameters simultaneously. For this, we used multiple error profiles, including heteroscedastic (variation changes throughout the experiment) and homoscedastic (variation stays the same), experimental designs (three individual experiments or one experiment with mean data), and different parameter boundary settings (0 to 1, 10, or 100). In none of those runs was the parameter estimation successful in capturing the biological qualities of the model. An example is shown in Figure 3.16, and the respective parameters of that example are in Table 3.12. Note that the confidence intervals are given as automatic outputs from the toolbox. While some parameters have very tight confident intervals (including some that are outputted as zero), others that are connected to those parameters have very wide ranges. Since these estimates are an intermediary step we will not discuss them further. The figure comprises the simulation of the updated Kulawik p38 MAPK-TTP model with the estimated parameters and the experimental BMDM data. In this run, we used a homoscedastic error profile set to 0.2 and three individual experiments for the experimental design. Figure 3.16 demonstrates that the identified parameter set was able to loosely capture the p38 MAPK phosphorylation dynamics with an initial peak and plateau phase as well as the plateau phase of DUSP1. However the parameter set was not able to capture the dynamics observed in the BMDM data for

unphosphorylated TTP, which was expressed at very low levels, and *Tnf* mRNA, which consequently increased unrestrained in the simulation. After obtaining similar results for all other parameter estimation runs (data not shown), we opted to divide the parameter estimation process into two steps. We first estimated the parameters of the p38 MAPK pathway and used the best parameter set to go back into the complete model to estimate the parameters of the downstream TTP pathway. This was possible because our model does currently not have any feedback loops from the downstream TTP pathway to the p38 MAPK pathway.

Table 3.12 Parameter set for the example one-step Kulawik p38 MAPK-TTP model parameter estimation

Parameter Estimation				
Symbol	**Description**	**PE value**	**Conf. interval**	**Dimension**
φ_{P1}	Phosphorylation rate 1 of p38	0.00	$6.84*10^{+5}$	min^{-1}
φ_{P2}	Phosphorylation rate 2 of p38	$3.13*10^{-1}$	0.00	$ng^{-1}min^{-1}mL$
ρ_{Pp1}	Dephosphorylation rate 1 of $p38_P$	$4.59*10^{-1}$	0.00	min^{-1}
ρ_{Pp2}	Dephosphorylation rate 2 of $p38_P$	$3.25*10^{-1}$	$9.02*10^{+4}$	$pg^{-1}min^{-1}\mu g$
γ_D	Synthesis rate of DUSP1	$1.0*10^{+1}$	0.00	$pg^{-1}min^{-1}\mu g$
δ_D	Degradation rate of DUSP1	$5.08*10^{-1}$	0.00	min^{-1}
γ_T	Synthesis rate of TTP	$0.51*10^{-2}$	$2.71*10^{-3}$	$pg^{-1}min^{-1}\mu g$
δ_T	Degradation rate of TTP	$0.11*10^{-2}$	$8.78*10^{-2}$	min^{-1}
φ_T	Phosphorylation rate of TTP	$0.51*10^{-2}$	$2.18*10^{-3}$	$pg^{-1}min^{-1}\mu g$
δ_{Tp}	Degradation rate of TTP_P	$0.11*10^{-2}$	$5.99*10^{-2}$	min^{-1}
ρ_{Tp}	Dephosphorylation rate of TTP_P	$0.68*10^{-1}$	$7.06*10^{-2}$	min^{-1}

γ_{Rm}	Synthesis rate of TNF_m	$0.79*10^{-2}$	$1.13*10^{-4}$	$pg^{-1}min^{-1}\mu g$
δ_{Rm1}	Degradation rate 1 TNF_m	0.00	$4.34*10^{-5}$	min^{-1}
δ_{Rm2}	Degradation rate 2 TNF_m	$0.96*10^{-4}$	$1.01*10^{-6}$	$pg^{-1}min^{-1}\mu g$

PE=Parameter estimation.

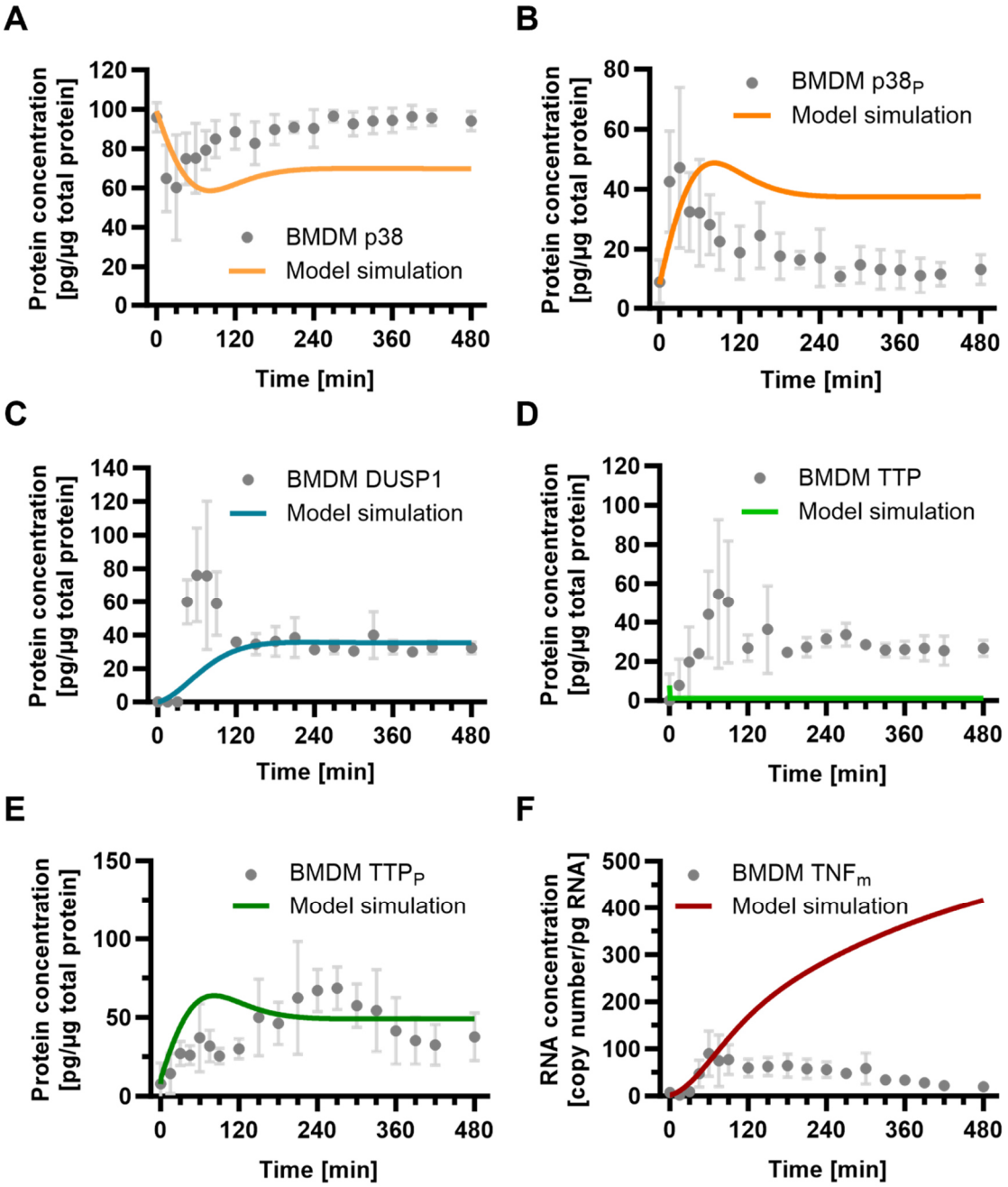


Figure 3.16 Computational simulation of the Kulawik p38 MAPK-TTP model using an exemplary estimated parameter set for LPS-treated BMDMs where all parameters were estimated simultaneously.

The data for the simulation of the Kulawik p38 MAPK-TTP model was generated in MATLAB, solving the ODE equations (3.14) to (3.19), as well as estimated parameter values and initial conditions presented in Table 3.12 and supplementary Table 7.1 for a time span of 480 min. The parameters were estimated using the NLSQ2 combined with the eSS2 nonlinear problem solver implemented in the AMIGO2 toolbox, and the experimental data of LPS-stimulated BMDMs, previously presented in Figure 3.13. In addition, a homoscedastic error profile set to 0.2, the

"individual" experiment design, and parameter boundaries between 0 and 1 were selected for the parameter estimation run. The graphs show the model simulation of A) unphosphorylated p38, B) phosphorylated p38, C) DUSP1, D) unphosphorylated TTP, E) phosphorylated TTP, and F) *Tnf* mRNA as lines in their respective colours together with the BMDM experimental data as symbols with error bars in grey. The full MATLAB script for parameter estimation and generation of the graphs can be found in Appendix 7.1.

3.4.2.2 Two-step model parameter estimation

For the separated model parameter estimation, we first estimated the parameters of the p38 MAPK model alone, which includes the ODEs of p38, $p38_P$, and DUSP1, and then chose the two best parameter sets to inform the estimation of the parameters of the TTP downstream model by fixing the parameters of the p38 MAPK pathway.

We ran similar data input variations for the p38 MAPK pathway parameter estimation as for the complete model estimation, including individual and combined experimental design, homoscedastic and heteroscedastic error profiles, and varying parameter boundaries. To compare the parameter estimation outcomes quantitatively, we calculated the relative mean of the absolute of the residuals. The residuals are a measurement of the goodness of fit of the model and are the values to be optimised in the process of parameter estimation. We aimed to reach a relative global MABS of the residual smaller or close to 20 % for our model. This decision was based on examples available in the AMIGO2 toolbox. Comparing the different parameter estimation runs, we identified that the run with a homoscedastic error profile set to 0.2, the "combined" experimental design, and 1 set as the upper boundary for the parameters delivered the lowest relative MABS of 19.37%. Figure 3.17 shows the model simulation of the best parameter set (Table 3.13) and the LPS-stimulated BMDM data used for the parameter estimation. The p38 MAPK expression profile followed the expected biological dynamics with an early peak and a plateau phase but did not cover the peak height adequately. For DUSP1, the parameter estimation covered primarily the plateau phase and could not capture the peak. The

relative MABS and main properties of the parameter estimation runs can be found in Table 3.14 ranked according to their global MABS, and the complete results in Appendix 7.5.

Kulawik et al. assumed that one phosphatase alone would be insufficient to simulate p38 MAPK dephosphorylation. We wanted to account for this possibility by performing parameter estimation with DUSP1 data excluded from the process in the next section. Where DUSP1 is insufficient to describe the phosphatase feedback loop of p38 MAPK sufficiently, as suggested by Kulawik et al., we also wanted to look at parameter estimation excluding DUSP1 data and compare the differences.

Now that parameter estimation of the upstream part of the model was completed, we continued to estimate the parameters of the complete Kulawik p38 MAPK-TTP model using the parameter sets and data input strategies of the parameter estimation runs with the lowest relative MABS from the previous two sections.

For the parameter set (Table 3.15), we received a global relative MABS of residuals of 23±8% (Figure 3.19), and from a qualitative visual evaluation, it appeared to possess a good fit overall. As can be seen in Figure 3.18, the model could not mimic the first peak of unphosphorylated TTP expression but followed its overall expression levels. The same is the case for phosphorylated TTP. Some of the expression behaviour of *Tnf* mRNA was a good fit; however, at later time points, the plateau of the simulation persisted, while the data continued to decrease. The measured initial double-peak was also not covered by the model. Looking at the individual parameters, we found that the constant dephosphorylation rate of p38 MAPK was estimated as zero, which is not true from a biological point of view but had no further impact on the overall properties of the model during the simulation of the inflammatory response. We further noticed that $\varphi_{P1}$and φ_{P1} have very wide confidence intervals, indicating that the experimental data was

not sufficient to give particularly reliable estimates for these parameters. We also found that the degradation rate of phosphorylated TTP was smaller than that of phosphorylated TTP, which is opposed to one of our core assumptions. We, therefore, repeated the parameter estimation for several iterations but always received the same relationship ($\delta_{Tp} > \delta_T$, data not shown). We tested whether altering the rates to reflect a biologically viable relationship had a significant impact on the model, by interchanging the degradation rates of TTP and TTP_P. We found that this switch only causes minimal changes to the model simulation (Figure 3.20). Therefore, to increase the value of the initial validation, we decided to go forward into the next chapter of model validation with the biologically viable option of switched TTP degradation rate. This will make it more likely that the model can simulate the mutant strains and does not impact on the modelling of the WT.

This discrepancy will be addressed in more detail in the discussion (Chapter 3.6.2).

Table 3.13 Parameter set of parameter estimation with best relative global MABS for the Kulawik p38 MAPK module

Parameter Estimation				
Symbol	**Description**	**PE value**	**Conf. interval**	**Dimension**
φ_{P1}	Phosphorylation rate 1 of p38	$6.91*10^{-4}$	$1.31*10^{+4}$	min^{-1}
φ_{P2}	Phosphorylation rate 2 of p38	$1.14*10^{-4}$	$1.31*10^{+3}$	$ng^{-1}min^{-1}mL$
ρ_{Pp1}	Dephosphorylation rate 1 of $p38_P$	0.00	$1.39*10^{-4}$	min^{-1}
ρ_{Pp2}	Dephosphorylation rate 2 of $p38_P$	$2.30*10^{-4}$	$4.45*10^{-6}$	$pg^{-1}min^{-1}\mu g$
γ_D	Synthesis rate of DUSP1	$4.23*10^{-3}$	$5.35*10^{-5}$	$pg^{-1}min^{-1}\mu g$
δ_D	Degradation rate of DUSP1	$1.61*10^{-3}$	$2.45*10^{-5}$	min^{-1}

PE=Parameter estimation.

Table 3.14 Global relative MABS ranking of p38 MAPK parameter estimation runs

Global relative MABS ranking of parameter estimation runs							
Short	**p38**		**p38-P**		**DUSP1**		**Global**
	Mean	Max	Mean	Max	Mean	Max	Mean
PDCHo	9.13	16.62	25.12	45.01	23.87	50.38	19.37
PDIHo	15.30	102.93	48.25	181.44	12.80	64.62	25.45
PDIHe	12.03	106.19	54.48	170.61	18.70	86.28	28.40
PDCHe	27.08	33.88	100.30	206.82	19.89	80.02	49.09

P=p38, D=DUSP1 data included C=combined experiments, I=individual experiments, Ho=homoscedastic error profile 0.2, He=heteroscedastic error profile.

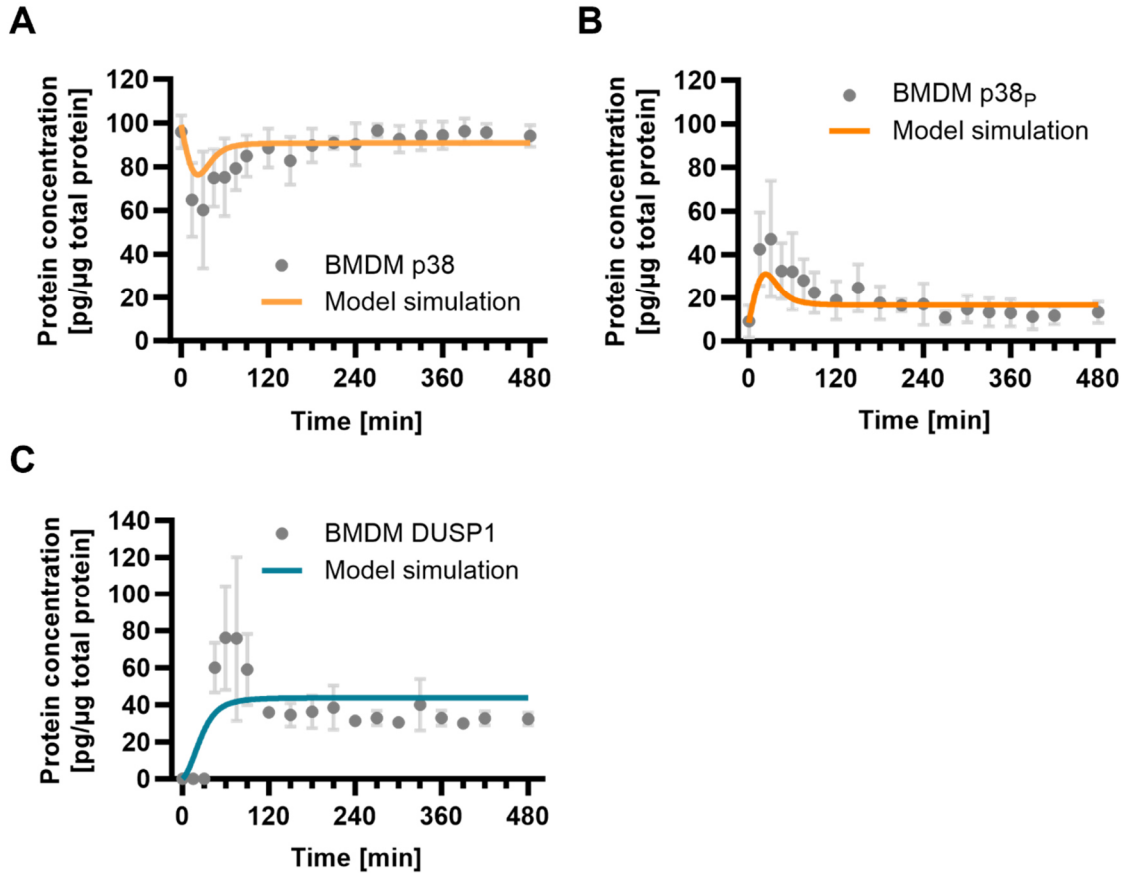


Figure 3.17 Computational simulation of the upstream p38 MAPK section of the Kulawik p38 MAPK-TTP model using an estimated parameter set with the best relative global MABS score for LPS-treated BMDMs.

The data for the simulation of the Kulawik p38 MAPK-TTP model was generated in MATLAB, solving the ODE equations (3.14) to (3.19) as well as the estimated parameter values and initial conditions in Table 3.13 and supplementary Table 7.1 for a time span of 480 min. The parameters were estimated using the NLSQ2 combined with the eSS2 nonlinear problem solver implemented in the AMIGO2 toolbox, and the experimental data of unphosphorylated, phosphorylated p38, and DUSP1 from the LPS-stimulated BMDMs presented in Figure 3.13. The values for unphosphorylated p38 were calculated by subtracting the $p38_P$ measurements from the mean total p38 measurements (99.09 pg/µg). In addition, a homoscedastic error profile set to 0.2, the "combined" experiment design, and parameter boundaries between 0 and 1 were selected for the parameter estimation run. The graphs show the model simulation of A) unphosphorylated p38, B) phosphorylated p38, and C) DUSP1 as lines in their respective colours together with the BMDM experimental data as symbols with error bars in grey. Estimation of the remaining parameters is shown in Figure 3.18. The full MATLAB script for parameter estimation and generation of the graphs can be found in Appendix 7.1

Table 3.15 Parameter set of parameter estimation for the Kulawik p38 MAPK-TTP model with fixed p38 MAPK parameters.

Parameter Estimation				
Symbol	**Description**	**PE value**	**Conf. interval**	**Dimension**
γ_T	Synthesis rate of TTP	$4.21*10^{-3}$	$3.37*10^{-5}$	$pg^{-1}min^{-1}\mu g$
δ_T	Degradation rate of TTP	$4.00*10^{-16}$	$4.24*10^{-6}$	min^{-1}
φ_T	Phosphorylation rate of TTP	$7.28*10^{-4}$	$5.41*10^{-5}$	$pg^{-1}min^{-1}\mu g$
δ_{Tp}	Degradation rate of TTP_P	$1.30*10^{-3}$	$1.62*10^{-4}$	min^{-1}
ρ_{Tp}	Dephosphorylation rate of TTP_P	$6.73*10^{-3}$	$6.05*10^{-4}$	min^{-1}
γ_{Rm}	Synthesis rate of TNF_m	$6.11*10^{-3}$	$3.32*10^{-5}$	$pg^{-1}min^{-1}\mu g$
δ_{Rm1}	Degradation rate 1 of TNF_m	$1.06*10^{-17}$	$1.06*10^{-6}$	min^{-1}
δ_{Rm2}	Degradation rate 2 of TNF_m	$6.51*10^{-5}$	$5.13*10^{-7}$	$pg^{-1}min^{-1}\mu g$

PE=Parameter estimation.

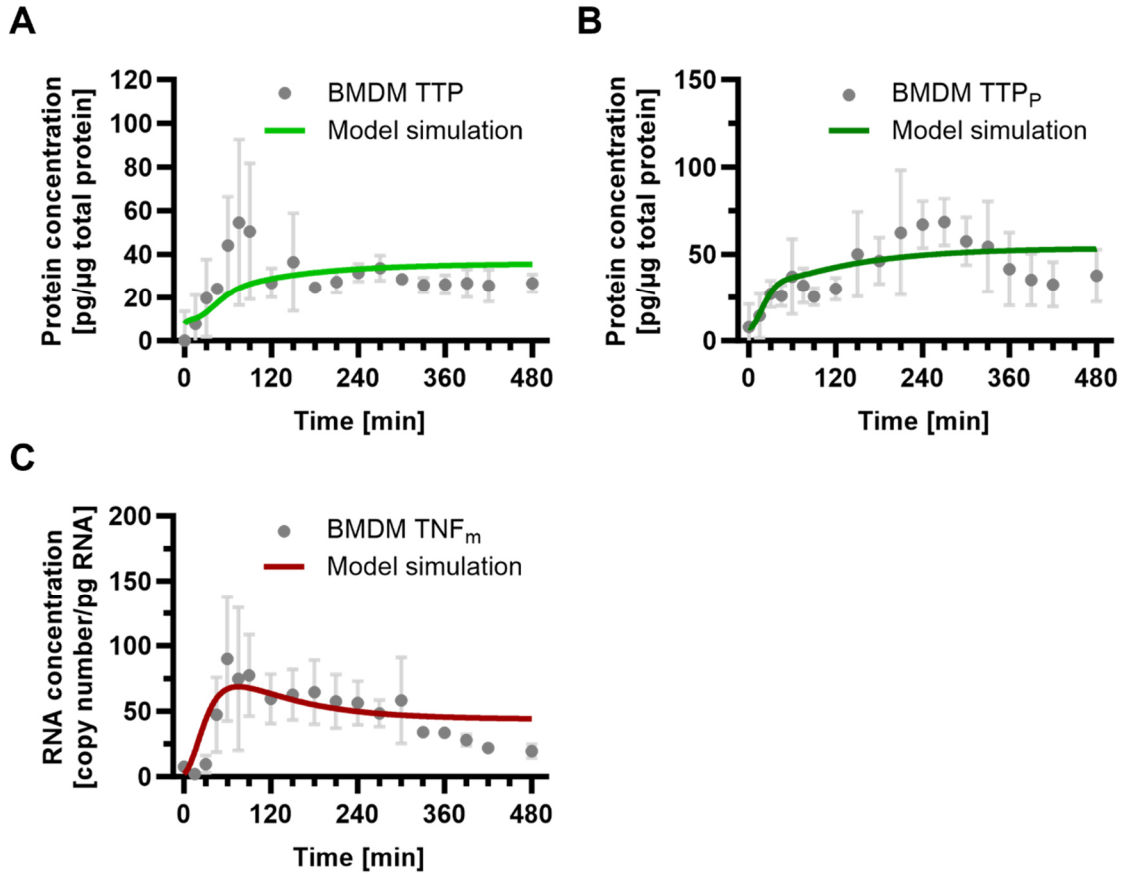


Figure 3.18 Computational simulation of the downstream TTP section of the Kulawik p38 MAPK-TTP model using an estimated parameter set with the best MABS score for LPS-treated BMDMs.

The data for the simulation of the Kulawik p38 MAPK-TTP model was generated in MATLAB, solving the ODE equations presented in Appendix 7.4, as well as the estimated parameter values and initial conditions in Table 3.15 and supplementary Table 7.1 for a time span of 480 min. The parameters were estimated using the NLSQ2 combined with the eSS2 nonlinear problem solver implemented in the AMIGO2 toolbox, and the experimental data of unphosphorylated and phosphorylated TTP and *Tnf* mRNA from the LPS-stimulated BMDMs presented in Figure 3.13. In addition, a homoscedastic error profile set to 0.2, the "combined" experiment design, and parameter boundaries between 0 and 1 were selected for the parameter estimation run. The graphs show the model simulation of A) unphosphorylated TTP, B) phosphorylated TTP, and C) *Tnf* mRNA as lines in their respective colours together with the BMDM experimental data as symbols with error bars in grey. The full MATLAB script for parameter estimation and generation of the graphs can be found in Appendix 7.1.

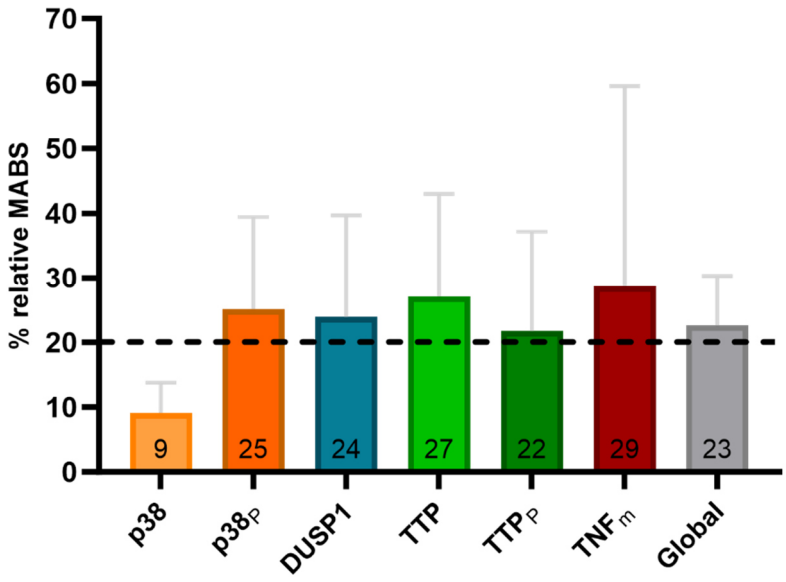


Figure 3.19 Relative MABS of residuals of the BMDM parameter estimation.

The relative differences between the data and the model simulation of the estimated BMDM parameters were obtained from the AMIGO2 parameter estimation result files, and the absolute mean was calculated for each variable and for all variables combined (global). The Figure shows MABS-mean as bar chart, and the standard deviation as error bars.

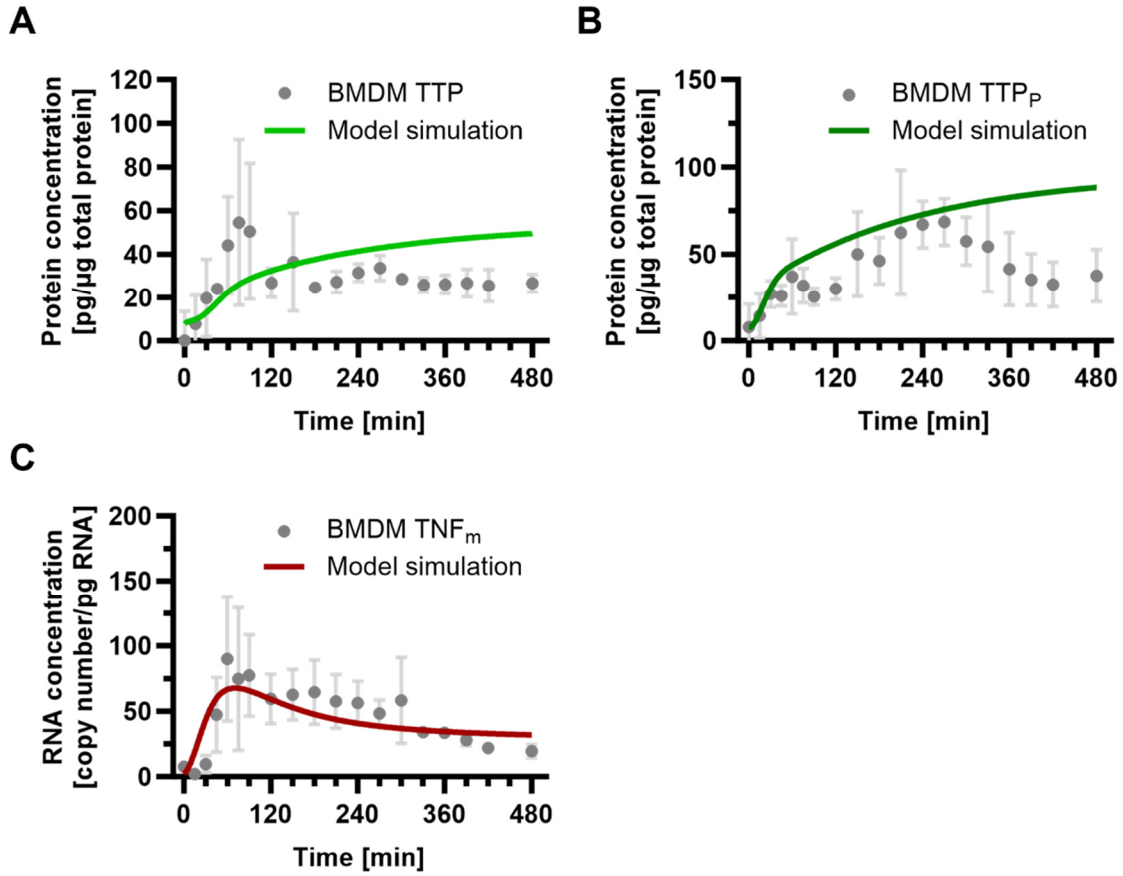


Figure 3.20 Computational simulation of the downstream TTP section of the Kulawik p38 MAPK-TTP model with switched TTP degradation rates.

The data for the simulation of the Kulawik p38 MAPK-TTP model simulation was generated in MATLAB, solving the ODE equations presented in Appendix 7.4, as well as the estimated parameter values and initial conditions in Table 3.13, Table 3.15 and supplementary Table 7.1 for a time span of 480 min. The parameters were estimated using the NLSQ2 combined with the eSS2 nonlinear problem solver implemented in the AMIGO2 toolbox, and the experimental data of unphosphorylated and phosphorylated TTP and *Tnf* mRNA from the LPS-stimulated BMDMs presented in Figure 3.13. In addition, a homoscedastic error profile set to 0.2, the "combined" experiment design, and parameter boundaries between 0 and 1 were selected for the parameter estimation run. Additionally, the estimated degradation rates of phosphorylated and unphosphorylated TTP were interchanged to describe better the biology of the data in the upcoming validation chapter. The graphs show the model simulation of A) unphosphorylated TTP, B) phosphorylated TTP, and C) *Tnf* mRNA as lines in their respective colours together with the BMDM experimental data as symbols with error bars in grey. The full MATLAB script for parameter estimation and generation of the graphs can be found in Appendix 7.1.

3.4.3 Model validation BMDMs

To compare data sets with model results, we simulated the model with the estimated parameters in MATLAB and compared them against the data from the respective experiment. We included the standard deviation of the mutant strain/inhibitor data to see if the model lies within this range, but omitted the standard deviation of the BMDM WT data, for clarity. For quantitative analysis, we calculated the relative MABS as before. First, we will present the data and describe how the model and reality differ for the *Dusp1*$^{-/-}$ and *Zfp36*$^{aa/aa}$ mutant strain experiments, as well as inhibitor treatment. For this purpose, we also included the BMDM nominal parameter values and compared them to the best-fit parameter estimates.

3.4.3.1 Comparison of WT and *Dusp1*$^{-/-}$ mutant BMDMs

DUSP1 is likely a key regulator of p38 MAPK-TTP pathway dynamics, which we aimed to dissect in the scope of our model. For this purpose, we employed the knockout mouse mutant line, *Dusp1*$^{-/-}$ (133). This mutant line does not exhibit any obvious phenotype under sterile conditions but shows increased p38 MAPK activation and expression of inflammatory cytokines when challenged with an inflammatory stimulus (118,131,134,135), which also renders them susceptible to various inflammatory diseases (136–139). DUSP1 is one of the p38 MAPK feedback regulators. Consequently, we expected an increase in p38 MAPK phosphorylation, increases in TTP phosphorylation, and *Tnf* mRNA expression when BMDMs from this mouse are subjected to an inflammatory stimulus. We were specifically interested in the exact dynamics and strength of the impact of the knockout on p38 MAPK phosphorylation and how it could affect the expression dynamics of TTP and *Tnf* mRNA; after all, DUSP1 might also be a potential target for drug intervention.

In this chapter, we examine the results of the time-course experiment performed with *Dusp1*$^{-/-}$ mice. The experiment, overall, follows the experimental scheme described for the WT BMDMs

and was repeated 3 times, with the cells of 6 mice combined for each experiment to allow the collection of protein and RNA samples for the time-course. Unfortunately, the cell yield was quite low for some of the experiments. Consequently, we could not measure all 19 time points, as was done with WT BMDMs, and the temporal resolution of the later stage of the inflammatory response is reduced.

In this chapter, we will first present and describe the data obtained from this experiment and follow with a comparison to WT BMDMs. The difference between the data sets is quantitatively assessed by utilising repeated measure (RM) two-way ANOVA and by Šidák post-hoc corrected multiple comparisons of individual means (individual experimental repeats are shown in Appendix 7.3.2), addressing the null hypothesis that there are no significant differences between the two groups overall or between individual time points, respectively. The layout of the graphs will draw on the same general structure as in previous chapters, which means proteins and mRNA of interest are shown in their respective signature colours which is maintained throughout the thesis. No data is reported on DUSP1 expression, which was, as expected, not detectable in *Dusp1*$^{-/-}$ mice, as shown in supplementary Figure 7.15.

p38 MAPK

Figure 3.21 A displays p38 MAPK expression patterns in *Dusp1*$^{-/-}$ BMDMs and WT BMDMs. For *Dusp1*$^{-/-}$ BMDMs, expression reached a global maximum at 87 pg/µg 0.5 h post-stimulation. Afterwards, expression decreases rapidly until the 2 h time point with a concentration of 28 pg/ µg and then more gradually reaching 12 pg/µg after 8 h.

Statistical analysis suggested that the overall characteristics of the phopho-p38 expression dynamics between WT BMDMs and *Dusp1*$^{-/-}$ BMDMs were indeed different (P value of combined column and row factors = 0.0024). However, multiple comparisons did not yield any

means at a specific time that would be classified as statistically significant. As such, the sum of smaller differences leads to a potential overall change in expression dynamics. For example, we measured increased phospho-p38 expression in unstimulated cells, with 5 pg/µg in WT and 18 pg/ in *Dusp1*$^{-/-}$, which could indicate a basal expression of DUSP1 in WT mice, where the phosphatase is constantly dephosphorylating low amounts of p38, followed by an increased expression intensity during the peak.

Unphosphorylated TTP

Figure 3.21 B shows unphosphorylated TTP (lower band WB) expression patterns in *Dusp1*$^{-/-}$ BMDMs and WT BMDM. In unstimulated *Dusp1*$^{-/-}$ cells, TTP expression remained below the detection limit, with the first expression measured 1 h after LPS stimulation. After 2 h, the maximum of 83 pg/µg was reached, after which the presence of unphosphorylated TTP appeared to briefly decline before picking up again to remain relatively steady with some fluctuation close to but not quite reaching the initial peak value. After 7 h, the expression slowly declined again. Although the exact dynamic and strength varied between the three repeats of the three experiments, a peak at around 2 h was observable in all three experiments (compare supplementary Figure 7.14, Figure 7.16 and Figure 7.18).

Comparing unphosphorylated TTP in BMDM WT vs. *Dusp1*$^{-/-}$, we observed differences in TTP expression dynamics throughout the inflammatory response. The statistical analysis backs this, reported as a P value of combined column and row factors = 0.0001. In WT BMDM, unphosphorylated TTP expression was already observable after 30 min, in contrast to only after 1 h in *Dusp1*$^{-/-}$. This is best reflected by the 0.75 h time point, which is analysed as statistically significantly different (P value = 0.0266) between the two groups. The expression peak appears to be delayed between the groups; in WT cells, we observed a peak in expression after 1.25 h, and in *Dusp1*$^{-/-}$ cells, only after 2 h. However, this qualitative observation is only covered by

the overall statistical difference, not by individual value difference P values. The measured total expression is generally higher in *Dusp1*$^{-/-}$ BMDMs, a fact not only reflected by the overall statistical analysis but also by the time points at 4 h (P value = 0.0032) and 5 h (P value = 0.0061) being flagged as significantly different in the multiple comparison analysis.

Phosphorylated TTP

Figure 3.21 C displays phosphorylated TTP (upper band) expression patterns in *Dusp1*$^{-/-}$ BMDMs. The first expression of phosphorylated TTP was measured 1 h after LPS stimulation. After 2 h, a local maximum was observed at around 78 pg/µg, followed by a short decline, reaching a local minimum at the 2.5 h time point. The global peak was reached at 131 pg/µg after 5 h, preceding a plateau-like phase before a decline after the 7 h time point.

Compared to phosphorylated TTP expression patterns in WT BMDMs, as for unphosphorylated TTP, we observed differences in the expression pattern (P value of combined column and row = 0.0106). Although none of these observations are backed by statistical significance in a multiple comparison analysis, the sum of these explains the overall difference in the measured time-courses. In WT BMDMs, Phospho-TTP expression was already observable after 0.25 h, and in *Dusp1*$^{-/-}$ cells, it was only after 1 h. In WT cells, we observed a peak after 1.25 h, while *Dusp1*$^{-/-}$ mice peaked delayed after 2 h. Following the initial local maximum in WT BMDMs, phospho-TTP expression reached a global maximum after 4.5 h, followed by a decline. In contrast, in *Dusp1*$^{-/-}$ BMDMs, the expression increased after an initial local minimum, and only reached a global maximum after 7 h, followed by a decline. As with the unphosphorylated species, the measured total expression was overall higher in *Dusp1*$^{-/-}$ BMDMs.

Tnf mRNA

Figure 3.21 D shows *Tnf* mRNA expression patterns in *Dusp1*$^{-/-}$ and WT BMDM. In *Dusp1*$^{-/-}$ cells, RNA expression in unstimulated cells was measured at around 1 cn/pg. Following stimulation, expression increased after 0.5 h and reached a local and global maximum at 257 cn/pg RNA, 1.5 h post-stimulation. After 1.5 h, expression decreased steeply at first and then gradually reaching 14 cn/pg after 8 h.

Comparing *Tnf* mRNA expression between WT BMDMs and *Dusp1*$^{-/-}$ BMDMs, we observed differences in *Tnf* expression during the inflammatory response (P value of combined column and row factors < 0.0001), with a much stronger but delayed expression peak followed by a steep decrease in expression that only reaches the gradual nature of the WT time-course 4 h after stimulation. In the multiple comparison analysis, this is also reflected in the peak value at 1.5 being flagged as statistically significantly different (P value = 0.0266).

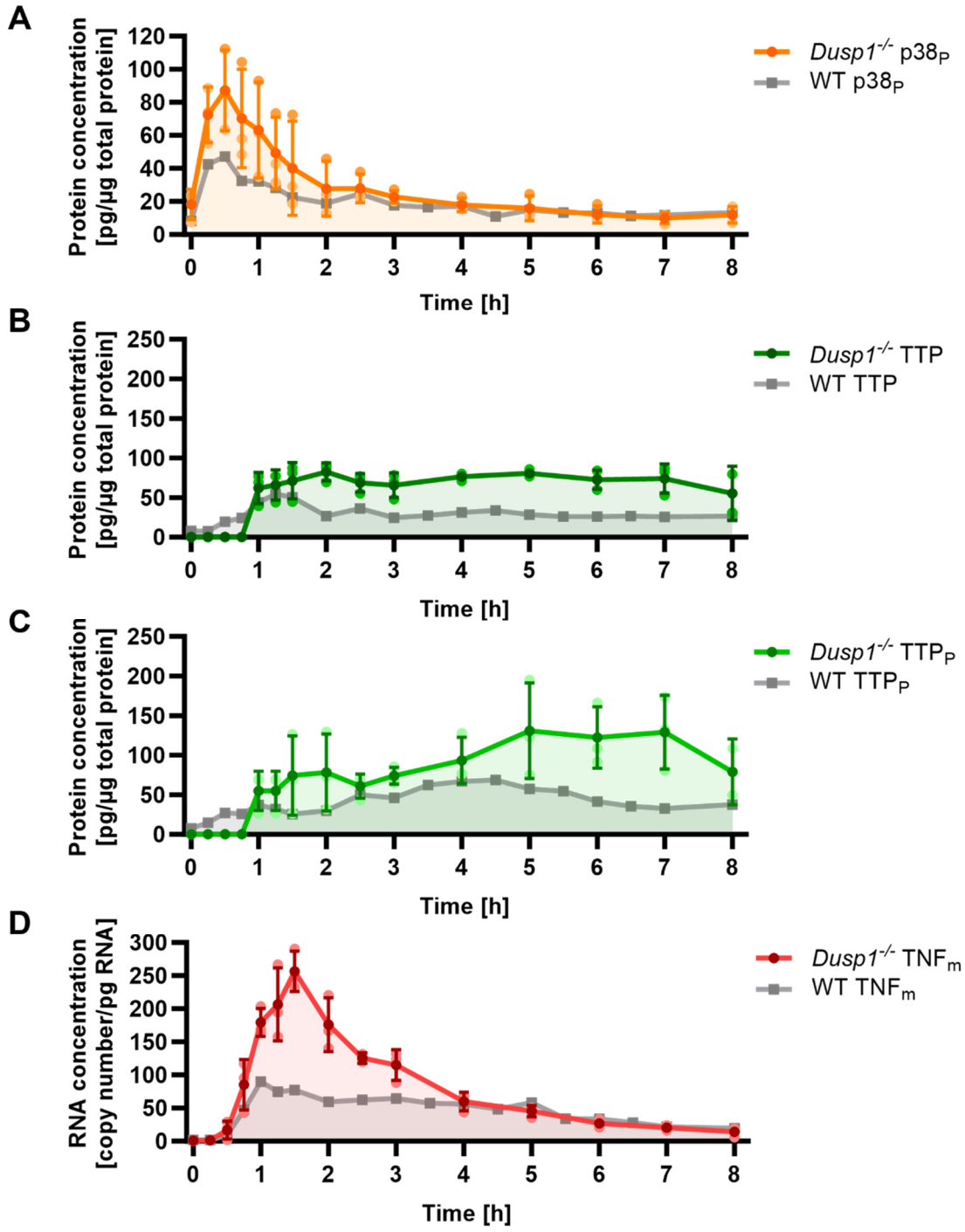


Figure 3.21 Measuring p38 MAPK-TTP pathway components by total quantification of Western blot and qPCR data obtained from *Dusp1*$^{-/-}$ and WT BMDMs treated with LPS over an 8 h time-course.

BMDMs derived from the bone marrow of 6 mice were combined and treated with 10 ng/mL LPS for a period of 8 h. Protein concentrations of phospho-p38, phospho-TTP and TTP, as well as *Tnf* mRNA levels, were measured using WB and qPCR, respectively (n=3). The Western blot data of A) phospho-p38 ($p38_P$), B) total (TTP_T) and

unphosphorylated TTP (TTP, lower band), and C) total and phosphorylated TTP (TTP_P, upper band) was quantified in Image Lab software, normalised to its Stain-Free signal, and the total protein concentrations were calculated using standard curves of recombinant protein. The total amount of D) *Tnf* mRNA was measured by running a standard curve consisting of known quantities of plasmid DNA alongside the samples for qPCR. Standard deviation is displayed as error bars, and the results of the individual experiments utilising *Dusp1*$^{-/-}$ BMDMs are included as lightly coloured symbols in the background to visualise variability. Results from Chapter 3.4.1 to enable comparison to WT BMDMs are shown in grey. RM two-way ANOVAs and Šidák post-hoc corrected multiple comparisons were performed to compare the results from *Dusp1*$^{-/-}$ BMDMs with WT BMDMs. Resulting P values of combined column and row factors as a measure for overall difference between the two curves and single multiple comparison P values, where statistical significance was reached: A) P value = 0.0024; B) P value = 0.0001, Multiple comparisons: P value (0.75 h) = 0.0266, P value (4 h) = 0.0032, P value (5 h) = 0.0061; C) P value = 0.0106 ; D) P value < 0.0001, Multiple comparisons: P value (1.5 h) = 0.0266.

Model comparison of WT and Dusp1$^{-/-}$ *BMDMs*

Figure 3.22 shows the computational simulation of $p38_P$, TTP, TTP_P, and TNF_m using the updated Kulawik p38 MAPK-TTP model (Equations 3.14 to 3.19) and the previously determined BMDM parameter set (Table 3.13 and Table 3.15) in WT and *Dusp1*$^{-/-}$ mutant cells. Additionally, the data obtained from *Dusp1*$^{-/-}$ BMDMs is shown as mean with standard deviation. For the simulation of the *Dusp1*$^{-/-}$ mutant, we set the parameter $\gamma_D = 0$ and the initial condition $D0 = 0$. DUSP1 expression is displayed, as it simulated at constant 0 and was not detected in the experiments. The data for the graphs was generated, as described in previous chapters, in MATLAB using the *ode23* solver.

The *Dusp1*$^{-/-}$ simulation resulted in an initial strong increase of p38 MAPK phosphorylation, followed by a plateau phase once all p38 MAPK molecules were phosphorylated (Figure 3.22 A). The observed dynamics were as expected, considering that DUSP1 in our model comprises the sole dephosphorylating agent of p38 MAPK. We did not find these dynamics in the *Dusp1*$^{-/-}$ BMDM experimental data; however, it confirmed that DUSP1 is not the only phosphatase regulating p38 MAPK.

An increase in p38 MAPK phosphorylation should subsequently lead to an increase in TTP synthesis and phosphorylation. For unphosphorylated TTP (Figure 3.22 B) in the *Dusp1*$^{-/-}$ simulation, we observed a linear increase throughout the simulated period, reaching more than double the concentration of the WT simulation after 480 min. In contrast, phosphorylated TTP (Figure 3.22 C) levels increased sharply up to 1400 pg/µg. This is contrasted by experimental data where we did not observe a linear increase of unphosphorylated TTP or a strong increase of phospho-TTP in the *Dusp1*$^{-/-}$ BMDMs. Again, this mismatch can be explained by the fact that our underlying model assumption of DUSP1 being sufficient to describe p38 MAPK dephosphorylation in our model, is likely wrong.

Increased p38 MAPK phosphorylation, together with increased TTP phosphorylation, which should equal functional inactivation, should also result in increased *Tnf* mRNA expression. Indeed, in the *Dusp1*$^{-/-}$ simulation (Figure 3.22 D), *Tnf* mRNA expression initially increased sharply, reaching a maximum of 250 cn/pg around the 135 min time point, followed by a decline to 80 cn/pg. In comparison, the WT simulation reached a maximum of 70 cn/pg around the 70 min time point and declined to 30 cn/pg. Interestingly, compared to the WT (Figure 3.17) the dynamics of the *Dusp1*$^{-/-}$ model simulation and experimental data were similar this time, regarding peak height and overall behaviour (Figure 3.22).

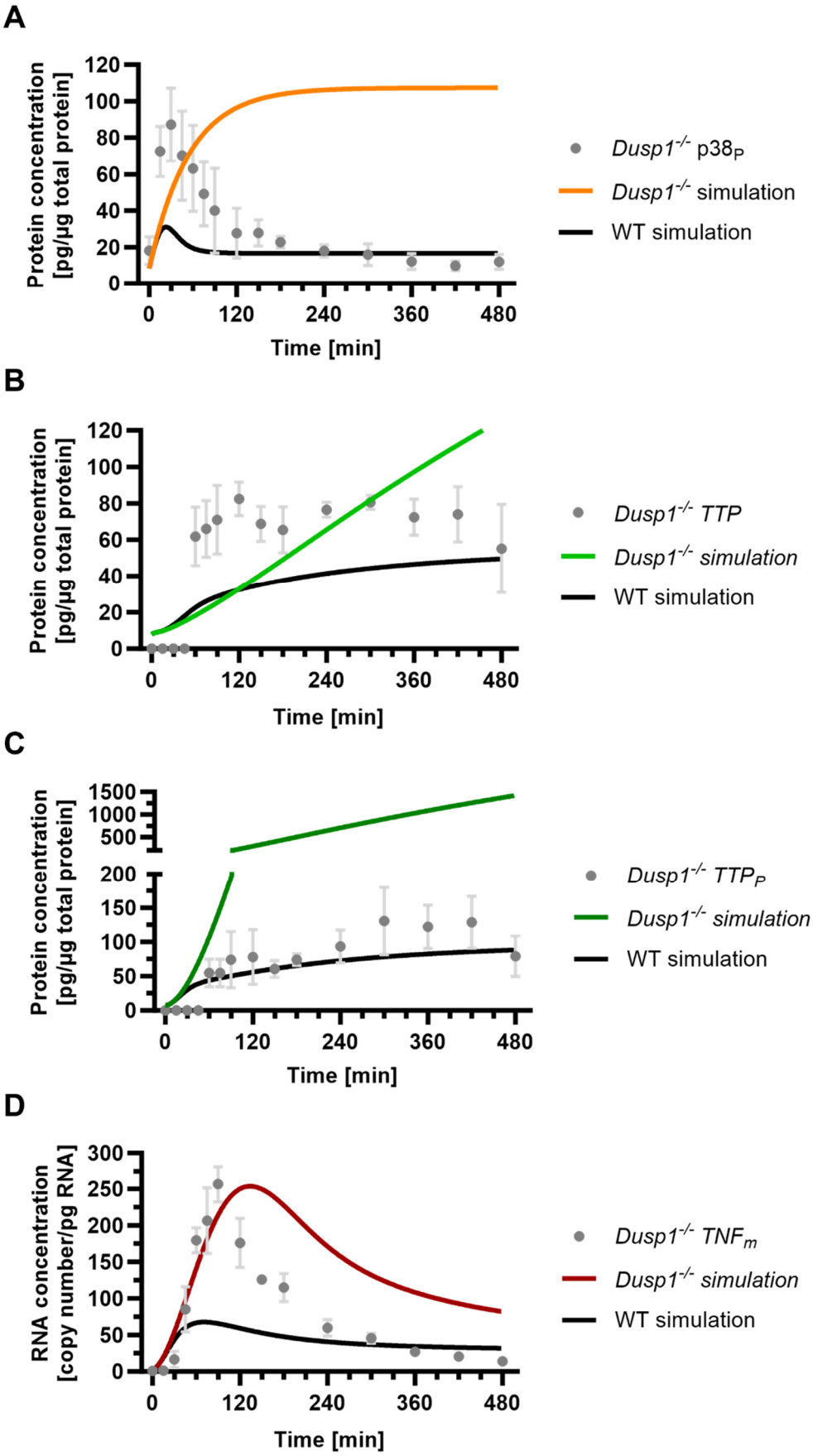

A
Protein concentration [pg/µg total protein]
120
100
80
60
40
20
0
0
120
240
360
480
Time [min]
Dusp1-/- p38P
Dusp1-/- simulation
WT simulation
B
Protein concentration [pg/µg total protein]
120
100
80
60
40
20
0
0
120
240
360
480
Time [min]
Dusp1-/- TTP
Dusp1-/- simulation
WT simulation
C
Protein concentration [pg/µg total protein]
1500
1000
500
200
150
100
50
0
0
120
240
360
480
Time [min]
Dusp1-/- TTPP
Dusp1-/- simulation
WT simulation
D
RNA concentration [copy number/pg RNA]
300
250
200
150
100
50
0
0
120
240
360
480
Time [min]
Dusp1-/- TNFm
Dusp1-/- simulation
WT simulation

Figure 3.22 Computational simulation of LPS-treated WT and *Dusp1*$^{-/-}$ BMDMs using the calibrated Kulawik p38 MAPK-TTP model.

The data for the simulation of the WT and *Dusp1*$^{-/-}$ Kulawik p38 MAPK-TTP model was generated in MATLAB, solving the ODE equations (3.14) to (3.19) as well as the estimated parameter values and initial conditions in Table 3.13 and supplementary Table 7.1 for a time span of 480 min. For the *Dusp1*$^{-/-}$ mutant simulation, the parameter $\boldsymbol{\varphi_D}$ and the initial condition $\boldsymbol{D0}$ were set to zero. The graphs show the model simulation of A) phosphorylated p38, B) unphosphorylated TTP, C) phosphorylated TTP, and D) TNF_m of WT of *Dusp1*$^{-/-}$ BMDMs together with the *Dusp1*$^{-/-}$ BMDM experimental data, presented in Chapter 3.4.3.1, as mean data points with standard deviation. The full MATLAB script for generating the simulated data can be found in Appendix 7.1.

3.4.3.2 Comparison of WT and *Zfp36*$^{aa/aa}$ mutant BMDMs

In *Zfp36*$^{aa/aa}$ mice, serines are replaced with alanines at positions Ser-52 and Ser-178, two of the main phosphorylation targets of p38 MAPK. This renders TTP non-phosphorylatable, which results in its constant activation. However, it also prevents its accumulation via stabilisation. The overall phenotype is described as normal, but mice appear protected from inflammation-related diseases (260).

In this chapter, we show the results of the time-course experiment performed with *Zfp36*$^{aa/aa}$ mice. The experiment, overall, follows the experimental scheme described for the WT BMDMs and was repeated 3 times with the cells of 6 mice combined for each experiment to allow the collection of protein and RNA samples for the time-course. Unfortunately, the cell yield was quite low for some of the experiments, and we could not measure the full 19 time points as for the WT mice, which resulted in some reduced temporal resolution later in the time-course. We will first present and describe the combined data obtained from *Zfp36*$^{aa/aa}$ time-course experiments (data from individual experiments is shown in Appendix 7.3.3). After describing the overall expression behaviour, we will present how it differs from WT BMDMs. This comparison will be quantitatively assessed by utilising repeated measure (RM) two-way ANOVA and by Šidák post-hoc corrected multiple comparisons of individual means. The

layout of the graphs, including the colour coding of targets, is presented the same as in previous chapters.

p38 MAPK

Figure 3.23 A shows phospho-p38 MAPK expression patterns in *Zfp36*$^{aa/aa}$ and WT BMDMs. In *Zfp36*$^{aa/aa}$ cells, phospho-p38 MAPK in unstimulated cells was measured at 8 pg/µg. Following stimulation, expression reached a local and global maximum at 67 pg/µg after 15 min. From the peak, expression decreased steadily, reaching 11.6 pg/µg after 2.5 h before; at the 3 h time point, phosphorylation increased to a small local maximum again. Afterwards, the concentration decreased steadily, underscoring the starting value in unstimulated cells after 6 h and reaching 4 pg/µg after 8 h.

Comparing p38 MAPK phosphorylation in WT BMDMs with *Zfp36*$^{aa/aa}$ revealed similar non-significantly different overall dynamics (P value of combined column and row factors = 0.0755). The initial peak was higher in *Zfp36*$^{aa/aa}$ BMDMs, primarily due to one experiment with a very strong response (106 pg/µg).

DUSP1

Figure 3.23 B displays DUSP1 expression patterns in *Zfp36*$^{aa/aa}$ and WT BMDMs. DUSP1 was not expressed in unstimulated cells and was only detectable after 0.5 h post-stimulation. A global maximum was detected after 1.25 h post-stimulation at 83 pg/µg. After the peak and the subsequent decrease in DUSP1 expression, the levels fell below the detection limit after 3 h. The presented plateau is assumed for modelling purposes based on observations in RAW264.7 and WT BMDM data (compare and supplementary Figure 7.25 and Figure 7.25).

For DUSP1, we were unfortunately unable to perform statistical analysis as for both the *Zfp36*$^{aa/aa}$ and the WT BMDMs, we could only include two experimental replicates. While this

does not impact utilising the values in mathematical modelling, it should be kept in mind that any comparison to BMDMs here is only of a qualitative nature and is not backed by quantitative statistical analysis. Here, we did not observe a big difference in the mean expression levels and dynamics, with a slight difference in the *Zfp36*$^{aa/aa}$ cells exhibiting a slower reduction of DUSP1 after the initial peak.

TTP

Figure 3.23 C displays TTP expression patterns in *Zfp36*$^{aa/aa}$ and WT BMDMs. For *Zfp36*$^{aa/aa}$ BMDMs, only one band and a cloud of signal noise (compare supplementary Figure 7.21) were distinguishable. Since TTP could not be phosphorylated at two sites, we assumed the signal to be unphosphorylated TTP. A signal was first detectable after 0.75 h post-stimulation, where an initial peak was reached at 5 pg/µg. Afterwards, the signal appeared only slightly to fluctuate for the remainder of the experiment.

For this measurement, we were unfortunately again unable to perform statistical analysis as for the *Zfp36*$^{aa/aa}$ BMDMs, we could only include two experimental replicates. Please keep in mind that any comparison to BMDMs here is only of a qualitative nature and is not backed by quantitative statistical analysis. The overall levels of expression were much lower than in WT BMDMs. The *Zfp36*$^{aa/aa}$ BMDMs did also not exhibit the, in WT BMDMs present, initial peak with a follow-up decrease.

Tnf mRNA

Tnf mRNA expression patterns in Zfp36$^{aa/aa}$ BMDMs are displayed in Figure 3.23 D. In unstimulated and 15 min post-stimulation cells, the expression of *Tnf* was low at 1 and 2 cn/pg, respectively. After 30 min, the expression increased, and two peaks were measured, the first after 1 h at 90 cn/pg and the second after 1.5 h at 99 cn/pg. Between these peaks, a dip was

observable at 73 cn/pg. One of the three experiments yielded especially high *Tnf* levels (143 copies per pg RNA) and did not exhibit a double peak, which leads to a quite high variation between experiments. After the initial peaks, the expression decreased to 52 cn/pg after 3 h, followed by an intermittent increase at 4.5 h. Finally, the levels gradually decreased, reaching 20 cn/pg after 8 h.

We observed only minor qualitative differences when comparing Tnf mRNA expression in WT vs. $Zfp36^{aa/aa}$ BMDMs. For example, the second peak in $Zfp36^{aa/aa}$ BMDMs was found to be a bit higher. These differences were not statistically significant individually or as an overall measurement (P value of combined column and row factors = 0.9409).

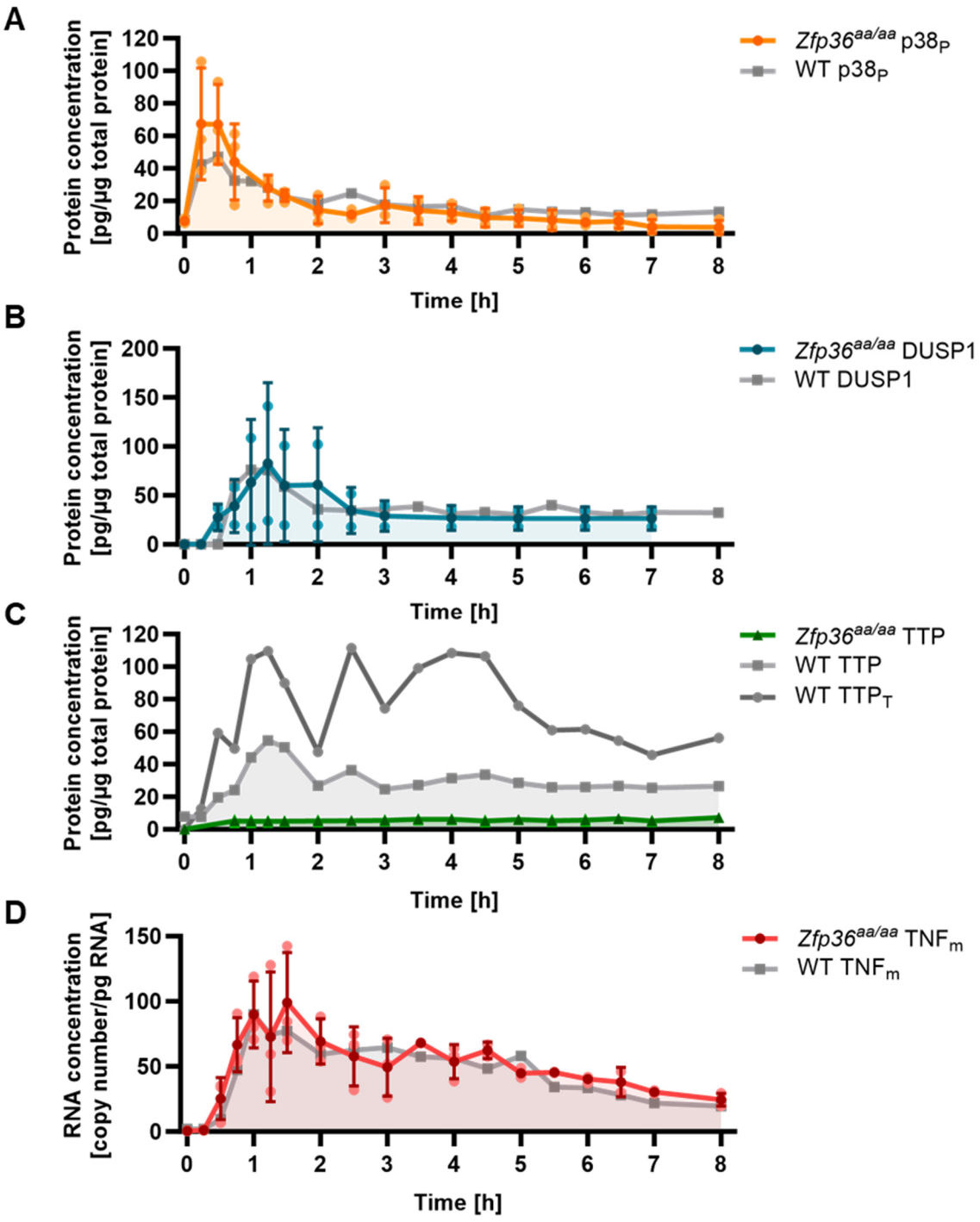


Figure 3.23 Measuring p38 MAPK-TTP pathway components by total quantification of Western blot and qPCR data obtained from *Zfp36*$^{aa/aa}$ and WT BMDMs treated with LPS over an 8 h time-course.

BMDMs derived from the bone marrow of 6 mice were combined and treated with 10 ng/mL LPS for a period of 8 h. Protein concentrations of phospho-p38, total p38, unphosphorylated TTP, as well as *Tnf* mRNA levels, were measured using WB and qPCR, respectively (n=3). The Western blot data of A) phospho-p38 ($p38_P$), B) DUSP1,

and C) total TTP (TTP_T) and unphosphorylated TTP (TTP) was quantified in Image Lab software, normalised to its Stain-Free signal, and the total protein concentrations were calculated using standard curves of recombinant protein. The total amount of D) *Tnf* mRNA was measured by running a standard curve consisting of known quantities of plasmid DNA alongside the samples for qPCR. Standard deviation is displayed as error bars, and the results of the individual experiments utilising *Zfp36*$^{aa/aa}$ BMDMs are included as lightly coloured symbols in the background to visualise variability. Results from Chapter 3.4.1, which enable comparison to WT BMDMs, are shown in grey. RM two-way ANOVAs were performed to compare the results from *Zfp36*$^{aa/aa}$ BMDMs with WT BMDMs; A) P value = 0.0755; B) could not be analysed due to incomplete dataset; C) could not be analysed due to incomplete dataset D) P value = 0.9409; No individual Šidák post-hoc corrected comparison yielded a statistically significant result.

Model comparison of WT and ZFP36$^{aa/aa}$ BMDMs

Figure 3.24 displays the computational simulation of TTP and TNF_m using the updated Kulawik p38 MAPK-TTP model (Equations (3.14) to (3.19)) and the previously determined BMDM parameter set (Table 3.13 and Table 3.15) in WT and *Zfp36*$^{aa/aa}$ mutant BMDMs. The parameter $\varphi_T = 0$ and the initial condition $T_P0 = 0$ are used for the simulation of the *Zfp36*$^{aa/aa}$ mutant. p38 and DUSP1 expression is not shown here because the values are identical between WT and mutant simulation, and phosphorylated TTP is not shown as it was not detected in the experiments. The data for the graphs was generated, as described in previous chapters, in MATLAB using the *ode23* solver.

The *Zfp36*$^{aa/aa}$ simulation resulted in an initial strong increase in TTP expression followed by a plateau phase at 50 pg/µg, which is around the same level as the WT simulation after 480 min. In contrast, the *Zfp36*$^{aa/aa}$ BMDM experimental data only reached 5 pg/µg total protein (Figure 3.24 A). In the simulation, this increase in unphosphorylated TTP led to a decrease in *Tnf* mRNA levels in the *Zfp36*$^{aa/aa}$ simulation compared to the WT (Figure 3.24 B). However, this is not reproduced by the experimental data which appeared more similar to the WT than the *Zfp36*$^{aa/aa}$ simulation. This discrepancy will be addressed in more detail in the discussion Chapter 3.6.3.

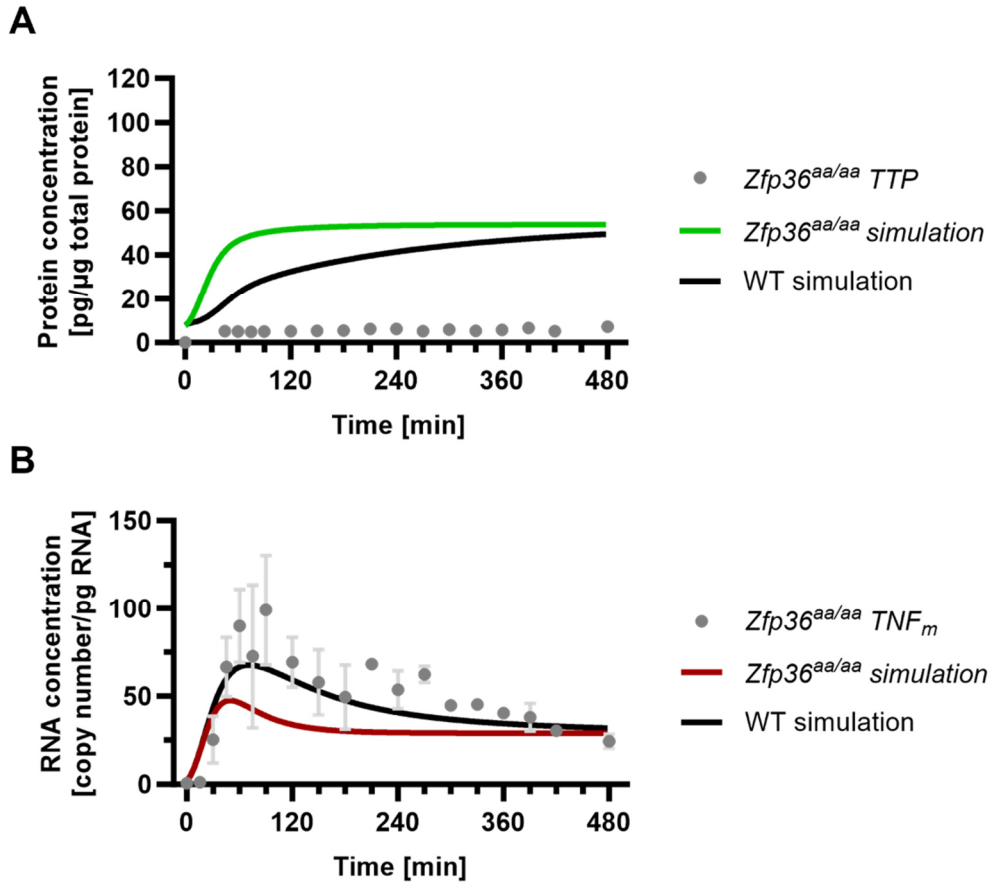


Figure 3.24 Computational simulation of LPS-treated WT and *Zfp36*$^{aa/aa}$ BMDMs using the calibrated Kulawik p38 MAPK-TTP model.

The data for the simulation of the WT and *Zfp36*$^{aa/aa}$ Kulawik p38 MAPK-TTP model was generated in MATLAB, solving the ODE equations (3.14) to (3.19) as well as the estimated parameter values and initial conditions in Table 3.13 and supplementary Table 7.1 for a time span of 480 min. For the simulation of the *Zfp36*$^{aa/aa}$ mutant, the parameter $\boldsymbol{\varphi_T}$ and the initial condition $\boldsymbol{T_P0}$ are set to zero. The graphs show the model simulation of A) unphosphorylated TTP, and B) TNF_m of WT and *Zfp36*$^{aa/aa}$ BMDMs together with the *Zfp36*$^{aa/aa}$ BMDM experimental data, presented in Chapter 3.4.3.2, as mean data points with standard deviation. The full MATLAB script for generating the simulated data can be found in Appendix 7.1.

3.4.3.3 BMDM inhibitor experiments

Inhibitor treatment was an interesting approach for us as it allows for manipulating the pathway without establishing a new cell or mouse line. Of course, this process is not as specific, as most inhibitors exhibit some off-target effects, and complete inhibition is not always possible. Also, inhibitors require some validation before being of value. In this chapter, we will present the

results of the time-course experiment in BMDMs, which were treated with 2.5 nM Calyculin A (a PP2A inhibitor) 30 min before the LPS stimulation. Identification of the concentrations and functional validation of the inhibitor is shown in Appendix 7.2.

Figure 3.25 displays the combined data obtained from the PP2A inhibitor time-course experiments with three repeats. The data layout is the same as that of the previous results chapters. Due to poor BMDM yield in some of the repeats, not all 19 time points could be covered, which reduces the temporal resolution at later time points. This experiment was performed alongside earlier presented experiments, with the same cells, from Chapter 3.4.1.

As a dephosphorylating agent of TTP, we expected to see an increase in phosphorylated TTP species combined with a decrease in unphosphorylated TTP and an increase in TTP target mRNA expression in Calyculin A treated BMDMs. While we observed the expected increase in *Tnf* mRNA expression compared to non-inhibitor treated cells (Figure 3.25 E), we did also observe strongly elevated p38 phosphorylation (Figure 3.25 A). As such, the overall readout from these experiments cannot be used for our model as the increase in *Tnf* mRNA expression cannot be attributed to changes in TTP phosphorylation and might very well be caused by the elevation of phospho-p38, which is in this case caused by an unknown factor, likely a cytotoxic effect of the inhibitor. Therefore, for brevity, we forgo a more detailed description here.

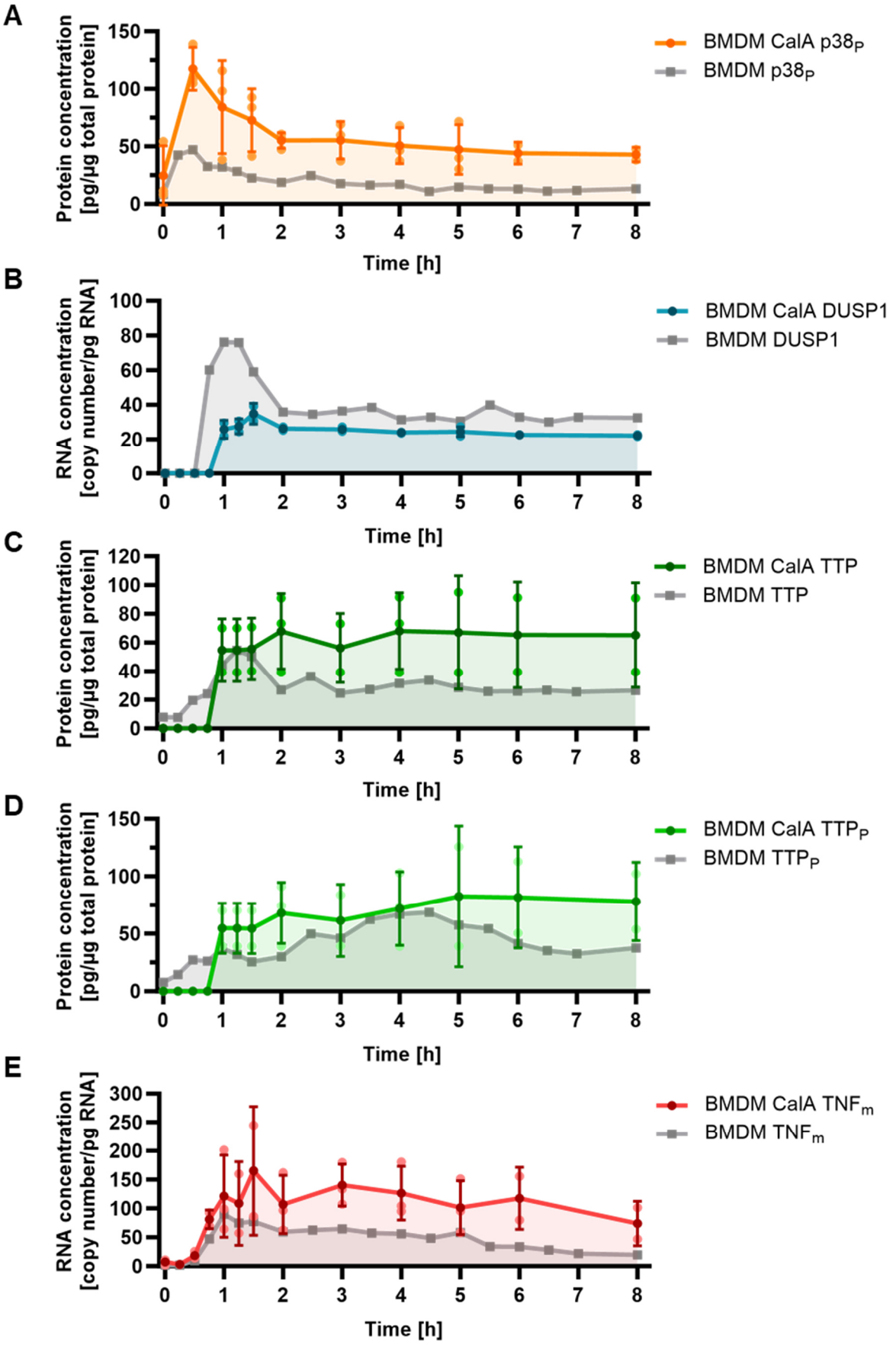

A
Protein concentration [pg/µg total protein]
150
100
50
0
0 1 2 3 4 5 6 7 8
Time [h]
BMDM CalA p38P
BMDM p38P
B
RNA concentration [copy number/pg RNA]
100
80
60
40
20
0
0 1 2 3 4 5 6 7 8
Time [h]
BMDM CalA DUSP1
BMDM DUSP1
C
Protein concentration [pg/µg total protein]
120
100
80
60
40
20
0
0 1 2 3 4 5 6 7 8
Time [h]
BMDM CalA TTP
BMDM TTP
D
Protein concentration [pg/µg total protein]
150
100
50
0
0 1 2 3 4 5 6 7 8
Time [h]
BMDM CalA TTPP
BMDM TTPP
E
RNA concentration [copy number/pg RNA]
300
250
200
150
100
50
0
0 1 2 3 4 5 6 7 8
Time [h]
BMDM CalA TNFm
BMDM TNFm

Figure 3.25 Measuring p38 MAPK-TTP pathway components by total quantification of Western blot and qPCR data obtained from WT BMDMs with or without Calyculin A stimulated with LPS over an 8 h time-course.

BMDMs derived from the bone marrow of 8 mice were combined and treated with 2.5 nM Calyculin A before stimulation with 10 ng/mL LPS for a period of 8 h. Protein concentrations of phospho-p38, tDUSP1, unphosphorylated TTP, as well as *Tnf* mRNA levels, were measured using WB and qPCR, respectively (n=3). The Western blot data of A) phospho-p38 ($p38_P$), B) DUSP1, C) unphosphorylated TTP (TTP, lower band), and D) total and phosphorylated (TTP_P, upper band) TTP, was quantified in Image Lab software, normalised to its Stain-Free signal, and the total protein concentrations were calculated using standard curves of recombinant protein. The total amount of E) *Tnf* mRNA, was measured by running a standard curve consisting of known quantities of plasmid DNA alongside the samples for qPCR. Standard deviation is displayed as error bars and the results of the individual experiments utilizing Calyculin A treated BMDMs are included as lightly coloured symbols in the background to visualise variability Results from Chapter 3.4.1 to enable comparison to untreated BMDMs are shown in grey. RM two-way ANOVAs were performed to compare the results from Calyculin A treated with untreated BMDMs; A) P value = 0.08, multiple comparisons: P value (2 h) = 0.0409, B) could not be analysed due to incomplete dataset; C) P value = 0.3262; D) P value = 0.1301.

3.5 Parameter estimation RAW264.7 cells

3.5.1 Comparison of BMDMs and the RAW264.7 cell line

As we and many other research groups in the past have used the RAW264.7 cell line to establish our current knowledge of TTP biology (250,320,344), we were curious about how these cell's pathway dynamics would differ compared to WT BMDMs. Furthermore, this experiment was used as the opportunity to test and optimise experimental setups and protocols for BMDMs. We performed a time-course experiment with the same layout as was done for BMDMs. Learning about differences in TTP pathway dynamics will allow our group to improve future experimental designs involving both cell types and to better understand historical data obtained from RAW264.7 cells. In this chapter, we will present and describe the combined data obtained from this experiment with 3 repeats, the data from individual experiments are shown in the Appendix 7.3.4. After describing the observed RAW264.7 cell expression behaviour, we will compare the dynamics to BMDMs, which are quantitatively assessed using repeated measure (RM) two-way ANOVA and by Šidák post-hoc corrected multiple comparisons of individual means.

The result of the RAW264.7 8 h time-course experiment (n=3) is shown Figure 3.26. As before, the protein concentration is shown as pg/µg of total protein and the time span in hours. RNA concentration is depicted as copy number per pg RNA. Targets of interest are displayed in their respective signature colours. Data symbols in a dark shade represent the mean of 3 experiments, light-coloured symbols show the measured data points of individual experiments, and the standard deviation is depicted as error bars. BMDM data is shown without standard deviation in grey in the background.

3.5.1.1 p38 MAPK

Figure 3.26 A displays p38 MAPK expression patterns in RAW264.7 cells and BMDM. In RAW264.7 cells, phospho-p38 MAPK in unstimulated cells was measured at around 5 pg/µg. Expression of $p38_p$ reaches the peak at around 82 pg/µg at 0.5 h post-stimulation. From this maximum, the expression steeply decreases reaching pre-stimulation levels after 1 h to 1.25 h with. Following this dip, the phospho-p38 levels slightly increased until the 2 h time point, after which the concentration slowly decreases over the next 6 h reaching 2 pg/µg at the 8 h time point. We observed one anomaly in the data where the phospho-p38 concentration, measured at the peak, was higher than the total amount of p38 present in the sample. This could have resulted from the stripping process, which will be addressed in the discussion of the experimental design. For our model, we decided to use the value of total p38 concentration at the peak because we have shown in other experiments, using a PhosTag gel (supplementary Figure 7.4), that around 100% of p38 MAPK is phosphorylated at this time point.

In both RAW264.7 and BMDM cells, we found a base expression of phospho-p38 at a level of around 5 pg/µg, and both cells rapidly responded to LPS stimulation with the peak at 0.5 h, whereby the RAW264.7 cells exhibited a higher level of phosphorylation. Interestingly, in RAW264.7 cells, phospho-p38 MAPK returns to pre-treatment levels within 1 h, followed by small fluctuations. In contrast, BMDMs exhibited a more slowly decreasing phenotype. However, these observations are not quantitatively backed by the multiple comparison analysis. While the overall curves are significantly different from each other (P value of combined column and row factors = 0.0022), none of the individual values differed statistically significantly. The peak, which is visually different, had to be excluded from statistical evaluation due to a missing value.

3.5.1.2 DUSP1

Figure 3.26 B shows the DUSP1 expression patterns during the LPS-induced inflammatory response in RAW264.7 cells. DUSP1 expression was not detectable including until 0.5 h after LPS stimulation. After 0.5 h, the expression rapidly increased, reaching the maximum at 1 h post-LPS stimulation at around 45 pg/µg. Following the peak, the expression decreased rapidly within 0.25 h and then gradually before bottoming out at 3 h with a concentration of 21 pg/µg, after which the concentration only slightly fluctuated during the remaining time.

For DUSP1, we were unfortunately unable to perform statistical analysis, as for WT BMDMs, we could only include two experimental replicates. While this does not impact utilising the values in mathematical modelling, it should be kept in mind that any comparison to BMDMs here is only of a qualitative nature and is not backed by quantitative statistical analysis. The overall expression levels of DUSP1 were higher in BMDMs than in RAW264.7 cells. Still, both cell types exhibited no expression of DUSP1 before the 45 min time point, and both exhibited a peak 1 h post-stimulation. This peak was followed in both cell types by a quick decline in concentration, whereas in BMDMs, this decline started later.

3.5.1.3 Unphosphorylated TTP

Figure 3.26 C shows the concentration changes of unphosphorylated TTP (lower band WB) over time during the LPS-induced inflammatory response in RAW264.7 cells and BMDM. In unstimulated RAW264.7 cells, unphosphorylated TTP expression was below the detection limit. The first detectable expression was observed after 30 min. The expression reaches the first maximum after 1 h with 50 pg/µg. The level then decreased, reaching a minimum at 27 pg/µg after 2 h, after which the levels of TTP increased again, reaching the second maximum

at 50 pg/µg after 4.5 h. Afterwards, the level slightly decreased from the maximum, reaching a fluctuating plateau for the remainder of the experiment.

Overall, compared with BMDMs, the dynamics appear strikingly similar. TTP expression was not detectable for the first 30 min post-stimulation for both cell types. The main difference would be that the initial peak was slightly delayed in BMDMs, at 1.25 h compared to 1 h, respectively. In both cell types, the expression levels also appeared quite similar. The similarity is also reflected in the statistical analysis, where the P value of combined column and row factors was found to be non-significant at 0.7024.

3.5.1.4 Phosphorylated TTP

Figure 3.26 D shows phosphorylated TTP and total TTP. Phosphorylated TTP in this context, as before, is derived from the measurement of the upper band of the TTP Western Blot. Expression of phospho-TTP was first detected 0.5 h post-stimulation, commencing a steady increase up to around 81 pg/µg after 3 h, followed by a dip at the 3.5 h time point. Following this, the level increased again until 4.5 h post-stimulation, where a level of around 116 pg/µg was measured, followed by another short dip at the 5 h time point. The level of phospho-TTP then continued to rise with a similar dynamic, dipping at 7 h and finally reaching 125 pg/µg at the 8 h time point.

Comparing unphosphorylated TTP dynamics between RAW264.7 cells and BMDMs yielded no significant differences, but this is not true for phospho-TTP. While again, no single values are statistically significantly different, the overall curves are (P value of combined column and row factors = 0.0376). Both exhibited similar expression levels up to 1 h, then phospho-TTP increased stepwise in RAW264.7 cells for the remaining time-course, while in BMDMs, it

increased less steeply until reaching a maximum at 4.5 h, followed by a steady decrease to a local minimum after 7 h

3.5.1.5 *Tnf* mRNA

Tnf mRNA expression during the LPS-induced inflammatory response is shown in Figure 3.26 E. In unstimulated RAW264.7 cells, 3 copies of *Tnf* per pg RNA were detected. Its expression increased after 30 min post-stimulation, first gradually and then steeply, reaching a global maximum after 1 h with 45 cn/pg. Afterwards, expression decreased, and fluctuations were measured, leading to 3 local maxima during the time-course of the experiment (at 2.5 h with 31 cn/pg, at 3.5 h with 36 cn/pg, and at 6 h with 22 cn/pg) before very slowly decreasing.

In both RAW264.7 and BMDMs, the expression was low in unstimulated cells and increased strongly after stimulation in BMDMs at 0.5 h and in RAW264.7 cells at 0.75 h. Both peak at 1 h, with RAW264.7 cells exhibiting roughly half the expression levels of BMDMs. This is interesting since RAW264.7 cells exhibited a stronger p38 MAPK response. However, they also display an earlier peak in unphosphorylated TTP expression, which might have affected *Tnf* mRNA expression levels. In BMDMs, the *Tnf* mRNA level fluctuations were also less apparent compared to RAW264.7 cells. The curves were found to be significantly different overall (P value of combined column and row factors = 0.0018); however, no single value was flagged as significantly different.

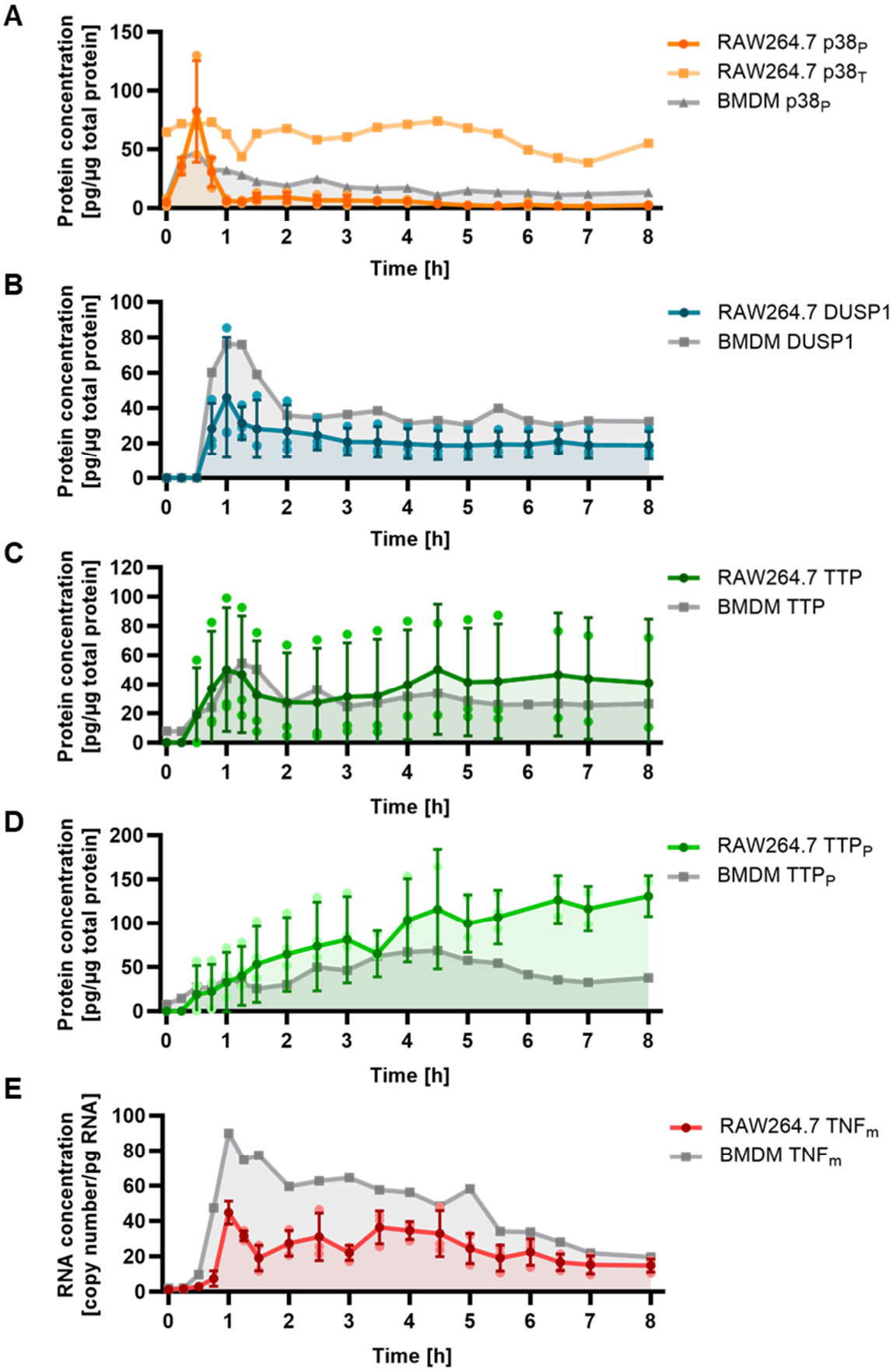

A
Protein concentration [pg/µg total protein]
150
100
50
0
0 1 2 3 4 5 6 7 8
Time [h]
RAW264.7 p38P
RAW264.7 p38T
BMDM p38P
B
Protein concentration [pg/µg total protein]
100
80
60
40
20
0
0 1 2 3 4 5 6 7 8
Time [h]
RAW264.7 DUSP1
BMDM DUSP1
C
Protein concentration [pg/µg total protein]
120
100
80
60
40
20
0
0 1 2 3 4 5 6 7 8
Time [h]
RAW264.7 TTP
BMDM TTP
D
Protein concentration [pg/µg total protein]
200
150
100
50
0
0 1 2 3 4 5 6 7 8
Time [h]
RAW264.7 TTPP
BMDM TTPP
E
RNA concentration [copy number/pg RNA]
100
80
60
40
20
0
0 1 2 3 4 5 6 7 8
Time [h]
RAW264.7 TNFm
BMDM TNFm

Figure 3.26 Measuring p38 MAPK-TTP pathway components by total quantification of Western blot and qPCR data obtained from RAW264.7 cells and WT BMDMs treated with LPS over an 8 h time-course.

Raw264.7 cells were treated with 10 ng/mL LPS for a period of 8 h. Protein concentrations of phospho-p38, total p38, phospho-TTP and TTP, as well as Tnf mRNA levels, were measured using WB and qPCR, respectively (n=3). The Western blot data of A) phospho-p38 ($p38_P$), B) DUSP1, C) total (TTP_T) and unphosphorylated TTP (TTP, lower band), and D) total and phosphorylated TTP (TTP_P, upper band) was quantified in Image Lab software, normalised to its Stain-Free signal, and the total protein concentrations were calculated using standard curves of recombinant protein. The total amount of E) *Tnf* mRNA was measured by running a standard curve consisting of known quantities of plasmid DNA alongside the samples for qPCR. Results from Chapter 3.4.1, which enable comparison to WT BMDMs, are shown in grey. RM two-way ANOVAs and Šidák post-hoc corrected multiple comparisons were performed to compare the results from RAW264.7 cells with WT BMDMs, except for B) where the BMDM experiment only contains two repeats; Resulting P values of combined column and row factors as a measure for overall difference between curves: A) P value = 0.0022; C) P value = 0.7024 ; D) P value = 0.0376, E) P value = 0.0018. No individual Šidák post-hoc corrected comparison yielded a statistically significant result.

3.5.2 Parameter estimation RAW264.7 cells

In this chapter, the parameter estimation results of the RAW264.7 data set will be presented. We took advantage of the best data input strategies identified in the previous BMDM parameter estimation chapter (Chapter 3.4.2.2). We again divided the parameter estimation process into two steps: First, identifying the parameter set of the p38 MAPK pathway and then using the result for the full p38 MAPK-TTP model. We then evaluated the global MABS, the qualitative fit of the data, and the biological plausibility of the parameters.

We ran the parameter estimation with a combined experimental design and homoscedastic error profile as data input with the upper boundary set to 1. The results of the parameter estimation are shown in Figure 3.28 and Table 3.16. For phosphorylated p38 MAPK (Figure 3.28 B), the simulation did not reach the peak height and ended in a higher plateau phase compared to the experimental data. Otherwise, the typical p38 MAPK activation dynamics were covered. DUSP1 (Figure 3.28 C) followed a gradual growth curve, increasing throughout the simulation period. The model, however, could not simulate the initial peak of the data. For

unphosphorylated TTP (Figure 3.28 D), the simulated data initially increased quickly before gradually rising. Although the model did not cover the initial peak, the remaining expression dynamics are represented well. In the model simulation, phosphorylated TTP levels (Figure 3.28 E) increased steadily over time, covering the overall trajectory of the experimental data, though with slightly reduced total values. The simulation did not cover the first and second peaks of the experimental *Tnf* mRNA measurements. Instead, it gradually increased for 135 min and then gradually declined. Apart from the peaks, the simulation fits the experimental data. Analysing the parameter values directly, we found no major inconsistencies with the biological data. The parameters ρ_{Pp1}, δ_{Tp}, and δ_{Rm1}, while not being zero, were represented by very low values in the range of 10^{-16} and 10^{-17}, which suggests that they are unimportant for the model simulation. The parameter estimates had a global relative MABS of 61% (Figure 3.27). The highest relative MABS had the variable $p38_P$ (283%). The lowest value was p38 (7%), which shows that the evaluation methodology is strongly skewed against variation at lower expression levels. The resulting set of parameters is shown in Table 3.16.

Table 3.16 Parameter set of parameter estimation for the RAW264.7 cell Kulawik p38 MAPK-TTP model.

Parameter Estimation				
Symbol	**Description**	**PE value**	**Conf. interval**	**Dimension**
φ_{P1}	Phosphorylation rate 1 of p38	$3.83*10^{-3}$	0.00	min^{-1}
φ_{P2}	Phosphorylation rate 2 of p38	$2.37*10^{-5}$	0.00	$ng^{-1}min^{-1}mL$
ρ_{Pp1}	Dephosphorylation rate 1 of $p38_P$	$4.03*10^{-17}$	$4.71*10^{-5}$	min^{-1}
ρ_{Pp2}	Dephosphorylation rate 2 of $p38_P$	$9.74*10^{-4}$	$1.85*10^{-5}$	$pg^{-1}min^{-1}\mu g$
γ_D	Synthesis rate of DUSP1	$5.39*10^{-4}$	$5.79*10^{-6}$	$pg^{-1}min^{-1}\mu g$
δ_D	Degradation rate of DUSP1	$2.15*10^{-4}$	$1.20*10^{-5}$	min^{-1}
γ_T	Synthesis rate of TTP	$2.72*10^{-3}$	$1.67*10^{-5}$	$pg^{-1}min^{-1}\mu g$

δ_T	Degradation rate of TTP	$4.60*10^{-4}$	$3.04*10^{-5}$	min^{-1}
φ_T	Phosphorylation rate of TTP	$5.91*10^{-2}$	$4.16*10^{-7}$	$pg^{-1}min^{-1}\mu g$
δ_{Tp}	Degradation rate of TTP_P	$3.19*10^{-17}$	$9.95*10^{-6}$	min^{-1}
ρ_{Tp}	Dephosphorylation rate of TTP_P	$1.58*10^{-1}$	$1.31*10^{-5}$	min^{-1}
γ_{Rm}	Synthesis rate of TNF_m	$1.20*10^{-3}$	$1.55*10^{-5}$	$pg^{-1}min^{-1}\mu g$
δ_{Rm1}	Degradation rate 1 TNF_m	$1.44*10^{-16}$	$3.28*10^{-5}$	min^{-1}
δ_{Rm2}	Degradation rate 2 TNF_m	$2.08*10^{-5}$	$9.81*10^{-7}$	$pg^{-1}min^{-1}\mu g$

Initial conditions: P0=77.92, P_P0=5.07, D0=0, T0=0, T_P0=0, T_m0=1.16.

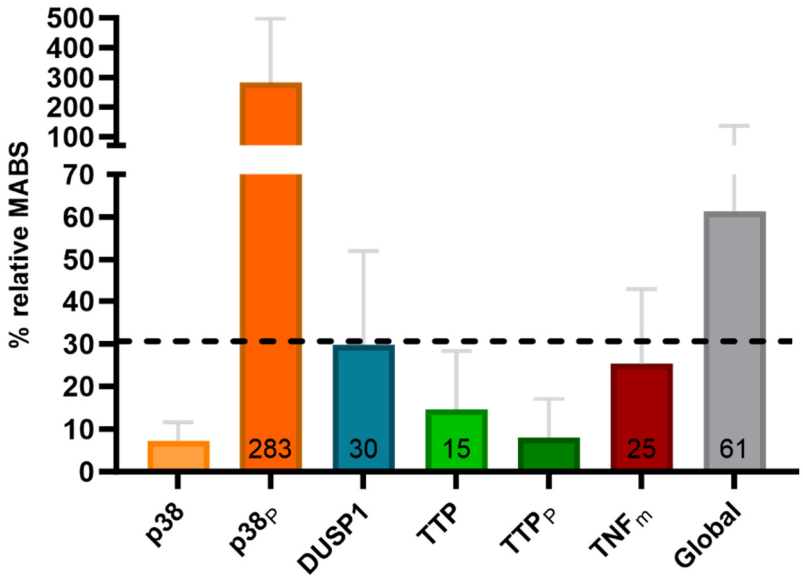


Figure 3.27 Relative MABS of the RAW264.7 parameter estimation.

The relative differences between the data and the model simulation of the estimated RAW264.7 parameters were obtained from the AMIGO2 parameter estimation result files, and the absolute mean was calculated for each variable and for all variables combined (global). The Figure shows the individual absolute relative differences as mean, and the standard deviation as error bars.

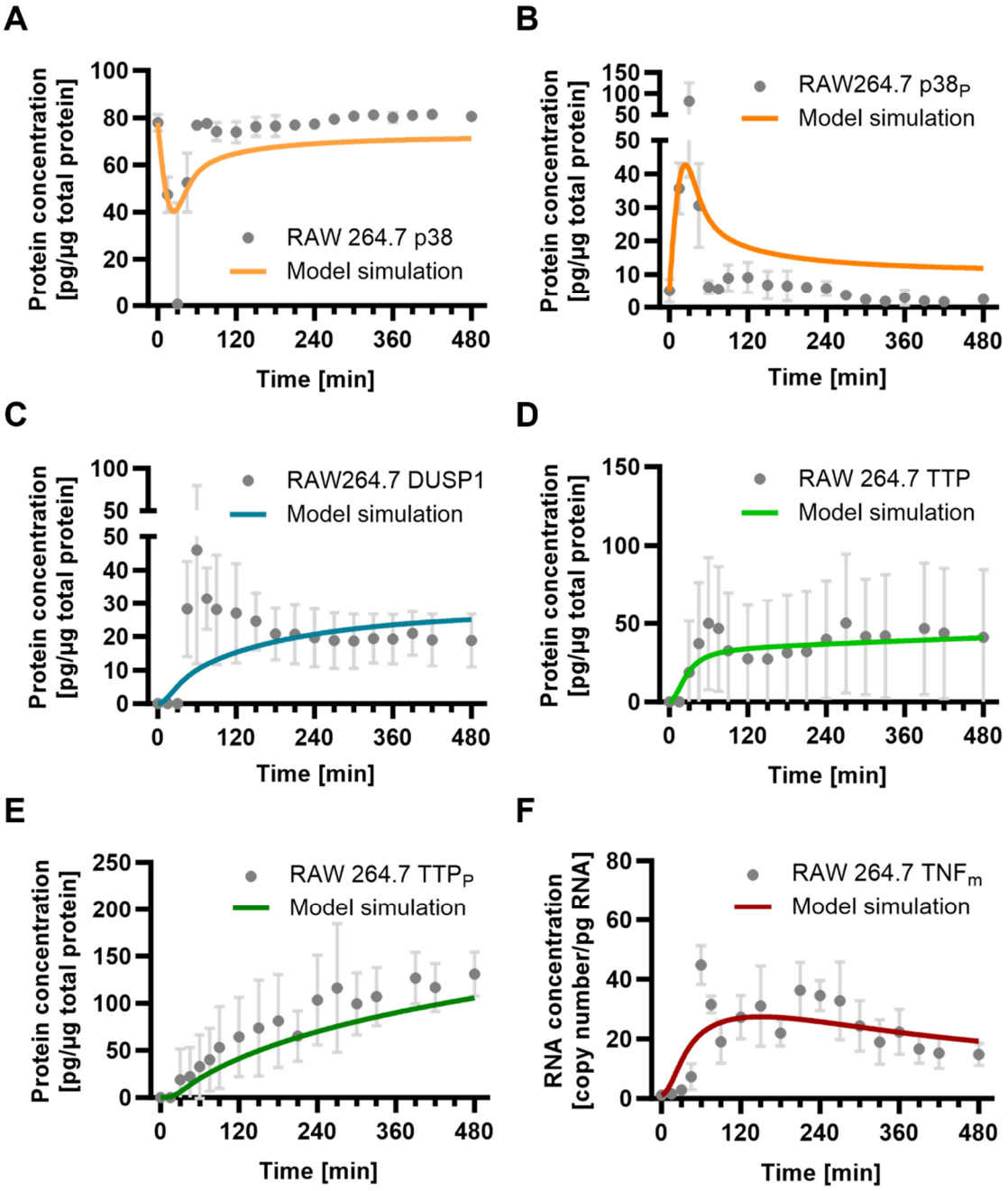


Figure 3.28 Computational simulation of the calibrated Kulawik p38 MAPK-TTP model for LPS-treated RAW264.7 cells.

The data for the simulation of the Kulawik p38 MAPK-TTP model was generated in MATLAB, solving the ODE equations (3.14) to (3.19), as well as estimated parameter values and initial conditions presented in Table 3.16 for a time span of 480 min. The parameters were estimated using the NLSQ2 combined with the eSS2 nonlinear problem solver implemented in the AMIGO2 toolbox, and the experimental data of LPS-stimulated RAW264.7 cells presented in Figure 3.26. In addition, a homoscedastic error profile set to 0.2, the "combined" experiment

design, and parameter boundaries between 0 and 1 were selected for the parameter estimation run. The graphs show the model simulation of A) unphosphorylated p38, B) phosphorylated p38, C) DUSP1, D) unphosphorylated TTP, E) phosphorylated TTP, and F) *Tnf* mRNA as lines in their respective colours together with the BMDM experimental data as symbols with error bars in grey. The full MATLAB script for parameter estimation and generation of the graphs can be found in Appendix 7.1.

3.5.3 Model comparison of RAW264.7 and BMDM simulations

The computational simulation of $p38_P$, DUSP1, TTP, TTP_P, and TNF_m using the updated Kulawik p38 MAPK-TTP model (Equations (3.14) to (3.19)) and the previously determined RAW264.7 (Table 3.16) and BMDM parameter set (Table 3.13 and Table 3.15) is shown in Figure 3.29. Unphosphorylated p38 MAPK expression is not shown to improve the clarity of the image because it does not convey any additional relevant information for the comparison. The data for the graphs was generated, as described in previous chapters, in MATLAB using the *ode23* solver. One of the main differences between the BMDM and RAW264.7 model for phosphorylated p38 MAPK was the higher peak in RAW264.7 cells. Another was the plateau phase observed for BMDMs after the initial peak, whereas in RAW264.7 cells the levels gradually declined. For DUSP1, the BMDMs showed an initial substantial increase followed by a constant plateau, while RAW264.7 cells exhibited an overall lower level and gradual growth. For unphosphorylated and phosphorylated TTP, the simulation dynamics were quite similar in overall levels and trajectories; however, with different outcomes of the full-time-course where RAW264.7 showed slightly higher levels in phosphorylated TTP and slightly lower levels in unphosphorylated TTP than BMDMs at the end of the simulation. *Tnf* mRNA expression exhibited a more defined peak and a generally higher level in BMDMs compared to RAW264.7 cells.

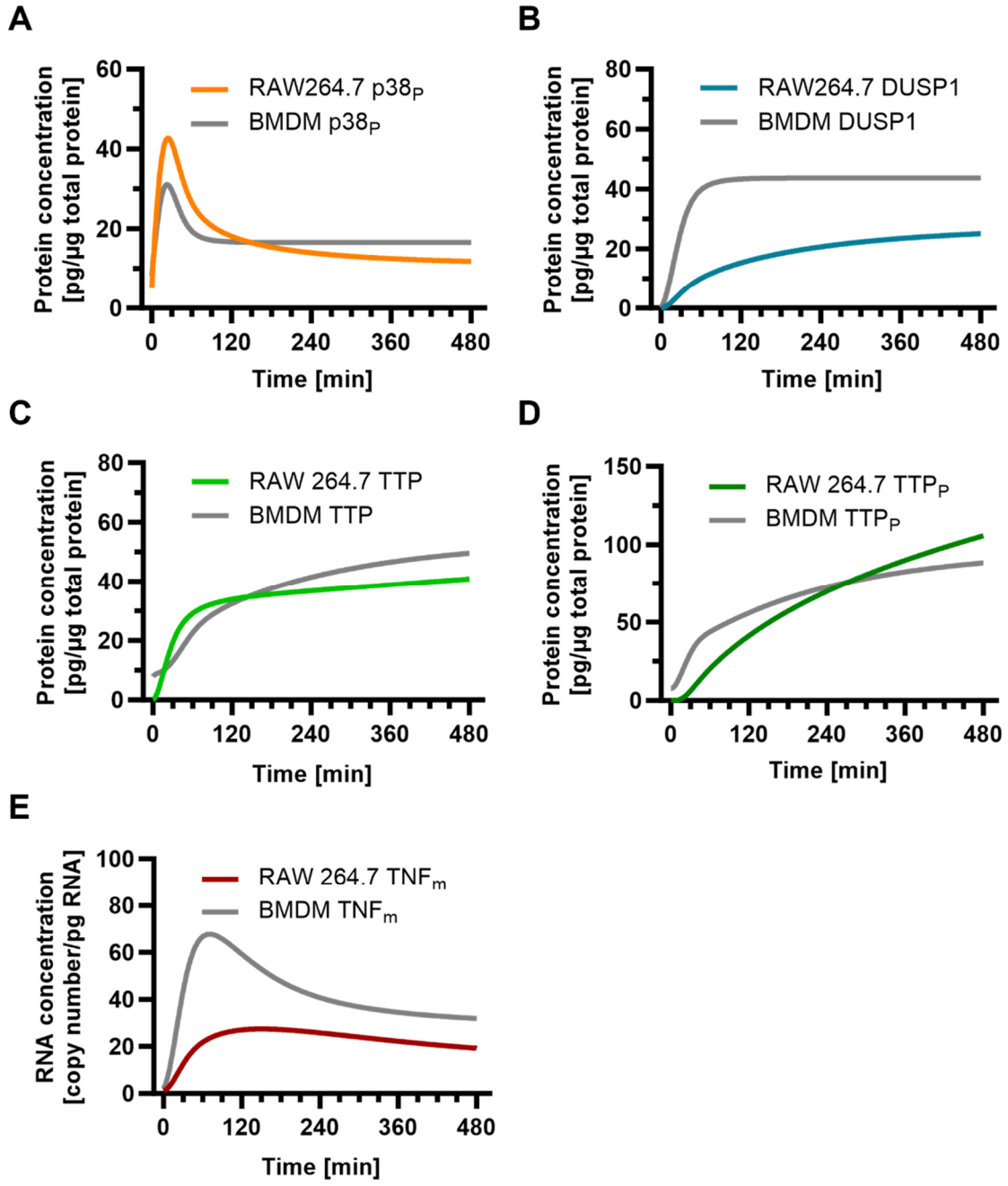


Figure 3.29 Computational simulation of LPS-treated WT RAW264.7 cells and BMDMs using the calibrated Kulawik p38 MAPK-TTP model.

The data for the simulation of the RAW264.7 and WT BMDM Kulawik p38 MAPK-TTP models was generated in MATLAB, solving the ODE equations 3.14 to 3.19 as well as the estimated parameter values and initial conditions in Table 3.16, Table 3.13, and supplementary Table 7.1 for a time span of 480 min. The graphs show the model simulation of A) phosphorylated p38, B) DUSP1, C) unphosphorylated TTP, D) phosphorylated TTP, and E) TNF_m in RAW264.7 cells and BMDMs. The full MATLAB script for generating the simulated data can be found in Appendix 7.1.

3.6 Discussion

For this discussion chapter, we first evaluate the experimental design, focusing on what worked and potential shortcomings. Afterwards, we discuss the BMDM data and Kulawik p38 MAPK model parameter estimation, followed by the data comparison and model validation against Dusp1$^{-/-}$ and Zfp36$^{aa/aa}$ BMDMs and finally, the comparison to RAW264.7 cells. We focus here on how the model fits the data and which adjustments of the model structure might be necessary to cover the observed expression dynamics fully.

3.6.1 Experimental Design

In this chapter, we critically evaluate the experimental design of the total quantification experiments, highlighting successful approaches and identifying potential problems. This analysis is vital for understanding the robustness of the data and provides a platform for suggesting improvements for future endeavours.

Kulawik et al. inspired the experimental design for total quantification of p38 MAPK-TTP pathway components. It was based on recombinant protein and pDNA standard curves, which were run alongside the samples and quantified using WB and qPCR (290).

The total quantification of the TTP-target mRNA *Tnf*, using qPCR, worked well and requires no further discussion. On the other hand, the WB approach has several limitations, where improvement is possible.

The utilisation of bought-in human recombinant protein as a standard curve was successful. Especially, identifying the percentage of phosphorylated p38 MAPK via PhosTag gels instead of using mass-spectrometry, like Kulawik et al., or not measuring it at all, like Hendriks et al., was a cost and time-efficient solution. Since the phospho-p38 standard curve was additionally very robust, the total quantification of phosphorylated p38 MAPK was successful. For total p38

MAPK, we encountered an unexpected issue. We decided to strip the phospho-p38 MAPK blots to measure the total p38 MAPK expression. The applied stripping method was well established in our laboratory and used regularly. When we analysed the first blots, however, we found that the basic protocol (20 min incubation time) was insufficient to remove the phospho-p38 MAPK signal. Longer incubation times or higher concentrations of the stripping solution unfortunately caused the stripping of target proteins (supplementary Figure 7.7). Consequently, our data set likely did not reflect the accurate total p38 MAPK levels; it also did not match the literature, where the level of total p38 MAPK is described as constant throughout the inflammatory response (148,290). Determining realistic total p38 MAPK levels requires a repeat of the WB without stripping. For our project, we assumed that the total p38 MAPK level would remain constant over time.

For DUSP1 and TTP, we encountered some challenges regarding the standard curve procedure. The standard curves were initially tested and appeared linear. The calculated R^2 values, which were used to evaluate the quality of the linear regression, reflected this with > 0.95 for all blots. However, we found the standard curves shifting towards a nonlinear relationship at lower concentrations. As some measurements (e.g., at the start of an experiment) lay within this area, we cannot determine how much of an error is introduced for these samples. When we researched the issue, we found that in other antibody-based quantification methods, such as ELISA, the measured intensity can follow a sigmoidal curve, requiring specialised analyses. We were, however, still looking for such information on WB, likely due to the rarity of absolute quantification employed using this methodology. For our dataset, we decided to stringently analyse all experiments assuming linearity in the standard curve, as this standardises the systematic error type across the dataset and because the general dimensions of the relationship between data points are maintained, i. e., a lower measurement always translates to a lower

concentration, albeit with an unknown inaccuracy. It would be possible to analyse the standard curves with nonlinear regression; one could argue that is precisely one of the benefits of utilising the absolute quantification approach. However, if we want to do this, it is necessary to include additional standard curve concentrations to effectively fit a nonlinear curve. Initially, we decided to commence with WB due to the high cost of ELISA. As additional standard curve samples would reduce the temporal resolution we could achieve in our experiments in WB, with this knowledge, we should revisit this approach, as ELISA, in general, has the benefit of enabling many more simultaneous measurements. When measuring TTP and even more so DUSP-1, some samples were outside the lower limit of the standard curve range. For DUSP-1, we were challenged with some blots where the lowest standard curve concentration could not be detected. One could mitigate these problems so much as to increase the resolution at the lower end of the curve up to a point where experimentally feasible. Along the way, detectability could be improved by changing from HR-coupled secondary antibodies to fluorescent ones, further optimising antibody concentrations, or finding alternative antibodies.

Another challenge that contributed to the above, e.g., with DUSP1 detection, is the variability in stimulation strength of the BMDMs, reflected in the uneven levels of phospho-p38 induction. This variability also affected comparing the BMDM WT experiments with *Dusp1*$^{-/-}$ and *Zfp36*$^{aa/aa}$ experiments. It can additionally be observed in the *Tnf* mRNA expression level readout (Figure 3.13), as quantification inaccuracies due to a nonlinear standard curve do not play a role here. Varying stimulation peaks of p38 MAPK phosphorylation made it more difficult to identify subtle changes in expression dynamics with increased SD, reducing the data quality for the model parameter estimation. Significant measurement errors, together with overparameterization and data scarcity, can lead to ill-conditioning of the parameter estimation, where small changes in input can cause large changes in dependent variables (342,345).

However, the variability also allowed some additional insights into the pathway. The data suggests some pathway dynamics might only appear or vary with sufficient p38 MAPK activation. For example, in experiments with strong p38 MAPK activation, phospho-p38 MAPK and DUSP1 expression were likely to exhibit a second local peak, while *Tnf* mRNA was downregulated more quickly and lost its initial double peak. Also, the overall level of DUSP1 during its plateau phase was higher (compare supplementary Figure 7.7 and Figure 7.19). Bhalla et al. proposed in their ERK1/2 MAPK model, where they combine a feedforward and an MKP-dependent feedback loop, that MAPK and MKPs exhibit a stable basal state, a metastable middle state, and a stable activated state, which results in switch-like behaviour from basal to activated at low concentrations and a proportional response at higher concentrations (346). As the p38 MAPK and ERK1/2 signalling pathways are almost identical in their network structure, likely, their observations are also applicable here. Implementing a similar strategy as Bhalla et al. might, therefore, allow to better cover the observed activation-state dependent properties. The LPS concentration employed was well-established within our group, though potentially, in these experiments, the chosen concentration might unexpectedly be at the tipping point between two activation states. To better understand p38-MAPK activity-dependent pathway changes, experiments comparing the effects of different concentrations of LPS might be helpful. Of course, there is the possibility that the variability is (partly) due to the experimenter. If this is the case, new experiments would likely be characterised by an altered variability profile due to experience effects or a different person performing the experiments.

3.6.2 BMDM data and parameter estimation

In this chapter, we discuss the BMDM time-course experiment results, whether the observations are consistent with the literature, and whether our Kulawik p38 MAPK-TTP model can capture the observed expression dynamics. Based on this, we suggest adjustments to the model structure

that might allow us to simulate the dynamics observed in the data and propose experiments to improve our understanding of them. Then, we address the overall outcome and quality of the parameter estimation.

p38 MAPK phosphorylation patterns were as expected, with low expression levels in unstimulated cells, an initial peak, followed by a slow decline (Figure 3.13 A). Our calibrated model fits the measured p38 MAPK data well regarding the relative MABS (p38: 9.13%, $p38_P$:25.12 %). However, it only completely covers some properties observed in the p38 MAPK data. First, the peak height is most likely inaccurate, considering the variability in individual experiments and the constant plateau of the model does not entirely describe the observed data. Improving the peak height and obtaining a gradual decline instead of a plateau phase would likely require changes to the phosphatase design within the model. We performed two-step parameter estimation as presented in Chapter 3.4.2.2 for the upstream p38 MAPK pathway while excluding the DUSP1 data from the process, just as Kulawik et al. did for their model (290). Indeed, we obtained a parameter set that fit to the p38 MAPK data well (relative global MABS 12.47 %). During the simulation, DUSP1 expression increased gradually, which resulted in an ideal description of the decline in p38 MAPK phosphorylation (Appendix 7.5, supplementary Table 7.4 and Figure 7.33). However, when employed in the downstream TTP pathway, it was insufficient to cover the observed biological behaviour, likely due to the quick initial rise in p38 MAPK phosphorylation. This observation still shows that better coverage of p38 MAPK dephosphorylation by the model could lead to the desired changes in model behaviour, i.e., an increased peak and gradual decline.

Based on the literature, the DUSP1 expression patterns were as expected (347). We observed an initial peak followed by a plateau phase (Figure 3.13 B). Although, with a relative MABS of 23.87%, the model fits the data reasonably well, the DUSP1 ODE currently cannot simulate

the observed data dynamics. Adding a delay to DUSP1 expression, for example, by introducing *Dusp1* mRNA as an independent variable, should allow for the simulation of the observed data dynamics as in our second, Tomida-based, model, where we have this variable included, we found peak and plateau represented across the cell population (Figure 4.6). We would need to include *Dusp1* mRNA measurements in our time-course experiments to estimate the respective parameters.

We are currently unable to measure p38 MAPK-mediated phosphorylation of TTP directly. Ammit et al. have previously eluded to and are currently working on a Mass spectrometry methodology based on parallel reaction monitoring for measuring TTP phosphorylation (267). We considered collaborating with them for this project, which would have involved travelling to Australia to learn the methodology and establish it here in Birmingham. However, this was impossible due to the pandemic. Instead, we measured the protein using WB, where two distinct bands formed on all blots, following separate dynamics. Cao et al. identified TTP as a hyperphosphorylated protein and showed the band-shift in SDS gels depending on the phosphorylation state, with phosphorylated TTP running slower than unphosphorylated protein species (337). Instead of only measuring total TTP, which would be insufficient for parameter estimation, we tested whether measuring individual bands might explain model dynamics between phosphorylated (upper band) and unphosphorylated (lower band) TTP. Both unphosphorylated and phosphorylated TTP exhibited an initial peak after stimulation (Figure 3.13 C and D), with unphosphorylated TTP being almost double the height compared to phosphorylated TTP. The intensity of the upper band continued to increase for the first 4 h of the experiment, while the lower band stayed relatively stable. These observations were consistent with our assumption that the lower band follows unphosphorylated TTP expression dynamics, which implies the accumulation of the stable phosphorylated TTP throughout the

inflammatory response and low steady levels of the unstable unphosphorylated TTP due to high turnover. Our current model achieved an MABS of 27.10 % for unphosphorylated TTP and 21.71% for phosphorylated TTP, which indicates a good fit. However, the current model structure cannot capture the initial peaks of the TTP expression dynamics. We already observed similar dynamics in our Kulawik p38 MAPK-TTP model simulations, where MK2 was initially included (Chapter 3.2.3.3), and the delay between p38 MAPK-mediated TTP synthesis and MK2-mediated phosphorylation resulted in such a peak (Figure 3.7). Therefore, adding a delay of TTP phosphorylation by re-adding MK2 and measuring its expression for parameter estimation could result in the desired dynamics. We will still likely be unable to simulate the decrease in the upper band after 4 h by reintroducing MK2 dynamics alone because we currently have no impulse in the model that would change the trajectory of phosphorylated protein from increase to decline. This change in the trajectory might be achieved by introducing the previously proposed gradual decline phase of p38 MAPK. However, an additional agent to actively induce TTP dephosphorylation might be needed to achieve the observed dynamics. One potential way to do this could involve the TTP phosphatase PP2A. Fey et al. explored the interaction of MAPK signalling pathways with PP2A as a central player in their model. One central theme of the model is p38 MAPK mediated induction of PP2A expression or activity (163–166). Therefore, reintroducing PP2A, not as an independent variable but as a dependent variable with its own ODE that changes its expression/activity dependent on p38 MAPK phosphorylation, might be the key to accurately covering the TTP phosphorylation dynamics. For PP2A, protein level and activity measurements could be performed to test whether their changes throughout the inflammatory response sufficiently explain TTP expression dynamics. If not, the finding would support the assumption that only a specific subunit is responsible for TTP regulation. Once the PP2A subunit targeting TTP is identified, measuring its expression

dynamics might allow a complete understanding of how TTP is regulated throughout the inflammatory response.

Overall, the calibrated model covered the observed expression dynamics of *Tnf* mRNA in BMDMs (Figure 3.13), as indicated by an MABS of 28.66%. However, it cannot simulate the decrease in *Tnf* mRNA expression in the last 3 h of the time-course, likely due to the stable plateau in p38 MAPK phosphorylation during this period. Therefore, fixing the p38 MAPK plateau would also result in better coverage of *Tnf* mRNA expression. The current model further does not allow the simulation of the double peak observed in the experiments. Interestingly, we observed a double peak for *Tnf* mRNA in our Kulawik p38 MAPK-TTP model simulation before the exclusion of MK2 (Figure 3.7). By reintroducing MK2, our model should also sufficiently cover the *Tnf* mRNA peak dynamic. This observation suggests that the initial peak in unphosphorylated TTP causes the double peak observed in the *Tnf* mRNA data, which again supports our assumption that the lower band of the TTP WB follows unphosphorylated TTP dynamics.

As our current model structure does not allow full coverage of all the expression dynamics observed in BMDMs, it is unsurprising that the model is practically non-identifiable with the current data set. This practical non-identifiability means the data does not allow for identifying one optimal parameter set; instead, it results in multiple parameter sets with the same residual MABS. Practical non-identifiability is further indicated by some minimal numbers in the range of 10^{-17}, estimated for the parameters φ_{P1}, ρ_{P1}, and δ_{Rm1}. Those are part of parameter pairs that depend on each other, such as DUSP1-dependent and independent p38 MAPK dephosphorylation. Together, both define the dephosphorylation dynamics of p38 MAPK. However, the DUSP1-independent phosphorylation rate has a negligible impact on the model outcome compared to the DUSP1-dependent one, as indicated by their relative global δ_{θ}^{msqr}

ranking (Figure 3.11) obtained during the global parameter ranking in Chapter 3.2.4.2. If such parameter pairs exist within the model, the parameter estimation process typically results in the less important one being set to zero or a minimal number. This circumstance does not affect the model's capability of simulating the expression dynamics during the inflammatory response. However, when simulating experimental designs where the basal dephosphorylation rate of p38 MAPK or the TTP-independent degradation rate of TNF_m plays an important role, such as when simulating unstimulated cells or a *Zfp36*$^{-/-}$ mutant, the model will then fail to predict the biological behaviour. With our current experiment input definition for the parameter estimation, identifying the values of those "unimportant" dependent parameters is not possible. For φ_{P1}, and ρ_{P1}, this could be solved by adding a simulation of unstimulated cells into the experimental design of the parameter estimation. For TTP-independent degradation of TNF_m, a dataset obtained from *Zfp36*$^{-/-}$ BMDM and its inclusion into the parameter estimation process would likely provide the required information. However, a more convenient option might be to leverage data provided by the TTP atlas, which includes degradation rates in *Zfp36*$^{-/-}$ BMDMs (348).

A specific discrepancy was observed in our measurements, where in multiple runs of parameter estimation, we found the degradation of unphosphorylated TTP to be lower than that of phosphorylated TTP. To maintain the biological coherence of the model, we tested if switching the two values would lead to significant changes in the model simulation. As we found the introduced changes negligible, we decided to switch the two TTP degradation rates for the model validation. We hoped this would allow us to simulate the *Zfp36*$^{aa/aa}$ mutant, which relies strongly on the discrepancy between the two degradation rates, while not affecting the quality of fit to our BMDM WT model. In the current data set, unphosphorylated TTP could be overestimated due to the nonlinearity of the standard curve. Revisiting this issue after choosing

a different analysis approach (see Chapter 3.6.1) might solve the conundrum. Alternatively, we could use a combined bottom-up and top-down approach by directly measuring the degradation rate of unphosphorylated TTP using a cycloheximide chase experiment. *Zfp36*$^{aa/aa}$ mice could be the key to identifying the degradation rate of unphosphorylated TTP. Interestingly, for the RAW264.7 cells, the estimation was automatically correct in assigning the higher degradation rate to unphosphorylated TTP. This correct assignment is likely because expression levels of phosphorylated TTP are higher in RAW264.7 cells.

Our current error input strategy for parameter estimation could be better, as it does not reflect the actual experimental error. We had to adjust the input as using the actual experimental error does not allow identifying a parameter set that captures the data dynamics in a combined experimental approach (supplementary Figure 7.32). Individual experiments as input strategy with homoscedastic error profile set to 0.2 gave better parameter results but were not as good as the combined approach with artificial minimal error, as indicated by the global relative MABS of 25.45% for the p38 MAPK pathway section (Table 3.14). For the future, using individual experiments as an input strategy for parameter estimation might be the best choice as it includes the actual variability of the data sets while still covering the data dynamics.

3.6.3 BMDM model validation through pathway disruptions

In this chapter, we discuss the comparison of the WT BMDM data and calibrated model with the *Dusp1*$^{-/-}$ and *Zfp36*$^{aa/aa}$ mutant. We use this comparison to identify shortcomings of the current model structure and present potential modelling or experimental solutions.

The expression patterns of phosphorylated p38 MAPK in *Dusp1*$^{-/-}$ BMDMs surprised us. Based on the literature and personal correspondence with colleagues, we assumed that DUSP1 would be responsible for most of the p38 MAPK dephosphorylation. If this had been the case, the p38

MAPK phosphorylation pattern was predicted to follow the model simulation dynamics, with an initial increase followed by a high plateau phase. However, from our data, one would assume that DUSP1 mainly affected p38 MAPK phosphorylation during its initial peak (Figure 3.21 A). We also expected a distinguishable change in expression levels. However, the mean results of *Dusp1*$^{-/-}$ BMDMs, while higher than in WT, were still within the observed range of p38 MAPK phosphorylation levels in individual experiments (Figure 3.13 A). The observed expression dynamics, therefore, suggest that DUSP1, at least in our model organisms, only covers a small portion of p38 MAPK dephosphorylation. Consequently, DUSP1 alone was insufficient to simulate p38 MAPK dephosphorylation in our model. There are two paths forward to adapting our model structure to reflect this. First, like Kulawik et al. (290), we could change DUSP1 back into a general MKP variable and not attempt to measure it further, Alternatively, we could keep DUSP1 and add another dependent variable to describe the remaining phosphatase activity. The latter option would have the advantage of allowing future evaluation of the impact of DUSP1-targeting treatment strategies. Having a model that can quantify the impact of DUSP1 on p38 MAPK might also be a valuable tool better to understand DUSP1 and its role within the inflammatory response, and identifying which and how many other phosphatases contribute to the regulation of p38 MAPK might be an interesting future direction one could explore with the help of our model. To estimate the parameters of the remaining phosphatases, we would need to measure p38 MAPK phosphorylation under complete inhibition of all phosphatase activity. Based on data from Tomida et al., the inhibitor triptolide seemed to block p38 MAPK dephosphorylation completely (148). For DUSP1, two expression patterns have been described in the literature; one group was classified as immediate-early and one as not-immediate-early, characterised by a linear increase upon

stimulation (349). Combining both in our model might allow us to simulate the desired dynamics.

Differences in *Tnf* expression between WT and *Dusp1*$^{-/-}$ BMDMs were more prominent than expected, considering the minor differences in p38 MAPK phosphorylation and TTP expression. *Tnf* varies from WT between the 1 h and 4 h time point, while we only observed differences in phosphorylated p38 MAPK between 30 min and 2 h. The *Tnf* levels of our model predictions for a total p38 MAPK phosphatase knockout fit in height and vary mainly in the duration of the expression peak. This data suggests that DUSP1 might affect other signalling pathways involved in regulating *Tnf* mRNA expression. However, further experiments are needed to confirm such a hypothesis.

As expected, the TTP expression was low in *Zfp36*$^{aa/aa}$ BMDMs. However, the expression levels obtained from the total quantification experiments likely overestimate the actual levels due to the non-linearity of the TTP standard curve at lower concentrations. For the *Zfp36*$^{aa/aa}$ mutant, based on the literature and previous experiments, we assumed that the overall TTP expression is low due to the instability of unphosphorylated TTP; it is still higher than active unphosphorylated TTP in WT BMDMs, which resulted in a decrease in TTP-target mRNAs. The value calculated for total TTP in Zfp36$^{aa/aa}$ mice is, however, in our data set, lower than what we measured for the lower band of TTP in WT. Because of these connections, it is unsurprising that the calibrated model does not reflect the described biological behaviour when simulating the *Zfp36*$^{aa/aa}$ phenotype. Consequently, measuring the lower band of TTP in WT BMDMs does not correspond in expression levels with the actual unphosphorylated, active TTP. Nevertheless, although the levels do not fit, the dynamics could still follow its actual activity pattern based on our observations. Suppose we cannot measure unphosphorylated TTP

directly. In that case, we can estimate the parameters of our model by including the *Zfp36*$^{aa/aa}$ mutant data in the parameter estimation process as an additional experiment.

Tnf mRNA expression levels in *Zfp36*$^{aa/aa}$ BMDMs were surprising, as they were the same as in WT BMDMs. We would have expected a decrease in *Tnf* expression. That we do not see any difference could be due to the variance between the experiments paired with a smaller effect size. For the *Zfp36*$^{aa/aa}$ experiments, p38 MAPK phosphorylation levels were as high as in the *Dusp1*$^{-/-}$ experiments. Although the *Zfp36*$^{aa/aa}$ mutant, according to our understanding of the pathway, should not have this effect on p38 MAPK phosphorylation. Based on the literature, TTP could affect p38 MAPK phosphorylation by destabilising *Dusp1* mRNA (145,146) or affecting TLR activity (350). However, it is unlikely that an effect on p38 MAPK phosphorylation levels in *Zfp36*$^{aa/aa}$ mutant mice has remained undetected until now, and the observed difference is consequently more likely due to experimental variability. We tried to control for this effect by normalising the measurements to the peak strength of p38 MAPK. Even after normalisation, only slight differences in mRNA expression between *Zfp36*$^{aa/aa}$ and WT were observed (Figure 3.30). When we compared our results to the online TTP atlas, we found only slight differences in mRNA expression between WT and *Zfp36*$^{-/-}$ cells (348). *Tnf* mRNA is a well-validated target of TTP; considering the severe phenotype of *Zfp36*$^{-/-}$ mice, which is dependent mainly on *Tnf* expression, this slight difference in mRNA expression is unlikely to paint the complete picture.

Ronkina et al. described significant differences in protein levels of *Tnf* in *Zfp36*$^{aa/aa}$ mice and MK2/3 knockout mice compared to WT mice (261). In summary, the literature actually suggests that *Tnf* might not be regulated by TTP-mediated mRNA decay alone. Translation inhibition is one of the proposed other modes of action for TTP (208,237–239). This was recognised early on but sidelined once the role of TTP in target mRNA decay was established.

To further investigate this, we performed an ELISA on the supernatant collected during our Zfp36$^{aa/aa}$ and WT experiments, and indeed, the difference between *Zfp36*$^{aa/aa}$ and WT TNF protein levels was clear (combined row and column factor P value=0.0214), despite the high variability of the WT BMDMs (Figure 3.31). This difference is unlikely to be introduced through mRNA degradation alone, where effects were minor, but is more likely due to TTP's role in translation inhibition. Other mRNAs, such as *Cxcl1* (351), display strong mRNA level changes induced by TTP; there may be some target mRNA dependency on whether TTP effects on the inflammatory state are mediated by degradation or translation inhibition. Other RBPs, such as HuR, might also play a role here. A factor in *Zfp36*$^{aa/aa}$ that shifts the scale towards translation inhibition could be that the third MK2 phosphorylation target at position Ser-316 is still phosphorylatable. The phosphorylation at Ser-316 has been shown to inhibit RNA degradation machinery recruitment (93,261). Consequently, it is likely that, in *Zfp36*$^{aa/aa}$ BMDMs, RNA decay might be hampered. Identifying which factors decide if degradation or translation inhibition are the main contributors might be an exciting question to tackle in the future by measuring different target mRNAs and their corresponding protein levels in similar experiments.

In WT BMDMs treated with the PP2A inhibitor Calyculin A, we observed an increase in p38 MAPK phosphorylation compared to WT cells (Figure 3.25). This made it difficult to discern what influence TTP had on the increased *Tnf* mRNA expression. On the one hand, this increase in p38 MAPK phosphorylation could be due to cytotoxicity and stress induced by the inhibitor. On the other hand, the observation could suggest that PP2A also targets p38 MAPK for dephosphorylation, which has been reported several times in the literature (157–162). Consequently, future experiments using PP2A inhibitors or activators should include not only TTP itself but also p38 MAPK phosphorylation measurements. Analysing the effect of PP2A-

mediated dephosphorylation of p38 MAPK on the model might result in interesting dynamics worth exploring.

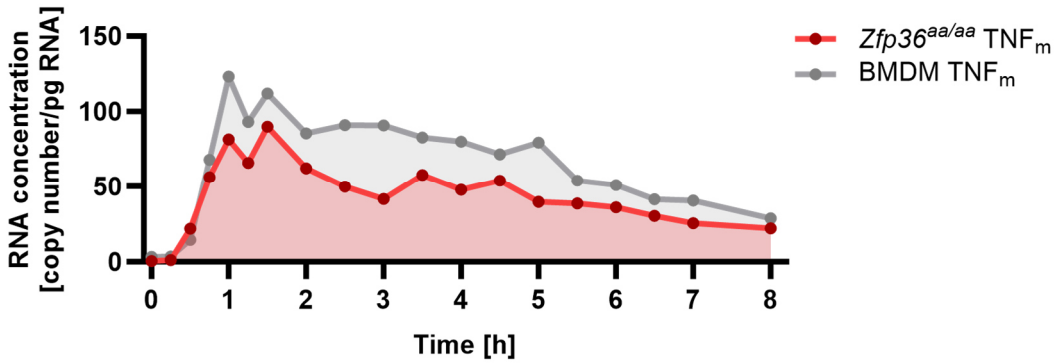


Figure 3.30 Comparison *Tnf* mRNA expression normalised to peak p38 MAPK phosphorylation between *Zfp36*$^{aa/aa}$ and WT BMDMs.

The *Tnf* mRNA data presented in Figure 3.13 and Figure 3.23 was normalised to peak p38 MAPK phosphorylation levels for WT and *Zfp36*$^{aa/aa}$ BMDMs. *Tnf* mRNA levels are shown in red for *Zfp36*$^{aa/aa}$ BMDMs and in grey for WT BMDMs. For clarity no standard deviation or individual data points are included. RM two-way ANOVAs and Šidák post-hoc corrected multiple comparisons were performed to compare the results from *Zfp36*$^{aa/aa}$ BMDMs with WT BMDMs; P value = 0.9409; No individual Šidák post-hoc corrected comparison yielded a statistically significant result.

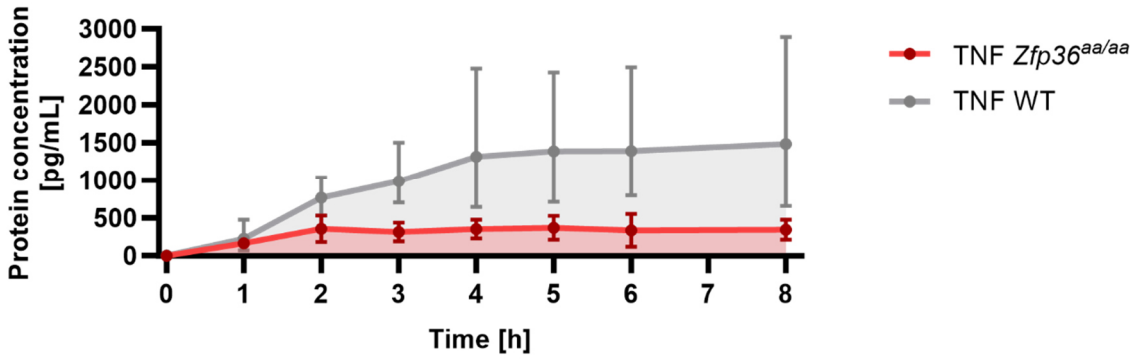


Figure 3.31 Comparison of secreted TNF-α protein expression between *Zfp36*$^{aa/aa}$ and WT BMDMs using ELISA.

WT and *Zfp36*$^{aa/aa}$ BMDMs derived from the bone marrow of 8/6 mice were combined and treated with 10 ng/mL LPS for a period of 8 h. Protein concentrations of secreted TNF-α were measured in the cell media using an ELISA

with included standard curve (n=3). Tnf protein levels are shown in red for *Zfp36*$^{aa/aa}$ BMDMs and in grey for WT BMDMs. Standard deviation is displayed as error bars. RM two-way ANOVAs and Šidák post-hoc corrected multiple comparisons were performed to compare the results from *Zfp36*$^{aa/aa}$ BMDMs with WT BMDMs; P value = 0.0214; No individual Šidák post-hoc corrected comparison yielded a statistically significant result.

3.6.4 Comparison of WT BMDMs and RAW264.7 cells

In this chapter, we discuss the comparison of the model and data obtained from WT BMDMs and RAW264.7 cells. As mentioned, RAW264.7 cells are a murine macrophage cell line we commonly use to test experimental settings before transitioning to BMDMs. This cell line also provided much of the groundwork for TTP biology. Understanding the differences between the two cell types will support the translatability of future work from RAW264.7 cells to BMDMs and, ultimately, patients. After all, these cells have a tumour origin and are potentially dysregulated in many aspects (352).

One major difference between BMDMs and RAW264.7 cells was the peak height of phosphorylated p38 MAPK, which we found >3 times higher in RAW264.7 cells. Indeed, in our preliminary PhosTag gel experiments, we found that p38 MAPK at its peak was likely close to 100% phosphorylated in RAW264.7 cells (supplementary Figure 7.4). This strong peak likely induced p38-specific phosphatases, which explains the steep downregulation after the peak, reaching starting phospho-p38 MAPK levels within 1.5 h. Apart from this, we observed similar expression patterns for DUSP1 and unphosphorylated TTP in RAW264.7 and BMDMs, with an initial peak followed by a plateau phase. We already discussed in the previous chapter that our current model structure could not simulate those dynamics and that we would need to include *Dusp1* mRNA and MK2 as dependent variables to achieve this. Phosphorylated TTP in RAW264.7 cells continued to increase throughout the inflammatory response, with a leap in expression levels around the 4 h time point. Initially, one would not attribute these dynamics to be solely mediated by the early peak in p38 MAPK phosphorylation. We identified four

potential explanations: 1) Contributions of other signalling pathways, 2) *Zfp36* mRNA stability, 3) Feedforward-loop of secreted pro-inflammatory cytokines or 4) oscillatory activation of p38 MAPK. We know from the literature that the NF-κB and ERK pathways (242,243,344), both activated by LPS, are involved in Zfp36 transcription. Additionally, MK2 has been reported to be involved in this process, explored by Ronkina et al. in a qualitative model (180). For the second option, we should consider that TTP reportedly destabilises its own mRNA and potentially also inhibits its translation (250,251). Therefore, the strong initial phosphorylation peak of p38 MAPK could lead to the formation of an mRNA pool that feeds into the protein levels for the remaining time-course. This hypothesis could be tested by measuring *Zfp36* mRNA. Third, throughout the inflammatory response, pro-inflammatory mediators accumulate in the medium which could contribute to the observed stepwise increase. The fourth option references the oscillatory activation of p38 MAPK phosphorylation, as described by Tomida et al. (148). According to their theory, due to cell-to-cell heterogeneity, oscillatory phosphorylation and activation of p38 MAPK are not visible in multicellular approaches such as WB and qPCR. Nevertheless, these oscillations are necessary for sufficient induction of the expression of inflammatory cytokines in their model. Similarly, sufficient TTP expression might rely on these, in our experiments, invisible oscillations. The four peaks observed in *Tnf* and the jump in TTP phosphorylation might hint in this direction. Oscillations might be visible in downstream targets of p38 MAPK and not p38 MAPK itself due to the amplification of the signal through mediating kinases such as MK2. However, apart from p38 MAPK, the NF-κB and ERK pathways also have been associated with oscillatory activation (286,353–355). and TTP and *Tnf* regulation. Therefore, to cover the observed expression behaviour in RAW264.7 cells, one could model each option and compare them to find the best fit for the data. Corresponding data measurements would then be necessary for parameter estimation. Overall,

the strong peak and the fast downregulation could imply that in RAW264.7 cells, the inflammatory response initiates faster than in BMDMs, and it might, therefore, be possible to observe dynamics that are otherwise outside the 8 h time-course experiment. To take the same line, it would be interesting to see if anti-inflammatory cytokines such as IL-10 are also expressed and produced earlier in RAW264.7 cells compared to BMDMs.

3.7 Chapter summary

The focus of this chapter was to build a mathematical p38 MAPK-TTP pathway model inspired by a previous p38 MAPK model published by Kulawik et al. to perform parameter estimation using total quantification data and to validate the newly established model. The model structure was selected based on the previously defined model aims and temporal scope, which led to a model that was defined as dynamic, continuous, deterministic, spatially homogenous, and open to environmental factors. The Kulawik p38 MAPK-TTP model was also defined in the form of the model components and their interactions summarised as model diagrams and ODEs. Following this, the model structure was evaluated using structural identifiability analysis and global parameter ranking, which found the model structurally identifiable and predicted the parameters that most affect the parameter estimation outcome. We then defined the experimental design based on the total quantification of proteins and mRNA. The experimental design was followed by the parameter estimation of the model, which included the description of the experimental data obtained from WT BMDMs, an update of the model and its nominal parameters, and their usage in the model parameter estimation. The BMDM data exhibited high variability between experiments, and we obtained multiple suboptimal solutions during the parameter estimation because of the practical non-identifiability of some model parameters. The current model structure was not suitable for covering every detail of the expression dynamics observed in the data. However, based on the relative global MABS we achieved an overall good fit of the model. We proposed several changes to the model and experiments that could allow us to cover the data dynamics more accurately and achieve a better fit of the model to the data during parameter estimation in the future. The changes included adding *Dusp1* mRNA, unphosphorylated and phosphorylated MK2, and PP2A expression or activity to the model as dependent variables.

The parameter set with the highest relative global MABS was validated against experimental data from *Dusp1*$^{-/-}$ and *Zfp36*$^{aa/aa}$ BMDMs. We found that Dusp1 alone was insufficient for modelling p38 MAPK dephosphorylation, so we proposed two strategies for implementing this knowledge into our model. The identified parameter set could not simulate the *Zfp36*$^{aa/aa}$ mutant accurately. Therefore, we proposed to include the *Zfp36*$^{aa/aa}$ data itself as an experiment in the parameter estimation process.

Comparing WT and *Zfp36*$^{aa/aa}$ data, we found out that the lower band of the WB TTP species was unsuitable for measuring unphosphorylated TTP levels quantitatively. We, therefore, proposed a combined bottom-up and top-down parameter estimation strategy and measurement of the degradation rate of unphosphorylated TTP directly using cycloheximide chase experiments in MK2/MK3 knockout mice or *Zfp36*$^{aa/aa}$ mice in the future. Additionally, we found no difference in *Tnf* mRNA expression between *Zfp36*$^{aa/aa}$ and WT BMDMs. However, we found a significant difference when we measured secreted TNF-α protein from *Zfp36*$^{aa/aa}$ and WT BMDMs. The observed difference in protein level, in combination with the literature, suggested that *Tnf* mRNA can be primarily regulated by TTP through translation inhibition instead of mRNA degradation in *Zfp36*$^{aa/aa}$ BMDMs. We concluded that the dominant way TTP regulates target mRNA might vary depending on the 3'UTR composition and other RBPs present. To cover this mode of regulation with our model, we proposed adding TNF-α secreted protein as a dependent variable.

We further evaluated data from BMDMs treated with a PP2A inhibitor. The inhibitor-treated WT BMDMs did not produce data usable for model validation as the data suggested that effects on *Tnf* mRNA might be due to changes in p38 MAPK phosphorylation rather than TTP dephosphorylation.

Finally, parameter estimation of the model was performed using RAW264.7 cells, and the data and computational model simulations were compared with BMDMs. We found some interesting dynamics in RAW264.7 cells that were not detectable in BMDMs. Based on the literature, we proposed potential mechanisms that would allow us to cover the observed dynamics if implemented into the model.

This chapter demonstrated the iterative nature of the modelling process. We proposed a model structure, used it to inform our experimental design, then amended it to fit our experimental design better, and by comparing the model and data, found ways to adjust the model to describe the biological system better. The model can now help us design the next set of experiments, test the newly proposed hypothesis computationally and repeat the cycle once we have new data sets. Overall, we achieved our goal of reaching a better and broader understanding of the pathway dynamics with this first iteration.

CHAPTER FOUR

Mathematical Modelling of the p38 MAPK-TTP signalling axis in individual cells

4 Mathematical Modelling of the p38 MAPK-TTP signalling axis in individual cells

4.1 Introduction

Total quantification methods, such as the WB and RT qPCR, were used in the previous chapter to describe the main dynamics of the p38 MAPK-TTP signalling axis. These assays all require many cells for a measurement and, as such, provide an average rather than what is happening within individual cells. Tomida et al. proposed a mathematical p38 MAPK model that described the oscillations of p38 MAPK activity on the single-cell level introduced through a DUSP1-mediated feedback mechanism (148). Oscillations in mathematical models are interesting as they can introduce unexpected behaviours but can also improve the robustness of a biochemical system towards perturbations. They further observed cell-to-cell heterogeneity of the oscillatory pattern after the initial peak, which they suggested led to the plateau of p38 MAPK phosphorylation observed in multicellular approaches such as WB. Although we observed some dynamics that might hint towards oscillatory regulation patterns, overall, the methods established in the previous chapter are unsuitable to capture single-cell p38 MAPK oscillations and their effects on the TTP pathway. However, understanding the implications of those oscillations might be essential to capture the pathway dynamics completely and understand how TTP and its target mRNAs are regulated.

For this purpose, we aimed to create a mathematical model that allows us to explore the consequences of oscillations on the p38 MAPK-TTP signalling axis as well as methods to capture this behaviour experimentally. Tomida et al. leveraged live-cell microscopy of p38 MAPK reporter activity to identify oscillatory patterns. Indeed, live-cell microscopy using fluorescent reporters appeared to be the only way to measure dynamic changes on a single-cell

level over longer periods. We were also drawn to this for the opportunity to establish a method that would allow us to measure TTP activity throughout the inflammatory response. Through literature research and based on previous experiments done in our lab, we identified potential readouts to visualise TTP activity. Unfortunately, due to challenges with establishing a robust live-cell microscopy protocol, we were delayed in our endeavour and could only start addressing one of these.

In this chapter, we will describe the formulation of our Tomida TTP model that implements an oscillatory p38 MAPK activity pattern upstream of TTP and its qualitative analysis and comparison to the Kulawik p38 MAPK-TTP model. This will be followed by the experimental design and results of the cloning of the fluorescent reporter constructs. Finally, we will present the experimental design of the live-cell microscopy, the preliminary microscopy results of those reporters and the challenges associated with the approach.

4.2 Model formulation

For the model building of the Tomida p38 MAPK-TTP model, we will first define the model scope. Then we will introduce the p38 MAPK model published by Tomida et al. and describe how we implemented and adapted it to our TTP core model. As part of this process, we defined all its components, including variables, parameters, processes, and their interactions, as well as the resulting equations.

4.2.1 Definition of the model scope

For setting the scope of the Tomida p38 MAPK-TTP model we defined its aim, data availability and constraints, temporal, and spatial resolution. The general approach here is the same as with the Kulawik p38 MAPK-TTP model (Chapter 3.2). We have already defined the model's aim and the main research questions to be addressed in Chapter 1.6. In short, the model aims to capture the oscillatory p38 MAPK activity and their effects on TTP and TTP-target mRNAs on the single-cell level during the early inflammatory response.

Regarding the data availability, while Tomida et al. demonstrated qualitatively oscillatory phosphorylation of p38 MAPK using a Foerster resonance energy transfer (FRET)-based KTR and live-cell microscopy, they did not explore the effect on downstream targets in the same way. To measure TTP activity dynamically in individual cells, we decided to clone fluorescent reporter proteins and use them in live-cell microscopy. The resulting data would be semi-quantitative as measuring the total amount of protein in this setting is impossible. For the temporal resolution, we decided to cover the same 8 h time frame as for our total quantification experiments in as much detail as possible without compromising experimental practicality. The number of sampling times for measurement is primarily dependent on how long the imaging process of each time point takes. For the spatial scope, we chose the complete protein or RNA

pool within an individual cell. We mentally marked the potential introduction of subcellular compartments (nucleus, cytoplasm, PBs) if experimental data recommends it. Based on these decisions, we kept the model structure, as defined in the previous chapter for our TTP core model and adapted the Tomida MAPK model accordingly.

4.2.2 Presentation of the Tomida p38 MAPK model

The Tomida p38 MAPK model, represented by the model diagram in Figure 4.1, consists of four ODEs, with its dependent variables being active MAP2K (M_P), active p38 MAPK (P_P), *DUSP1* mRNA (D_m), and DUSP1 protein (D) (Table 4.1). Its sole independent variable is the inflammatory cytokine IL-1β (S) (Table 4.1). Like in the Kulawik p38 MAPK model, the signalling complex of the IL-1R was strongly reduced, summarised as stimulus-mediated MAP2K and subsequent p38 MAPK activation. MAP2K comprises all upstream kinases involved in p38 MAPK phosphorylation. Contrary to our previously described model, the unphosphorylated protein species were not included as own variables. Instead, they were represented as the total amount of p38 MAPK protein minus the phosphorylated protein species. The model did not include a basal activation of p38 MAPK. As negative feedback inhibitors, they included DUSP1 protein and *DUSP1* mRNA. The mRNA was necessary to create an additional delay between p38 MAPK phosphorylation and DUSP1 expression, which is essential to obtain the oscillatory activity pattern (356). For both, the synthesis term was structured similarly to the phosphorylation term used for MAP2K and p38 MAPK, being defined as 1 minus their own concentration. The included parameters describe the synthesis, degradation, phosphorylation, and dephosphorylation rates of the dependent variables. A summary of all interactions and resulting parameters can be found in Table 4.2 and Table 4.3, respectively.

The mathematical equations presented by Tomida et al. were adapted to fit our naming conventions to simplify compatibility between models but were otherwise left unchanged. To introduce oscillatory behaviour, they further included a Michaelis Menten function for DUSP1-mediated p38 MAPK dephosphorylation. This results in the following set of equations:

$$\frac{dM_P}{dt} = +\varphi_{Mp}{}^{*}S^{*}(1 - M_P) - \rho_{Mp}{}^{*}M_P, \tag{4.1}$$

$$\frac{dP_P}{dt} = +\varphi_{Pp}{}^{*}M_P{}^{*}(1 - P_P) - \frac{\rho_{Pp}{}^{*}D^{*}P_P}{k_M + P_P}, \tag{4.2}$$

$$\frac{dD_m}{dt} = +\gamma_{Dm}{}^{*}P_p{}^{*}(1 - D_m) - \delta_{Dm}{}^{*}D_m, \tag{4.3}$$

$$\frac{dD}{dt} = +\gamma_D{}^{*}D_m{}^{*}(1 - D) - \delta_D{}^{*}D, \tag{4.4}$$

with the initial conditions $M_P(0) = M_P0$, $P_P(0) = P_P0$, $D_m(0) = D_m0$, and $D(0) = D0$. Here '*' represents a multiplication sign, which is introduced for improved readability of the equations.

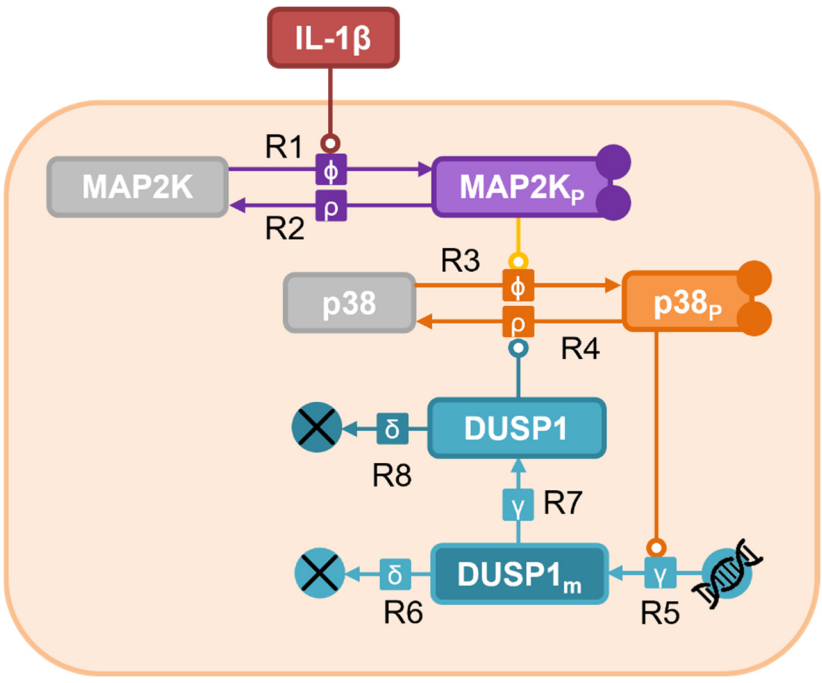


Figure 4.1 Model diagram of the Tomida p38 MAPK model.

The graphic summarises the model components, reactions, and interactions included in the Tomida p38 MAPK model. The dependent variables comprise phosphorylated MAP2K ($MAP2K_P$, violet), phosphorylated p38 ($p38_p$, orange), *DUSP1* mRNA ($DUSP1_m$, light blue), and DUSP1 protein (dark blue). The sole independent variable is the stimulus IL-1β (red). Circles on the side of the variable mark phosphorylated protein species. Arrows indicate the flow of material between variables and represent the main reactions within the model numbered R1 to R8. Circles with a DNA helix indicate that new mRNA or, ultimately, protein is synthesised and enters the model. Circles with an X refer to the degradation of mRNA or protein, therefore material leaving the model. The lines with circles at their ends represent a flow of information and connect a variable with the reactions they are affecting. The parameters are represented as small squares on the reaction arrows labelled with the Greek letters γ, δ, φ, or ρ, referring to the specific type of reactions, namely the rate of synthesis, degradation, phosphorylation, and dephosphorylation, respectively.

Table 4.1 Variables of the Tomida p38 MAPK model.

Variables

Symbol	Description	Initial condition	Dimension
S	Concentration of stimulus IL-1β	$S = 1$	$a.u.$
M_P	Concentration of active MAP2K	$M_P0 = 0$	$a.u.$
P_P	Concentration of active p38	$P_P0 = 0$	$a.u.$
D_m	Concentration of DUSP1 mRNA	$D_m0 = 0$	$a.u.$
D	Concentration of DUSP1	$D0 = 0$	$a.u.$

Table 4.2 Interactions of the Tomida p38 MAPK model.

Interactions

Reaction	Description	No.	Ref.
$\emptyset \xrightarrow{IL-1\beta} MAP2K_P$	IL-1β-dependent activation of MAP2K	R1	(148)
$\emptyset \leftarrow MAP2K_P$	Deactivation of MAP2K	R2	(148)
$\emptyset \xrightarrow{MAP2Kp} p38_P$	MAP2K-dependent activation of p38	R3	(148)
$\emptyset \xleftarrow[DUSP1]{} p38_P$	DUSP1-dependent deactivation of p38	R4	(148)
$\emptyset \xrightarrow{p38_P} DUSP1_m$	Phospho-p38-dependent DUSP1 mRNA transcription	R5	(148)

$\emptyset \leftarrow DUSP1_m$	*DUSP1* mRNA degradation	R6	(148)
$\emptyset \xrightarrow{DUSP1m} DUSP1$	*DUSP1* mRNA translation	R7	(148)
$\emptyset \leftarrow DUSP1$	DUSP1 degradation	R8	(148)

Table 4.3 Parameters of the Tomida p38 MAPK model.

Parameters			
Symbol	**Description**	**Nominal value**	**Dimension**
φ_{Mp}	Phosphorylation rate of MAP2K	0.06	min^{-1}
ρ_{Mp}	Dephosphorylation rate of MAP2K	0.15	min^{-1}
φ_{Pp}	Phosphorylation rate of p38 MAPK	0.15	min^{-1}
ρ_{Pp}	Dephosphorylation rate of p38 MAPK	0.16	min^{-1}
k_M	Michaelis Menten constant	0.0001	$a.u.$
γ_{Dm}	Synthesis rate of DUSP1 mRNA	0.055	min^{-1}
δ_{Dm}	Degradation rate of DUSP1 mRNA	0.05	min^{-1}
γ_D	Synthesis rate of DUSP1	0.2	min^{-1}
δ_D	Degradation rate of DUSP1	0.02	min^{-1}

How the parameter values of the Tomida et al. model were estimated initially was not included in their publication (148). This, together with the rounded numbers (see Table 4.3), could suggest that the parameter set was obtained through trial and error until the desired behaviour matched the observations in their microscopy data during model simulations. These parameter values, and the initial conditions found in Table 4.4, resulted in the model simulation shown in Figure 4.2. The MATLAB script can be found in Appendix 7.1. The simulation in Figure 4.2 B

shows the oscillatory activation pattern of p38 MAPK, with the initial strong peak followed by oscillations. Oscillations can also be found in the *DUSP1* mRNA and DUSP1 protein simulation.

Like Tomida et al. (148), we created a multicellular variation of the model by randomising the DUSP1 degradation rate (n=30), which will be addressed in more detail in the discussion Chapter 4.5.1. The results are shown in Figure 4.3, which is supposed to capture the cell-to-cell variability of the oscillations. Tomida et al. based this decision on a paper published by Crowell et al. (347), where they found that DUSP1 degradation is controlled by phosphorylation. In the multicellular model variation, the disappearance of overall oscillation behaviour could be partially observed. As shown in Figure 4.3 B, with only 30 cells in the simulation, one can already observe how an average measurement could hide oscillations, with the oscillations still visible but dampened. The behaviour of mean p38 MAPK activation, including more cells, would then express itself, as we know it from our Kulawik p38 MAPK-TTP model, with an initial strong peak at around 0.5 h post-stimulation, followed by a plateau phase. The same is the case for *DUSP1* mRNA and protein, whereas in the latter one, the effect on oscillations was strongest, with 30 included cells almost completely abolished. The oscillations found in the real-life imaging data of Tomida et al. were still less synchronous than in the model and vary in height and length (Figure 1.10). Considering this, one can imagine that in multicellular assays, with millions of cells, the first peak would remain detectable while the later oscillations become covered up entirely by cell-to-cell variability, resulting in plateaus. In the next section, we will combine our TPP core model and the Tomida p38 MAPK pathway model.

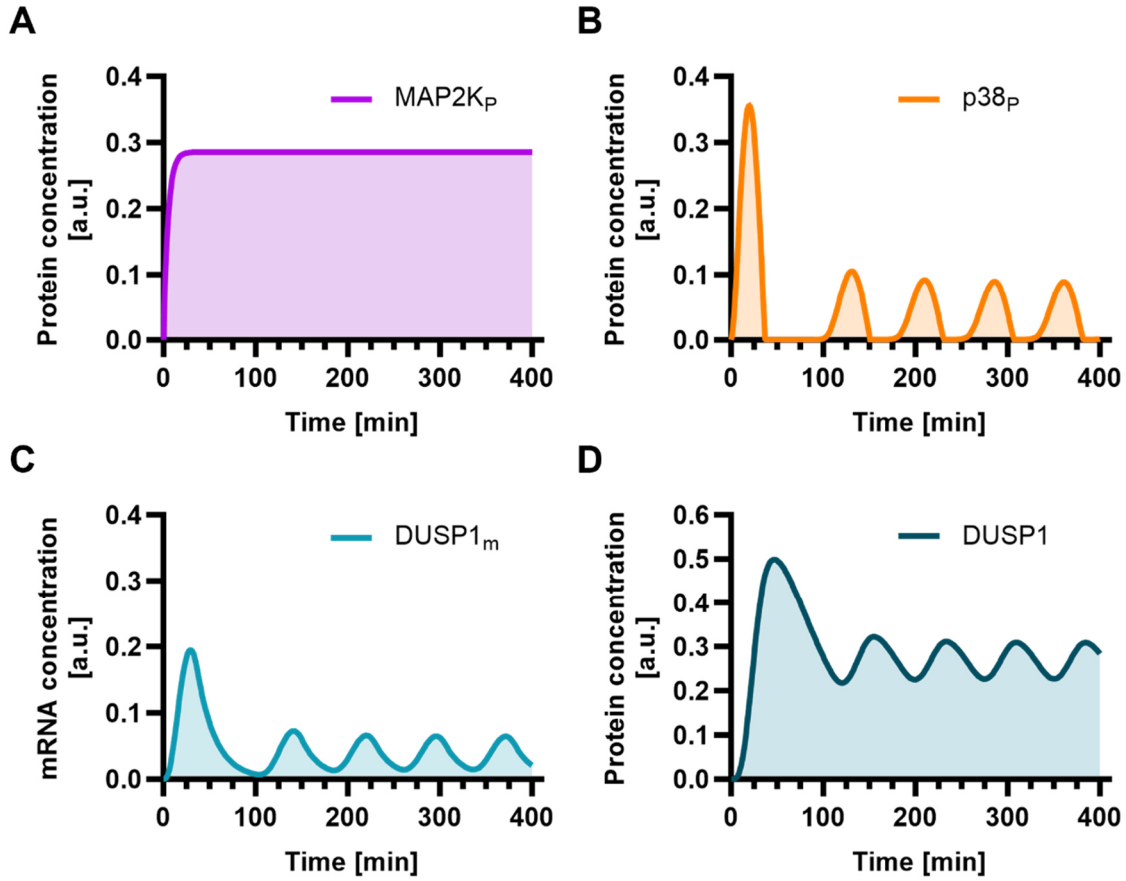


Figure 4.2 Computational single-cell simulation of the Tomida p38 MAPK model.

The data for the simulation of the Tomida p38 MAPK model was generated in MATLAB using the *ode23* function to solve the ODE equations (4.1) to (4.4) as well as the nominal parameter values and initial conditions shown in Table 4.3 and Table 4.1 for a time span of 400 min. The graphs display the expression change of A) active MAP2K, B) active p38 MAPK, C) *DUSP1* mRNA, and D) DUSP1 protein, following IL-1β treatment within an individual HeLa cell. The full MATLAB script for generating the graphs can be found in Appendix 7.1.

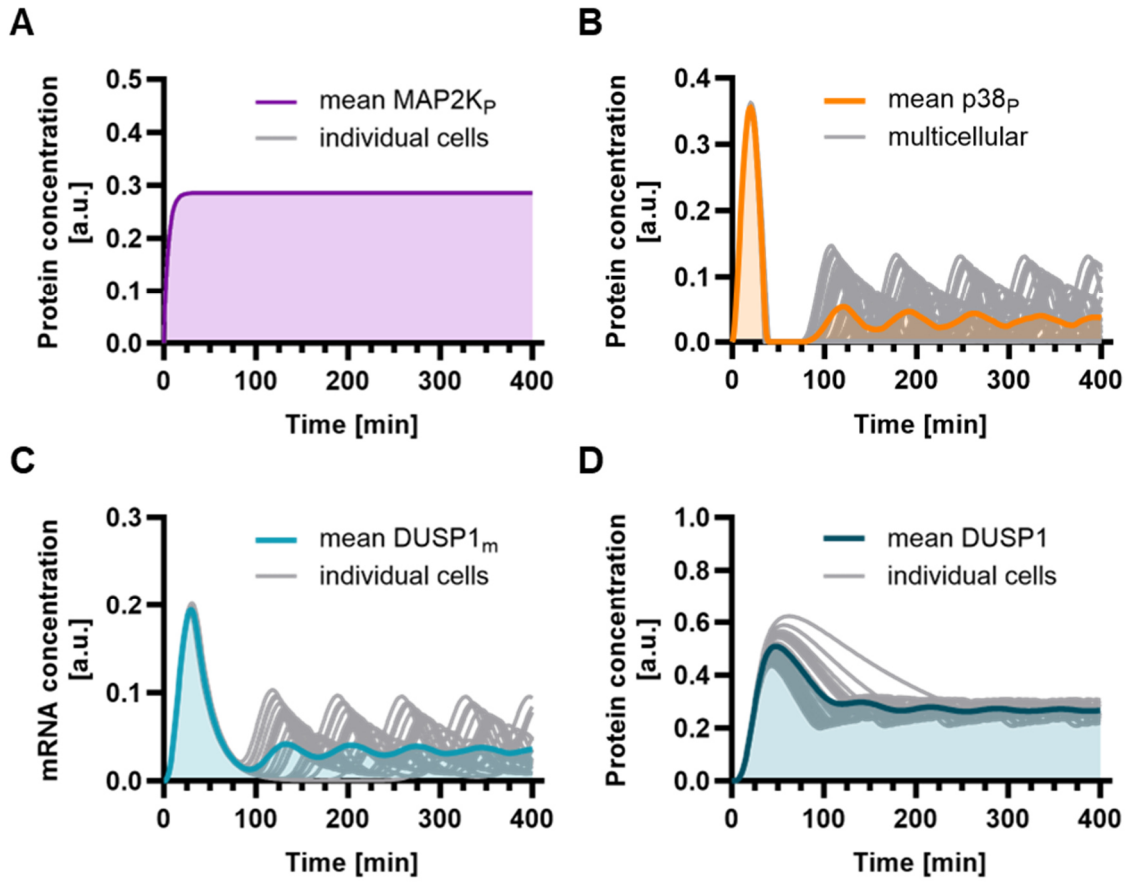


Figure 4.3 Computational multicellular simulation of the Tomida p38 MAPK model.

The data for the multicellular simulation of the Tomida p38 MAPK model was generated in MATLAB using the *ode23* function to solve the ODE equations (4.1) to (4.4) as well as the nominal parameter values and initial conditions shown in Table 4.3 and Table 4.1 for a time span of 400 min with randomised DUSP1 degradation rate. The graphs show the expression change of A) active MAP2K, B) active p38 MAPK, C) *DUSP1* mRNA D), and DUSP1 protein, following IL-1β treatment within multiple (n=30) individual HeLa cells (grey) together with the mean expression levels (coloured). The full MATLAB script for generating the graphs can be found in Appendix 7.1.

4.2.3 Design of the Tomida p38 MAPK-TTP model

We combined the Tomida p38 MAPK model and the TTP core model presented in Chapter 3.2.3.1. The resulting model diagram is shown in Figure 4.4, and the model components are listed in Table 4.4, Table 4.5, and Table 4.6. To achieve this, we removed the MAP2K kinase as a variable, added unphosphorylated p38 MAPK as a variable, and adapted the equations to the principles of mass action kinetics. This resulted in the following set of ODEs:

$$\frac{dP}{dt} = -\varphi_{P2}{}^{*}S^{*}P + \rho_{Pp1}{}^{*}P_P + \frac{\rho_{Pp2}{}^{*}D^{*}P_P}{k_M + P_P}, \quad (4.5)$$

$$\frac{dP_P}{dt} = +\varphi_{P2}{}^{*}S^{*}P - \rho_{Pp1}{}^{*}P_P - \frac{\rho_{Pp2}{}^{*}D^{*}P_P}{k_M + P_P}, \quad (4.6)$$

$$\frac{dD_m}{dt} = +\gamma_{Dm}{}^{*}P_P - \delta_{Dm}{}^{*}D_m, \quad (4.7)$$

$$\frac{dD}{dt} = +\gamma_{D}{}^{*}D_m - \delta_{D}{}^{*}D, \quad (4.8)$$

$$\frac{dT}{dt} = +\gamma_{T}{}^{*}P_P - \delta_{T}{}^{*}T - \varphi_{T}{}^{*}T^{*}P_P + \rho_{Tp}{}^{*}T_P, \quad (4.9)$$

$$\frac{dT_P}{dt} = -\delta_{Tp}{}^{*}T_P + \varphi_{T}{}^{*}P_P{}^{*}T - \rho_{Tp}{}^{*}T_P, \quad (4.10)$$

$$\frac{dR_m}{dt} = +\gamma_{Rm}{}^{*}P_P - \delta_{Rm1}{}^{*}R_m - \delta_{Rm2}{}^{*}T^{*}R_m, \quad (4.11)$$

with initial conditions $P(0) = P0$, $P_P(0) = P_P0$, $D_m(0) = D_m0$, $D(0) = D0$, $T(0) = T0$, $T_P(0) = T_P0$, and $R_m(0) = R_m0$.

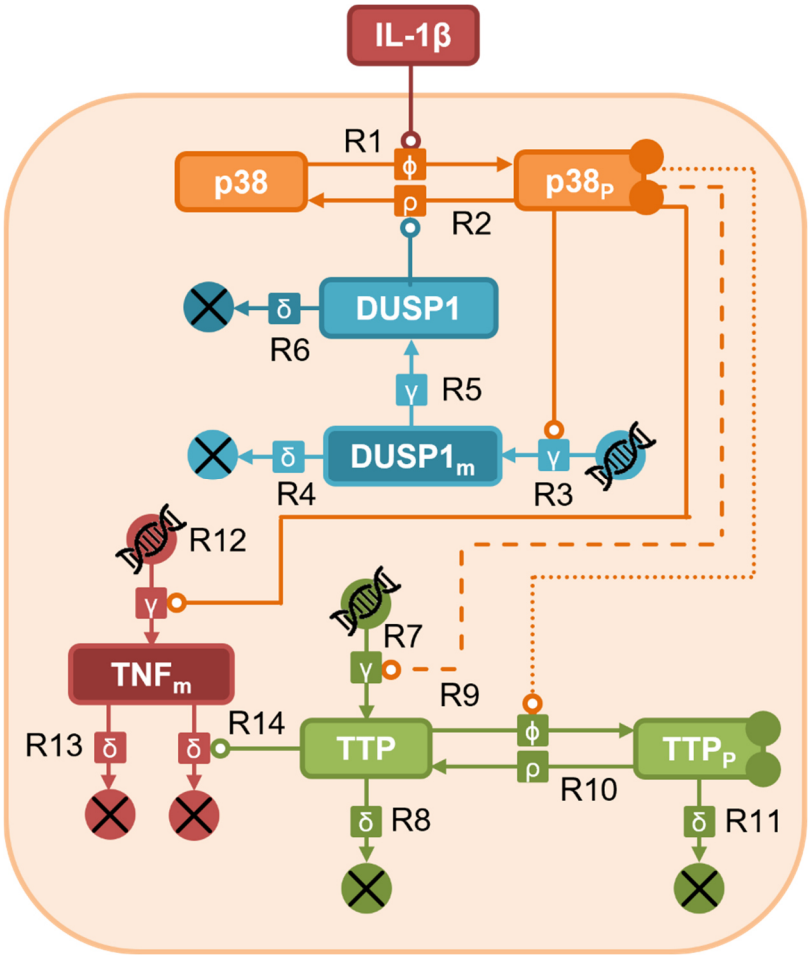


Figure 4.4 Model diagram of the Tomida p38 MAPK-TTP pathway.

The graphic summarises the model components, reactions, and interactions included in the Kulawik p38 MAPK-TTP model. The dependent variables comprise unphosphorylated and phosphorylated p38 (orange), DUSP1 mRNA and DUSP1 protein (blue), unphosphorylated and phosphorylated TTP (green), and TTP-target mRNA (red). The sole independent variable is the stimulus IL-1β. Circles on the side of the variable mark phosphorylated protein species. Arrows indicate the flow of material between variables and represent the main reactions within the model numbered R1 to R14. Circles with a DNA helix indicate that new mRNA or, ultimately, protein is synthesised and enters the model. Circles with an X refer to the degradation of mRNA or protein, therefore material leaving the model. The lines with circles at their ends represent a flow of information and connect a variable with the reactions they are affecting. The parameters are represented as small squares on the reaction arrows labelled with the Greek letters γ, δ, φ, or ρ, referring to the specific type of reactions, namely the rate of synthesis, degradation, phosphorylation, and dephosphorylation, respectively.

Table 4.4 Variables of the Tomida p38 MAPK-TTP model.

Variables			
Symbol	**Description**	**Initial condition**	**Dimension**
S	Concentration stimulus IL-1β	$S = 1$	$a.u.$
P	Concentration of inactive p38	$P0 = 1$	$a.u.$
P_P	Concentration of active p38	$P_P0 = 0$	$a.u.$
D_m	Concentration of DUSP1 mRNA	$D_m0 = 0$	$a.u.$
D	Concentration of DUSP1	$D0 = 0$	$a.u.$
T	Concentration of active TTP	$T0 = 0$	$a.u.$
T_P	Concentration of inactive TTP	$T_P0 = 0$	$a.u.$
R_m	Concentration of TTP TNF_m	$R_m0 = 0$	$a.u.$

Table 4.5 Interactions of the Tomida p38 MAPK-TTP model.

Interactions			
Reaction	**Description**	**No.**	**Ref.**
$p38 \xrightarrow{IL-1\beta} p38_P$	IL-1β-dependent activation of p38 MAPK	R1	(148)
$p38 \xleftarrow[DUSP1]{} p38_P$	DUSP1-dependent deactivation of p38 MAPK	R2	(148)
$\emptyset \xrightarrow{p38_P} DUSP1_m$	Phospho-p38-dependent DUSP1 mRNA synthesis	R3	(148)
$\emptyset \leftarrow DUSP1_m$	DUSP1 mRNA degradation	R4	(148)
$\emptyset \xrightarrow{DUSP1m} DUSP1$	DUSP1 mRNA translation	R5	(148)
$\emptyset \leftarrow DUSP1$	DUSP1 mRNA degradation	R6	(148)
$\emptyset \xrightarrow{p38_P} TTP$	Phospho-p38-dependent TTP synthesis	R7	(319)
$\emptyset \leftarrow TTP$	Degradation of unphosphorylated TTP	R8	(319)
$\emptyset \leftarrow TTP$	Degradation of unphosphorylated TTP	R9	(319)

$TTP \xrightarrow{p38_P} TTP_P$	Phospho-p38 MAPK-mediated TTP phosphorylation	R10	(319)
$\emptyset \leftarrow TTP_P$	Degradation of phosphorylated TTP	R11	(319)
$TTP \leftarrow TTP_P$	TTP dephosphorylation	R12	(319)
$\emptyset \xrightarrow{p38_P} RNA_m$	p38 MAPK-dependent synthesis of TNF_m	R13	(319)
$\emptyset \leftarrow RNA_m$	TTP-independent degradation of TNF_m	R14	(319)
$\emptyset \underset{TTP}{\longleftarrow} RNA_m$	TTP-dependent degradation of TNF_m	R15	(319)

Table 4.6 Parameters of the Tomida p38 MAPK-TTP model.

Parameters			
Symbol	**Description**	**Nominal value**	**Dimension**
φ_{Pp}	Phosphorylation rate of p38 MAPK	0.15	min^{-1}
ρ_{Pp}	Dephosphorylation rate of p38 MAPK	0.16	min^{-1}
k_M	Michaelis Menten constant	0.0001	$a.u.$
γ_D	Synthesis rate of DUSP1 mRNA	0.055	min^{-1}
δ_D	Degradation rate of DUSP1 mRNA	0.05	min^{-1}
γ_D	Synthesis rate of DUSP1	0.2	min^{-1}
δ_D	Degradation rate of DUSP1	0.02	min^{-1}
γ_T	Synthesis rate of TTP	0.18	min^{-1}
δ_T	Degradation rate of TTP	0.023	min^{-1}
φ_T	Phosphorylation rate of TTP	50	min^{-1}
δ_{Tp}	Degradation rate of phosphorylated TTP	0.05	min^{-1}
ρ_{Tp}	Dephosphorylation rate of TTP_P	0.0029	min^{-1}
γ_{Rm}	Synthesis rate of TNF_m	1	min^{-1}

δ_{Rm1}	Degradation rate 1 TNF_m	0.005	min^{-1}
δ_{Rm2}	Degradation rate 2 TNF_m	10	min^{-1}

Simulation of the equations (4.5) to (4.11) and parameters from Table 4.6, using the *ode23* solver in MATLAB, are shown in Figure 4.5. Since we removed MAP2K from the equations, we had to adapt the p38 MAPK phosphorylation rate of the Tomida p38 MAPK model to account for the signal amplification of the stimulus S through MAP2K. The nominal parameters of the TTP core model vary in some instances from the parameters used for the Tomida p38 MAPK model, a change introduced to adjust to the altered p38 MAPK activation dynamics (Table 4.6). The oscillatory activation pattern of p38 MAPK resulted in an initial peak and subsequent oscillations for unphosphorylated TTP, phosphorylated TTP, and TTP-target mRNA. We also included total TTP, which was simulated by adding the variables of unphosphorylated and phosphorylated TTP because the planned time-course microscopy experiments only allowed for the measurement of total TTP. Figure 4.6 shows the multicellular variation of the model (n=50). As before for the non-combined Tomida p38 MAPK model, the mean expression introduced dampened the observability of oscillations for all pathway components.

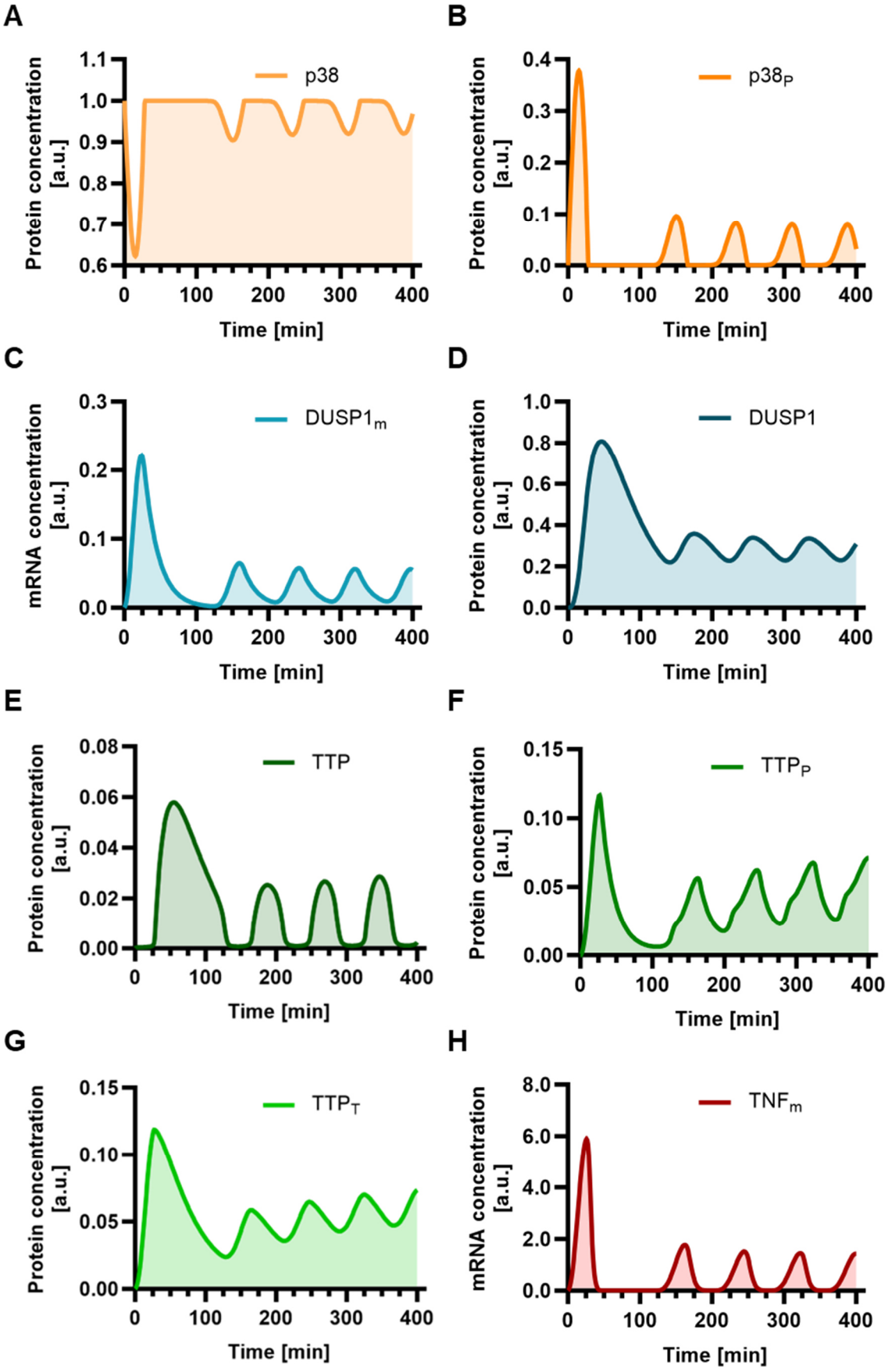

A
p38
Protein concentration [a.u.]
Time [min]
B
p38P
Protein concentration [a.u.]
Time [min]
C
DUSP1m
mRNA concentration [a.u.]
Time [min]
D
DUSP1
Protein concentration [a.u.]
Time [min]
E
TTP
Protein concentration [a.u.]
Time [min]
F
TTPP
Protein concentration [a.u.]
Time [min]
G
TTPT
Protein concentration [a.u.]
Time [min]
H
TNFm
mRNA concentration [a.u.]
Time [min]

Figure 4.5 Computational single-cell simulation of the Tomida p38 MAPK-TTP model.

The data for the simulation of the Tomida p38 MAPK-TTP model was generated in MATLAB using the *ode23* function to solve the ODE equations (4.5) to (4.11) as well as the nominal parameter values and initial conditions shown in Table 4.6 and Table 4.4 for a time span of 400 min. The graphs show the expression change of A) unphosphorylated p38, B) phosphorylated p38, C) *DUSP1* mRNA, D) DUSP1 protein, E) unphosphorylated TTP, F) phosphorylated TTP, G) total TTP, and H) *TNF* mRNA, following treatment with IL-1β in an individual HeLa cell. The full MATLAB script for generating the graphs can be found in Appendix 7.1.

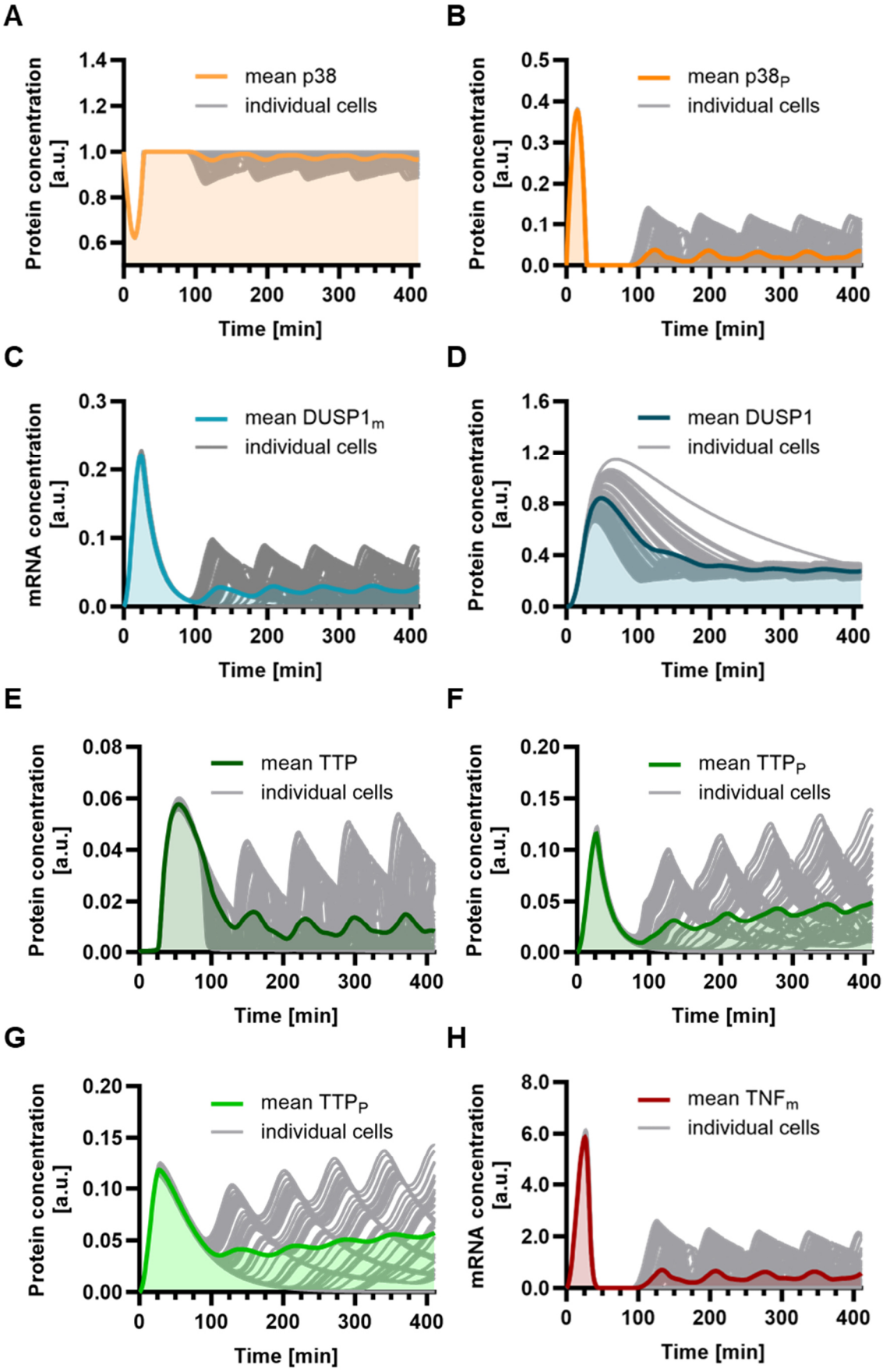

A
Protein concentration [a.u.]
1.4
1.2
1.0
0.8
0.6
mean p38
individual cells
0
100
200
300
400
Time [min]
B
Protein concentration [a.u.]
0.5
0.4
0.3
0.2
0.1
0.0
mean p38P
individual cells
0
100
200
300
400
Time [min]
C
mRNA concentration [a.u.]
0.3
0.2
0.1
0.0
mean DUSP1m
individual cells
0
100
200
300
400
Time [min]
D
Protein concentration [a.u.]
1.6
1.2
0.8
0.4
0.0
mean DUSP1
individual cells
0
100
200
300
400
Time [min]
E
Protein concentration [a.u.]
0.08
0.06
0.04
0.02
0.00
mean TTP
individual cells
0
100
200
300
400
Time [min]
F
Protein concentration [a.u.]
0.20
0.15
0.10
0.05
0.00
mean TTPP
individual cells
0
100
200
300
400
Time [min]
G
Protein concentration [a.u.]
0.20
0.15
0.10
0.05
0.00
mean TTPP
individual cells
0
100
200
300
400
Time [min]
H
mRNA concentration [a.u.]
8.0
6.0
4.0
2.0
0.0
mean TNFm
individual cells
0
100
200
300
400
Time [min]

Figure 4.6 Computational multicellular simulation of the Tomida p38 MAPK-TTP model.

The data for the multicellular simulation of the Tomida p38 MAPK-TTP model was generated in MATLAB using the *ode23* function to solve the ODE equations (4.5) to (4.11) as well as the nominal parameter values and initial conditions shown in Table 4.6 and Table 4.4 for a time span of 400 min with randomised DUSP1 degradation rate. The graphs show the expression change of A) unphosphorylated p38, B) phosphorylated p38, C) *DUSP1* mRNA, D) DUSP1 protein, E) unphosphorylated TTP, F) phosphorylated TTP, G) total TTP, H) *TNF* mRNA, following treatment with IL-1β within multiple (n=50) individual HeLa cells (grey), together with the mean expression levels (coloured). The full MATLAB script for generating the graphs can be found in Appendix 7.1.

4.2.4 Comparison of the Tomida and Kulawik p38 MAPK-TTP models

Figure 4.7 shows the computational simulation of $p38_P$, DUSP1, TTP, TTP_P, and TNF_m using the Tomida p38 MAPK-TTP model (Equations (4.5) to (4.11), Table 4.6), the calibrated Kulawik p38 MAPK-TTP model (Equations (3.14) to (3.19), Table 3.13, Table 3.15) and the WT BMDM data set. Unphosphorylated p38 MAPK expression is not shown as it does not convey additional information for the comparison. As described in previous chapters, the model simulation data was generated in MATLAB using the *ode23* solver. The main differences between the Tomida and Kulawik models are, of course, the oscillations. For the comparison, we focused on the qualitative behaviour of the models and, specifically, the peaks of the Tomida model. As the presented Tomida model displays the simulation of a single cell, it is interesting to analyse the behaviour of oscillating peaks and interpret how millions of cells, measured in the BMDM data, demonstrating heterogenous oscillating behaviour, could lead to such measurements. For phosphorylated p38 MAPK, the peaks of the Tomida-based model followed the expression dynamics of the WT BMDM data, forming the classical peak and extrapolated to millions of cells, the plateau phase patterns (Figure 4.7 A). For DUSP1, the Tomida model covered the expression profile of the BMDMs better than the Kulawik model, as this model only covered the plateau phase (Figure 4.7 B). Also, the expression dynamics of unphosphorylated TTP were covered by the Tomida model, which captured the initial peak and

the plateau phase with its oscillation peaks quite like the readout of $p38_p$. The Kulawik model did not cover the initial peak but followed the overall expression levels of the plateau phase in WT BMDMs, albeit in the form of an asymptotic rise (Figure 4.7 C). The Tomida model bore some resemblance, with the initial peak and rising pattern for phosphorylated TTP. However, the BMDM data displayed a decline later during the measurements, which the model did not capture. The Kulawik model also did not capture this behaviour. It displayed a gradual increase and did not cover the initial peak (Figure 4.7 D). The *Tnf* mRNA simulation of the Tomida-based model followed the initial peak and gradual decline. This pattern did not cover all data dynamics, precisely not the double peak followed by a gradual biphasic decrease over the period. The double peak and biphasic decline were also not covered by the Kulawik-based model; however, the gradual decline is also represented (Figure 4.7 E).

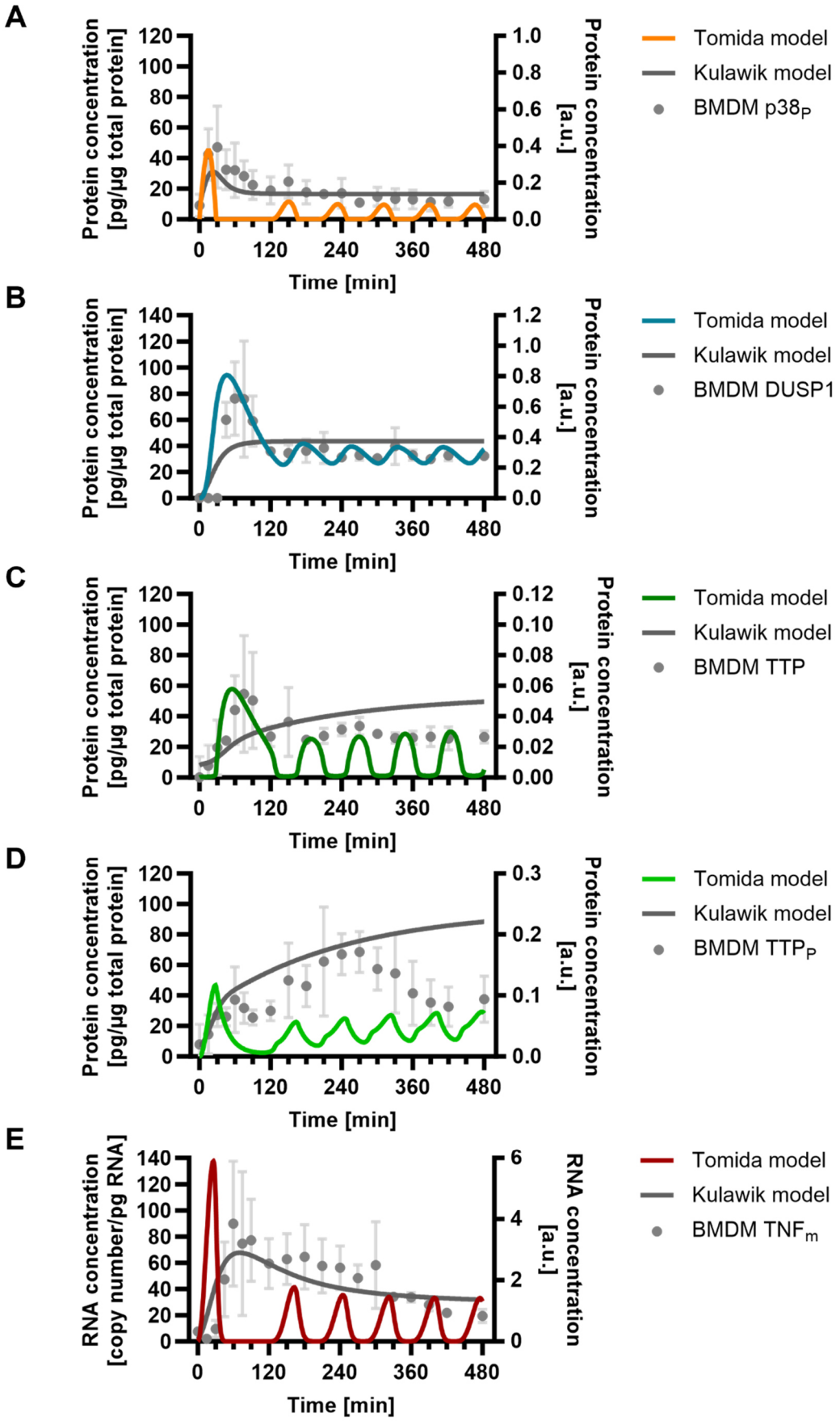

A
Protein concentration [pg/µg total protein]
Protein concentration [a.u.]
Time [min]
Tomida model
Kulawik model
BMDM p38P
B
Protein concentration [pg/µg total protein]
Protein concentration [a.u.]
Time [min]
Tomida model
Kulawik model
BMDM DUSP1
C
Protein concentration [pg/µg total protein]
Protein concentration [a.u.]
Time [min]
Tomida model
Kulawik model
BMDM TTP
D
Protein concentration [pg/µg total protein]
Protein concentration [a.u.]
Time [min]
Tomida model
Kulawik model
BMDM TTPP
E
RNA concentration [copy number/pg RNA]
RNA concentration [a.u.]
Time [min]
Tomida model
Kulawik model
BMDM TNFm

Figure 4.7 Computational simulation of LPS-treated WT BMDMs using the nominal Tomida and calibrated Kulawik p38 MAPK-TTP model.

The data for the simulation of the Kulawik p38 MAPK-TTP model was generated in MATLAB, solving the ODE equations (3.14) to (3.19) as well as the estimated parameter values and initial conditions in Table 3.13 and supplementary Table 7.1 for a time span of 480 min. The data for the simulation of the Tomida p38 MAPK-TTP model of a single cell was generated in MATLAB, solving the ODE equations (4.5) to (4.11) as well as the nominal parameter values and initial conditions in Table 4.4 and Table 4.6 for a time span of 480 min. The graphs show the Tomida and Kulawik model simulations of A) phosphorylated p38 MAPK, B) DUSP1, C) unphosphorylated TTP, D) phosphorylated TTP, and E) *Tnf* mRNA together with the WT BMDM experimental data, presented in Chapter 3.4.1, as mean and standard deviation. The full MATLAB script for generating of the simulated data can be found in Appendix 7.1.

4.3 Establishing microscopy reporter cell lines

To investigate TTP activity dynamics in single cells, we produced mNeonGreen-tagged TTP and TTP mutants for Doxycycline-dependent overexpression as well as mRuby2-tagged kinase translocation and colocalisation reporters in the HeLa cell line. In this chapter, the reasoning behind these constructs and how the reporter cell lines were established will be described.

4.3.1 Experimental design of cloning

The initial goal of the experimental design process was to identify a way to measure p38 MAPK and TTP activity in individual living cells to obtain data for validating the Tomida p38 MAPK-TTP model. Taking inspiration from the methods applied by Tomida et al., we decided to use fluorescent reporter constructs for live-cell microscopy. As a delivery method for the constructs, we chose lentiviral transduction, which enabled easier experimentation due to the non-transient nature of overexpression. We chose HeLa cells as the target cell line since these are commonly used TTP model cells, easy to transduce, and, due to their size, easy to image.

To measure p38 MAPK activity, we decided to use p38 MAPK-specific KTRs, which allow measurements of their activity through changes in their subcellular localisation. We obtained a p38 MAPK KTR generated by Regot et al. (357,358) through Addgene. However, we could not transduce cells with these constructs efficiently, likely due to the incompatibility of the lentiviral vector with our packaging plasmids and decided to use an MK2-reporter plasmid instead. MK2 functions as a natural KTR due to its p38 MAPK-mediated translocation from the nucleus to the cytoplasm (111,112). This method has been previously validated by Miura et al. in comparison to other p38 MAPK KTRs.

To visualise TTP activity in live-cell microscopy, during an inflammatory response, through literature research, and based on previous experiments done in our lab, we identified four

potential readouts to visualise TTP activity: 1) Through its subcellular localisation, 2) through the differences in degradation speed between phosphorylated and unphosphorylated TTP, 3) through protein-protein interactions, and 4) through TTP-target degradation. We set out to clone lentivirus-based cellular reporters that would allow us to test the first three prospects and obtain plasmids for the fourth one. Due to challenges in establishing a robust live-cell microscopy protocol, we were delayed in our endeavour and could only address the first approach. Therefore, we will not detail the cloning procedure; we will only briefly mention the concept of the latter three.

We identified potential subcellular localisations that might allow indirect measurement of TTP activity. On the one hand, the activity-dependent cytoplasmic and nuclear shuttling of TTP, which has been reported (191). We also have some preliminary data from our lab suggesting this is the case in HeLa cells (Appendix 7.8). On the other hand, phosphorylation-dependent localisation of TTP to P-bodies has been reported (229,268–270). To identify localisation to the nucleus, we decided to use the live-cell nuclear stain DRAQ5 (far-red) for colocalisation and to observe P-body localisation, we created a mRuby2-labelled DCP1a overexpression reporter, which is commonly used as a P-body marker (268). We also created a reporter construct for the stress-granule marker G3BP1. However, we have not used it for experiments yet and will therefore not mention it further.

As an activity-dependent TTP interaction partner, we chose the scaffolding protein 14-3-3, for which we also created a mRuby2-labelled overexpressor. To measure their interaction, we aimed to use FRET. As for G3BP1, we have not used it for experiments yet and, therefore, will not go into more detail. The last approach would have focused on measuring TTP-target mRNA degradation. This has been described by Horvathova et al. (234), and we obtained their plasmids from Addgene. Again, this approach won't be addressed in this thesis.

We required fluorescently labelled TTP reporters of WT TTP and its AA and EE mutants for the first three approaches. The AA mutant corresponds to the *Zfp36*$^{aa/aa}$ mutant BMDMs, used in the previous chapter (Chapter 3.4.3.2), which exhibits Ser to Ala substitutions (human Ser-60 and Ser-186) that render the mutant non-phosphorylatable at the two most important p38 MAPK-specific phosphorylation sites. In the EE mutant, the same two Ser were replaced with Glu, which is supposed to mimic the negative charge of phosphorylation sites. Regot et al. (357) used Glu as phospho-mimetic control for their p38 MAPK KTR model validation, and Carreño et al. established the TTP EE mutant and showed that it stabilised its target mRNAs (359). Due to the reported cytotoxicity of stable TTP overexpression (215,360), we decided to use a lentiviral vector with a Doxycycline-inducible expression system, as previously used by Tiedje et al. for high throughput transcriptomics and iCLIP experiments (215). We also used their design of the TTP reporter regarding fluorophore positioning and spacer design, which they kindly provided.

4.3.2 Establishing TTP mutant reporter cell lines

To generate human TTP WT, AA, and EE mutant fluorescent reporter constructs for usage in HeLa cells, we transferred the TTP sequence into a plasmid containing the fluorophore mNeonGreen, introduced the amino acid substitutions for the mutants through SDM, and transferred the tagged TTP mutants into a Doxycycline-inducible lentiviral vector system. The cloning scheme is shown in Figure 4.8.

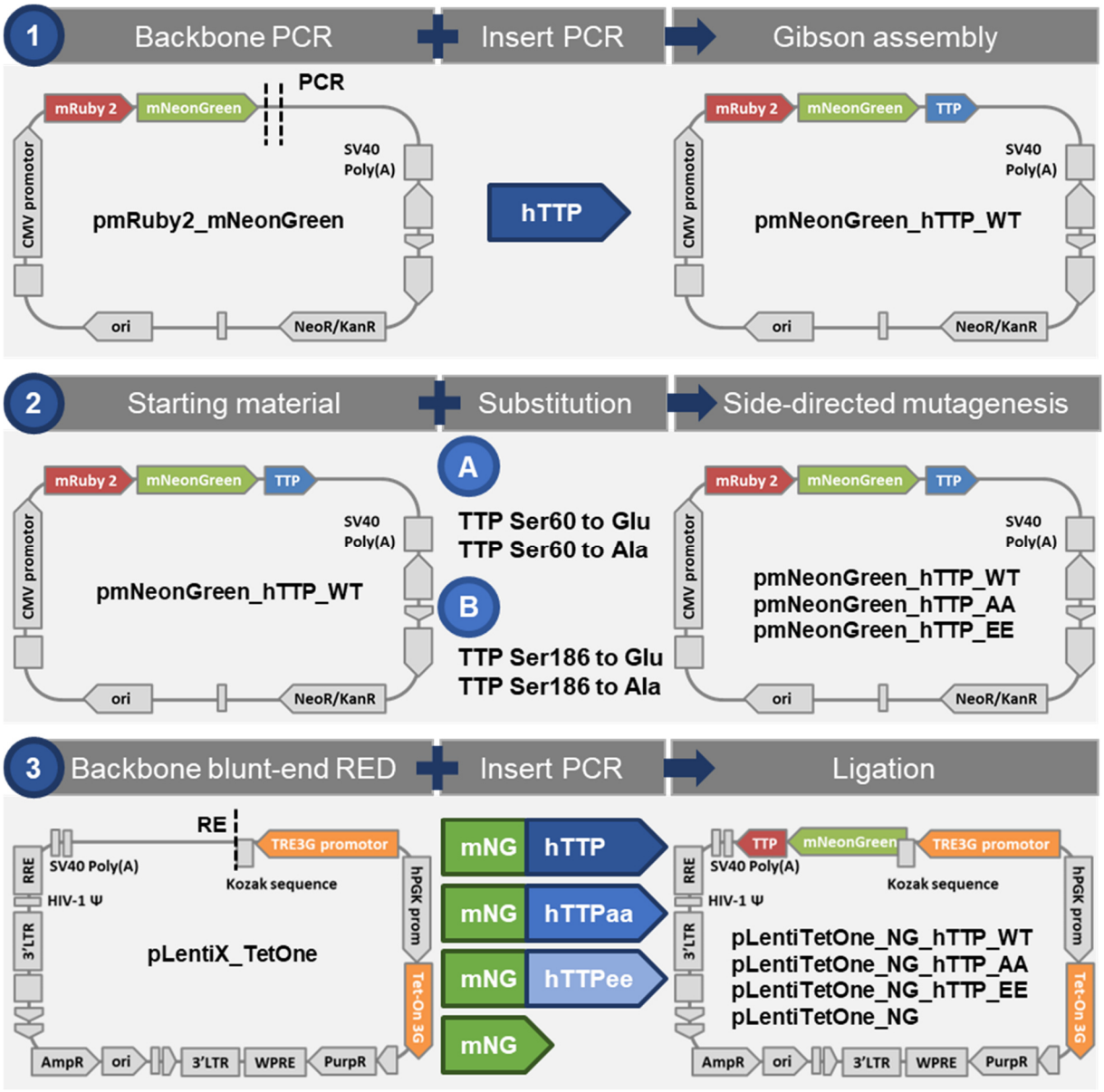


Figure 4.8 Cloning scheme of the TTP mutant reporter constructs for live-cell microscopy.

The graphic summarises the cloning scheme of the TTP mutant reporter constructs. It can be divided into three main steps: (1) Transfer of the hTTP inserts into the backbone pmRuby2_mNeonGreen via Gibson assembly. (2) SDM of hTTP within pmNeonGreen_hTTP by substituting Ser-60 and Ser-186 with alanine for the AA and glutamic acid for the EE mutant in two cloning rounds. (3) Transfer of mNeonGreen labelled hTTP, hTTPaa, hTTPee, and mNeonGreen on its own (control) to the pLentiX_TetOne_Puro lentiviral vector by blunt-end cloning. The plasmids are shown with all their main functional components. For pmRuby2_mNeonGreen this includes a CMV promoter and enhancer for mammalian expression, the fluorophores mRuby2 and mNeonGreen, a Neomycin (NeoR) and Kanamycin (KanR) resistance factor for bacterial selection, SV40 Poly(A) signal, ori and promoter, and ori for plasmid replication. For LentiX_TetOne_Puro this includes the TRE3G promoter, SV40 Poly(A) signal, ori and promoter, Rev response element (RRE), HIV-1ψ, two 3'Long terminal repeats (LTR),

AmpR promoter and signal, ori, lac promoter, WPRE, Puromycin resistance (PuroR), TetOn® 3G, and a hPGK promoter. Of those, WPRE, RRE, 3'LTR, and HIV-1ψ are essential for generating viral particles and TetOn® 3G and the TRE3G promoter for Doxycycline-dependent expression. Abbreviations: hTTP = human TTP, mNG/NG = mNeonGreen, LVX = LentiX, AA/aa = hTTP Ser-60 and Ser-186 alanine substitution, EE/ee = hTTP Ser-60 and Ser-186 glutamic acid substitution.

Human TTP was transferred from plasmid pFRT-TODestFLAGHAhTTP (Addgene) to plasmid pmRuby2-mNeonGreen using Gibson assembly. The PCR amplification of the mNeonGreen backbone plasmid and the TTP insert PCR were controlled via agarose gel electrophoresis, as shown in Figure 4.9. The successful PCR amplifications resulted in an individual band around the correct size (hTTP 0.98 kB, backbone 5.38 kB). The resulting plasmids were transformed into competent bacteria and grown on selective plates. For each construct, 3 to 5 colonies were picked, and their DNA was isolated, measured, and sent for Sanger sequencing.

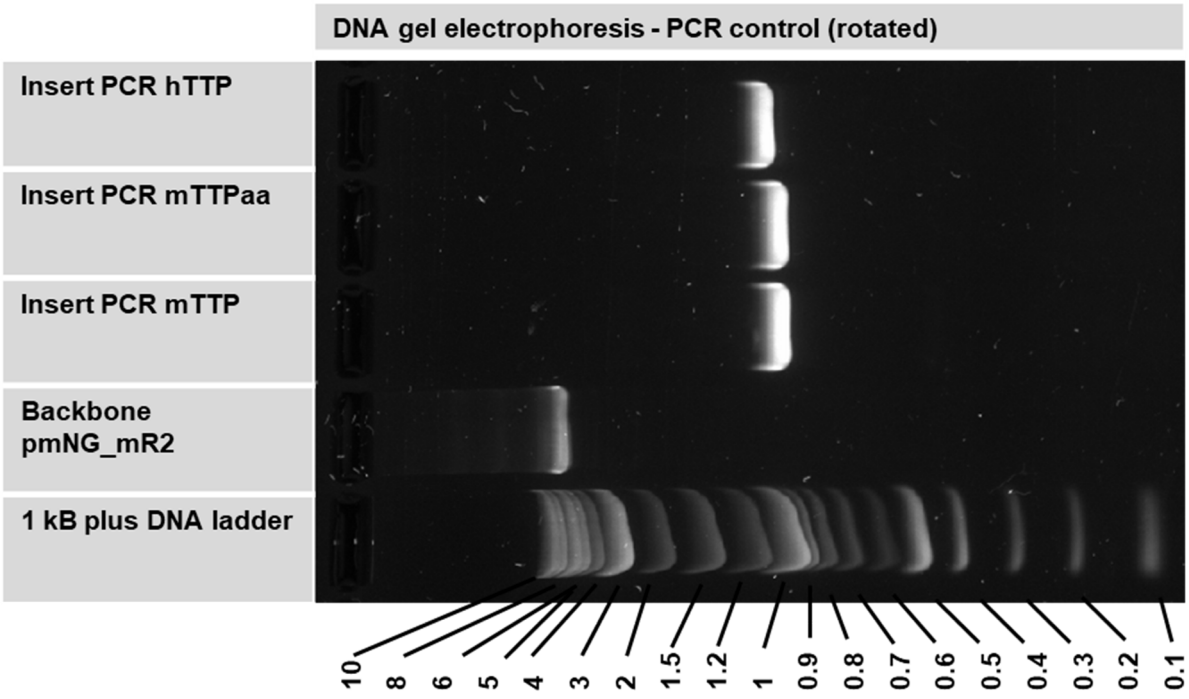


Figure 4.9 DNA gel electrophoresis verifying the correct PCR amplifications of the hTTP insert and the pmRuby2_mNeonGreen backbone for Gibson assembly.

For the transfer of hTTP into the pmRuby2_mNeonGreen via Gibson assembly, the insert and the backbone were amplified using PCR. This work step was controlled with DNA gel electrophoresis. The gel shows the labelled 1

kB plus DNA ladder, the PCR product of the pmRuby2_mNeonGreen backbone (5.38 kB), the hTTP wildtype insert (0.98 kB), as well as the murine mTTP and mTTPaa inserts (0.92 kB), the cloning of which was performed at the same time for potential later use.

We then performed SDM of hTTP at position Ser-60 and position Ser-186 from serine to alanine for our AA mutant and to glutamic acid for the EE mutant. The PCR steps were again controlled using agarose gel electrophoresis, which, for the first round of SDM, showed one band each around the expected size (6.4 kB) together with an off-target amplification at 0.4 kB (Figure 4.10). As this off-target amplification was unlikely to contain bacterial resistance factors, we continued with the transformation into bacteria. The resulting construct DNA was isolated and sequenced. The mutations were successfully introduced in two cloning rounds.

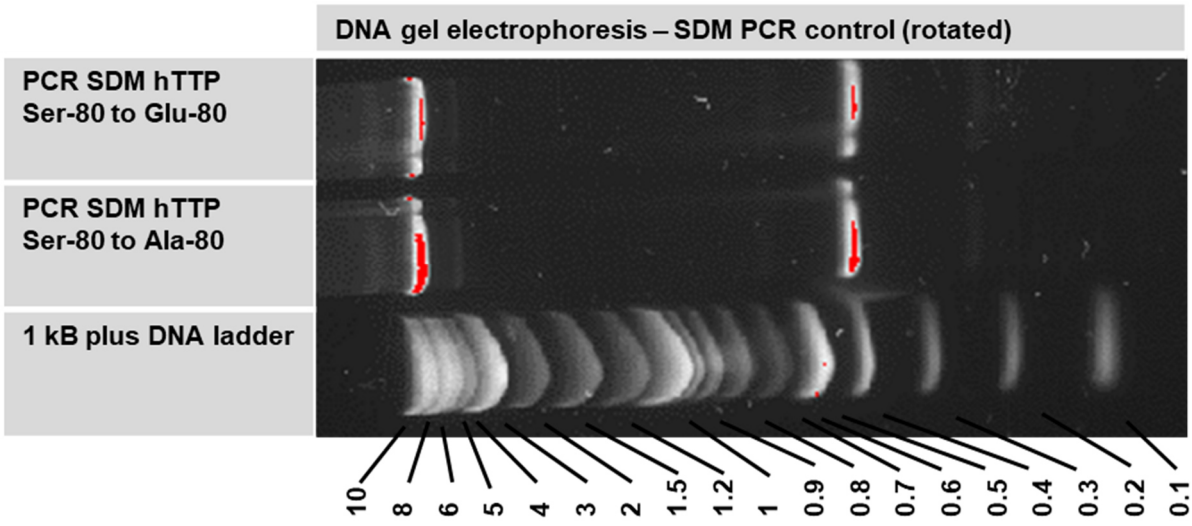


Figure 4.10 Control DNA gel electrophoresis verifying the correct PCR amplifications for SDMs of hTTP at position Ser-80.

For the SDM of hTTP at position Ser-80 from serine to alanine (TTPaa) and glutamic acid (TTPee), the whole plasmid pmNeonGreen_hTTP was amplified via PCR using a specific primer to introduce the substitutions. This work step was controlled by DNA gel electrophoresis. The gel shows the labelled 1 kB plus DNA ladder, the PCR product of the SDM for hTTPaa and hTTPee (6.4 kB). Apart from the expected band, an off-target amplification at 0.4 kB was detected, which did not affect downstream applications.

The next cloning step involved transferring the fluorescently labelled TTP mutant reporters into the Doxycycline-inducible lentiviral vector pLentiX_TetOne_Puro. Lentiviral vectors are large and contain repetitive elements, which makes them difficult for PCR-based methods such as Gibson assembly. Therefore, we used a blunt-end cloning approach. We digested the pLentiX_TetOne_Puro backbone plasmid with the RE BstZ17I-HF, and dephosphorylated it to reduce backbone re-ligation, followed by a DNA clean-up. The inserts were amplified using PCR, and the original plasmids were digested using DpnI, followed by a PCR clean-up and phosphorylation. PCR and digest were again controlled using Agarose gel electrophoresis (example for hTTP see Figure 4.11) (hTTP 0.98 kB, mNeonGreen 0.71 kB, and pLentiX_TetOne_Puro 9.18 kB). The backbone and inserts were ligated and transformed into NEB-Stable bacteria, which allow for better stability of large and sequence-repetitive plasmids. We expected three potential outcomes for blunt-end cloning: Correct insertion, reverse insertion, or backbone re-ligation. Consequently, we performed a diagnostic digest before sequencing to identify constructs with the correct insert. Virtual digests of the correct orientation, inverse orientation, and backbone re-ligation, along with an example diagnostic digest for wildtype hTTP, are shown in Figure 4.12. We picked 10 to 40 colonies to identify the correct inserted constructs. The identified constructs with the correct insertion were then sequenced to control for sequence integrity. Next, we produced lentiviral particles in Hek293T cells, concentrated the viral particles, and transduced HeLa cells to generate stable cell lines using antibiotic selection.

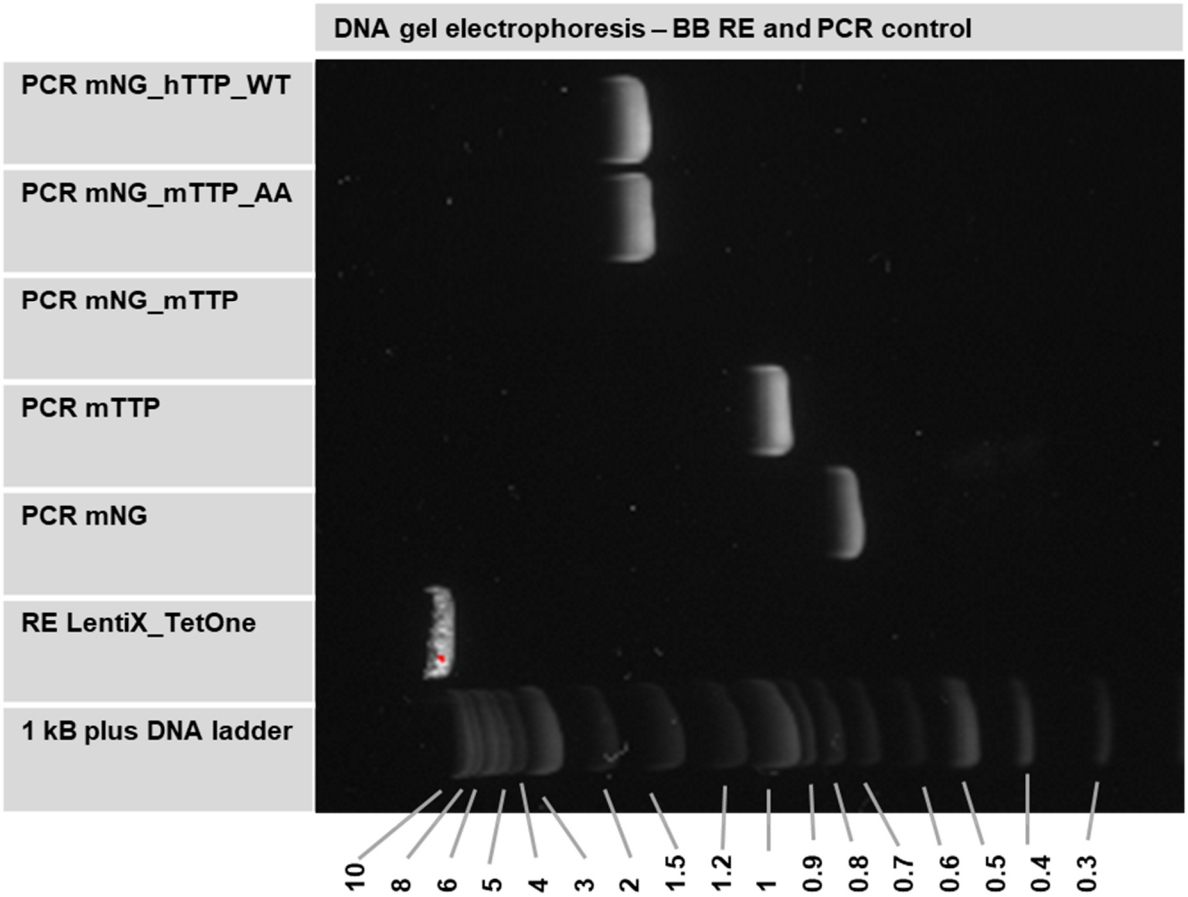


Figure 4.11 Control DNA gel electrophoresis verifying the correct PCR amplifications of the mNeonGreen_hTTP_WT insert and RE digest of the pLentiX_TetOne_Puro backbone for blunt-end ligation.

For the transfer of mNeonGreen_hTTP_WT into the Doxycycline-inducible lentiviral vector pLentiX_TetOne_Puro via blunt-end cloning, the insert was amplified using PCR and the backbone linearised using RE digest. These work steps were controlled with DNA gel electrophoresis. The gel shows the labelled 1 kB plus DNA ladder, the linearised pLentiX_TetOne_Puro backbone, and the PCR products of the mNeonGreen_hTTP_WT (1.69 kB) and mNeonGreen (0.71) inserts as well as the mNeonGreen_mTTP_WT (1.63 kB), mNeonGreen_mTTP_AA (1.63 kB), and mTTP (0.92 kB) inserts, the cloning of which was done at the same time for potential later use.

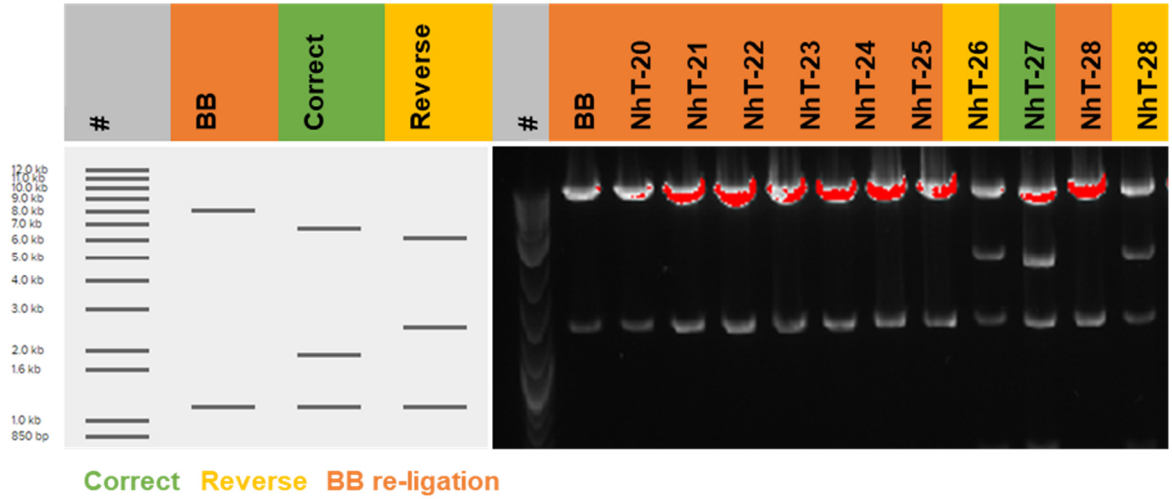


Figure 4.12 Example diagnostic RE digests of the newly generated construct pLentiX_TetOne_mNG_hTTP_WT to identify bacterial colonies with the correct insert orientation following blunt-end cloning.

The TTP reporter plasmid pLentiX_TetOne_mNG_hTTP_WT was generated using blunt-end cloning, transformed into NEB-Stable competent bacteria, and grown on selective agar plates. The grown colonies were picked and grown in a selective LB medium overnight, and the DNA was isolated via Miniprep. The isolated DNA was then digested with the RE NcoI to create a specific pattern to identify the correct insert orientation. The virtual digests were performed on the online cloning platform Benchling and showed the expected patterns for a backbone (BB) re-ligation (orange), a correct (green), and a reverse insertion (yellow) of the amplified insert. The right-hand side of the image displays example diagnostic digests of the colonies 20 to 28 of the insert mNeonGreen_hTTP_WT (NhT) and the backbone pLentiX_TetOne_Puro ligation. The correct insertion was confirmed after, by Sanger sequencing.

4.3.3 Establishment of KTR and TTP-colocalisation reporters

The P-body marker DCP1a and the KTR MK2 were tagged with the fluorescent protein mRuby2 using Gibson assembly and transferred in the overexpressor lentiviral vector pWPI-IRES-Bla-Ak via blunt-end cloning. The cloning scheme is shown in Figure 4.13 and follows the same principles described above (Chapter 4.3.2). The agarose gels and diagnostic digests can be found in Appendix 7.6. The newly generated constructs pWPI_mRuby2_DCP1a and pWPI_mRuby2_MK2 were used to produce lentiviral particles, which were concentrated and utilised for transductions into the already established TTP-reporter cell lines.

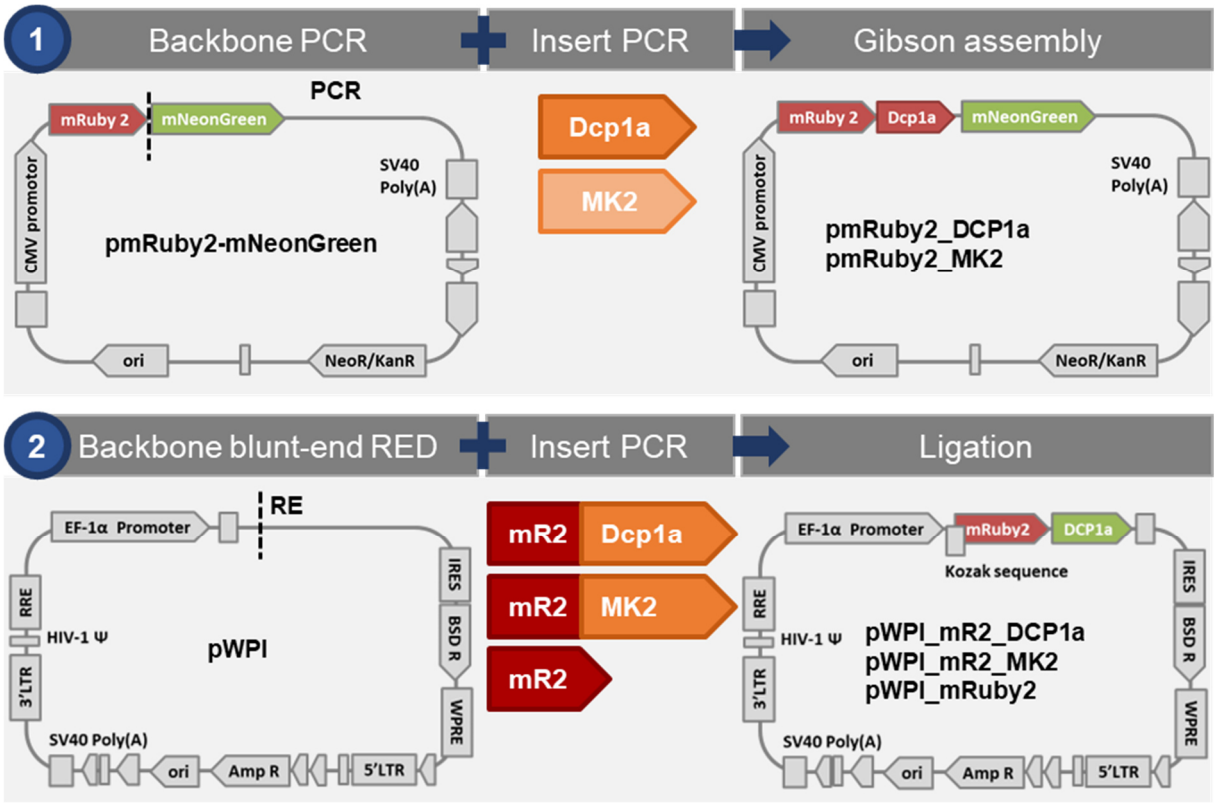


Figure 4.13 Cloning scheme of the DCP1a (P-body) Colocalisation and MK2 KTR reporter constructs for live-cell microscopy.

The graphic summarises the cloning schemes of the DCP1a (P-body) colocalisation and MK2 KTR reporter constructs. The approach can be divided into two main steps: (1) Transfer of the DCP1a and MK2 inserts into the pmRuby2_mNeonGreen backbone via Gibson assembly. (2) Transfer of mRuby2 labelled DCP1a and MK2, and mRuby2 on its own (control), to the pWPI-IRES-Bla-Ak lentiviral vector via blunt-end cloning. The plasmids are shown with all their main building elements. For pmRuby2_mNeonGreen this includes a CMV promoter and enhancer for mammalian expression, the fluorophores mRuby2 and mNeonGreen, Neomycin (NeoR) and Kanamycin (KanR) resistance factor for mammalian selection, SV40 Poly(A) signal, ori and promoter, Ampicillin resistance factor (AmpR) and promoter for bacterial selection, and ori for plasmid replication. For pWPI-IRES-Bla-Ak, this includes the Rev response element (RRE), an EF-1α promoter, WPRE, a 5'and 3'Long terminal repeat (LTR) AmpR promoter and signal, ori, SV40 promoter, ori and poly(A) signal, and HIV-1ψ. Of those, WPRE, RRE, 3'LTR, and HIV-1ψ are essential for generating viral particles. Abbreviations: hTTP= human TTP, mNG/NG= mNeonGreen, LVX=LentiX, AA/aa= hTTP Ser60 and Ser-186 alanine substitution, EE/ee= hTTP Ser-60 and Ser-186 glutamic acid substitution.

4.4 Microscopy setup and time-course experiments

4.4.1 Experimental design live-cell microscopy

Once the TTP reporter cell lines were established, we started with setting up the microscopy experiments. We first identified the correct dosage and timing of Doxycycline for TTP induction using WB. Figure 4.14 displays a time-course of TetOne_mNG-TTP HeLa cells stimulated with different concentrations of Doxycycline (100 ng/mL, 500 ng/mL, 1000 ng/mL) over a period of 24 h. In contrast to Tiedje et al., we did not observe a plateau in expression after 4 h (215). Instead, the expression of the reporter continued to increase for the whole 24 h period. Also, the expression levels after 4 h were only increased 1.6-fold compared to untreated cells, potentially not enough for successful microscopy. Longer Doxycycline stimulations (5-9 h) would have led to difficult working hour scheduling. Therefore, we decided to employ a 24 h stimulation period. The results suggested that the strongest induction of TTP expression was reached at 1000 ng/mL, which might not be the maximum of expression one could induce, but preliminary microscopy suggested that adequate signals were reached and the stimulation is in line with the concentrations used by Tiedje et al. (215).

For the live-cell microscopy experiments, we chose specific imaging slides that allow for the growth and staining of cells in small volumes directly on the slides. We decided to use the live-cell nuclear stain Draq5 in far-red for our live-cell experiment, as this fluorescent spectrum was unused and would allow more flexibility for introducing additional reporter constructs and cell stains in the future.

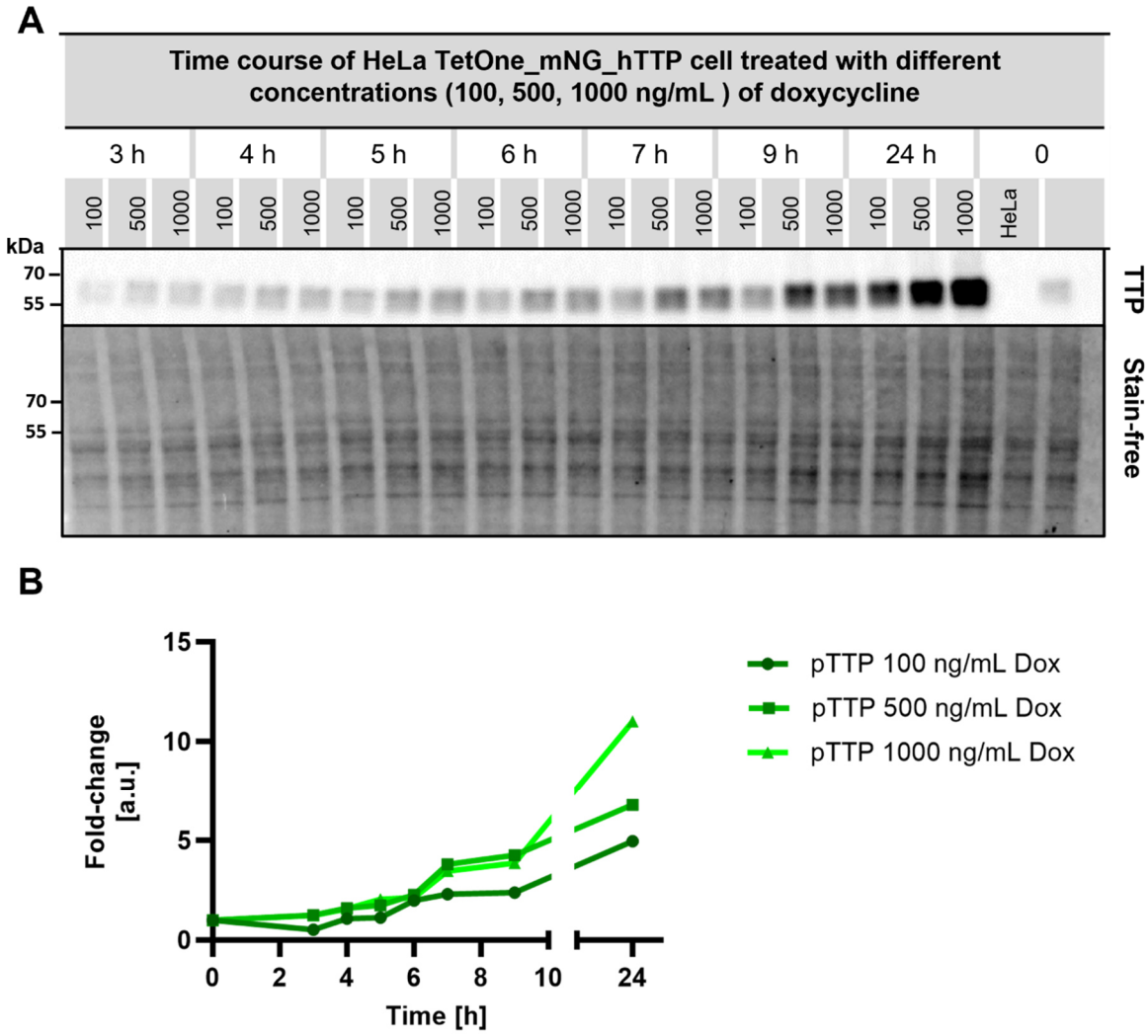


Figure 4.14 Time-course of Doxycycline treated TetOne_hTTP_WT HeLa cells.

TetOne_hTTP_WT HeLa cells were treated with varying concentrations of Doxycycline (Dox, 100 ng/mL, 500 ng/mL, and 1000 ng/mL) over a period of 24 h. The lysates of the cells at 8 different time points were harvested, and the TTP protein concentration was measured by WB. For normalisation, total protein measurements were obtained through the Stain-Free signal of the blot. A) shows the Western blot of TTP with the respective Stain-Free image used for normalisation, which was quantified using Image Lab software and is displayed as a fold-change of the adjusted total band volume in B) (n=1) displays the fold-change over untreated TetOne_hTTP_WT HeLa cells. No statistics were performed.

We initially used a confocal microscope to set up the experiments (LSM780) in the imaging suite of the Institute of Biomedical Research A preliminary experiment of TetOne_mNG-TTP HeLa, stimulated with 1000 ng/mL Doxycycline for 24h and 30 ng/mL IL-1β, demonstrated

the accumulation of TTP in foci reminiscent of the patterns formed by P-body or SG-markers in the literature (Figure 4.15 A). However, when this experiment was repeated with cells stimulated with only Doxycycline as controls, seeded on the same imaging slides as the IL-1β stimulated cells, we found the same foci forming in the control (Figure 4.15 B). One of these cells forming speckles even seemed to undergo apoptosis (Figure 4.15 B zoom). Both observations hinted towards a stress-mediated induction of these foci through the imaging process itself rather than them being induced by IL-1β. Consequently, we started with the troubleshooting process to identify the cause. There could be several potential stressors, including photo-toxicity, cell transportation (physical stress and temperature stress) to the IBR imaging suite, potential adverse effects of the nuclear stain Draq5, insufficient CO_2 levels, and evaporation. We optimised transportation, CO_2 levels, and evaporation and repeated the time-course experiment without Draq5 (Figure 4.15 C). Over the time-course TTP was again localised to foci. However, this time, the IL-1β unstimulated control cells did not show TTP localization to foci when imaged before and after the IL-1β time-course experiment. This suggests that Draq5 induced the foci formation in the control cells in the previous experiment. However, we still had not confirmed, if phototoxicity might play a role in foci formation observed during the live-cell microscopy experiment. Phototoxicity during live-cell microscopy is thought to be in large parts mediated through light-induced ROS production (361). ROS production and the associated oxidative stress are a known activator of p38 MAPK activation and stress granule formation (362). To evaluate whether phototoxicity induces the foci, we decided to perform a time-course experiment with fixed cells. Unfortunately, this was the point where we ran out of time and were not able to perform further live-cell microscopy with the adjusted settings. Major hurdles here were the reduced access to the imaging facilities because of the COVID-19 pandemic measures, as well as frequent breakdowns of the confocal

microscopes. We, therefore, decided to expand the fixed-cell microscopy experiment also to include the TTP mutants AA and EE, the P-body marker DCP1a and the KTR MK2, which will be shown in the next section.

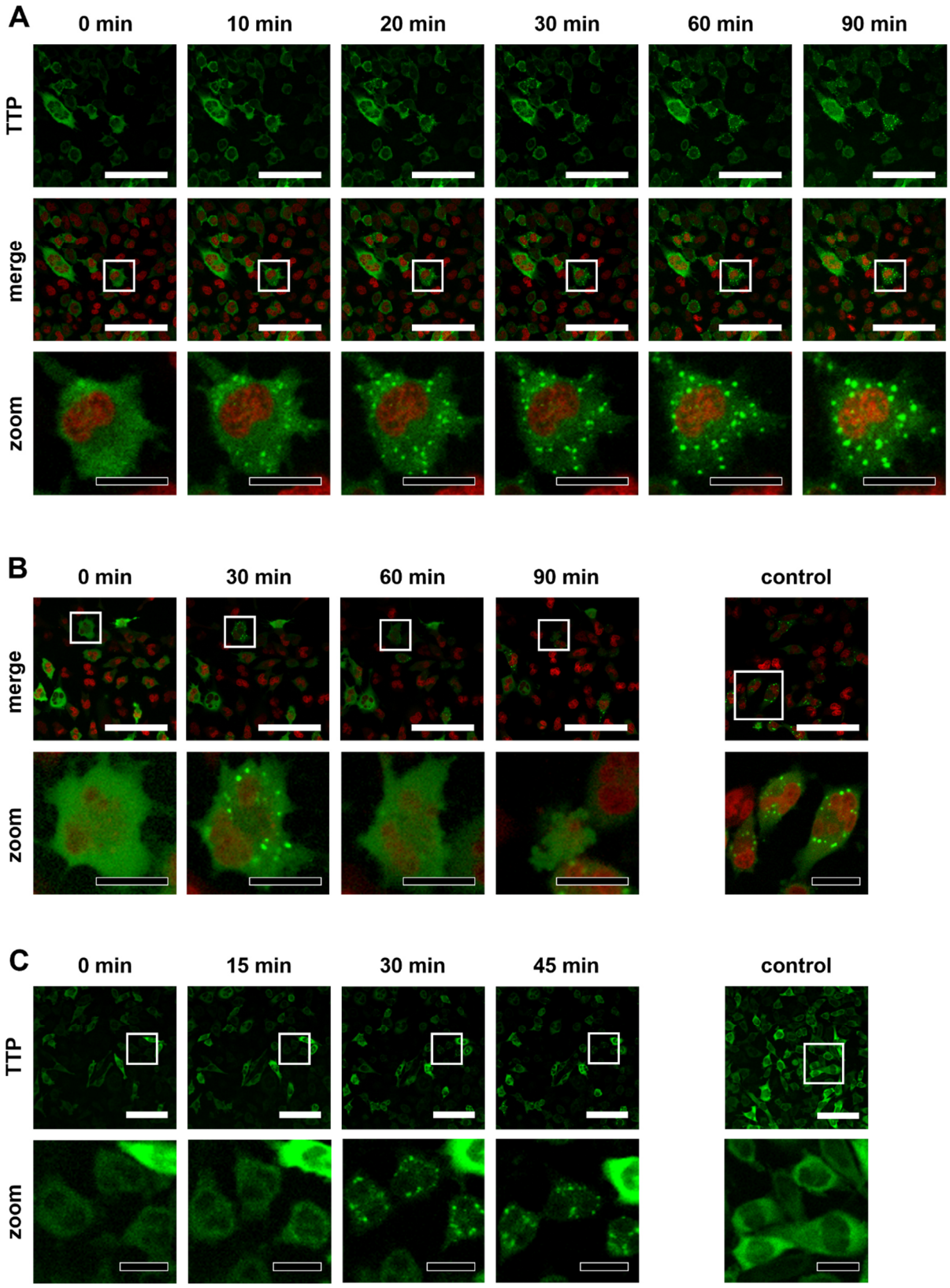


Figure 4.15 Time-lapse analysis of TetOne_mNG_hTTP_WT HeLa cells stimulated with IL-1β.

TetOne_hTTP_WT HeLa cells were seeded in imaging slides and treated for 24h with 1000 ng/mL of Doxycycline and 30 ng/mL IL-1β. TTP (green) expression was assessed using time-lapse microscopy. For A) and B), the cells were further stained with Draq5 (red), functioning as a nuclear counterstain, for 1 h prior to imaging. A) Representative images of a preliminary live-cell microscopy experiment of TetOne_mNG_hTTP_WT HeLa cells stained with Draq5 with pictures taken every 5 min for 105 min. The images show TTP alone, Draq5 and TTP combined, and the magnification of an individual cell. B) Representative images of a live-cell microscopy experiment of TetOne_mNG_hTTP_WT HeLa cells stained with Dragq5. Images were taken every 5 min for the first 40 min and afterwards every 10 min for up to 100 min. In addition, control images of IL-1β unstimulated cells, seeded on the same imaging slides, were taken after the time-lapse experiment. C) Representative images of a live-cell microscopy experiment of TetOne_mNG_hTTP_WT HeLa cells without Draq5 nuclear staining with images taken for 45 min. The control shows IL-1β unstimulated cells seeded on the same imaging slides imaged after the time-lapse experiment. The white box represents a region of magnification. White bar: 100 µm, black bar: 20 µm.

4.4.2 Microscopy experiments of fixed HeLa-TTP reporters

As presented in the previous chapter (Chapter 4.5.2.1), we were not confident whether the changes observed in the live-cell microscopy preliminary experiments were due to the inflammatory stimulus treatment or environmental stressors introduced through the microscopy procedure. The fixed-cell microscopy experiments aimed to explore TTP subcellular behaviour throughout the early inflammatory response, removing all potential cell stressors. As such, a time-course experiment with HeLa-TTP reporter cells co-expressing either DCP1a or MK2 was set up. For DCP1a, apart from WT TTP, the AA and EE mutants were included. The cells were seeded on imaging dishes and treated with 1000 ng/µg Doxycycline, 24h prior to 30 ng/mL IL-1β stimulation, to ensure sufficient TTP expression. After an IL-1β time-course treatment (DCP1a: 0 min, 10 min, 30 min, 60 min, 120 min, 240 min, 360 min, 480 min; MK2: 0 min, 10 min, 30 min, 60 min), the cells were fixed and stained with either Draq5 (counterstain nucleus, DCP1a experiment) or DAPI (counterstain nucleus, MK2 experiment). The cells were then imaged using an LSM780 confocal microscope, with at least four images taken per condition.

We also used these experiments to set up and evaluate an automated image analysis approach in Python, which is needed due to the large dataset that was produced.

4.4.2.1 Microscopy of HeLa-TTP reporter cells co-expressing DCP1a

Figure 4.16 displays representative images of fixed HeLa-TTP WT, AA, and EE reporter cells prior to IL-1β stimulation. Shown are cropped images (for clarity) of the TTP channel, the DCP1a channel, the merged channels, and zoom for an individual cell. Cells overexpressing DCP1a formed P-bodies as described by the literature (268). DCP1a formed P-bodies colocalised with TTP-foci in all three TTP species, with varying intensity.

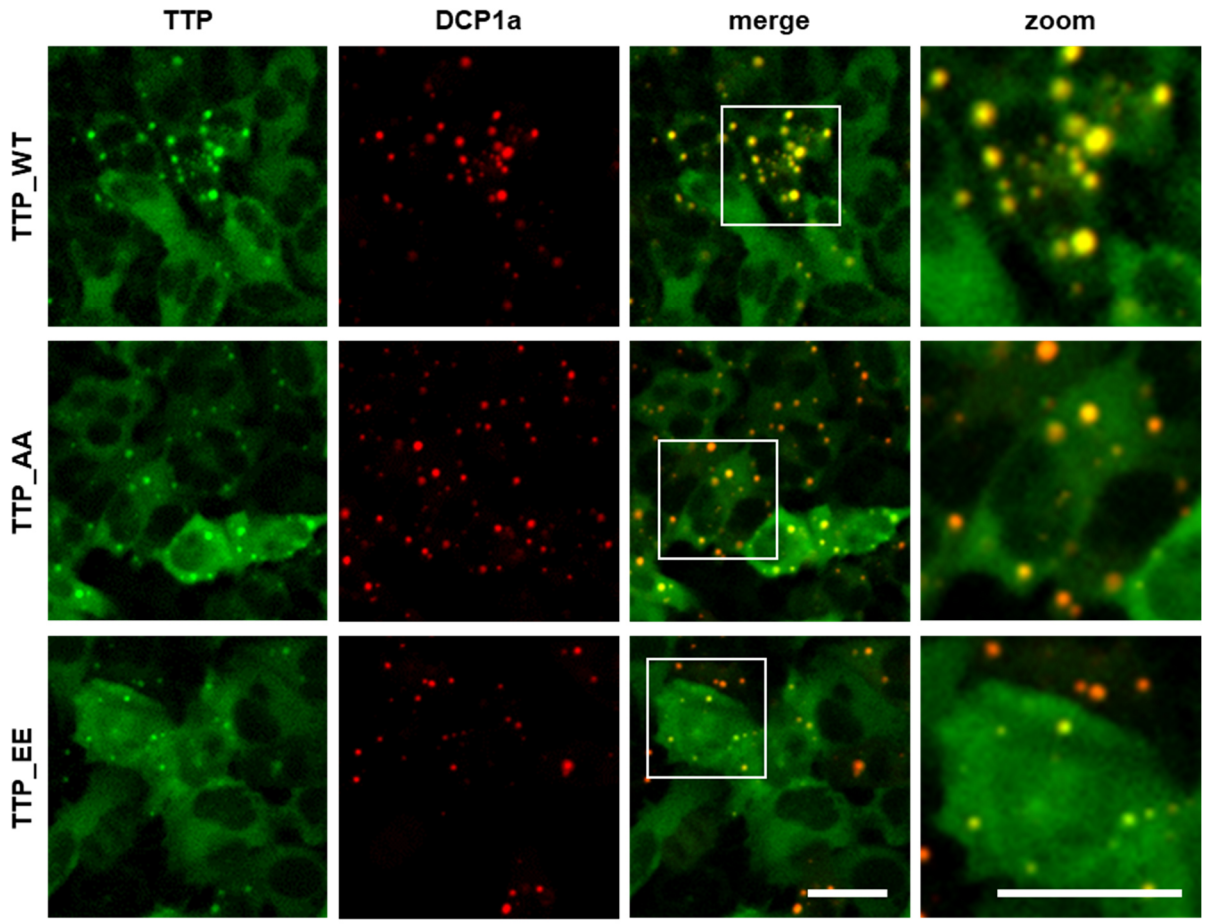
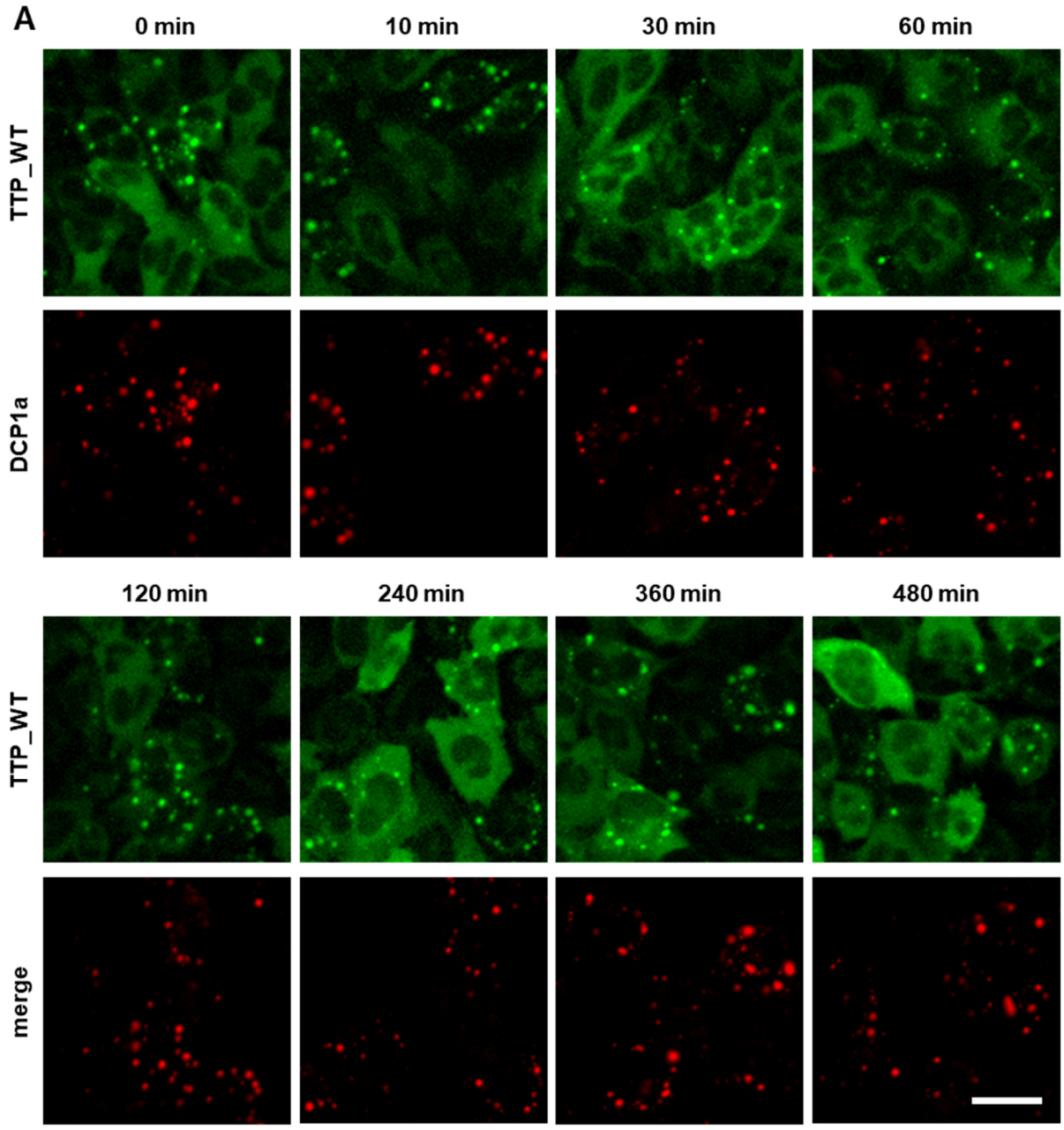


Figure 4.16 Representative images of fixed TetOne_mNG_hTTP_WT/AA/EE HeLa cells co-expressing mR2_DCP1a.

TetOne_hTTP_WT/AA/EE HeLa cells were seeded in imaging slides and treated for 24h with 1000 ng/mL of Doxycycline. TTP (green) and DCP1a (red) expression were assessed using confocal microscopy. After fixation, the cells were also stained with DRAQ5 nuclear stain (not shown for clarity). The representative images show cropped images for TTP and DCP1a alone; both merged and the magnification of an individual cell. The white box represents the region of magnification. White bar: 20 μm.

Figure 4.17 A shows representative images of the fixed-cell HeLa_TTP_WT reporter time-course experiment. TTP co-localised with P-bodies in both untreated and IL-1β stimulated cells. As we did not select cells after the transduction of HeLa-TTP reporter cells with the DCP1a reporter, we observed a heterogeneous population, with some of the HeLa-TTP reporter cells not expressing DCP1a. We did not identify TTP-positive cells forming foci without the induction of P-bodies by DCP1a. We did not observe changes in the localisation of TTP to P-bodies, and the protein was located primarily in the cytoplasm throughout the time-course.

Figure 4.17 B shows the cytoplasm to P-body (C/P) ratio throughout the experiment for TTP WT, AA, and EE reporter cells. At the start of the time-course, a slight increase in the ratio was observed in all reporters. However, whether this was an actual change requires further experiments and proper validation of the analysis methods. The C/P ratio was similar between the TTP mutant variations.


A
0 min
10 min
30 min
60 min
TTP_WT
DCP1a
120 min
240 min
360 min
480 min
TTP_WT
merge

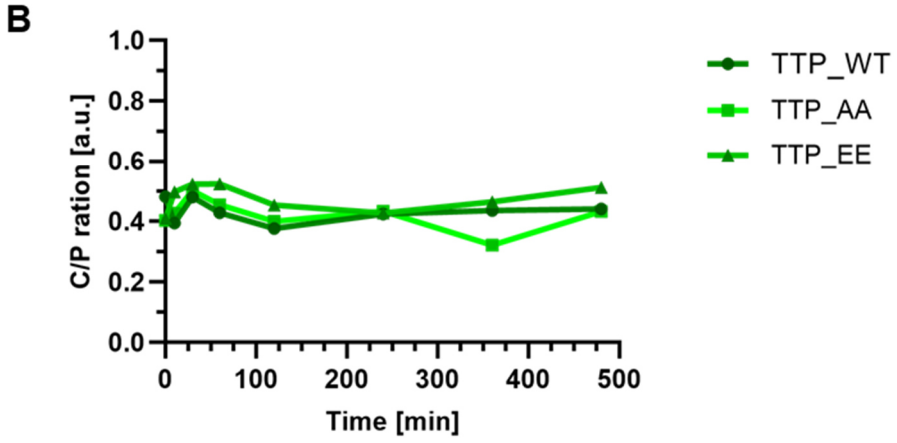

B
C/P ration [a.u.]
1.0
0.8
0.6
0.4
0.2
0.0
0
100
200
300
400
500
Time [min]
TTP_WT
TTP_AA
TTP_EE

Figure 4.17 Time-course experiment of fixed TetOne_mNG_hTTP_WT/AA/EE HeLa cells co-expressing mR2_DCP1a treated with 30 ng/mL IL-1β.

TetOne_hTTP_WT/AA/EE HeLa cells were seeded in imaging slides and treated for 24h with 1000 ng/mL of Doxycycline and 20 ng/mL IL-1β. TTP (green) and DCP1a (red) expression were assessed using confocal microscopy. After fixation, the cells were also stained with Draq5 nuclear stain (not shown for clarity). A) The representative images of the time-course in TetOne_mNG_hTTP_WT/mR2_Dcp1a HeLa cells show cropped images for TTP and DCP1a expression alone. B) Analysis of time-course microscopy data of the TetOne_hTTP_WT/AA/EE HeLa cells, using the automated Python script. The analysis workflow included tagging the cells using the Cellpose software and creating a P-body mask in ImageJ via thresholding. The figure shows the ratio of the mean fluorescence intensity of TTP in the cytoplasm compared to the mean fluorescence intensity of P-bodies. For each time point, 200 to 900 cells were analysed (n=1). No statistics were performed. White bar: 20 µm.

4.4.2.2 Microscopy of HeLa-TTP reporter cells co-expressing MK2

Figure 4.18 A shows representative images of HeLa_TTP_WT cell reporters, co-expressing MK2 stimulated with IL-1β. The images show the MK2 and TTP channels individually, as well as merged with the nuclear DAPI counterstain. Additionally, a magnification of the merged image is shown. This experiment was performed to detect MK2 translocation from the nucleus to the cytoplasm and to test if we can quantify this translocation using our automated analysis methodology. MK2 was expressed throughout whole cells, with higher concentrations usually localised to the nucleus in both unstimulated and stimulated cells. We did not observe any apparent changes in MK2 localisation throughout the experiment. TTP was expressed primarily in the cytoplasm and did not form foci throughout the time-course.

Figure 4.18 B displays the quantitative evaluation of the microscopy experiment in the form of the cytoplasm to nucleus (C/N) ratio of the mean expression intensity for TTP and MK2. Both did not show strong changes over time. Although the C/N ratio is smaller for MK2 than TTP, it is still smaller than 1 for TTP, suggesting that the concentration of TTP is higher in the nucleus than in the cytoplasm. Looking at the images, this is clearly not the case. Consequently, the analysis method requires improvement.

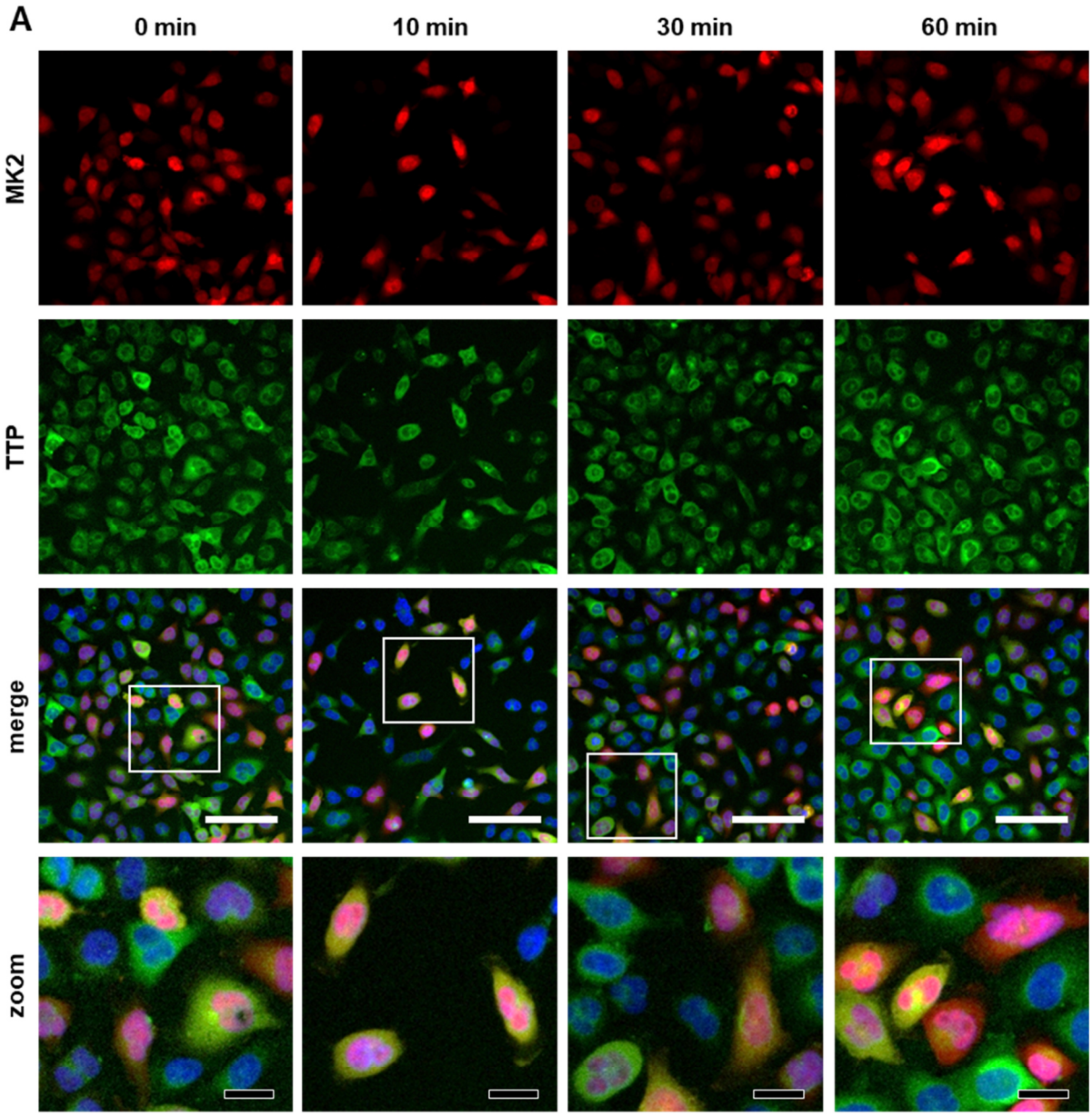

A
0 min
10 min
30 min
60 min
MK2
TTP
merge
zoom
B
C/N ration [a.u.]
1.0
0.8
0.6
0.4
0.2
0.0
0
20
40
60
Time [min]
MK2
TTP

Figure 4.18 Time-course experiment of fixed TetOne_mNG_hTTP_WT HeLa cells co-expressing mR2_MK2 treated with 30 ng/mL IL-1β.

TetOne_hTTP_WT HeLa cells were seeded in imaging slides and treated for 24h with 1000 ng/mL of Doxycycline and 30 ng/mL IL-1β. TTP (green) and MK2 (red) expression were assessed using confocal microscopy. After fixation, the cells were also stained with DAPI for a nuclear stain (blue, merge). A) The representative images of the time-course in TetOne_mNG_hTTP_WT/mR2_MK2 HeLa cells show images for TTP and MK2 expression alone, merged with nuclear counter stain, and the magnification of a group of cells (merged). B) Analysis of time-course microscopy data of the TetOne_hTTP_WT HeLa cells, using the automated Python script. The analysis workflow includes tagging the cells and nuclei using the Cellpose software and creating a cytoplasm mask in ImageJ. The figure shows the mean fluorescence intensity ratio of TTP and MK2 in the cytoplasm compared to the nucleus. For each time point, 100 to 500 cells were analysed (n=1). No statistics were performed. The white box represents the region of magnification. White bar: 100 µm, black bar: 20 µm.

4.5 Discussion

4.5.1 Tomida p38 MAPK-TTP model

In this chapter, we discuss the design of the nominal Tomida p38 MAPK-TTP model and its comparison to the data obtained from WT BMDM and the calibrated Kulawik p38 MAPK-TTP model.

For the Tomida model, we generated two model variations, a single cell and a multicellular one. We created the multicellular one like Tomida et al. by randomising the DUSP1 degradation rate, with the rationale that DUSP1 is phosphorylated by the ERK pathway, which changes DUSP1 stability throughout the inflammatory response and that ERK oscillates asynchronously (347). Tomida et al. proposed that this might add the variations needed to generate the desired cell-to-cell heterogeneity. By doing so, they indeed found a way to simulate heterogenous cells. However, the oscillations within each cell maintain the same strength. Their imaging data (Figure 1.10) shows that the oscillations within individual cells change in peak height during the inflammatory response. Consequently, the varying degradation rate of DUSP1 does not fully cover the observed biological variability, which is more unpredictable and random. Concerning the randomness, it might be interesting to explore if adding randomisation factors to multiple processes within the ODE system would allow for a better simulation of the multicellular model.

Understanding how well the model dynamics cover the BMDM data allowed us to challenge our model assumptions and find ways to improve the model structure, while comparing our two p38 MAPK-TTP models enabled us to identify their strengths and shortcomings. As the Tomida model represents the oscillatory expression in an individual cell, while BMDM data and the Kulawik model are multicellular, we mainly focused on the peaks during oscillations.

For phosphorylated p38 MAPK, the Tomida and Kulawik models fit the data similarly well. Possible avenues for improvement of the Tomida model concerning phosphorylated p38 MAPK include reducing the gap between the first and second peak, adjusting the oscillations in a way that they decline throughout the time-course and adding the constant phosphorylation and dephosphorylation rates we used in the Kulawik model. The adjustments might be achieved by optimising the nominal parameter set. In contrast to the Kulawik model, the Tomida model can simulate the initial peak observed in DUSP1, unphosphorylated TTP and phosphorylated TTP. However, the gradual increase in phosphorylated TTP is currently not covered by the Tomida model. This increase could likely be achieved through a lower degradation rate of phosphorylated TTP to allow its accumulation during the time-course. To cover the subsequent decrease, like for the Kulawik et al. model, one would need to add PP2A as the dependent variable to increase the TTP dephosphorylation rate over time. The sum of the proposed changes above could also be sufficient to change *Tnf* mRNA expression to fit the data better.

4.5.2 Microscopy

4.5.2.1 Live-cell microscopy

During the initial live-cell microscopy experiments, we observed foci formation in HeLa TetOne_mNG_TTP cells in the presence and the absence of an inflammatory stimulus. Spontaneous localisation of overexpressed TTP to foci, specifically SGs, has been reported by Stoecklin et al. (256). They further showed that upon stimulation with arsenite, which induces oxidative stress in a p38 MAPK-dependent manner, TTP dissociated from the SGs (256). We did not see the foci dissipate upon stimulation with the p38 MAPK-activating cytokine IL-1β in our live-cell experiment. Instead, foci formed specifically after starting the imaging process. When we optimised our sample handling, we identified the DRAQ5 nuclear live-cell stain as one of the inducers of foci formation and as a potential inducer of cell death. After removing

DRAQ5 from the imaging process, we did not observe the spontaneous foci formation in the TTP reporter cells outside of the live-cell microscopy imaging process. In live-cell microscopy, counter-stains of the nucleus and cytoplasm membrane are important for image analysis, especially in our case, where we aim to employ automated large-scale analysis techniques using Cellpose. Alternatives to live-cell stains include fluorescent reporter proteins that localise to these areas of interest and ideally do not affect the p38 MAPK-TTP signalling pathway. Miura et al. used a reporter construct expressing iRFP flanked by two nuclear reporter signals for this purpose, which could be suitable for our purposes (112). Using the same approach but with an NES signal should allow visualisation of the cytoplasm.

The fixed-cell experiments with the MK2-reporter construct further suggested that no foci are formed during an IL-1β induced inflammatory response if no environmental stressors are present. In contrast, in the live-cell microscopy experiment shown in Figure 4.15 C, foci already formed after 30 min. The observation suggests that the foci seen in this microscopy experiment, resulted from phototoxicity rather than IL-1β stimulation. It might be worth further investigating this using the not-yet applied stress-granule marker construct that was also prepared during this work. Limiting phototoxicity could be achieved by two approaches in the environment of the University of Birmingham. The first one involves the AiryScan technology available on the confocal microscope LSM880 in the imaging suite. AiryScan allows faster imaging with reduced laser strength, limiting the exposure time of the cells (363). Another solution would be a switch to LED-based microscopy methods. Here, the Cell Discoverer 7 microscope optimised for large-scale time-lapse microscopy at the Bioscience building is especially interesting. The author received training for this microscope and performed some initial setup experiments. However, we could not perform time-course experiments on the microscope due to access restrictions introduced during the COVID-19 lockdown. For these

experiments, it would have been necessary to validate if TTP expression is high enough for the usage of LEDs and if the resolution is sufficient to measure structures such as P-bodies. Lastly, it is important to note that while the microscope setup allows for stimulus application, this is not straightforward and requires validation and extended training before any experiment can be performed.

4.5.2.2 DCP1a fixed cell experiment

When co-expressing DCP1a in HeLa-TTP cells, we observed P-body-TTP colocalization with all three overexpressors, WT, AA, and EE.

As expected, we observed that DCP1a overexpression nucleates P-bodies. This was previously described, among others, by Kedersha et al. (268). We also observed that TTP localises to these P-bodies in unstimulated cells. This was explored by Qi et al. (269), who also showed that the ratio of TTP-positive P-bodies varies between TTP WT and AA overexpressing reporter cells. However, in our experiments, we were not able to confirm this observation. Neither by comparison with the naked eye nor our automated image analysis strategy did we observe any difference in TTP localisation regarding P-bodies between TTP_WT, TTP_AA, and TTP_EE mutant in unstimulated cells. Also, upon stimulation with IL-1β, we did not observe any changes over time. In contrast, Qi et al. showed dissociation of TTP from P-bodies upon stimulation with TNF-α in a p38 MAPK-dependent manner (269). As Qi et al. and we used a similar strategy, there is likely an underlying complication with our TTP reporter cells. Therefore, identifying the problem, will be an important next step in our way towards measuring TTP-activity during live-cell microscopy.

4.5.2.3 MK2 fixed cell experiment

We did not observe major changes in MK2 or TTP translocation between the cytoplasm and the nucleus when imaging HeLa-TTP reporter cells co-expressing MK2. Miura et al. showed that MK2 functions as a KTR for p38 MAPK. They measured the C/N ratio of the MK2-based KTR in anisomycin and IL-1β (10 ng/mL) treated HeLa reporter cells and observed a clear change in subcellular localisation over time. This ratio followed the expected peak and plateau patterns of p38 MAPK phosphorylation (112). The MK2-based p38 MAPK KTR is also supported by the scientific literature, which identified the mechanisms behind the p38 MAPK-mediated translocation of MK2 from the nucleus to the cytoplasm (109,110). Our MK2 constructs were validated by sequencing and contained the complete MK2 sequence without mutations. Additionally the construct is designed similarly to the one used by Miura et al. (112). Non-observable translocation initially hints towards issues with the stimulus, IL-1β. However, we confirmed p38 MAPK activation previously by IL-1β stimulation through WB (supplementary Figure 7.40). To exclude experimental error, running a WB alongside the imaging experiments, measuring p38 MAPK phosphorylation, would be a way to validate the stimulation. Transfecting the original MK2-reporter plasmid, obtained from Miura et al. (Addgene), into HeLa cells and testing for translocation could test for unknown mistakes introduced during the cloning process. If we are unable to identify the issue with the MK2-based KTR following the proposed troubleshooting steps, we still have the option to test the original p38 MAPK KTRs used by Regot et al. (357) again, which we have set aside because of transduction issues. To solve this transduction inefficiency, which could be caused by an incompatibility of the lentiviral vector with our packaging plasmids, we could transfer the KTR payload to our pWPI-IRES-Bla-Ak lentiviral vector. Here, an initial transfection experiment,

validating subcellular translocation, should be performed upstream to identify challenges early and save time later.

We also did not observe a translocation of TTP during the inflammatory response. Johnson et al. reported that, in transfected HeLa cells, TTP is primarily localised to the nucleus and co-expression of 14-3-3 increases its cytoplasmic localisation (264). In contrast, Qi et al. found TTP primarily in the cytoplasm in unstimulated HeLa cells transfected with a TTP reporter (269). A previous group member generated imaging data, suggesting that the translocation of TTP from the nucleus to the cytoplasm and vice versa happens in HeLa cells (Appendix 7.8). This suggests that the reporter design might affect the subcellular localisation of TTP. We used the TTP reporter design by Tiedje et al. based on their functional experiments with the construct (215). Comparing our reporter with those used in other microscopy experiments, such as Johnson et al. and Qi et al., might be a good starting point to identify the next steps (264,269).

4.5.2.4 Automated image analysis

The automation of the analysis workflow (compare Chapter 2.3.3)enabled us to analyse the whole data set within several minutes using a single command line in Python. The only hands-on step is the initial thresholding of DCP1a. For automation of this step, however, a reliable method to identify the best thresholding for the whole data set would need to be validated first. Writing and troubleshooting this code in a reasonable time frame was possible due to Chat-GPT 4.0, as the author is not an experienced programmer but self-taught in understanding written code, mainly in MATLAB. The Large Language Model (LLM) was used to generate a starting code for a specific problem and to rewrite the code multiple times for troubleshooting. As a side note, during that, the LLM regularly imagined commands that were not provided or switched the coding language, and the application could not find solutions to problems in the

image analysis strategy. The troubleshooting strategy with the most success, solving various issues, was to break down and process isolated analysis steps.

The DCP1a analysis currently compares the mean signal intensity within P-bodies within TTP-positive cells to the mean signal intensity in the remaining cells using two masks. However, some of the cells are lost during the mask generation process, which makes it challenging to automatically identify which measurements of P-bodies belong to which cytoplasm measurement. A better approach would be to create two masks of foci for DCP1a and TTP individually in each cell and overlap them to precisely measure the difference, which would leave us with the measurement of the ratio of TTP-positive P-bodies per total P-bodies for each cell. This approach is impossible currently due to the varying intensities of TTP expression between individual cells. Because of this varying intensity, we cannot identify a single threshold that manages capturing all P-bodies and no cytoplasm within a picture. A potential solution would be to evaluate individual cells instead of the whole image. This could be done by creating cell masks in Cellpose followed by cropping the individual cells using the x- and y-coordinates of the region of interest of each individual cell. The threshold for the identification of foci would then need to be identified for each cell. However, without automation of this step, this would be a very tedious task.

During the MK2 analysis, we initially received implausible results for the TTP C/N-ratio. The numbers indicated higher concentration in the nucleus, while visual qualitative evaluation suggested otherwise. This is most likely due to the nuclear mask, generated using Cellpose, being too large, measuring parts of the cytoplasm. In addition, generating the cytoplasm mask by cutting out the nucleus ROIs from the whole cell mask results in the loss of multiple cells, which prevents direct comparison between cytoplasm and nuclei in individual cells. As before, this could be solved by cropping for individual cells before measuring the intensities. To

optimise the size of the nuclei, one could adapt the *cellprob_threshold* and *flow_threshold* settings in Cellpose to reduce the size of the mask created. Overall, it will be a good idea and preparation for future experiments to train our own model in Cellpose using the imaging data to optimise the cell and nucleus segmentation for our data.

4.6 Chapter summary

The focus of this chapter was to build a mathematical p38 MAPK-TTP pathway model inspired by a p38 MAPK model published by Tomida et al. to simulate oscillatory activation patterns and establish a toolset to observe these oscillations experimentally. The Tomida p38 MAPK-TTP model was defined as the model components and their interactions summarised as model diagrams, a set of nominal parameter values, and ODEs. The model structure was evaluated by comparing it qualitatively to the BMDM data and the calibrated Kulawik p38 MAPK-TTP model from the previous chapter. Interestingly, the oscillatory Tomida p38 MAPK-TTP model described some features of the BMDM data set qualitatively better than the Kulawik one. We identified potential improvements such as adding a randomisation factor for simulating multiple cells, adding the dependent variable PP2A, and optimising the nominal parameter set in the future.

We then defined the experimental design for establishing live-cell microscopy reporters that might allow quantifying the oscillatory p38 MAPK and TTP activity. We established three human TTP mutant reporter cell lines and the colocalisation/interaction reporters for G3BP1, 14-3-3b, MK2, and DCP1a. Afterwards, we described the experimental design and setup for our live-cell microscopy experiments. Unfortunately, we could not complete these experiments as the imaging process induced foci formation in TTP cells independent of the inflammatory stimuli. Through troubleshooting, we identified the contributing factors and updated the live-cell microscopy strategy but could not progress further due to access restrictions introduced during the COVID-19 pandemic. Instead, we conducted preliminary fixed-cell experiments using TTP-DCP1a and TTP-MK2 reporter cells. We set up an automated image analysis strategy using Python, Cellpose, and ImageJ to analyse the time-course experiments. By setting up the image analysis strategy, a challenge for the live-cell microscopy project is now solved.

In the fixed-cell experiments with IL-1β stimulated HeLa reporter cell lines, we found no changes in subcellular localisation for TTP concerning nuclei and P-bodies or between the TTP phosphorylation mutants TTP_AA and TTP_EE during the inflammatory response. Observing no changes brings up the question if our initial assumptions on TTP behaviour were wrong. However, it is important to remember that this was preliminary experimentation. Therefore, repeating the experiment and excluding experimental errors as potential causes for the absence of change in subcellular localisation will be a crucial next step in our endeavour to measure TTP activity. Nevertheless, we established a valuable toolkit and skillset that brought us closer to our goals.

CHAPTER FIVE

Conclusion

5 Conclusion

In this work, we have established two p38 MAPK-TTP signalling pathway model variations. We calibrated the first one using total quantification data sets from BMDMs and RAW264.7 cells and established the experimental toolset to investigate the other. By combining experimental and mathematical modelling approaches, we changed our and explored the pathway from a new perspective. We showed the first round of the iterative model-building process and proposed the next steps.

For the first model (based on Kulawik et al.), we described the dynamic changes of the model components in BMDMs and RAW264.7 cells during the inflammatory response. We found that the current structure of the model needs to be revised to cover the expression patterns completely and proposed adjustments, which should mitigate the observed discrepancies. When we simulated system perturbations and compared them to respective experimental data, we found that our model structure and identified parameter set were insufficient to simulate these. We demonstrated that DUSP1 is only responsible for a small portion of phospho-p38 MAPK dephosphorylation and, therefore, insufficient as a sole phosphatase in our model. Measuring TTP by WB alone was insufficient to evaluate expression levels of unphosphorylated TTP but might still give insights into its activity pattern. During these experiments, we observed *Tnf* mRNA to likely be primarily regulated through TTP translational inhibition rather than mRNA destabilisation, and because of that, our model is missing a critical variable, namely secreted TNF-α to represent regulation outside of mRNA expression and stability.

Inhibitor experiments with Calyculin A showed that this PP2A inhibitor affects p38 MAPK-phosphorylation and, therefore, is unsuitable for studying the downstream TTP pathway. From

a different perspective our data could support reports that PP2A dephosphorylates p38 MAPK, which would be an interesting addition to our model.

In a comparison, we analysed the expression dynamics between BMDMs and RAW264.7 cells, finding them to vary and that different adjustments to the model structure are needed for the simulation to fit the data. There were also hints of oscillatory activity in the RAW264.7 cell data. As such, adapting the model to include those was identified as a potential way to achieve data coverage.

For the second model (based on Tomida et al.), we captured the effects of oscillatory p38 MAPK activity on the TTP pathway and TTP-target mRNA expression during the inflammatory response. The oscillations in p38 MAPK activity extended to the downstream TTP and Tnf mRNA pathway components. We established the reporter constructs to test the hypothesis and performed a preliminary fixed-cell microscopy time-course experiment. We found no changes in expression levels and subcellular localisation to the nucleus or P-bodies during the inflammatory response and between TTP phosphorylation mutants, in contrast to what is reported in the literature. Since the chosen MK2-based KTR did not perform as expected, we are still establishing a way to measure p38 MAPK and TTP-activity and oscillations in individual cells. We compared the nominal Tomida model with the BMDM data and the Kulawik model simulations and found the Tomida model to fit the data qualitatively. In some respects, it even outperformed the calibrated Kulawik model. We then proposed some adjustments that would enable an even better fit to the data. Consequently, continuing with both models will allow us to explore multiple facets of the p38 MAPK-TTP pathway.

Compared to the extensive regulatory pathways presented in the introduction (Figure 1.4, Figure 1.5, and Figure 1.7), our two p38 MAPK-TTP models only cover the essential

components and interactions. Even the proposed changes will not change the proportion significantly. The reasons for this have been addressed in Chapter 3.2.2 and 3.3. For p38 MAPK specifically, the three-tiered kinase cascade, changes in subcellular localisation, the effects of protein interactions on its stability or activity and the negative feedback loop via TAK1, are not covered. For TTP, we have not included other transcriptional regulators than p38 MAPK, no posttranscriptional regulation through miRNA or itself, no subcellular translocation, and no interaction with 14-3-3 and the mRNA decay machinery. Also, the TTP-mediated degradation of DUSP1 mRNA is not included. Exploring some of these regulatory components systematically would be an interesting future project. Especially, feedback mechanisms of the already included or soon to be included model components would be a good starting point.

Our models currently describe the classical inflammatory response in isolated cells. To bear relevance for clinical work, we would need to extend the models to simulate chronic inflammatory diseases such as RA. One way could be to implement an RA mouse model to obtain data for this purpose. Transferring the model from murine to human cells is essential. Furthermore, implementing optimal design strategies as available in the AMIGO toolbox allows us to directly evaluate potential treatment strategies using our model once we have improved the model structure and parameter sets to fit the BMDM data.

Due to the iterative nature of the modelling process, we could propose the next important steps. For the Kulawik-based model, we will need to adjust our model structure and evaluate different possibilities to simulate the expression dynamics better. Then, we can use the optimal experimental design feature of the AMIGO toolbox to help identify the best set of experiments for the next round of parameter estimation. For the Tomida model, future steps include implementing and testing the proposed adjustments and continuing to set up the live-cell microscopy experiments. An important step is to validate one of the available KTRs and obtain

a nuclear and cytoplasm reporter construct. With this interdisciplinary work, we have combined mathematical and experimental toolkits to improve our knowledge of the p38 MAPK-TTP signalling axis, which is relevant to various inflammatory diseases.

CHAPTER SIX

References

6 References

1. Newton K, Dixit VM. Signaling in Innate Immunity and Inflammation. Cold Spring Harb Perspect Biol [Internet]. 2012 Mar [cited 2024 Jul 23];4(3). Available from: /pmc/articles/PMC3282411/

2. Fullerton JN, Gilroy DW. Resolution of inflammation: a new therapeutic frontier. Nat Rev Drug Discov [Internet]. 2016 Aug 29 [cited 2018 Nov 18];15(8):551–67. Available from: http://www.ncbi.nlm.nih.gov/pubmed/27020098

3. Watanabe S, Alexander M, Misharin A V., Budinger GRS. The role of macrophages in the resolution of inflammation. J Clin Invest [Internet]. 2019 May 5 [cited 2024 Jul 23];129(7):2619. Available from: /pmc/articles/PMC6597225/

4. Murphy K, Weaver C. Janeway's Immunobiology [Internet]. 9th ed. Garland Science; 2016 [cited 2018 Jun 30]. 1–855 p. Available from: https://books.google.de/books/about/Janeway_s_Immunobiology_9th_edition.html?id=GmPLCwAAQBAJ&redir_esc=y

5. Serhan CN, Ward PA, Gilroy DW, Ayoub SS. Fundamentals of Inflammation. [Internet]. Cambridge University Press; 2010 [cited 2018 Nov 19]. 489 p. Available from: https://books.google.co.uk/books/about/Fundamentals_of_Inflammation.html?id=cJq1RMPKEYkC&printsec=frontcover&source=kp_read_button&redir_esc=y#v=onepage&q&f=false

6. Misharin A V., Cuda CM, Saber R, Turner JD, Gierut AK, Kenneth Haines GK, et al. Nonclassical Ly6C(-) monocytes drive the development of inflammatory arthritis in mice. Cell Rep [Internet]. 2014 [cited 2024 Jul 23];9(2):591–604. Available from: https://pubmed.ncbi.nlm.nih.gov/25373902/

7. Scientific Image and Illustration Software | BioRender [Internet]. [cited 2024 Jul 23]. Available from: https://www.biorender.com/

8. Fox S, Rossi AG. Macrophages. Fundam Inflamm [Internet]. 2010 Apr 26 [cited 2024 Jul 23];96–106. Available from: https://www.cambridge.org/core/books/fundamentals-of-inflammation/macrophages/DD001DC11C72017E9967C81503252D8E

9. Wynn TA, Chawla A, Pollard JW. Macrophage biology in development, homeostasis and disease. Nature [Internet]. 2013 Apr 24 [cited 2018 Dec 16];496(7446):445–55. Available from: http://www.ncbi.nlm.nih.gov/pubmed/23619691

10. Takeuchi O, Akira S. Pattern Recognition Receptors and Inflammation. Cell [Internet]. 2010 Mar 19 [cited 2018 Dec 16];140(6):805–20. Available from: http://www.ncbi.nlm.nih.gov/pubmed/20303872

11. Hoeffel G, Ginhoux F. Fetal monocytes and the origins of tissue-resident macrophages. Cell Immunol. 2018 Aug 1;330:5–15.

12. Helft J, Böttcher J, Chakravarty P, Zelenay S, Huotari J, Schraml BU, et al. GM-CSF Mouse Bone Marrow Cultures Comprise a Heterogeneous Population of CD11c(+)MHCII(+) Macrophages and Dendritic Cells. Immunity [Internet]. 2015 Jun 16 [cited 2024 Jul 23];42(6):1197–211. Available from: https://pubmed.ncbi.nlm.nih.gov/26084029/

13. Italiani P, Boraschi D. From monocytes to M1/M2 macrophages: Phenotypical vs. functional differentiation. Front Immunol. 2014 Oct 17;5(OCT):116283.

14. Haubruck P, Pinto MM, Moradi B, Little CB, Gentek R. Monocytes, Macrophages, and Their Potential Niches in Synovial Joints – Therapeutic Targets in Post-Traumatic Osteoarthritis? Front Immunol [Internet]. 2021 Nov 4 [cited 2024 Jul 23];12. Available from: /pmc/articles/PMC8600114/

15. Paolicelli RC, Bolasco G, Pagani F, Maggi L, Scianni M, Panzanelli P, et al. Synaptic pruning by microglia is necessary for normal brain development. Science [Internet]. 2011 Sep 9 [cited 2024 Jul 23];333(6048):1456–8. Available from: https://pubmed.ncbi.nlm.nih.gov/21778362/

16. Amit I, Winter DR, Jung S. The role of the local environment and epigenetics in shaping macrophage identity and their effect on tissue homeostasis. Nat Immunol 2015 171 [Internet]. 2015 Dec 17 [cited 2024 Jul 23];17(1):18–25. Available from: https://www.nature.com/articles/ni.3325

17. Ganz T. Macrophages and systemic iron homeostasis. J Innate Immun [Internet]. 2012 Aug [cited 2024 Jul 23];4(5–6):446–53. Available from: https://pubmed.ncbi.nlm.nih.gov/22441209/

18. Nathan CF, Murray HW, Wlebe IE, Rubin BY. Identification of interferon-gamma as the lymphokine that activates human macrophage oxidative metabolism and antimicrobial activity. J Exp Med [Internet]. 1983 Sep 1 [cited 2024 Jul 24];158(3):670–89. Available from: https://pubmed.ncbi.nlm.nih.gov/6411853/

19. Atri C, Guerfali FZ, Laouini D. Role of Human Macrophage Polarization in Inflammation during Infectious Diseases. Int J Mol Sci [Internet]. 2018 Jun 19 [cited 2024 Jul 24];19(6). Available from: https://pubmed.ncbi.nlm.nih.gov/29921749/

20. Xue J, Schmidt S V., Sander J, Draffehn A, Krebs W, Quester I, et al. Transcriptome-based network analysis reveals a spectrum model of human macrophage activation. Immunity [Internet]. 2014 Feb 20 [cited 2024 Jul 24];40(2):274–88. Available from: https://pubmed.ncbi.nlm.nih.gov/24530056/

21. Martinez FO, Gordon S. The M1 and M2 paradigm of macrophage activation: time for reassessment. F1000Prime Rep [Internet]. 2014 Mar 3 [cited 2024 Jul 24];6. Available from: https://pubmed.ncbi.nlm.nih.gov/24669294/

22. Kerneur C, Cano CE, Olive D. Major pathways involved in macrophage polarization in cancer. Front Immunol. 2022 Oct 17;13:1026954.

23. Medzhitov R. Origin and physiological roles of inflammation. Nature [Internet]. 2008 Jul 24 [cited 2024 Jul 24];454(7203):428–35. Available from: https://pubmed.ncbi.nlm.nih.gov/18650913/

24. Smolen JS, Aletaha D, McInnes IB. Rheumatoid arthritis. Lancet [Internet]. 2016 Oct 22 [cited 2018 Nov 18];388(10055):2023–38. Available from: https://linkinghub.elsevier.com/retrieve/pii/S0140673616301738

25. Smolen JS, Aletaha D, Barton A, Burmester GR, Emery P, Firestein GS, et al. Rheumatoid arthritis. Nat Rev Dis Prim [Internet]. 2018 Feb 8 [cited 2018 Nov 18];4:18001. Available from: http://www.nature.com/articles/nrdp20181

26. Muller S, Radic M. Citrullinated Autoantigens: From Diagnostic Markers to Pathogenetic Mechanisms. Clin Rev Allergy Immunol [Internet]. 2015 Oct 30 [cited 2018 Nov 19];49(2):232–9. Available from: http://link.springer.com/10.1007/s12016-014-8459-2

27. Holers VM. Autoimmunity to citrullinated proteins and the initiation of rheumatoid arthritis.

Curr Opin Immunol [Internet]. 2013 Dec [cited 2018 Nov 19];25(6):728–35. Available from: https://linkinghub.elsevier.com/retrieve/pii/S0952791513001957

28. Arend WP, Firestein GS. Pre-rheumatoid arthritis: predisposition and transition to clinical synovitis. Nat Rev Rheumatol [Internet]. 2012 Oct 21 [cited 2018 Nov 19];8(10):573–86. Available from: http://www.nature.com/articles/nrrheum.2012.134

29. Alivernini S, MacDonald L, Elmesmari A, Finlay S, Tolusso B, Gigante MR, et al. Distinct synovial tissue macrophage subsets regulate inflammation and remission in rheumatoid arthritis. Nat Med [Internet]. 2020 Aug 1 [cited 2024 Jul 24];26(8):1295–306. Available from: https://pubmed.ncbi.nlm.nih.gov/32601335/

30. Wang Y, Han C chen, Cui D, Li Y, Ma Y, Wei W. Is macrophage polarization important in rheumatoid arthritis? Int Immunopharmacol [Internet]. 2017 Sep 1 [cited 2024 Jul 24];50:345–52. Available from: https://pubmed.ncbi.nlm.nih.gov/28750350/

31. Sun W, Zhang H, Wang H, Chiu YG, Wang M, Ritchlin CT, et al. Targeting Notch-Activated M1 Macrophages Attenuates Joint Tissue Damage in a Mouse Model of Inflammatory Arthritis. J Bone Miner Res [Internet]. 2017 Jul 1 [cited 2023 Oct 5];32(7):1469–80. Available from: https://onlinelibrary.wiley.com/doi/full/10.1002/jbmr.3117

32. Siouti E, Andreakos E. The many facets of macrophages in rheumatoid arthritis. Biochem Pharmacol. 2019 Jul 1;165:152–69.

33. Sokolove J, Zhao X, Chandra PE, Robinson WH. Immune complexes containing citrullinated fibrinogen costimulate macrophages via toll-like receptor 4 and Fcγ receptor. Arthritis Rheum. 2011 Jan;63(1):53–62.

34. Elshabrawy HA, Chen Z, Volin M V., Ravella S, Virupannavar S, Shahrara S. The Pathogenic Role of Angiogenesis in Rheumatoid Arthritis. Angiogenesis [Internet]. 2015 Oct 1 [cited 2024 Jul 24];18(4):433. Available from: /pmc/articles/PMC4879881/

35. Schett G, Gravallese E. Bone erosion in rheumatoid arthritis: mechanisms, diagnosis and treatment. Nat Rev Rheumatol [Internet]. 2012 Nov [cited 2018 Nov 19];8(11):656–64. Available from: http://www.ncbi.nlm.nih.gov/pubmed/23007741

36. Ramamoorthy S, Cidlowski JA. Corticosteroids-Mechanisms of Action in Health and Disease. Rheum Dis Clin North Am [Internet]. 2016 [cited 2024 Jul 24];42(1):15. Available from: /pmc/articles/PMC4662771/

37. Abbasi M, Mousavi MJ, Jamalzehi S, Alimohammadi R, Bezvan MH, Mohammadi H, et al. Strategies toward rheumatoid arthritis therapy; the old and the new. J Cell Physiol [Internet]. 2019 Jul 1 [cited 2024 Jul 24];234(7):10018–31. Available from: https://pubmed.ncbi.nlm.nih.gov/30536757/

38. FDA requires warnings about increased risk of serious heart-related events, cancer, blood clots, and death for JAK inhibitors that treat certain chronic inflammatory conditions | FDA [Internet]. [cited 2024 Jul 24]. Available from: https://www.fda.gov/drugs/fda-drug-safety-podcasts/fda-requires-warnings-about-increased-risk-serious-heart-related-events-cancer-blood-clots-and-death

39. Ganguly P, Macleod T, Wong C, Harland M, McGonagle D. Revisiting p38 Mitogen-Activated Protein Kinases (MAPK) in Inflammatory Arthritis: A Narrative of the Emergence of MAPK-Activated Protein Kinase Inhibitors (MK2i). Pharmaceuticals [Internet]. 2023 Sep 1 [cited 2024 May 22];16(9). Available from: /pmc/articles/PMC10537904/

40. Arthur JSC, Ley SC. Mitogen-activated protein kinases in innate immunity. Nat Rev Immunol [Internet]. 2013 Sep 19 [cited 2019 Jan 8];13(9):679–92. Available from: http://www.nature.com/articles/nri3495

41. Moens U, Kostenko S, Sveinbjørnsson B. The Role of Mitogen-Activated Protein Kinase-Activated Protein Kinases (MAPKAPKs) in Inflammation. Genes (Basel) [Internet]. 2013 [cited 2024 May 14];4:101–33. Available from: www.mdpi.com/journal/genes

42. Meloche S, Pouysségur J. The ERK1/2 mitogen-activated protein kinase pathway as a master regulator of the G1- to S-phase transition. Oncogene [Internet]. 2007 May 14 [cited 2024 May 14];26(22):3227–39. Available from: https://pubmed.ncbi.nlm.nih.gov/17496918/

43. Remy G, Risco AM, Iñesta-Vaquera FA, González-Terán B, Sabio G, Davis RJ, et al. Differential activation of p38MAPK isoforms by MKK6 and MKK3. Cell Signal. 2010 Apr;22(4):660–7.

44. Sabio G, Davis RJ. TNF and MAP kinase signaling pathways. Semin Immunol [Internet]. 2014 [cited 2024 May 15];26(3):237. Available from: /pmc/articles/PMC4099309/

45. Freshney NW, Rawlinson L, Guesdon F, Jones E, Cowley S, Hsuan J, et al. Interleukin-1 activates a novel protein kinase cascade that results in the phosphorylation of Hsp27. Cell [Internet]. 1994 Sep 23 [cited 2024 May 15];78(6):1039–49. Available from: https://pubmed.ncbi.nlm.nih.gov/7923354/

46. Park BS, Song DH, Kim HM, Choi BS, Lee H, Lee JO. The structural basis of lipopolysaccharide recognition by the TLR4-MD-2 complex. Nature [Internet]. 2009 Apr 30 [cited 2024 May 15];458(7242):1191–5. Available from: https://pubmed.ncbi.nlm.nih.gov/19252480/

47. Wright SD, Ramos RA, Tobias PS, Ulevitch RJ, Mathison JC. CD14, a Receptor for Complexes of Lipopolysaccharide (LPS) and LPS Binding Protein. Science (80-) [Internet]. 1990 Sep 21 [cited 2024 May 15];249(4975):1431–3. Available from: https://www.science.org/doi/10.1126/science.1698311

48. Kuzmich NN, Sivak K V., Chubarev VN, Porozov YB, Savateeva-Lyubimova TN, Peri F. TLR4 Signaling Pathway Modulators as Potential Therapeutics in Inflammation and Sepsis. Vaccines [Internet]. 2017 Dec 1 [cited 2024 May 15];5(4). Available from: /pmc/articles/PMC5748601/

49. O'Neill LAJ, Bowie AG. The family of five: TIR-domain-containing adaptors in Toll-like receptor signalling. Nat Rev Immunol 2007 75 [Internet]. 2007 May [cited 2024 May 15];7(5):353–64. Available from: https://www.nature.com/articles/nri2079

50. Irie T, Muta T, Takeshige K. TAK1 mediates an activation signal from toll-like receptor(s) to nuclear factor-kappaB in lipopolysaccharide-stimulated macrophages. FEBS Lett [Internet]. 2000 Feb 11 [cited 2024 May 15];467(2–3):160–4. Available from: https://pubmed.ncbi.nlm.nih.gov/10675530/

51. Cuevas BD, Abell AN, Johnson GL. Role of mitogen-activated protein kinase kinase kinases in signal integration. Oncogene [Internet]. 2007 [cited 2024 May 14];26:3159–71. Available from: www.nature.com/onc

52. Hayakawa T, Matsuzawa A, Noguchi T, Takeda K, Ichijo H. The ASK1–MAP kinase pathways in immune and stress responses. Microbes Infect. 2006 Apr 1;8(4):1098–107.

53. Huang Q, Yang J, Lin Y, Walker C, Cheng J, Liu ZG, et al. Differential regulation of interleukin 1 receptor and Toll-like receptor signaling by MEKK3. Nat Immunol [Internet]. 2004 Jan [cited

2024 May 15];5(1):98–103. Available from: https://pubmed.ncbi.nlm.nih.gov/14661019/

54. Brancho D, Tanaka N, Jaeschke A, Ventura JJ, Kelkar N, Tanaka Y, et al. Mechanism of p38 MAP kinase activation in vivo. Genes Dev. 2003 Aug 15;17(16):1969–78.

55. Salvador JM, Mittelstadt PR, Guszczynski T, Copeland TD, Yamaguchi H, Appella E, et al. Alternative p38 activation pathway mediated by T cell receptor–proximal tyrosine kinases. Nat Immunol 2005 64 [Internet]. 2005 Feb 27 [cited 2024 May 15];6(4):390–5. Available from: https://www.nature.com/articles/ni1177

56. Ge B, Gram H, Di Padova F, Huang B, New L, Ulevitch RJ, et al. MAPKK-independent activation of p38α mediated by TAB1-dependent autophosphorylation of p38α. Science (80-) [Internet]. 2002 Feb 15 [cited 2024 May 15];295(5558):1291–4. Available from: https://www.science.org/doi/10.1126/science.1067289

57. Eliopoulos AG, Wang CC, Dumitru CD, Tsichlis PN. Tpl2 transduces CD40 and TNF signals that activate ERK and regulates IgE induction by CD40. EMBO J [Internet]. 2003 Aug 1 [cited 2024 May 15];22(15):3855–64. Available from: https://pubmed.ncbi.nlm.nih.gov/12881420/

58. Han J, Lee JD, Bibbs L, Ulevitch RJ. A MAP kinase targeted by endotoxin and hyperosmolarity in mammalian cells. Science [Internet]. 1994 [cited 2024 May 17];265(5173):808–11. Available from: https://pubmed.ncbi.nlm.nih.gov/7914033/

59. Jiang Y, Chen C, Li Z, Guo W, Gegner JA, Lin S, et al. Characterization of the structure and function of a new mitogen-activated protein kinase (p38beta). J Biol Chem [Internet]. 1996 [cited 2024 May 17];271(30):17920–6. Available from: https://pubmed.ncbi.nlm.nih.gov/8663524/

60. Lechner C, Zahalka MA, Giot JF, Møller NPH, Ullrich A. ERK6, a mitogen-activated protein kinase involved in C2C12 myoblast differentiation. Proc Natl Acad Sci U S A [Internet]. 1996 Apr 30 [cited 2024 May 17];93(9):4355–9. Available from: https://pubmed.ncbi.nlm.nih.gov/8633070/

61. Wang XS, Diener K, Manthey CL, Wang SW, Rosenzweig B, Bray J, et al. Molecular cloning and characterization of a novel p38 mitogen-activated protein kinase. J Biol Chem [Internet]. 1997 Sep 19 [cited 2024 May 17];272(38):23668–74. Available from: https://pubmed.ncbi.nlm.nih.gov/9295308/

62. Jiang Y, Gram H, Zhao M, New L, Gu J, Feng L, et al. Characterization of the structure and function of the fourth member of p38 group mitogen-activated protein kinases, p38delta. J Biol Chem [Internet]. 1997 Nov 28 [cited 2024 May 17];272(48):30122–8. Available from: https://pubmed.ncbi.nlm.nih.gov/9374491/

63. Sabio G, Arthur JSC, Kuma Y, Peggie M, Carr J, Murray-Tait V, et al. p38γ regulates the localisation of SAP97 in the cytoskeleton by modulating its interaction with GKAP. EMBO J [Internet]. 2005 Mar 23 [cited 2024 May 21];24(6):1134–45. Available from: https://www.embopress.org/doi/10.1038/sj.emboj.7600578

64. Aouadi M, Binetruy B, Caron L, Le Marchand-Brustel Y, Bost F. Role of MAPKs in development and differentiation: lessons from knockout mice. Biochimie. 2006 Sep 1;88(9):1091–8.

65. Beardmore VA, Hinton HJ, Eftychi C, Apostolaki M, Armaka M, Darragh J, et al. Generation and Characterization of p38β (MAPK11) Gene-Targeted Mice. Mol Cell Biol [Internet]. 2005 Dec 1 [cited 2024 May 21];25(23):10454. Available from: /pmc/articles/PMC1291241/

66. Allen M, Svensson L, Roach M, Hambor J, McNeish J, Gabel CA. Deficiency of the stress kinase p38alpha results in embryonic lethality: characterization of the kinase dependence of stress responses of enzyme-deficient embryonic stem cells. J Exp Med [Internet]. 2000 Mar 6 [cited 2024 May 21];191(5):859–69. Available from: https://pubmed.ncbi.nlm.nih.gov/10704466/

67. Canovas B, Nebreda AR. Diversity and versatility of p38 kinase signalling in health and disease. Nat Rev Mol Cell Biol [Internet]. [cited 2024 May 8]; Available from: www.nature.com/nrm

68. Tanoue T, Adachi M, Moriguchi T, Nishida E. A conserved docking motif in MAP kinases common to substrates, activators and regulators. Nat Cell Biol [Internet]. 2000 [cited 2024 May 7];2(2):110–6. Available from: https://pubmed.ncbi.nlm.nih.gov/10655591/

69. Gaestel M. Specificity of signaling from MAPKs to MAPKAPKs: kinases' tango nuevo. Front Biosci [Internet]. 2008 May 1 [cited 2024 May 7];13(16):6050–9. Available from: https://pubmed.ncbi.nlm.nih.gov/18508642/

70. Tiedje C, Holtmann H, Gaestel M. The Role of Mammalian MAPK Signaling in Regulation of Cytokine mRNA Stability and Translation. J Interf Cytokine Res [Internet]. 2014 Apr 3 [cited 2019 Jan 15];34(4):220–32. Available from: http://www.liebertpub.com/doi/10.1089/jir.2013.0146

71. Gaestel M. MAPK-activated protein kinases (MKs): Novel insights and challenges. Front Cell Dev Biol. 2016 Jan 8;3(JAN):172821.

72. Joshi S, Platanias LC. Mnk kinase pathway: Cellular functions and biological outcomes. World J Biol Chem [Internet]. 2014 Aug 8 [cited 2024 May 21];5(3):321. Available from: /pmc/articles/PMC4160526/

73. Trempolec N, Dave-Coll N, Nebreda AR. SnapShot: P38 MAPK substrates. Cell [Internet]. 2013 Feb 14 [cited 2024 May 21];152(4):924-924.e1. Available from: http://www.cell.com/article/S0092867413001396/fulltext

74. Herbert K, Binet R, Lambert JP, Louphrasitthiphol P, Kalkavan H, Sesma-Sanz L, et al. BRN2 suppresses apoptosis, reprograms DNA damage repair, and is associated with a high somatic mutation burden in melanoma. Genes Dev [Internet]. 2019 Mar 1 [cited 2024 May 21];33(5–6):310–32. Available from: https://pubmed.ncbi.nlm.nih.gov/30804224/

75. Li W, Zhu J, Dou J, She H, Tao K, Xu H, et al. Phosphorylation of LAMP2A by p38 MAPK couples ER stress to chaperone-mediated autophagy. Nat Commun 2017 81 [Internet]. 2017 Nov 24 [cited 2024 May 21];8(1):1–14. Available from: https://www.nature.com/articles/s41467-017-01609-x

76. Phong MS, Horn RD Van, Li S, Tucker-Kellogg G, Surana U, Ye XS. p38 Mitogen-Activated Protein Kinase Promotes Cell Survival in Response to DNA Damage but Is Not Required for the G2 DNA Damage Checkpoint in Human Cancer Cells. Mol Cell Biol [Internet]. 2010 Aug 1 [cited 2024 May 21];30(15):3816. Available from: /pmc/articles/PMC2916406/

77. Dolado I, Nebreda AR. Regulation of Tumorigenesis by p38α MAP Kinase. Top Curr Genet [Internet]. 2007 [cited 2024 May 21];20:99–128. Available from: https://link.springer.com/chapter/10.1007/4735_2007_0245

78. Bost F, Aouadi M, Caron L, Binétruy B. The role of MAPKs in adipocyte differentiation and obesity. Biochimie [Internet]. 2005 [cited 2024 May 21];87(1):51–6. Available from: https://pubmed.ncbi.nlm.nih.gov/15733737/

79. Rodríguez-Carballo E, Gámez B, Ventura F. p38 MAPK Signaling in Osteoblast Differentiation. Front Cell Dev Biol [Internet]. 2016 May 6 [cited 2024 May 21];4(MAY):40. Available from: /pmc/articles/PMC4858538/

80. Segalés J, Perdiguero E, Muñoz-Cánoves P. Regulation of Muscle Stem Cell Functions: A Focus on the p38 MAPK Signaling Pathway. Front cell Dev Biol [Internet]. 2016 Aug 30 [cited 2024 May 21];4(AUG). Available from: https://pubmed.ncbi.nlm.nih.gov/27626031/

81. Whitmarsh AJ, Yang S-H, Su MS-S, Sharrocks AD, Davis RJ. Role of p38 and JNK mitogen-activated protein kinases in the activation of ternary complex factors. Mol Cell Biol [Internet]. 1997 May 1 [cited 2024 May 21];17(5):2360–71. Available from: https://pubmed.ncbi.nlm.nih.gov/9111305/

82. Ramsauer K, Sadzak I, Porras A, Pilz A, Nebreda AR, Decker T, et al. p38 MAPK enhances STAT1-dependent transcription independently of Ser-727 phosphorylation. Proc Natl Acad Sci U S A [Internet]. 2002 Oct 1 [cited 2024 May 21];99(20):12859–64. Available from: https://pubmed.ncbi.nlm.nih.gov/12232043/

83. Breitwieser W, Lyons S, Flenniken AM, Ashton G, Bruder G, Willington M, et al. Feedback regulation of p38 activity via ATF2 is essential for survival of embryonic liver cells. Genes Dev [Internet]. 2007 Aug 15 [cited 2024 May 8];21(16):2069–82. Available from: https://pubmed.ncbi.nlm.nih.gov/17699753/

84. Schett G, Zwerina J, Firestein G. The p38 mitogen-activated protein kinase (MAPK) pathway in rheumatoid arthritis. Ann Rheum Dis [Internet]. 2008 Jul [cited 2024 May 21];67(7):909. Available from: /pmc/articles/PMC2754165/

85. Clark AR, Dean J LE. The p38 MAPK Pathway in Rheumatoid Arthritis: A Sideways Look. Open Rheumatol J [Internet]. 2012 [cited 2019 Apr 4];6:209–19. Available from: http://www.ncbi.nlm.nih.gov/pubmed/23028406

86. Lopez-Bergami P, Lau E, Ronai Z. Emerging roles of ATF2 and the dynamic AP1 network in cancer. Nat Rev Cancer 2010 101 [Internet]. 2010 Jan [cited 2024 May 21];10(1):65–76. Available from: https://www.nature.com/articles/nrc2681

87. Janknecht R, Ernst WH, Pingoud V, Nordheim A. Activation of ternary complex factor Elk-1 by MAP kinases. EMBO J [Internet]. 1993 Dec [cited 2024 May 21];12(13):5097–104. Available from: https://pubmed.ncbi.nlm.nih.gov/8262053/

88. Saccani S, Pantano S, Natoli G. p38-Dependent marking of inflammatory genes for increased NF-kappa B recruitment. Nat Immunol [Internet]. 2002 [cited 2024 May 21];3(1):69–75. Available from: https://pubmed.ncbi.nlm.nih.gov/11743587/

89. Morgan D, Berggren KL, Spiess CD, Smith HM, Tejwani A, Weir SJ, et al. Mitogen-activated protein kinase-activated protein kinase-2 (MK2) and its role in cell survival, inflammatory signaling, and migration in promoting cancer. Mol Carcinog [Internet]. 2022 Feb 1 [cited 2024 May 21];61(2):173. Available from: /pmc/articles/PMC8799529/

90. Tan Y, Rouse J, Zhang A, Cariati S, Cohen P, Comb MJ. FGF and stress regulate CREB and ATF-1 via a pathway involving p38 MAP kinase and MAPKAP kinase-2. EMBO J [Internet]. 1996 Sep 9 [cited 2024 May 21];15(17):4629. Available from: /pmc/articles/PMC452194/?report=abstract

91. Reyskens KMSE, Arthur JSC. Emerging roles of the mitogen and stress activated kinases MSK1 and MSK2. Front Cell Dev Biol. 2016 Jun 10;4(JUN):195179.

92. Naqvi S, Martin KJ, Arthur JSC. CREB phosphorylation at Ser133 regulates transcription via distinct mechanisms downstream of cAMP and MAPK signalling. Biochem J [Internet]. 2014 Mar 15 [cited 2024 May 22];458(3):469–79. Available from: /biochemj/article/458/3/469/46535/CREB-phosphorylation-at-Ser133-regulates

93. Chrestensen CA, Schroeder MJ, Shabanowitz J, Hunt DF, Pelo JW, Worthington MT, et al. MAPKAP kinase 2 phosphorylates tristetraprolin on in vivo sites including Ser178, a site required for 14-3-3 binding. J Biol Chem [Internet]. 2004 Mar 12 [cited 2019 Jan 16];279(11):10176–84. Available from: http://www.ncbi.nlm.nih.gov/pubmed/14688255

94. Bollig F, Winzen R, Gaestel M, Kostka S, Resch K, Holtmann H. Affinity purification of ARE-binding proteins identifies poly(A)-binding protein 1 as a potential substrate in MK2-induced mRNA stabilization. Biochem Biophys Res Commun. 2003 Feb 14;301(3):665–70.

95. Rousseau S, Morrice N, Peggie M, Campbell DG, Gaestel M, Cohen P. Inhibition of SAPK2a/p38 prevents hnRNP A0 phosphorylation by MAPKAP-K2 and its interaction with cytokine mRNAs. EMBO J [Internet]. 2002 Dec 1 [cited 2024 May 22];21(23):6505–14. Available from: https://www.embopress.org/doi/10.1093/emboj/cdf639

96. Tiedje C, Ronkina N, Tehrani M, Dhamija S, Laass K, Holtmann H, et al. The p38/MK2-Driven Exchange between Tristetraprolin and HuR Regulates AU-Rich Element-Dependent Translation. PLoS Genet. 2012 Sep;8(9).

97. Ronkina N, Kotlyarov A, Dittrich-Breiholz O, Kracht M, Hitti E, Milarski K, et al. The Mitogen-Activated Protein Kinase (MAPK)-Activated Protein Kinases MK2 and MK3 Cooperate in Stimulation of Tumor Necrosis Factor Biosynthesis and Stabilization of p38 MAPK. Mol Cell Biol [Internet]. 2007 Jan 1 [cited 2024 May 22];27(1):170. Available from: /pmc/articles/PMC1800641/

98. Uchida Y, Chiba T, Kurimoto R, Asahara H. Post-transcriptional regulation of inflammation by RNA-binding proteins via cis-elements of mRNAs [Internet]. Vol. 166, Journal of Biochemistry. Oxford University Press; 2019 [cited 2020 Nov 19]. p. 375–82. Available from: https://pubmed.ncbi.nlm.nih.gov/31511872/

99. Rabani M, Levin JZ, Fan L, Adiconis X, Raychowdhury R, Garber M, et al. Metabolic labeling of RNA uncovers principles of RNA production and degradation dynamics in mammalian cells. Nat Biotechnol [Internet]. 2011 May 24 [cited 2019 Mar 31];29(5):436–42. Available from: http://www.nature.com/articles/nbt.1861

100. Elkon R, Zlotorynski E, Zeller KI, Agami R. Major role for mRNA stability in shaping the kinetics of gene induction. BMC Genomics [Internet]. 2010 Apr 21 [cited 2020 Nov 19];11(1). Available from: https://pubmed.ncbi.nlm.nih.gov/20409322/

101. Mendoza H, Campbell DG, Burness K, Hastie J, Ronkina N, Shim JH, et al. Roles for TAB1 in regulating the IL-1-dependent phosphorylation of the TAB3 regulatory subunit and activity of the TAK1 complex. Biochem J [Internet]. 2008 Feb 1 [cited 2024 May 22];409(3):711–22. Available from: https://pubmed.ncbi.nlm.nih.gov/18021073/

102. Ananieva O, Darragh J, Johansen C, Carr JM, McIlrath J, Park JM, et al. The kinases MSK1 and MSK2 act as negative regulators of Toll-like receptor signaling. Nat Immunol. 2008;9(9):1028–36.

103. White A, Pargellis CA, Studts JM, Werneburg BG, Farmer BT. Molecular basis of MAPK-activated protein kinase 2:p38 assembly. Proc Natl Acad Sci U S A [Internet]. 2007 Apr 4 [cited 2024 May 3];104(15):6353. Available from: /pmc/articles/PMC1851067/

104. Kotlyarov A, Yannoni Y, Fritz S, Laaß K, Telliez J-B, Pitman D, et al. Distinct Cellular Functions of MK2. Mol Cell Biol [Internet]. 2002 Jul 1 [cited 2024 May 6];22(13):4827. Available from: /pmc/articles/PMC133920/

105. Sudo T, Kawai K, Matsuzaki H, Osada H. p38 mitogen-activated protein kinase plays a key role in regulating MAPKAPK2 expression. Biochem Biophys Res Commun. 2005 Nov 18;337(2):415–21.

106. Alexa A, Gógl G, Glatz G, Garai Á, Zeke A, Varga J, et al. Structural assembly of the signaling competent ERK2-RSK1 heterodimeric protein kinase complex. Proc Natl Acad Sci U S A [Internet]. 2015 Mar 3 [cited 2024 May 6];112(9):2711–6. Available from: /pmc/articles/PMC4352816/

107. Ronkina N, Menon MB, Schwermann J, Arthur JSC, Legault H, Telliez JB, et al. Stress induced gene expression: A direct role for MAPKAP kinases in transcriptional activation of immediate early genes. Nucleic Acids Res. 2011 Apr;39(7):2503–18.

108. Kobayashi M, Nishita M, Mishima T, Ohashi K, Mizuno K. MAPKAPK-2-mediated LIM-kinase activation is critical for VEGF-induced actin remodeling and cell migration. EMBO J [Internet]. 2006 Feb 2 [cited 2024 May 3];25(4):713. Available from: /pmc/articles/PMC1383554/

109. Meng W, Swenson LL, Fitzgibbon MJ, Hayakawa K, Haar E Ter, Behrens AE, et al. Structure of mitogen-activated protein kinase-activated protein (MAPKAP) kinase 2 suggests a bifunctional switch that couples kinase activation with nuclear export. J Biol Chem [Internet]. 2002 Oct 4 [cited 2024 May 6];277(40):37401–5. Available from: http://www.jbc.org/article/S0021925818364597/fulltext

110. Engel K, Kotlyarov A, Gaestel M. Leptomycin B-sensitive nuclear export of MAPKAP kinase 2 is regulated by phosphorylation. EMBO J [Internet]. 1998 Jun 6 [cited 2024 May 6];17(12):3363. Available from: /pmc/articles/PMC1170674/?report=abstract

111. Anton R, Bauer SM, Keck PRWEF, Laufer S, Rothbauer U. A p38 Substrate-Specific MK2-EGFP Translocation Assay for Identification and Validation of New p38 Inhibitors in Living Cells: A Comprising Alternative for Acquisition of Cellular p38 Inhibition Data. PLoS One [Internet]. 2014 [cited 2024 May 6];9(4):95641. Available from: www.plosone.org

112. Miura H, Kondo Y, Matsuda M, Aoki K. Cell-to-Cell Heterogeneity in p38-Mediated Cross-Inhibition of JNK Causes Stochastic Cell Death. Cell Rep [Internet]. 2018 Sep 4 [cited 2024 May 6];24(10):2658–68. Available from: http://www.cell.com/article/S2211124718312749/fulltext

113. Ben-Levy R, Hooper S, Wilson R, Paterson HF, Marshall CJ. Nuclear export of the stress-activated protein kinase p38 mediated by its substrate MAPKAP kinase-2. [cited 2024 May 6]; Available from: http://biomednet.com/elecref/0960982200801049

114. Nishimoto S, Nishida E. MAPK signalling: ERK5 versus ERK1/2. EMBO Rep [Internet]. 2006 Aug [cited 2024 May 16];7(8):782–6. Available from: https://pubmed.ncbi.nlm.nih.gov/16880823/

115. David Wood C, Thornton TM, Sabio G, Davis RA, Rincon M. Nuclear Localization of p38 MAPK in Response to DNA Damage. Int J Biol Sci [Internet]. 2009 [cited 2024 May 6];5(5):428–37. Available from: http://www.biolsci.org428

116. Brand P, Plochmann S, Valk E, Zahn S, Saloga J, Knop J, et al. Activation and translocation of p38 mitogen-activated protein kinase after stimulation of monocytes with contact sensitizers. J Invest Dermatol [Internet]. 2002 Jul 1 [cited 2024 May 6];119(1):99–106. Available from:

http://www.jidonline.org/article/S0022202X15417099/fulltext

117. Zehorai E, Seger R. Beta-Like Importins Mediate the Nuclear Translocation of MAPKs. Cell Physiol Biochem [Internet]. 2019 [cited 2024 May 6];52(4):802–21. Available from: https://pubmed.ncbi.nlm.nih.gov/30946556/

118. Salojin K, Oravecz T. Regulation of innate immunity by MAPK dual-specificity phosphatases: knockout models reveal new tricks of old genes. J Leukoc Biol [Internet]. 2007 Apr 1 [cited 2024 May 8];81(4):860–9. Available from: https://dx.doi.org/10.1189/jlb.1006639

119. Liu Y, Shepherd EG, Nelin LD. MAPK phosphatases — regulating the immune response. Nat Rev Immunol 2007 73 [Internet]. 2007 Mar [cited 2024 May 8];7(3):202–12. Available from: https://www.nature.com/articles/nri2035

120. Dickinson RJ, Keyse SM. Diverse physiological functions for dual-specificity MAP kinase phosphatases. J Cell Sci [Internet]. 2006 Nov 15 [cited 2024 May 8];119(22):4607–15. Available from: https://dx.doi.org/10.1242/jcs.03266

121. Wu JJ, Zhang L, Bennett AM. The noncatalytic amino terminus of mitogen-activated protein kinase phosphatase 1 directs nuclear targeting and serum response element transcriptional regulation. Mol Cell Biol [Internet]. 2005 Jun 1 [cited 2024 May 8];25(11):4792–803. Available from: https://pubmed.ncbi.nlm.nih.gov/15899879/

122. Sun H, Charles CH, Lau LF, Tonks NK. MKP-1 (3CH134), an immediate early gene product, is a dual specificity phosphatase that dephosphorylates MAP kinase in vivo. Cell [Internet]. 1993 Nov 5 [cited 2024 May 8];75(3):487–93. Available from: https://pubmed.ncbi.nlm.nih.gov/8221888/

123. Groom LA, Sneddon AA, Alessi DR, Dowd S, Keyse SM. Differential regulation of the MAP, SAP and RK/p38 kinases by Pyst1, a novel cytosolic dual-specificity phosphatase. EMBO J [Internet]. 1996 Jul 7 [cited 2024 May 8];15(14):3621. Available from: /pmc/articles/PMC451978/?report=abstract

124. Hutter D, Chen P, Barnes J, Liu Y. Catalytic activation of mitogen-activated protein (MAP) kinase phosphatase-1 by binding to p38 MAP kinase: critical role of the p38 C-terminal domain in its negative regulation. Biochem J [Internet]. 2000 Nov 11 [cited 2024 May 8];352(Pt 1):155. Available from: /pmc/articles/PMC1221442/?report=abstract

125. Muda M, Theodosiou A, Rodrigues N, Boschert U, Camps M, Gillieron C, et al. The dual specificity phosphatases M3/6 and MKP-3 are highly selective for inactivation of distinct mitogen-activated protein kinases. J Biol Chem [Internet]. 1996 [cited 2024 May 8];271(44):27205–8. Available from: https://pubmed.ncbi.nlm.nih.gov/8910287/

126. Chu Y, Solski PA, Khosravi-Far R, Der CJ, Kelly K. The mitogen-activated protein kinase phosphatases PAC1, MKP-1, and MKP-2 have unique substrate specificities and reduced activity in vivo toward the ERK2 sevenmaker mutation. J Biol Chem [Internet]. 1996 Mar 15 [cited 2024 May 8];271(11):6497–501. Available from: https://pubmed.ncbi.nlm.nih.gov/8626452/

127. Tanoue T, Yamamoto T, Maeda R, Nishida E. A Novel MAPK phosphatase MKP-7 acts preferentially on JNK/SAPK and p38 alpha and beta MAPKs. J Biol Chem [Internet]. 2001 Jul 13 [cited 2024 May 8];276(28):26629–39. Available from: https://pubmed.ncbi.nlm.nih.gov/11359773/

128. Theodosiou A, Smith A, Gillieron C, Arkinstall S, Ashworth A. MKP5, a new member of the MAP kinase phosphatase family, which selectively dephosphorylates stress-activated kinases.

Oncogene [Internet]. 1999 Nov 25 [cited 2024 May 8];18(50):6981–8. Available from: https://pubmed.ncbi.nlm.nih.gov/10597297/

129. Franklin CC, Kraft AS. Conditional expression of the mitogen-activated protein kinase (MAPK) phosphatase MKP-1 preferentially inhibits p38 MAPK and stress-activated protein kinase in U937 cells. J Biol Chem [Internet]. 1997 Jul 4 [cited 2024 May 8];272(27):16917–23. Available from: https://pubmed.ncbi.nlm.nih.gov/9202001/

130. Zhang Y, Blattman JN, Kennedy NJ, Duong J, Hguyen T, Wang Y, et al. Regulation of innate and adaptive immune responses by MAP kinase phosphatase 5. Nature [Internet]. 2004 Aug 12 [cited 2024 May 8];430(7001):793–7. Available from: https://pubmed.ncbi.nlm.nih.gov/15306813/

131. Zhao Q, Wang X, Nelin LD, Yao Y, Matta R, Manson ME, et al. MAP kinase phosphatase 1 controls innate immune responses and suppresses endotoxic shock. J Exp Med [Internet]. 2006 Jan 23 [cited 2024 May 8];203(1):131–40. Available from: https://pubmed.ncbi.nlm.nih.gov/16380513/

132. Jeffrey KL, Brummer T, Rolph MS, Liu SM, Callejas NA, Grumont RJ, et al. Positive regulation of immune cell function and inflammatory responses by phosphatase PAC-1. Nat Immunol [Internet]. 2006 Mar [cited 2024 May 8];7(3):274–83. Available from: https://pubmed.ncbi.nlm.nih.gov/16474395/

133. Dorfman K, Carrasco D, Gruda M, Ryan C, Lira SA, Bravo R. Disruption of the erp/mkp-1 gene does not affect mouse development: normal MAP kinase activity in ERP/MKP-1-deficient fibroblasts. Oncogene [Internet]. 1996 Sep 1 [cited 2023 Sep 30];13(5):925–31. Available from: https://europepmc.org/article/med/8806681

134. Hammer M, Mages J, Dietrich H, Servatius A, Howells N, Cato ACB, et al. Dual specificity phosphatase 1 (DUSP1) regulates a subset of LPS-induced genes and protects mice from lethal endotoxin shock. J Exp Med [Internet]. 2006 Jan 23 [cited 2019 Apr 10];203(1):15–20. Available from: http://www.ncbi.nlm.nih.gov/pubmed/16380512

135. Zhao Q, Shepherd EG, Manson ME, Nelin LD, Sorokin A, Liu Y. The role of mitogen-activated protein kinase phosphatase-1 in the response of alveolar macrophages to lipopolysaccharide: attenuation of proinflammatory cytokine biosynthesis via feedback control of p38. J Biol Chem [Internet]. 2005 Mar 4 [cited 2024 May 8];280(9):8101–8. Available from: https://pubmed.ncbi.nlm.nih.gov/15590669/

136. Zhang T, Lu X, Arnold P, Liu Y, Baliga R, Huang H, et al. Mitogen-activated protein kinase phosphatase-1 inhibits myocardial TNF-α expression and improves cardiac function during endotoxemia. Cardiovasc Res [Internet]. 2012 Mar 3 [cited 2024 May 8];93(3):471. Available from: /pmc/articles/PMC3282576/

137. Frazier WJ, Wang X, Wancket LM, Li X-A, Meng X, Nelin LD, et al. Increased Inflammation, Impaired Bacterial Clearance, and Metabolic Disruption after Gram-Negative Sepsis in Mkp-1-Deficient Mice 1. J Immunol [Internet]. 2009 [cited 2024 May 8];183:7411–9. Available from: www.jimmunol.org/cgi/doi/10.4049/jimmunol.0804343

138. Sartori R, Li F, Kirkwood KL. MAP Kinase Phosphatase-1 Protects against Inflammatory Bone Loss. J Dent Res [Internet]. 2009 Dec [cited 2024 May 8];88(12):1125. Available from: /pmc/articles/PMC3144051/

139. Salojin K V., Owusu IB, Millerchip KA, Potter M, Platt KA, Oravecz T. Essential Role of MAPK Phosphatase-1 in the Negative Control of Innate Immune Responses. J Immunol [Internet]. 2006

Feb 1 [cited 2024 May 8];176(3):1899–907. Available from: https://dx.doi.org/10.4049/jimmunol.176.3.1899

140. Matta R, Barnard JA, Wancket LM, Yan J, Xue J, Grieves J, et al. Knockout of Mkp-1 exacerbates colitis in Il-10-deficient mice. Am J Physiol Gastrointest Liver Physiol [Internet]. 2012 [cited 2024 May 8];302:1322–35. Available from: http://www.ajpgi.org

141. Maier J V., Brema S, Tuckermann J, Herzer U, Klein M, Stassen M, et al. Dual specificity phosphatase 1 knockout mice show enhanced susceptibility to anaphylaxis but are sensitive to glucocorticoids. Mol Endocrinol [Internet]. 2007 Nov [cited 2024 May 8];21(11):2663–71. Available from: https://pubmed.ncbi.nlm.nih.gov/17636038/

142. Vattakuzhi Y, Abraham SM, Freidin A, Clark AR, Horwood NJ. Dual-specificity phosphatase 1-null mice exhibit spontaneous osteolytic disease and enhanced inflammatory osteolysis in experimental arthritis. Arthritis Rheum. 2012 Jul;64(7):2201–10.

143. Staples CJ, Owens DM, Maier J V., Cato ACB, Keyse SM. Cross-talk between the p38alpha and JNK MAPK pathways mediated by MAP kinase phosphatase-1 determines cellular sensitivity to UV radiation. J Biol Chem [Internet]. 2010 Aug 20 [cited 2024 May 8];285(34):25928–40. Available from: https://pubmed.ncbi.nlm.nih.gov/20547488/

144. Cho IJ, Woo NR, Shin IC, Kim SG. H89, an inhibitor of PKA and MSK, inhibits cyclic-AMP response element binding protein-mediated MAPK phosphatase-1 induction by lipopolysaccharide. Inflamm Res [Internet]. 2009 Dec [cited 2024 May 8];58(12):863–72. Available from: https://pubmed.ncbi.nlm.nih.gov/19547917/

145. Wong HR, Dunsmore KE, Page K, Shanley TP. Heat shock-mediated regulation of MKP-1. Am J Physiol - Cell Physiol [Internet]. 2005 Nov [cited 2024 May 8];289(5 58-5):1152–8. Available from: https://journals.physiology.org/doi/10.1152/ajpcell.00138.2005

146. Emmons J, Townley-Tilson WHD, Deleault KM, Skinner SJ, Gross RH, Whitfield ML, et al. Identification of TTP mRNA targets in human dendritic cells reveals TTP as a critical regulator of dendritic cell maturation. RNA. 2008 May;14(5):888–902.

147. Hu JH, Chen T, Zhuang ZH, Kong L, Yu MC, Liu Y, et al. Feedback control of MKP-1 expression by p38. Cell Signal [Internet]. 2007 [cited 2024 May 8];19(2):393–400. Available from: https://pubmed.ncbi.nlm.nih.gov/16978838/

148. Tomida T, Takekawa M, Saito H. Oscillation of p38 activity controls efficient pro-inflammatory gene expression. Nat Commun [Internet]. 2015 Sep 24 [cited 2019 Jan 7];6(1):1–9. Available from: http://www.ncbi.nlm.nih.gov/pubmed/26399197

149. Brondello JM, Pouysségur J, McKenzie FR. Reduced MAP kinase phosphatase-1 degradation after p42/p44MAPK-dependent phosphorylation. Science [Internet]. 1999 Dec 24 [cited 2024 May 8];286(5449):2514–7. Available from: https://pubmed.ncbi.nlm.nih.gov/10617468/

150. Li L, Chen SF, Liu Y. MAP kinase phosphatase-1, a critical negative regulator of the innate immune response. Int J Clin Exp Med [Internet]. 2009 [cited 2024 May 8];2(1):48. Available from: /pmc/articles/PMC2680050/

151. Sohaskey ML, Ferrell JE. Activation of p42 mitogen-activated protein kinase (MAPK), but not c-Jun NH(2)-terminal kinase, induces phosphorylation and stabilization of MAPK phosphatase XCL100 in Xenopus oocytes. Mol Biol Cell [Internet]. 2002 [cited 2024 May 8];13(2):454–68. Available from: https://pubmed.ncbi.nlm.nih.gov/11854404/

152. Su J, Xie Q, Wilson I, Li L. Differential regulation and role of interleukin-1 receptor associated kinase-M in innate immunity signaling. Cell Signal [Internet]. 2007 Jul [cited 2024 May 8];19(7):1596–601. Available from: https://pubmed.ncbi.nlm.nih.gov/17379480/

153. Cao W, Bao C, Padalko E, Lowenstein CJ. Acetylation of mitogen-activated protein kinase phosphatase-1 inhibits Toll-like receptor signaling. J Exp Med [Internet]. 2008 Jun 9 [cited 2024 May 8];205(6):1491–503. Available from: https://pubmed.ncbi.nlm.nih.gov/18504304/

154. Toh ML, Yang Y, Leech M, Santos L, Morand EF. Expression of mitogen-activated protein kinase phosphatase 1, a negative regulator of the mitogen-activated protein kinases, in rheumatoid arthritis: up-regulation by interleukin-1beta and glucocorticoids. Arthritis Rheum [Internet]. 2004 Oct [cited 2024 May 8];50(10):3118–28. Available from: https://pubmed.ncbi.nlm.nih.gov/15476200/

155. Kassel O, Sancono A, Krätzschmar J, Kreft B, Stassen M, Cato ACB. Glucocorticoids inhibit MAP kinase via increased expression and decreased degradation of MKP-1. EMBO J [Internet]. 2001 Dec 17 [cited 2024 May 8];20(24):7108–16. Available from: https://pubmed.ncbi.nlm.nih.gov/11742987/

156. Lasa M, Abraham SM, Boucheron C, Saklatvala J, Clark AR. Dexamethasone Causes Sustained Expression of Mitogen-Activated Protein Kinase (MAPK) Phosphatase 1 and Phosphatase-Mediated Inhibition of MAPK p38. Mol Cell Biol. 2002 Nov 15;22(22):7802–11.

157. Takekawa M, Adachi M, Nakahata A, Nakayama I, Itoh F, Tsukuda H, et al. p53-inducible Wip1 phosphatase mediates a negative feedback regulation of p38 MAPK-p53 signaling in response to UV radiation. EMBO J [Internet]. 2000 Dec 1 [cited 2024 May 8];19(23):6517–26. Available from: https://www.embopress.org/doi/10.1093/emboj/19.23.6517

158. Takekawa M, Maeda T, Saito H. Protein phosphatase 2Cα inhibits the human stress-responsive p38 and JNK MAPK pathways. EMBO J [Internet]. 1998 Aug 17 [cited 2024 May 8];17(16):4744–52. Available from: https://www.embopress.org/doi/10.1093/emboj/17.16.4744

159. Deb I, Manhas N, Poddar R, Rajagopal S, Allan AM, Lombroso PJ, et al. Neuroprotective Role of a Brain-Enriched Tyrosine Phosphatase, STEP, in Focal Cerebral Ischemia. J Neurosci [Internet]. 2013 Nov 11 [cited 2024 Jul 25];33(45):17814. Available from: /pmc/articles/PMC3818554/

160. Francis DM, Rä B, Koveal D, Hummer G, Page R, Peti W. Structural basis of p38α regulation by hematopoietic tyrosine phosphatase. Nat Chem Biol [Internet]. 2011 [cited 2024 Jul 25];7(12):916–24. Available from: /pmc/articles/PMC3657131/

161. Muñoz JJ, Tárrega C, Blanco-Aparicio C, Pulido R. Differential interaction of the tyrosine phosphatases PTP-SL, STEP and HePTP with the mitogen-activated protein kinases ERK1/2 and p38alpha is determined by a kinase specificity sequence and influenced by reducing agents. Biochem J [Internet]. 2003 May 15 [cited 2024 Jul 25];372(Pt 1):193–201. Available from: https://pubmed.ncbi.nlm.nih.gov/12583813/

162. Lee T, Kim SJ, Sumpio BE. Role of PP2A in the regulation of p38 MAPK activation in bovine aortic endothelial cells exposed to cyclic strain. J Cell Physiol [Internet]. 2003 Mar 1 [cited 2024 May 8];194(3):349–55. Available from: https://pubmed.ncbi.nlm.nih.gov/12548554/

163. Fey D, Croucher DR, Kolch W, Kholodenko BN, Barberis M. Crosstalk and signaling switches in mitogen-activated protein kinase cascades. 2012 [cited 2024 May 8]; Available from: www.frontiersin.org

164. Westermarck J, Li S-P, Kallunki T, Han J, Kähäri V-M. p38 mitogen-activated protein kinase-dependent activation of protein phosphatases 1 and 2A inhibits MEK1 and MEK2 activity and collagenase 1 (MMP-1) gene expression. Mol Cell Biol [Internet]. 2001 Apr 1 [cited 2024 May 8];21(7):2373–83. Available from: https://pubmed.ncbi.nlm.nih.gov/11259586/

165. Junttila MR, Li S, Westermarck J. Phosphatase-mediated crosstalk between MAPK signaling pathways in the regulation of cell survival. FASEB J [Internet]. 2008 Apr [cited 2024 Jul 25];22(4):954–65. Available from: https://pubmed.ncbi.nlm.nih.gov/18039929/

166. Grethe S, Pörn-Ares MI. p38 MAPK regulates phosphorylation of Bad via PP2A-dependent suppression of the MEK1/2-ERK1/2 survival pathway in TNF-α induced endothelial apoptosis. Cell Signal. 2006 Apr 1;18(4):531–40.

167. Li D, Ren W, Jiang Z, Zhu L. Regulation of the NLRP3 inflammasome and macrophage pyroptosis by the p38 MAPK signaling pathway in a mouse model of acute lung injury. Mol Med Rep [Internet]. 2018 Nov 1 [cited 2024 May 22];18(5):4399–409. Available from: https://pubmed.ncbi.nlm.nih.gov/30152849/

168. Romero-Becerra R, Santamans AM, Folgueira C, Sabio G. p38 MAPK Pathway in the Heart: New Insights in Health and Disease. Int J Mol Sci [Internet]. 2020 Oct 1 [cited 2024 May 22];21(19):1–19. Available from: https://pubmed.ncbi.nlm.nih.gov/33049962/

169. Zou X, Blank M. Targeting p38 MAP kinase signaling in cancer through post-translational modifications. Cancer Lett. 2017 Jan 1;384:19–26.

170. Böhm C, Hayer S, Kilian A, Zaiss MM, Finger S, Hess A, et al. The α-Isoform of p38 MAPK Specifically Regulates Arthritic Bone Loss. J Immunol. 2009 Nov 1;183(9):5938–47.

171. Mbalaviele G, Anderson G, Jones A, De Ciechi P, Settle S, Mnich S, et al. Inhibition of p38 mitogen-activated protein kinase prevents inflammatory bone destruction. J Pharmacol Exp Ther [Internet]. 2006 Jun [cited 2024 May 17];317(3):1044–53. Available from: https://pubmed.ncbi.nlm.nih.gov/16501068/

172. Underwood DC, Osborn RR, Bochnowicz S, Webb EF, Rieman DJ, Lee JC, et al. SB 239063, a p38 MAPK inhibitor, reduces neutrophilia, inflammatory cytokines, MMP-9, and fibrosis in lung. Am J Physiol Lung Cell Mol Physiol [Internet]. 2000 [cited 2024 May 17];279(5). Available from: https://pubmed.ncbi.nlm.nih.gov/11053025/

173. Pietersma A, Tilly BC, Gaestel M, De Jong N, Lee JC, Koster JF, et al. p38 mitogen activated protein kinase regulates endothelial VCAM-1 expression at the post-transcriptional level. Biochem Biophys Res Commun [Internet]. 1997 Jan 3 [cited 2024 May 22];230(1):44–8. Available from: https://pubmed.ncbi.nlm.nih.gov/9020057/

174. Read MA, Whitley MZ, Gupta S, Pierce JW, Best J, Davis RJ, et al. Tumor necrosis factor alpha-induced E-selectin expression is activated by the nuclear factor-kappaB and c-JUN N-terminal kinase/p38 mitogen-activated protein kinase pathways. J Biol Chem [Internet]. 1997 [cited 2024 May 22];272(5):2753–61. Available from: https://pubmed.ncbi.nlm.nih.gov/9006914/

175. Schindler JF, Monahan JB, Smith WG. p38 pathway kinases as anti-inflammatory drug targets. J Dent Res [Internet]. 2007 Sep [cited 2024 May 22];86(9):800–11. Available from: https://pubmed.ncbi.nlm.nih.gov/17720847/

176. Damjanov N, Kauffman RS, Spencer-Green GT. Efficacy, pharmacodynamics, and safety of VX-702, a novel p38 MAPK inhibitor, in rheumatoid arthritis: results of two randomized, double-blind, placebo-controlled clinical studies. Arthritis Rheum [Internet]. 2009 May [cited

2024 May 22];60(5):1232–41. Available from: https://pubmed.ncbi.nlm.nih.gov/19404957/

177. Genovese MC, Cohen SB, Wofsy D, Weinblatt ME, Firestein GS, Brahn E, et al. A 24-week, randomized, double-blind, placebo-controlled, parallel group study of the efficacy of oral SCIO-469, a p38 mitogen-activated protein kinase inhibitor, in patients with active rheumatoid arthritis. J Rheumatol [Internet]. 2011 May [cited 2024 May 22];38(5):846–54. Available from: https://pubmed.ncbi.nlm.nih.gov/21285160/

178. Genovese MC. Inhibition of p38: Has the fat lady sung? Arthritis Rheum [Internet]. 2009 Feb 1 [cited 2019 Feb 15];60(2):317–20. Available from: http://doi.wiley.com/10.1002/art.24264

179. Hedström U, Norberg M, Evertsson E, Lever SR, Munck af Rosenschöld M, Lönn H, et al. An Angle on MK2 Inhibition-Optimization and Evaluation of Prevention of Activation Inhibitors. ChemMedChem [Internet]. 2019 Oct 4 [cited 2024 May 22];14(19):1701–9. Available from: https://pubmed.ncbi.nlm.nih.gov/31325352/

180. Ronkina N, Menon MB, Schwermann J, Tiedje C, Hitti E, Kotlyarov A, et al. MAPKAP kinases MK2 and MK3 in inflammation: Complex regulation of TNF biosynthesis via expression and phosphorylation of tristetraprolin. Biochem Pharmacol. 2010 Dec 15;80(12):1915–20.

181. Schlapbach A, Feifel R, Hawtin S, Heng R, Koch G, Moebitz H, et al. Pyrrolo-pyrimidones: A novel class of MK2 inhibitors with potent cellular activity. Bioorg Med Chem Lett. 2008 Dec 1;18(23):6142–6.

182. Mourey RJ, Burnette BL, Brustkern SJ, Daniels JS, Hirsch JL, Hood WF, et al. A Benzothiophene Inhibitor of Mitogen-Activated Protein Kinase-Activated Protein Kinase 2 Inhibits Tumor Necrosis Factor α Production and Has Oral Anti-Inflammatory Efficacy in Acute and Chronic Models of Inflammation. J Pharmacol Exp Ther [Internet]. 2010 Jun 1 [cited 2024 May 22];333(3):797–807. Available from: https://jpet.aspetjournals.org/content/333/3/797

183. Wang C, Hockerman S, Jacobsen EJ, Alippe Y, Selness SR, Hope HR, et al. Selective inhibition of the p38α MAPK-MK2 axis inhibits inflammatory cues including inflammasome priming signals. J Exp Med [Internet]. 2018 May 1 [cited 2024 May 22];215(5):1315–25. Available from: https://pubmed.ncbi.nlm.nih.gov/29549113/

184. Gordon D, Hellriegel ET, Hope HR, Burt D, Monahan JB. Safety, Tolerability, Pharmacokinetics, and Pharmacodynamics of the MK2 Inhibitor ATI-450 in Healthy Subjects: A Placebo-Controlled, Randomized Phase 1 Study. Clin Pharmacol [Internet]. 2021 [cited 2024 May 22];13:123–34. Available from: https://pubmed.ncbi.nlm.nih.gov/34140814/

185. Sanduja S, Blanco FF, Dixon DA. The roles of TTP and BRF proteins in regulated mRNA decay. Wiley Interdiscip Rev RNA [Internet]. 2011 Jan [cited 2021 Feb 16];2(1):42–57. Available from: /pmc/articles/PMC3030256/

186. Varnum BC, Lim RW, Sukhatme VP, Herschman HR. Nucleotide sequence of a cDNA encoding TIS11, a message induced in Swiss 3T3 cells by the tumor promoter tetradecanoyl phorbol acetate. Oncogene [Internet]. 1989 Jan [cited 2019 Mar 27];4(1):119–20. Available from: http://www.ncbi.nlm.nih.gov/pubmed/2915901

187. Phillips RS, Ramos SBV, Blackshear PJ. Members of the tristetraprolin family of tandem CCCH zinc finger proteins exhibit CRM1-dependent nucleocytoplasmic shuttling. J Biol Chem. 2002 Mar 29;277(13):11606–13.

188. Lai WS, Carballo E, Thorn JM, Kennington EA, Blackshear PJ. Interactions of CCCH zinc finger proteins with mRNA. Binding of tristetraprolin-related zinc finger proteins to Au-rich elements

and destabilization of mRNA. J Biol Chem [Internet]. 2000 Jun 9 [cited 2019 Mar 31];275(23):17827–37. Available from: http://www.ncbi.nlm.nih.gov/pubmed/10751406

189. Lai WS, Stumpo DJ, Blackshear PJ. Rapid insulin-stimulated accumulation of an mRNA encoding a proline-rich protein. J Biol Chem [Internet]. 1990 Sep 25 [cited 2019 Mar 27];265(27):16556–63. Available from: http://www.ncbi.nlm.nih.gov/pubmed/2204625

190. Lykke-Andersen J, Wagner E. Recruitment and activation of mRNA decay enzymes by two ARE-mediated decay activation domains in the proteins TTP and BRF-1. Genes Dev [Internet]. 2005 Jan 13 [cited 2019 Mar 31];19(3):351–61. Available from: http://www.ncbi.nlm.nih.gov/pubmed/15687258

191. Murata T, Yoshino Y, Morita N, Kaneda N. Identification of nuclear import and export signals within the structure of the zinc finger protein TIS11. Biochem Biophys Res Commun [Internet]. 2002 May 17 [cited 2019 Dec 5];293(4):1242–7. Available from: http://www.ncbi.nlm.nih.gov/pubmed/12054509

192. Taylor GA, Carballo E, Lee DM, Lai WS, Thompson MJ, Patel DD, et al. A pathogenetic role for TNF alpha in the syndrome of cachexia, arthritis, and autoimmunity resulting from tristetraprolin (TTP) deficiency. Immunity [Internet]. 1996 May 1 [cited 2019 Mar 27];4(5):445–54. Available from: http://www.ncbi.nlm.nih.gov/pubmed/8630730

193. Taylor GA, Thompson MJ, Lai WS, Blackshear PJ. Phosphorylation of tristetraprolin, a potential zinc finger transcription factor, by mitogen stimulation in intact cells and by mitogen-activated protein kinase in vitro. J Biol Chem [Internet]. 1995 Jun 2 [cited 2024 May 14];270(22):13341–7. Available from: https://pubmed.ncbi.nlm.nih.gov/7768935/

194. DuBois RN, McLane MW, Ryder K, Lau LF, Nathans D. A growth factor-inducible nuclear protein with a novel cysteine/histidine repetitive sequence. J Biol Chem [Internet]. 1990 Nov 5 [cited 2019 Mar 27];265(31):19185–91. Available from: http://www.ncbi.nlm.nih.gov/pubmed/1699942

195. Heximer SP, Forsdyke DR. A human putative lymphocyte G0/G1 switch gene homologous to a rodent gene encoding a zinc-binding potential transcription factor. DNA Cell Biol [Internet]. [cited 2019 Mar 27];12(1):73–88. Available from: http://www.ncbi.nlm.nih.gov/pubmed/8422274

196. Carballo E, Lai WS, Blackshear PJ. Feedback Inhibition of Macrophage Tumor Necrosis Factor-α Production by Tristetraprolin. Science (80-) [Internet]. 1998 Aug 14 [cited 2024 May 14];281(5379):1001–5. Available from: https://www.science.org/doi/10.1126/science.281.5379.1001

197. Lai WS, Carballo E, Strum JR, Kennington EA, Phillips RS, Blackshear PJ. Evidence that Tristetraprolin Binds to AU-Rich Elements and Promotes the Deadenylation and Destabilization of Tumor Necrosis Factor Alpha mRNA. Mol Cell Biol. 1999 Jun 1;19(6):4311–23.

198. Chen CY, Shyu AB. AU-rich elements: characterization and importance in mRNA degradation. Trends Biochem Sci [Internet]. 1995 Nov [cited 2019 Mar 31];20(11):465–70. Available from: http://www.ncbi.nlm.nih.gov/pubmed/8578590

199. Caput D, Beutler B, Hartog K, Thayer R, Brown-Shimer S, Cerami A. Identification of a common nucleotide sequence in the 3'-untranslated region of mRNA molecules specifying inflammatory mediators. Proc Natl Acad Sci U S A [Internet]. 1986 Mar [cited 2019 Mar 31];83(6):1670–4. Available from: http://www.ncbi.nlm.nih.gov/pubmed/2419912

200. Shaw G, Kamen R. A conserved AU sequence from the 3′ untranslated region of GM-CSF mRNA mediates selective mRNA degradation. Cell [Internet]. 1986 Aug 29 [cited 2021 Jan 19];46(5):659–67. Available from: https://pubmed.ncbi.nlm.nih.gov/3488815/

201. García-Mauriño SM, Rivero-Rodríguez F, Velázquez-Cruz A, Hernández-Vellisca M, Díaz-Quintana A, De la Rosa MA, et al. RNA binding protein regulation and cross-talk in the control of AU-rich mRNA Fate [Internet]. Vol. 4, Frontiers in Molecular Biosciences. Frontiers Media S.A.; 2017 [cited 2021 Feb 11]. p. 71. Available from: www.frontiersin.org

202. Gruber AR, Fallmann J, Kratochvill F, Kovarik P, Hofacker IL. AREsite: A database for the comprehensive investigation of AU-rich elements. Nucleic Acids Res [Internet]. 2011 Jan [cited 2021 Jan 19];39(SUPPL. 1):66–9. Available from: https://pubmed.ncbi.nlm.nih.gov/21071424/

203. Halees AS, El-badrawi R, Khabar KSA. ARED Organism: Expansion of ARED reveals AU-rich element cluster variations between human and mouse. Nucleic Acids Res [Internet]. 2008 Jan [cited 2021 Jan 19];36(SUPPL. 1):D137. Available from: /pmc/articles/PMC2238997/?report=abstract

204. Kontoyiannis D, Pasparakis M, Pizarro TT, Cominelli F, Kollias G. Impaired on/off regulation of TNF biosynthesis in mice lacking TNF AU- rich elements: Implications for joint and gut-associated immunopathologies. Immunity [Internet]. 1999 [cited 2020 Nov 14];10(3):387–98. Available from: https://pubmed.ncbi.nlm.nih.gov/10204494/

205. Gherzi R, Lee KY, Briata P, Wegmüller D, Moroni C, Karin M, et al. A KH domain RNA binding protein, KSRP, promotes ARE-directed mRNA turnover by recruiting the degradation machinery. Mol Cell [Internet]. 2004 Jun 4 [cited 2021 Feb 16];14(5):571–83. Available from: https://pubmed.ncbi.nlm.nih.gov/15175153/

206. Brewer G. An A + U-rich element RNA-binding factor regulates c-myc mRNA stability in vitro. Mol Cell Biol [Internet]. 1991 May [cited 2021 Feb 16];11(5):2460–6. Available from: /pmc/articles/PMC360010/?report=abstract

207. Brennan CM, Steitz JA. HuR and mRNA stability. Vol. 58, Cellular and Molecular Life Sciences. Birkhauser Verlag Basel; 2001. p. 266–77.

208. Brooks SA, Blackshear PJ. Tristetraprolin (TTP): interactions with mRNA and proteins, and current thoughts on mechanisms of action. Biochim Biophys Acta [Internet]. 2013 [cited 2019 Jan 8];1829(6–7):666–79. Available from: http://www.ncbi.nlm.nih.gov/pubmed/23428348

209. Blackshear PJ, Lai WS, Kennington EA, Brewer G, Wilson GM, Guan X, et al. Characteristics of the interaction of a synthetic human tristetraprolin tandem zinc finger peptide with AU-rich element-containing RNA substrates. J Biol Chem [Internet]. 2003 May 30 [cited 2019 Mar 31];278(22):19947–55. Available from: http://www.ncbi.nlm.nih.gov/pubmed/12639954

210. Lai WS, Stumpo DJ, Qiu L, Faccio R, Blackshear PJ. A Knock-In Tristetraprolin (TTP) Zinc Finger Point Mutation in Mice: Comparison with Complete TTP Deficiency. Mol Cell Biol [Internet]. 2018 Feb 1 [cited 2024 Jun 4];38(4). Available from: https://pubmed.ncbi.nlm.nih.gov/29203639/

211. Hudson BP, Martinez-Yamout MA, Dyson HJ, Wright PE. Recognition of the mRNA AU-rich element by the zinc finger domain of TIS11d. Nat Struct Mol Biol. 2004 Mar;11(3):257–64.

212. Carballo E, Blackshear PJ. Roles of tumor necrosis factor-alpha receptor subtypes in the pathogenesis of the tristetraprolin-deficiency syndrome. Blood [Internet]. 2001 Oct 15 [cited 2024 May 15];98(8):2389–95. Available from: https://pubmed.ncbi.nlm.nih.gov/11588035/

213. Carballo E, Lai WS, Blackshear PJ. Evidence that tristetraprolin is a physiological regulator of granulocyte-macrophage colony-stimulating factor messenger RNA deadenylation and stability. Blood. 2000 Mar 15;95(6):1891–9.

214. Sedlyarov V, Fallmann J, Ebner F, Huemer J, Sneezum L, Ivin M, et al. Tristetraprolin binding site atlas in the macrophage transcriptome reveals a switch for inflammation resolution. Mol Syst Biol [Internet]. 2016 May [cited 2024 May 16];12(5). Available from: https://pubmed.ncbi.nlm.nih.gov/27178967/

215. Tiedje C, Diaz-Muñoz MD, Trulley P, Ahlfors H, Laaß K, Blackshear PJ, et al. The RNA-binding protein TTP is a global post-transcriptional regulator of feedback control in inflammation. Nucleic Acids Res [Internet]. 2016 Sep 6 [cited 2019 Jan 16];44(15). Available from: https://pubmed.ncbi.nlm.nih.gov/27220464/

216. Wolf J, Passmore LA. MRNA deadenylation by Pan2-Pan3. Biochem Soc Trans [Internet]. 2014 Feb [cited 2021 May 27];42(1):184–7. Available from: https://pubmed.ncbi.nlm.nih.gov/24450649/

217. Collart MA. The Ccr4-Not complex is a key regulator of eukaryotic gene expression [Internet]. Vol. 7, Wiley Interdisciplinary Reviews: RNA. Blackwell Publishing Ltd; 2016 [cited 2021 May 27]. p. 438–54. Available from: https://pubmed.ncbi.nlm.nih.gov/26821858/

218. Chang C Te, Bercovich N, Loh B, Jonas S, Izaurralde E. The activation of the decapping enzyme DCP2 by DCP1 occurs on the EDC4 scaffold and involves a conserved loop in DCP1. Nucleic Acids Res [Internet]. 2014 [cited 2021 Jun 14];42(8):5217–33. Available from: https://pubmed.ncbi.nlm.nih.gov/24510189/

219. Eulalio A, Behm-Ansmant I, Izaurralde E. P bodies: At the crossroads of post-transcriptional pathways [Internet]. Vol. 8, Nature Reviews Molecular Cell Biology. Nat Rev Mol Cell Biol; 2007 [cited 2021 May 19]. p. 9–22. Available from: https://pubmed.ncbi.nlm.nih.gov/17183357/

220. Garneau NL, Wilusz J, Wilusz CJ. The highways and byways of mRNA decay [Internet]. Nature Reviews Molecular Cell Biology Nature Publishing Group; Feb 1, 2007 p. 113–26. Available from: http://www.nature.com/articles/nrm2104

221. Fabian MR, Frank F, Rouya C, Siddiqui N, Lai WS, Karetnikov A, et al. Structural basis for the recruitment of the human CCR4-NOT deadenylase complex by tristetraprolin. Nat Struct Mol Biol. 2013 Jun;20(6):735–9.

222. Bulbrook D, Brazier H, Mahajan P, Kliszczak M, Fedorov O, Marchese FP, et al. Tryptophan-Mediated Interactions between Tristetraprolin and the CNOT9 Subunit Are Required for CCR4-NOT Deadenylase Complex Recruitment. J Mol Biol [Internet]. 2018 Mar 2 [cited 2021 May 18];430(5):722–36. Available from: https://pubmed.ncbi.nlm.nih.gov/29291391/

223. Sandler H, Kreth J, Timmers HTM, Stoecklin G. Not1 mediates recruitment of the deadenylase Caf1 to mRNAs targeted for degradation by tristetraprolin. Nucleic Acids Res [Internet]. 2011 May [cited 2019 Mar 31];39(10):4373–86. Available from: https://academic.oup.com/nar/article-lookup/doi/10.1093/nar/gkr011

224. Tiedje C, Kotlyarov A, Gaestel M. Molecular mechanisms of phosphorylation-regulated TTP (tristetraprolin) action and screening for further TTP-interacting proteins. In: Biochemical Society Transactions. 2010. p. 1632–7.

225. Hau HH, Walsh RJ, Ogilvie RL, Williams DA, Reilly CS, Bohjanen PR. Tristetraprolin recruits functional mRNA decay complexes to ARE sequences. J Cell Biochem [Internet]. 2007 Apr 15

[cited 2021 May 19];100(6):1477–92. Available from: https://pubmed.ncbi.nlm.nih.gov/17133347/

226. Luo Y, Na Z, Slavoff SA. P-Bodies: Composition, Properties, and Functions [Internet]. Vol. 57, Biochemistry. American Chemical Society; 2018 [cited 2021 May 19]. p. 2424–31. Available from: https://pubmed.ncbi.nlm.nih.gov/29381060/

227. Stoecklin G, Anderson P. In a tight spot: ARE-mRNAs at processing bodies [Internet]. Vol. 21, Genes and Development. Cold Spring Harbor Laboratory Press; 2007 [cited 2021 May 19]. p. 627–31. Available from: http://www.genesdev.org/cgi/doi/10.1101/gad.1538807.

228. Standart N, Weil D. P-Bodies: Cytosolic Droplets for Coordinated mRNA Storage [Internet]. Vol. 34, Trends in Genetics. Elsevier Ltd; 2018 [cited 2021 May 19]. p. 612–26. Available from: http://www.cell.com/article/S0168952518300908/fulltext

229. Franks TM, Lykke-Andersen J. TTP and BRF proteins nucleate processing body formation to silence mRNAs with AU-rich elements. Genes Dev. 2007 Mar 15;21(6):719–35.

230. Tian S, Curnutte HA, Trcek T. RNA granules: A view from the RNA perspective [Internet]. Vol. 25, Molecules. MDPI AG; 2020 [cited 2021 May 19]. Available from: https://pubmed.ncbi.nlm.nih.gov/32650583/

231. Chan LY, Mugler CF, Heinrich S, Vallotton P, Weis K. Non-invasive measurement of mRNA decay reveals translation initiation as the major determinant of mRNA stability. Elife. 2018 Sep 1;7.

232. Mugridge JS, Coller J, Gross JD. Structural and molecular mechanisms for the control of eukaryotic 5′–3′ mRNA decay. Nat Struct Mol Biol [Internet]. 2018 Dec 1 [cited 2021 May 25];25(12):1077–85. Available from: https://doi.org/10.1038/s41594-018-0164-z

233. Wang C, Schmich F, Srivatsa S, Weidner J, Beerenwinkel N, Spang A. Context-dependent deposition and regulation of mRNAs in P-bodies. Elife [Internet]. 2018 Jan 3 [cited 2021 May 19];7. Available from: https://pubmed.ncbi.nlm.nih.gov/29297464/

234. Horvathova I, Voigt F, Kotrys A V., Zhan Y, Artus-Revel CG, Eglinger J, et al. The Dynamics of mRNA Turnover Revealed by Single-Molecule Imaging in Single Cells. Mol Cell [Internet]. 2017 Nov 2 [cited 2021 Mar 3];68(3):615-625.e9. Available from: https://pubmed.ncbi.nlm.nih.gov/29056324/

235. Fenger-Grøn M, Fillman C, Norrild B, Lykke-Andersen J. Multiple processing body factors and the ARE binding protein TTP activate mRNA decapping. Mol Cell [Internet]. 2005 Dec 22 [cited 2024 May 16];20(6):905–15. Available from: https://pubmed.ncbi.nlm.nih.gov/16364915/

236. Blanco FF, Sanduja S, Deane NG, Blackshear PJ, Dixon DA. Transforming growth factor β regulates P-body formation through induction of the mRNA decay factor tristetraprolin. Mol Cell Biol [Internet]. 2014 Jan 1 [cited 2024 May 24];34(2):180–95. Available from: https://pubmed.ncbi.nlm.nih.gov/24190969/

237. Schichl YM, Resch U, Hofer-Warbinek R, de Martin R. Tristetraprolin Impairs NF-κB/p65 Nuclear Translocation. J Biol Chem [Internet]. 2009 Oct 10 [cited 2024 May 16];284(43):29571. Available from: /pmc/articles/PMC2785590/

238. Tu Y, Wu X, Yu F, Dang J, Wang J, Wei Y, et al. Tristetraprolin specifically regulates the expression and alternative splicing of immune response genes in HeLa cells. BMC Immunol [Internet]. 2019 May 2 [cited 2024 May 16];20(1). Available from: /pmc/articles/PMC6498542/

239. Jing Q, Huang S, Guth S, Zarubin T, Motoyama A, Chen J, et al. Involvement of microRNA in AU-rich element-mediated mRNA instability. Cell [Internet]. 2005 Mar 11 [cited 2024 May 23];120(5):623–34. Available from: https://pubmed.ncbi.nlm.nih.gov/15766526/

240. Taylor GA, Lai WS, Oakey RJ, Seldin MF, Shows TB, Eddy RL, et al. The human TTP protein: sequence, alignment with related proteins, and chromosomal localization of the mouse and human genes. Nucleic Acids Res [Internet]. 1991 [cited 2019 Mar 27];19(12):3454. Available from: https://www.ncbi.nlm.nih.gov/pmc/articles/PMC328350/

241. Saunders AM, Seldin MF. A molecular genetic linkage map of mouse chromosome 7. Genomics [Internet]. 1990 [cited 2024 May 23];8(3):525–35. Available from: https://pubmed.ncbi.nlm.nih.gov/1981054/

242. Lai WS, Thompson MJ, Taylor GA, Liu Y, Blackshear PJ. Promoter analysis of Zfp-36, the mitogen-inducible gene encoding the zinc finger protein tristetraprolin. J Biol Chem [Internet]. 1995 Oct 20 [cited 2024 May 23];270(42):25266–72. Available from: http://www.jbc.org/article/S0021925818871186/fulltext

243. Fallahi M, Amelio AL, Cleveland JL, Rounbehler RJ. CREB Targets Define the Gene Expression Signature of Malignancies Having Reduced Levels of the Tumor Suppressor Tristetraprolin. PLoS One [Internet]. 2014 Dec 26 [cited 2024 Jul 25];9(12). Available from: /pmc/articles/PMC4277357/

244. Florkowska M, Tymoszuk P, Balwierz A, Skucha A, Kochan J, Wawro M, et al. EGF activates TTP expression by activation of ELK-1 and EGR-1 transcription factors. BMC Mol Biol [Internet]. 2012 Mar 20 [cited 2021 May 20];13. Available from: https://pubmed.ncbi.nlm.nih.gov/22433566/

245. Patial S, Curtis AD, Lai WS, Stumpo DJ, Hill GD, Flake GP, et al. Enhanced stability of tristetraprolin mRNA protects mice against immune-mediated inflammatory pathologies. Proc Natl Acad Sci U S A [Internet]. 2016 Feb 16 [cited 2024 Jul 25];113(7):1865–70. Available from: /pmc/articles/PMC4763790/

246. Guo J, Li J, Zhao J, Yang S, Wang L, Cheng G, et al. MiRNA-29c regulates the expression of inflammatory cytokines in diabetic nephropathy by targeting tristetraprolin. Sci Reports 2017 71 [Internet]. 2017 May 24 [cited 2024 Jul 25];7(1):1–13. Available from: https://www.nature.com/articles/s41598-017-01027-5

247. Liu J, Sisk JM, Gama L, Clements JE, Witwer KW. Tristetraprolin expression and microRNA-mediated regulation during simian immunodeficiency virus infection of the central nervous system. Mol Brain [Internet]. 2013 Sep 2 [cited 2024 Jul 25];6(1):1–10. Available from: https://molecularbrain.biomedcentral.com/articles/10.1186/1756-6606-6-40

248. Semaan N, Frenzel L, Alsaleh G, Suffert G, Gottenberg JE, Sibilia J, et al. miR-346 Controls Release of TNF-α Protein and Stability of Its mRNA in Rheumatoid Arthritis via Tristetraprolin Stabilization. PLoS One [Internet]. 2011 [cited 2024 Jul 25];6(5):e19827. Available from: https://journals.plos.org/plosone/article?id=10.1371/journal.pone.0019827

249. Gebeshuber CA, Zatloukal K, Martinez J. miR-29a suppresses tristetraprolin, which is a regulator of epithelial polarity and metastasis. EMBO Rep [Internet]. 2009 Feb 27 [cited 2024 Jul 25];10(4):400–5. Available from: https://www.embopress.org/doi/10.1038/embor.2009.9

250. Tchen CR, Brook M, Saklatvala J, Clark AR. The stability of tristetraprolin mRNA is regulated by mitogen-activated protein kinase p38 and by tristetraprolin itself. J Biol Chem. 2004 Jul 30;279(31):32393–400.

251. Brooks SA, Connolly JE, Rigby WFC. The role of mRNA turnover in the regulation of tristetraprolin expression: evidence for an extracellular signal-regulated kinase-specific, AU-rich element-dependent, autoregulatory pathway. J Immunol [Internet]. 2004 Jun 15 [cited 2024 May 23];172(12):7263–71. Available from: https://pubmed.ncbi.nlm.nih.gov/15187101/

252. Cao H, Deterding LJ, Blackshear PJ. Phosphorylation site analysis of the anti-inflammatory and mRNA-destabilizing protein tristetraprolin. Expert Rev Proteomics [Internet]. 2007 Dec 9 [cited 2019 Mar 31];4(6):711–26. Available from: http://www.ncbi.nlm.nih.gov/pubmed/18067411

253. TTP (mouse) [Internet]. [cited 2024 May 23]. Available from: https://www.phosphosite.org/proteinAction.action?id=4832&showAllSites=true

254. Hitti E, Iakovleva T, Brook M, Deppenmeier S, Gruber AD, Radzioch D, et al. Mitogen-activated protein kinase-activated protein kinase 2 regulates tumor necrosis factor mRNA stability and translation mainly by altering tristetraprolin expression, stability, and binding to adenine/uridine-rich element. Mol Cell Biol [Internet]. 2006 Mar 1 [cited 2024 May 16];26(6):2399–407. Available from: https://pubmed.ncbi.nlm.nih.gov/16508014/

255. Cao H. Expression, purification, and biochemical characterization of the antiinflammatory tristetraprolin: A zinc-dependent mRNA binding protein affected by posttranslational modifications. In: Biochemistry. 2004. p. 13724–38.

256. Stoecklin G, Stubbs T, Kedersha N, Wax S, Rigby WFC, Blackwell TK, et al. MK2-induced tristetraprolin:14-3-3 complexes prevent stress granule association and ARE-mRNA decay. EMBO J [Internet]. 2004 Mar 24 [cited 2024 Jun 4];23(6):1313–24. Available from: https://pubmed.ncbi.nlm.nih.gov/15014438/

257. Clement SL, Scheckel C, Stoecklin G, Lykke-Andersen J. Phosphorylation of tristetraprolin by MK2 impairs AU-rich element mRNA decay by preventing deadenylase recruitment. Mol Cell Biol [Internet]. 2011 Jan 1 [cited 2024 Jul 25];31(2):256–66. Available from: https://pubmed.ncbi.nlm.nih.gov/21078877/

258. Marchese FP, Aubareda A, Tudor C, Saklatvala J, Clark AR, Dean JLE. MAPKAP Kinase 2 Blocks Tristetraprolin-directed mRNA Decay by Inhibiting CAF1 Deadenylase Recruitment. J Biol Chem [Internet]. 2010 Sep 3 [cited 2019 Jan 16];285(36):27590–600. Available from: http://www.ncbi.nlm.nih.gov/pubmed/20595389

259. Sun L, Stoecklin G, Van Way S, Hinkovska-Galcheva V, Guo RF, Anderson P, et al. Tristetraprolin (TTP)-14-3-3 complex formation protects TTP from dephosphorylation by protein phosphatase 2a and stabilizes tumor necrosis factor-α mRNA. J Biol Chem. 2007;282(6):3766–77.

260. Ross EA, Smallie T, Ding Q, O'Neil JD, Cunliffe HE, Tang T, et al. Dominant Suppression of Inflammation via Targeted Mutation of the mRNA Destabilizing Protein Tristetraprolin. J Immunol [Internet]. 2015 Jul 1 [cited 2019 Jan 15];195(1):265–76. Available from: http://www.ncbi.nlm.nih.gov/pubmed/26002976

261. Ronkina N, Shushakova N, Tiedje C, Yakovleva T, Tollenaere MAX, Scott A, et al. The Role of TTP Phosphorylation in the Regulation of Inflammatory Cytokine Production by MK2/3. J Immunol. 2019 Oct 15;203(8):2291–300.

262. Liu Q, Hofmann PA. Protein phosphatase 2A-mediated cross-talk between p38 MAPK and ERK in apoptosis of cardiac myocytes. Am J Physiol Heart Circ Physiol [Internet]. 2004 Jun [cited 2024 May 8];286(6). Available from: https://pubmed.ncbi.nlm.nih.gov/14962831/

263. Taylor GA, Thompson MJ, Lai WS, Blackshear PJ. Mitogens stimulate the rapid nuclear to cytosolic translocation of tristetraprolin, a potential zinc-finger transcription factor. Mol Endocrinol [Internet]. 1996 Feb [cited 2024 May 23];10(2):140–6. Available from: https://pubmed.ncbi.nlm.nih.gov/8825554/

264. Johnson BA, Stehn JR, Yaffe MB, Keith Blackwell T. Cytoplasmic localization of tristetraprolin involves 14-3-3-dependent and -independent mechanisms. J Biol Chem. 2002 May 17;277(20):18029–36.

265. Cao H, Tuttle JS, Blackshear PJ. Immunological characterization of tristetraprolin as a low abundance, inducible, stable cytosolic protein. J Biol Chem. 2004 May 14;279(20):21489–99.

266. Brook M, Tchen CR, Santalucia T, McIlrath J, Arthur JSC, Saklatvala J, et al. Posttranslational regulation of tristetraprolin subcellular localization and protein stability by p38 mitogen-activated protein kinase and extracellular signal-regulated kinase pathways. Mol Cell Biol [Internet]. 2006 Mar [cited 2019 Jan 16];26(6):2408–18. Available from: http://www.ncbi.nlm.nih.gov/pubmed/16508015

267. Rezcallah MC, Al-mazi T, Ammit AJ. Cataloguing the phosphorylation sites of tristetraprolin (TTP): Functional implications for inflammatory diseases. Cell Signal. 2021 Feb 1;78:109868.

268. Kedersha N, Stoecklin G, Ayodele M, Yacono P, Lykke-Andersen J, Fitzler MJ, et al. Stress granules and processing bodies are dynamically linked sites of mRNP remodeling. J Cell Biol. 2005 Jun;169(6):871–84.

269. Qi MY, Song JW, Zhang Z, Huang S, Jing Q, Matera AG. P38 activation induces the dissociation of tristetraprolin from Argonaute 2 to increase ARE-mRNA stabilization. Mol Biol Cell [Internet]. 2018 Apr 15 [cited 2024 May 24];29(8):988–1002. Available from: https://pubmed.ncbi.nlm.nih.gov/29444957/

270. Sandler H, Stoecklin G. Control of mRNA decay by phosphorylation of tristetraprolin. Biochem Soc Trans [Internet]. 2008 Jun 1 [cited 2024 Jul 25];36(3):491–6. Available from: /biochemsoctrans/article/36/3/491/66012/Control-of-mRNA-decay-by-phosphorylation-of

271. Schwerk J, Savan R. Translating the Untranslated Region. J Immunol [Internet]. 2015 Oct 1 [cited 2024 Jul 25];195(7):2963–71. Available from: https://pubmed.ncbi.nlm.nih.gov/26386038/

272. Sandberg R, Neilson JR, Sarma A, Sharp PA, Burge CB. Proliferating cells express mRNAs with shortened 3′ untranslated regions and fewer microRNA target sites. Science (80-) [Internet]. 2008 Jun 20 [cited 2024 Jul 25];320(5883):1643–7. Available from: https://www.science.org/doi/10.1126/science.1155390

273. Edwalds-Gilbert G, Veraldi KL, Milcarek C. Alternative poly(A) site selection in complex transcription units: means to an end? Nucleic Acids Res [Internet]. 1997 Jul 7 [cited 2024 Jul 25];25(13):2547. Available from: /pmc/articles/PMC146782/?report=abstract

274. Elkon R, Ugalde AP, Agami R. Alternative cleavage and polyadenylation: extent, regulation and function. Nat Rev Genet [Internet]. 2013 Jul [cited 2024 Jul 25];14(7):496–506. Available from: https://pubmed.ncbi.nlm.nih.gov/23774734/

275. Haneklaus M, O'Neil JD, Clark AR, Masters SL, O'Neill LAJ. The RNA-binding protein Tristetraprolin (TTP) is a critical negative regulator of the NLRP3 inflammasome. J Biol Chem. 2017 Apr 28;292(17):6869–81.

276. Linker K, Pautz A, Fechir M, Hubrich T, Greeve J, Kleinert H. Involvement of KSRP in the post-transcriptional regulation of human iNOS expression-complex interplay of KSRP with TTP and HuR. Nucleic Acids Res [Internet]. 2005 [cited 2024 Jul 25];33(15):4813–27. Available from: https://pubmed.ncbi.nlm.nih.gov/16126846/

277. Fischer HP. Mathematical modeling of complex biological systems: from parts lists to understanding systems behavior. Alcohol Res Health [Internet]. 2008 [cited 2019 Apr 6];31(1):49–59. Available from: http://www.ncbi.nlm.nih.gov/pubmed/23584751

278. Bringing cells to life … and to Minecraft: $30 million NSF grant supports whole-cell modeling research | School of Molecular & Cellular Biology | UIUC [Internet]. [cited 2024 Jul 27]. Available from: https://mcb.illinois.edu/news/2023-09-07/bringing-cells-life-and-minecraft-30-million-nsf-grant-supports-whole-cell-modeling

279. Voit EO. A First Course in Systems Biology [Internet]. Garland Science; 2018. Available from: https://books.google.de/books?id=0dY6ngAACAAJ

280. Balsa-Canto E, Henriques D, Gábor A, Banga JR. AMIGO2, a toolbox for dynamic modeling, optimization and control in systems biology. Bioinformatics. 2016 Nov 1;32(21):3357–9.

281. Balsa-Canto E, Alonso AA, Banga JR. An iterative identification procedure for dynamic modeling of biochemical networks. BMC Syst Biol [Internet]. 2010 Dec 17 [cited 2020 Jan 30];4(1):11. Available from: https://bmcsystbiol.biomedcentral.com/articles/10.1186/1752-0509-4-11

282. Balsa-Canto E, Banga JR. Computational Procedures for Optimal Model Identification in Systems Biology. In: IFAC Proceedings Volumes [Internet]. IFAC; 2009 [cited 2020 Jan 20]. p. 1247–52. Available from: http://dx.doi.org/10.3182/20090706-3-FR-2004.00207

283. Banga JR, Balsa-Canto E, Moles CG, Alonso AA. Dynamic optimization of bioprocesses: efficient and robust numerical strategies. J Biotechnol [Internet]. 2005 Jun 29 [cited 2024 May 31];117(4):407–19. Available from: https://pubmed.ncbi.nlm.nih.gov/15888349/

284. Banga JR, Balsa-Canto E. Parameter estimation and optimal experimental design. Essays Biochem [Internet]. 2008 Sep 30 [cited 2024 Jul 31];45:195–209. Available from: /essaysbiochem/article/doi/10.1042/bse0450195/78346/Parameter-estimation-and-optimal-experimental

285. Zhang Y, Liu H, Yan F, Zhou J. Oscillatory dynamics of p38 activity with transcriptional and translational time delays. Sci Rep [Internet]. 2017 Dec 13 [cited 2019 Apr 7];7(1):11495. Available from: http://www.nature.com/articles/s41598-017-11149-5

286. Zambrano S, de Toma I, Piffer A, Bianchi ME, Agresti A. NF-κB oscillations translate into functionally related patterns of gene expression. Elife [Internet]. 2016 Jan 14 [cited 2024 Jun 3];5(JANUARY2016). Available from: /pmc/articles/PMC4798970/

287. Waters KM, Cummings BS, Shankaran H, Scholpa NE, Weber TJ. ERK oscillation-dependent gene expression patterns and deregulation by stress response. Chem Res Toxicol [Internet]. 2014 Sep 15 [cited 2024 Jun 3];27(9):1496–503. Available from: https://pubs.acs.org/doi/full/10.1021/tx500085u

288. Shankaran H, Ippolito DL, Chrisler WB, Resat H, Bollinger N, Opresko LK, et al. Rapid and sustained nuclear-cytoplasmic ERK oscillations induced by epidermal growth factor. Mol Syst Biol [Internet]. 2009 Jan 20 [cited 2024 Jun 3];5:332. Available from: https://www.embopress.org/doi/10.1038/msb.2009.90

289. Hendriks BS, Hua F, Chabot JR. Analysis of Mechanistic Pathway Models in Drug Discovery: p38 Pathway. Biotechnol Prog [Internet]. 2008 Feb 1 [cited 2020 Aug 25];24(1):96–109. Available from: http://doi.wiley.com/10.1021/bp070084g

290. Kulawik A, Engesser R, Ehlting C, Raue A, Albrecht U, Hahn B, et al. IL-1-induced and p38MAPK-dependent activation of the mitogen-Activated protein kinase-Activated protein kinase 2 (MK2) in hepatocytes: Signal transduction with robust and concentration-independent signal amplification. J Biol Chem. 2017 Apr 14;292(15):6291–302.

291. Brown KS, Sethna JP. Statistical mechanical approaches to models with many poorly known parameters. Phys Rev E Stat Nonlin Soft Matter Phys [Internet]. 2003 [cited 2024 Jun 3];68(2 Pt 1):9. Available from: https://pubmed.ncbi.nlm.nih.gov/14525003/

292. Fähling M, Persson AB, Klinger B, Benko E, Steege A, Kasim M, et al. Multilevel regulation of HIF-1 signaling by TTP. Mol Biol Cell [Internet]. 2012 Oct 15 [cited 2024 Jun 3];23(20):4129–41. Available from: https://pubmed.ncbi.nlm.nih.gov/22918951/

293. Kholodenko BN, Kiyatkin A, Bruggeman FJ, Sontag E, Westerhoff H V., Hoek JB. Untangling the wires: a strategy to trace functional interactions in signaling and gene networks. Proc Natl Acad Sci U S A [Internet]. 2002 Oct 1 [cited 2024 Jun 3];99(20):12841–6. Available from: https://pubmed.ncbi.nlm.nih.gov/12242336/

294. BRUGGEMAN FJ, WESTERHOFF H V., HOEK JB, KHOLODENKO BN. Modular Response Analysis of Cellular Regulatory Networks. J Theor Biol. 2002 Oct 21;218(4):507–20.

295. Aslam N, Zaheer I. The biosynthesis characteristics of TTP and TNF can be regulated through a posttranscriptional molecular loop. J Biol Chem [Internet]. 2011 Feb 4 [cited 2024 Jun 3];286(5):3767–76. Available from: https://pubmed.ncbi.nlm.nih.gov/21088298/

296. Takeichi M, Okada TS. Roles of magnesium and calcium ions in cell-to-substrate adhesion. Exp Cell Res. 1972 Sep 1;74(1):51–60.

297. Pear WS, Nolan GP, Scott ML, Baltimore D. Production of high-titer helper-free retroviruses by transient transfection. Proc Natl Acad Sci [Internet]. 1993 Sep 15 [cited 2023 Oct 1];90(18):8392–6. Available from: https://www.pnas.org/doi/abs/10.1073/pnas.90.18.8392

298. Scherer WF, Hoogasian AC. Preservation at Subzero Temperatures of Mouse Fibroblasts (Strain L) and Human Epithelial Cells (Strain HeLa).∗. https://doi.org/103181/00379727-87-21419 [Internet]. 1954 Nov 1 [cited 2023 Oct 8];87(2):480–7. Available from: https://journals.sagepub.com/doi/abs/10.3181/00379727-87-21419

299. Raschke WC, Baird S, Ralph P, Nakoinz I. Functional macrophage cell lines transformed by abelson leukemia virus. Cell [Internet]. 1978 Sep 1 [cited 2023 Oct 1];15(1):261–7. Available from: http://www.cell.com/article/0092867478901010/fulltext

300. Addgene: pWPI [Internet]. [cited 2024 Jul 3]. Available from: https://www.addgene.org/12254/

301. Tetracycline inducible expression—Tet-One systems [Internet]. [cited 2024 Jul 3]. Available from: https://www.takarabio.com/products/gene-function/tet-inducible-expression-systems/tet-one-systems

302. NEB Tm Calculator [Internet]. [cited 2024 Jul 3]. Available from: https://tmcalculator.neb.com/#!/main

303. Free Electronic Lab Notebook & Molecular Biology Software for Academics | Benchling [Internet]. [cited 2024 Jul 3]. Available from: https://www.benchling.com/academic

304. NEBioCalculator [Internet]. [cited 2024 Jul 3]. Available from: https://nebiocalculator.neb.com/#!/ligation

305. NEBuilder [Internet]. [cited 2024 Jul 4]. Available from: https://nebuilder.neb.com/#!/

306. NEBaseChanger [Internet]. [cited 2024 Jul 4]. Available from: https://nebasechanger.neb.com/

307. Pronobis MI, Deuitch N, Peifer M. The Miraprep: A Protocol that Uses a Miniprep Kit and Provides Maxiprep Yields. PLoS One [Internet]. 2016 Aug 1 [cited 2024 Jul 4];11(8). Available from: https://pubmed.ncbi.nlm.nih.gov/27486871/

308. Jiang W, Hua R, Wei M, Li C, Qiu Z, Yang X, et al. An optimized method for high-titer lentivirus preparations without ultracentrifugation. Sci Rep [Internet]. 2015 Sep 8 [cited 2024 Jul 4];5. Available from: https://pubmed.ncbi.nlm.nih.gov/26348152/

309. Hellemans J, Mortier G, De Paepe A, Speleman F, Vandesompele J. qBase relative quantification framework and software for management and automated analysis of real-time quantitative PCR data. Genome Biol [Internet]. 2007 Feb 9 [cited 2024 Aug 3];8(2). Available from: https://pubmed.ncbi.nlm.nih.gov/17291332/

310. Chiş O, Banga JR, Balsa-Canto E. GenSSI: A software toolbox for structural identifiability analysis of biological models. Bioinformatics. 2011 Sep;27(18):2610–1.

311. Chis OT, Banga JR, Balsa-Canto E. Structural identifiability of systems biology models: A critical comparison of methods. PLoS One. 2011 Nov 22;6(11).

312. Ross EA, Devitt A, Johnson JR. Macrophages: The Good, the Bad, and the Gluttony. Front Immunol. 2021 Aug 12;12:708186.

313. Fukui S, Iwamoto N, Takatani A, Igawa T, Shimizu T, Umeda M, et al. M1 and M2 Monocytes in rheumatoid arthritis: A contribution of imbalance of M1/M2 monocytes to osteoclastogenesis. Front Immunol. 2018 Jan 8;8(JAN):307698.

314. Midwood K, Sacre S, Piccinini AM, Inglis J, Trebaul A, Chan E, et al. Tenascin-C is an endogenous activator of Toll-like receptor 4 that is essential for maintaining inflammation in arthritic joint disease. Nat Med 2009 157 [Internet]. 2009 Jun 28 [cited 2023 Oct 5];15(7):774–80. Available from: https://www.nature.com/articles/nm.1987

315. Bianchi ME. DAMPs, PAMPs and alarmins: all we need to know about danger. J Leukoc Biol [Internet]. 2007 Jan 1 [cited 2023 Oct 5];81(1):1–5. Available from: https://dx.doi.org/10.1189/jlb.0306164

316. Roelofs MF, Joosten LAB, Abdollahi-Roodsaz S, Van Lieshout AWT, Sprong T, Van Den Hoogen FH, et al. The expression of Toll-like receptors 3 and 7 in rheumatoid arthritis synovium is increased and costimulation of Toll-like receptors 3, 4, and 7/8 results in synergistic cytokine production by dendritic cells. Arthritis Rheum. 2005 Aug;52(8):2313–22.

317. Sacre SM, Andreakos E, Kiriakidis S, Amjadi P, Lundberg A, Giddins G, et al. The toll-like receptor adaptor proteins MyD88 and Mal/TIRAP contribute to the inflammatory and destructive processes in a human model of rheumatoid arthritis. Am J Pathol [Internet]. 2007 Feb 1 [cited 2023 Oct 5];170(2):518–25. Available from: http://ajp.amjpathol.org/article/S0002944010608759/fulltext

318. Rappl P, Brüne B, Schmid T. Role of Tristetraprolin in the Resolution of Inflammation. Biology (Basel) [Internet]. 2021 Jan 1 [cited 2022 Nov 9];10(1):1–12. Available from: /pmc/articles/PMC7832405/

319. Clark AR, Dean JLE. The control of inflammation via the phosphorylation and dephosphorylation of tristetraprolin: a tale of two phosphatases. Biochem Soc Trans [Internet]. 2016 Oct 15 [cited 2019 Jan 7];44(5):1321–37. Available from: http://www.biochemsoctrans.org/content/44/5/1321

320. Mahtani KR, Brook M, Dean JL, Sully G, Saklatvala J, Clark AR. Mitogen-activated protein kinase p38 controls the expression and posttranslational modification of tristetraprolin, a regulator of tumor necrosis factor alpha mRNA stability. Mol Cell Biol [Internet]. 2001 Oct [cited 2019 Jan 16];21(19):6461–9. Available from: http://www.ncbi.nlm.nih.gov/pubmed/11533235

321. Rangamani P, Iyengar R. Modelling cellular signalling systems. Essays Biochem [Internet]. 2008 [cited 2019 Apr 8];45:83–94. Available from: http://www.ncbi.nlm.nih.gov/pubmed/18793125

322. Voit EO. Biochemical Systems Theory: A Review. ISRN Biomath. 2013 Jan 16;2013:1–53.

323. Ngoc LV, Wauquier C, Soin R, Bousbata S, Twyffels L, Kruys V, et al. Rapid proteasomal degradation of posttranscriptional regulators of the TIS11/tristetraprolin family is induced by an intrinsically unstructured region independently of ubiquitination. Mol Cell Biol [Internet]. 2014 Dec 1 [cited 2024 Jun 4];34(23):4315–28. Available from: https://pubmed.ncbi.nlm.nih.gov/25246635/

324. Blazek M, Santisteban TS, Zengerle R, Meier M. Analysis of fast protein phosphorylation kinetics in single cells on a microfluidic chip. Lab Chip [Internet]. 2015 Jan 22 [cited 2024 Aug 4];15(3):726–34. Available from: https://pubs.rsc.org/en/content/articlehtml/2015/lc/c4lc00797b

325. Adelman K, Kennedy MA, Nechaev S, Gilchrist DA, Muse GW, Chinenov Y, et al. Immediate mediators of the inflammatory response are poised for gene activation through RNA polymerase II stalling. Proc Natl Acad Sci U S A [Internet]. 2009 Oct 27 [cited 2024 Aug 4];106(43):18207–12. Available from: https://www.pnas.org/doi/abs/10.1073/pnas.0910177106

326. Hoppstädter J, Ammit AJ. Role of dual-specificity phosphatase 1 in glucocorticoid-driven antiinflammatory responses. Front Immunol [Internet]. 2019 Jun 26 [cited 2024 Aug 4];10(JUN):466136. Available from: www.frontiersin.org

327. Albrecht U, Yang X, Asselta R, Keitel V, Tenchini ML, Ludwig S, et al. Activation of NF-kappaB by IL-1beta blocks IL-6-induced sustained STAT3 activation and STAT3-dependent gene expression of the human gamma-fibrinogen gene. Cell Signal [Internet]. 2007 Sep [cited 2024 Aug 4];19(9):1866–78. Available from: https://pubmed.ncbi.nlm.nih.gov/17543500/

328. Raue A, Steiert B, Schelker M, Kreutz C, Maiwald T, Hass H, et al. Data2Dynamics: a modeling environment tailored to parameter estimation in dynamical systems: Fig. 1. Bioinformatics [Internet]. 2015 Nov 1 [cited 2020 Jan 31];31(21):3558–60. Available from: https://academic.oup.com/bioinformatics/article-lookup/doi/10.1093/bioinformatics/btv405

329. Pohjanpalo H. System identifiability based on the power series expansion of the solution. Math Biosci. 1978;41(1–2):21–33.

330. Walter E, Lecourtier Y. Global approaches to identifiability testing for linear and nonlinear state space models. Math Comput Simul. 1982;24(6):472–82.

331. Denis-Vidal L, Joly-Blanchard G. An easy to check criterion for (Un)identifiability of uncontrolled systems and its applications. IEEE Trans Automat Contr. 2000;45(4):768–71.

332. Hengl S, Kreutz C, Timmer J, Maiwald T. Data-based identifiability analysis of non-linear dynamical models. Bioinformatics [Internet]. 2007 Oct 1 [cited 2020 Feb 3];23(19):2612–8. Available from: https://academic.oup.com/bioinformatics/article-lookup/doi/10.1093/bioinformatics/btm382

333. Ligon TS, Fröhlich F, Chiş OT, Banga JR, Balsa-Canto E, Hasenauer J. GenSSI 2.0: Multi-experiment structural identifiability analysis of SBML models. Bioinformatics. 2018 Apr 15;34(8):1421–3.

334. Brun R, Reichert P, Künsch HR. Practical identifiability analysis of large environmental simulation models. Water Resour Res [Internet]. 2001 Apr 1 [cited 2020 Apr 21];37(4):1015–30. Available from: https://agupubs.onlinelibrary.wiley.com/doi/full/10.1029/2000WR900350

335. Pfeiffer JR, Brooks SA. Cullin 4B is recruited to tristetraprolin-containing messenger ribonucleoproteins and regulates TNF-α mRNA polysome loading. J Immunol [Internet]. 2012 Feb 15 [cited 2024 May 16];188(4):1828–39. Available from: https://pubmed.ncbi.nlm.nih.gov/22262661/

336. Werno C, Schmid T, Schnitzer SE, Peters K, Milke L, Brüne B. A combination of hypoxia and lipopolysaccharide activates tristetraprolin to destabilize proinflammatory mRNAs such as tumor necrosis factor-α. Am J Pathol. 2010;177(3):1104–12.

337. Cao H, Deterding LJ, Venable JD, Kennington EA, Yates JR, Tomer KB, et al. Identification of the anti-inflammatory protein tristetraprolin as a hyperphosphorylated protein by mass spectrometry and site-directed mutagenesis. Biochem J [Internet]. 2006 Feb 2 [cited 2024 Jul 31];394(Pt 1):285. Available from: /pmc/articles/PMC1386027/

338. Carballo E, Gilkeson GS, Blackshear PJ. Bone marrow transplantation reproduces the tristetraprolin-deficiency syndrome in recombination activating gene-2 (-/-) mice. Evidence that monocyte/macrophage progenitors may be responsible for TNFalpha overproduction. J Clin Invest [Internet]. 1997 Sep 1 [cited 2019 Mar 27];100(5):986–95. Available from: http://www.ncbi.nlm.nih.gov/pubmed/9276715

339. Smallie T, Ross EA, Ammit AJ, Cunliffe HE, Tang T, Rosner DR, et al. Dual-Specificity Phosphatase 1 and Tristetraprolin Cooperate To Regulate Macrophage Responses to Lipopolysaccharide. J Immunol. 2015 Jul 1;195(1):277–88.

340. Dennis JE, Gay DM, Welsch RE. An Adaptive Nonlinear Least Square Algorithm [Internet]. 1977 [cited 2024 Jul 29]. Available from: https://papers.ssrn.com/abstract=225158

341. Egea JA, Martí R, Banga JR. An evolutionary method for complex-process optimization. Comput Oper Res. 2010 Feb 1;37(2):315–24.

342. Gábor A, Banga JR. Robust and efficient parameter estimation in dynamic models of biological systems. BMC Syst Biol 2015 91 [Internet]. 2015 Oct 29 [cited 2024 Nov 26];9(1):1–25. Available from: https://bmcsystbiol.biomedcentral.com/articles/10.1186/s12918-015-0219-2

343. Runarsson TP, Yao X. Stochastic ranking for constrained evolutionary optimization. IEEE Trans Evol Comput. 2000;4(3):284–94.

344. Deleault KM, Skinner SJ, Brooks SA. Tristetraprolin regulates TNF TNF-α mRNA stability via a proteasome dependent mechanism involving the combined action of the ERK and p38 pathways. Mol Immunol [Internet]. 2008 Jan [cited 2019 Apr 14];45(1):13–24. Available from: https://linkinghub.elsevier.com/retrieve/pii/S0161589007002271

345. Kravaris C, Hahn J, Chu Y. Advances and selected recent developments in state and parameter estimation. Comput Chem Eng. 2013 Apr 5;51:111–23.

346. Bhalla US, Ram PT, Iyengar R. MAP kinase phosphatase as a locus of flexibility in a mitogen-activated protein kinase signaling network. Science [Internet]. 2002 Aug 9 [cited 2024 May 24];297(5583):1018–23. Available from: https://pubmed.ncbi.nlm.nih.gov/12169734/

347. Crowell S, Wancket LM, Shakibi Y, Xu P, Xue J, Samavati L, et al. Post-translational regulation of mitogen-activated protein kinase phosphatase (MKP)-1 and MKP-2 in macrophages following lipopolysaccharide stimulation: the role of the C termini of the phosphatases in determining their stability. J Biol Chem [Internet]. 2014 Oct 17 [cited 2019 Jan 14];289(42):28753–64. Available from: http://www.ncbi.nlm.nih.gov/pubmed/25204653

348. ttp-atlas Tnf [Internet]. [cited 2024 Aug 1]. Available from: https://ttp-atlas.univie.ac.at/wsgi/results/?conditions_field=%22*ICLIP_TTP3_FALL%22&genetextbox2=Tnf&submit=Submit

349. Liu Y, Shepherd EG, Nelin LD. MAPK phosphatases - Regulating the immune response. Vol. 7, Nature Reviews Immunology. 2007. p. 202–12.

350. Tsai CS, Chen DL, Lin SJ, Tsai JC, Lin TC, Lin CY, et al. TNF-alpha inhibits toll-like receptor 4 expression on monocytic cells via tristetraprolin during cardiopulmonary bypass. Shock [Internet]. 2009 Jul [cited 2024 Aug 1];32(1):40–8. Available from: https://pubmed.ncbi.nlm.nih.gov/19106809/

351. ttp-atlas [Internet]. [cited 2024 Aug 1]. Available from: https://ttp-atlas.univie.ac.at/wsgi/results/?conditions_field=%22*ICLIP_TTP3_FALL%22&genetextbox2=Cxcl1&submit=Submit

352. RAW 264.7 - TIB-71 | ATCC [Internet]. [cited 2024 Aug 1]. Available from: https://www.atcc.org/products/tib-71

353. Ho KKY, Srivastava S, Kinnunen PC, Garikipati K, Luker GD, Luker KE. Oscillatory ERK Signaling and Morphology Determine Heterogeneity of Breast Cancer Cell Chemotaxis via MEK-ERK and p38-MAPK Signaling Pathways. Bioengineering [Internet]. 2023 Feb 1 [cited 2024 Jun 3];10(2). Available from: /pmc/articles/PMC9952091/

354. Monk NAM. Oscillatory expression of Hes1, p53, and NF-κB driven by transcriptional time delays. Curr Biol. 2003 Aug 19;13(16):1409–13.

355. Mengel B, Hunziker A, Pedersen L, Trusina A, Jensen MH, Krishna S. Modeling oscillatory control in NF-κB, p53 and Wnt signaling. Vol. 20, Current Opinion in Genetics and Development. 2010. p. 656–64.

356. Ferrell JE. Self-perpetuating states in signal transduction: positive feedback, double-negative feedback and bistability. Curr Opin Cell Biol [Internet]. 2002 Apr 1 [cited 2019 Jan 14];14(2):140–8. Available from: https://www.sciencedirect.com/science/article/pii/S0955067402003149?via%3Dihub

357. Regot S, Hughey JJ, Bajar BT, Carrasco S, Covert MW. High-sensitivity measurements of multiple kinase activities in live single cells. Cell [Internet]. 2014 Jun 19 [cited 2021 Mar 1];157(7):1724–34. Available from: http://www.ncbi.nlm.nih.gov/pubmed/24949979

358. Kudo T, Jeknić S, Macklin DN, Akhter S, Hughey JJ, Regot S, et al. Live-cell measurements of kinase activity in single cells using translocation reporters. Nat Protoc 2017 131 [Internet]. 2017

Dec 21 [cited 2024 Nov 26];13(1):155–69. Available from: https://www.nature.com/articles/nprot.2017.128

359. Carreño A, Lykke-Andersen J. The Conserved CNOT1 Interaction Motif of Tristetraprolin Regulates ARE-mRNA Decay Independently of the p38 MAPK-MK2 Kinase Pathway. Mol Cell Biol [Internet]. 2022 Sep 1 [cited 2024 Aug 4];42(9). Available from: /pmc/articles/PMC9476947/

360. Johnson BA, Geha M, Blackwell TK. Similar but distinct effects of the tristetraprolin/TIS11 immediate-early proteins on cell survival. Oncogene [Internet]. 2000 [cited 2024 Aug 4];19(13):1657–64. Available from: https://pubmed.ncbi.nlm.nih.gov/10763822/

361. Icha J, Weber M, Waters JC, Norden C. Phototoxicity in live fluorescence microscopy, and how to avoid it. Bioessays [Internet]. 2017 Aug 1 [cited 2024 Dec 9];39(8). Available from: https://pubmed.ncbi.nlm.nih.gov/28749075/

362. Kedersha N, Anderson P. Stress granules: Sites of mRNA triage that regulate mRNA stability and translatability. In: Biochemical Society Transactions. 2002. p. 963–9.

363. Korobchevskaya K, Lagerholm BC, Colin-York H, Fritzsche M. Exploring the Potential of Airyscan Microscopy for Live Cell Imaging. Photonics 2017, Vol 4, Page 41 [Internet]. 2017 Jul 7 [cited 2024 Aug 1];4(3):41. Available from: https://www.mdpi.com/2304-6732/4/3/41/htm

364. Brook M, Tchen CR, Santalucia T, McIlrath J, Arthur JSC, Saklatvala J, et al. Posttranslational regulation of tristetraprolin subcellular localization and protein stability by p38 mitogen-activated protein kinase and extracellular signal-regulated kinase pathways. Mol Cell Biol [Internet]. 2006 Mar 1 [cited 2024 May 23];26(6):2408–18. Available from: https://pubmed.ncbi.nlm.nih.gov/16508015/

365. Hahn B, D'Alessandro LA, Depner S, Waldow K, Boehm ME, Bachmann J, et al. Cellular ERK phospho-form profiles with conserved preference for a switch-like pattern. J Proteome Res [Internet]. 2013 Feb 1 [cited 2024 Nov 26];12(2):637–46. Available from: https://pubs.acs.org/doi/abs/10.1021/pr3007232

CHAPTER SEVEN

Appendix

7 APPENDIX

Large files were reposited to the UBIRA eData repository (https://edata.bham.ac.uk/) under the name:

Supplementary data for the thesis "An interdisciplinary approach to understanding the TTP pathway" by Victoria Veronika Rink.

7.1 MATLAB scripts

MATLAB scripts are available at UBIRA eData repository (https://edata.bham.ac.uk/) (Supplementary data for the thesis "An interdisciplinary approach to understanding the TTP pathway" by Victoria Veronika Rink) under the name:

“ModelSimulation”

Below is an example script for data generation of model simulations, in this case, the TTP core model simulation:

```
clear
clcDependent Variables
```

```
 LPS= 1;%ng/mL
 PP = 1; % [PP2A]
```

Parameters

```
% gammai = synthesis rate of i
% deltai = degradation rate of i
% phii = phosphorylation rate of i
% rhoi = de-phosphorylation rate of i


% p38_P (Pp)
phiPp = 0.1;
rhoPp = 0.01;
%rhoPp = 0; % Simulation DUSP KO (linear does not work)
```

```
% TTP (T),
gammaT= 1; % tbc, testing
%gammaT= 0; % Simulation TTP KO phenotype
deltaT = 0.2; % tbc, resting state
phiT = 50; % tbc, testing
%phiT = 0; % Simulation AA mutant


% TTP_P (Tp),
deltaTp = 0.000001;
rhoTp = 0.05; %tbc,
%rhoTp = 0; % Simulation PP2A inhibitor


% Target mRNA (Rm),
gammaRm = 1; % tbc
deltaRm1 = 0.001; % tbc, resting state: gammam1=deltam1*mRNA+deltam2*TTP
deltaRm2 = 0.1; % tbc
```

Initial conditions

```
Pp0=0;
T0=0;
Tp0=0;
Rm0=0;
```

Final timepoint

```
tend = 480; % [min]
```

```
% filename = sprintf('TablesTTP/TTP_simulation_202406011.csv');


% TTP KO
% filename = sprintf('TablesTTP/TTP_KO_simulation_20240612.csv');
% gammaT = 0;


% % DUSP KO
```

```
% filename = sprintf('TablesTTP/TTP_DUSPKO_simulation_20240612.csv');
% rhoPp = 0;


% % AA
% filename = sprintf('TablesTTP/TTP_AA_simulation_20240612.csv');
% phiT = 0;


% % PP2Ai
% filename = sprintf('TablesTTP/TTP_PP2Ai_simulation_20240612.csv');
% rhoTp = 0;
```

ODE Solver

```
options = odeset('RelTol',1e-5); %


% Solve ODEs


[t,x]        =        ode23(@TTP_v1,[0        tend],[Pp0        T0        Tp0
Rm0],options,LPS,PP,phiPp,rhoPp,gammaT,deltaT,phiT,deltaTp,rhoTp,gammaRm,delta
Rm1,deltaRm2);
% tbc ode23 (Ffion uses differnt ode solver: ode15s)
```

Data generation

```
% define figure labels
ylabs= {'p38-P [a.u]'; 'TTP [a.u.]'; 'TTP-P [a.u.]'; 'target mRNA [a.u]'};
% define fontsize and style for consistent use below and physical figure size


% plot figure
for k=1:4 % forloop
    subplot(2,2,k), hold all %
 plot(t, x(:,k));
 xlabel('Time (min)')
 ylabel(ylabs(k))
end


dx = linspace(0,tend,tend+1);
dy = interp1(t,x,dx);
```

```
Tv1 = table(dx',dy);
writetable(Tv1,filename);
```

Function TTP

```
function
f=TTP_v1(t,x,LPS,PP,phiPp,rhoPp,gammaT,deltaT,phiT,deltaTp,rhoTp,gammaRm,delta
Rm1,deltaRm2)


Pp = x(1);
T = x(2);
Tp = x(3);
Rm = x(4);


Ppdiff=phiPp*LPS - rhoPp*Pp*t;


Tdiff = gammaT*Pp - phiT*T*Pp - deltaT*T + rhoTp*Tp*PP;


Tpdiff = phiT*T*Pp - deltaTp*Tp - rhoTp*Tp*PP;


Rmdiff = gammaRm*Pp - deltaRm1*Rm - deltaRm2*T*Rm;




f=[Ppdiff Tdiff Tpdiff Rmdiff]';


end
```

Below is an example for a parameter estimation problem file, in this case, the p38 MAPK pathway with combined experimental design, homoscedastic error profile set to 0.2.:

```
%                                                                    $Header:
svn://.../trunk/AMIGO2R2016/Examples/Arabidopsis_circadian/circadian_pe.m     2410
2015-12-07 13:58:57Z evabalsa $
%%%%%%%%%%%%%%%%%%%%%%%%%%%%%%%%%%%%%%%%%%%%%%%%%%%%%%%%%%%%%%%%%%%%%%%%%%%%%%%
% TITLE: KulawikTTP model calibration using data derived from WT BMDM
```

```
%
%        Type :
%                > help KulawikTTP_tutorial (Write!)
%        for a more detailed description of the model.
%%%%%%%%%%%%%%%%%%%%%%%%%%%%%%%%%%%%%%%%%%%%%%%%%%%%%%%%%%%%%%%%%%%%%%%%%%%%
%
%        INPUT FILE TO ESTIMATE MODEL UKNOWNS
%
%        This is the minimum input file to simualate with real data.
%        Default values are assigned to non defined inputs.
%
%        Minimum required inputs:
%           > Paths related data
%           > Model:               model_type; n_st; n_par; n_stimulus;
%                                  st_names; par_names; stimulus_names;
%                                  eqns; par
%           > Experimental scheme: n_exp; exp_y0{iexp}; t_f{iexp};
%                                  u_interp{iexp}; t_con{iexp}; u{iexp}
%                                  n_obs{iexp}; obs_names{iexp}; obs{iexp}
%
%                (AMIGO_PE)==>>    n_s{iexp}; t_s{iexp};
%                                  data_type; noise_type;
%                                  exp_data{iexp}; [error_data{iexp}]
%                                  id_global_theta; [id_global_theta_y0]
%
[id_local_theta{iexp}];[id_local_theta_y0{iexp}]global_theta_max; global_theta_min
%                                  [global_theta_y0_max];[global_theta_y0_min]
%                                  [local_theta_max{iexp}];[local_theta_min{iexp}]
%                            [local_theta_y0_max{iexp}];[local_theta_yo_min{iexp}]
%                                  [global_theta_guess];[global_theta_y0_guess];
%                           [local_theta_guess{iexp}];[local_theta_y0_guess{iexp}]
%                                  [PEcost_type];[lsq_type];[llk_type]
%                                  []:optional inputs
%
%%%%%%%%%%%%%%%%%%%%%%%%%%%%%%%%%%%%%%%%%%%%%%%%%%%%%%%%%%%%%%%%%%%%%%%%%%%%


%======================
% PATHS RELATED DATA
%======================

inputs.pathd.results_folder='VKBcom_homo_p38_PE';         % Folder to keep results
(in Results) for a given problem
inputs.pathd.short_name='VKBcomhomop38';                     % To identify figures
and reports for a given problem
inputs.pathd.runident='240628_VKBcom_p38_homo_PE_05';

%======================
% MODEL RELATED DATA
%======================

inputs.model.input_model_type='charmodelC';                  % Model introduction:
'charmodelC'|'c_model'|'charmodelM'|'matlabmodel'|'sbmlmodel'|
                                                            %
'blackboxmodel'|'blackboxcost
inputs.model.n_st=3;                                       % Number of states
inputs.model.n_par=6;                                    % Number of model parameters
```

```
inputs.model.n_stimulus=1;                                          % Number of inputs,
stimuli or control variables
inputs.model.st_names=char('Pn','Pp','D');     % Names of the states
inputs.model.par_names=char('phiPn1','phiPn2','rhoPp1','rhoPp2','gammaD','deltaD')
; % Names of the parameters
inputs.model.stimulus_names=char('S');% Names of the stimuli, inputs or controls
inputs.model.eqns=...                                               % Equations describing
system dynamics. Time derivatives are regarded 'd'st_name''
               char('dPn=-(+(Pn*phiPn1)+(S*Pn*phiPn2)-(rhoPp1*Pp)-
(D*rhoPp2*Pp))',...
                    'dPp=+(Pn*phiPn1)+(S*Pn*phiPn2)-(rhoPp1*Pp)-(D*rhoPp2*Pp)',...
                    'dD=+(gammaD*Pp)-(D*deltaD)');

% 'dPn=-(+(Pn*phiPn1)+((S*Pn*phiPn2)/(S*Skm))-(rhoPp1*Pp)-(D*rhoPp2*Pp))'
%inputs.model.par=[0.000151 0.00908 0.525 3.1 0.00841 0.01 1 0.2 50 0 0.05
%1 0.005 1]; % old version
inputs.model.par=[0.00015 0.01 0.0001 0.003 0.03 0.0001]; % Update 17/01/2024
%==================================
% EXPERIMENTAL SCHEME RELATED DATA
%==================================

%  inputs.exps.n_exp=1;                                    % Number of experiments
%   inputs.exps.n_obs{1}=2;                                      % Number of observed
quantities per experiment
%  inputs.exps.obs_names{iexp}=char('totalTTP','p38_P');     % Name of the observed
quantities per experiment
%  inputs.exps.obs{iexp}=char('totalTTP=Tt','p38_P=Pp');
%  inputs.exps.exp_y0{iexp}=[8.291371 0 7.833826667  7.699146667   1.948337333];
% Initial conditions for each experiment
%
%  inputs.exps.u_interp{1}='sustained';
%  inputs.exps.t_f{1}=360;                                % Experiment duration
%  inputs.exps.t_con{1}=[0 360];                          % Input swithching times:
Initial and final time
%  inputs.exps.u{1}=[1;1];                                  % Values of the inputs
%  inputs.exps.n_s{1}=10;                                 % Number of sampling times
for each experiment.
%
% 5
inputs.exps.n_exp=1;                                    %Number of experiments
 for iexp=1:inputs.exps.n_exp
 inputs.exps.exp_y0{iexp}=[99.09829141 8.291371     0];        %Initial conditions
for each experiment
 inputs.exps.t_f{iexp}=480;                              %Experiments duration

% OBSEVABLES DEFINITION
 inputs.exps.n_obs{iexp}=3;                            % Number of observed quantities
per experiment
 inputs.exps.obs_names{iexp}=char('p38','p38_P','DUSP1');          %  Name  of  the
observed quantities per experiment
 inputs.exps.obs{iexp}=char('p38=Pn','p38_P=Pp','DUSP1=D');        %   Observation
function
% STIMULUS DEFINITION
 inputs.exps.u_interp{iexp}='sustained';                   %Stimuli definition for
experiment.    OPTIONS:u_interp:    'sustained'    |'step'|'linear'(default)|'pulse-
up'|'pulse-down'
```

```
 inputs.exps.t_con{iexp}=[0 480];                          % Input swithching times:
Initial and final time
 inputs.exps.u{iexp}=10;                                  % Values of the inputs

 end

%  inputs.exps.exp_y0{4}=[1 0 0 0 0.06 0 0.06];       %Initial conditions for each
experiment
%  inputs.exps.t_f{4}=300;
%  inputs.exps.n_obs{4}=5;                            % Number of observed quantities
per experiment
%      inputs.exps.obs_names{4}=char('total_p38','p38_P','DUSP1','TTP','TNFmRNA');
% Name of the observed quantities per experiment
%
inputs.exps.obs{4}=char('total_p38=Pt','p38_P=Pp','DUSP1=D','TTP=Tt','TNFmRNA=Am')
;   % Observation function
%
%  inputs.exps.u_interp{4}='sustained';                    %Stimuli definition for
experiment 1:
%                                                              %OPTIONS:u_interp:
'sustained' |'step'|'linear'(default)|'pulse-up'|'pulse-down'
%  inputs.exps.t_con{4}=[0 300];                          % Input swithching times:
Initial and final time
%  inputs.exps.u{4}=10;                                 % Values of the inputs

%
%==================================
% EXPERIMENTAL DATA RELATED INFO
%==================================
 inputs.exps.n_s{1}=19;                                % [] Number of sampling times
for each experiment.
 % inputs.exps.n_s{2}=19;                                    %    Optative input. By
default "continuous" measurements are assumed.
 % inputs.exps.n_s{3}=19;
% inputs.exps.n_s{4}=11;


inputs.exps.t_s{1}=[0 15 30 45 60 75 90 120 150 180 210 240 270 300 330 360 390 420
480]; % [] Sampling times for each experiment, by default equidistant
% inputs.exps.t_s{2}=[0 15 30 45 60 75 90 120 150 180 210 240 270 300 330 360 390
420 480]; % [] Sampling times for each experiment, by default equidistant
% inputs.exps.t_s{3}=[0 15 30 45 60 75 90 120 150 180 210 240 270 300 330 360 390
420 480]; % [] Sampling times for each experiment, by default equidistant
%inputs.exps.t_s{4}=[0 7.5 22.5 37.5 52.5 67.5 82.5 120 180 240 300]; % [] Sampling
times for each experiment, by default equidistant


 inputs.exps.data_type='real';                          % Type of experimental data:
'real'|'pseudo'|'pseudo_pos'(>=0)
 inputs.exps.noise_type='homo';                        % Type of experimental noise:
Gaussian with zero mean and
%     inputs.exps.std_dev{1}=[0.001   0.001];                                    %
Homoscedastic with constant variance: 'homo'
                                                       %
Homoscedastic with varying variance:'homo_var'
                                                       %
Heteroscedastic: 'hetero'
```

```
inputs.exps.exp_data{1}=[                                   % Experimental data per
experiment n_s{iexp}x n_obs{iexp}
             99.09829141   8.291371     0
64.88382574  42.50583667   0
60.17685907  47.21280333   0
74.94643241  32.44323      60.040545
75.24253241  32.14713      76.17594
79.18929574  28.20036667   75.849445
84.88209241  22.50757      58.97302
88.54236074  18.84730167   35.86407
82.80051907  24.58914333   34.5104
89.70730207  17.68236033   36.3126
90.93404241  16.45562      38.429335
90.29788741  17.091775     31.282115
96.48715941  10.902503     32.825675
92.56447374  14.82518867   30.460085
94.12967241  13.25999      39.901705
94.37425774  13.01540467   32.83019
96.18807607  11.20158633   30
95.68658841  11.703074     32.728435
94.12594991  13.2637125    32.38618
             ];

 inputs.exps.error_data{1}=[                                  % Experimental noise,
n_s{iexp}x n_obs{iexp}
             1.6582742     1.6582742     0
8.501167333  8.501167333   0
9.442560667  9.442560667   0
6.488646     6.488646      12.008109
6.429426     6.429426      15.235188
5.640073333  5.640073333   15.169889
4.501514     4.501514      11.794604
3.769460333  3.769460333   7.172814
4.917828667  4.917828667   6.90208
3.536472067  3.536472067   7.26252
3.291124     3.291124      7.685867
3.418355     3.418355      6.256423
2.1805006    2.1805006     6.565135
2.965037733  2.965037733   6.092017
2.651998     2.651998      7.980341
2.603080933  2.603080933   6.566038
2.240317267  2.240317267   6
2.3406148    2.3406148     6.545687
2.6527425    2.6527425     6.477236
             ];

%==================================
% UNKNOWNS RELATED DATA
%==================================

% GLOBAL UNKNOWNS (SAME VALUE FOR ALL EXPERIMENTS)


inputs.PEsol.id_global_theta='all';
%char('phiP','rhoPp1','gammaT','deltaT','phiT','deltaTp','rhoTp');   %   'all'|User
selected
```

```
inputs.PEsol.global_theta_max=[1 1 1 1 1 1];  % Maximum allowed values for the
paramters
inputs.PEsol.global_theta_min=[0 0 0 0 0 0]; % Minimum allowed values for the
paramters
%('Px','phiPn1','phiPn2','Skm','rhoPp1','rhoPp2','gammaD','deltaD','gammaTn','delt
aTn','phiTn','deltaTp','rhoTp','gammaAm','deltaAm1','deltaAm2');
%inputs.model.par=[1 0.000151 0.00908 0.525 0.00001 3.1 0.00841 0.01 1 0.2 50 0 0.05
1 0.005 1];

% inputs.PEsol.global_theta_guess=[   5.082824695230836
%    0.745885509439732
%    7.750612254239743
%    3.167859540291811
%    2.476253863567990
%    6.008054327045663
%    4.696372709251819
%    3.346472917415490
%    3.185933721977777]';
%  inputs.PEsol.global_theta_max=2.*inputs.PEsol.global_theta_guess;    %  Maximum
allowed values for the paramters
%  inputs.PEsol.global_theta_min=0*ones(1,9);  %  Minimum  allowed  values  for  the
paramters




% GLOBAL INITIAL CONDITIONS
%inputs.PEsol.id_global_theta_y0='none';                % [] 'all'|User selected|
'none' (default)
% inputs.PEsol.global_theta_y0_max=[];                % Maximum allowed values for
the initial conditions
% inputs.PEsol.global_theta_y0_min=[];                % Minimum allowed values for
the initial conditions
% inputs.PEsol.global_theta_y0_guess=[];              % [] Initial guess

% LOCAL UNKNOWNS (DIFFERENT VALUES FOR DIFFERENT EXPERIMENTS)

%inputs.PEsol.id_local_theta{1}='none';                 % [] 'all'|User selected|
'none' (default)
% inputs.PEsol.local_theta_max{iexp}=[];              % Maximum allowed values for
the paramters
% inputs.PEsol.local_theta_min{iexp}=[];              % Minimum allowed values for
the parameters
% inputs.PEsol.local_theta_guess{iexp}=[];            % [] Initial guess
%inputs.PEsol.id_local_theta_y0{1}='none';              % [] 'all'|User selected|
'none' (default)
% inputs.PEsol.local_theta_y0_max{iexp}=[];           % Maximum allowed values for
the initial conditions
% inputs.PEsol.local_theta_y0_min{iexp}=[];           % Minimum allowed values for
the initial conditions
% inputs.PEsol.local_theta_y0_guess{iexp}=[];         % [] Initial guess


%==================================
% COST FUNCTION RELATED DATA
```

```
%==================================

inputs.PEsol.PEcost_type='llk';                    % 'lsq' (weighted least squares
default) | 'llk' (log likelihood) | 'user_PEcost'
inputs.PEsol.llk_type='homo';                        % [] To be defined for llk
function, 'homo' | 'homo_var' | 'hetero'



%==================================
% NUMERICAL METHODS
%==================================

%
% SIMULATION
%
 inputs.ivpsol.ivpsolver='cvodes';                                % [] IVP solver:
'radau5'(default, fortran)|'rkf45'|'lsodes'|


 inputs.ivpsol.senssolver='cvodes';                    % [] Sensitivities solver:
'cvodes' (C)


 inputs.ivpsol.rtol=1.0D-7;                           % [] IVP solver integration
tolerances
 inputs.ivpsol.atol=1.0D-7;

%
% % OPTIMIZATION
%
inputs.nlpsol.nlpsolver='eSS';                       % [] NLP solver:
%                                                                    % LOCAL:
'local_fmincon'|'local_n2fb'|'local_dn2fb'|'local_dhc'|
%                                                                         %
'local_ipopt'|'local_solnp'|'local_nomad'||'local_nl2sol'
%                                                      %        'local_lsqnonlin'
%                                                                         %
MULTISTART:'multi_fmincon'|'multi_n2fb'|'multi_dn2fb'|'multi_dhc'|
%                                                                         %
'multi_ipopt'|'multi_solnp'|'multi_nomad'|'multi_nl2sol'
%                                                    %           'multi_lsqnonlin'
%                                                       % GLOBAL: 'de'|'sres'
%                                                                  % HYBRID:
'hyb_de_fmincon'|'hyb_de_n2fb'|'hyb_de_dn2fb'|'hyb_de_dhc'|'hyp_de_ipopt'|
%                                           %       'hyb_de_solnp'|'hyb_de_nomad'|
%                                                                         %
'hyb_sres_fmincon'|'hyb_sres_n2fb'|'hyb_sres_dn2fb'|'hyb_sres_dhc'|
%                                                                         %
'hyp_sres_ipopt'|'hyb_sres_solnp'|'hyb_sres_nomad'
%                                                       % METAHEURISTICS:
%                                                       % 'ess' or 'eSS' (default)
%                                                     % Note that the corresponding
defaults are in files:
%                                                   % OPT_solvers\DE\de_options.m;
OPT_solvers\SRES\sres_options.m;
%                                                % OPT_solvers\eSS_**\ess_options.m
```

```
%

%inputs.nlpsol.eSS.log_var = 1:9;
inputs.nlpsol.eSS.maxeval = 10000000000; % as high as possible
inputs.nlpsol.eSS.maxtime = 1800; %100000; % more than 24h

inputs.nlpsol.eSS.local.solver = 'nl2sol';
inputs.nlpsol.eSS.local.finish = 'nl2sol';

% % OPTIMIZATION
% inputs.nlpsol.nlpsolver='ess';                    % In this case the problem will
be solved with eSS
% inputs.nlpsol.eSS.maxeval=20000;                    % Maximum number of function
evaluations
% inputs.nlpsol.eSS.maxtime=600;                    % Maximum allowed time in s for
eSS
% inputs.nlpsol.eSS.local.solver='nl2sol';              % Local solver in eSS -
recommended for PE
% inputs.nlpsol.eSS.local.iterprint=0;                % Do not print intermediate
results

% % OPTIMIZATION DE
% inputs.nlpsol.nlpsolver='multi_nl2sol';
%
% inputs.nlpsol.multi_starts=500;                         % [] Number of different
initial guesses to run local methods in the multistart approach
% inputs.nlpsol.multistart.maxeval = 10000000000;             % Maximum number of
function evaluations for the multistart
% inputs.nlpsol.multistart.maxtime = 100000;               % Maximum allowed time
for the optimization

% % OPTIMIZATION DE
% inputs.nlpsol.nlpsolver='DE';                    % In this case the problem will
be solved with
%                                                  % a global evolutionary
%                                                  % approach SRES
% inputs.nlpsol.DE.NP = 9*10;                           % Initial population size
(around 10*npar)
% inputs.nlpsol.DE.itermax = 200000;                          % Maximum number of
iteratios in DE
% inputs.nlpsol.DE.F = 1; %0.75;  %1                    % F: DE-stepsize F ex [0,
2]
% inputs.nlpsol.DE.CR =0.85;                           %CR: crossover probabililty
constant ex [0, 1]
% inputs.nlpsol.DE.strategy =2;                           % strategy        1 -->
DE/best/1/exp
%                                                         %               2 -->
DE/rand/1/exp
%                                                         %               3 -->
DE/rand-to-best/1/exp
%                                                         %               4 -->
DE/best/2/exp
%                                                         %               5 -->
DE/rand/2/exp

% % OPTIMIZATION SRES
```

```
% inputs.nlpsol.nlpsolver='sres';                    % In this case the problem will
be solved with
%                                                    % a global evolutionary
%                                                    % approach SRES
% inputs.nlpsol.SRES.NP=200;                            % Size of population (200,
default)
% inputs.nlpsol.SRES.itermax= 10000;                  % Maximum number of iterations
(1000, default)
%                                                      % Each iteration 200 funtion
evaluations
% inputs.nlpsol.SRES.pf=0.45;                        % Pressure on fitness in [0 0.5]
try around 0.45
%                                                     %       for unconstrained cases
try >0.5
% inputs.nlpsol.SRES.varphi=1;                       % Expected rate of convergence
% inputs.nlpsol.SRES.cvarmax=1.0e-12;                % Stopping criterium: population
variance

% OPTIMIZATION hybrid
% inputs.nlpsol.nlpsolver='hyb_de_nl2sol';     % In this case the problem will be
solved with a
%                                             % sequential hybrid - DE + nl2sol
% inputs.nlpsol.DE.NP=100;                      % Size of population - recommended
10*N variables
% inputs.nlpsol.DE.itermax=200;                   % Maximum number of iterations -
100*200 function
%                                             % evaluations
% inputs.nlpsol.DE.strategy=7;                % Strategy in DE 2:DE/rand/1/exp
% inputs.nlpsol.DE.cvarmax=1e-4;              % Maximum variance for the population



% inputs.nlpsol.multi_starts=500;                          % [] Number of different
initial guesses to run local methods in the multistart approach
% inputs.nlpsol.multistart.maxeval = 100000;           % Maximum number of function
evaluations for the multistart
% inputs.nlpsol.multistart.maxtime = 300;              % Maximum allowed time for
the optimization
%
% inputs.nlpsol.DE.NP = 9*10;                            % Initial population size
(around 10*npar)
% inputs.nlpsol.DE.itermax = 2000;                    % Maximum number of iteratios
in DE
% inputs.nlpsol.DE.F = 1; %0.75;  %1                    % F: DE-stepsize F ex [0,
2]
% inputs.nlpsol.DE.CR =0.85;                           %CR: crossover probabililty
constant ex [0, 1]
% inputs.nlpsol.DE.strategy =2;                           % strategy        1 -->
DE/best/1/exp
%                                                         %                 2 -->
DE/rand/1/exp
%                                                         %                 3 -->
DE/rand-to-best/1/exp
%                                                         %                 4 -->
DE/best/2/exp
%                                                         %                 5 -->
DE/rand/2/exp
```

```
%
% %==================================
% % RIdent or GRank DATA
% %==================================
% %
%
% inputs.rid.conf_ntrials=500;                              % [] Number of trials for
the robust confidence computation (default: 500)
% inputs.rank.gr_samples=10000;                            % [] Number of samples for
global sensitivities and global rank within LHS (default: 10000)
%
%
% %==================================
% % DISPLAY OF RESULTS
% %==================================
%
%
inputs.plotd.plotlevel='full';                             % [] Display of figures:
'full'|'medium'(default)|'min' |'noplot'
%inputs.plotd.figsave=1;
% inputs.plotd.epssave=0;                                  % [] Figures may be saved in
.eps (1) or only in .fig format (0) (default)
% inputs.plotd.number_max_states=8;                        % [] Maximum number of states
per figure
% inputs.plotd.number_max_obs=8;                           % [] Maximum number of
observables per figure
% inputs.plotd.n_t_plot=100;                               % [] Number of times to be
used for observables and states plots
% inputs.plotd.number_max_hist=8;                          % [] Maximum number of
unknowns histograms per figure (multistart)
%inputs.plotd.nx_contour=100;                              % Number of points for
plotting the contours x and y direction
%inputs.plotd.ny_contour=100;                              % ADVISE: >50
```

7.2 Preliminary experiments of Chapter 3

7.2.1 Dose-response curve of Calyculin A

Brook et al. previously demonstrated that Calyculin A inhibition leads to the accumulation of TTP within the cells (364). In our preliminary experiments, performing dose-response curves in RAW264.7, we observed increased TTP expression after 2.5 h of inhibitor treatment with 1 to 2.5 nM concentrations in RAW264.7 cells (Figure 7.1). At higher concentrations, TTP levels dropped below those of untreated cells, and cells treated with these concentrations of Calyculin A displayed altered phenotypes and signs of cell death. We opted to use 2.5 nM in subsequent experiments.

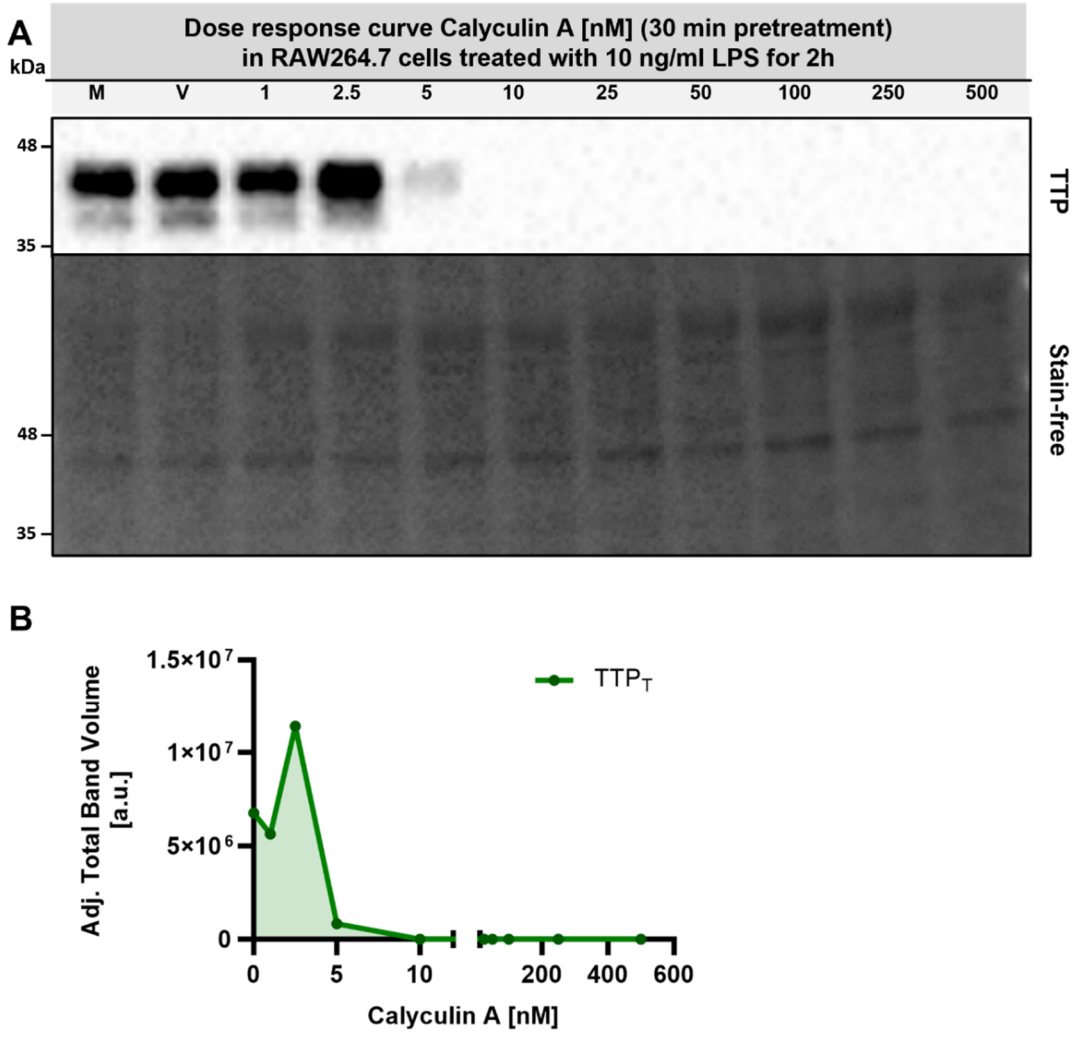


Figure 7.1 Dose-response curve of the PP2A inhibitor Calyculin A in RAW264.7 cells.

RAW264.7 cells were treated with varying concentrations of Calyculin A 30 min prior to stimulation with 10 ng/mL LPS and incubated for 2 h. The lysates of the cells were harvested, and protein concentration of TTP was measured using WB. For normalisation, total protein measurements were obtained through the Stain-Free signal of the blot. A) shows the Western blot of TTP with the respective Stain-Free image used for normalisation, which was quantified using Image Lab software and is displayed as adjusted total band volume in B) (n=1). No statistics were performed.

7.2.2 Standard curve total protein

Total protein measurement needed to be conducted for TTP and DUSP1, and for this purpose, we obtained human recombinant protein from Abcam. These proteins were directly used in our Western blots. The recombinant TTP protein included the full-length protein produced by wheat germ and has a predicted molecular weight of 62 kDa, including tags. The same applied to DUSP1, with a predicted size of 66 kDa.

We conducted preliminary experiments in RAW264.7 cells to identify concentration ranges for the standard curve, as shown in Figure 7.2 and Figure 7.3. For both TTP and DUSP1, we decided to start with the following concentrations of recombinant protein per lane: 200 ng, 100 ng, 50 ng, 25 ng, 10 ng, and 5 ng. Additionally, we conducted a time-course experiment by stimulating RAW264.7 cells with 10 ng/mL LPS for varying durations, including 0 h, 0.75 h, 3 h, and 6 h. The protein samples generated by this experiment were run alongside the recombinant protein standard. Our first observation was that for both TTP and DUSP1, the recombinant standard had the expected molecular weight of 62 kDa and 66 kDa, respectively. The observed size difference between endogenous and recombinant protein was primarily attributed to the presence of the tag, the details of which were not provided by Abcam.

Based on the TTP expression profile observed in Figure 7.2, we chose to include 50 ng, 25 ng, 10 ng, 5 ng, and 0 ng of TTP standard per lane. Subsequently, after the first time-course

experiment in RAW264.7 cells, we updated it to 10 ng, 5 ng, 2.5 ng, 1 ng and 0.5 ng per lane. Finally, we needed to adapt the standard curve to 1 ng, 0.5 ng, 0.25 ng, 0.1 ng, and 0.05 ng per lane to account for our mouse mutant strain *Zfp36*$^{aa/aa}$, which displayed lower TTP expression levels.

For DUSP1, we started with a standard curve that ranged from 5 ng, 1 ng, 0.5 ng, 0.1 ng, and 0 ng per lane in the first RAW264.7 time-course experiment. This was later updated to 5 ng, 2.5 ng, 1 ng, 0.5 ng, and 0.25 ng per lane in the second experiment and eventually set at 2.5 ng, 1 ng, 0.5 ng, 0.25 ng, 0.1 ng per lane for the first WT murine BMDM experiment.

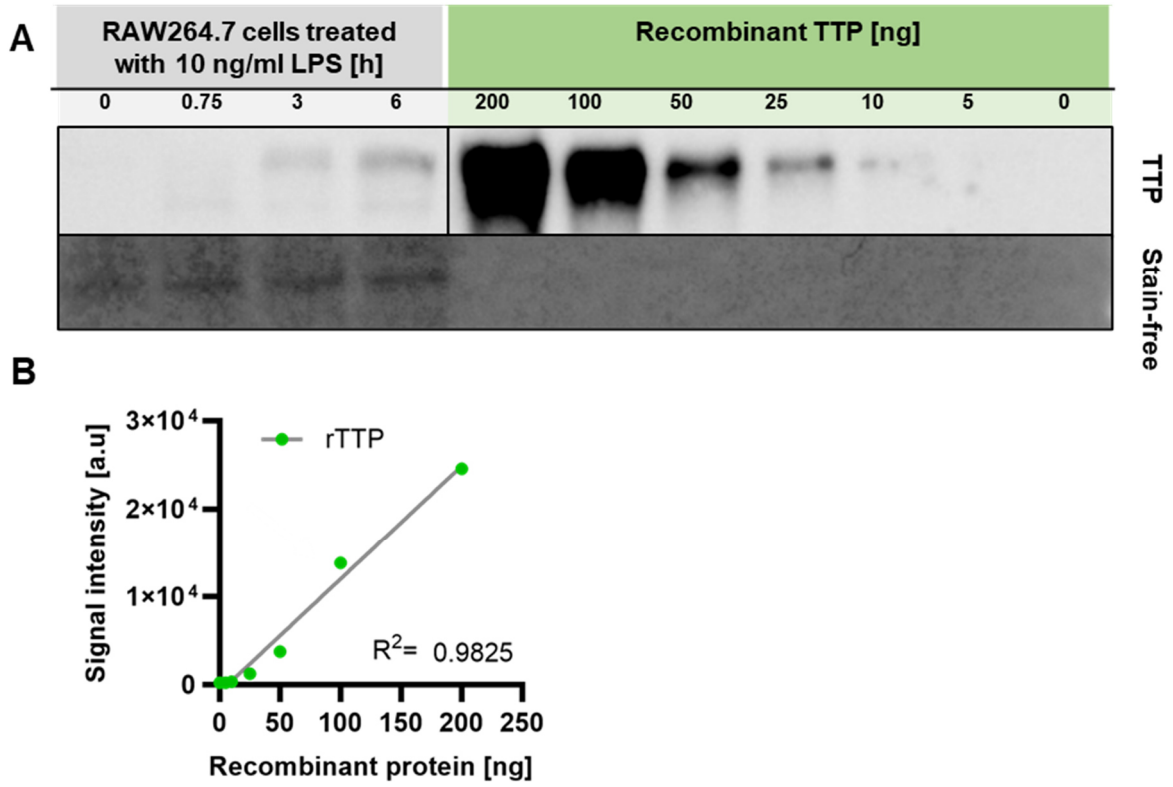


Figure 7.2 Preliminary experiment for identification of the TTP standard curve for total quantification.

RAW264.7 cells were treated with 10 ng/mL LPS and incubated for 45 min, 1 h, 3 h, and 6 h. The lysates of the cells were harvested, and protein concentration of endogenous TTP together with varying amounts of recombinant TTP protein (200 ng, 100 ng, 50 ng, 25 ng, 10 ng, 5 ng) was measured using WB. A) shows the Western blot of TTP with the respective Stain-Free image used for normalisation. As endogenous TTP and the recombinant protein vary in size, the blots were cut for better visualisation. The unedited blots can be found in Appendix 7.3. B) The signal intensity of the recombinant protein standard curve was quantified using Image Lab software (n=1). No statistics were performed. Linear regression was performed on the standard curve.

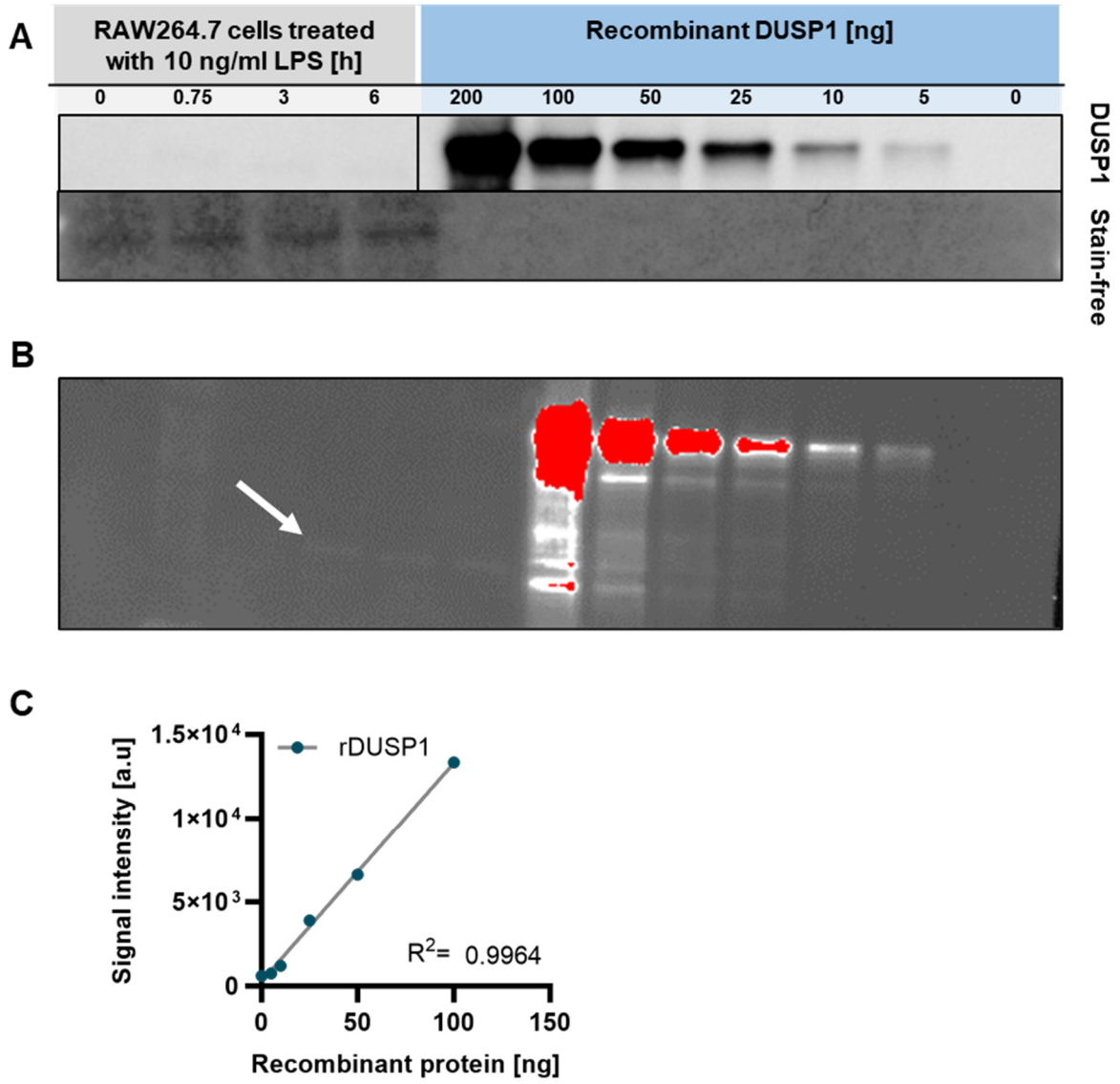


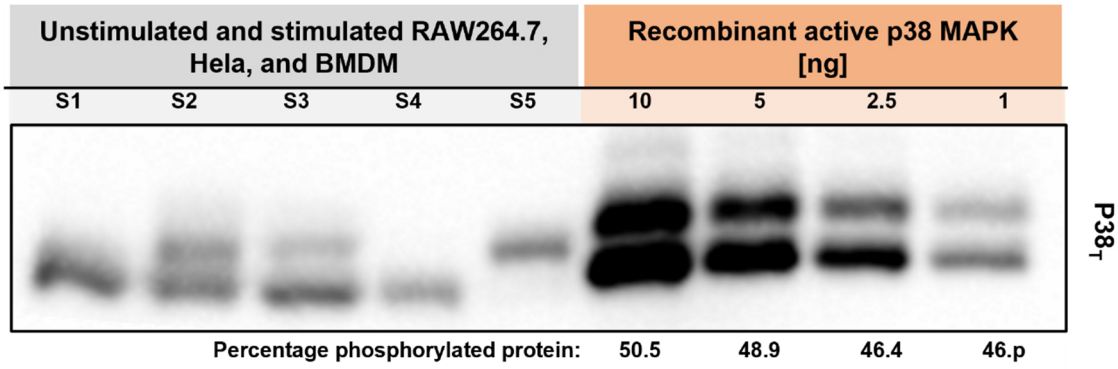
Figure 7.3 Preliminary experiment for identification of the DUSP1 standard curve for total quantification.

RAW264.7 cells were treated with 10 ng/mL LPS and incubated for 0.75 h, 1 h, 3 h, and 6 h. The lysates of the cells were harvested, and protein concentration of endogenous DUSP1 together with varying amounts of recombinant DUSP1 protein (200 ng, 100 ng, 50 ng, 25 ng, 10 ng, 5 ng) was measured using WB. A) shows the Western blot of TTP with the respective Stain-Free image used for normalisation. As endogenous DUSP1 and the recombinant protein vary in size, the blots were cut for better visualisation. The unedited blots can be found in Appendix 7.3. B) Because DUSP1 expression is not visible using imaging times to measure the standard curve in A), B) shows the blot with longer imaging times to show DUSP1 expression. C) The signal intensity of the recombinant protein standard curve was quantified using Image Lab software (n=1). Linear regression was performed on the standard curve.

7.2.3 Standard curve phosphorylated protein

For the protein standard of p38 MAPK, we obtained recombinant protein isolated from Sf9 cells infected with baculovirus. The baculovirus infection induces p38 MAPK phosphorylation, which results in phosphorylated recombinant protein. The recombinant protein, which includes a His-tag for purification, has a predicted molecular weight of 42 kDa. To determine the percentage of phosphorylated p38 MAPK in the recombinant protein standard, Kulawik et al. employed a mass spectrometry approach. This approach has been previously described by Hahn et al. (365). When we contacted our local mass spectrometry facility, they indicated that implementing this method would exceed our time and budget constraints.

Consequently, we found an alternative approach, which involved quantification of phosphorylated p38 MAPK via PhosTag gels. PhosTag gels contain chemical compounds with phosphate binding groups that increase the molecular weight of phosphorylated proteins. This alteration in molecular weight results in different running velocities of unphosphorylated and phosphorylated proteins, allowing the observation of separate bands after SDS PAGE. By quantifying total p38 MAPK of the individual bands we can identify the percentage of its phosphorylation. Figure 7.4 displays the gel and quantified results, identifying the percentage of phosphorylated p38 MAPK in our recombinant standard to be 46.6±0.23%. For this average, we excluded the two highest concentrations as the lanes were overloaded, and the bands were not clearly separated. Similar to TTP and DUSP1, we conducted a preliminary experiment with different concentrations, as shown in Figure 7.5, to determine the initial concentrations for the standard curve. For p38 MAPK, endogenous and recombinant proteins exhibited the same size. We started with a standard curve ranging from 10, 5, 1, 0.5 and 0 ng/lane in the first RAW264.7 time-course experiment, which was updated to 10, 5, 1, 0.5 and 0.25 ng/lane in the second experiment.



S1: unstimulated HeLa cells

S2: HeLa cells stimulated with 30 ng/ml IL-1β for 30 min

S3: RAW cells stimulated with 10 ng/ml LPS for 30 min

S4: unstimulated BMDM

S5: BMDM stimulated with 10 ng/ml LPS for 30 min

Figure 7.4 Measurement of the percentage of phosphorylated p38 MAPK in the active recombinant protein of p38 MAPK using PhosTag gel Western Blotting.

Samples from previous preliminary experiments comprising HeLa cells, RAW264.7 cells and WT BMDMs were run alongside different concentrations (10, 5, 2.5, 1 ng) of recombinant active p38 MAPK protein on a PhosTag gel to identify the percentage of phosphorylated protein within the p38 MAPK recombinant protein. The samples from previous experiments included unstimulated HeLa cells (S1), HeLa cells stimulated with 30 ng/mL IL-β for 30 min, RAW264.7 cells treated with 10 ng/mL LPS for 30 min, untreated BMDMs, and BMDMs stimulated with 10 ng/mL LPS for 30 min. For the calculation of the percentage of phosphorylated protein (upper band) of total p38 MAPK protein (lower and upper band), the bands were quantified in Image Lab. The measured percentage is shown beneath the respective row (n=1).

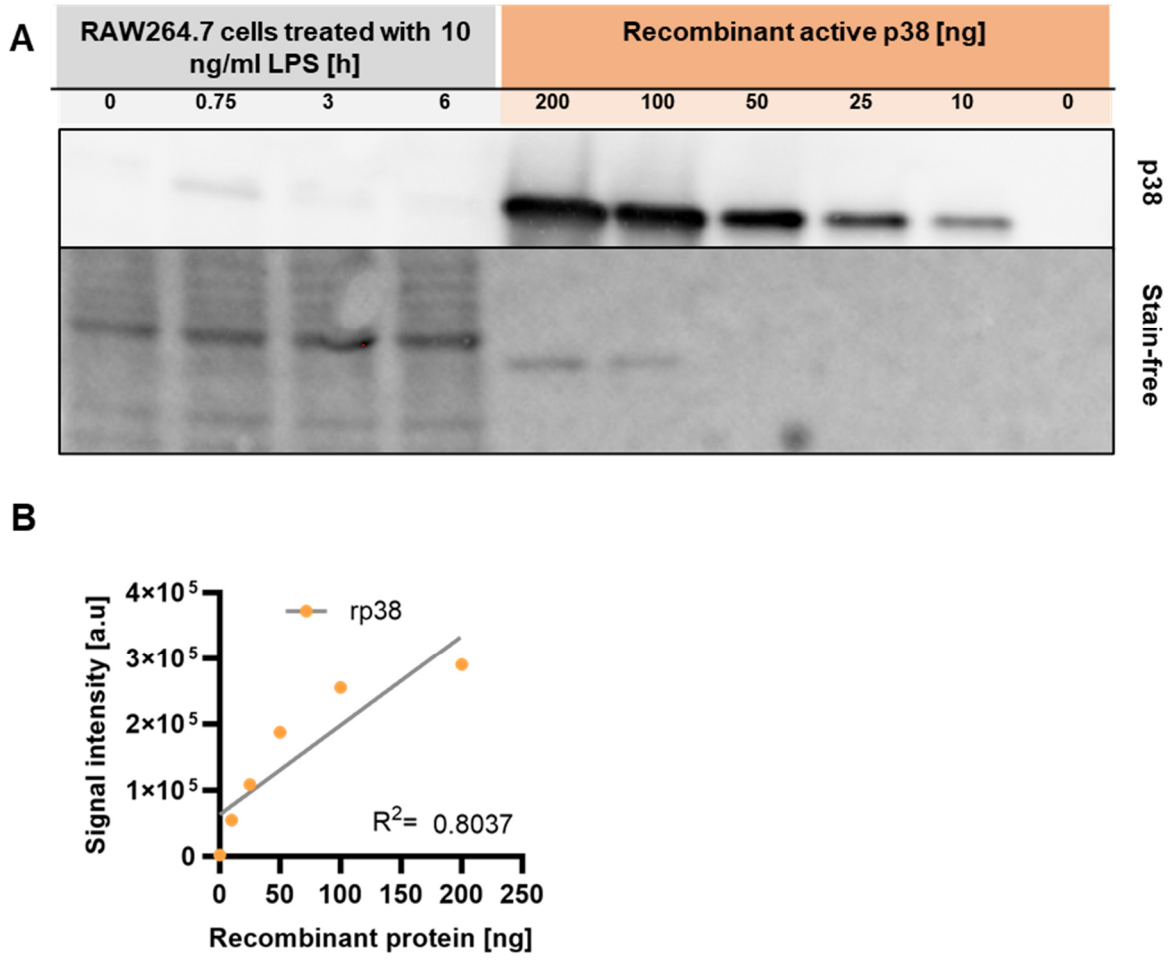


Figure 7.5 Preliminary experiment for identification of the p38 MAPK standard curve for total quantification.

RAW264.7 cells were treated with 10 ng/mL LPS and incubated for 0.75 h, 1 h, 3 h, and 6 h. The lysates of the cells were harvested, and protein concentration of endogenous p38 MAPK together with varying amounts of recombinant active p38 protein (200 ng, 100 ng, 50 ng, 25 ng, 10 ng) were measured using WB. A) shows the Western blot of p38 MAPK with the respective Stain-Free image used for normalisation. B) The signal intensity of the recombinant protein standard curve was quantified using Image Lab software (n=1). Linear regression was performed on the standard curve.

7.2.4 Standard curve qPCR

We obtained the *Tnf* plasmid from Addgene, and after preparing the plasmid stocks, we confirmed the integrity of the *Tnf* sequence through Sanger sequencing. We then linearised the plasmid using the restriction enzyme AgeI. We confirmed the quality of linearisation using DNA gel electrophoresis; the results are shown in Figure 7.6. For qPCR, we did not preliminarily determine standard curve performance; the performance can be observed in individual experiments in Appendix 7.3.

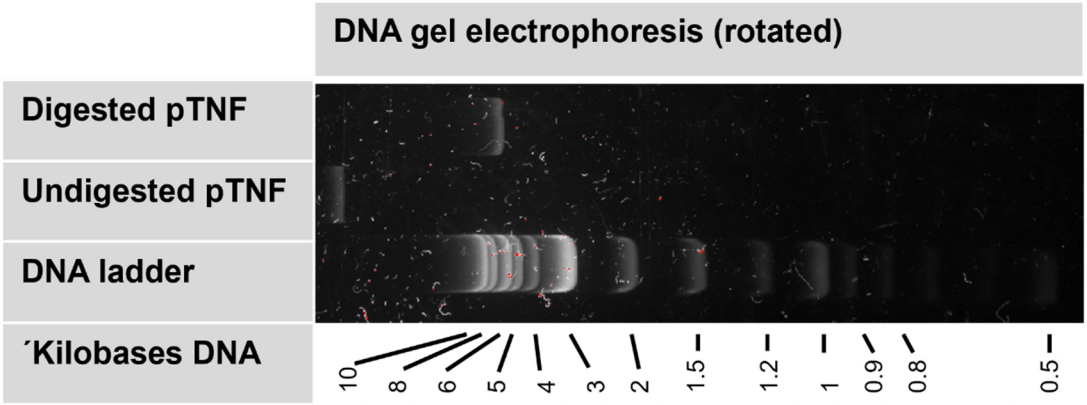


Figure 7.6 Control DNA gel electrophoresis verifying correct linearisation of the TNF plasmid following AgeI RE digest.

The TNF plasmid used as the standard for total quantification qPCR was linearised using the single cutting RE AgeI. The linearised plasmid, together with a 1 kB plus DNA ladder and undigested plasmid, were separated using DNA gel electrophoresis and visualised using SybrSafe under UV light to verify correct complete digestion.

7.3 Individual experiments of Chapter 3

We exemplarily describe the experiment outcome and thinking process on how data was processed for the first WT BMDM experiment below. The same process was applied to all other experiments shown here.

7.3.1 WT BMDMs

7.3.1.1 Experiment 1

Figure 7.7 shows the Western blot data for the first individual experiment conducted in WT BMDMs, while Figure 7.8 displays the respective quantification of these blots alongside the qPCR data. We present the first experiment here in more detail to emphasise how the data was treated to obtain values for parameter estimation and to allow observation of the individual standard curves. The following experiments will only be described in bullet points.

p38 MAPK

In Figure 7.7, the first section displays images of the p38 MAPK Western blot from Experiment 1. The first one was obtained by staining for phosphorylated p38 MAPK ($p38_P$), the second one by stripping and re-staining of the blot for total p38 MAPK ($p38_T$) and the last one by imaging the Stain-Free signal of the blot directly after the membrane transfer. Both phosphorylated and total p38 MAPK Western Blots exhibited a single band between 35 and 45 kDa for the endogenous protein of the time-course samples as well as the recombinant protein of the standard curve. The Stain-Free signal produced the band profile of total protein, which was used for normalisation between the lanes prior to total quantification.

The 0.1 ng recombinant p38 MAPK standard was below the detection limit and, as a result, was excluded from calculations for total quantification. The resulting standard curve, depicted in Figure 7.8 (A), exhibits an R^2 value of 0.87 for total and 0.9994 for phosphorylated p38 MAPK.

The R^2 value is a measure of goodness of fit of the regression line (grey line) to the data. For our standard curve, we considered values above 0.99 an ideal fit, above 0.9 a good fit and above 0.8 a moderate fit and everything below 0.8 as not sufficient for total quantification. In case of an R^2 below 0.9, we were further considering excluding standard curve values, if possible. For total p38 MAPK, the standard curve appears nonlinear, particularly at the highest concentration of 10 ng/well, where the standard curve seems to reach a plateau. Considering this behaviour, it might be advisable to exclude this data point for a more reliable standard curve. Especially since none of our samples lay above the 5 ng/well standard range. Removing the 10 ng/well data point from the standard curve results in an R^2 value of 0.9953. All samples lay within the range of the resulting standard curves for both total and phosphorylated p38.

We then calculated the standard deviation of the normalisation factors obtained during the quantification of Western Blots. Subsequently, we compared this standard deviation with the average of the normalisation factors. The underlying concept is that transfer issues, such as bubbles or inefficient transfer, can significantly skew the normalisation factor calculated from the Stain-Free signal and, as such, the values of our measurements. We aim to confirm the validity of the normalisation approach and establish a quantifiable and reproducible practice for identifying and removing unreliable data measurements. For each value exceeding the standard deviation we qualitatively examined the Stain-Free blots for obvious transfer issues in the affected lanes and evaluated whether variance could be explained by differences in protein loading. For p38, the calculated SD was exceeded by the 4 h and 8 h time points. Both lanes exhibited a bubble in one of the main bands of the Stain-Free blot that skewed the normalisation and were therefore excluded. The excluded values are shown with a light grey symbol, and the connection lines are dashed. The first 3 lanes of total p38 MAPK are unexpectedly low. It is well established in the scientific community that total p38 MAPK is stably expressed

throughout the inflammatory response. The low expression levels are also not reflected in the Stain-Free blots or phosphorylated p38 MAPK. We concluded that this had to be an experimental issue, more precisely due to uneven stripping of the blot. Consequently, those three values were excluded from calculating the mean total p38 MAPK expression, which will later be used to calculate unphosphorylated p38 MAPK expression for the model parameter estimation.

DUSP1

The next section of the Western blot image in Figure 7.7 shows the DUSP1 time-course and standard curve as well as the respective Stain-Free blot used for normalisation. Endogenous DUSP1 formed a single band between 35 kDa and 48 kDa. The recombinant protein formed a single band between 63 kDa and 75 kDa. The two lowest concentrations of the standard curve were below the detection limit and, therefore, excluded from calculating total quantification values (grey symbols). The R^2 value of the standard curve was identified as 0.9859, which accounts for reasonable linearity within the measured region. Of those samples that were above the detection limit, only the 6.5 h time point measurement lay outside the standard curve range. Also, the first three time points of the time-course were below the detection limit. We decided to assume those three values to be 0 for our parameter estimation. The initially measured values (background signal) are shown as light grey symbols. All other values were above the detection limit, which was found at 30 pg/µg total protein and displayed as a thick grey dashed line. The variance of the normalisation factor was higher than the standard deviation for the 0.15 for 0 h, 1.5 h, 2 h, 2.5 h, 4.5 h, 6 h and 6.5 h time points. After checking the Stain-Free lane profile, we decided to exclude the 2 h time point due to a transfer issue within the lane and the 6.5 h time point because of a bubble in one of the main bands.

TTP

The next section of the WB shows TTP expression patterns and the corresponding quantification can be found in Figure 7.8 E, and F. Endogenous TTP formed two distinct bands between 35 and 48 kDa. The upper band has been shown to be caused by hyperphosphorylation of TTP, and we therefore decided to measure the two bands individually for our model parameter estimation. The standard curve exhibited an individual band between 63 kDa and 75 kDa. We further show two images of the TTP blot, TTPa with 12.6 sec and TTPb with 180 sec of exposure time. In TTPa, the entire standard curve was within range, but some early time points were below the detection limit. By imaging for longer in TTPb, some bands were oversaturated, but we received a better understanding of the expression in the early time points. Therefore, we used a calibration method to improve the resolution of the first 3.5 h of the time-course. This is a commonly used technique in other applications to allow for plate-to-plate comparison and should also work for WB. Ideally, we would have used the standard here, but to do this, we would have needed at least 3 values and most of the standard signal was oversaturated with the higher exposure time. We used the standard lane of 0.5 ng to calibrate between the blots using the resulting calibration factor of 0.036927. Even after this adaption, the 0 h time point of phosphorylated (TTP_P) and unphosphorylated TTP (TTP), as well as the 0.25 h time point of unphosphorylated TTP, are still below the detection limit of 19 pg/µg total protein (thick grey dashed line). The original measurements were included as light grey symbols. As with DUSP1, we assumed a concentration of 0 for simplicity. The standard curve was linear over the whole range of concentrations and exhibited an R^2 value of 0.9995. However, unfortunately during analysis, we found that using the adjusted intensity value as a reference, some of the samples lay outside of the standard range (0.25, 0.5, 0.75 1, 1.25 phos, 1.5 phos, 2-3, 3.5 unphos, 6.5 unphos, 7 unphos). We decided to assume linearity of the standard

curve for the calculations for now (see also Chapter 3.6.1). Regarding the standard deviation of the normalisation factors, which was found to be 0.1, the 0 h, 1.5 h, 2 h, 5 h and 6 h time points exhibited higher variation. However, all variations could be explained by differences in loading and no further values were excluded.

Tnf mRNA

The qPCR measurement of *Tnf* is shown in Figure 7.8 G and H. The detection limit was between 300 and 1000 copies per reaction. None of the sample was below that threshold. No triplicates exhibited a standard deviation above 0.2 and none of them had to be excluded. The 5 h time point variation appeared irregular, but there was no justifiable reason to exclude it.

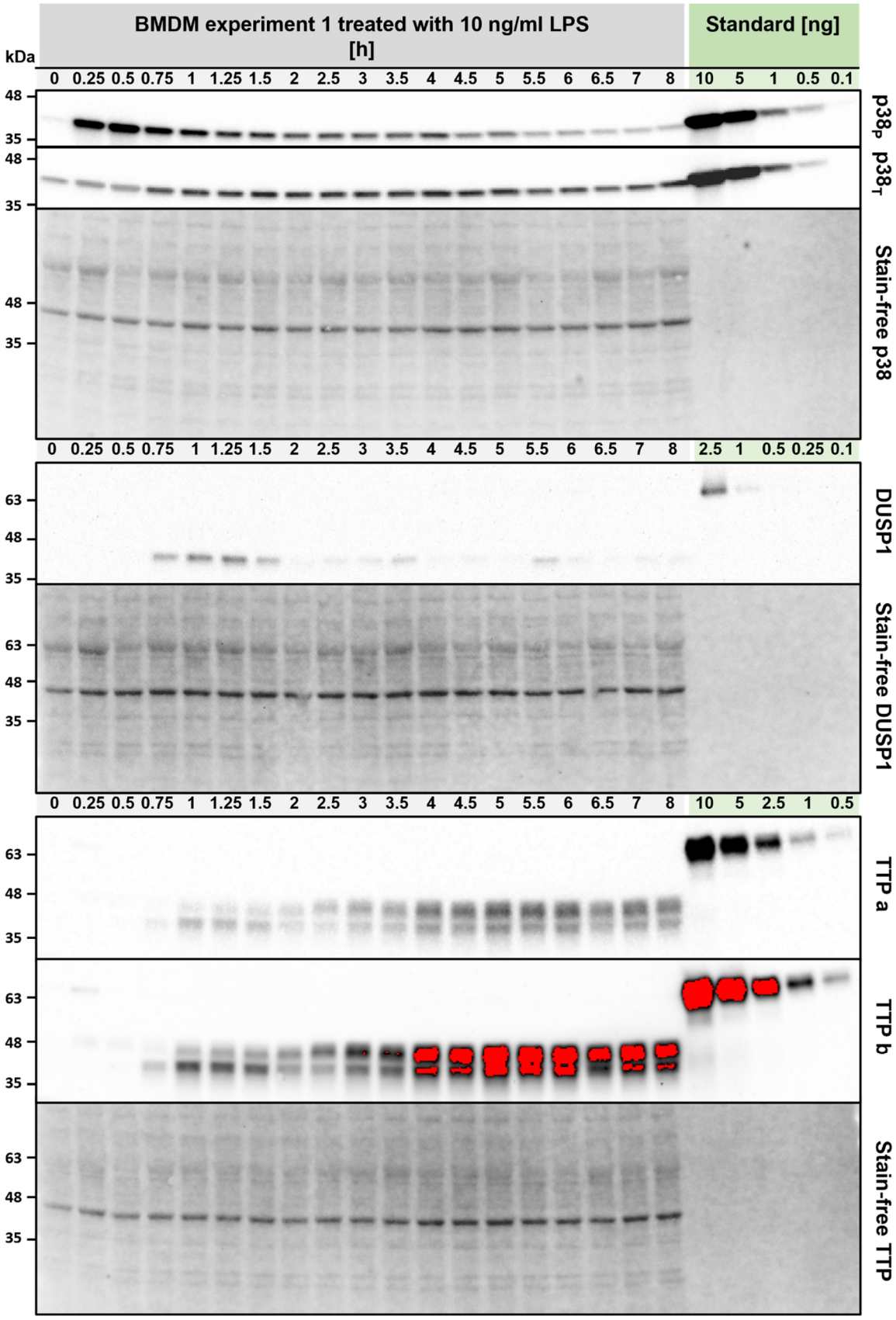

BMDM experiment 1 treated with 10 ng/ml LPS
[h]
Standard [ng]
kDa
0 0.25 0.5 0.75 1 1.25 1.5 2 2.5 3 3.5 4 4.5 5 5.5 6 6.5 7 8
10 5 1 0.5 0.1
48
35
p38P
p38T
Stain-free p38
2.5 1 0.5 0.25 0.1
63
DUSP1
Stain-free DUSP1
10 5 2.5 1 0.5
TTP a
TTP b
Stain-free TTP

Figure 7.7 WT BMDM Experiment 1: Total quantification Western blot data of BMDMs treated with LPS over an 8 h time-course measuring p38 MAPK-TTP pathway components.

BMDMs derived from the bone marrow of 8 mice were combined and treated with 10 ng/mL LPS for a period of 8 h. Protein concentration of phospho-p38 ($p38_P$), total p38 ($p38_T$), DUSP1 and TTP were measured on individual blots together with recombinant protein standard curve using WB. For TTP, two distinct exposure times, 12.6 sec (TTPa) and 180 sec (TTPb), are shown to increase the resolution of early time points. Shown are measurements of chemiluminescence for each protein as well as their respective Stain-Free blots. The protein size is indicated by relevant marks of the protein ladder in kDa.

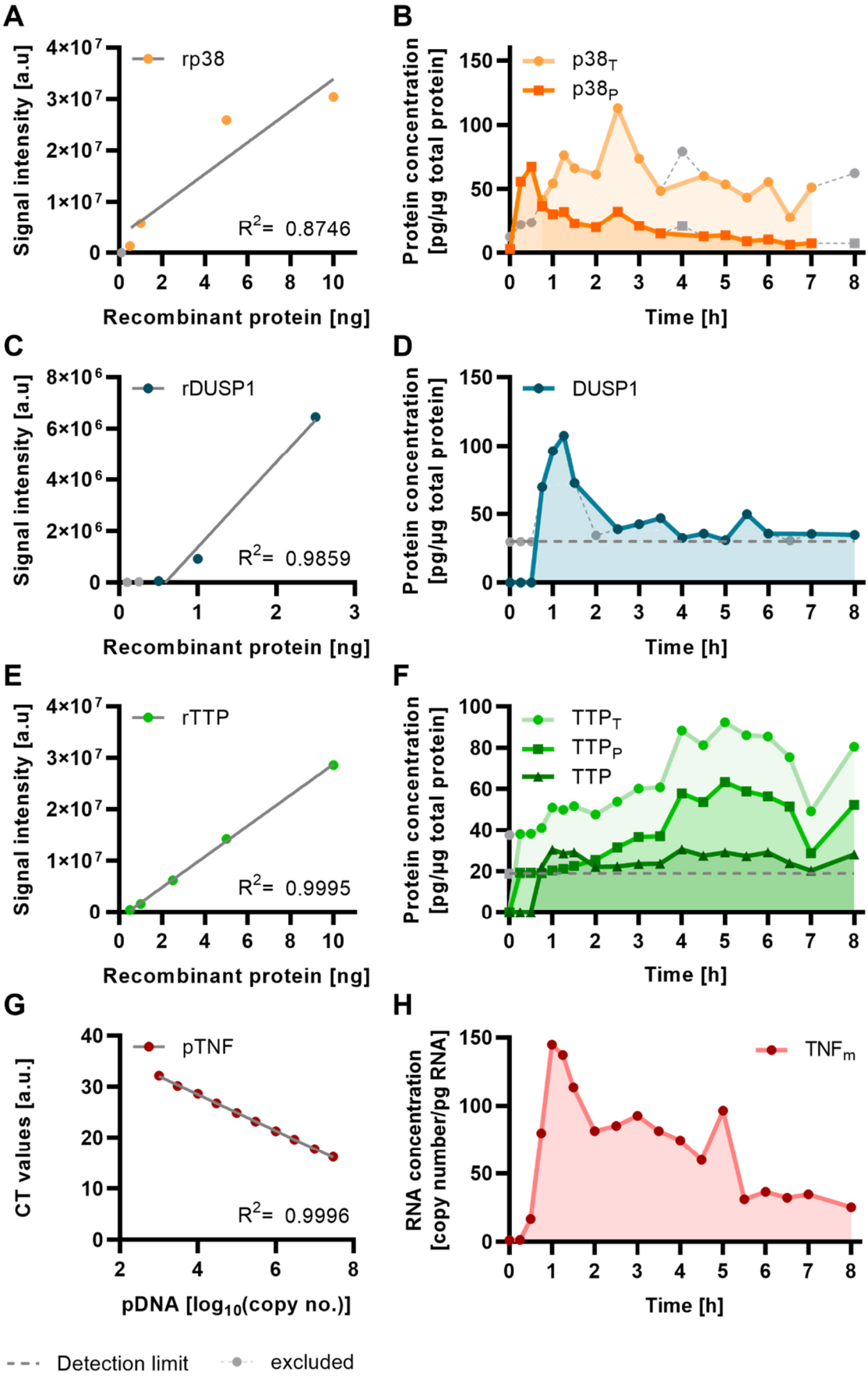

A
Signal intensity [a.u]
rp38
R²= 0.8746
Recombinant protein [ng]
B
Protein concentration [pg/µg total protein]
p38T
p38P
Time [h]
C
Signal intensity [a.u]
rDUSP1
R²= 0.9859
Recombinant protein [ng]
D
Protein concentration [pg/µg total protein]
DUSP1
Time [h]
E
Signal intensity [a.u]
rTTP
R²= 0.9995
Recombinant protein [ng]
F
Protein concentration [pg/µg total protein]
TTPT
TTPP
TTP
Time [h]
G
CT values [a.u.]
pTNF
R²= 0.9996
pDNA [log10(copy no.)]
H
RNA concentration [copy number/pg RNA]
TNFm
Time [h]
Detection limit
excluded

Figure 7.8 BMDM WT Experiment 1: Standard curves and total quantification of Western blot and qPCR data obtained from BMDMs treated with LPS over an 8 h time-course measuring p38 MAPK-TTP pathway components.

BMDMs derived from the bone marrow of 8 mice were combined and treated with 10 ng/mL LPS for a period of 8 h. Protein concentration of phospho-p38 (p38P), total p38 (p38T), DUSP1 and TTP, as well as *Tnf* mRNA levels, were measured using WB and qPCR, respectively. The Western blot data was quantified in Image Lab software, normalised to its Stain-Free signal and the total protein concentration of B) p38 total ($p38_T$) and phospho-p38 ($p38_P$, orange), D) DUSP1 (blue), F) total (TTP_T) unphosphorylated (TTP, lower band) and phosphorylated (TTP_P, upper band) TTP (green) was calculated using the relevant standard curves in A), C), and E). The total amount of *Tnf* mRNA (red), shown in H), was identified by running a standard curve, displayed in G), consisting of known quantities of plasmid DNA alongside the samples for qPCR. Excluded values are shown in light grey symbols with a thin dotted line indicating the change in interpolation. If relevant, the detection limit was indicated by a thick grey dotted line.

7.3.1.2 Experiment 2

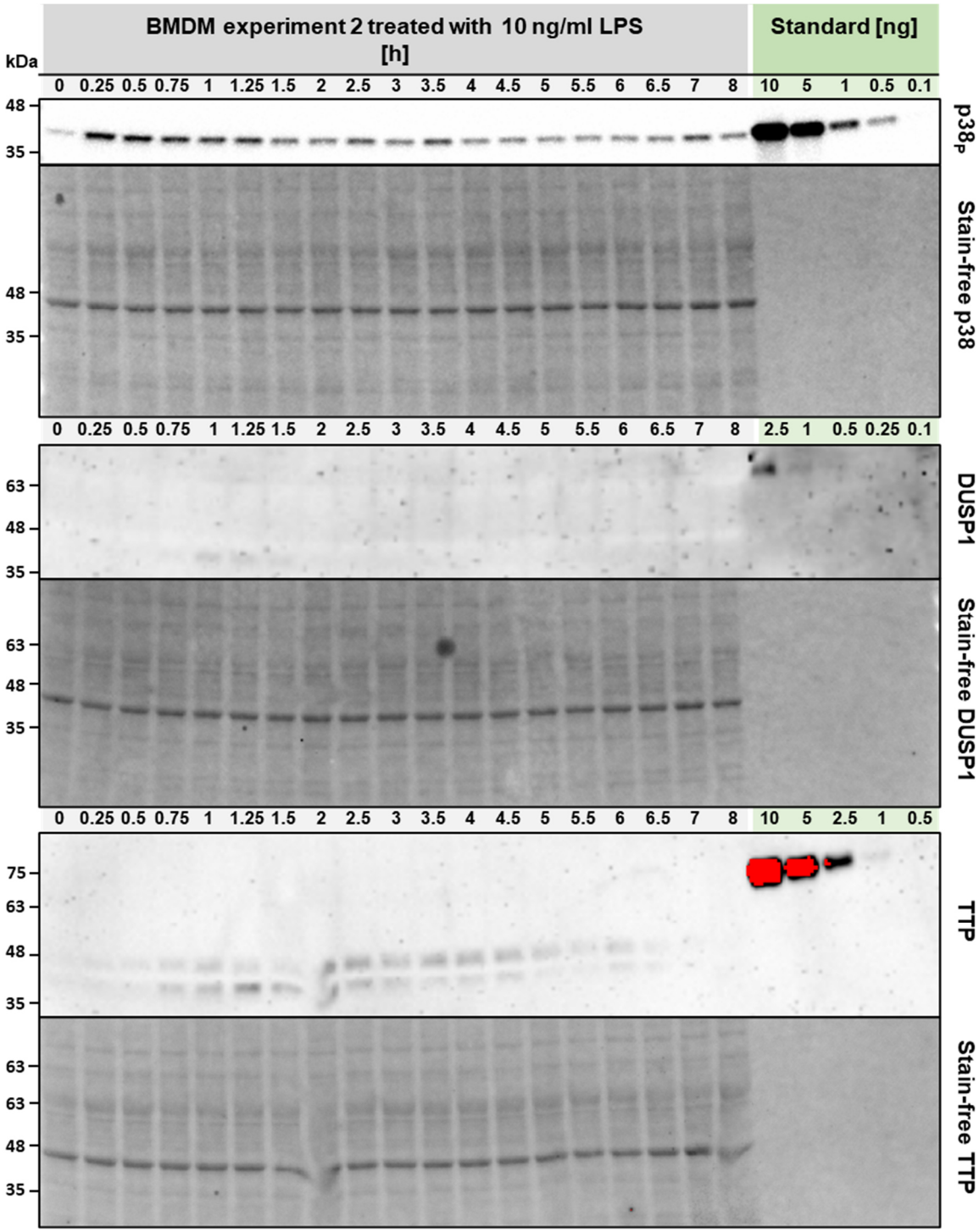


Figure 7.9 WT BMDM Experiment 2: Total quantification Western blot data of BMDMs treated with LPS over an 8 h time-course measuring p38 MAPK-TTP pathway components.

BMDMs derived from the bone marrow of 8 mice were combined and treated with 10 ng/mL LPS for a period of 8 h. Protein concentration of phospho-p38 ($p38_P$), DUSP1, and TTP were measured on individual blots together

with recombinant protein standard curve using WB. Shown are measurements of chemiluminescence for each protein as well as their respective Stain-Free blots. The protein size is indicated by relevant marks of the protein ladder in kDa.

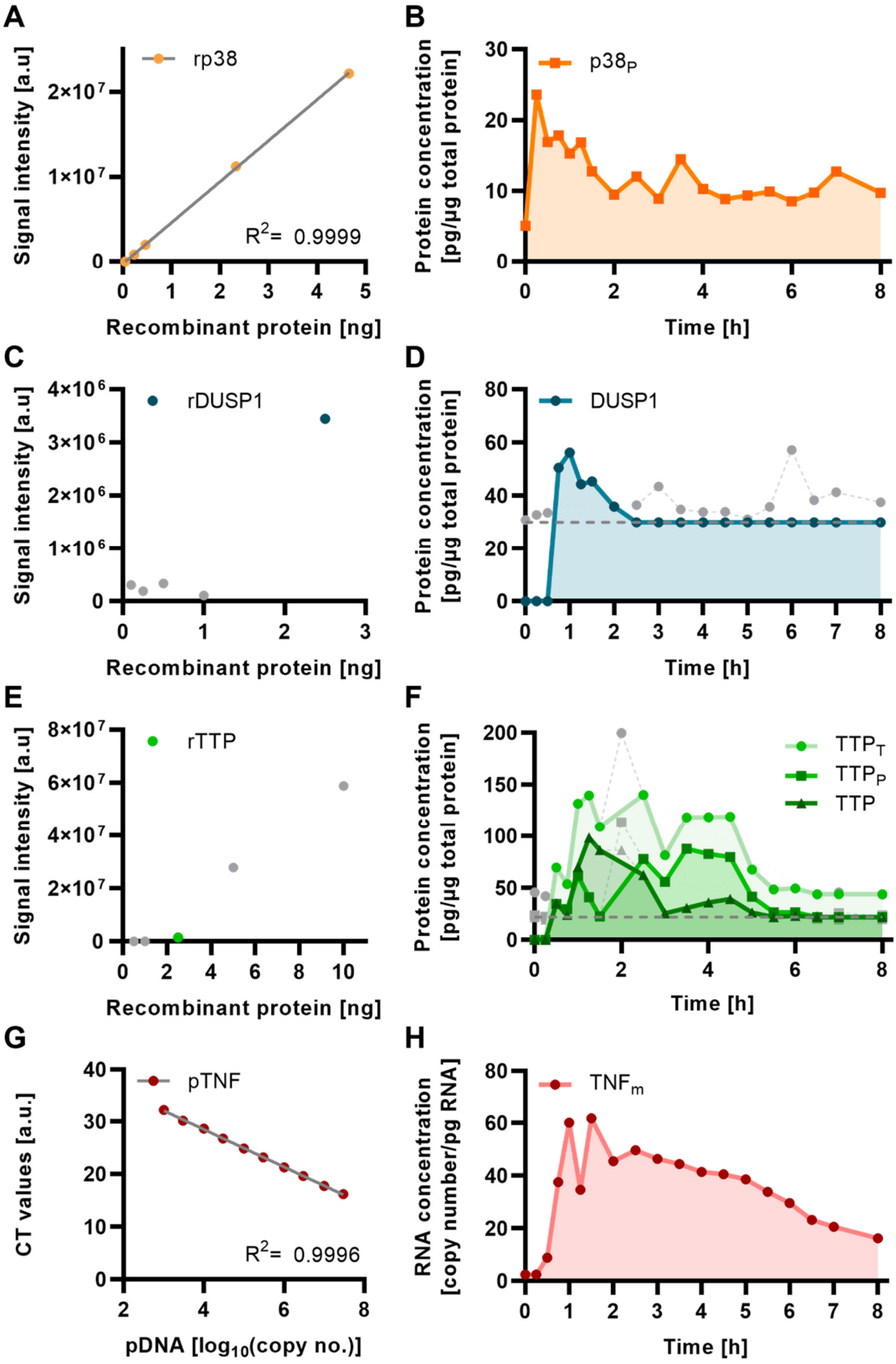

A
rp38
Signal intensity [a.u]
2×10^7
1×10^7
0
R^2= 0.9999
0 1 2 3 4 5
Recombinant protein [ng]
B
p38P
Protein concentration [pg/µg total protein]
30
20
10
0
0 2 4 6 8
Time [h]
C
rDUSP1
Signal intensity [a.u]
4×10^6
3×10^6
2×10^6
1×10^6
0
0 1 2 3
Recombinant protein [ng]
D
DUSP1
Protein concentration [pg/µg total protein]
80
60
40
20
0
0 1 2 3 4 5 6 7 8
Time [h]
E
rTTP
Signal intensity [a.u]
8×10^7
6×10^7
4×10^7
2×10^7
0
0 2 4 6 8 10
Recombinant protein [ng]
F
TTPT
TTPP
TTP
Protein concentration [pg/µg total protein]
200
150
100
50
0
0 2 4 6 8
Time [h]
G
pTNF
CT values [a.u.]
40
30
20
10
0
R^2= 0.9996
2 4 6 8
pDNA [log10(copy no.)]
H
TNFm
RNA concentration [copy number/pg RNA]
80
60
40
20
0
0 1 2 3 4 5 6 7 8
Time [h]

Figure 7.10 WT BMDM Experiment 2: Standard curves and total quantification of Western blot and qPCR data obtained from BMDMs treated with LPS over an 8 h time-course measuring p38 MAPK-TTP pathway components.

BMDMs derived from the bone marrow of 8 mice were combined and treated with 10 ng/mL LPS for a period of 8 h. Protein concentration of phospho-p38 (p38P), total p38 (p38T), DUSP1 and TTP, as well as *Tnf* mRNA levels, were measured using WB and qPCR, respectively. The Western blot data was quantified in Image Lab software, normalised to its Stain-Free signal and the total protein concentration of B) p38 total ($p38_T$) and phospho-p38 ($p38_P$, orange), D) DUSP1 (blue), F) total (TTP_T) unphosphorylated (TTP, lower band) and phosphorylated (TTP_P, upper band) TTP (green) was calculated using the relevant standard curves in A), C), and E). The total amount of *Tnf* mRNA (red), shown in H), was identified by running a standard curve, displayed in G), consisting of known quantities of plasmid DNA alongside the samples for qPCR. Excluded values are shown in light grey symbols with a thin dotted line indicating the change in interpolation. If relevant, the detection limit was indicated by a thick grey dotted line.

7.3.1.3 Experiment 3

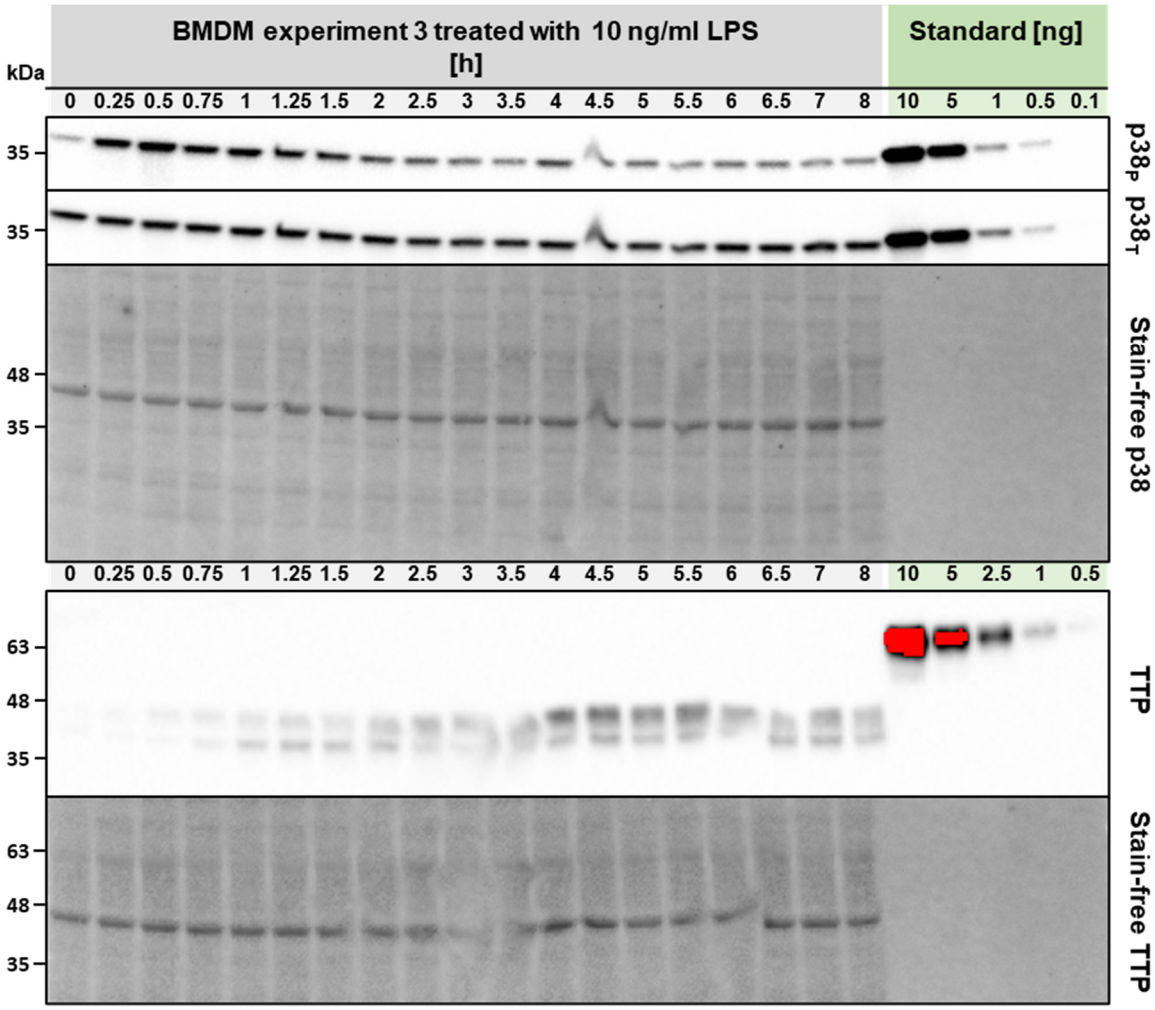


Figure 7.11 WT BMDM Experiment 3: Total quantification Western blot data of BMDMs treated with LPS over an 8 h time-course measuring p38 MAPK-TTP pathway components.

BMDMs derived from the bone marrow of 8 mice were combined and treated with 10 ng/mL LPS for a period of 8 h. Protein concentration of phospho-p38 ($p38_P$), total p38 ($p38_T$), and TTP were measured on individual blots together with recombinant protein standard curve using WB. Shown are measurements of chemiluminescence for each protein as well as their respective Stain-Free blots. The protein size is indicated by relevant marks of the protein ladder in kDa. A DUSP1 blot image is missing due to an error with the Stain-Free that prevented imaging, unfortunately there was not enough sample left to repeat the WB.

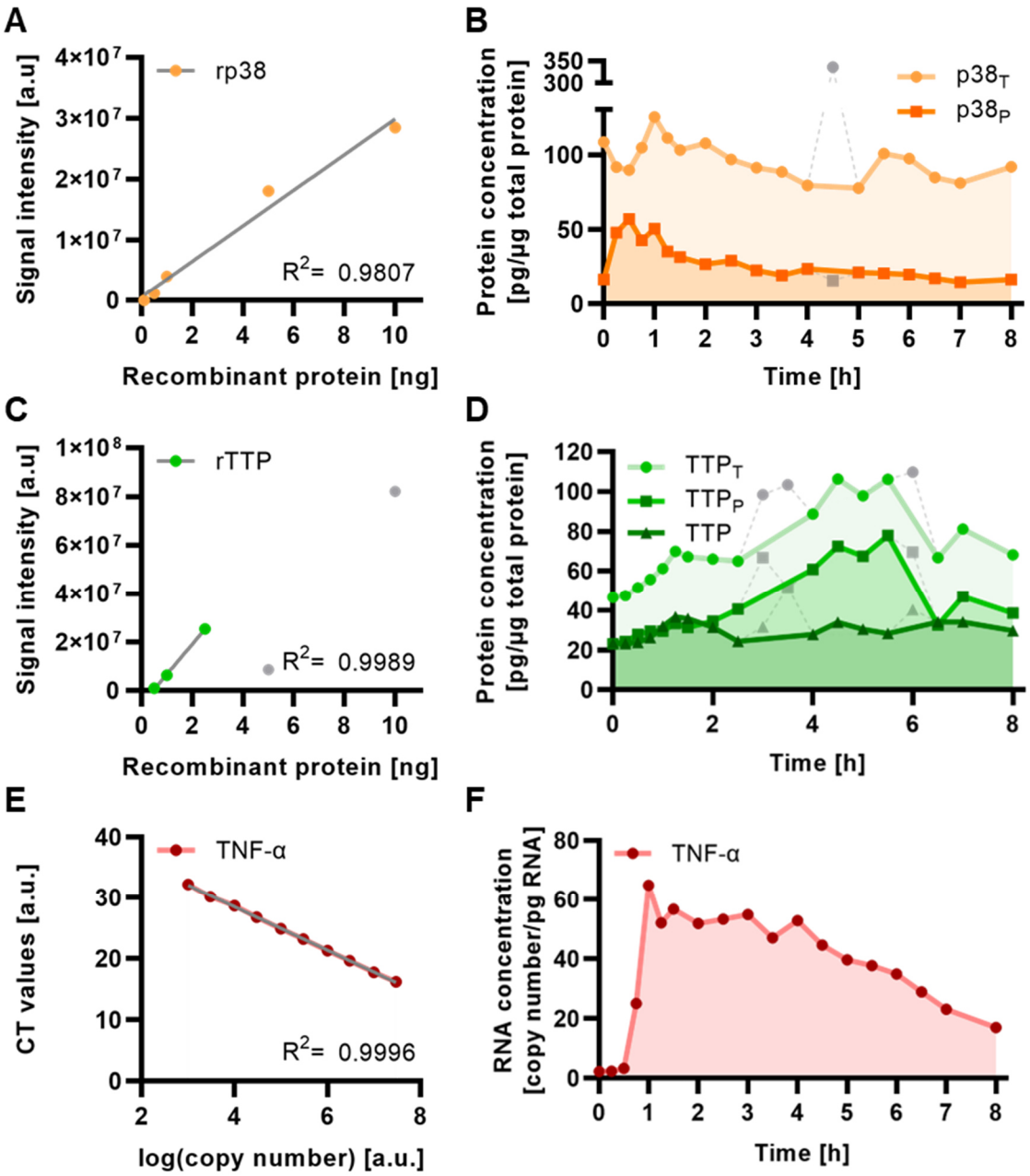


Figure 7.12 WT BMDM Experiment 3: Standard curves and total quantification of Western blot and qPCR data obtained from BMDMs treated with LPS over an 8 h time-course measuring p38 MAPK-TTP pathway components.

BMDMs derived from the bone marrow of 8 mice were combined and treated with 10 ng/mL LPS for a period of 8 h. Protein concentration of phospho-p38 (p38P), total p38 (p38T), and TTP, as well as *Tnf* mRNA levels, were measured using WB and qPCR, respectively. The Western blot data was quantified in Image Lab software, normalised to its Stain-Free signal and the total protein concentration of B) p38 total ($p38_T$) and phospho-p38

($p38_P$, orange), D) total (TTP_T) unphosphorylated (TTP, lower band) and phosphorylated (TTP_P, upper band) TTP (green) was calculated using the relevant standard curves in A), and C). The total amount of *Tnf* mRNA (red), shown in F), was identified by running a standard curve, displayed in E), consisting of known quantities of plasmid DNA alongside the samples for qPCR. Excluded values are shown in light grey symbols with a thin dotted line indicating the change in interpolation.

7.3.2 *Dusp1*$^{-/-}$ BMDMs

7.3.2.1 Experiment 1

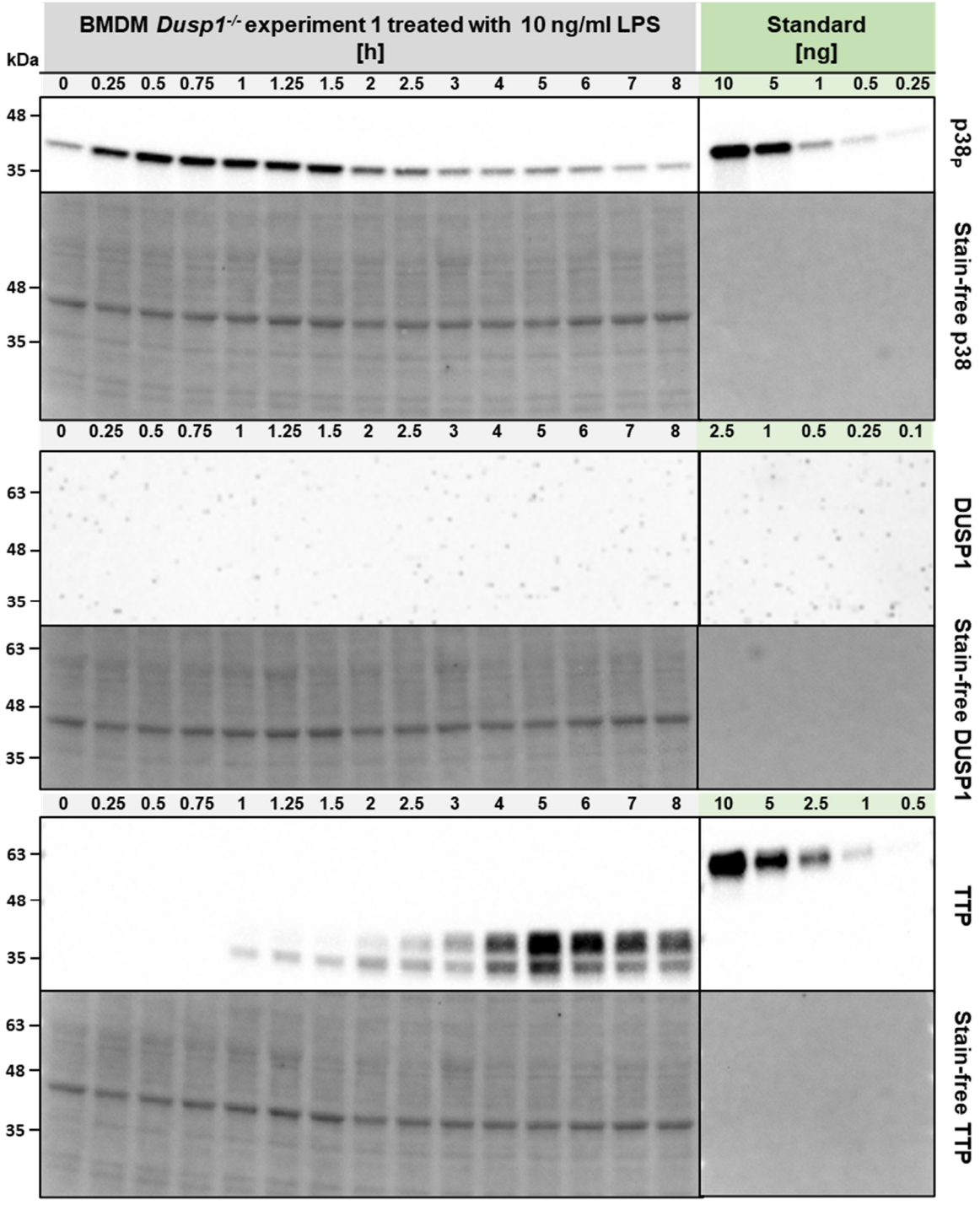


Figure 7.13 *Dusp1*$^{-/-}$ BMDM Experiment 1: Representative total quantification Western blot data of *Dusp1*$^{-/-}$ BMDMs treated with LPS over an 8 h time-course measuring p38 MAPK-TTP pathway components.

Dusp1$^{-/-}$ BMDMs derived from the bone marrow of 6 mice were combined and treated with 10 ng/mL LPS for a period of 8 h. Protein concentration of Phospho-p38 ($p38_P$), DUSP1, and TTP were measured on individual blots together with recombinant protein standard curve using WB. Shown are measurements of chemiluminescence for each protein as well as their respective Stain-Free blots. The protein size is indicated by relevant marks of the protein ladder in kDa.

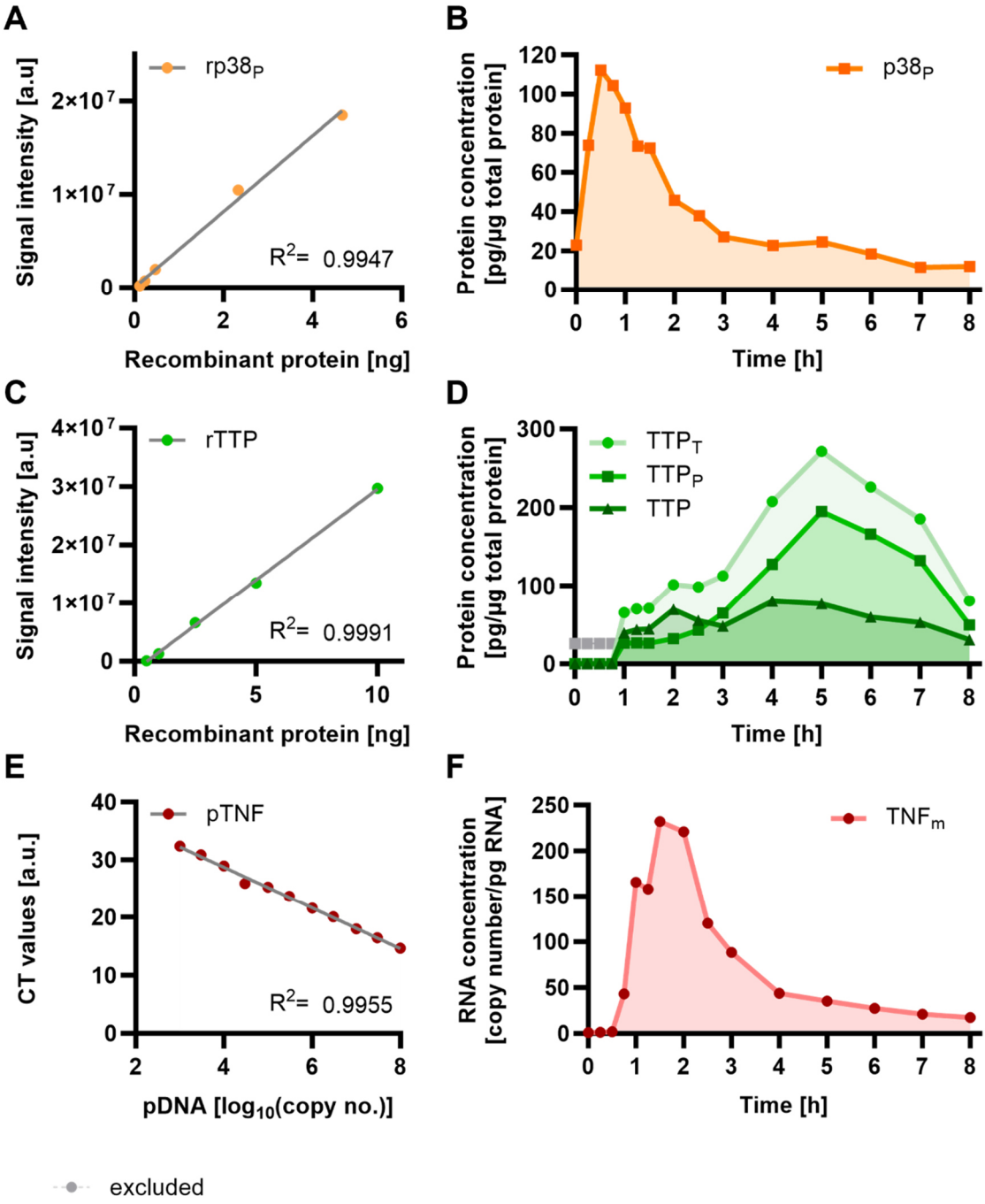


Figure 7.14 *Dusp1*$^{-/-}$ BMDM Experiment 1: Total quantification of Western blot and qPCR data obtained from *Dusp1*$^{-/-}$ BMDMs treated with LPS over an 8 h time-course measuring p38 MAPK-TTP pathway components.

Dusp1$^{-/-}$ BMDMs derived from the bone marrow of 6 mice were combined and treated with 10 ng/mL LPS for a period of 8 h. Protein concentration of Phospho-p38 (p38P) and TTP, as well as *Tnf* mRNA levels, were measured using WB and qPCR, respectively. The Western blot data was quantified in Image Lab software, normalised to its

Stain-Free signal and the total protein concentration of B) p38 total ($p38_T$) and phospho-p38 ($p38_P$, orange), D) total (TTP_T) unphosphorylated (TTP, lower band) and phosphorylated (TTP_P, upper band) TTP (green) was calculated using the relevant standard curves in A), and C). The total amount of *Tnf* mRNA (red), shown in F), was identified by running a standard curve, displayed in E), consisting of known quantities of plasmid DNA alongside the samples for qPCR. Excluded values are shown in light grey symbols with a thin dotted line indicating the change in interpolation.

7.3.2.2 Experiment 2

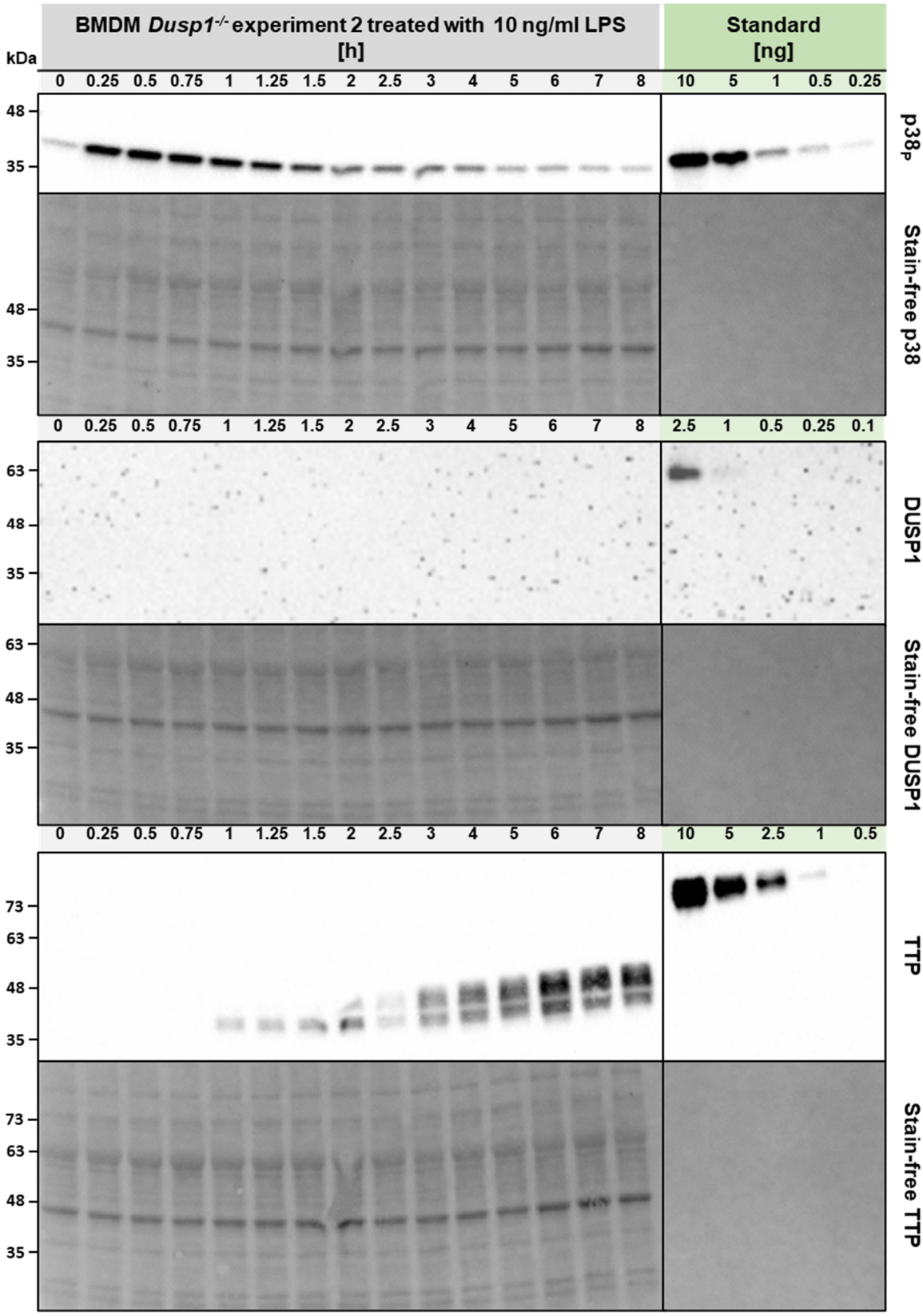


Figure 7.15 *Dusp1*$^{-/-}$ BMDM Experiment 2: Total quantification Western blot data of *Dusp1*$^{-/-}$ BMDMs treated with LPS over an 8 h time-course measuring p38 MAPK-TTP pathway components.

Dusp1$^{-/-}$ BMDMs derived from the bone marrow of 6 mice were combined and treated with 10 ng/mL LPS for a period of 8 h. Protein concentration of phospho-p38 ($p38_P$), total p38 ($p38_T$), DUSP1, and TTP were measured on individual blots together with recombinant protein standard curve using WB. Shown are measurements of chemiluminescence for each protein as well as their respective Stain-Free blots. The protein size is indicated by relevant marks of the protein ladder in kDa.

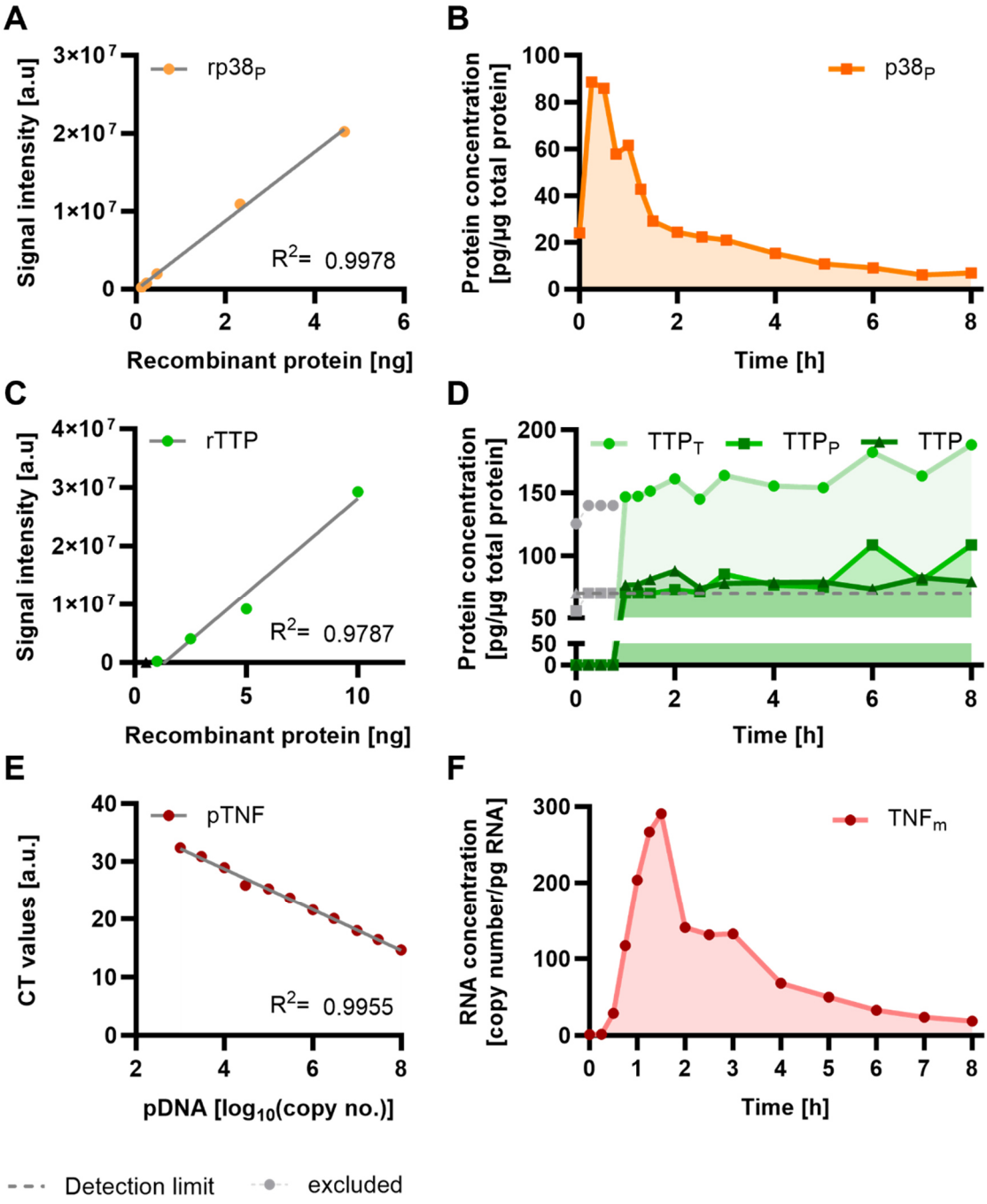


Figure 7.16 *Dusp1*$^{-/-}$ BMDM Experiment 2: Standard curves and total quantification of Western blot and qPCR data obtained from *Dusp1*$^{-/-}$ BMDMs treated with LPS over an 8 h time-course measuring p38 MAPK-TTP pathway components.

Dusp1$^{-/-}$ BMDMs derived from the bone marrow of 6 mice were combined and treated with 10 ng/mL LPS for a period of 8 h. Protein concentration of phospho-p38 (p38P) and TTP, as well as *Tnf* mRNA levels, were measured using WB and qPCR, respectively. The Western blot data was quantified in Image Lab software, normalised to its Stain-Free signal and the total protein concentration of B) p38 total ($p38_T$) and phospho-p38 ($p38_P$, orange), D)

total (TTP_T) unphosphorylated (TTP, lower band) and phosphorylated (TTP_P, upper band) TTP (green) was calculated using the relevant standard curves in A), and C). The total amount of *Tnf* mRNA (red), shown in F), was identified by running a standard curve, displayed in E), consisting of known quantities of plasmid DNA alongside the samples for qPCR. Excluded values are shown in light grey symbols with a thin dotted line indicating the change in interpolation. If relevant, the detection limit was indicated by a thick grey dotted line.

7.3.2.3 Experiment 3

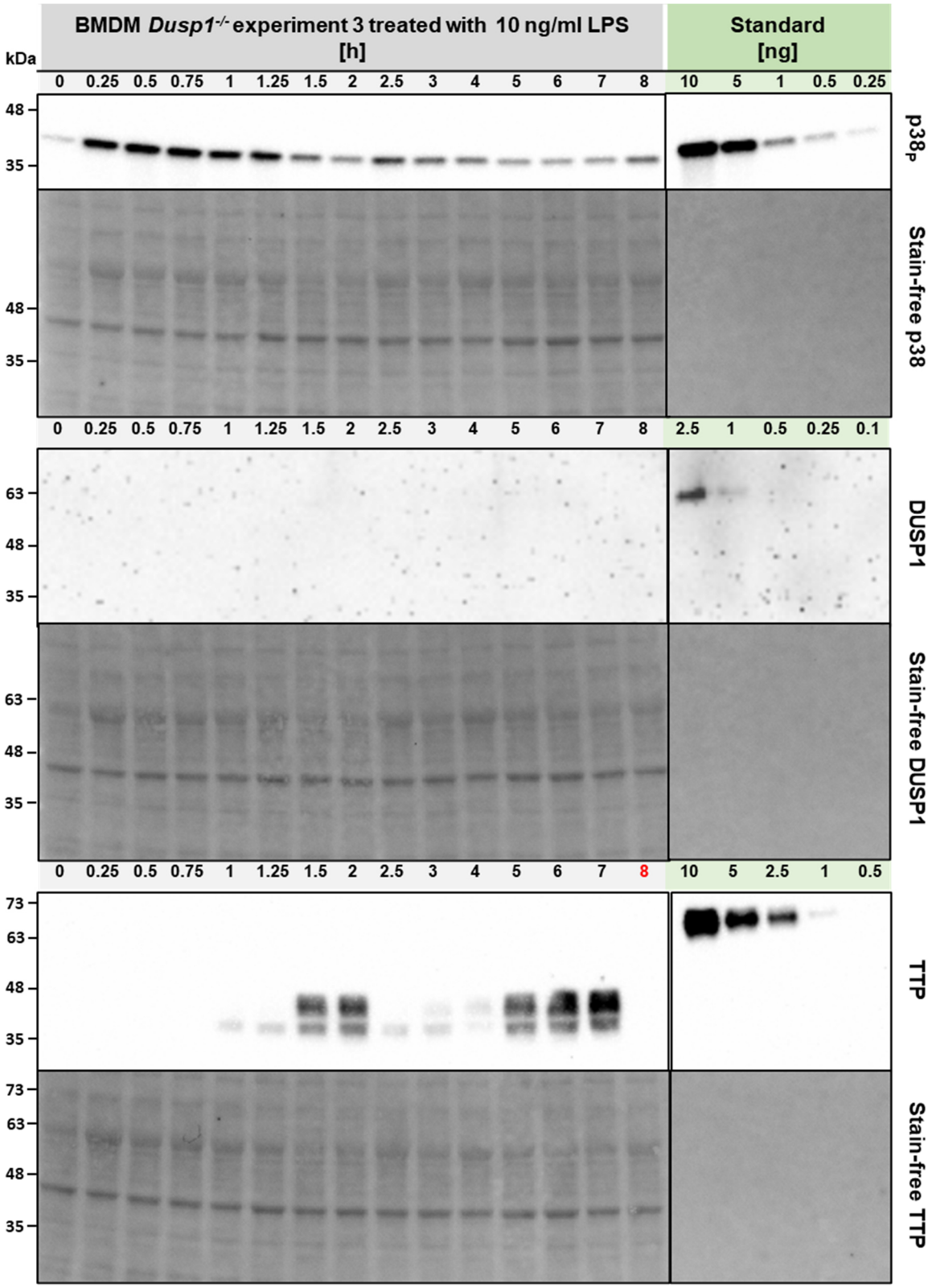


Figure 7.17 *Dusp1*$^{-/-}$ BMDM Experiment 3: Total quantification Western blot data of *Dusp1*$^{-/-}$ BMDMs treated with LPS over an 8 h time-course measuring p38 MAPK-TTP pathway components.

Dusp1$^{-/-}$ BMDMs derived from the bone marrow of 6 mice were combined and treated with 10 ng/mL LPS for a period of 8 h. Protein concentration of phospho-p38 ($p38_P$), DUSP1 and TTP were measured on individual blots together with recombinant protein standard curve using WB. Shown are measurements of chemiluminescence for each protein as well as their respective Stain-Free blots. The protein size is indicated by relevant marks of the protein ladder in kDa.

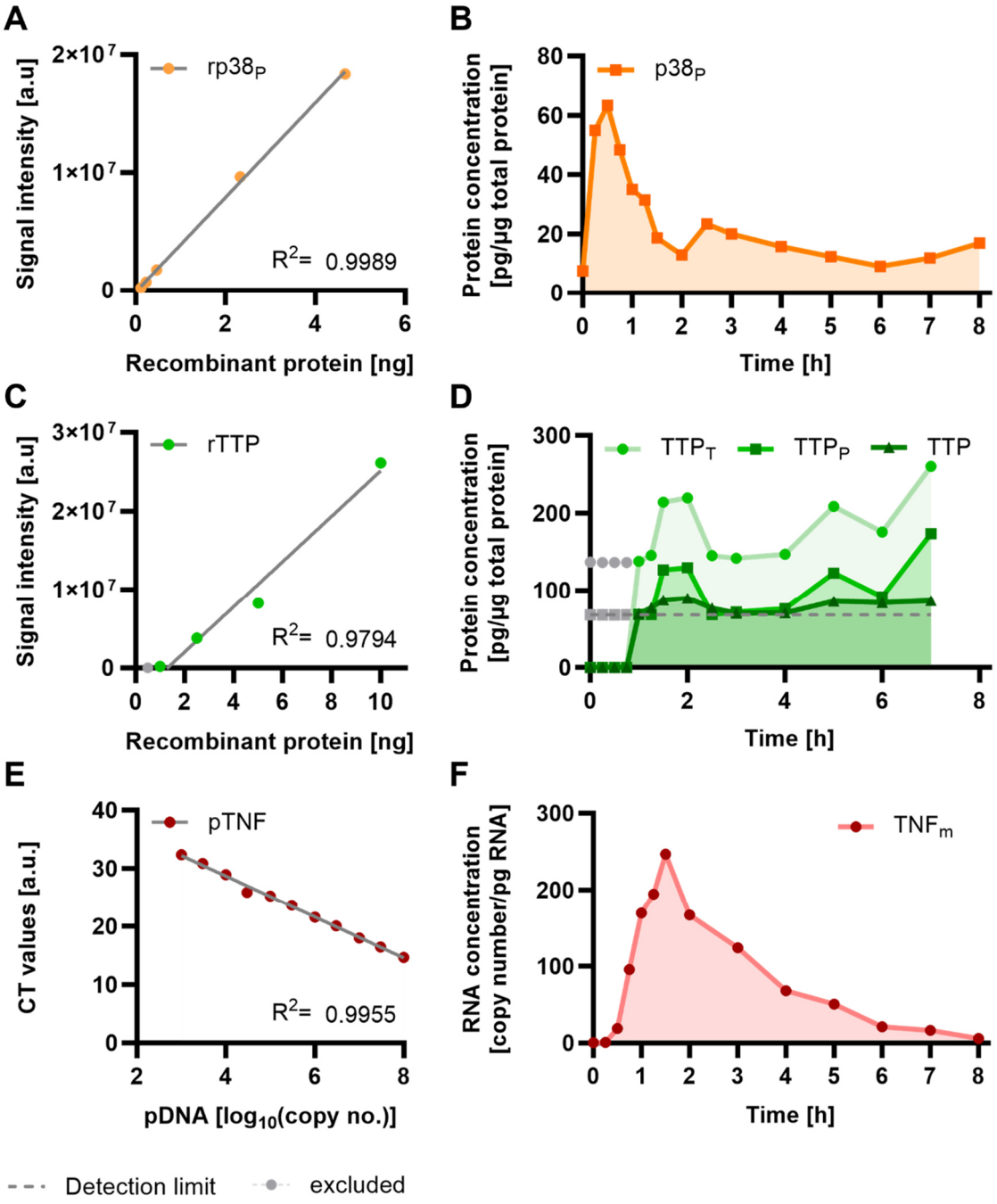


Figure 7.18 *Dusp1*$^{-/-}$ BMDM Experiment 3: Standard curves and total quantification of Western blot and qPCR data obtained from *Dusp1*$^{-/-}$ BMDMs treated with LPS over an 8 h time-course measuring p38 MAPK-TTP pathway components.

Dusp1$^{-/-}$ BMDMs derived from the bone marrow of 6 mice were combined and treated with 10 ng/mL LPS for a period of 8 h. Protein concentration of phospho-p38 (p38P), and TTP, as well as *Tnf* mRNA levels, were measured using WB and qPCR, respectively. The Western blot data was quantified in Image Lab software, normalised to its Stain-Free signal and the total protein concentration of B) phospho-p38 ($p38_P$, orange), D) total (TTP_T)

unphosphorylated (TTP, lower band) and phosphorylated (TTP_P, upper band) TTP (green) was calculated using the relevant standard curves in A), and C). The total amount of *Tnf* mRNA (red), shown in F), was identified by running a standard curve, displayed in E), consisting of known quantities of plasmid DNA alongside the samples for qPCR. Excluded values are shown in light grey symbols with a thin dotted line indicating the change in interpolation. If relevant, the detection limit was indicated by a thick grey dotted line.

7.3.3 *Zfp36*$^{aa/aa}$ BMDMs

7.3.3.1 Experiment 1

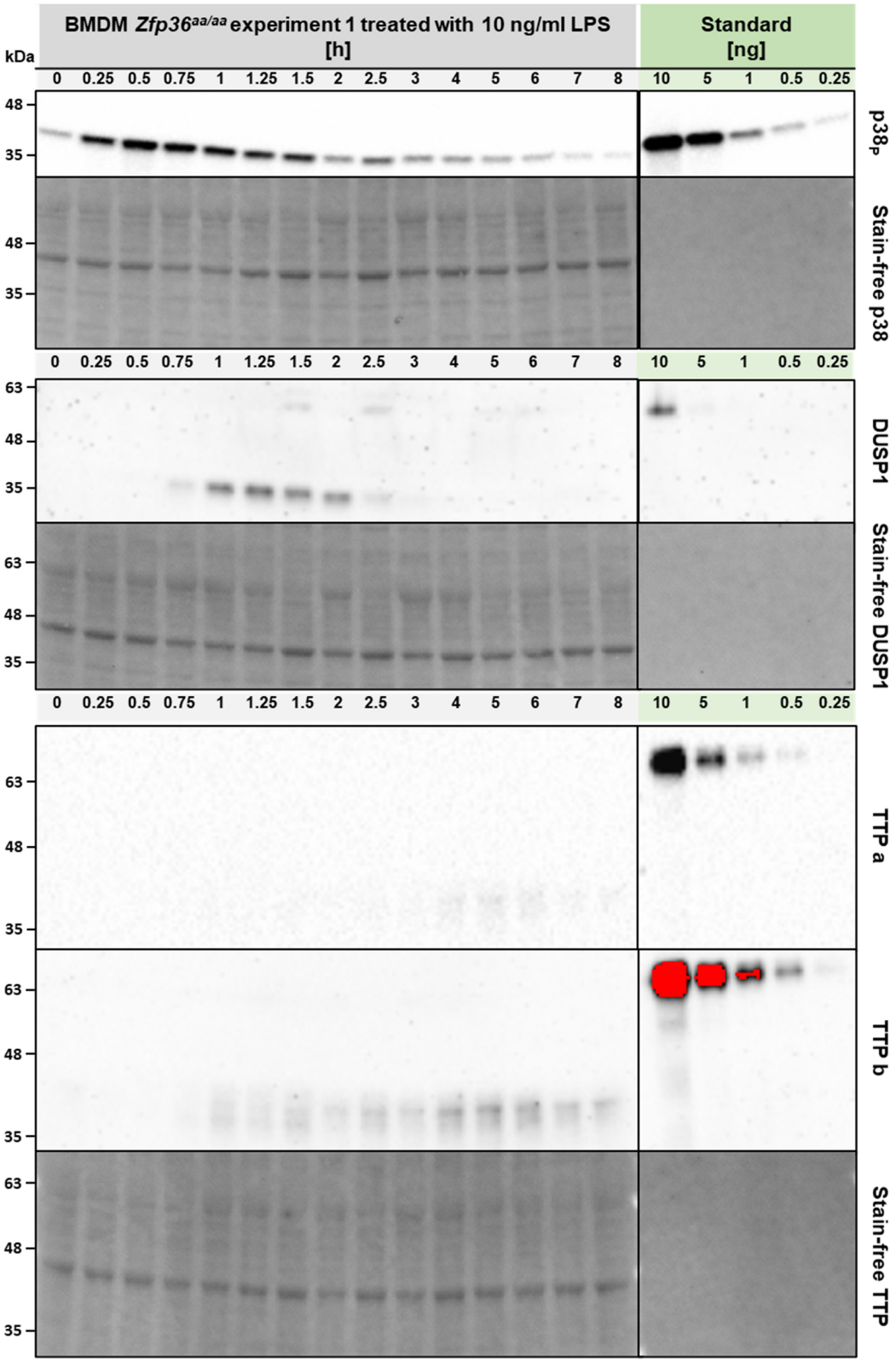


Figure 7.19 *Zfp36*$^{aa/aa}$ BMDM Experiment 1: Representative total quantification Western blot data of *Zfp36*$^{aa/aa}$ BMDMs treated with LPS over an 8 h time-course measuring p38 MAPK-TTP pathway components.

Zfp36$^{aa/aa}$ BMDMs derived from the bone marrow of 6 mice were combined and treated with 10 ng/mL LPS for a period of 8 h. Protein concentration of phospho-p38 ($p38_P$), DUSP1 and TTP were measured on individual blots together with recombinant protein standard curve using WB. For TTP, two distinct exposure times, 60 sec (TTPa) and 600 sec (TTPb), are shown to increase resolution of early time points. Shown are measurements of chemiluminescence for each protein as well as their respective Stain-Free blots. The protein size is indicated by relevant marks of the protein ladder in kDa.

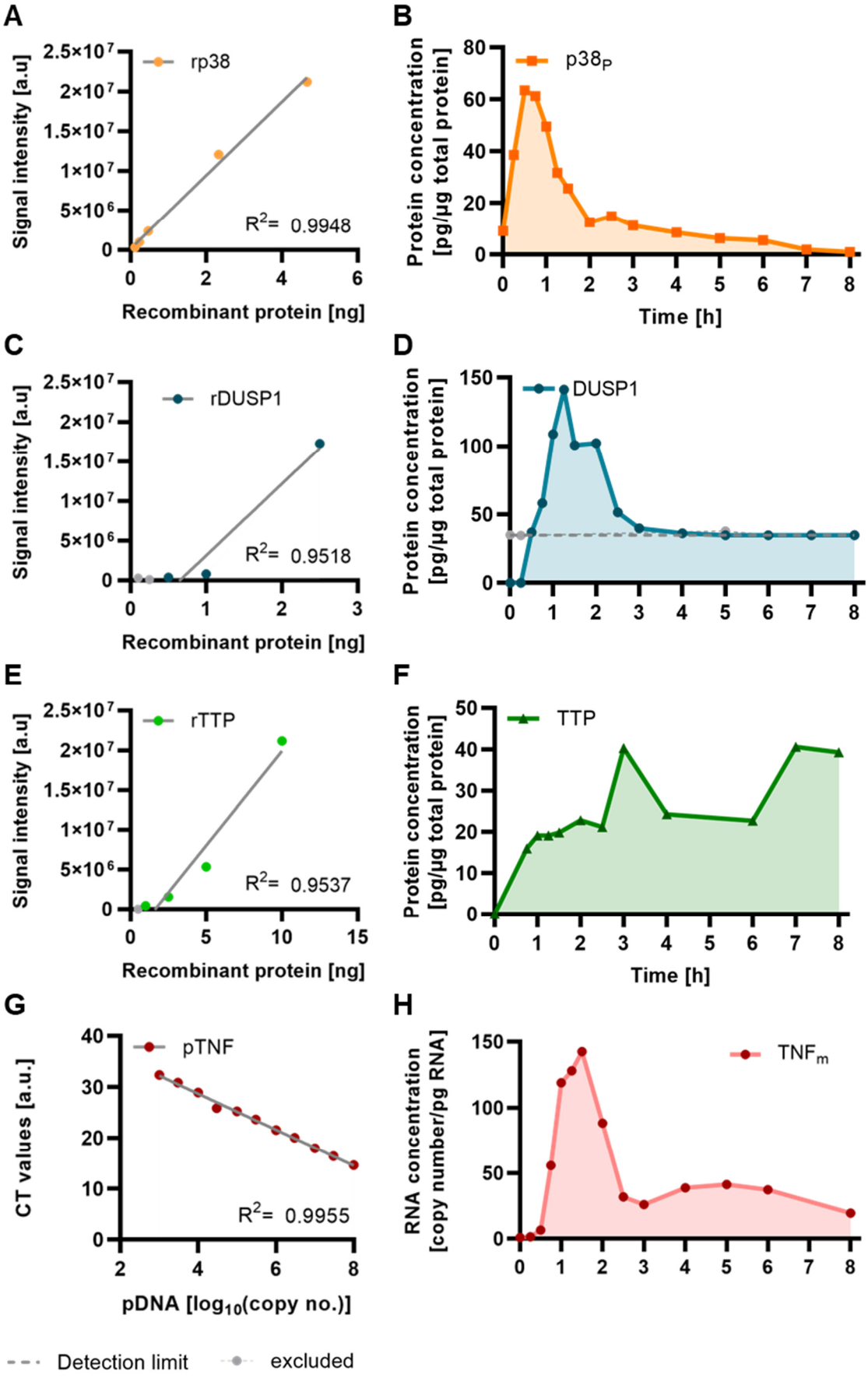

A
Signal intensity [a.u]
rp38
R²= 0.9948
Recombinant protein [ng]
B
Protein concentration [pg/µg total protein]
p38P
Time [h]
C
Signal intensity [a.u]
rDUSP1
R²= 0.9518
Recombinant protein [ng]
D
Protein concentration [pg/µg total protein]
DUSP1
E
Signal intensity [a.u]
rTTP
R²= 0.9537
Recombinant protein [ng]
F
Protein concentration [pg/µg total protein]
TTP
Time [h]
G
CT values [a.u.]
pTNF
R²= 0.9955
pDNA [log10(copy no.)]
H
RNA concentration [copy number/pg RNA]
TNFm
Detection limit
excluded

Figure 7.20 *Zfp36*$^{aa/aa}$ BMDM Experiment 1: Standard curves and total quantification of Western blot and qPCR data obtained from *Zfp36*$^{aa/aa}$ BMDMs treated with LPS over an 8 h time-course measuring p38 MAPK-TTP pathway components.

Zfp36$^{aa/aa}$ BMDMs derived from the bone marrow of 6 mice were combined and treated with 10 ng/mL LPS for a period of 8 h. Protein concentration of phospho-p38 (p38P), DUSP1, and TTP, as well as *Tnf* mRNA levels, were measured using WB and qPCR, respectively. The Western blot data was quantified in Image Lab software, normalised to its Stain-Free signal and the total protein concentration of B) phospho-p38 ($p38_P$, orange), D) DUSP1, E) unphosphorylated TTP (green) was calculated using the relevant standard curves in A), C) and E). The total amount of *Tnf* mRNA (red), shown in H), was identified by running a standard curve, displayed in G), consisting of known quantities of plasmid DNA alongside the samples for qPCR. Excluded values are shown in light grey symbols with a thin dotted line indicating the change in interpolation. If relevant, the detection limit was indicated by a thick grey dotted line. The TTP data set was excluded, because we accidentally run the wrong standard curve.

7.3.3.2 Experiment 2

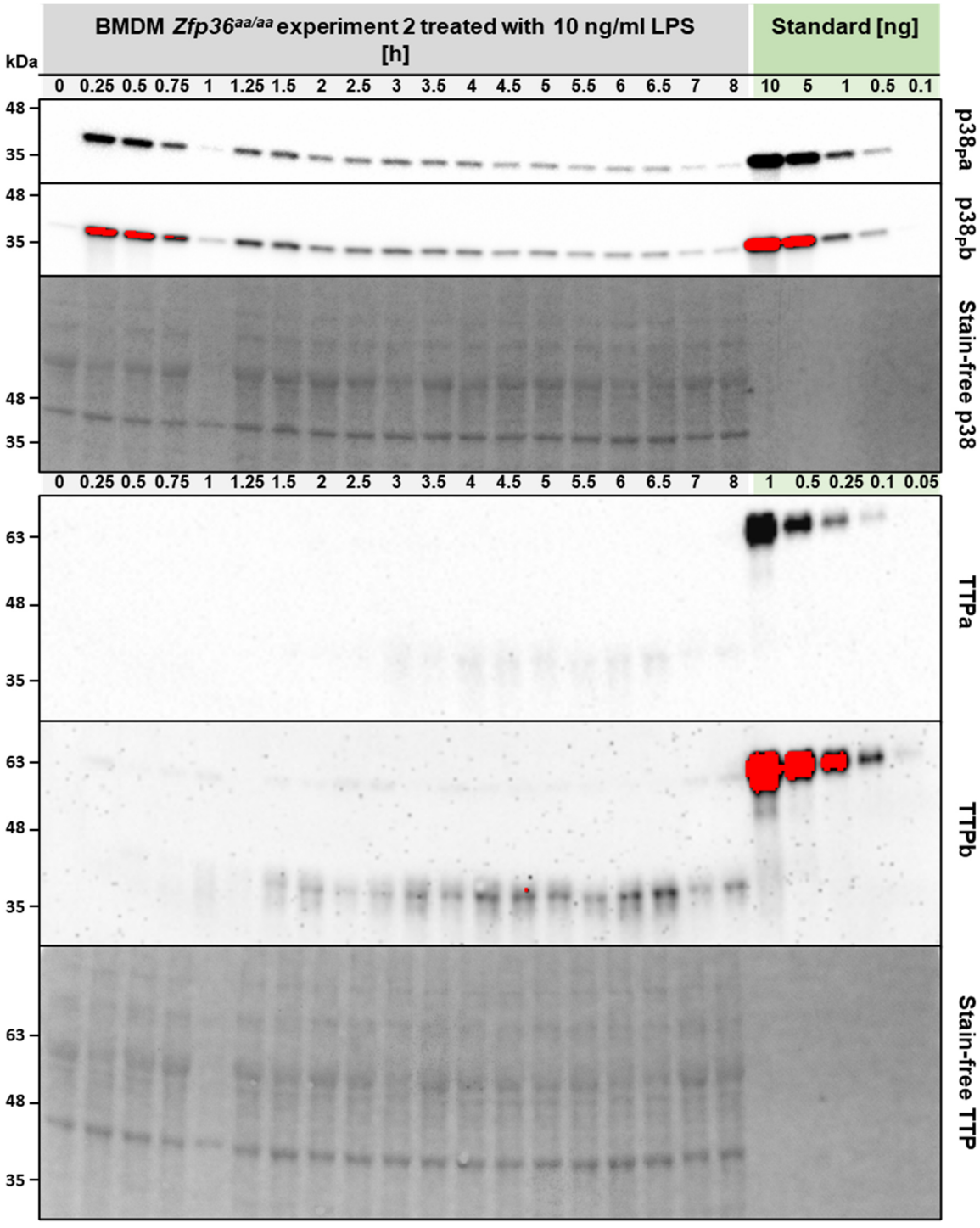


Figure 7.21 *Zfp36*$^{aa/aa}$ BMDM Experiment 2: total quantification Western blot data of *Zfp36*$^{aa/aa}$ BMDMs treated with LPS over an 8 h time-course measuring p38 MAPK-TTP pathway components.

Zfp36$^{aa/aa}$ BMDMs derived from the bone marrow of 6 mice were combined and treated with 10 ng/mL LPS for a period of 8 h. Protein concentration of phospho-p38 ($p38_P$), and TTP were measured on individual blots together

with recombinant protein standard curve using WB. For TTP, two distinct exposure times are shown (TTPa 60 sec, TTPb 600 sec). Shown are measurements of chemiluminescence for each protein as well as their respective Stain-Free blots. The protein size is indicated by relevant marks of the protein ladder in kDa.

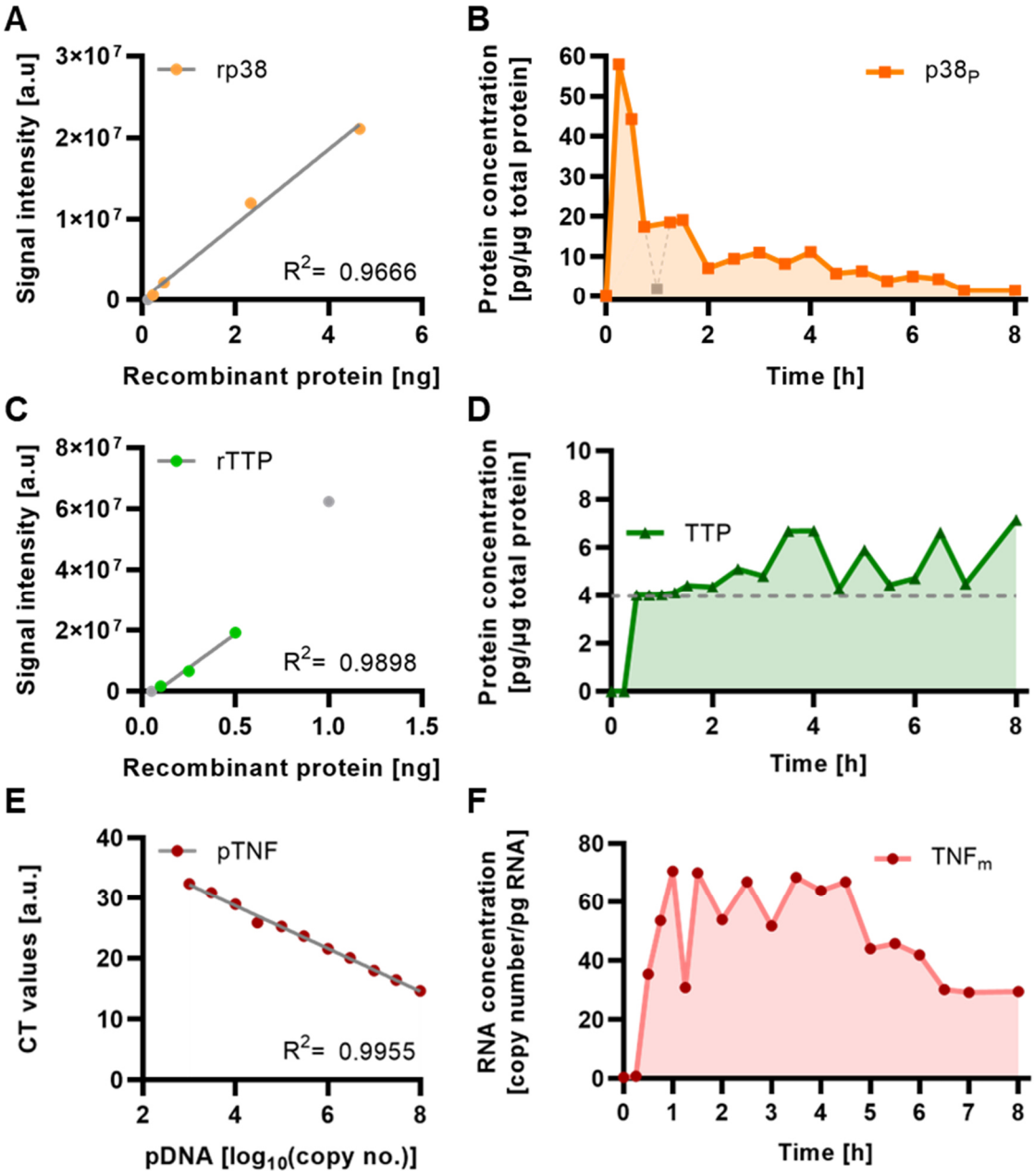


Figure 7.22 *Zfp36*$^{aa/aa}$ BMDM Experiment 2: Standard curves and total quantification of Western blot and qPCR data obtained from *Zfp36*$^{aa/aa}$ BMDMs treated with LPS over an 8 h time-course measuring p38 MAPK-TTP pathway components.

Zfp36$^{aa/aa}$ BMDMs derived from the bone marrow of 6 mice were combined and treated with 10 ng/mL LPS for a period of 8 h. Protein concentration of phospho-p38 (p38P), and TTP, as well as *Tnf* mRNA levels, were measured using WB and qPCR, respectively. The Western blot data was quantified in Image Lab software, normalised to its Stain-Free signal and the total protein concentration of B) phospho-p38 ($p38_P$, orange), D) unphosphorylated TTP (green) was calculated using the relevant standard curves in A), and C). The total amount of *Tnf* mRNA (red), shown in F), was identified by running a standard curve, displayed in E), consisting of known quantities of plasmid DNA alongside the samples for qPCR. Excluded values are shown in light grey symbols with a thin dotted line indicating the change in interpolation. If relevant, the detection limit was indicated by a thick grey dotted line.

7.3.3.3 Experiment 3

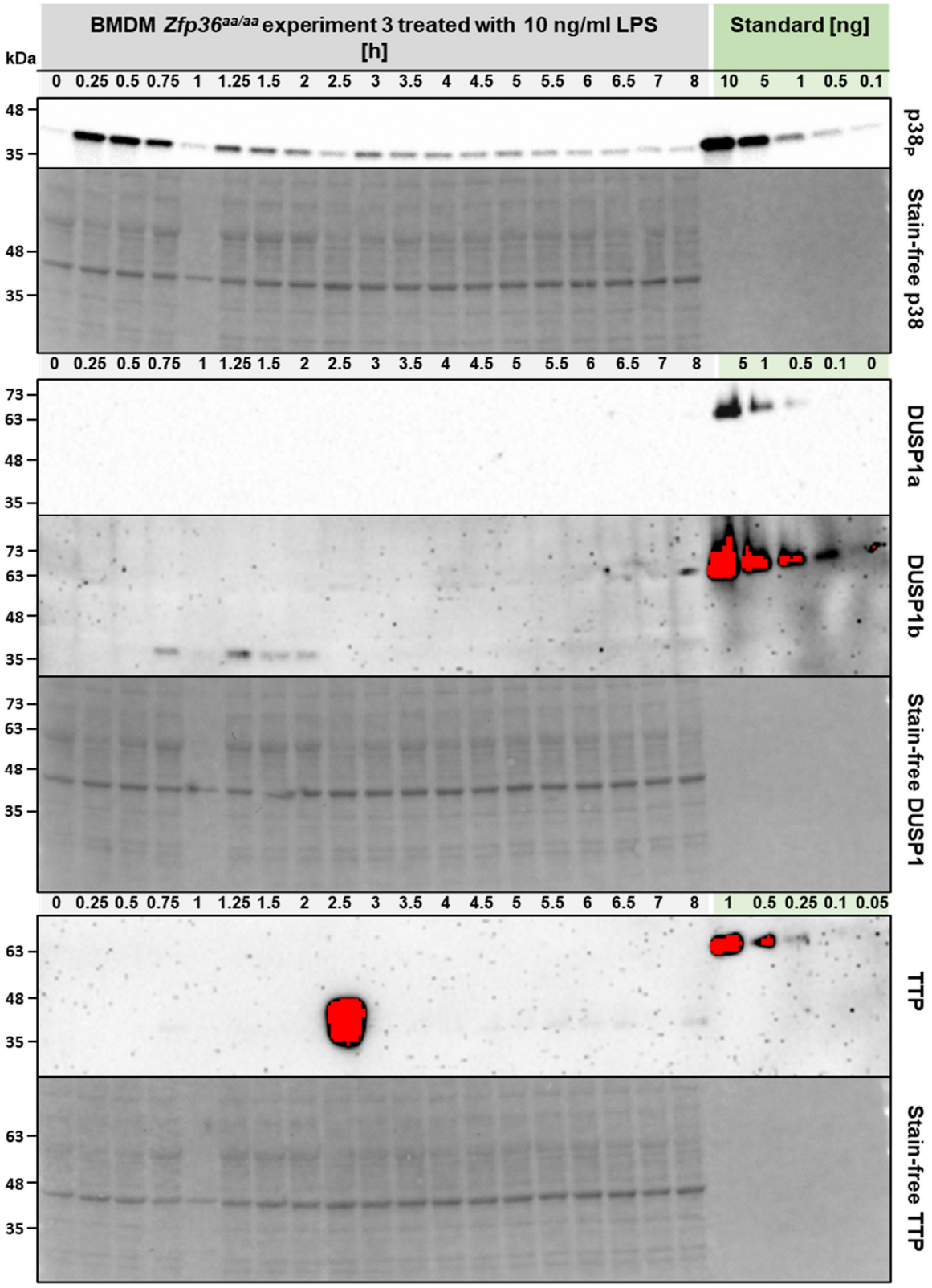


Figure 7.23 *Zfp36*$^{aa/aa}$ BMDM Experiment 3: Total quantification Western blot data of *Zfp36*$^{aa/aa}$ BMDMs treated with LPS over an 8 h time-course measuring p38 MAPK-TTP pathway components.

Zfp36$^{aa/aa}$ BMDMs derived from the bone marrow of 6 mice were combined and treated with 10 ng/mL LPS for a period of 8 h. Protein concentration of phospho-p38 ($p38_P$), DUSP1, and TTP were measured on individual blots together with recombinant protein standard curve using WB. For DUSP1, two distinct exposure times are shown. Shown are measurements of chemiluminescence for each protein as well as their respective Stain-Free blots. The protein size is indicated by relevant marks of the protein ladder in kDa.

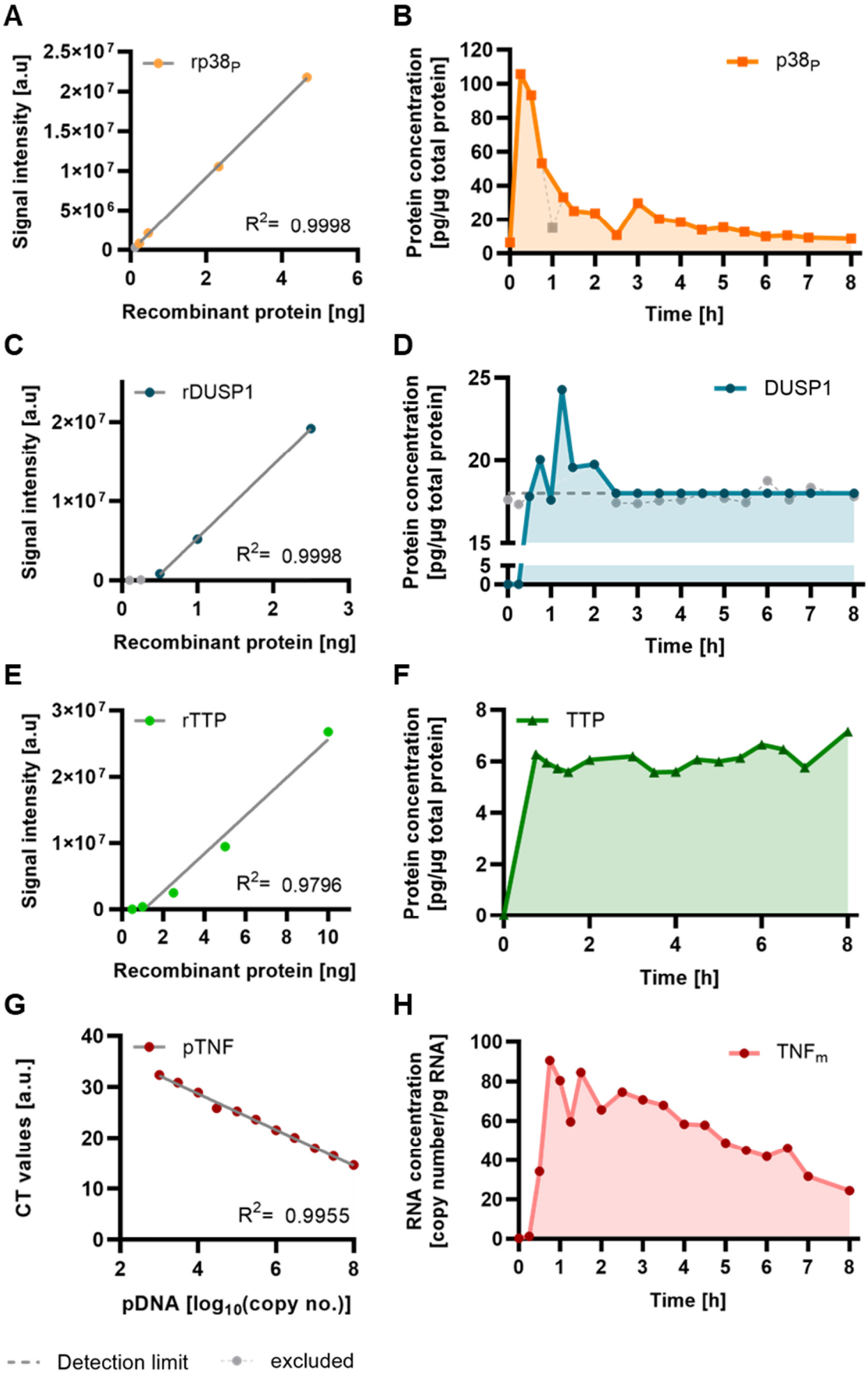

A
Signal intensity [a.u]
rp38P
R2= 0.9998
Recombinant protein [ng]
B
Protein concentration [pg/µg total protein]
p38P
Time [h]
C
Signal intensity [a.u]
rDUSP1
R2= 0.9998
Recombinant protein [ng]
D
Protein concentration [pg/µg total protein]
DUSP1
Time [h]
E
Signal intensity [a.u]
rTTP
R2= 0.9796
Recombinant protein [ng]
F
Protein concentration [pg/µg total protein]
TTP
Time [h]
G
CT values [a.u.]
pTNF
R2= 0.9955
pDNA [log10(copy no.)]
H
RNA concentration [copy number/pg RNA]
TNFm
Time [h]
Detection limit
excluded

Figure 7.24 *Zfp36*$^{aa/aa}$ BMDM Experiment 3: Standard curves and total quantification of Western blot and qPCR data obtained from *Zfp36*$^{aa/aa}$ BMDMs treated with LPS over an 8 h time-course measuring p38 MAPK-TTP pathway components.

Zfp36$^{aa/aa}$ BMDMs derived from the bone marrow of 6 mice were combined and treated with 10 ng/mL LPS for a period of 8 h. Protein concentration of phospho-p38 (p38P), DUSP1, and TTP, as well as *Tnf* mRNA levels, were measured using WB and qPCR, respectively. The Western blot data was quantified in Image Lab software, normalised to its Stain-Free signal and the total protein concentration of B) phospho-p38 ($p38_P$, orange), D) DUSP1, E) unphosphorylated TTP (green) was calculated using the relevant standard curves in A), C) and E). The total amount of *Tnf* mRNA (red), shown in H), was identified by running a standard curve, displayed in G), consisting of known quantities of plasmid DNA alongside the samples for qPCR. Excluded values are shown in light grey symbols with a thin dotted line indicating the change in interpolation. If relevant, the detection limit was indicated by a thick grey dotted line.

7.3.4 RAW264.7 cells

7.3.4.1 Experiment 1

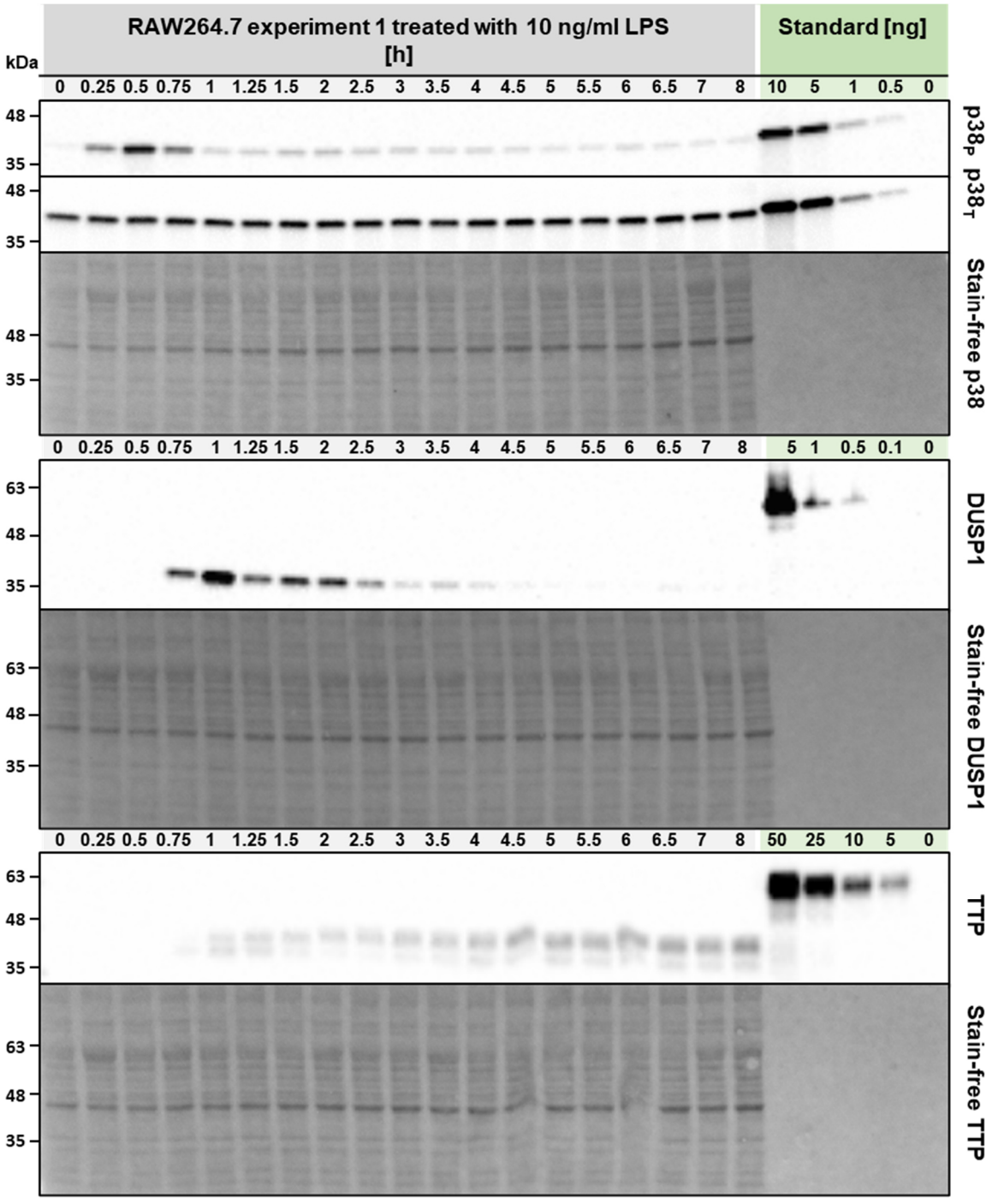


Figure 7.25 RAW264.7 Experiment 1: Total quantification Western blot data of RAW264.7 cells treated with LPS over an 8 h time-course measuring p38 MAPK-TTP pathway components.

RAW264.7 cells were treated with 10 ng/mL LPS for a period of 8 h. Protein concentration of phospho-p38 ($p38_P$), total p38 ($p38_T$), DUSP1 and TTP were measured on individual blots together with recombinant protein standard curve using WB. Shown are measurements of chemiluminescence for each protein as well as their respective Stain-Free blots. The protein size is indicated by relevant marks of the protein ladder in kDa.

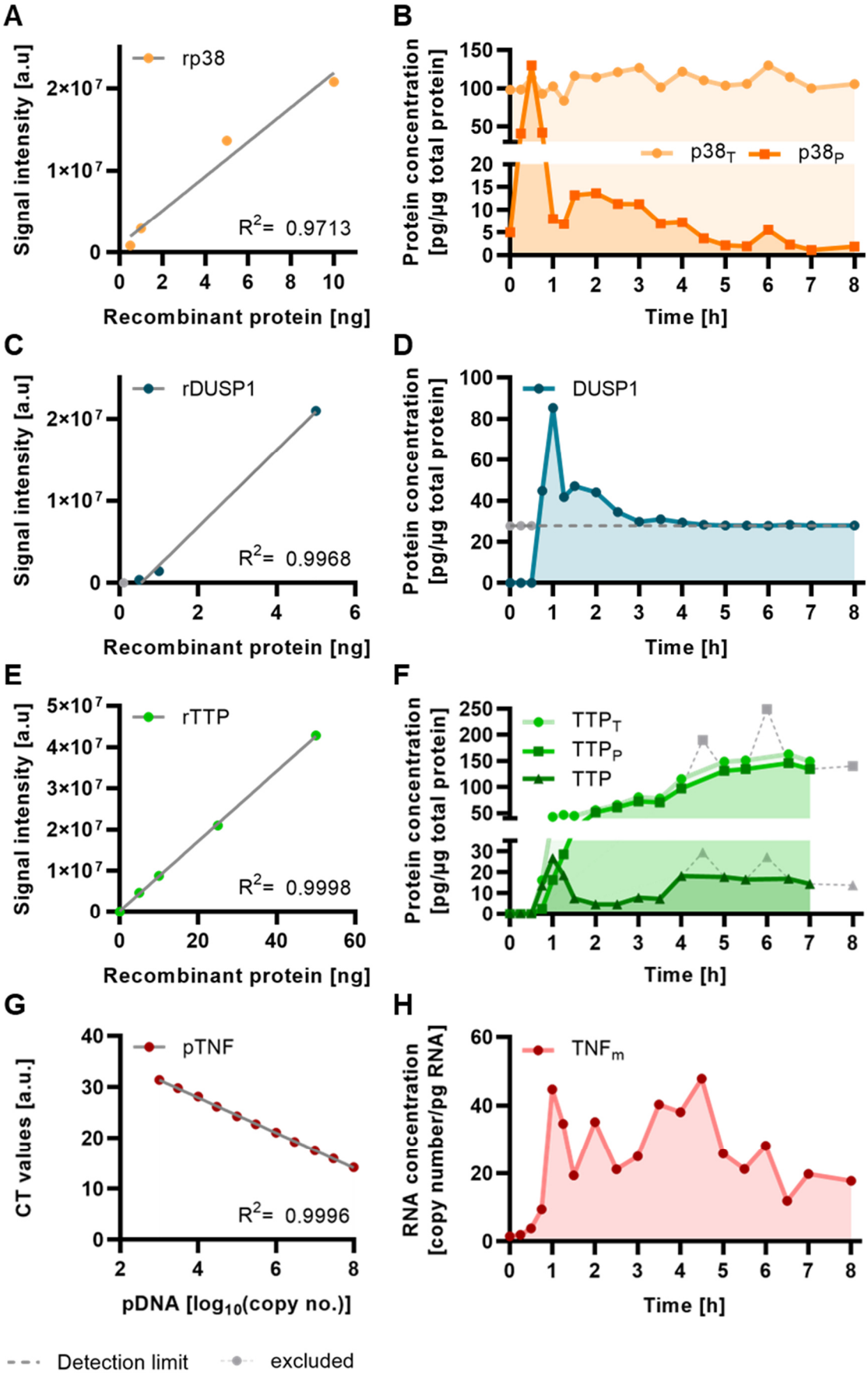

A
rp38
Signal intensity [a.u]
Recombinant protein [ng]
R²= 0.9713
B
Protein concentration [pg/µg total protein]
p38T
p38P
Time [h]
C
rDUSP1
Signal intensity [a.u]
Recombinant protein [ng]
R²= 0.9968
D
DUSP1
Protein concentration [pg/µg total protein]
Time [h]
E
rTTP
Signal intensity [a.u]
Recombinant protein [ng]
R²= 0.9998
F
TTPT
TTPP
TTP
Protein concentration [pg/µg total protein]
Time [h]
G
pTNF
CT values [a.u.]
pDNA [log10(copy no.)]
R²= 0.9996
H
TNFm
RNA concentration [copy number/pg RNA]
Time [h]
Detection limit
excluded

Figure 7.26 RAW264.7 Experiment 1: Standard curves and total quantification of Western blot and qPCR data obtained from RAW264.7 cells treated with LPS over an 8 h time-course measuring p38 MAPK-TTP pathway components.

RAW264.7 cells were treated with 10 ng/mL LPS for a period of 8 h. Protein concentration of phospho-p38 (p38P), total p38 (p38T), DUSP1 and TTP, as well as *Tnf* mRNA levels, were measured using WB and qPCR, respectively. The Western blot data was quantified in Image Lab software, normalised to its Stain-Free signal and the total protein concentration of B) p38 total ($p38_T$) and phospho-p38 ($p38_P$, orange), D) DUSP1 (blue), F) total (TTP_T) unphosphorylated (TTP, lower band) and phosphorylated (TTP_P, upper band) TTP (green) was calculated using the relevant standard curves in A), C), and E). The total amount of *Tnf* mRNA (red), shown in H), was identified by running a standard curve, displayed in G), consisting of known quantities of plasmid DNA alongside the samples for qPCR. Excluded values are shown in light grey symbols with a thin dotted line indicating the change in interpolation. If relevant, the detection limit was indicated by a thick grey dotted line.

7.3.4.2 Experiment 2

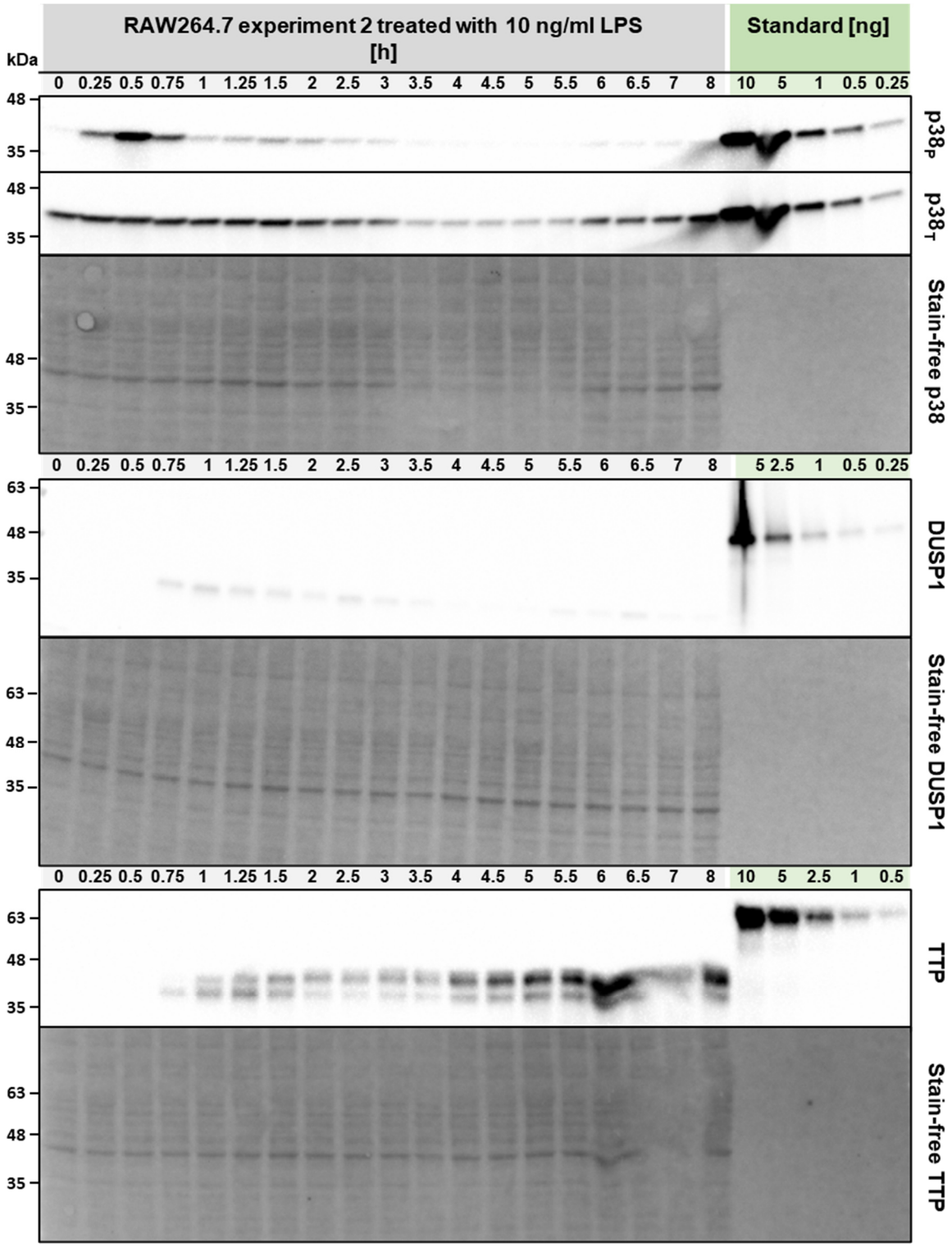


Figure 7.27 RAW264.7 Experiment 2: Total quantification Western blot data of RAW264.7 cells treated with LPS over an 8 h time-course measuring p38 MAPK-TTP pathway components.

RAW264.7 cells were treated with 10 ng/mL LPS for a period of 8 h. Protein concentration of phospho-p38 ($p38_P$), total p38 ($p38_T$), DUSP1 and TTP were measured on individual blots together with recombinant protein standard curve using WB. Shown are measurements of chemiluminescence for each protein as well as their respective Stain-Free blots. The protein size is indicated by relevant marks of the protein ladder in kDa.

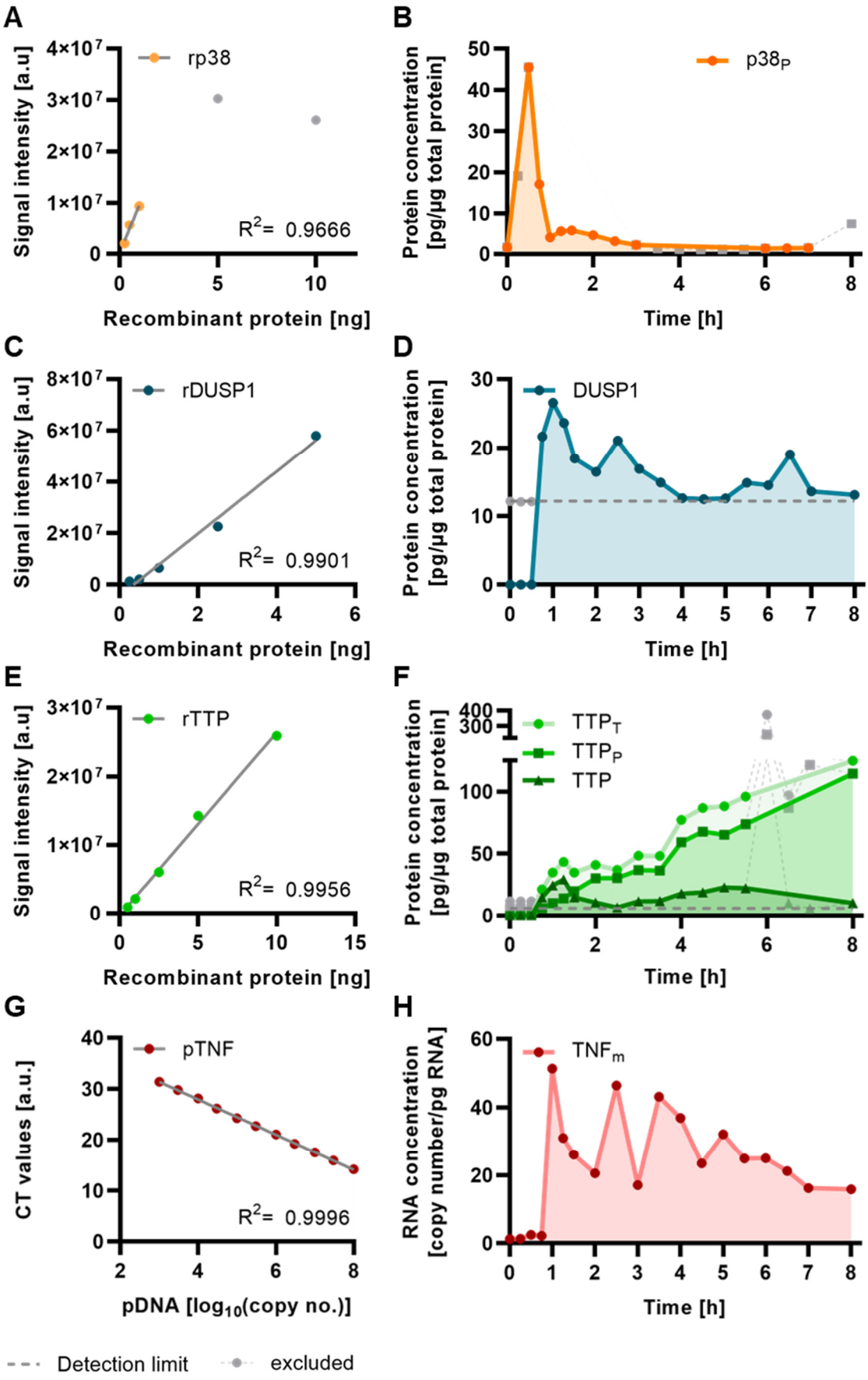

A
Signal intensity [a.u]
rp38
R²= 0.9666
Recombinant protein [ng]
B
Protein concentration [pg/µg total protein]
p38P
Time [h]
C
Signal intensity [a.u]
rDUSP1
R²= 0.9901
Recombinant protein [ng]
D
Protein concentration [pg/µg total protein]
DUSP1
Time [h]
E
Signal intensity [a.u]
rTTP
R²= 0.9956
Recombinant protein [ng]
F
Protein concentration [pg/µg total protein]
TTPT
TTPP
TTP
Time [h]
G
CT values [a.u.]
pTNF
R²= 0.9996
pDNA [log10(copy no.)]
H
RNA concentration [copy number/pg RNA]
TNFm
Time [h]
Detection limit
excluded

Figure 7.28 RAW264.7 Experiment 2: Standard curves and total quantification of Western blot and qPCR data obtained from RAW264.7 cells treated with LPS over an 8 h time-course measuring p38 MAPK-TTP pathway components.

RAW264.7 cells were treated with 10 ng/mL LPS for a period of 8 h. Protein concentration of Phospho-p38 (p38P), total p38 (p38T), DUSP1 and TTP, as well as *Tnf* mRNA levels, were measured using WB and qPCR, respectively. The Western blot data was quantified in Image Lab software, normalised to its Stain-Free signal and the total protein concentration of B) p38 total ($p38_T$) and phospho-p38 ($p38_P$, orange), D) DUSP1 (blue), F) total (TTP_T) unphosphorylated (TTP, lower band) and phosphorylated (TTP_P, upper band) TTP (green) was calculated using the relevant standard curves in A), C), and E). The total amount of *Tnf* mRNA (red), shown in H), was identified by running a standard curve, displayed in G), consisting of known quantities of plasmid DNA alongside the samples for qPCR. Excluded values are shown in light grey symbols with a thin dotted line indicating the change in interpolation. If relevant, the detection limit was indicated by a thick grey dotted line.

7.3.4.3 Experiment 3

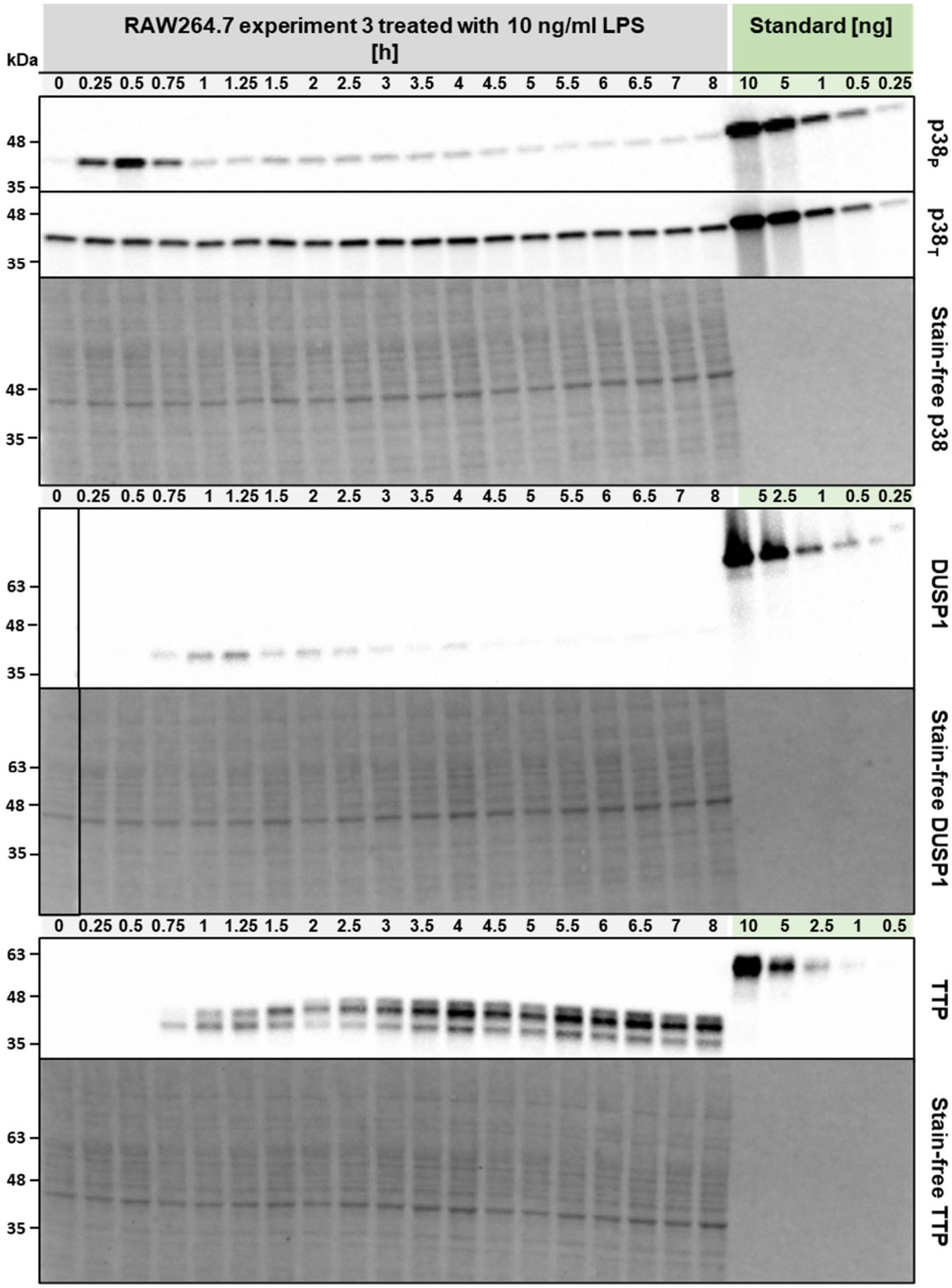


Figure 7.29 RAW264.7 Experiment 3: Total quantification Western blot data of RAW264.7 cells treated with LPS over an 8 h time-course measuring p38 MAPK-TTP pathway components.

RAW264.7 cells were treated with 10 ng/mL LPS for a period of 8 h. Protein concentration of phospho-p38 ($p38_P$), total p38 ($p38_T$), DUSP1 and TTP were measured on individual blots together with recombinant protein standard curve using WB. For TTP, two distinct exposure times, 12.6 sec (TTPa) and 180 sec (TTPb), are shown to increase resolution of early time points. Shown are measurements of chemiluminescence for each protein as well as their respective Stain-Free blots. The protein size is indicated by relevant marks of the protein ladder in kDa.

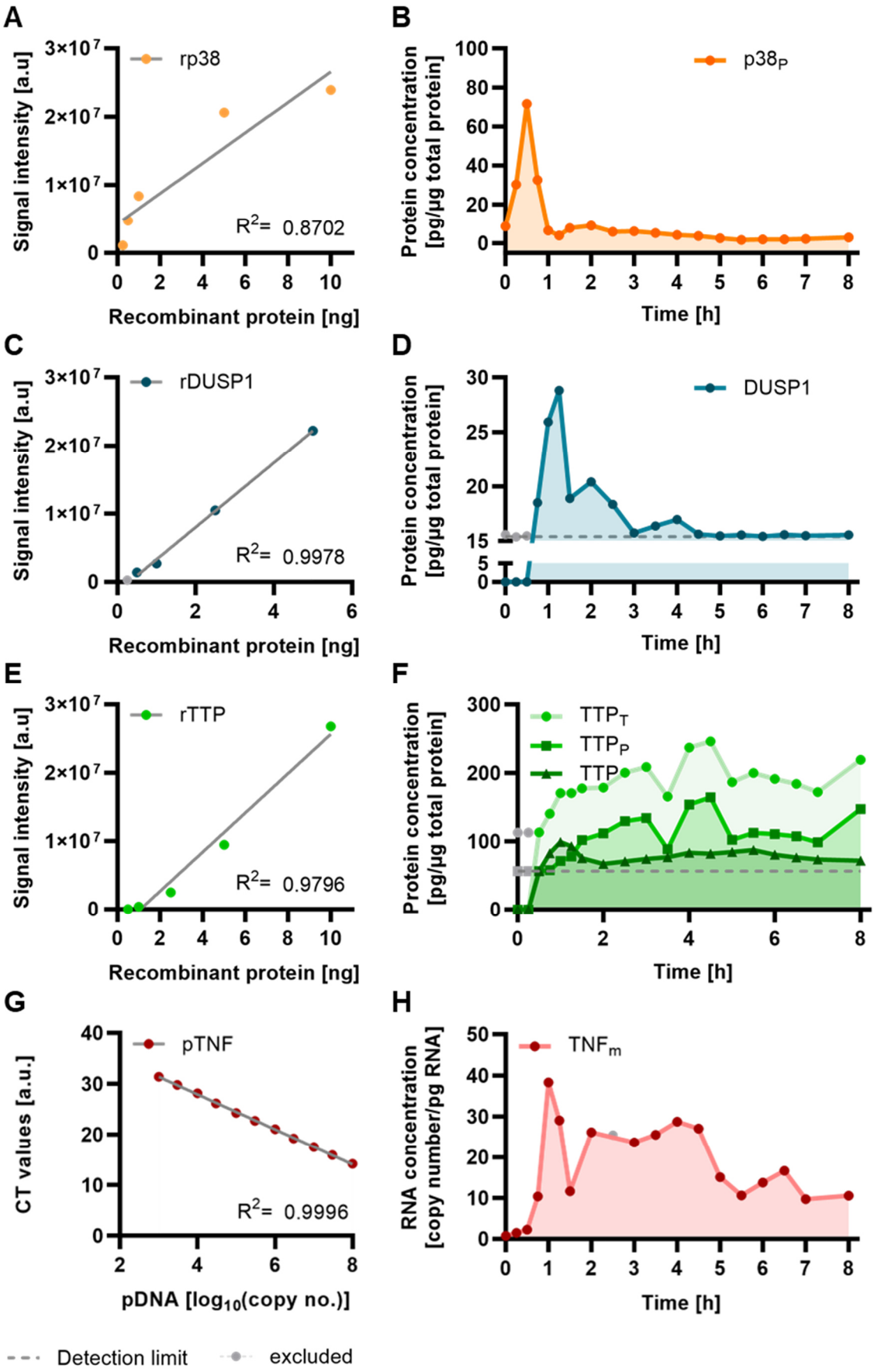

A
Signal intensity [a.u]
rp38
R²= 0.8702
Recombinant protein [ng]
B
Protein concentration [pg/µg total protein]
p38P
Time [h]
C
Signal intensity [a.u]
rDUSP1
R²= 0.9978
Recombinant protein [ng]
D
Protein concentration [pg/µg total protein]
DUSP1
Time [h]
E
Signal intensity [a.u]
rTTP
R²= 0.9796
Recombinant protein [ng]
F
Protein concentration [pg/µg total protein]
TTPT
TTPP
TTP
Time [h]
G
CT values [a.u.]
pTNF
R²= 0.9996
pDNA [log10(copy no.)]
H
RNA concentration [copy number/pg RNA]
TNFm
Time [h]
Detection limit
excluded

Figure 7.30 RAW264.7 Experiment 3: Standard curves and total quantification of Western blot and qPCR data obtained from RAW264.7 cells treated with LPS over an 8 h time-course measuring p38 MAPK-TTP pathway components.

RAW264.7 cells were treated with 10 ng/mL LPS for a period of 8 h. Protein concentration of phospho-p38 (p38P), total p38 (p38T), DUSP1 and TTP, as well as *Tnf* mRNA levels, were measured using WB and qPCR, respectively. The Western blot data was quantified in Image Lab software, normalised to its Stain-Free signal and the total protein concentration of B) p38 total ($p38_T$) and phospho-p38 ($p38_P$, orange), D) DUSP1 (blue), F) total (TTP_T) unphosphorylated (TTP, lower band) and phosphorylated (TTP_P, upper band) TTP (green) was calculated using the relevant standard curves in A), C), and E). The total amount of *Tnf* mRNA (red), shown in H), was identified by running a standard curve, displayed in G), consisting of known quantities of plasmid DNA alongside the samples for qPCR. Excluded values are shown in light grey symbols with a thin dotted line indicating the change in interpolation. If relevant, the detection limit was indicated by a thick grey dotted line.

7.4 Adaption of the Kulawik p38 MAPK-TTP model

In this section, we first summarise our adaptions to the model structure during the model analysis and experimental design. This was necessary for the next step of parameter estimation.

To improve structural identifiability, we removed the saturation rate σ_S, which was originally used by Kulawik et al. to simulate the stimulus concentration-dependent saturation of p38 MAPK phosphorylation. Removing it was possible because we were not evaluating model behaviour at different stimulus concentrations.

We could not measure unphosphorylated p38 MAPK directly. Instead, we aimed to calculate the model input by subtracting phospho-p38 MAPK measurements from total p38 MAPK. Consequently, we did not need to modify the equations for p38 MAPK.

Instead of combining all MKP enzymes, we chose to include and thus measure only DUSP1. If our experiments indicated that DUSP1 alone could not sufficiently mimic p38 MAPK pathway behaviour, we would modify the model components to include MKP enzymes in the future.

Next, we temporarily removed the dependent variable MK2 from the model. By doing so, we aimed to slim down the model and the experimental design for our initial parameter estimation. MK2, according to our understanding, served primarily as an amplifying factor within the model. However, as it is an interesting drug target, we aim to measure MK2 in the future once our experimental data and the parameter estimation are validated. Using optimised experimental design while doing so, would allow us to reduce the required number of samples and Western blot gels for MK2.

For TTP, we assumed that the dynamics of hyperphosphorylation in WB are equivalent to p38 MAPK-dependent phosphorylation. This assumption needs to be validated or dismissed. We

aim to do this in this thesis by comparing model simulation with the experimental data in WT and mutant BMDMs. Therefore, for now, no changes to the equations of the Kulawik p38 MAPK-TTP model were necessary regarding TTP.

We removed the independent variable PP2A to achieve structural identifiability of the model in Chapter 3.2.4.1. For now, we decided to remove it, as it is currently only a symbolic placeholder.

Regarding the TTP-target mRNA, we decided to focus on *Tnf* mRNA, which we measured in the BMDM experiments. Apart from changing the name of the target mRNA to TNF_m, no alterations to the model structure were necessary.

The above modifications resulted in the model diagram in Figure 3.15 and the following set of equations:

$$\frac{dP}{dt} = -P^*\varphi_{P1} - S^*P^*\varphi_{P2} + P_P{}^*\rho_{Pp1} + D^*P_P{}^*\rho_{Pp2}, \quad 3.14$$

$$\frac{dP_P}{dt} = +P^*\varphi_{P1} + S^*P^*\varphi_{P2} - P_P{}^*\rho_{Pp1} - D^*P_P{}^*\rho_{Pp2}, \quad 3.15$$

$$\frac{dD}{dt} = +\gamma_D{}^*P_P{}^*D - \delta_D{}^*D, \quad 3.16$$

$$\frac{dT}{dt} = +\gamma_T{}^*P_P + \rho_{Tp}{}^*T_P - \delta_T{}^*T - \varphi_T{}^*T^*P_P, \quad 3.17$$

$$\frac{dT_P}{dt} = +\varphi_T{}^*T^*P_P - \delta_{Tp}{}^*T_P - \rho_{Tp}{}^*T_P, \quad 3.18$$

$$\frac{dR_m}{dt} = +\gamma_{Rm}{}^*P_P - \delta_{Rm1}{}^*R_m - \delta_{Rm2}{}^*R_m{}^*T, \quad 3.19$$

with the initial conditions $P(0) = P0$, $P_P(0) = P_P0$, $D(0) = D0$, $K(0) = K0$, $K_P(0) = K_P0$, $T(0) = T0$, $T_P(0) = T_P0$, and $R_m(0) = R_m0$. Here '*' represents a multiplication sign, which is introduced for improved readability of the equations.

Following the update of the model structure, we also updated the nominal parameter values. The aim of this last update before the actual parameter estimation was to obtain a parameter set in the same range as our experimental data. We started with the p38 MAPK pathway and then continued with the TTP pathway. The updated parameters and graphs, containing variables and nominal parameters, are shown in Table 7.2, Table 7.1, and Figure 7.31.

For phospho-p38 MAPK, we adjusted the parameters to obtain a peak at the same time and height as in the experimental data. We also adapted the parameters to result in a plateau phase at a similar height. For DUSP1, we aimed for the simulation to follow the peak dynamics and specifically focused on the delayed onset of DUSP1 expression. For TTP, we aimed for the simulation to follow the overall dynamics and height of the data. For the *Tnf* mRNA, we focused on and adapted the timing of the peak and the overall expression height.

Table 7.1 Variables and initial conditions of the Kulawik p38 MAPK-TTP model adapted to LPS-stimulated BMDMs

Variables			
Symbol	**Description**	**Initial condition**	**Dimension**
S	Concentration stimulus LPS	10	$mL^{-1}ng$
P	Concentration of unphosphorylated p38	$P0 = 99.09$	$\mu g^{-1}pg$
P_P	Concentration of phosphorylated p38	$P_P0 = 8.29$	$\mu g^{-1}pg$
D	Concentration of DUSP1	$D0 = 0.001$	$\mu g^{-1}pg$
T	Concentration un-phosphorylated TTP	$T0 = 7.83$	$\mu g^{-1}pg$
T_P	Concentration phosphorylated TTP	$T_P0 = 7.70$	$\mu g^{-1}pg$
R_m	Concentration of *Tnf* mRNA	$R_m0 = 1.95$	$\mu g^{-1}pg$

Table 7.2 Nominal parameter values of the Kulawik p38 MAPK-TTP model adapted to LPS-stimulated BMDMs

Parameters			
Symbol	**Description**	**Nominal value**	**Dimension**
φ_{P1}	Phosphorylation rate 1 of p38	$0.15*10^{-4}$	min^{-1}
φ_{P2}	Phosphorylation rate 2 of p38	$0.1*10^{-2}$	$ng^{-1}min^{-1}mL$
ρ_{Pp1}	Dephosphorylation rate 1 of $p38_P$	$0.1*10^{-4}$	min^{-1}
ρ_{Pp2}	Dephosphorylation rate 2 of $p38_P$	$0.3*10^{-3}$	$pg^{-1}min^{-1}\mu g$
γ_D	Synthesis rate of DUSP1	$0.3*10^{-2}$	$pg^{-1}min^{-1}\mu g$
δ_D	Degradation rate of DUSP1	$0.1*10^{-4}$	min^{-1}
γ_T	Synthesis rate of TTP	$0.2*10^{-2}$	$pg^{-1}min^{-1}\mu g$
δ_T	Degradation rate of TTP	$0.2*10^{-2}$	min^{-1}
φ_T	Phosphorylation rate of TTP	$0.3*10^{-3}$	$pg^{-1}min^{-1}\mu g$
δ_{Tp}	Degradation rate of TTP_P	$0.1*10^{-5}$	min^{-1}
ρ_{Tp}	Dephosphorylation rate of TTP_P	$0.2*10^{-2}$	min^{-1}
γ_{Rm}	Synthesis rate of TNF_m	$0.4*10^{-2}$	$pg^{-1}min^{-1}\mu g$
δ_{Rm1}	Degradation rate 1 TNF_m	$0.1*10^{-4}$	min^{-1}
δ_{Rm2}	Degradation rate 2 TNF_m	$0.2*10^{-3}$	$pg^{-1}min^{-1}\mu g$

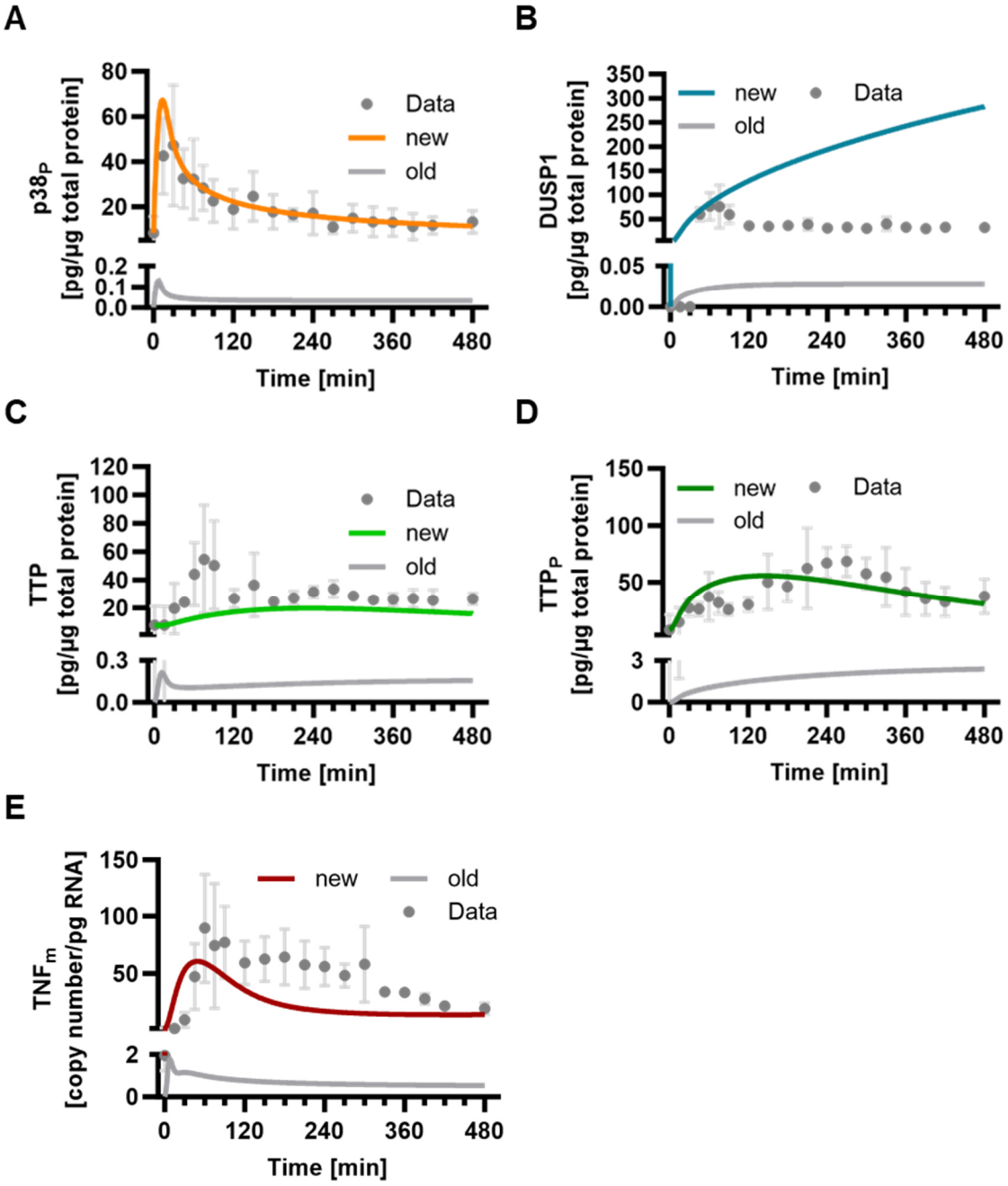


Figure 7.31 Computational simulation of the Kulawik p38 MAPK-TTP model comparing two sets of nominal parameters.

The data for the "old" simulation of the Kulawik p38 MAPK-TTP model was generated in MATLAB solving the ODE equations presented in Chapter 3.2.3.3 as well as nominal parameter values and initial conditions in Table 3.10 and Table 3.8 for a time span of 480 min. For the "new" simulation nominal parameter values (Table 7.2) updated to fit the LPS-stimulated BMDM data presented in Figure 3.13, initial values in Table 7.1, equations (3.14) to (3.19), were used. The graphs show the model simulation of A) phosphorylated p38, B) DUSP1, C)

unphosphorylated TTP, D) phosphorylated TTP, and E) *Tnf* mRNA as lines in their respective colours for the adapted nominal parameter values, as grey lines for the original parameter set, together with the BMDM experimental data as symbols with error bars in grey. The full MATLAB script for generating the graphs can be found in Appendix 7.1.

7.5 Parameter estimation results

7.5.1 Example images parameter estimation

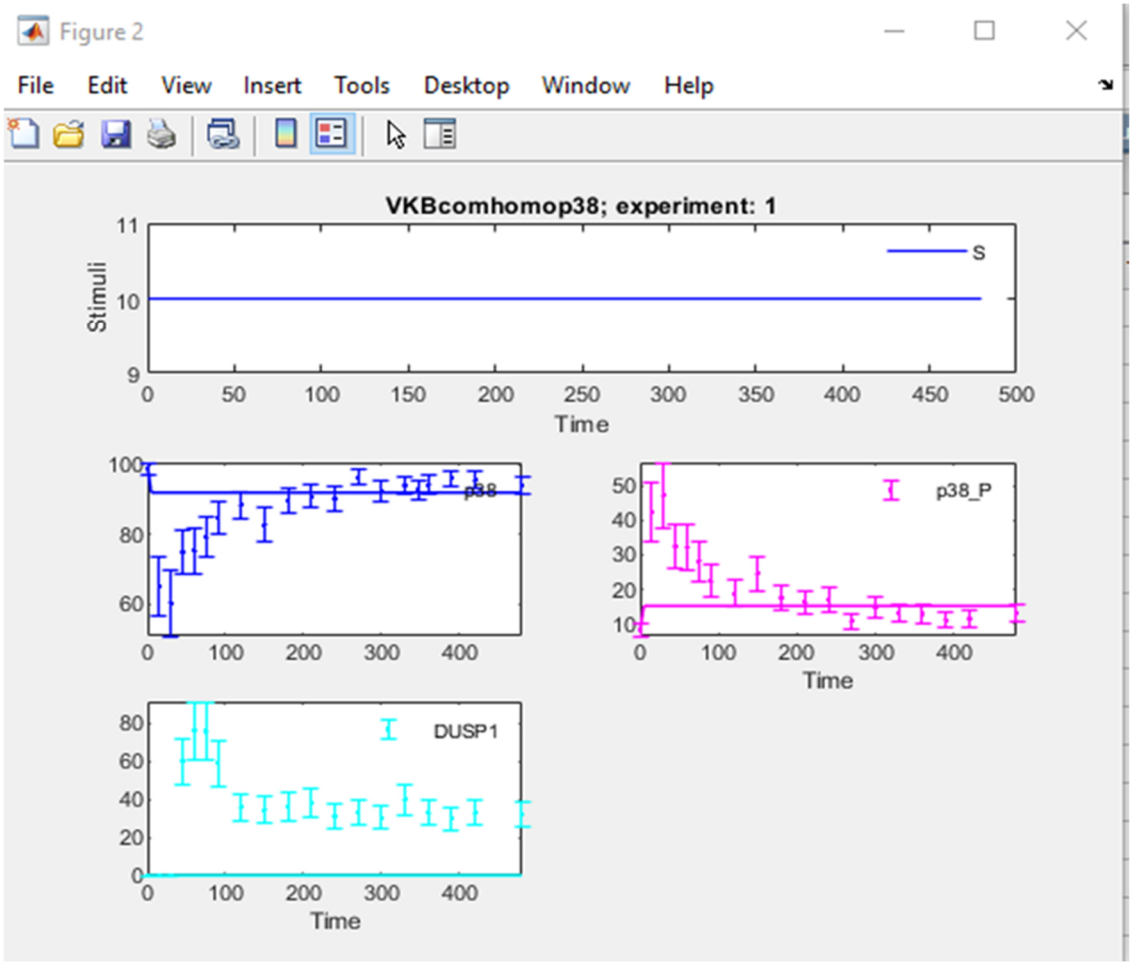


Figure 7.32 Example image of parameter estimation output with a realistic error profile of the p38 MAPK pathway.

The MATLAB graphs show the stimulus profile at the top. The input data as points with error bars and the simulated model as solid lines for p38, phosphorylated p38 and DUSP1 are shown as smaller graphs.

7.5.2 p38 MAPK parameter estimation without DUSP1 data

The global relative MABS of the parameter estimation runs where DUSP1 data was excluded are shown in Table 7.4. Here, the homoscedastic error profile (set to 0.2) with "combined" experimental design and 10 as the upper boundary reached the best result with a relative global MABS of residuals of 12.47%. This and the estimated parameter set itself and its simulation

are shown in Figure 7.33 and Table 7.3. Here, p38 phosphorylation experienced an immediate, almost vertical increase followed by an asymptotic decrease towards the plateau. Qualitatively, the parameter set could not mirror the exact p38 MAPK phosphorylation dynamics of the peak. However, the dynamics of the plateau phase were well covered. The DUSP1 values increased throughout the time-course, and the expression levels were generally higher compared to the previous parameter estimation where DUSP1 data was included. Comparing the two approaches, the resulting combined MKP expression pattern was more realistic after removing the DUSP1 data from the parameter estimation.

Table 7.3 Parameter set of parameter estimation with best relative global MABS for the Kulawik p38 MAPK module with DUSP1 data excluded

Parameter Estimation				
Symbol	**Description**	**PE value**	**Conf. interval**	**Dimension**
φ_{P1}	Phosphorylation rate 1 of p38	$9.43*10^{-1}$	$1.12*10^{+7}$	min^{-1}
φ_{P2}	Phosphorylation rate 2 of p38	$3.01*10^{-1}$	$1.12*10^{+6}$	$ng^{-1}min^{-1}mL$
ρ_{Pp1}	Dephosphorylation rate 1 of $p38_P$	$1.00*10^{+1}$	$2.24*10^{+3}$	min^{-1}
ρ_{Pp2}	Dephosphorylation rate 2 of $p38_P$	$4.13*10^{-1}$	0.00	$pg^{-1}min^{-1}\mu g$
γ_D	Synthesis rate of DUSP1	$1.21*10^{-3}$	0.00	$pg^{-1}min^{-1}\mu g$
δ_D	Degradation rate of DUSP1	0.00	$1.70*10^{-5}$	min^{-1}

Table 7.4 Global relative MABS ranking of p38 MAPK parameter estimation runs without DUSP1 data

Global relative MABS ranking of parameter estimation runs							
Short	**p38**		**p38-P**		**DUSP1**		**Global**
	Mean	Max	Mean	Max	Mean	Max	Mean
PCHo	6.80	14.41	18.3	35.80	-	-	12.47
PIHo	10.20	64.33	36.56	170.61	-	-	23.38

PCHe	5.11	21.42	52.43	67.27	-	-	28.77
PIHe	10.78	79.12	48.66	170.61	-	-	29.72

P=p38, C=combined experiments, I=individual experiments, Ho=homoscedastic error profile 0.2, He=heteroscedastic error profile.

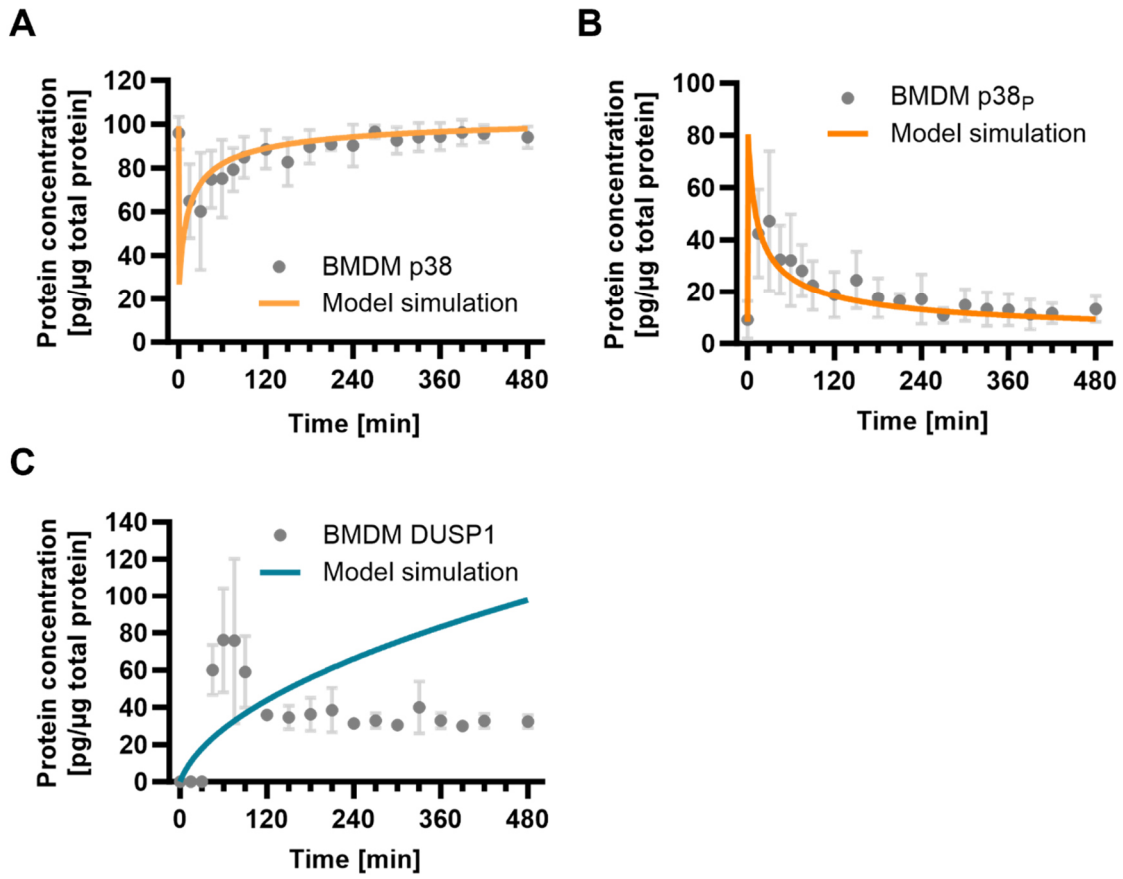


Figure 7.33 Computational simulation of the upstream p38 MAPK section of the Kulawik p38 MAPK-TTP model using an estimated parameter set with the best MABS score for LPS-treated BMDMs with DUSP1 data excluded from the parameter estimation process.

The data for the simulation of the Kulawik p38 MAPK-TTP model was generated in MATLAB, solving the ODE equations (3.14) to (3.19) as well as the estimated parameter values and initial conditions in Table 7.3 and Table 7.1 for a time span of 480 min. The parameters were estimated using the NLSQ2 combined with the eSS2 nonlinear problem solver implemented in the AMIGO2 toolbox and the experimental data of unphosphorylated and phosphorylated p38 from the LPS-stimulated BMDMs presented in Figure 3.13. The values for unphosphorylated p38 were calculated by subtracting the $p38_P$ measurements from the mean total p38 measurements. In addition, a homoscedastic error profile set to 0.2, the "combined" experiment design, and parameter boundaries between 0 and 10 were selected for the parameter estimation run. The graphs show the model simulation of A)

unphosphorylated p38, B) phosphorylated p38, and C) DUSP1 as lines in their respective colours together with the BMDM experimental data as symbols with error bars in grey. The full MATLAB script for parameter estimation and generation of the graphs can be found in Appendix 7.1.

For the parameter set without DUSP1 input data (Table 7.5), the parameter estimation did not achieve a good fit for the TTP pathway data (Figure 7.34). Although the strong peak profile fits the p38 MAPK data very well, this stimulus profile did not allow for the simulation of TTP and *Tnf* mRNA in a way that matches the data. Due to these problems with the parameter set obtained from the parameter estimation without DUSP1 data, we decided to only proceed with the DUSP1 data including parameter set.

Table 7.5 Parameter set of parameter estimation for the Kulawik p38 MAPK-TTP model with fixed p38 MAPK parameters and DUSP1 data excluded

Parameter Estimation				
Symbol	**Description**	**PE value**	**Conf. interval**	**Dimension**
γ_T	Synthesis rate of TTP	$5.92*10^{-2}$	$8.41*10^{-3}$	$pg^{-1}min^{-1}\mu g$
δ_T	Degradation rate of TTP	$7.74*10^{-3}$	$1.15*10^{-3}$	min^{-1}
φ_T	Phosphorylation rate of TTP	$4.63*10^{-2}$	$5.41*10^{-5}$	$pg^{-1}min^{-1}\mu g$
δ_{Tp}	Degradation rate of TTP_P	$3.42*10^{-2}$	$1.62*10^{-4}$	min^{-1}
ρ_{Tp}	Dephosphorylation rate of TTP_P	$1.00*10^{+1}$	$6.71*10^{+2}$	min^{-1}
γ_{Rm}	Synthesis rate of TNF_m	$1.00*10^{+1}$	$3.92*10^{+2}$	$pg^{-1}min^{-1}\mu g$
δ_{Rm1}	Degradation rate 1 TNF_m	$7.51*10^{-9}$	$1.86*10^{-2}$	min^{-1}
δ_{Rm2}	Degradation rate 2 TNF_m	$1.44*10^{-2}$	$5.68*10^{-2}$	$pg^{-1}min^{-1}\mu g$

PE=Parameter estimation.

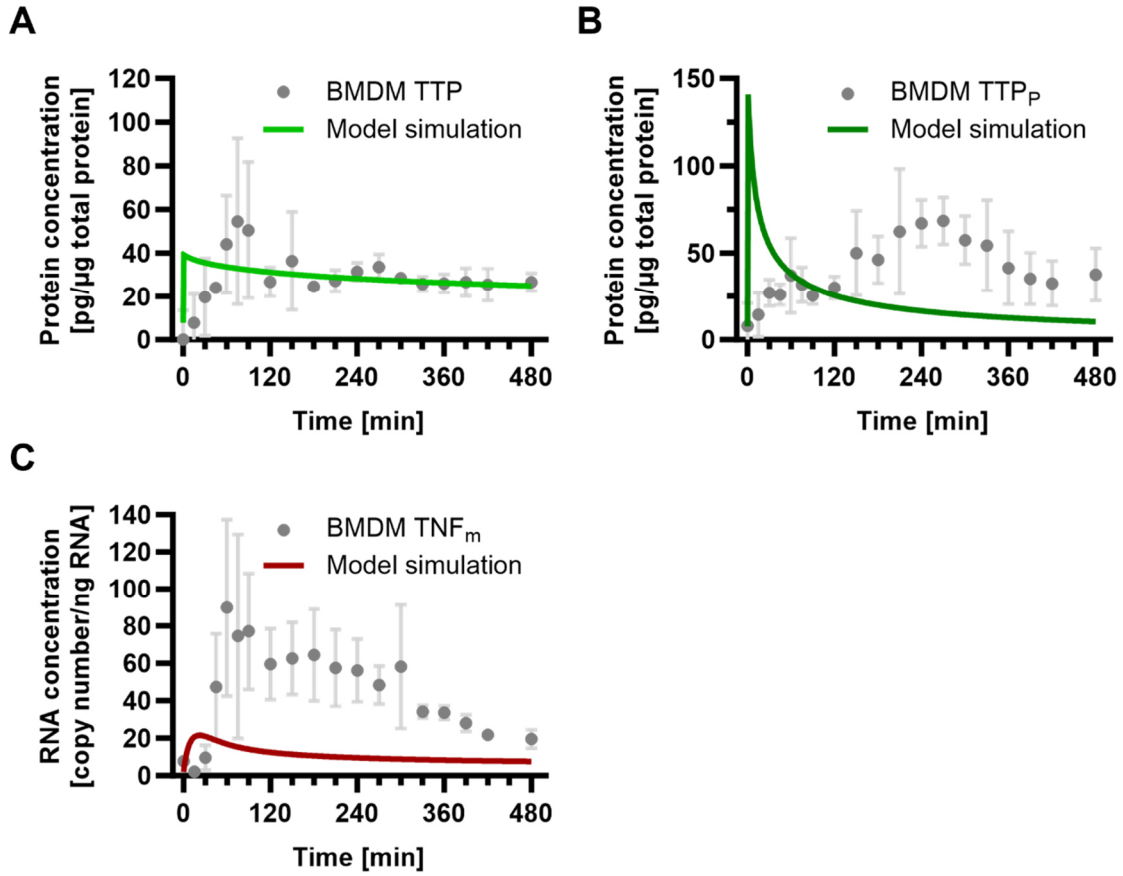


Figure 7.34 Computational simulation of the of the downstream TTP section of the Kulawik p38 MAPK-TTP model using an estimated parameter set with the best MABS score for LPS-treated BMDMs with DUSP1 data excluded from the parameter estimation process.

The data for the simulation of the Kulawik p38 MAPK-TTP model was generated in MATLAB, solving the ODE equations presented in Appendix 7.4 as well as the estimated parameter values and initial conditions in Table 7.5 and Table 7.1 for a time span of 480 min. The parameters were estimated using the NLSQ2 combined with the eSS2 nonlinear problem solver implemented in the AMIGO2 toolbox, and the experimental data of unphosphorylated and phosphorylated TTP and *Tnf* mRNA from the LPS-stimulated BMDMs presented in Figure 3.13. In addition, a homoscedastic error profile set to 0.2, the "combined" experiment design, and parameter boundaries between 0 and 10 were selected for the parameter estimation run. The graphs show the model simulation of A) unphosphorylated TTP, B) phosphorylated TTP, and C) *Tnf* mRNA as lines in their respective colours together with the BMDM experimental data as symbols with error bars in grey. The full MATLAB script for parameter estimation and generation of the graphs can be found in Appendix 7.1.

7.6 Cloning Results – Agarose Gels

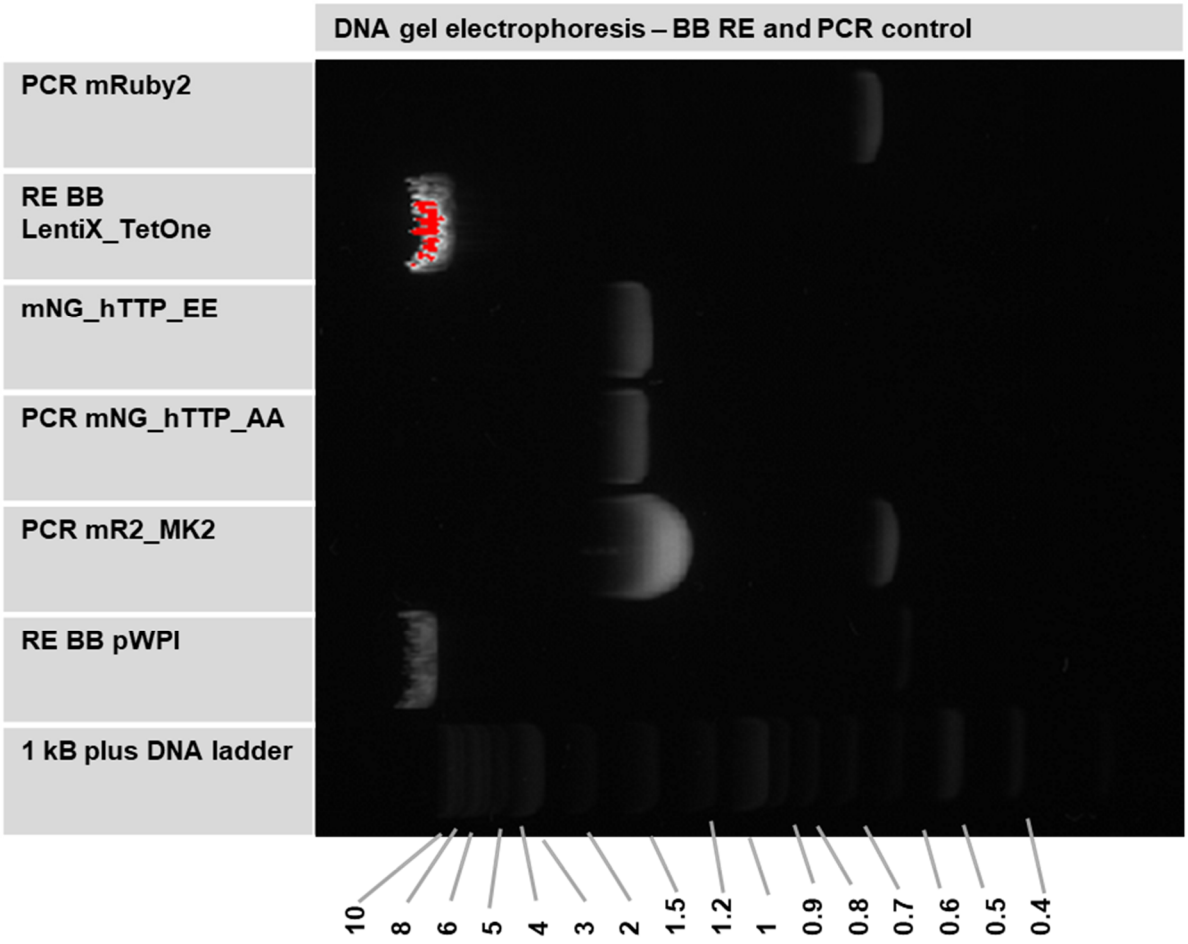
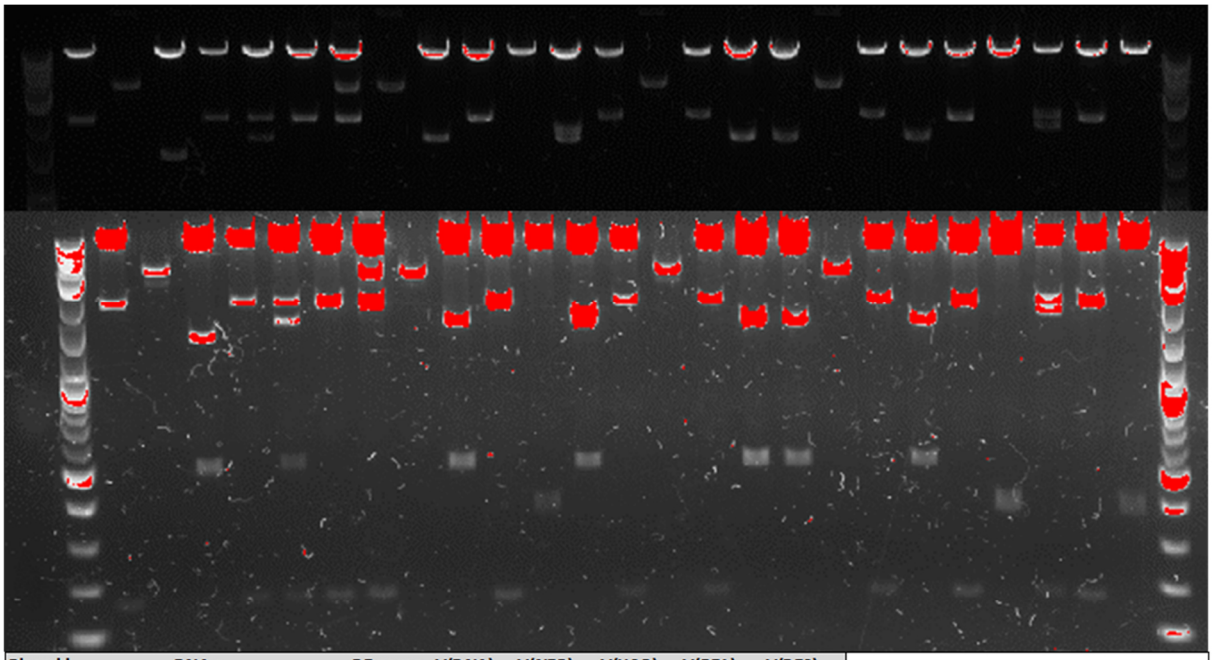


Figure 7.35 Control DNA gel electrophoresis verifying the correct RE digest of pLentiX_TetOne_Puro and PCR amplifications of the inserts mNeonGreen_hTTP_AA and mNeonGreen_hTTP_EE.

For the blunt end cloning of the mNeonGreen-tagged proteins, hTTP_AA and hTTP_EE were amplified via PCR, and the backbone pLentiX_TetOne_Puro linearised using the RE BstZ17I-HF. This work step was controlled by DNA gel electrophoresis. The gel shows the labelled 1 kB plus DNA ladder, the RE digest of pLentiX_TetOne_Puro (9.18 kB), and mNeonGreen_hTTP_AA/EE (1.69 kB). Other samples were run alongside, including the PCR product of mRuby2, mRuby2_MK2, and RE digest of pWPI-IRES-Bla-Ak.



Plasmid	DNA c (µg/µL)	RE name	V(DNA) 500 ng	V(NEB) 2 µL	V(H2O) to 20 µl	V(RE1)	V(RE2)	200	500/400	2000	weird
A1		302.10 BamHI/Xh	1.66	2	13.34	1.5	1.5	+	-	+	-
A2		302.10 BamHI/Xh	1.66	2	13.34	1.5	1.5	-	-	-	+
A3		302.10 BamHI/Xh	1.66	2	13.34	1.5	1.5	-	+	-	-
A4		302.10 BamHI/Xh	1.66	2	13.34	1.5	1.5	+	-	+	-
A6		302.10 BamHI/Xh	1.66	2	13.34	1.5	1.5	+	+	+	+
A6*		302.10 BamHI/Xh	1.66	2	13.34	1.5	1.5	+	-	+	-
A7		302.10 BamHI/Xh	1.66	2	13.34	1.5	1.5	+	-	+	+
A8		302.10 BamHI/Xh	1.66	2	13.34	1.5	1.5	-	-	-	+
A9		302.10 BamHI/Xh	1.66	2	13.34	1.5	1.5	-	+	-	-
A10		302.10 BamHI/Xh	1.66	2	13.34	1.5	1.5	+	-	+	-
A11		302.10 BamHI/Xh	1.66	2	13.34	1.5	1.5	-	+	-	-
A12		302.10 BamHI/Xh	1.66	2	13.34	1.5	1.5	-	+	+	+
E1		302.10 BamHI/Xh	1.66	2	13.34	1.5	1.5	+	-	+	-
E2		302.10 BamHI/Xh	1.66	2	13.34	1.5	1.5	-	-	-	+
E3		302.10 BamHI/Xh	1.66	2	13.34	1.5	1.5	+	-	+	-
E8		302.10 BamHI/Xh	1.66	2	13.34	1.5	1.5	-	+	-	-
E9		302.10 BamHI/Xh	1.66	2	13.34	1.5	1.5	-	+	-	-
E10		302.10 BamHI/Xh	1.66	2	13.34	1.5	1.5	-	-	-	+
E11		302.10 BamHI/Xh	1.66	2	13.34	1.5	1.5	+	-	+	-
E12		302.10 BamHI/Xh	1.66	2	13.34	1.5	1.5	-	+	-	-
E13		302.10 BamHI/Xh	1.66	2	13.34	1.5	1.5	+	-	+	-
E14		302.10 BamHI/Xh	1.66	2	13.34	1.5	1.5	-	+	-	-
E15		302.10 BamHI/Xh	1.66	2	13.34	1.5	1.5	+	-	+	+
E16		302.10 BamHI/Xh	1.66	2	13.34	1.5	1.5	+	-	+	-
TeOne	1:10 dil	1728.3 BamHI/Xh	0.29	2	16.21	1.5	1.5	-	+	-	-

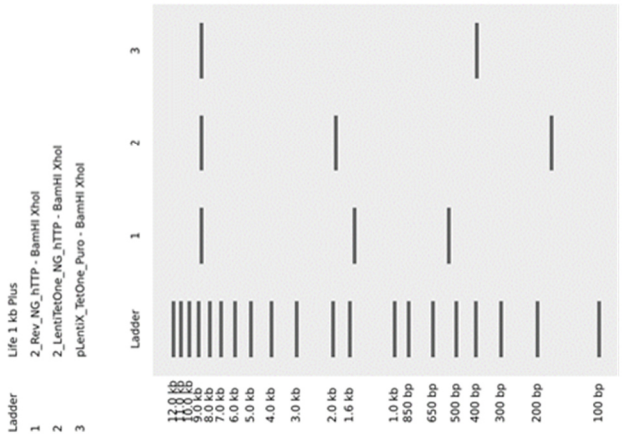


Figure 7.36 Diagnostic RE digests of the newly generated constructs pLentiTetOne_mNG_hTTP_AA/EE to identify bacterial colonies with the correct insert orientation following blunt-end cloning.

The TTP reporter plasmids pLentiTetOne_mNG_hTTP_AA/EE were generated using blunt-end cloning, transformed into NEB-Stable competent bacteria, and grown on selective agar plates. The grown colonies were picked and grown in a selective LB medium overnight, and the DNA was isolated via Miniprep. The isolated DNA was then digested with the REs BamHI and XhoI to create a specific pattern to identify the correct insert orientation. The virtual digests were performed on the online cloning platform Benchling and showed the expected patterns for a BB re-ligation, a correct, and a reverse insertion of the amplified insert (bottom). The diagnostic digests of the colonies A1 to A12 and E1 to E16 of the insert mNeonGrenn_hTTP_AA/EE is shown. An excerpt from the analysis sheet is shown highlighting the correctly inserted inserts (green). The correct insertion was confirmed afterwards by Sanger sequencing.

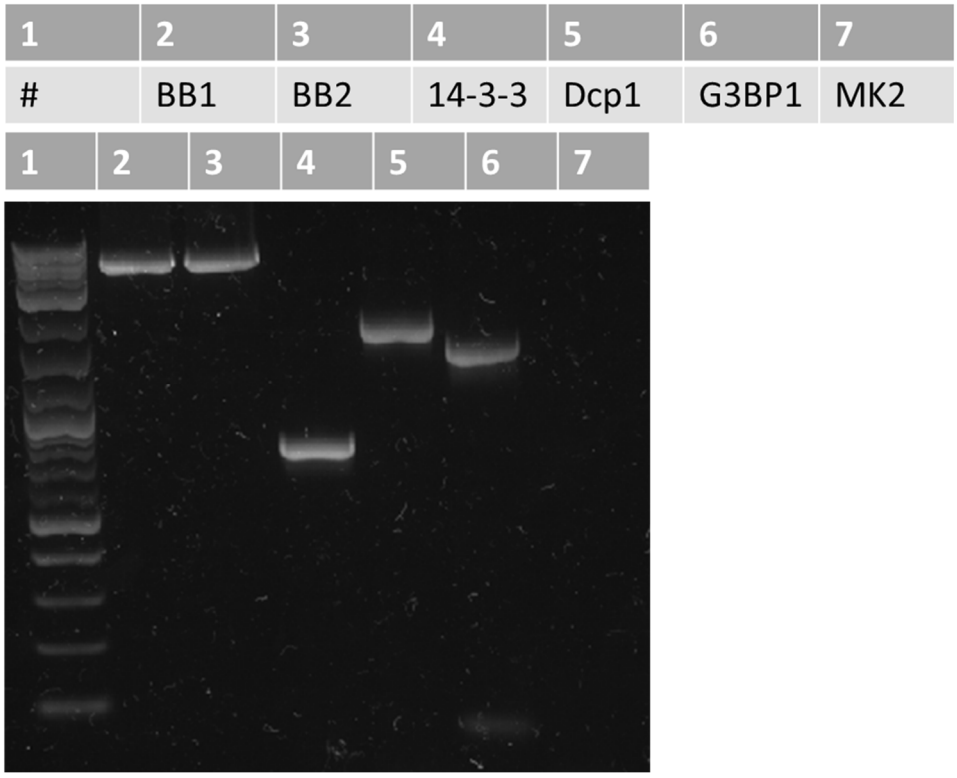


Figure 7.37 Control DNA gel electrophoresis verifying the correct PCR amplification of the BB pmNeonGreen-mRuby2-FRET-10 and the inserts 14-3-3, DCP1a, GRBP1, and MK2 for Gibson assembly.

For Gibson assembly, the pmNeonGreen-mRuby2-FRET-10 with the inserts DCP1a, G3BP1, 14-3-3b, and MK2 were amplified via PCR. This work step was controlled by DNA gel electrophoresis. The gel shows the labelled 1 kB plus DNA ladder and the PCR product of pmNeonGreen-mRuby2-FRET-10 (4.65 kB), DCP1a (1.75 kB), G3BP1 (1.4 kB), 14-3-3b (0.74 kB) and MK2 (1.2 kB).

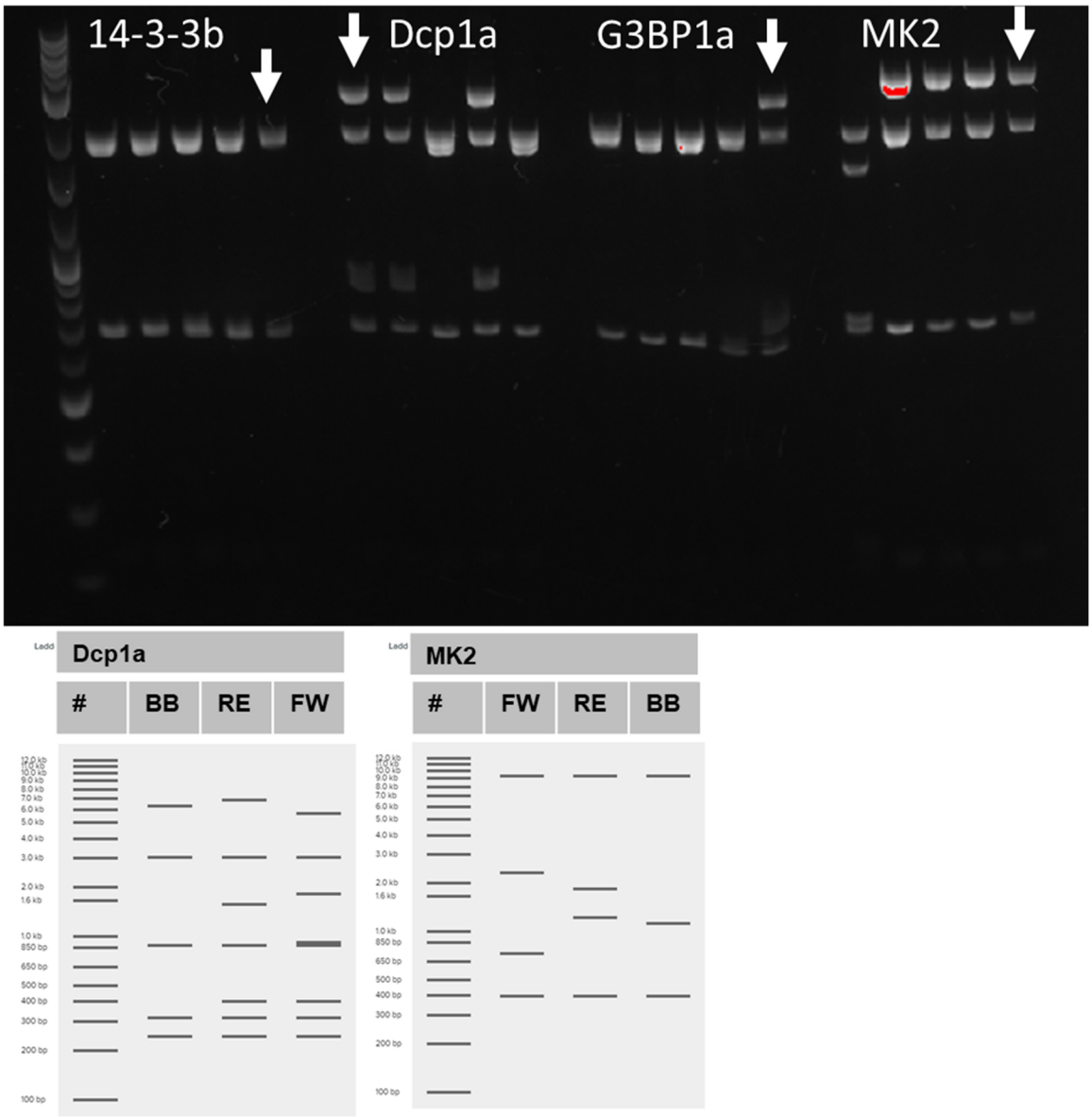


Figure 7.38 Diagnostic RE digests of the newly generated construct pWPI_mRuby2_DCP1a/MK2 to identify bacterial colonies with the correct insert orientation following blunt-end cloning.

The reporter plasmids pWPI_mRuby2_DCP1a/MK2 were generated using blunt-end cloning, transformed into NEB-Stable competent bacteria, and grown on selective agar plates. The grown colonies were picked and grown in a selective LB medium overnight, and the DNA was isolated as Miniprep. The isolated DNA was then digested with the RE NcoI/XbaI (DCP1a) and XhoI (MK2) to create a specific pattern to identify the correct insert orientation. The virtual digests were performed on the online cloning platform Benchling and showed the expected patterns for a BB re-ligation, a correct (FW), and a reverse insertion (RE) of the amplified insert. The diagnostic digests of the colonies in shown at the top. The RE digest of the constructs pWPI_mRuby2_G3BP1/14-3-3 were run on the same gel. Arrows indicate correct insertion of the insert. A correct insertions was confirmed afterwards by Sanger sequencing.

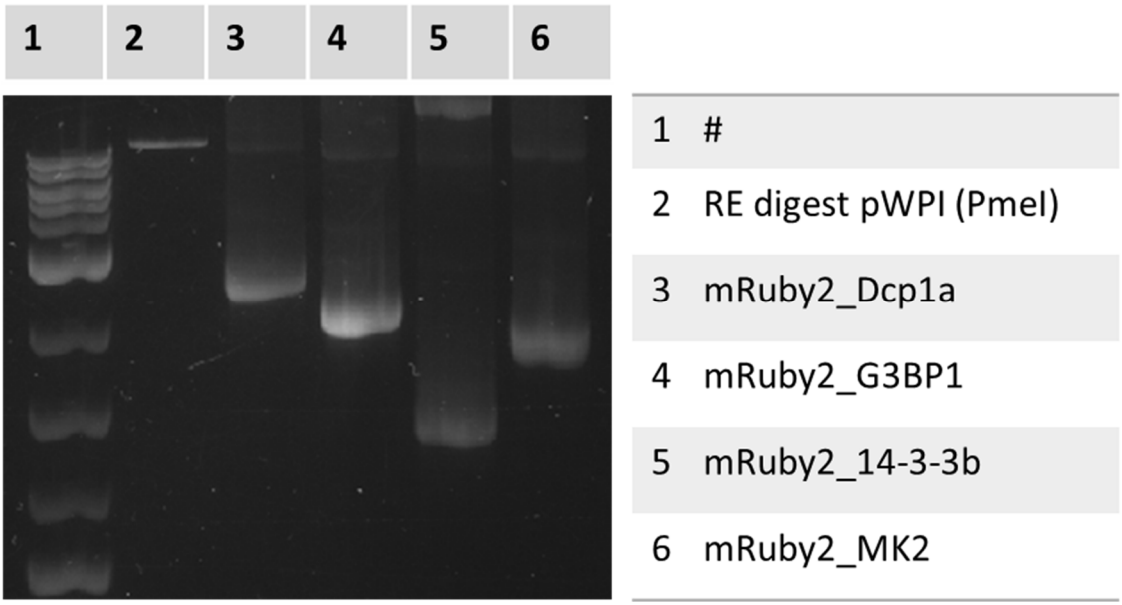


Figure 7.39 Control DNA gel electrophoresis verifying the correct RE digest of pWPI-IRES-Bla-Ak and PCR amplifications of the inserts R2_DCP1a, R2_G3BP1, R2_14-3-3b, and R2_MK2 for blunt end ligation.

For the blunt end cloning of the mRuby2-tagged proteins, DCP1a, G3BP1, 14-3-3b, and MK2 were amplified via PCR and the backbone pWPI-IRES-Bla-Ak linearised using the RE PmeI. This work step was controlled by DNA gel electrophoresis. The gel shows the labelled 1 kB plus DNA ladder, the RE digest of pWPI-IRES-Bla-Ak (10.8 kB), and the PCR product of R2_DCP1a (2.48 kB), R2_G3BP1 (2.18), R2_14-3-3b (1.46 kB) and R2_MK2 (1.92 kB). Apart from the expected band, an off-target amplification at 0.4 kB was detected, which did not affect downstream applications.

7.7 Full plasmid sequences and plasmid maps

Plasmid maps are available at UBIRA eData repository (https://edata.bham.ac.uk/) (Supplementary data for the thesis "An interdisciplinary approach to understanding the TTP pathway" by Victoria Veronika Rink) under the name: “PlasmidMaps”.

7.8 Microscopy

The video showing TTP translocation between nucleus and cytoplasm in HeLa cells is available at UBIRA eData repository (https://edata.bham.ac.uk/) (Supplementary data for the thesis "An interdisciplinary approach to understanding the TTP pathway" by Victoria Veronika Rink) under the name: “HeLaTTPshuttling”.

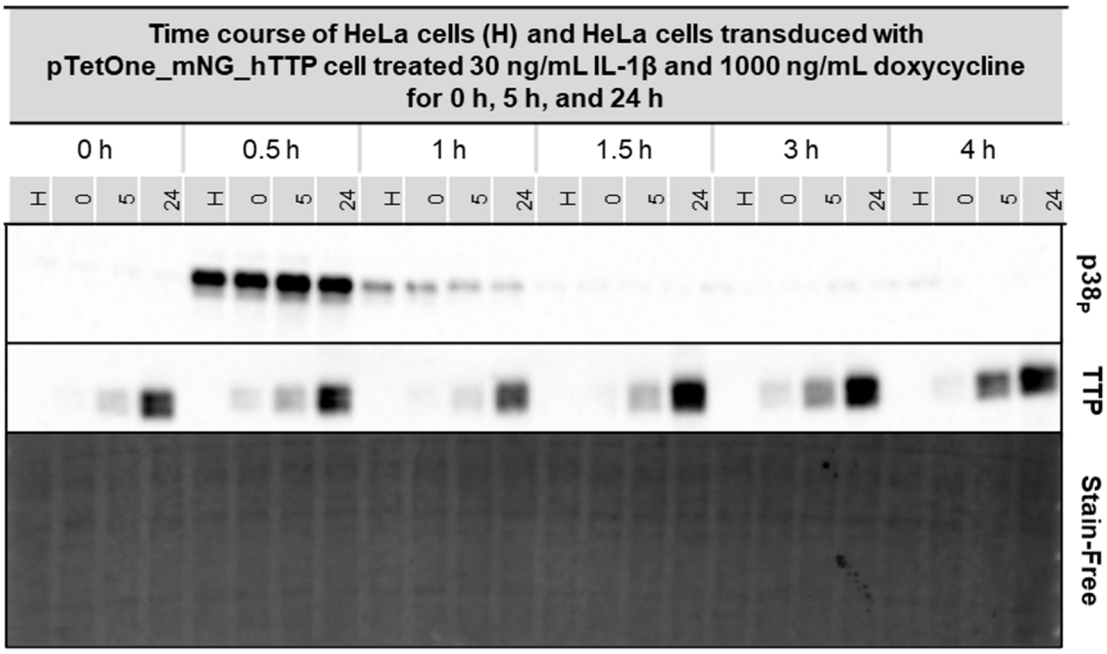


Figure 7.40 Example for p38 MAPK activation by 30 ng/mL IL-1β.

TetOne_hTTP_WT HeLa cells were treated with 1000 ng/mL Doxycycline for 0 h, 5 h, and 24 h. Then, the cells were stimulated with 30 ng/mL IL-1β over a period of 4h. The lysates of the cells at 6 different time points were harvested, and the phospho-p38 and TTP protein concentration was measured by Western Blotting. For normalisation, total protein measurements were obtained through the Stain-Free signal of the blot. This image shows the successful stimulation of p38 MAPK phosphorylation in HeLa cells using a 30 ng/mL concentration.

7.9 Image analysis

Image analysis scripts are available at UBIRA eData repository (https://edata.bham.ac.uk/) (Supplementary data for the thesis "An interdisciplinary approach to understanding the TTP pathway" by Victoria Veronika Rink) under the names: “Dcp1aTTPanalysis” and “MK2TTPanalysis”.